Synthesis of Organic-Inorganic Nanocomposite Materials and Their Various Applications

A Thesis Submitted for the Award of the Degree of

Doctor of Philosophy in Science

By

SUNANDA PAL

Ph.D. Registration No. SCHEM1510019

Date of Registration: 17th September, 2019

Department of Chemistry

Inorganic Chemistry Section, Department of Chemistry

Jadavpur University, Kolkata-700032, India

September, 2024

Dr. Bibhuti Bhushan Show
Associate Proffessor
Department of Chemistry

JADAVPUR UNIVERSITY
KOLKATA – 700 032, INDIA
Email: bibhutishow1978@gmail.com
bibhutib.show@jadavpuruniversity.in
Mobile: +919477222456/9836210392

CERTIFICATE FROM THE SUPERVISOR

This is to certify that the thesis titled **"Synthesis of Organic-Inorganic Nanocomposite Materials and Their Various Applications"** submitted by **Sunanda Pal** ***(Index No.: 100/19/Chem./26)*** who got her name registered on 17.09.2019 for the award of Ph. D. (Science) Degree of Jadavpur University, is absolutely based upon his own work under the supervision of **Dr. Bibhuti Bhushan Show** and that neither this thesis nor any part of it has been submitted for either any degree/diploma or any other academic award anywhere before.

Bibhuti Bhushan Show
Dt. 24th September, 2024.

Dr. Bibhuti Bhushan Show
Associate Professor,
Inorganic Chemistry Section
Department of Chemistry
Jadavpur University,
Kolkata, India

Dr. Bibhuti Bhushan Show
Associate Professor
Inorganic Chemistry Section, Dept. of Chemi
Jadavpur University
Kolkata - 700032, W.B. India

Declaration

*I hereby declare that the thesis entitled "**Synthesis of Organic-Inorganic Nanocomposite Materials and Their Various Applications**" submitted for the degree of Doctor of Philosophy (Science) of Jadavpur University is based on the original work done by me under the guidance of Dr. Bibhuti Bhushan Show, Associate Professor, Department of Chemistry, Jadavpur University, Kolkata-700 032, and this work has not been included in any other thesis submitted previously for the award of any other degree.*

Sunanda Pal
Index No.: 100/19/Chem./26
Department of Chemistry
Jadavpur University
Kolkata, India

Dedicated

to

My Parents

Late Dhruba Paul

Smt. Bina Paul

Acknowledgement

At first, I wish to convey my deepest gratitude and utmost respect to my Ph.D. supervisor, Dr. Bibhuti Bhushan Show. His invaluable guidance, unwavering encouragement, and profound intellectual support throughout my research have been indispensable. Without his trust and continuous support, the successful completion of this work would not have been possible.

I would like to extend my heartfelt thanks to Prof. Kajal Krishna Rajak, Head of the Department (Chemistry), and express my sincere gratitude to all the esteemed faculty members for their continuous guidance and encouragement.

I am sincerely grateful to the Director and Deans of Jadavpur University, Jadavpur, for providing me the opportunity to pursue my doctoral studies by offering the necessary instrumental facilities and financial support.

I am deeply grateful to all other faculty members of Jadavpur University for their continued support and collaboration. I would like to extend my sincere thanks to all the official staff, whose secretarial assistance ensured the timely submission of various evaluation documents.

I also wish to acknowledge the financial support provided by the RUSA 2.0 grant from the Government of India, which was crucial in upgrading both the software and the electrodes of our electrochemical workstation. Additionally, I express my appreciation to the Inorganic Chemistry Research Fund within the Department of Chemistry at Jadavpur University, Kolkata.

I am profoundly grateful to Professor Bibhutosh Adhikary, IIEST, Shibpur, for his guidance and encouragement throughout this journey, as well as his unwavering support and belief in my ability to complete my research work. I am deeply appreciative of Mr. Abhimanyu Sarkar, Mrs. Purbali Roy, Farhin Sultana, Dr. Papri Mondal, Dr. Jit Satra and Dr. Uday Kumar Ghorui for their invaluable cooperation, guidance, and unwavering support throughout my research. Their friendship and assistance have been truly instrumental in completing this work.

Words cannot fully capture my gratitude towards my family. My parents, the late Dhruba Paul and Mrs. Bina Paul; my brother, Dr. Nanda Dulal Paul, associate Prof. of IIEST, Shibpur; my husband, Mr Uttam Kumar Mal; and my well wisher Smt. Samita Naskar have been a continual source of inspiration and support through every challenge. My two cherished daughters, Tanisa Mal and Tiana Mal, have also played a crucial role with their love, patience, and understanding. The success of this thesis is a testament to their steadfast encouragement, love, and belief in me. This achievement would not have been possible without their presence and support.

Sunanda Pal
Department of Chemistry
Jadavpur University
Kolkata-700032
September, 2024

Preface

This research focuses on synthesizing and evaluating Bi and Cu-based organic-inorganic nanocomposites using solvothermal methods to enhance their electrochemical and photoelectrochemical properties. The study examines surface modifications, embedded defects, and electronic property optimization to improve their potential in energy hervesting and environmental remediation.

Chapter 1 provides an in-depth literature review of recent research and advancements, highlighting the potential of Bi and Cu-based metal oxides, decorated with organic matrices, to meet the increasing demand for energy harvesting and efficient environmental remediation strategies.

Chapter 2 provides an overview of various advanced tools, their fundamental principles, and their applications for synthesizing and characterizing nanocomposites. It includes detailed structural, morphological, optical, and electrochemical analyses to ensure thorough characterization.

Chapter 3 explores the development of a selective electrode using Bi_2MoO_6/H_2TPP nanocomposites for oxygen reduction reaction (ORR) and the electrocatalytic reduction of p-nitrophenol (p-NP). Fabricated on a glassy carbon electrode, this sensor demonstrated significant electrocatalytic performance with an E_{onset} of 0.942 V and an $E_{½}$ of 0.704 V vs. RHE. The electrode exhibited high sensitivity (0.4683 $\mu A\ \mu M^{-1}\ cm^{-2}$) for p-NP detection with a low detection limit of 0.0940 μM and good stability, making it effective for practical applications.

Chapter 4 addresses the environmental and health hazards of hexavalent chromium (Cr^{6+}) and proposes a β-Bi_2O_3-Bi_2WO_6/H_2TPP nanocomposite for selective electrocatalytic and photoelectrocatalytic Cr^{6+} reduction. This hybrid material demonstrated remarkable sensitivity (8.005 $\mu A\ mM\ cm^{-2}$), low detection limit (8.0 nM), and stability under light irradiation, showing potential for environmental remediation.

Chapter 5 introduces a method for synthesizing $CuWO_4/CuO$ and its rGO blended derivatives for HER and OER, respectively. $CuWO_4$/CuO-rGO showed impressive OER activity with low overpotential (η_{10} = 161 mV) and small Tafel slope (60.82 mV dec^{-1}), while $CuWO_4$/CuO exhibited low overpotential (16 mV) and small Tafel slope (16.33 mV dec^{-1}) for HER. These findings underscore their remarkable performance in water splitting.

This research advances the understanding of organic-inorganic nanocomposites in energy conversion and environmental applications, providing a foundation for future innovations in energy harvesting and environmental remediation strategies.

List of Abbreviation

A	Ampere
ACCN	amine-functionalized crystalline carbon nanodots
BE	Binding Energy
BET	Brunauer-Emmett-Teller
BGE	Band Gap Energy
BQ	p-benzoquinone
BTU	British Thermal Unit
CB	Conduction Band
CTAB	Cetyltrimethylammonium bromide
CA	Chronoamperometry
C_{dl}	Double layer capacitance
CoO/N–MoS_2/CF	cobalt oxide (CoO) decorated on nitrogen-doped MoS_2 supported on carbon fibers
CV	Cyclic Voltammetry
DFT	Density Funtional Theory
DRS	Diffuse reflectance spectroscopy
ECSA	Electrochemical Active Surface Area
EDX	Energy Dispersive X-ray
E_{fb}	Flat band potential
EG	Ethylene Glycol
EIA	Energy Information Administration
EIS	electrochemical impedance spectroscopy
E_{onset}	Onset potential
EPR	Electron Paramagnetic Resonance
$E_{½}$	Half-wave potential
FE-SEM	Field Emission Scanning Electron Microscopy
FFT	Fast Fourier Transform
FTIR	Fourier Transform Infrared Spectroscopy
FTO	Fluorine doped tin oxide
GCE	Glassy Carbon Electrode
GF	Graphite Felt
HER	Hydrogen Evolution Reaction
HOMO	Highest Occupied Molecular Orbital
HOR	Hydrogen Oxidation Reaction
HR-TEM	High Resolution Transmission Electron Microscopy
IFFT	Inverse Fast Fourier Transform
IPA	Isopropanol
J_d	Current density
KE	Kinetic Energy

LOD	Limit of Detection
LSV	Linear Sweep Voltammetry
LUMO	Lowest Unoccupied Molecular Orbital
MABs	Metal-Air Batteries
MXenes	a two-dimensional material composed of transition metal carbides or nitrides
NComp	Nanocomposite
NPs	Nanoparticles
NSs	Nanosheets
OER	Oxygen Evolution Reaction
ORR	Oxygen Reduction Reaction
OV	Oxygen Vacancy
OWS	Overall water splitting
PL	Photoluminescence
Porphy/H_2TPP	Porphyrin
p-NP	4-nitrophenol/p-nitrophenol
PXRD	Powder X-ray diffraction
qd	Quadrillion
RDS	Rate Determining Step
R_{ct}	Charge transfer resistance
R_f	Roughness factor
rGO	Reduced Graphene Oxide
RHE	Reversible Hydrogen Electrode
RMABs	Rechargeable Metal-Air Batteries
RRDE	Rotating Ring Disc Electrode
R_s	Solution resistance
SAED	Selected Area Electron Diffraction
SC	Semiconductor
TMOs	Ternery Metal Oxides
TMSs	Ternery Metal Sulfides
TOF	Turn Over Frequency
UV-Vis	Ultraviolet Visible Spectroscopy
V	Volt
VB	Valence Band
XPS	X-ray Photoelectron Spectroscopy
η	Overpotential
η_{10}	Overpotential at current density of 10 mA cm^{-2}

Goals and Targets

Goal: The objective of this research is to develop and enhance organic-inorganic nanocomposites to improve their catalytic performance for energy conversion and environmental remediation applications.

Targets:

- **Synthesis and evaluation:** To fabricate ternary metal oxides containing bismuth and copper, and to characterize these materials through different sophisticated tools and detais of electrochemistry to evaluate their electrochemical properties and their applications in different aspects.
- **Surface enhancement:** To modify the surface of different mixed metal oxides with porhhyrin and rGO to achieve synergism conditions. This enhancement aims to boost their performance in electrocatalytic activities (such as ORR, OER, and HER) and in environmental applications such as sensing hazardous contaminants through photoelectrochemical analysis.
- **Performance optimization:** To optimize the catalytic performance of the synthesized catalysts by adjusting the weight percentages of organic molecules within the organic-inorganic nanocomposites.
- **Understanding catalytic mechanisms:** To explore the catalytic mechanisms and assess how surface modifications impact the functionality of the mixed metal oxides. This will help elucidate the role of these modifications in improving electrochemical and photoelectrochemical activities.
- **Impact of mixed-valence oxides:** To examine how metal oxides with multiple oxidation states influence the electrocatalytic performance, correlating changes in electrochemical behavior with variying weight percentages of organic molecules, and to evaluate the potential of Bi- and Cu-based hybrid materials to enhance catalytic activity.

These targets are designed to advance the development and application of advanced catalysts for energy conversion and environmental remediation.

Outline of the Work

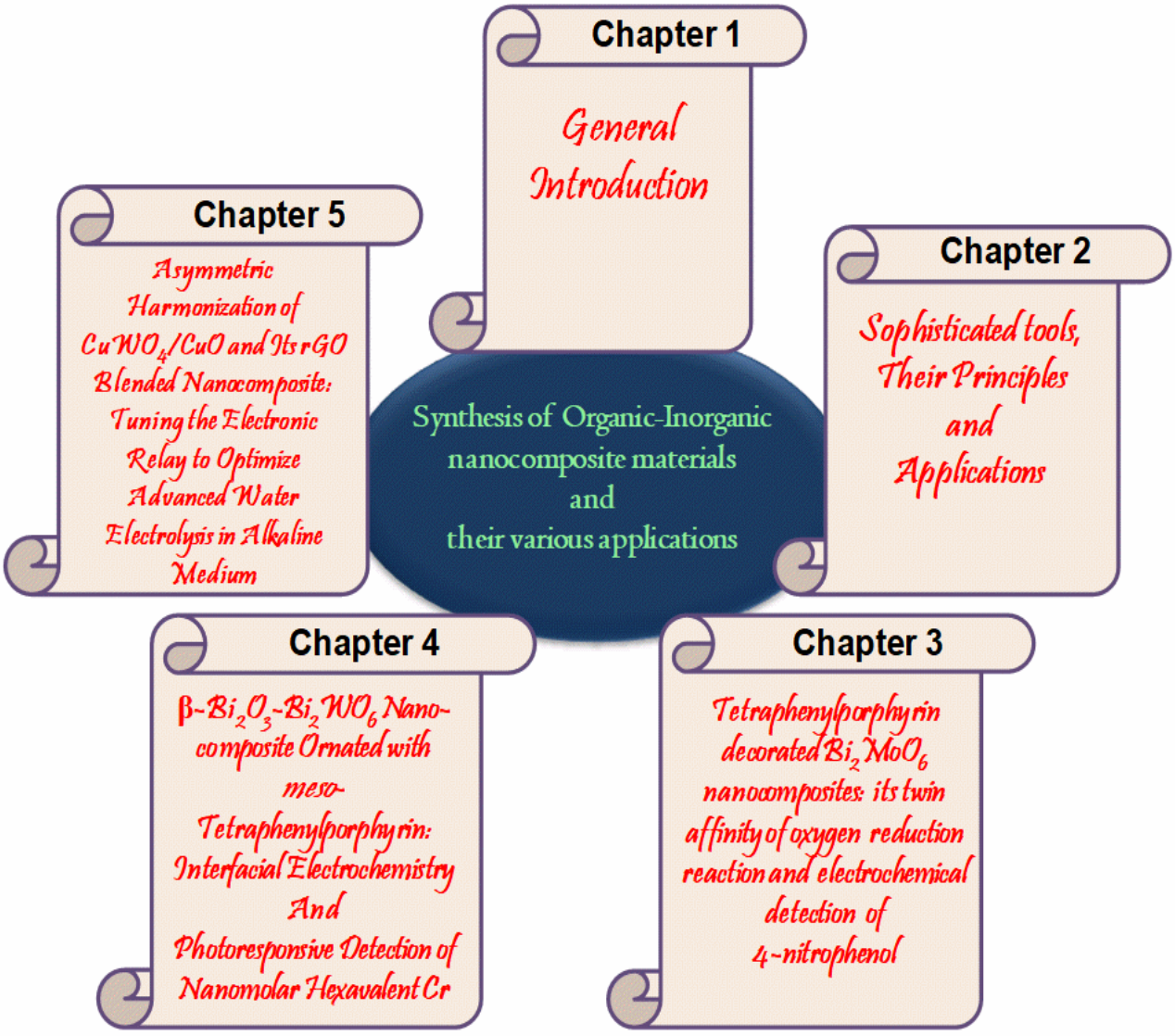

CONTENTS

CHAPTER 1

General Introduction

Objectives

Overview of the topic, establishing its relevance and outlining the research scope

1.1. CIRCUMSTANCES

Expanding urbanization and rapid industrialization have posed a major threat to the world's energy outlook and environmental sustainability in recent decades. In addition, fossil fuel use has increased significantly over the last two decades, and projections suggest that it will continue to grow at a faster rate in the decades to come. This trend is leading to the exhaustion of fossil fuel resources and making fossil fuel discovery and extraction increasingly difficult. The U.S. Energy Information Administration (EIA) has already projected a substantial increase in global energy consumption, expected to rise from 629 quadrillion (qd) British thermal units (Btu) in 2020 to 815 qd Btu by 2040. This translates to approximately 30% growth over a span of 20 years. Although conventional fossil fuels contribute nearly 80% of the world's total energy consumption, their combustion releases harmful greenhouse gases that pose a significant threat to the environment. As a result, the pressing need for global energy supply, coupled with escalating concerns about climate change, environmental pollution, and ecological degradation, has sparked extensive research efforts. These efforts are directed towards the advancement of clean and sustainable energy solutions, as well as the innovation of novel systems for electrochemical energy conversion and storage.[1] Extensive endeavors have been dedicated to improving the efficiencies of systems where electrochemistry plays a pivotal role, involving a sequence of catalytic reactions. These reactions include the oxygen reduction reaction (ORR) occurring at the cathode in both metal-air batteries (MABs) and fuel cells.[2-4] In rechargeable metal-air batteries (RMABs), both the ORR and oxygen evolution reaction (OER) takes place (Figure 1.1a). Additionally, the hydrogen oxidation reaction (HOR) is significant in fuel cells[5] (Figure 1.1.b). In water electrolysis,[6] the OER occurs at the anode and the hydrogen evolution reaction (HER) at the cathode (Figure 1.1c). These reactions are also relevant in devices aimed at carbon dioxide reduction.

Nevertheless, the sluggish kinetics and substantial overpotential associated with pivotal redox reactions (such as ORR, OER, and HER) within these energy devices[7-9] pose significant obstacles to their practical utility. These limitations markedly curtail both energy density and cycle lifespan. Hence, there exists a pressing demand for efficacious electrocatalysts capable of expediting reaction rates, facilitating high current density at minimal overpotential (η), and augmenting catalytic resilience. To address this, the need for efficient electrocatalysts is paramount-ones that can quicken reaction rates, enable high current density even under low overpotential conditions, and bolster catalytic stability. Currently, materials based on Pt and Pt-alloys are recognized as proficient ORR and HER catalysts,[10,11] while those derived from Ir and Ru are established as standard OER catalysts[12,13] due to their exemplary catalytic efficiency. However, none of these materials exhibit the

bifunctional OER/ORR (MABs) or OER/HER (within OWS) performance. Moreover, their extensive adoption is hindered by exorbitant costs, limited availability, compromised durability, and inadequate bifunctional activity.

Furthermore, the majority of cost-effective alternatives for OER and HER catalysts exhibit heightened OER efficiency in alkaline electrolytes while showcasing better HER performance in acidic electrolytes. As a result, the differing pH requirements impose limitations on their practical applications. This issue is particularly significant in the context of water electrolysis devices, where overall water splitting should ideally occur in a consistent electrolyte to minimize operational costs.

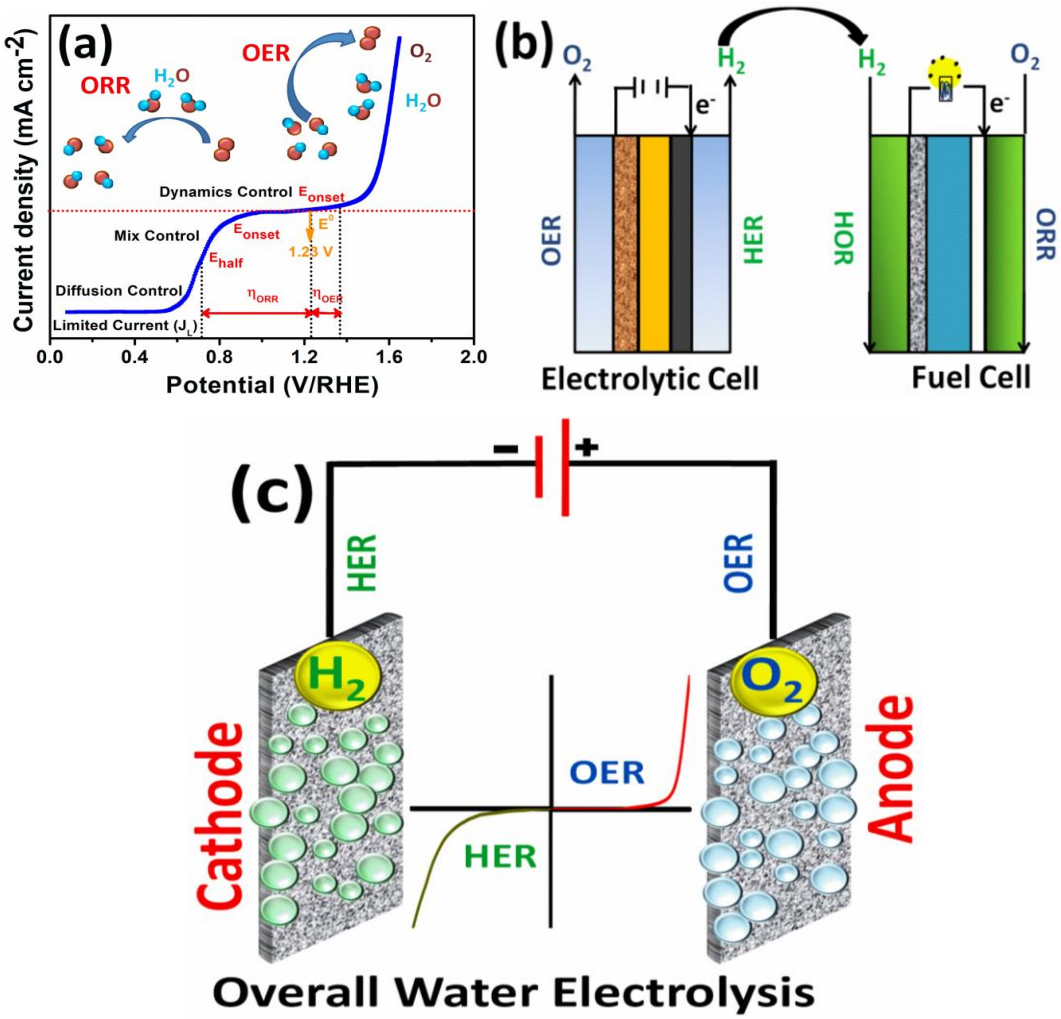

Figure 1.1. Schematic representation of (a) ORR and OER LSV Plots, (b) Electrolytic Cell and Fuel Cell, and (c) Overall Water Electrolysis (HER and OER).

In addition to the escalating concerns surrounding air emissions and their adverse ecological implications,[14] another critical environmental issue emerges due to the extensive use of As, Hg, and Cd and various organic pollutants. Antibiotics, used extensively in veterinary medicine and human healthcare, contribute to environmental pollution and the development of antibacterial resistance, adversely affecting ecosystems and human health. Reports from the U.S. Geological Survey indicate that pharmaceutical effluents contain active pharmaceutical ingredients (APIs) at concentrations 10-1000 times higher than those found in effluents[15] from other sources. Additionally, textile dyeing accounts for about 17-20% of industrial water pollution, according to the World Bank.

Addressing these challenges requires the development of effective, sustainable technologies for contaminant removal. Traditional methods, such as biological treatments, physical methods (e.g., membrane filtration and adsorption), and chemical treatments, have limitations such as high costs, incomplete removal of contaminants, and generation of harmful by-products. Photocatalytic degradation has emerged as a promising technique due to its advantages, including minimal harm to living organisms, cost-effectiveness, high efficiency, and complete mineralization of contaminants into non-toxic products like CO_2 and H_2O (Figure 1.2). However, improving the stability and efficiency of photocatalysts remains a key challenge. The advancement of photocatalytic degradation as a method for treating toxic organic effluents is significantly hindered by the poor photostability and rapid recombination of photogenerated electron-hole pairs in semiconductor (SC) catalysts.

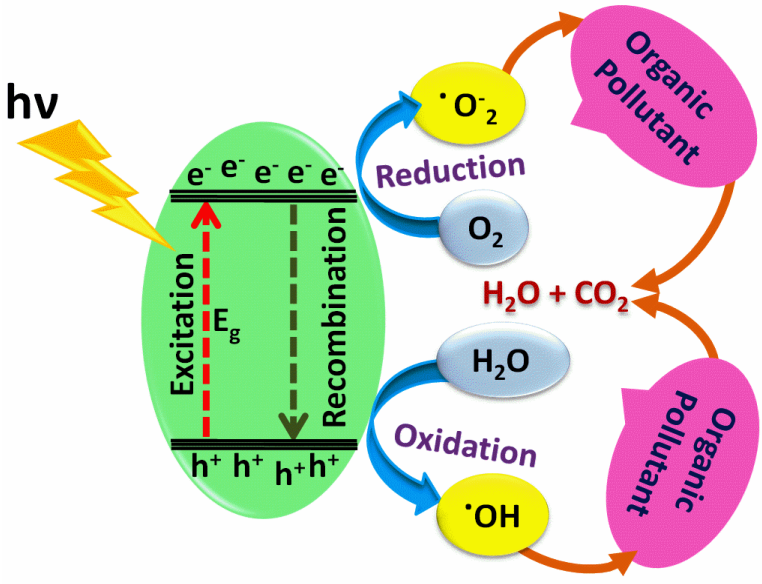

Figure 1.2. Schematic diagram illustrating the processes occurring during photocatalysis.

The development of advanced organic-inorganic nanocomposites could provide significant benefits for both energy applications and environmental remediation. These materials have the potential to address critical issues such as enhancing electrocatalytic processes and improving methods for the removal of hazardous contaminants from wastewater

1.2. INSPIRATION

This thesis seeks to address this challenge by developing a novel catalyst that combines the benefits of non-precious materials, specifically through the integration of bismuth and copper. The research begins with the synthesis of ternary metal oxides, laying the groundwork for creating a catalyst with enhanced properties. Subsequent stages involve the precise construction of the ternary catalyst, characterized by the combination of bismuth and copper, and a detailed examination of its structure and properties.

The study also extends to practical evaluations of the catalyst's performance and stability over time. Assessing these factors is crucial for determining the catalyst's practical applicability. Additionally, this research aims to uncover the underlying catalytic mechanisms, providing insights into how surface modifications can enhance the performance of bismuth and copper-based ternary metal oxides. These insights are expected to contribute to optimizing these catalysts for various applications, including the degradation of organic pollutants, addressing significant environmental challenges.

In summary, this thesis is focused on advancing catalyst development by creating an exceptionally efficient, cost-effective, and environmentally friendly catalyst with dual capabilities in electrochemical and photocatalytic applications.

1.3. Bi- and Cu-Based Ternary Metal Oxides (TMOs) and their fabrication strategies for the concerned applications

1.3.1. Advantages of Ternary Metal Oxides (TMOs) over Binary Oxides

Ternary metal oxides (TMOs) offer several distinct advantages compared to binary oxides, making them highly desirable in various applications:

(i) Improved catalytic activity: TMOs often demonstrate superior catalytic performance compared to binary oxides. This enhancement arises from the increased number of active sites and the synergistic interactions among the different metal components, leading to higher reaction rates and efficiencies.

(ii) Greater stability: TMOs typically exhibit better stability under operational conditions. This improved stability ensures that TMOs remain effective over extended periods, reducing the frequency of replacements and maintenance.

(iii) Tailorable properties: The properties of TMOs can be adjusted through variations in composition and structure. This flexibility enables the design of TMOs specifically tailored to meet the requirements of various applications, optimizing their performance.

(iv) Wide range of applications: TMOs are versatile and can be applied beyond catalysis, including in energy storage, sensing, and environmental remediation. Their multifunctionality enhances their utility across diverse technological fields.

(v) Enhanced synergistic effects: The presence of multiple metal components in TMOs often leads to synergistic effects, which can result in improved performance, including increased activity and efficiency, compared to systems with fewer components.

(vi) Cost effectiveness: TMOs can be more economical than binary oxides, particularly when they reduce the need for expensive metals during their synthesis. This can lower production costs and make advanced materials more accessible.

(vii) Support for environmental sustainability: TMOs contribute to more sustainable practices by facilitating greener processes. Their efficiency and stability often lead to reduced waste and lower energy consumption, aligning with environmental sustainability goals.

Overall, the benefits of TMOs, including their enhanced catalytic activity, stability, and versatility, combined with their cost-effectiveness and support for sustainability, highlight their significant advantages over binary oxides.

1.3.2. Benefits of Ternary Metal Oxides (TMOs) in different electrocatalysis

Recent advancements have highlighted the significant potential of ternary metal oxides (TMOs) in advancing photocatalytic and electrocatalytic technologies. Unlike noble metal-based catalysts, which are highly effective but hindered by their high cost and limited stability, TMOs offer a compelling alternative. Their cost-effectiveness, enhanced stability, and versatile compositional flexibility make them particularly attractive for large-scale applications.

TMOs have garnered attention as a new class of catalytic materials due to their distinct properties. These include exceptional redox reversibility, a high density of redox-active sites, and superior electrical conductivity and capacitance. Additionally, TMOs exhibit impressive photo- and electrochemical activity. The advantages of TMOs can be summarized as follows:

(i) Structural flexibility: TMOs can undergo structural changes that allow modifications in lattice symmetry and cell parameters. This adaptability can be tailored to enhance their performance in various catalytic processes.

(ii) Electrochemical property adjustments: Quantum confinement effects within TMOs can alter their electrochemical characteristics. This ability to modify electronic properties helps improve their effectiveness in catalytic reactions.

(iii) Surface property modification: TMOs can experience changes in their surface properties that significantly impact their band gap. Adjustments in the band gap influence both conductivity and catalytic activity, optimizing their performance for specific applications.

(iv) Versatile Applications: These TMOs are widely used in various fields, including life science, energy harvesting, portable energy devices as well as different type of catalysis. This property supports selective sensing of biomolecules,[16] expanding their utility in sensing applications.

In conclusion, TMOs represent a versatile and promising alternative to noble metals in various catalytic applications. Their cost-effectiveness, stability, and customizable properties, along with their significant electrochemical advantages, underscore their potential in advancing both electrcatalytic and photoelectrocatalytic applications.

1.3.3. Rationale for focusing on Bismuth (Bi) and Copper (Cu) in Ternary Metal Oxides (TMOs)

This thesis focuses on the development of ternary metal oxides incorporating both bismuth (Bi) and copper (Cu) due to their distinctive electronic structures, dielectric and semiconductor properties, and their advantages in terms of low toxicity and catalytic potential. Bismuth oxides are known for their high dielectric constants,[17] which enhance their performance in electronic applications, while copper oxides exhibit semiconductor behavior,[18] contributing to their utility in a range of technological applications. Both metals are environmentally friendly and demonstrate significant potential across various fields of electrochemical applications as well as environmental remediation (Figure 1.3). Furthermore, their role in environmental remediation is notable, as they can be employed in processes to clean up pollutants or neutralize contaminants, thus advancing materials science and contributing to sustainable technological and biomedical solutions.

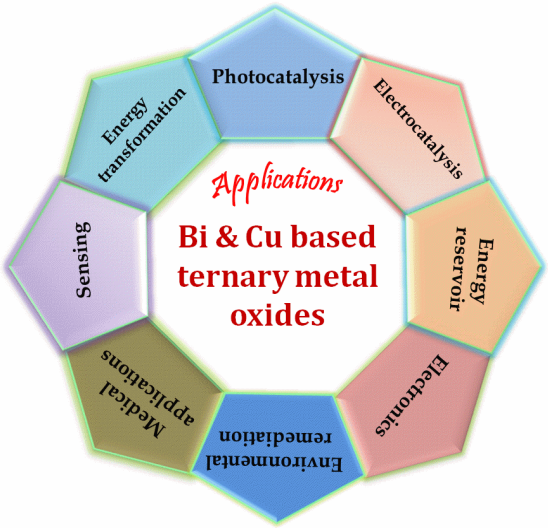

Figure 1.3. Overview of different applications for Bi- and Cu-based ternary metal oxides.

This thesis employs various fabrication techniques to enhance the performance of Bi- and Cu-based catalysts (Figure 1.4), addressing and overcoming the inherent limitations. When materials are modified or decorated with various organic moieties, the enhancement of active sites takes place. The design and alignment of smaller crystallites can be carefully managed through different organic systems, which greatly affect the electrocatalytic performance of metal oxides, producing a more pronounced response compared to other materials.

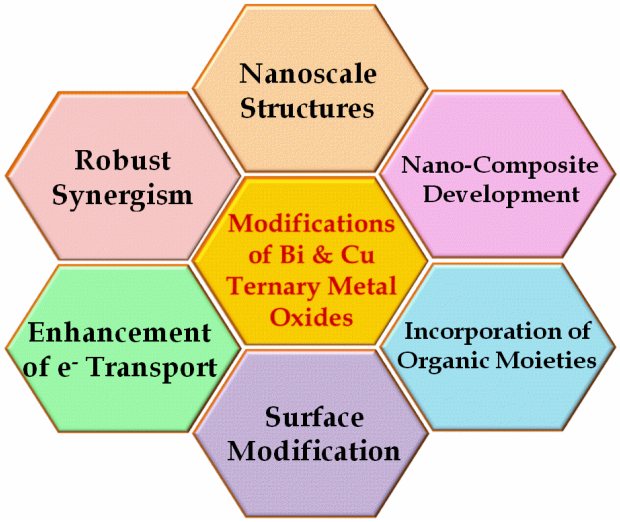

Figure 1.4. Strategies for enhancing the performance of advanced catalyst.

1.4. Approaches for enhancing catalytic performance through fabrication techniques

1.4.1. Development of nanoscale structures

Nanomaterials have significant potential in a variety of advanced applications, such as biomedicine,[19] which includes imaging,[20] drug carriers,[21] and sensing,[22] data storage,[23] energy storage,[24] environmental remediation,[25] catalysis,[26] and lighting technologies.[27] A key factor in their effectiveness is the ability to precisely control their elemental composition, which enhances their intrinsic properties and performance. One of the most notable advantages of nanomaterials is their exceptionally high surface area-to-volume ratio. This increased surface area is crucial for catalytic processes, as it provides more active sites for reactions compared to bulk materials. Additionally, the atomic interactions within nanostructures differ markedly from those in larger-scale materials, leading to unique physicochemical properties. The nanoscale dimensions induce changes in the material's structure and energy levels, which can fundamentally alter their physical, electronic, and optical characteristics.

Nanomaterials often bridge the gap between homogeneous and heterogeneous catalysts, combining the benefits of both types. They typically exhibit enhanced activity, selectivity, efficiency, and reusability in catalytic processes. Furthermore, nanomaterials are characterized by exceptional porosity, diverse morphologies, and various forms, including composites, compounds, alloys, and elemental solids. These features make them highly advantageous for catalytic applications.

1.4.1.1. Traditional materials with nanoscale structures

Research into nanoscale structures of classical metal oxides based on bismuth (Bi) and copper (Cu) has shown their effectiveness in a range of applications. Here are examples of these traditional TMO nanostructures:

Bi-Based metal oxides nanostructures:

Bi_2O_3 Nanoparticles: Bismuth oxide nanoparticles have been widely studied for their photocatalytic activity, making them valuable in degrading organic pollutants and harnessing solar energy.

$BiFeO_3$ nanowires: Bismuth ferrite ($BiFeO_3$) nanowires exhibit multiferroic properties and are explored for their potential in memory devices and data storage applications.

Bi_2MoO_6 nanospheres: Bismuth molybdate (Bi_2MoO_6) nanospheres exhibit unique properties and are studied for their potential in various applications, including photocatalysis, sensing, and energy storage. These nanospheres offer a promising avenue for harnessing their distinctive characteristics in advanced technologies.

Bi_2WO_6 nanosheets: Bismuth tungstate nanosheets have shown promise in photocatalysis and are used in the degradation of organic dyes and pollutants in water.

Bi_2S_3 Nanorods: Bismuth sulfide nanorods are employed in photodetectors and photovoltaic devices due to their unique electronic properties and light-absorbing capabilities.

Cu-Based metal oxide nanostructures:

CuO nanoparticles: Copper oxide nanoparticles, particularly CuO, are utilized in gas sensors and catalysts for their exceptional surface reactivity and catalytic activity.

Cu_2O nanocubes: Copper oxide nanocubes are employed in the development of solar cells and photoelectrochemical devices for their ability to capture and convert solar energy.

$CuWO_4$ nanoparticles: Copper tungstate ($CuWO_4$) nanoparticles possess intriguing properties that make them valuable in diverse applications. These nanoparticles are being investigated for their potential use in areas such as photocatalysis, energy storage, and sensors, highlighting their versatility and significance in the realm of nanomaterials.

$CuFe_2O_4$ nanoparticles: Copper ferrite ($CuFe_2O_4$) nanoparticles are explored for their magnetic properties and potential applications in data storage and magnetic resonance imaging (MRI).

These examples showcase the versatility of classical TMO nanostructures based on Bi and Cu in various fields, including catalysis, energy conversion, electronics, and biomedical applications. Recent studies highlighting some examples of Bi- and Cu-based materials are summarised in Table 1.1.

FE-SEM, HR-TEM, and SAED images of the selected materials that were synthesized in our laboratory are presented in Figures 1.5, 1.6, and 1.7.

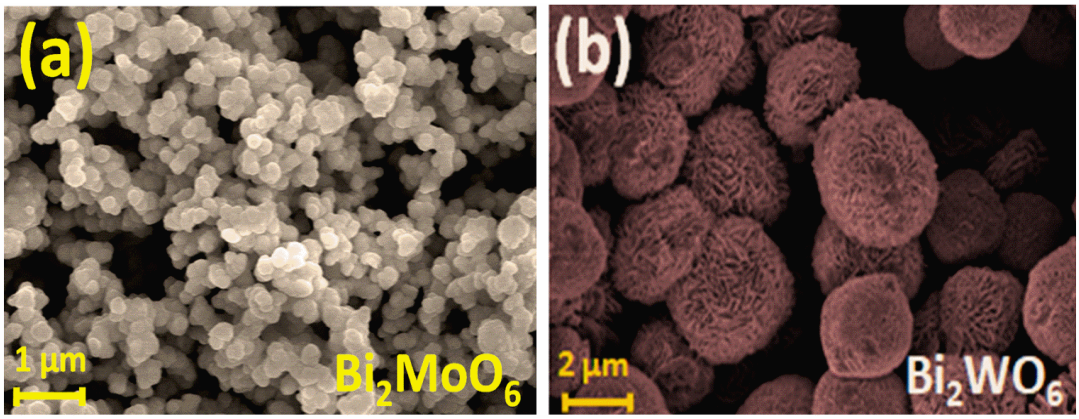

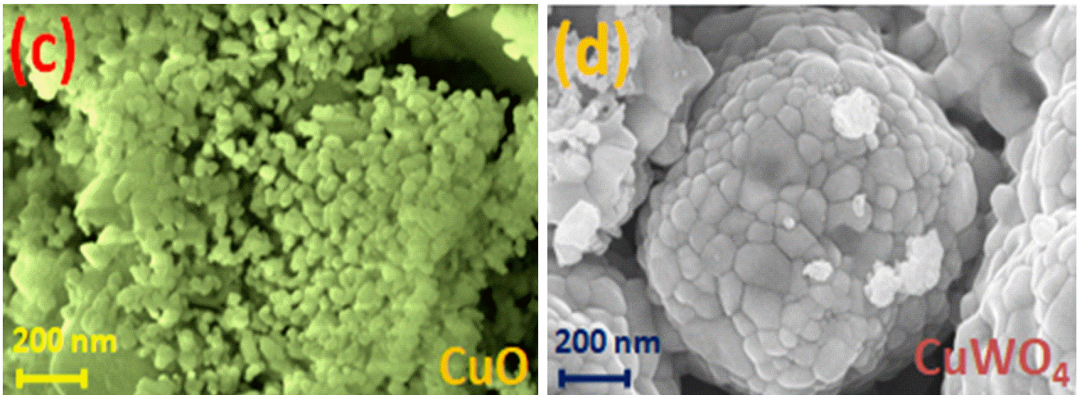

Figure 1.5. FE-SEM images of (a) Bi_2MoO_6, (b) Bi_2WO_6, (c) CuO, and (d) $CuWO_4$ nanoparticles.

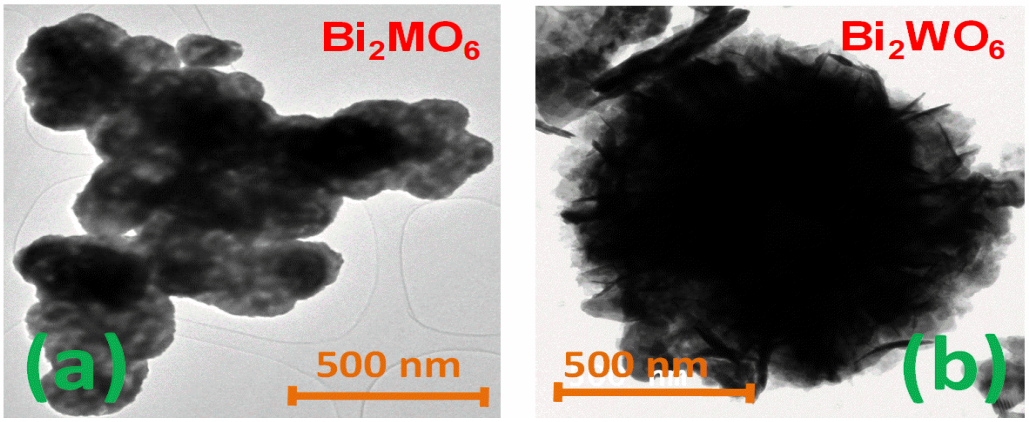

Figure 1.6. HR-TEM images of (a) Bi_2MoO_6, (b) Bi_2WO_6 nanomaterials.

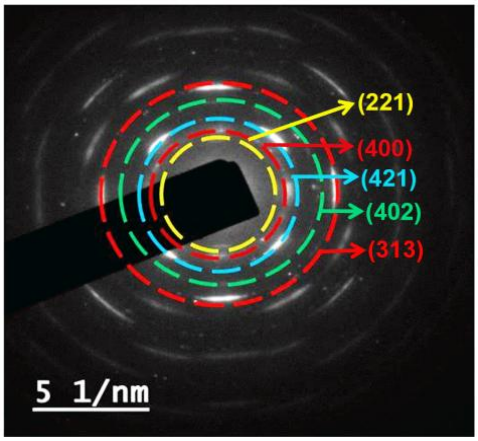

Figure 1.7. SAED image of (a) Bi_2MoO_6 nanomaterial.

Table 1.1: Classical nanomaterials for energy applications and environmental remediation.

Catalyst	Morphology	Distinctive behaviour	Relevant applications	Ref.
$BiFeO_3$	Nanoparticles	Photocatalyst	Photocatalytic degradation of RhB	28
Bi_2MoO_6	Nanosheets	Photocatalyst	Photocatalytic degradation of sulfamethoxazole and Escherichia coli bacteria disinfection	29
Bi_2WO_6	Nanoparticles	Photocatalyst	Photocatalytic hydrogen evolution from water splitting	30
$BiVO_4$	Nanoparticles	Photocatalyst	Photocatalytic degradation of methylene blue dye	31
CuO	Nanoparticles	Electrocatalyst	CO_2 reduction	32
$CuWO_4$	Nanofilm	Photocatalyst	Photoelectrochemical water splitting	33
$CuFe_2O_4$	Nanoparticles	Electrocatalyst and photocatalyst	Photocatalytic and electrocatalytic hydrogen generation	34
$CuMoO_4$	Nanoparticles	Photocatalyst	Photocatalytic degradation of RhB	35

1.4.2. Nano-composite development

Current research is increasingly directed towards creating nano-composites (NComps), to address the limitations of conventional nanomaterials and markedly improve their catalytic performance. NComps are advanced composite materials made up of multiple phases, where the resulting material exhibits properties that are significantly different from those of the individual components. The central aim in developing NComps is to exploit the synergies among different materials, resulting in multifunctional capabilities that surpass those of traditional binary or ternary nanometal oxides.

These NComps integrate at least one organic or inorganic element at the nanoscale. Their enhanced properties arise from both the unique characteristics of each component and the interactions at their interfaces. This approach is crucial for creating highly effective catalytic materials, improving electrical conductivity, facilitating better charge separation at interfaces, optimizing light absorption, increasing adsorption capacity, and expanding surface area, all of which contribute to a higher number of active sites. For instance, Boukherroub and colleagues successfully developed a composite material combining CoO with nitrogen-doped MoS_2 on carbon fibers (CoO/N-MoS_2/CF). This composite exhibited significantly improved bifunctional electrocatalytic performance over MoS_2/CF and N-MoS_2/CF. Additionally, it demonstrated notable photoinduced electron-hole separation and decreased rate of recombination, which is particularly beneficial for photocatalytic applications.

Figure 1.8 illustrates the enhanced electron-hole separation and transport in a Z-scheme system of ZnO nanosheets decorated with Bi_2WO_6 nanolayers,[36] making it a highly effective photocatalyst for removing environmental pollutants and for photoelectrochemical solar water oxidation. Further examples of bismuth-based nano-composites are detailed in Table 1.2.

Table 1.2. Modification of conventional nanomaterials for various applications.

Catalyst	Distinctive behaviour	Relevant applications	Ref.
α-NiS/Bi_2O_3	Photocatalyst	Photocatalytic Degradation Tramadol	37
W-doped Bi_2MoO_6	Photocatalyst	Photocatalytic N_2 fixation	38
polyaniline/Bi_2MoO_6 nanocomposites	Photocatalyst	Photocatalytic Degradation RhB	39
ACCN/Bi_2WO_6	Photocatalyst	Photocatalytic degradation of tetracycline and ciprofloxacin	40
$CuWO_4$/ZnO	Photocatalyst	Wastewater control	41
$CuWO_4$/$BiVO_4$/$FeCoO_x$	Photoelectrocatalyst	Photoelectrochemical water oxidation	42
Ti_3C_2TxMXene/Graphene Oxide/CuO/ZnO	Gas sensor	Ammonia Gas Sensor	43
$CuWO_4$-RGO nanocomposite	Photocatalyst	Photocatalytic degradation of brilliant green and malachite green	44
Graphene oxide decorated $CuWO_4$	Gas Sensor	NO_2 Gas Sensor	45

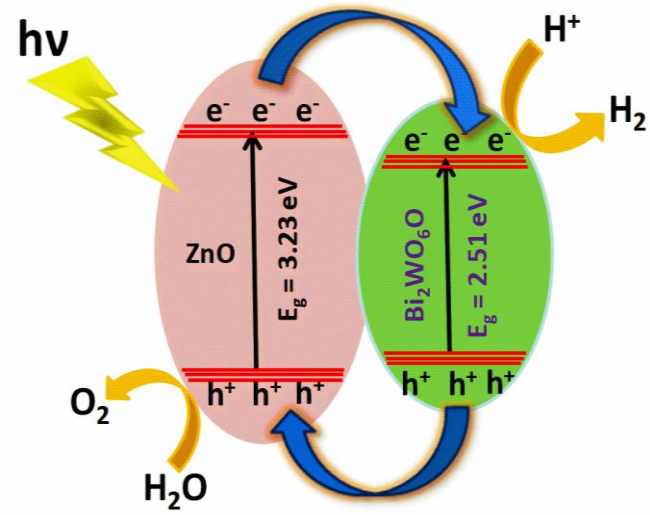

Figure 1.8. Schematic representation of Z-scheme water electrolysis.

1.4.2.1. Organic matrices

In the realm of organic compounds, tetraphenylporphyrin[46] and reduced graphene oxide (rGO)[47] stand out due to their unique properties and wide-ranging applications. Both materials play crucial roles in advancing various scientific and technological fields.

Tetraphenylporphyrin is a significant organic compound known for its distinctive macrocyclic structure. It features four phenyl rings surrounding a central porphyrin core, which imparts it with notable characteristics such as vivid coloration and strong visible light absorption. These photophysical properties make tetraphenylporphyrin an important component in multiple applications. It serves as a useful model for studying heme-containing proteins like hemoglobin and myoglobin due to its ability to coordinate metal ions within the porphyrin ring. This property is especially valuable in catalytic and sensing applications. Additionally, conjugated structure and adjustable properties of tetraphenylporphyrin make it a key material in designing functional components for organic electronics and photovoltaics.

On the other hand, reduced graphene oxide (rGO) is derived from graphene oxide through a reduction process. While rGO retains some of exceptional properties of graphene, such as high electrical conductivity and mechanical strength, the reduction introduces defects and disruptions in the graphene lattice. These imperfections can be advantageous for certain applications. The presence of oxygen-containing functional groups on rGO enhances its compatibility with various organic

molecules, making it a versatile material for functionalization and hybridization. Consequently, rGO is extensively used in energy storage, sensing technologies, and catalytic processes.

In summary, tetraphenylporphyrin and rGO exemplify the diversity of organic compounds and their potential to drive innovation. Macrocyclic structure of tetraphenylporphyrin and metal coordination capabilities are pivotal for catalysis and sensing, while electrical conductivity, mechanical strength, and organic compatibility of rGO make it an essential material for a range of advanced applications.[48] Together, these compounds highlight the vast potential of organic materials in advancing technology and scientific research.

1.4.3. Incorporation of organic matrices into nanodimensional materials

Advancements in material science enable the synthesis of diverse nanomaterials, with component regulation crucial for modifying their electronic structure and properties. Introduction and variation of weight percentages of organic components alter electron transfer and band structures, impacting electronic, optical, and catalytic activities. Composition engineering, morphological control and functionalization enhance catalytic activity and conductivity in nanomaterials. Polypyrrole modified oxygen vacancy-rich exhibits enhanced electrocatalytic behavior towards CO_2 reduction.[49] Similarly, polyaniline fabricated Bi_2MoO_6 nanosheets exhibited enhanced photocatalytic activity[50] while incorporating polyaniline into CuO enhances its selective sensing capabilities for H_2S.[51]

1.4.4. Surface modification and heterostructure engineering

Surface modification and heterostructure engineering (Figure 1.9) are synergistic techniques used to enhance material performance and functionality across a range of applications. Surface modification involves altering the outer layer of a material to improve its properties or tailor its behavior for specific uses. Methods such as coating, doping, and chemical functionalization are employed to enhance the catalytic activity. This is crucial in fields such as energy storage, where improved electrode surfaces can boost charge/discharge rates and cycle stability, and in sensing technologies, where tailored surfaces increase sensitivity and selectivity. Heterostructure engineering, on the other hand, involves creating composite structures from two or more different materials or phases. By combining materials with complementary properties at the nanoscale, heterostructures can exhibit unique characteristics that surpass those of individual components. This approach is particularly effective in applications like photovoltaics, where integrating different semiconductor materials enhances light absorption and charge separation, or in catalysis, where the synergy between materials can lead to improved activity and selectivity. When used together, surface modification and

heterostructure engineering can significantly advance the performance of materials in diverse fields, including energy, sensing, and environmental remediation. These techniques enable the development of more efficient, durable, and multifunctional materials, fostering innovation and progress in scientific and industrial applications. Together, these techniques drive the advancement of materials with enhanced catalytic properties, better energy performance, and improved sensing capabilities, supporting progress in various fields including energy, environmental remediation, and beyond.[52,53]

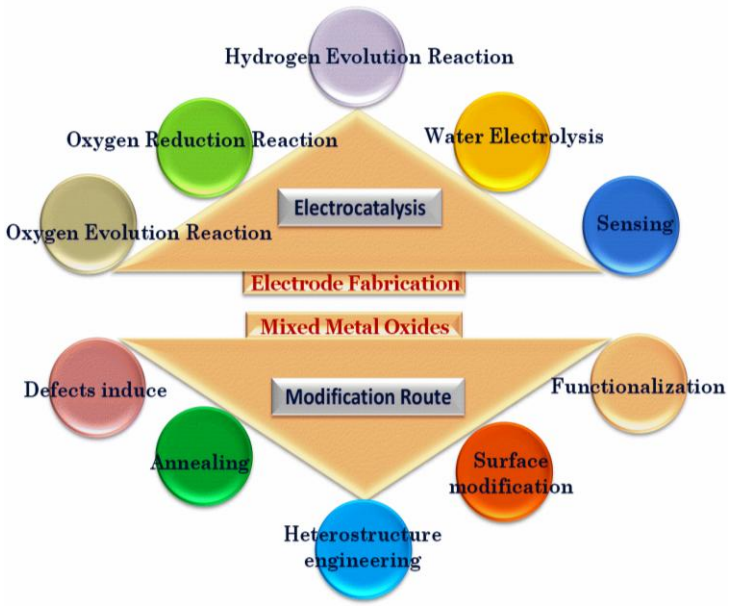

Figure 1.9. Schematic diagram depicting surface modification/heterostructure engineering techniques for creating effective catalysts in renewable energy technologies.

1.4.5. Enhancement of electron transport properties

Improving the properties of charge carriers and ensuring their efficient separation is essential for developing effective catalysts. One crucial aspect of this strategy is optimizing the band diagram of a heterojunction.[54] This design facilitates the directional movement of electron at the catalyst's interface and minimizes the recombination process. Integrating highly conductive non-metallic materials, such as carbon-based substances and π-conjugated organic compounds, with the base catalyst can offer substantial benefits. This combination results in a material with enhanced properties, including a higher density of charge carriers.

Additionally, creating an internal electric field through well-aligned band structure often resembling a Z-scheme configuration[55] can further improve the transfer and separation of

photoinduced charge carriers. This leads to enhanced photocatalytic activity and selectivity. For instance, the hybrid organic/inorganic g-C_3N_4/$Cs_3Bi_2Br_9$ Z-scheme photocatalyst has demonstrated improved photocatalytic activity and stability for CO_2 reduction.

1.4.6. Establishment of robust synergism

To substantially boost the catalytic activity of oxides, one effective strategy is to harness the effective synergism achieved by combining different components. This approach capitalizes on the beneficial interactions among these components, which result in enhanced overall performance. The primary advantages of this strategy include: (i) a larger surface area available for catalytic activity; (ii) improved charge and mass transport; (iii) increased electrical conductance; (iv) better adsorption of reaction intermediates during electrocatalytic processes[56] and (v) more efficient photoinduced electron-hole separation.[57] For example, Li et al. developed an efficient electrocatalyst OER by combining α-Fe_2O_3 with NiFeOOH, which led to improved photoelectrochemical water splitting.[58] Similarly, Jiangquan et al. proposed a z-scheme heterojunction of $CdIn_2S_4$ and Bi_2WO_6, which exhibited enhanced piezo-photo synergistic performance.[59]

1.4.7. Rational for selecting solvothermal synthesis method

The solvothermal process offers several advantages for the synthesis of nanomaterials and other advanced materials:

(i) Enhanced control over nucleation and growth: The solvothermal method allows precise control over reaction conditions such as temperature, pressure, and solvent composition. This control facilitates the uniform nucleation and growth of nanoparticles, leading to materials with well-defined sizes, shapes, and crystallinity.

(ii) High purity and homogeneity: By conducting reactions in a closed system, solvothermal synthesis minimizes exposure to contaminants and reduces the formation of impurities. This results in high-purity products with consistent properties, which is crucial for applications requiring reliable and reproducible material performance.

(iii) Versatility in material synthesis: The solvothermal technique is adaptable to a wide range of materials, including metals, metal oxides, sulfides, and complex heterostructures. It can be used to synthesize various nanostructures and composites with tailored properties for diverse applications.

(iv) Scalability: Solvothermal synthesis can be scaled up from laboratory to industrial production. This scalability allows for the synthesis of larger quantities of materials while maintaining control over their properties, making it suitable for commercial applications.

(v) Improved crystallinity and structure: The high temperatures and pressures in solvothermal reactions often lead to improved crystallinity and well-defined structural properties of the resulting nanomaterials. This can enhance their performance in various applications, such as catalysis, electronics, and energy storage.

(vi) Favorability of functionalization: The solvothermal process allows for the incorporation of functional groups, doping elements, and other modifications during synthesis. This functionalization can tailor the electronic, optical, and chemical properties of the nanomaterials to meet specific requirements.

(vii) Ease of complex structure formation: Solvothermal synthesis is capable of forming complex and hierarchical nanostructures that might be challenging to achieve through other methods. This includes core-shell structures, hierarchical assemblies, and other advanced architectures.

(viii) Reduced processing times: Compared to some traditional methods, solvothermal synthesis can achieve desired material properties more quickly due to the high reaction rates and enhanced diffusion processes under solvothermal conditions.

These advantages make the solvothermal process a valuable technique for producing high-quality nanomaterials with tailored properties for a wide range of scientific and industrial applications.

1.4.8. Optimizing Key Parameters and Conditions for Enhanced Performance of TMOs: Key reaction parameters such as LOD, LOQ, linearity, selectivity, and sensitivity must be optimized to effectively use TMOs systems decorated with organic moieties in practical applications. Additionally, optimizing the pH and temperature of the sensor is crucial. Recent literature highlights the importance of pH and temperature adjustments for enhancing sensor performance[60,61].

1.5. CONCLUSIONS

In conclusion, the advancements in oxide-based nanoparticles represent a significant leap forward in both scientific research and practical applications. The recent progress highlighted in this chapter demonstrates the growing potential of these materials in energy harvesting and environmental remediation. The innovative fabrication techniques discussed offer promising aspects for further enhancement, potentially leading to more effective and sustainable solutions. As the field continues to evolve, ongoing research and development will be crucial in unlocking the full potential of oxide-based nanocomposites, ultimately contributing to advancements in energy conversion and environmental protection.

REFERENCES

1. Kabeyi, M.J.B. and Olanrewaju, O.A. Sustainable energy transition for renewable and low carbon grid electricity generation and supply. *Front. Energy Res.* **2022**, *9*, 743114 (1-45).

2. Cheng, F. and Chen, J. Metal-air batteries: from oxygen reduction electrochemistry to cathode catalysts. *J. Chem. Soc. Rev*. **2012**, *41*, 2172-2192.

3. Liu, N.; Liang, Z.; Yang, F.; Wang, X.; Zhong, J.; Gui, X.; Yang, G.; Zeng, Z. and Yu, D. Flexible solid-state metal-air batteries: the booming of portable energy supplies. *ChemSusChem* **2023**, *16*, 202202192 (1-16).

4. Chang, J. and Yang, Y. Recent advances in zinc-air batteries: self-standing inorganic nanoporous metal films as air cathodes. *Chem. Commun.* **2023**, *59*, 5823-5838.

5. Sanati, S., Morsali, A. and Garcia, H., Metal-organic framework-based materials as key components in electrocatalytic oxidation and reduction reactions. *J. Energy Chem*. **2023**, 87, 540-567.

6. Ibn Shamsah, S.M. Earth-abundant electrocatalysts for water splitting: current and future directions. *Catalysts* **2021**, *11*, 429 (1-21).

7. Ji, Z.; Liu, J.; Deng, Y.; Zhang, S.; Zhang, Z.; Du, P.; Zhao, Y. and Lu, X. Accurate synergy effect of Ni-Sn dual active sites enhances electrocatalytic oxidation of urea for hydrogen evolution in alkaline medium. *J. Mater. Chem.* **2020**, *8*, 14680-14689.

8. Shi, Y. and Zhang, B. Recent advances in transition metal phosphide nanomaterials: synthesis and applications in hydrogen evolution reaction. *Chem. Soc. Rev*. **2016**, *45*, 1529-1541.

9. Suen, N.T.; Hung, S.F.; Quan, Q.; Zhang, N.; Xu, Y.J. and Chen, H.M. Electrocatalysis for the oxygen evolution reaction: recent development and future perspectives. *Chem. Soc. Rev*. **2017**, *46*, 337-365.

10. Wu, X.; Niu, Y.; Feng, B.; Yu, Y.; Huang, X.; Zhong, C.; Hu, W. and Li, C.M. Mesoporous hollow nitrogen-doped carbon nanospheres with embedded $MnFe_2O_4$/Fe hybrid nanoparticles as efficient bifunctional oxygen electrocatalysts in alkaline media. *ACS Appl. Mater. Interfaces* **2018**, *10*, 20440-20447.

11. Yu, J., Guo, Y., Miao, S., Ni, M., Zhou, W. and Shao, Z. Spherical ruthenium disulfide-sulfur-doped graphene composite as an efficient hydrogen evolution electrocatalyst. *ACS Appl. Mater. Interfaces* **2018**, *10*, 34098-34107.

12. Hu, C.; Liu, J.; Wang, J.; She, W.; Xiao, J.; Xi, J.; Bai, Z. and Wang, S. Coordination-assisted polymerization of mesoporous cobalt sulfide/heteroatom (N, S)-doped double-layered carbon tubes as an efficient bifunctional oxygen electrocatalyst. *ACS Appl. Mater. Interfaces* **2018**, *10*, 33124-33134.

13. Kim, B.; Oh, A.; Kabiraz, M.K.; Hong, Y.; Joo, J.; Baik, H.; Choi, S.I. and Lee, K. NiOOH exfoliation-free nickel octahedra as highly active and durable electrocatalysts toward the oxygen evolution reaction in an alkaline electrolyte. *ACS Appl. Mater. Interfaces* **2018**, *10*, 10115-10122.

14. Velusamy, S.; Roy, A.; Sundaram, S. and Kumar Mallick, T. A review on heavy metal ions and containing dyes removal through graphene oxide-based adsorption strategies for textile wastewater treatment. *Chem. Rec.* **2021**, *21*, 1570-1610.

15. Guo, R.; Liu, H.; Yang, K.; Wang, S.; Sun, P.; Gao, H.; Wang, B. and Chen, F. β-Cyclodextrin polymerized in cross-flowing channels of biomass sawdust for rapid and highly efficient pharmaceutical pollutants removal from water. *ACS Appl. Mater. Interfaces* **2020**, *12*, 32817-32826.

16. Li, L., Wang, S., Xiao, Y. and Wang, Y. Recent advances in immobilization strategies for biomolecules in sensors using organic field-effect transistors. *Trans. Tianjin. Univ.* **2020**, *26*, 424-440.

17. Feng, Z.; Hao, Y.; Zhang, J.; Qin, J.; Guo, L. and Bi, K. Dielectric properties of two-dimensional Bi_2Se_3 hexagonal nanoplates modified PVDF nanocomposites. *Adv. Poly. Technol.* **2019**, *2019*, 8720678 (1-8).

18. Legaspi, E.D.R. and Regulacio, M.D. Nanocomposites of Cu_2O with plasmonic metals (Au, Ag): design, synthesis, and photocatalytic applications. *Nanoscale Adv.* **2023**, 5, 5683-5704

19. Mitragotri, S.; Anderson, D.G.; Chen, X.; Chow, E.K.; Ho, D.; Kabanov, A.V.; Karp, J.M.; Kataoka, K.; Mirkin, C.A.; Petrosko, S.H. and Shi, J. Accelerating the translation of nanomaterials in biomedicine. *ACS Nano*, **2015**, *9*, 6644-6654.

20. Wolfbeis, O.S. An overview of nanoparticles commonly used in fluorescent bioimaging. *Chem. Soc. Rev.* **2015**, *44*, 4743-4768.

21. Jijie, R.; Barras, A.; Boukherroub, R. and Szunerits, S. Nanomaterials for transdermal drug delivery: beyond the state of the art of liposomal structures. *J. Mater. Chem. B* **2017**, *5*, 8653-8675.

22. Zhu, C.; Yang, G.; Li, H.; Du, D. and Lin, Y. Electrochemical sensors and biosensors based on nanomaterials and nanostructures. *Anal. Chem.* **2015**, *87*, 230-249.

23. Chen, K.; Kong, J.; Zhu, J.; Ermann, N.; Predki, P. and Keyser, U.F. Digital data storage using DNA nanostructures and solid-state nanopores. *Nano Lett.* **2018**, *19*, 1210-1215.

24. Gogotsi, Y. and Penner, R.M. Energy storage in nanomaterials-capacitive, pseudocapacitive, or battery-like? *ACS Nano*, **2018**, *12*, 2081-2083.

25. Zou, Y.; Wang, X.; Khan, A.; Wang, P.; Liu, Y.; Alsaedi, A.; Hayat, T. and Wang, X. Environmental remediation and application of nanoscale zero-valent iron and its composites for the removal of heavy metal ions: a review. *Environ. Sci. Technol.* **2016**, *50*, 7290-7304.

26. Li, Z.; Ji, S.; Liu, Y.; Cao, X.; Tian, S.; Chen, Y.; Niu, Z. and Li, Y. Well-defined materials for heterogeneous catalysis: from nanoparticles to isolated single-atom sites. *Chem. Rev.* **2019**, *120*, 623-682.

27. Shirasaki, Y.; Supran, G.J.; Bawendi, M.G. and Bulovic, V. Emergence of colloidal quantum-dot light-emitting technologies. *Nat. Photonics* **2013**, *7*, 13-23.

28. Fourmont, P.; Nechache, R. and Cloutier, S.G. Reusable $BiFeO_3$ nanofiber-based membranes for photo-activated organic pollutant removal with negligible colloidal release. *ACS Appl. Nano Mater.* **2021**, *4*, 12261-12269.

29. Chen, Y.; Yang, W.; Gao, S.; Sun, C. and Li, Q. Synthesis of Bi_2MoO_6 nanosheets with rich oxygen vacancies by postsynthesis etching treatment for enhanced photocatalytic performance. *ACS Appl. Nano Mater.* **2018**, *1*, 3565-3578.

30. Wu, S.; Sun, J.; Li, Q.; Hood, Z.D.; Yang, S.; Su, T.; Peng, R.; Wu, Z.; Sun, W.; Kent, P.R. and Jiang, B. Effects of surface terminations of 2D Bi_2WO_6 on photocatalytic hydrogen evolution from water splitting. *ACS Appl. Mater.* **2020**, *12*, 20067-20074.

31. Ganeshbabu, M.; Kannan, N.; Venkatesh, P.S.; Paulraj, G.; Jeganathan, K. and MubarakAli, D. Synthesis and characterization of $BiVO_4$ nanoparticles for environmental applications. *RSC Adv.* **2020**, *10*, 18315-18322.

32. Hsu, J.; Eid, A.M.; Randall, C.; Houache, M.S.; Abu-Lebdeh, Y. and Al-Abadleh, H.A. Mechanistic in situ ATR-FTIR studies on the adsorption and desorption of major intermediates in CO_2 electrochemical reduction on CuO nanoparticles. *Langmuir* **2022**, *38*, 14789-14798.

33. Chen, L.; Li, W.; Qiu, W.; He, G.; Wang, K.; Liu, Y.; Wu, Q. and Li, J. Oriented $CuWO_4$ films for improved photoelectrochemical water splitting. *ACS Appl. Mater.Interfaces* **2022**, *14*, 47737-47746.

34. Mehtab, A.; Banerjee, S.; Mao, Y. and Ahmad, T. Type-II $CuFe_2O_4$/graphitic carbon nitride heterojunctions for high-efficiency photocatalytic and electrocatalytic hydrogen generation. *ACS Appl. Mater. Interfaces* **2022**, *14*, 44317-44329.

35. Tan, W. and Luan, J. Investigation into the synthesis conditions of $CuMoO_4$ by an in situ method and its photocatalytic properties under visible light irradiation. *RSC Adv.* **2020**, *10*, 9745-9759.

36. Majhi, D.; Samal, P.K.; Das, K.; Gouda, S.K.; Bhoi, Y.P. and Mishra, B.G. α-NiS/Bi_2O_3 nanocomposites for enhanced photocatalytic degradation of tramadol. *ACS Appl. Nano Mater.* **2018**, *2*, 395-407.

37. Sharma, M.; Kumar, A.; Gill, D.; Jaiswal, S.; Patra, A.; Bhattacharya, S. and Krishnan, V. Boosting photocatalytic nitrogen fixation via nanoarchitectonics using oxygen vacancy regulation in W-doped Bi_2MoO_6 nanosheets. *ACS Appl. Mater. Interfaces* **2023**, *15*, 55765-55778.

38. Bisht, K.; Kumar, G. and Dutta, R.K. Amine-functionalized crystalline carbon nanodots decorated on Bi_2WO_6 nanoplates as solar photocatalysts for efficient degradation of tetracycline and ciprofloxacin. *Indus. Eng. Chem. Res.* **2022**, *61*, 16946-16961.

39. Feng, T.; Yin, H.; Jiang, H.; Chai, X.; Li, X.; Li, D.; Wu, J.; Liu, X. and Sun, B. Design and fabrication of polyaniline/Bi_2MoO_6 nanocomposites for enhanced visible-light-driven photocatalysis. *New J. Chem.* **2019**, *43*, 9606-9613.

40. Cao, J.; He, J.; Ye, J.; Ge, K.; Zhang, Y. and Yang, Y. Urchin-like Bi_2S_3/Ag nanostructures for photocatalytic reduction of Cr (VI). *ACS Appl. Nano Mater.* **2021**, *4*, 1260-1269.

41. Chen, C.; Bi, W.; Xia, Z.; Yuan, W. and Li, L. Hydrothermal synthesis of the $CuWO_4$/ZnO composites with enhanced photocatalytic performance. *ACS Omega* **2020**, *5*, 13185-13195.

42. Seekaew, Y.; Kamlue, S. and Wongchoosuk, C. Room-temperature ammonia gas sensor based on $Ti_3C_2T_x$ MXene/graphene oxide/CuO/ZnO nanocomposite. *ACS Appl. Nano Mater.* **2023**, *6*, 9008-9020.

43. El-Khoury, P.Z.; Honkala, K. and Hess, W.P. Electronic and vibrational properties of meso-tetraphenylporphyrin on silver substrates. *J. Phys. Chem. A* **2014**, *118*, 8115-8123.

44. Babu, M.J.; Botsa, S.M.; Rani, S.J.; Venkateswararao, B. and Muralikrishna, R. Enhanced photocatalytic degradation of cationic dyes under visible light irradiation by $CuWO_4$-RGO nanocomposite. A*dv. Compos. Hybrid Mater.* **2020**, *3*, 205-212.

45. Zhang, W.; Zhang, D. and Zhang, Y. High-performance NO_2 gas sensor based on bimetallic oxide $CuWO_4$ decorated with reduced graphene oxide. *J. Mater. Sci.: Mater. Electron.* **2020**, *31*, 6706-6715.

46. Caliskan, S.; Wang, A.; Qin, F.; House, S.D. and Lee, J.K. Molybdenum carbide-reduced graphene oxide composites as electrocatalysts for hydrogen evolution. *ACS Appl. Nano Mater.* **2022**, *5*, 3790-3798.

47. Sakthinathan, S.; Kubendhiran, S.; Chen, S.M.; Karuppiah, C. and Chiu, T.W. Novel bifunctional electrocatalyst for ORR activity and methyl parathion detection based on reduced graphene oxide/palladium tetraphenylporphyrin nanocomposite. *J. Phys. Chem. C* **2017**, *121*, 14096-14107.

48. Ying, H.; Bi, J.; Xu, H.; Wu, G.; Wu, X.;, Hao, J. and Li, Z. Mn-doped Bi_2O_3 nanosheets from a deep eutectic solvent toward enhanced electrocatalytic N_2 reduction. *ACS Sustain. Chem. Eng.* **2022**, *10*, 6766-6774.

49. Xu, Y.; Guo, Y.; Sheng, Y.; Yu, H.; Deng, K.; Wang, Z.; Li, X.; Wang, H. and Wang, L. Selective CO_2 electroreduction to formate on polypyrrole-modified oxygen vacancy-rich Bi_2O_3 nanosheet precatalysts by local microenvironment modulation. *Small*, **2023**, *19*, 2300001.

50. Feng, T.; Yin, H.; Jiang, H.; Chai, X.; Li, X.; Li, D.; Wu, J.; Liu, X. and Sun, B. Design and fabrication of polyaniline/Bi_2MoO_6 nanocomposites for enhanced visible-light-driven photocatalysis. *New J. Chem.* **2019**, *43*, 9606-9613.

51. Zhang, B.; Shang, F.; Shi, X.; Yao, R.; Wei, F.; Hou, X.; Li, W. and Zhang, J. Polyaniline/CuO nanoparticle composites for use in selective H_2S sensors. *ACS Appl. Nano Mater.* **2023**, *6*, 18413-18425.

52. Qin, Y.; Fang, F.; Xie, Z.; Lin, H.; Zhang, K.; Yu, X. and Chang, K. La, Al-codoped $SrTiO_3$ as a photocatalyst in overall water splitting: significant surface engineering effects on defect engineering. *ACS Catal.* **2021**, *11*, 11429-11439.

53. Saeed, S.W.; Norby, T. and Bjorheim, T.S. Charge-carrier enrichment at $BaZrO_3$/$SrTiO_3$ interfaces. *J. Phys. Chem. C* **2019**, *123*, 20808-20816.

54. Wang, H.; Chen, Z.; Shang, Y.; Lv, C.; Zhang, X.; Li, F.; Huang, Q.; Liu, X.; Liu, W.; Zhao, L. and Ye, L. Boosting carrier separation on a BiOBr/$Bi_4O_5Br_2$ direct z-scheme heterojunction for superior photocatalytic nitrogen fixation. *ACS Catal.* **2024**, *14*, 5779-5787.

55. Baghdadi, Y.; Temerov, F.; Cui, J.; Daboczi, M.; Rattner, E.; Sena, M.S.; Itskou, I. and Eslava, S. $Cs_3Bi_2Br_9$/g-C_3N_4 direct z-scheme heterojunction for enhanced photocatalytic reduction of CO_2 to CO. *Chem. Mater.* **2023**, *35*, 8607-8620.

56. Li, L.; Yang, H.; Miao, J.; Zhang, L.; Wang, H.Y.; Zeng, Z.; Huang, W.; Dong, X. and Liu, B. Unraveling oxygen evolution reaction on carbon-based electrocatalysts: effect of oxygen doping on adsorption of oxygenated intermediates. *ACS Energy Lett.* **2017**, *2*, 294-300.

57. Liu, T.T.; Liu, T.F.; Wu, X.P. and Gong, X.Q. Modulating photoinduced charge separation in metal-azolate frameworks. *J. Phys. Chem. C* **2021**, *125*, 2064-2073.

58. Lin, Y.; Qin, A.; Fang, W.; Xv, R. and Fu, L. Synergistic effect of Ni^{2+} and Fe^{3+} of bimetallic oxyhydroxide NiFeOOH as OER cocatalyst for Fe_2O_3 photoanode with enhanced photoelectrochemical water splitting. *Energ. Fuel.* **2022**, *36*, 2890-2900.

59. Li, N.; Shi, M.; Sun, G.; Wu, M.; Li, Q.; Shen, W. and Ma, J. Z-scheme $CdIn_2S_4/Bi_2WO_6$ heterojunction for high piezo-photo synergetic performance. *Inorg. Chem.* **2023**, *62*, 8261-8270.

60. Guo, Y.; Zhou, C.; Fang, L.; Liu, Z.; Li, W. and Yang, M. Effect of pH on the catalytic degradation of rhodamine B by synthesized CDs/g-C_3N_4/Cu_xO composites. *ACS Omega* **2021**, *6*, 8119-8130.

61. Chen, Q.; Hao, Y.; Song, Z.; Liu, M.; Chen, D.; Zhu, B.; Chen, J. and Chen, Z. Optimization of photocatalytic degradation conditions and toxicity assessment of norfloxacin under visible light by new lamellar structure magnetic ZnO/g-C_3N_4. *Ecotoxicol. Environ. Saf.* **2021**, *225*, 112742.

CHAPTER 2

Sophisticated tools, their Principles and Applications

Objectives

Focusing on the characterization and efficiency of nanomaterials

Instrumentation and Analytical Techniques

The following content outlines the sophisticated tools and methodologies used in this research, detailing their operational principles and applications. Understanding these techniques is essential for interpreting experimental results and ensuring the accuracy of the findings. Below is an overview of each instrument and its role in the study.

2.1 Structural Analysis:

2.1.1. Powder X-ray Diffraction (PXRD): Powder X-ray Diffraction is a pivotal analytical methode employed to investigate the crystallographic properties of substances in powdered form. By directing X-rays at a powdered sample and analyzing the resulting diffraction pattern, PXRD provides comprehensive insights into the atomic arrangement of the material, phase composition, and structural parameters. This technique is indispensable for the identification and characterization of crystalline phases, which are crucial for understanding the physical properties of the material, stability, and potential applications.[1]

Principles: PXRD operates on the principle of Bragg's Law, which relates the angle of incidence and the wavelength of X-rays to the interplanar spacing of a crystal. When X-rays interact with the crystal lattice, they are diffracted in specific directions according to the lattice planes' spacing and the wavelength of the X-rays. The constructive interference of diffracted X-rays produces a diffraction pattern that is unique to the crystal structure of the sample.

Bragg's Law is mathematically expressed as:

$$n\lambda = 2d \sin\theta \qquad \text{Eq. 2.1}$$

Where, n represents the diffraction order, λ denotes the X-ray wavelength, d indicates the spacing between crystal planes, and θ is the angle of incidence.

By measuring the angles and intensities of the diffracted X-rays, the diffraction pattern can reveal information about the lattice parameters, phase purity, and crystallite size of the material.

Instrumentation and Experimental Procedure: The typical PXRD setup consists of an X-ray source, a sample holder, and a detector. The X-ray source generates X-rays that are collimated and directed towards the powdered sample. The sample is usually placed in a holder that allows for uniform exposure to the X-rays and ensures reproducibility. As the X-rays interact with the sample, the detector measures the intensity of the diffracted X-rays at various angles. The experimental procedure involves the following steps:

- **Sample Preparation:** The sample is finely ground to a powder and loaded into a sample holder. Ensuring a homogeneous powder and proper packing is essential for accurate results.
- **Data Collection:** The X-ray source and detector are aligned, and the sample is irradiated with X-rays. The diffraction pattern is recorded as the sample holder is rotated, or the X-ray source and detector are moved to cover a range of diffraction angles.
- **Data Analysis:** The recorded diffraction pattern is analyzed using software to identify the peaks and determine the corresponding 2θ angles. These peaks are matched against known reference patterns to identify the phases present and calculate lattice parameters.

Applications: PXRD is widely used in various fields for its ability to provide detailed structural information. Key applications include:

- **Phase Identification:** PXRD is employed to identify and quantify crystalline phases within a material. By comparing the experimental diffraction pattern with standard reference patterns, the phases present in the sample can be determined.
- **Lattice Parameter Determination:** The technique allows for the precise measurement of lattice parameters, which are crucial for understanding the structure of the material and properties.
- **Purity Assessment:** PXRD can detect the presence of impurities or secondary phases in a sample, providing insights into its purity and quality.
- **Crystallite Size and Strain Analysis:** The width of the diffraction peaks can be used to estimate the size of the crystallites and any internal strain within the material.

Powder X-ray Diffraction remains an essential tool in materials science and chemistry for its ability to provide detailed information about crystalline materials. Its application in phase identification, lattice parameter determination, and purity assessment underscores its significance in both research and industrial settings. Despite its limitations, ongoing advancements in PXRD instrumentation and analysis techniques continue to enhance its capabilities and accuracy.

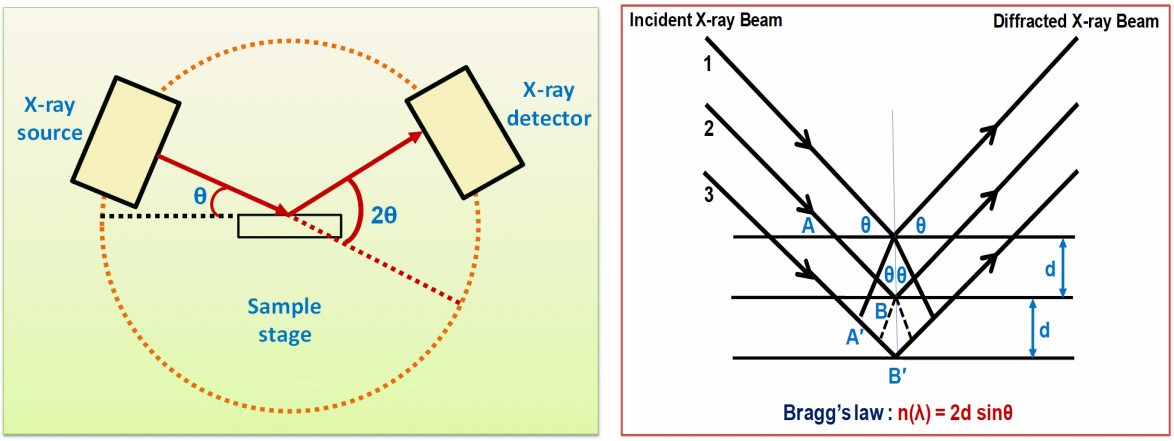

Figure 2.1. Schematic representation on the working principle of powder X ray diffraction.

2.1.2. X-ray Photoelectron Spectroscopy (XPS): X-ray Photoelectron Spectroscopy is a powerful surface-sensitive analytical technique used to characterize the elemental composition and chemical state of materials. By analyzing the kinetic energy of photoelectrons emitted from a sample when it is irradiated with X-rays, XPS provides detailed information about the surface chemistry of materials. This following discussion explores the principles of XPS, its instrumentation, experimental procedure, applications, and the advantages and limitations of the technique.[2]

Principles: XPS is based on the photoelectric effect, in which photons (X-rays) incident on a material's surface eject photoelectrons from the atoms. The kinetic energy of these emitted photoelectrons is measured to determine the binding energy of the electrons in the material. This binding energy is characteristic of the specific elements and their chemical states within the sample. The relationship between the kinetic energy E_k of the emitted photoelectrons and their binding energy E_b is given by:

$$E_b = h\nu - E_k - \phi \qquad \text{Eq. 2.2}$$

Where hν is the energy of the incident X-rays, ϕ denotes the spectrometer's work function, and E_k indicates the kinetic energy of the photoelectrons that are emitted.

By analyzing the binding energies and their corresponding intensities, XPS can provide qualitative and quantitative information about the elements present on the surface and their chemical states.

Instrumentation and Experimental Procedure: The XPS setup typically consists of an X-ray source, an electron energy analyzer, and a vacuum chamber to maintain an ultra-high vacuum

environment. The sample is irradiated with X-rays, and the emitted photoelectrons are collected and analyzed.

Instrumentation Components:

1. **X-ray Source:** Commonly employs monochromatic Al-Kα or Mg-Kα or Cu-Kα X-rays, which are suitable for exciting photoelectrons in most materials.
2. **Electron Energy Analyzer:** Measures the kinetic energy of the emitted photoelectrons. Common types include hemispherical analyzers and time-of-flight analyzers.
3. **Vacuum System:** Maintains an ultra-high vacuum environment to prevent photoelectron scattering and contamination.

Experimental Procedure:

1. **Sample Preparation:** The sample surface is cleaned and possibly etched to remove contaminants and ensure a representative surface analysis.
2. **Data Acquisition:** The sample is placed in the vacuum chamber, and X-rays are directed onto the surface. The emitted photoelectrons are collected and analyzed by the energy analyzer.
3. **Data Analysis:** The resulting spectra are analyzed to identify peaks corresponding to different elements and their chemical states. Peak positions are compared to reference data to determine binding energies and interpret the chemical environment of the elements.

Applications: XPS is widely used in various fields for its ability to provide detailed surface chemical information. Key applications include:

- **Elemental Composition Analysis:** XPS can identify and quantify the elements present on the sample surface, providing insights into surface composition.
- **Chemical State Identification:** The technique helps determine the oxidation states and chemical bonding environments of the elements, crucial for understanding material properties and reactivity.
- **Surface Contamination Analysis:** XPS is used to detect and analyze surface contaminants, which is important for semiconductor processing and material cleanliness.
- **Thin Film Characterization:** XPS provides valuable information on the composition and chemical states of thin films and coatings, essential for material science and engineering applications.

XPS is a crucial technique in surface science and materials characterization. Its ability to provide detailed information about elemental composition and chemical states makes it invaluable for

understanding surface properties, reactivity, and performance of materials. Despite its limitations, XPS continues to be a key tool in research and industry, offering critical insights into material surfaces and interfaces.

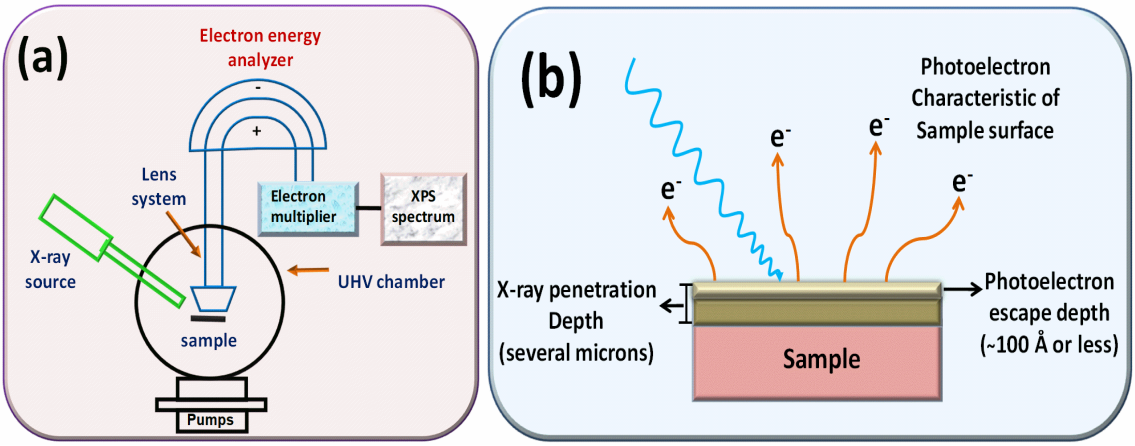

Figure 2.2. (a) Schematic diagram of XPS instrument and (b) Principle of XPS.

2.2. Morphological Analysis

2.2.1. Field Emission Scanning Electron Microscopy (FE-SEM): Field Emission Scanning Electron Microscopy is an advanced method that provides high-resolution images of the surface morphology and topography of samples. FE-SEM is an advanced variant of scanning electron microscopy (SEM) that uses a field emission gun (FEG) as its electron source, enabling superior resolution and imaging capabilities. The discussion covers the principles of FE-SEM, its instrumentation, experimental procedures, applications, and the advantages and limitations of the technique.[3,4]

Principles: FE-SEM operates on the principle of scanning a focused electron beam over a sample to produce high-resolution images based on secondary and backscattered electron emission. The technique relies on a field emission gun, which generates a highly collimated and stable electron beam by applying a strong electric field to a sharp tungsten or lanthanum hexaboride (LaB_6) or cerium hexaboride (CeB_6) tip. The field emission gun produces electrons with high brightness and low energy spread, which contributes to the improved resolution and depth of focus in FE-SEM imaging. The electron beam is scanned across the sample surface, and the emitted electrons are collected by a detector to form an image. The resulting image provides detailed information about the surface structure, morphology, and composition of the sample.

Instrumentation and Experimental Procedure: A typical FE-SEM setup includes a field emission gun, an electron column, scanning coils, detectors, and a computer system for image acquisition and analysis.

Instrumentation Components:

1. **Field Emission Gun (FEG):** Generates a stable and focused electron beam with high brightness. The FEG can be a tungsten or LaB_6 or CeB_6 tip, which emits electrons when subjected to a strong electric field.
2. **Electron Column:** Focuses and directs the electron beam onto the sample. It includes electromagnetic lenses and deflecting coils to control beam convergence and scanning.
3. **Detectors:** Collect emitted secondary and backscattered electrons to form the image. Common detectors include Everhart-Thornley detectors for secondary electrons and solid-state detectors for backscattered electrons.
4. **Computer System:** Processes the signals from the detectors, generates the image, and allows for image analysis and enhancement.

Experimental Procedure:

1. **Sample Preparation:** Samples are often coated with a thin conductive layer if they are non-conductive to prevent charging effects. The sample is then placed in the FE-SEM chamber.
2. **Vacuum System:** The FE-SEM operates under high vacuum conditions to prevent scattering of electrons by air molecules. The sample chamber is evacuated to achieve the required vacuum level.
3. **Imaging:** The electron beam is focused and scanned across the sample surface. Secondary and backscattered electrons are collected by the detectors to produce an image.
4. **Data Analysis:** The acquired images are analyzed to determine surface morphology, texture, and other features. The high resolution of FE-SEM allows for detailed examination of surface structures at the nanometer scale.

Applications: FE-SEM is widely used in various fields due to its high resolution and detailed imaging capabilities. Key applications include:

- **Material Science:** Characterizes the surface morphology and microstructure of materials such as metals, ceramics, and polymers. It is used to study grain boundaries, phase distributions, and surface defects.
- **Nanotechnology:** Provides high-resolution imaging of nanostructures, nanoparticles, and nanocomposites, enabling the design and development of nanoscale materials and devices.

- **Semiconductor Industry:** Analyzes semiconductor devices and integrated circuits to investigate fabrication defects, surface features, and material interfaces.
- **Biology and Medicine:** Examines biological samples, including cells and tissues, to study their ultrastructure and understand cellular processes and disease mechanisms.
- **Forensic Science:** Analyzes forensic samples, such as fibers, gunshot residues, and surface traces, to provide evidence in criminal investigations.

FE-SEM is a sophisticated imaging technique that provides high-resolution, detailed images of sample surfaces. Its ability to reveal fine structural details and surface characteristics makes it an invaluable tool in materials science, nanotechnology, and various other fields. Despite its limitations, FE-SEM remains a crucial technique for advancing our understanding of surface morphology and microstructural features.

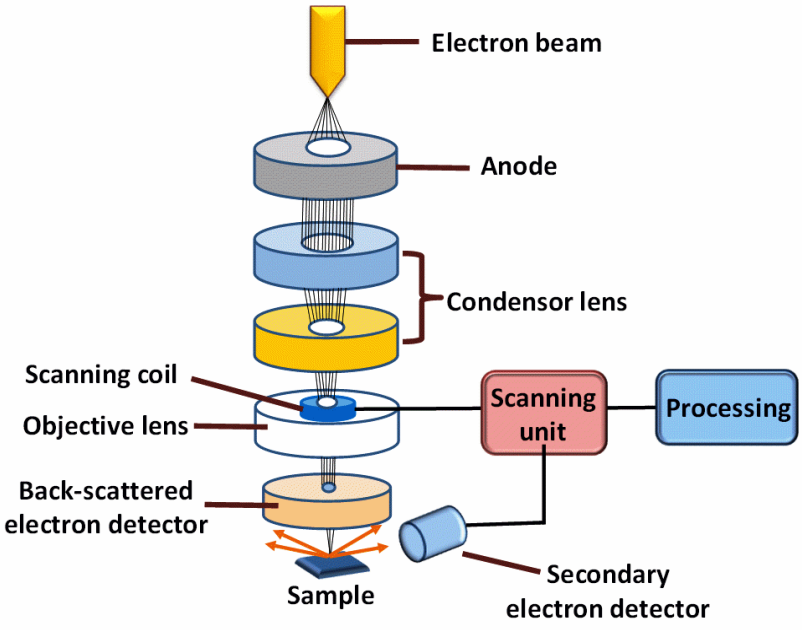

Figure 2.3. Schematic diagram of FE-SEM measurement set up.

2.2.2. High-Resolution Transmission Electron Microscopy (HR-TEM): High-Resolution Transmission Electron Microscopy is a sophisticated imaging method that allows for the visualization of materials at atomic resolution. By using transmitted electrons rather than visible light, HR-TEM provides unprecedented detail of the internal structure of samples, revealing information about atomic arrangements, defects, and interfaces. The following discussion the principles of HR-TEM, its

instrumentation, experimental procedures, applications, and the advantages and limitations of this powerful technique.[5,6,7]

Principles: HR-TEM relies on the transmission of high-energy electrons through a thin sample to produce images with atomic-level resolution. When an electron beam passes through a sample, it interacts with the atomic potentials of the material. These interactions cause variations in the phase and amplitude of the transmitted electrons, which are then used to form high-resolution images.

Key Principles:

- **Electron Wavelength:** The resolution of HR-TEM is related to the wavelength of the electrons used. Electrons have much shorter wavelengths compared to visible light, enabling the imaging of structures at the atomic scale. The wavelength of the electrons is inversely proportional to their energy, which is typically in the range of 100 keV to 300 keV for HR-TEM.
- **Phase Contrast:** HR-TEM images are formed based on phase contrast, where variations in the phase of the transmitted electron wave are converted into intensity variations in the final image. This contrast allows for the visualization of atomic planes and lattice fringes.
- **Aberration Correction:** Advanced HR-TEM systems employ aberration-correcting optics to minimize distortions and achieve higher resolution. These corrections are crucial for imaging at the atomic scale and improving image quality.

Instrumentation and Experimental Procedure: A typical HR-TEM system includes an electron source, a sample holder, electromagnetic lenses, and a detector. The following components are crucial for HR-TEM operation:

Instrumentation Components:

1. **Electron Source:** Provides a high-energy electron beam, usually generated by a field emission gun (FEG) for high brightness and coherence.
2. **Electromagnetic Lenses:** Focus and control the electron beam, including condenser lenses to focus the beam onto the sample and objective lenses to form the image.
3. **Sample Holder:** Holds the sample, which must be very thin (typically less than 100 nm) to allow electrons to pass through. The sample is usually prepared as a thin foil or film.
4. **Detector:** Captures the transmitted electron beam and converts it into an image. Detectors commonly used in HR-TEM include charge-coupled devices (CCDs) and direct electron detectors.

Experimental Procedure:

Sample Preparation: The sample must be extremely thin and uniform. Techniques such as ion milling, ultramicrotomy, or chemical etching are used to prepare thin samples. Proper sample preparation is crucial for obtaining high-resolution images.

1. **Imaging:** The electron beam is transmitted through the sample, and the interaction between the electrons and the atomic structure produces a high-resolution image. The microscope's objective lens focuses the electron beam to form an image of the sample's internal structure.
2. **Data Analysis:** The acquired HR-TEM images are analyzed to determine the atomic arrangement, lattice parameters, and defects. Advanced image processing techniques can enhance contrast and resolution, aiding in detailed structural analysis.

Applications: HR-TEM is used in various fields due to its ability to provide atomic-scale imaging. Key applications include:

- **Materials Science:** Analyzes the atomic structure of materials, including metals, semiconductors, and nanomaterials. HR-TEM reveals details such as grain boundaries, dislocations, and interface structures.
- **Nanotechnology:** Investigates nanostructures and nanoparticles, providing insights into their size, shape, and internal structure. This information is crucial for designing and optimizing nanomaterials.
- **Semiconductor Industry:** Examines the atomic arrangement in semiconductor devices, such as integrated circuits and thin films, to detect defects and ensure quality control.
- **Catalysis:** Studies the structure of catalyst particles and their active sites at the atomic level, improving our understanding of catalytic processes and enhancing catalyst design.
- **Biology and Medicine:** Provides detailed images of biological specimens, including cells and organelles, contributing to the understanding of cellular processes and disease mechanisms.

HR-TEM is a cutting-edge technique for imaging materials at the atomic scale. Its ability to provide detailed structural information with atomic resolution makes it a valuable tool in materials science, nanotechnology, and various other fields. Despite its challenges, such as sample preparation and high cost, HR-TEM remains a critical technique for advancing our understanding of the atomic structure and properties of materials.

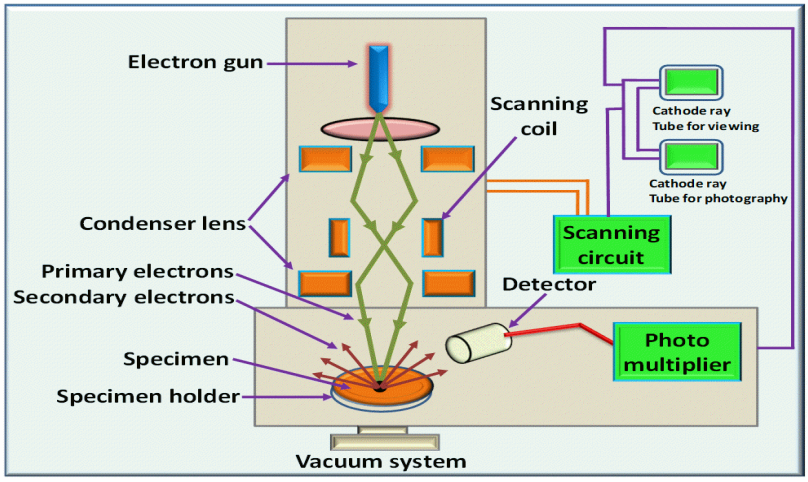

Figure 2.4. Schematic diagram of HR-TEM set up.

2.2.3. Energy Dispersive X-ray (EDX) Spectroscopy: Energy Dispersive X-ray Spectroscopy (EDX), also known as Energy Dispersive Spectroscopy, is an analytical method employed to identify the elemental composition of materials. EDX is commonly employed in conjunction with scanning electron microscopy (SEM) or transmission electron microscopy (TEM) to provide detailed chemical information about a sample. The principles of EDX spectroscopy, its instrumentation, experimental procedures, applications, and the advantages and limitations of the technique[8] are discussed.

Principles: EDX Spectroscopy is based on the interaction of X-rays with matter. When a sample is irradiated with an electron beam or X-rays, the atoms in the sample emit characteristic X-rays as they return to their ground state after being excited. These characteristic X-rays have energies specific to the elements present in the sample.

The principle behind EDX is that each element emits X-rays at distinct energy levels when excited. By analyzing the energy and intensity of these emitted X-rays, EDX can identify the elements present in the sample and determine their relative abundances. The resulting spectrum displays peaks corresponding to different elements, which are used for qualitative and quantitative analysis.

The energy of the emitted X-rays is measured using an energy-dispersive detector, and the energy spectrum is analyzed to determine the elemental composition of the sample.

Instrumentation and Experimental Procedure: A typical EDX system is integrated with an electron microscope and consists of several key components: an X-ray source, an energy-dispersive detector, and a computer for data analysis.

Instrumentation Components:

1. **X-ray Source:** In an SEM setup, the electron beam serves as the excitation source, while in other setups; X-rays from an external source may be used.
2. **Energy-Dispersive Detector:** Detects and measures the energy of the emitted X-rays. Common detectors include silicon drift detectors (SDD) and lithium-drifted silicon detectors (Si (Li)).
3. **Spectrometer:** Analyzes the X-ray energy spectrum and generates the EDX spectrum.
4. **Computer System:** Processes the data, displays the spectrum, and performs quantitative and qualitative analysis.

Experimental Procedure:

1. **Sample Preparation:** The sample is prepared for analysis, often by coating with a conductive layer if it is non-conductive, to prevent charging effects.
2. **Data Acquisition:** The sample is placed in the electron microscope, and the electron beam or X-ray source excites the sample. The emitted X-rays are collected by the detector.
3. **Data Analysis:** The energy spectrum of the emitted X-rays is recorded. Peaks in the spectrum are analyzed to identify the elements and determine their concentrations. The spectrum is compared to known standards or reference spectra for accurate identification.

Applications: EDX Spectroscopy has a wide range of applications in various scientific and industrial fields due to its ability to provide detailed elemental analysis.

Key applications include:

- **Material Characterization:** Identifies and quantifies elements in materials such as metals, ceramics, and polymers. It is used to study composition, alloying, and contaminants.
- **Semiconductor Analysis:** Assesses the elemental composition of semiconductor materials and devices, crucial for quality control and failure analysis.
- **Environmental Analysis:** Detects and quantifies trace elements and pollutants in environmental samples, such as soil, water, and atmospheric particles.
- **Forensic Analysis:** Analyzes materials from crime scenes, including paint, glass, and fibers, to provide evidence for forensic investigations.
- **Biomedical Research:** Investigates the elemental composition of biological samples, such as tissues and cells, to understand their structure and function.

EDX Spectroscopy is a powerful analytical tool for determining the elemental composition of materials. Its ability to provide detailed chemical information, combined with its integration with

electron microscopy techniques, makes it invaluable in materials science, environmental analysis, and forensic investigations. Despite its limitations, EDX remains an essential technique for understanding the composition and properties of various samples.

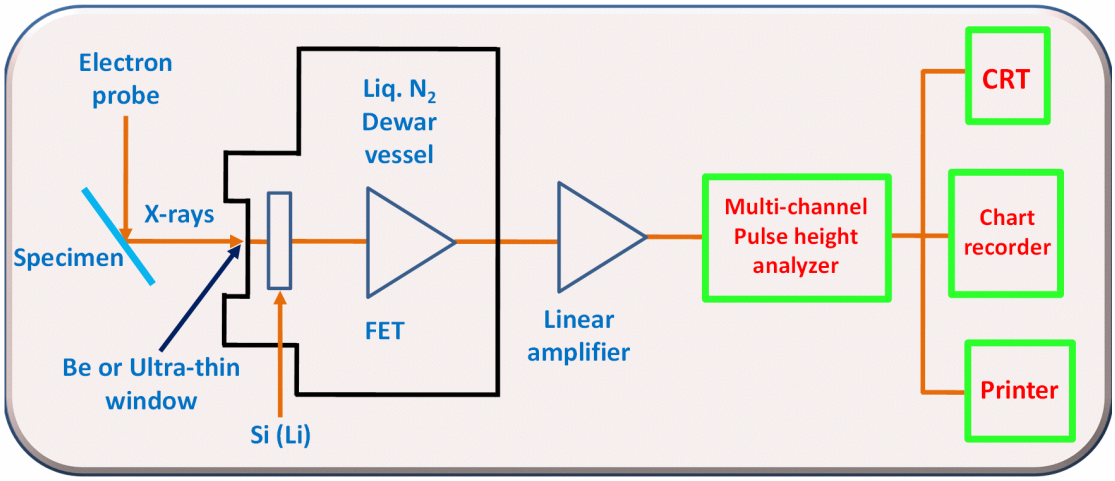

Figure 2.5. Schematic diagram of EDX instrument set up.

2.2.4. Brunauer-Emmett-Teller Surface Area Analysis (BET): BET analysis is a widely used method for determining the specific surface area of materials. This method is crucial in various fields, including materials science, chemistry, and environmental science, as surface area is a key property influencing the performance and behavior of porous materials and catalysts. The principles behind BET Surface Area Analysis, its instrumentation, experimental procedures, applications, and the advantages and limitations of the technique[9] are discussed.

Principles: The BET method is based on the adsorption of nitrogen gas onto the surface of a material. By measuring the amount of gas adsorbed at different relative pressures, the surface area of the material can be determined. The technique extends the Langmuir adsorption theory to multilayer adsorption, allowing for the calculation of surface area from the adsorption data.

Key Concepts:

- **Adsorption Isotherm:** The BET method measures how the amount of gas adsorbed changes with pressure. This is described by the BET equation, which relates the volume of adsorbed gas to the relative pressure.

- **Monolayer Coverage:** The BET theory assumes that gas molecules initially adsorb to form a monolayer on the surface. Once the monolayer is formed, additional layers are adsorbed, and the total amount of gas adsorbed can be used to estimate the surface area.
- **Specific Surface Area Calculation:** The specific surface area is calculated based on the volume of gas adsorbed when the surface is covered by a monolayer. This is expressed in units of area per mass of sample (e.g., $m^2\ g^{-1}$).

The BET equation is given by:

$$\frac{V_m}{V(V_0 - V)} = \frac{1}{V_m}\left(\frac{P}{p_0} - 1\right) + \left(\frac{C - 1}{V_m}\right)\frac{P}{P_0} \qquad \text{Eq. 2.3}$$

Where V represents the volume of gas adsorbed at pressure P, V_m denotes the volume of gas adsorbed at monolayer coverage, P is the equilibrium pressure of the adsorptive, P_0 refers to the saturation pressure of the adsorptive, and C is the BET constant related to the adsorption energy.

Instrumentation and Experimental Procedure: A typical BET surface area analyzer includes a gas adsorption system, a pressure measurement system, and a temperature control system. The instrument measures the adsorption and desorption of nitrogen gas to determine the surface area.

Instrumentation Components:

1. **Gas Adsorption System:** Introduces a controlled amount of gas (usually nitrogen) into the sample chamber. The system measures the volume of gas adsorbed at various pressures.
2. **Pressure Measurement System:** Monitors the pressure of the gas in the sample chamber. Accurate pressure measurements are crucial for calculating adsorption isotherms.
3. **Temperature Control System:** Maintains the sample at a constant temperature during the analysis, as temperature variations can affect gas adsorption.

Experimental Procedure:

1. **Sample Preparation:** The sample is degassed to remove any adsorbed impurities or moisture. This is usually done by heating the sample under vacuum or flowing a gas over it.
2. **Adsorption Measurement:** The sample is exposed to nitrogen gas at a series of relative pressures. The volume of nitrogen adsorbed at each pressure is recorded.
3. **Data Analysis:** The BET equation is applied to the adsorption data to calculate the specific surface area. The data is plotted as a BET plot, which is a linear representation of the BET equation, allowing for the determination of surface area from the slope and intercept.

Applications: BET Surface Area Analysis is used in a variety of applications due to its ability to provide detailed information about the surface properties of materials. Key applications include:

- **Catalyst Characterization:** Measures the surface area of catalysts, which is essential for understanding their activity and performance in chemical reactions.
- **Material Science:** Evaluates the surface area of porous materials, such as zeolites, metal-organic frameworks (MOFs), and carbon-based materials, to assess their suitability for various applications.
- **Pharmaceuticals:** Analyzes the surface area of drug powders and formulations, which can influence the drug's dissolution rate and bioavailability.
- **Environmental Science:** Studies adsorbents used in pollution control, such as activated carbon, to determine their effectiveness in removing contaminants from air and water.

BET Surface Area Analysis is a critical technique for determining the specific surface area of materials, with wide-ranging applications in materials science, catalysis, pharmaceuticals, and environmental science. Its ability to provide accurate surface area measurements makes it an invaluable tool for characterizing porous materials and understanding their performance. Despite some limitations, such as the need for thorough sample preparation and the reliance on nitrogen gas, the BET method remains a cornerstone in surface area analysis.

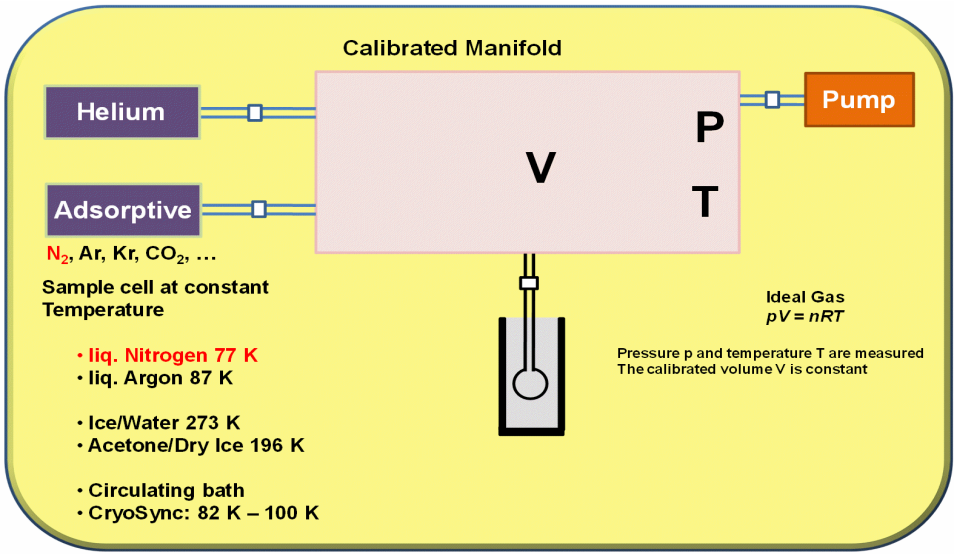

Figure 2.6. Schematic measurement set up of BET analysis.

2.3. Optical Analysis

2.3.1. Diffuse Reflectance Spectroscopy (DRS): Diffuse Reflectance Spectroscopy is a widely used analytical technique[10] for characterizing the optical properties and band gaps of solid samples. By measuring the diffuse reflection of light from a powdered or granular sample, DRS provides valuable information about the electronic and optical characteristics of materials. The principles of DRS, its instrumentation, experimental procedure, applications, and its advantages and limitations are listed.

Principles: Diffuse Reflectance Spectroscopy is based on the interaction of light with a sample. When light is incident on a rough or powdered sample, it scatters in many directions rather than reflecting specularly. The diffuse reflected light is collected and analyzed to obtain information about the sample's absorption and electronic transitions.

The fundamental principle of DRS is that the diffuse reflectance of a sample can be related to its absorption properties. According to the Kubelka-Munk theory, the diffuse reflectance R of a sample is related to its absorption α and scattering S coefficients through the following relationship:

$$F(R) = \frac{(1-R)^2}{2R} \qquad \text{Eq. 2.4}$$

Where F(R) represents the Kubelka-Munk function, which is proportional to the absorption coefficient α. By analyzing the spectrum of diffuse reflectance, one can determine the band gap and other optical properties of the material.

Instrumentation and Experimental Procedure: The typical DRS setup includes a light source, a sample holder, and a detector. The setup is designed to measure the intensity of light reflected from the sample and to analyze its spectrum.

Instrumentation Components:

1. **Light Source:** Usually, a broad-spectrum light source such as a halogen lamp or a Xenon lamp is used to provide a continuous range of wavelengths.
2. **Sample Holder:** The sample is typically ground into a fine powder and placed in a sample holder that ensures uniform illumination and collection of the reflected light.
3. **Detector:** A photodetector or spectrometer collects the reflected light and measures its intensity across different wavelengths.

Experimental Procedure:

1. **Sample Preparation:** The sample is finely powdered to ensure that it scatters light diffusely. The powder is then placed in a sample holder.

2. **Data Acquisition:** The sample is illuminated with a broad spectrum of light, and the diffuse reflected light is collected. The intensity of the reflected light is measured as a function of wavelength.
3. **Data Analysis:** The reflectance spectrum is analyzed to determine the optical band gap and other properties. The Kubelka-Munk function is often used to convert reflectance data into absorption spectra.

Applications: DRS is employed in various fields for its ability to provide detailed optical information. Key applications include:

- **Band Gap Determination:** DRS is widely used to estimate the optical band gap of semiconductors and other materials by analyzing the absorption edge in the reflectance spectrum.
- **Material Characterization:** Provides insights into the electronic structure and optical transitions of materials, which is important for developing new materials and devices.
- **Catalyst and Photocatalyst Evaluation:** Used to study the light absorption properties of catalysts and photocatalysts, which are crucial for their performance in photochemical reactions.
- **Quality Control:** DRS can be used for quality control in manufacturing processes, such as verifying the consistency of optical properties in batch production.

DRS is an essential technique for investigating the optical properties and electronic structure of materials. Its ability to determine band gaps, evaluate material characteristics, and support various applications in research and industry highlights its importance in material science. Despite its limitations, DRS remains a valuable tool for understanding the optical behavior of solid materials.

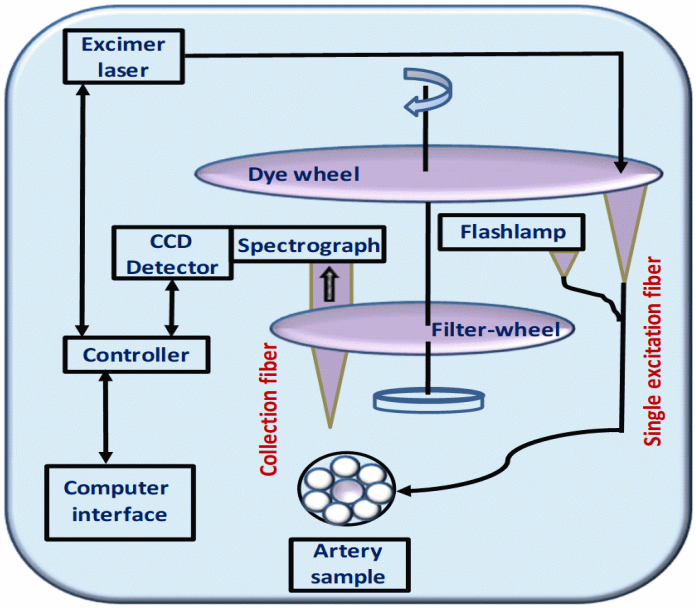

Figure 2.7. Schematic diagram of Diffuse Reflection measurement set up.

2.3.2. UV-Vis Absorption Spectroscopy: Ultraviolet-Visible Spectroscopy is a widely utilized analytical method that measures how a sample absorbs ultraviolet and visible light. This technique provides valuable information about the electronic transitions within molecules and is instrumental in determining the concentration and nature of various compounds. The principles of UV-Vis spectroscopy, its instrumentation, experimental procedure, applications, and the advantages and limitations of the technique[11] are explored.

Principles: UV-Vis Spectroscopy is based on the interaction between ultraviolet or visible light and the electrons in a sample. When light passes through a sample, certain wavelengths are absorbed by electronic transitions between different energy levels of the molecules. The amount of light absorbed at each wavelength is measured and recorded to produce an absorption spectrum.

The absorption of light at a specific wavelength corresponds to the excitation of electrons from lower to higher energy states. The relationship between the absorbance A, the concentration c, the path length l, and the molar absorptivity ε is described by Beer's Law:

$$A = \log\frac{I_0}{I} = \varepsilon Cl \qquad \text{Eq. 2.5}$$

Where I_0 represents the intensity of the incident light, I denotes the intensity of the transmitted light, ε is the molar absorptivity coefficient, c is the concentration of the sample, and l indicates the path length of the sample.

The absorption spectrum obtained can provide information about the electronic structure of the sample, including the presence of chromophores and their respective absorption maxima.

Instrumentation and Experimental Procedure: A typical UV-Vis spectrometer includes a light source, a monochromator, a detector and, a sample holder. The spectrometer measures the intensity of light absorbed by the sample as a function of wavelength.

Instrumentation Components:

1. **Light Source:** Usually, a deuterium lamp (for UV range) and a tungsten-halogen lamp (for visible range) are used to cover the full UV-Vis spectrum.
2. **Monochromator:** Disperses the light into its constituent wavelengths and selects a specific wavelength to pass through the sample.
3. **Sample Holder:** Contains the sample and ensures that light passes through it uniformly. It is often equipped with quartz cuvettes for UV-Vis measurements.
4. **Detector:** Measures the intensity of light after passing through the sample and converts it into an electronic signal for analysis.

Experimental Procedure:

1. **Sample Preparation:** Samples are typically prepared in a suitable solvent and placed in a clean cuvette. The concentration and path length are chosen based on the expected absorbance.
2. **Baseline Correction:** A blank cuvette containing only the solvent is used to zero the instrument and account for any background absorbance.
3. **Data Acquisition:** The sample is exposed to light across the UV-Vis spectrum, and the absorbance is measured at different wavelengths.
4. **Data Analysis:** The resulting spectrum is analyzed to determine the absorption peaks, which correspond to specific electronic transitions within the sample. The intensity of these peaks can be used to infer concentration and identify chemical species.

Applications: UV-Vis Spectroscopy has diverse applications across various fields due to its ability to provide detailed electronic and quantitative information. Key applications include:

- **Quantitative Analysis:** UV-Vis spectroscopy is commonly used to determine the concentration of solutes in solution based on Beer's Law. It is widely applied in chemical analysis, pharmaceuticals, and environmental monitoring.

- **Identification of Compounds:** The absorption spectrum can help identify compounds based on their characteristic peaks. This is particularly useful in organic chemistry and material science.
- **Characterization of Materials:** UV-Vis spectroscopy is used to study the electronic structure of materials, including metals, semiconductors, and nanomaterials. It provides insights into band gaps and electronic transitions.
- **Kinetics Studies:** The technique can be employed to monitor reaction progress and study the kinetics of chemical reactions by measuring changes in absorbance over time.

UV-Vis Spectroscopy is a fundamental technique in analytical chemistry and material science, providing valuable information about the electronic properties and concentration of substances. Its wide range of applications, coupled with its sensitivity and speed, makes it an essential tool for researchers and industry professionals alike.

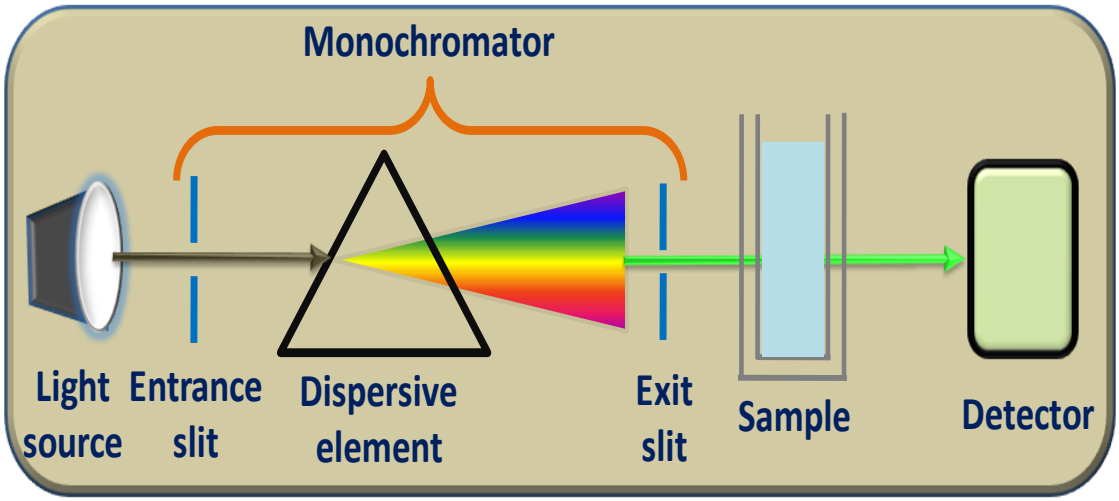

Figure 2.8. Schematic diagram for the experimental simple set up of UV-Vis Spectroscopy.

2.3.3. Fourier Transform Infrared (FTIR) Spectroscopy: Fourier Transform Infrared Spectroscopy is a versatile analytical method employed to identify and characterize the molecular composition and structure of materials. By measuring the absorption of infrared light at various wavelengths, FTIR provides detailed information about the vibrational modes of molecules, which is crucial for understanding chemical bonding and molecular interactions. The principles of FTIR spectroscopy, its instrumentation, experimental procedures, applications, and the advantages and limitations of the technique[12,13] are explored.

Principles: FTIR Spectroscopy is based on the principle that molecules absorb infrared light at specific frequencies corresponding to their vibrational modes. When a sample is exposed to infrared radiation, different molecular bonds absorb light at characteristic frequencies, leading to an absorption spectrum that reflects the molecular structure of the sample.

The technique utilizes the Fourier Transform method to convert the time-domain signal from an interferometer into a frequency-domain spectrum. The interferometer splits the infrared beam into two paths, recombines them, and measures the resulting interference pattern. This pattern, known as an interferogram, is then mathematically transformed into an absorption spectrum using Fourier transformation. The fundamental equation describing the relationship between absorbance and concentration is:

$$A = \log\frac{I_0}{I} \qquad \text{Eq. 2.6}$$

Where I_0 represents the intensity of the incident infrared light, I denotes the intensity of the transmitted light.

Instrumentation and Experimental Procedure: A typical FTIR spectrometer comprises a light source, an interferometer, a sample holder, and a detector. The spectrometer measures the absorbance of infrared light across a wide range of wavelengths to produce a detailed spectrum.

Instrumentation Components:

1. **Light Source:** Provides a broad spectrum of infrared light, commonly using sources like Globar or Mercury-Cadmium-Telluride (MCT) for different infrared regions.
2. **Interferometer:** Contains a beam splitter and mirrors that create an interferogram by producing interference patterns between two beams of infrared light.
3. **Sample Holder:** Holds the sample, which can be a liquid, solid, or gas, and ensures that infrared light passes through or reflects from the sample.
4. **Detector:** Measures the intensity of the transmitted or reflected infrared light and converts it into an electronic signal.

Experimental Procedure:

1. **Sample Preparation:** Depending on the sample type, preparation methods include grinding solids with KBr to form a pellet, placing liquids in an IR-transparent cell, or using attenuated total reflectance (ATR) for direct analysis.
2. **Data Collection:** The sample is exposed to infrared radiation, and the interferogram is recorded by the detector.

3. **Data Analysis:** The interferogram is transformed into an absorption spectrum using Fourier transformation. The resulting spectrum is analyzed to identify characteristic peaks corresponding to various molecular vibrations.

Applications: FTIR Spectroscopy has extensive applications across various fields, including chemistry, materials science, and environmental analysis. Key applications include:

- **Molecular Identification:** Provides detailed information about functional groups and molecular structure by analyzing absorption bands.
- **Quantitative Analysis:** Used to determine the concentration of compounds in a mixture by measuring absorbance at specific wavelengths.
- **Material Characterization:** Characterizes polymers, coatings, and other materials by identifying functional groups and assessing chemical composition.
- **Quality Control:** Ensures the consistency and purity of materials in manufacturing processes by comparing FTIR spectra with reference standards.
- **Environmental Monitoring:** Analyzes pollutants and contaminants in air, water, and soil by detecting specific molecular signatures.

FTIR Spectroscopy is a powerful and versatile technique for molecular characterization and analysis. Its ability to provide detailed information about molecular vibrations and functional groups makes it an essential tool in many scientific and industrial applications. Despite its limitations, FTIR spectroscopy remains a key technique for understanding molecular structure and composition.

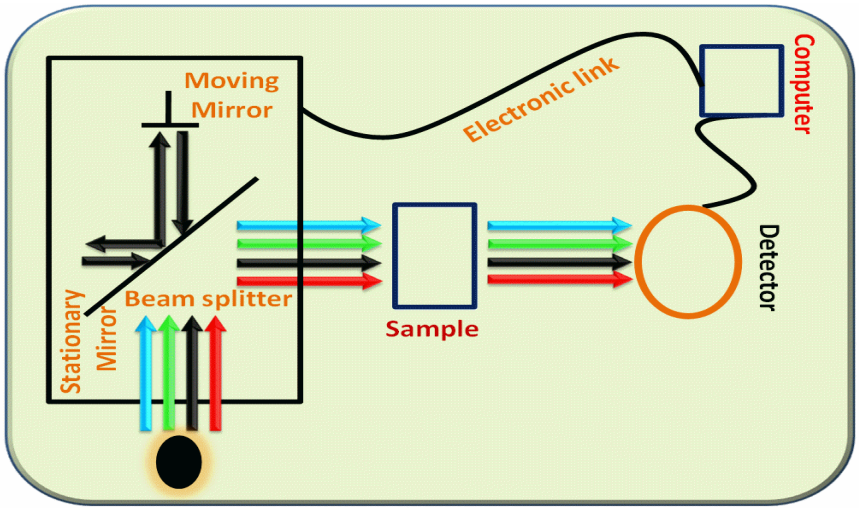

Figure 2.9. Schematic diagram of FTIR instrumentation.

2.3.4. Raman Spectroscopy: Raman Spectroscopy is a non-destructive analytical technique[14] that provides detailed information about molecular vibrations and chemical composition based on the scattering of monochromatic light. It is widely used for characterizing the structure and properties of materials, from organic compounds to inorganic solids and complex mixtures. The following content discusses the principles of Raman Spectroscopy, its instrumentation, experimental procedures, applications, and the advantages and limitations of the technique.

Principles: Raman Spectroscopy relies on the principle of inelastic photon scattering by molecules. When monochromatic light, typically from a laser, strikes a sample, most photons are scattered elastically (Rayleigh scattering). However, a small fraction of photons are scattered inelastically, resulting in a shift in their energy corresponding to molecular vibrations. The Raman shift is defined as the difference in energy between the incident photons and the scattered photons, and it provides information about the vibrational modes of the molecules in the sample. The Raman spectrum is a plot of scattered light intensity versus Raman shift, which reveals the vibrational frequencies of molecular bonds.

The Raman shift $\Delta\nu$ is given by:

$$\Delta\nu = \nu_{0-} \nu \qquad \text{Eq. 2.7}$$

Where ν_0 denotes the frequency of the incident light, ν is the frequency of the scattered light.

This shift corresponds to the vibrational modes of the sample and can be used to identify molecular structures and interactions.

Instrumentation and Experimental Procedure: A typical Raman spectrometer consists of a laser light source, an optical setup for light collection and dispersion, and a detector. The instrument measures the intensity of Raman-scattered light and analyzes its frequency components.

Instrumentation Components:

1. **Laser Light Source:** Provides a monochromatic and intense light source, usually in the visible, near-infrared, or near-ultraviolet regions.
2. **Optical System:** Includes lenses, mirrors, and beam splitters to focus the laser light onto the sample and collect the scattered light.
3. **Spectrometer:** Disperses the scattered light into its component wavelengths using a diffraction grating or prism.
4. **Detector:** Measures the intensity of the dispersed light and records the Raman spectrum. Common detectors include charge-coupled devices (CCDs) and photomultiplier tubes (PMTs).

Experimental Procedure:

1. **Sample Preparation:** Samples are typically prepared as powders, liquids, or thin films. The sample should be placed in a suitable holder to ensure proper interaction with the laser light.
2. **Data Collection:** The sample is irradiated with laser light, and the scattered light is collected. The Raman spectra are recorded by analyzing the scattered light with the spectrometer.
3. **Data Analysis:** The resulting spectrum is analyzed to identify peaks corresponding to different vibrational modes. These peaks provide information about the chemical composition, molecular structure, and interactions of the sample.

Applications: Raman Spectroscopy is used in various fields due to its ability to provide molecular-level information. Key applications include:

- **Material Characterization:** Provides insights into the molecular composition and structure of materials, including polymers, minerals, and nanomaterials.
- **Chemical Identification:** Identifies and characterizes compounds based on their unique Raman spectra, useful in organic and inorganic chemistry.
- **Biological Studies:** Analyzes biological tissues and cells, helping to understand molecular interactions and detect diseases at the cellular level.
- **Pharmaceuticals:** Assesses the composition and quality of pharmaceutical products, including drug formulation and identification.
- **Forensic Analysis:** Detects and identifies substances in forensic investigations, such as drugs and explosives.

Raman Spectroscopy is a powerful analytical tool for obtaining detailed information about molecular vibrations and chemical composition. Its non-destructive nature, minimal sample preparation requirements, and high chemical specificity make it valuable in a wide range of scientific and industrial applications. Despite its limitations, Raman Spectroscopy continues to be an essential technique for characterizing materials and understanding molecular interactions.

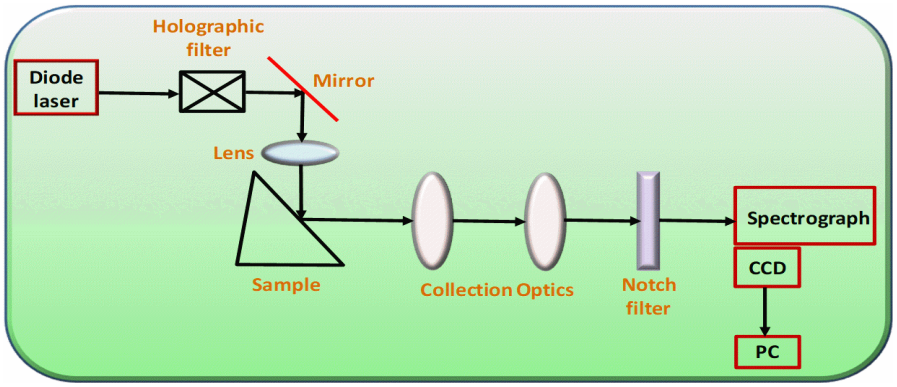

Figure 2.10. Schematic diagram of Raman platform set up.

2.3.5. Photoluminescence (PL) Spectroscopy: Photoluminescence Spectroscopy is a powerful analytical technique[15] used to investigate the optical properties of materials by measuring the light emitted from a sample after it has absorbed photons. This technique is crucial for studying a wide range of materials, including semiconductors, insulators, and biological samples, and provides insights into their electronic structure, optical transitions, and environmental interactions. The discussion includes the principles of PL spectroscopy, its instrumentation, experimental procedures, applications, and the advantages and limitations of the technique.

Principles: Photoluminescence spectroscopy involves the absorption of photons by a material, which excites electrons from a lower energy state to a higher energy state. When these excited electrons transition back to their ground state, they release photons with specific energies. The emitted light is detected and analyzed to gain information about the electronic and optical properties of the material.

Key Concepts:

- **Excitation and Emission:** The process begins with the excitation of electrons by absorbing photons (usually from a UV or visible light source). The electrons then relax back to their ground state, emitting photons in the process. The energy of the emitted photons corresponds to the difference between the excited and ground states.
- **Spectral Information:** The PL spectrum provides information about the energy levels of the material, including band gaps, defect states, and electronic transitions. Peaks in the spectrum correspond to specific optical transitions.
- **Stokes Shift:** The difference between the peak positions of the excitation and emission spectra is known as the Stokes shift. It provides insight into the energy loss mechanisms and relaxation processes within the material.

Instrumentation and Experimental Procedure: A typical PL spectroscopy setup includes a light source for excitation, an optical system for collecting emitted light, a monochromator or spectrograph for dispersion, and a detector for measuring the intensity of the emitted light.

Instrumentation Components:

1. **Light Source:** Provides the excitation energy needed to excite electrons in the sample. Common sources include mercury lamps, xenon lamps, and lasers, with the selection depending on the specific excitation wavelength required.
2. **Optical System:** Includes lenses and mirrors to focus the excitation light on the sample and to collect the emitted light. The optical system ensures that the maximum amount of emitted light reaches the detector.
3. **Monochromator/Spectrograph:** Dispenses the collected light into its constituent wavelengths. This component separates the light into its spectral components, allowing for detailed analysis of the emission spectrum.
4. **Detector:** Measures the intensity of the emitted light at various wavelengths. Common detectors include photomultiplier tubes (PMTs), charge-coupled devices (CCDs), and photodiodes.

Experimental Procedure:

1. **Sample Preparation:** The sample is prepared and placed in the spectrometer. It should be optically clean and, in some cases, need to be cooled to reduce thermal effects that may affect luminescence.
2. **Excitation:** The sample is illuminated with light from the chosen excitation source. The wavelength and intensity of the excitation light are carefully controlled.
3. **Emission Collection:** The emitted light from the sample is collected and directed through the monochromator or spectrograph.
4. **Spectral Analysis:** The spectrum of the emitted light is recorded. The peaks and their intensities are analyzed to determine the optical properties and electronic transitions of the material.

Applications: PL Spectroscopy is employed in a diverse range of fields due to its ability to provide detailed information about electronic and optical properties. Key applications include:

- **Semiconductor Research:** Analyzes band gaps, exciton binding energies, and defect states in semiconductors. It is essential for the development and characterization of optoelectronic devices such as LEDs and solar cells.

- **Material Science:** Investigates the optical properties of novel materials, including nanomaterials and quantum dots, to understand their potential applications and performance.
- **Biology and Medicine:** Studies the photoluminescence of fluorescent probes and biomarkers to track biological processes, visualize cellular structures, and diagnose diseases.
- **Environmental Science:** Assesses the fluorescence properties of environmental samples, such as pollutants and natural substances, to monitor contamination and study environmental interactions.
- **Quantum Computing:** Examines the optical properties of quantum dots and other quantum materials to explore their potential use in quantum computing and information processing.

PL Spectroscopy is a versatile and informative technique for investigating the optical and electronic properties of materials. Its ability to provide detailed information about electronic transitions, energy levels, and defect states makes it invaluable in fields such as materials science, biology, and environmental science. Despite some limitations, such as the need for careful sample preparation and potential interference issues, PL spectroscopy remains a fundamental tool for advancing our understanding of material properties and developing new technologies.

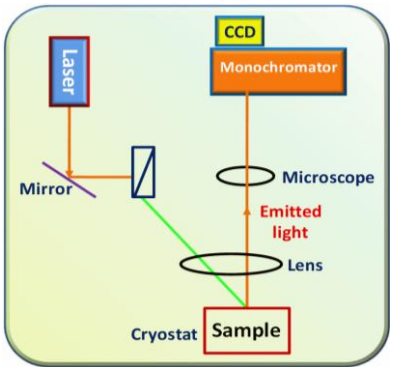

Figure 2.11. Schematic diagram of the Photoluminescence set up.

2.4. Electrochemical Analysis: Electrochemical analysis is a pivotal technique in both fundamental and applied chemistry, enabling the investigation of chemical reactions and processes through the measurement of electrical properties.[16,17] Techniques such as cyclic voltammetry, linear sweep voltammetry and electrochemical impedance spectroscopy (EIS) assess the catalytic performance of the material. This technique involves studying the relationship between electrical currents and chemical changes, providing insights into reaction mechanisms, material properties, and sensor

development. The following content outlines the principles of electrochemical analysis, details its instrumentation and experimental procedures, discusses its applications, and explores its advantages and limitations.

Principles: Electrochemical analysis is based on the principles of electrochemistry, which explores the interaction between electrical energy and chemical reactions. The technique typically involves measuring parameters such as current, voltage, and charge to study redox reactions, conductance, and electrode processes.

Key Concepts:

- **Electrochemical Cells:** An electrochemical cell comprises two electrodes (anode and cathode) placed in an electrolyte solution. Reactions occur at the electrodes, leading to changes in current and potential that can be measured.
- **Redox Reactions:** Electrochemical analysis often focuses on redox (reduction-oxidation) reactions, where electrons are transferred between species. The electrode potentials associated with these reactions are critical for understanding reaction mechanisms.
- **Electrode Potential:** The potential difference between the working electrode and a reference electrode is used to drive the electrochemical reactions. The measured electrode potential provides information about the reaction's driving force and equilibrium.

Instrumentation and Experimental Procedure: Electrochemical analysis involves several key components: electrochemical cells, electrodes, and measurement systems. Each component plays a role in the accurate measurement and analysis of electrochemical processes.

Instrumentation Components:

1. **Electrochemical Cell:** Comprises the working electrode, counter electrode, and reference electrode, all placed in an electrolyte solution. The cell setup ensures proper contact and reaction conditions.
2. **Electrodes:**
    - **Working Electrode:** The electrode where the reaction of interest occurs. It can be made from materials such as glassy carbon, platinum, or gold.
    - **Counter Electrode:** Completes the circuit by allowing current to flow through the cell. It is typically made of an inert material like platinum.
    - **Reference Electrode:** Provides a stable and known reference potential, such as a silver/silver chloride (Ag/AgCl) or calomel electrode.

3. **Potentiostat/Galvanostat:** Controls the potential difference between the working and reference electrodes and measures the resulting current. This instrument is essential for performing techniques like cyclic voltammetry and chronoamperometry.
4. **Data Acquisition System:** Records and analyzes the data obtained from the potentiostat/galvanostat, generating plots and curves for interpretation.

Experimental Procedure:

1. **Cell Preparation:** Assemble the electrochemical cell with the chosen electrodes and electrolyte solution. Ensure that the cell is properly sealed and free from contamination.
2. **Electrode Conditioning:** Prepare and condition the electrodes to ensure reproducibility and accuracy of measurements. This may involve polishing or cleaning the electrode surfaces.
3. **Measurement:** Apply a controlled potential or current to the working electrode and measure the resulting response. Techniques such as cyclic voltammetry (CV), chronoamperometry (CA), and impedance spectroscopy can be used depending on the analysis requirements.
4. **Data Analysis:** Analyze the recorded data to determine key electrochemical parameters such as redox potentials, current densities, and reaction kinetics. Interpret the results in the context of the material or reaction being studied.

2.4.1. Key Techniques in Electrochemistry: In electrochemical research, a variety of techniques are employed to analyze and optimize electrochemical processes. Among these, cyclic voltammetry (CV), linear sweep voltammetry (LSV), chronoamperometry (CA), and electrochemical impedance spectroscopy (EIS) are fundamental for investigating the electrochemical behavior of materials. Each technique provides unique insights into different aspects of electrochemical systems.

2.4.1.1. Cyclic Voltammetry. CV is a widely used technique to study the redox properties of electrochemical systems. In CV, the electrode potential is swept back and forth between two values at a constant scan rate ν. The resulting current response is recorded to generate a cyclic voltammogram. CV provides information about the electrochemical reversibility of reactions, the kinetics of electron transfer, and the stability of the electrochemical system. Key features of the CV curve include the peak current I_p, peak potential E_p, and the separation between the anodic and cathodic peaks, which can be used to infer reaction mechanisms and kinetics.

The Randles-Sevcik equation provides a crucial relationship in CV that describes how the peak current (I_p) of a redox reaction depends on the scan rate (ν) during an electrochemical experiment. This equation helps to understand the kinetics of the electrochemical reaction and the diffusion characteristics of the electrochemical process under study.

The Randles-Sevcik equation is given by:

$$I_p = 2.69 \times 10^5 n^{3/2} A D^{1/2} C_0 \nu^{1/2} \quad \text{Eq. 2.8}$$

Where I_p denotes the peak current (in amperes, A), n represents the number of electrons transferred in the redox reaction, A is the electrode area (in cm^2), D is the diffusion coefficient of the electroactive species (in $cm^2\ s^{-1}$), C_0 is the concentration of the electroactive species in the bulk solution (in mol cm^{-3}), ν is the scan rate (in $V\ s^{-1}$).

2.4.1.2. Linear Sweep Voltammetry. LSV involves a continuous, linear change in the electrode potential over time. The resulting current response is plotted against the potential to produce a voltammogram.

The current I in LSV can be described by:

$$I = I_a(E - E_a) \quad \text{Eq. 2.9}$$

Where I_a is the current due to the anodic reaction, E is the applied potential, and E_a is the anodic peak potential.

LSV is particularly useful for determining the onset potential of a reaction and assessing the catalytic activity of electrochemical systems. By examining the shape and position of the voltammogram, researchers can evaluate the efficiency and performance of catalysts and optimize operating conditions.

2.4.1.3. Chronoamperometry. CA involves applying a step change in electrode potential and measuring the resulting current as a function of time.

The current I(t) following a potential step can be described by the Cottrell equation:

$$I(t) = \frac{nFAD^{1/2}C_0}{\sqrt{\pi t}} \quad \text{Eq. 2.10}$$

Where n is the number of electrons involved in the reaction, F is the Faraday constant, A is the electrode area, D is the diffusion coefficient, C_0 is the concentration of the electroactive species, and t is time.

CA is used to study reaction kinetics, mass transport processes, and the stability of electrochemical systems. The time-dependent current response provides insights into the rate of reaction and the durability of the electrode material.

2.4.1.4. Electrochemical Impedance Spectroscopy (EIS). EIS is a technique used to analyze the impedance of an electrochemical system over a range of frequencies.[18]

The impedance Z is given by:

$$Z = \frac{V}{I} = Z' + jZ'' \qquad \text{Eq. 2.11}$$

Where Z' is the real part, Z'' is the imaginary part, and j is the imaginary unit.

The impedance can also be expressed in polar form as:

$$Z = |Z| e^{j\theta} \qquad \text{Eq. 2.12}$$

Where $|Z|$ is the magnitude and θ is the phase angle.

The Nyquist plot is a common way to represent EIS data, where the real part Z' is plotted against the negative imaginary part $-Z''$.

Nyquist plot: Z' vs. $-Z''$

This plot typically exhibits semicircles, where the diameter of the semicircle corresponds to the charge transfer resistance R_{ct}, and the high-frequency intercept with the real axis provides the solution resistance R_s.

Equivalent circuit models are used to interpret EIS data. The Randles circuit, a simple but widely used model, includes:

- **Solution Resistance (R_s):** Represents the resistance of the electrolyte.
- **Charge Transfer Resistance (R_{ct}):** Represents the resistance to charge transfer at the electrode surface.
- **Double-Layer Capacitance (C_{dl}):** Represents the capacitance of the electrical double layer.

The impedance of the Randles circuit is given by:

$$Z_{Randles} = R_S + \frac{1}{\frac{1}{R_{ct}} + jwC_{dl}} \qquad \text{Eq. 2.13}$$

Where ω is the angular frequency of the AC signal ($\omega = 2\pi f$).

For more complex systems, additional elements such as Warburg impedance and constant phase elements (CPE) may be included.

Warburg impedance Z_W can be expressed as:

$$Z_w = \frac{\sigma}{\sqrt{jw}} \qquad \text{Eq. 2.14}$$

and a CPE can be described by:

$$Z_{CPE} = \frac{1}{Q(jw)^n} \qquad \text{Eq. 2.15}$$

Where Q is the CPE constant and n is the exponent.

Together, CV, LSV, CA, and EIS provide a comprehensive toolkit for analyzing electrochemical systems. Each technique offers unique insights into different aspects of electrochemical behavior, from redox properties and reaction kinetics to impedance characteristics and system performance. By utilizing these techniques, researchers can gain a deeper understanding of electrochemical processes and optimize the design and functionality of electrochemical devices.

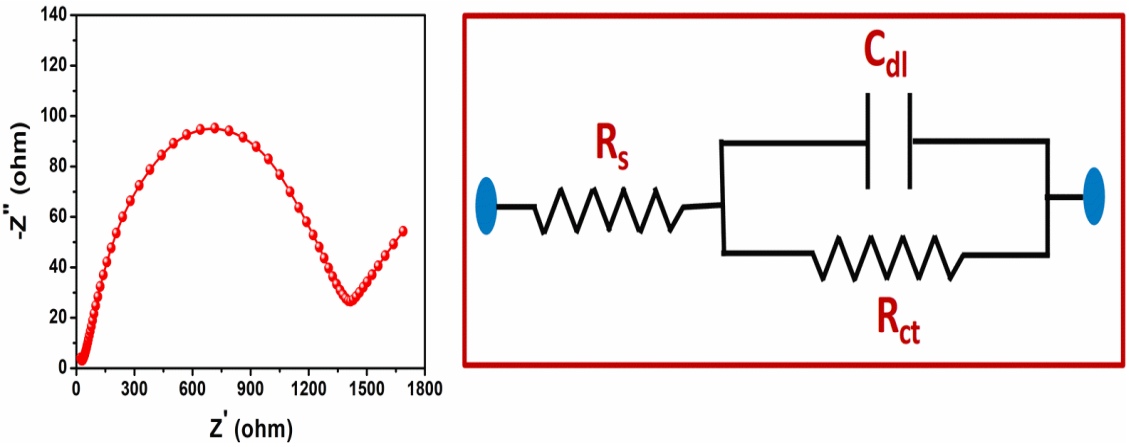

Figure 2.12. (a) Nyquist's plot (b) equivalent circuit model based on the Randles cell model.

2.4.2. Applications: Electrochemical analysis is instrumental in evaluating and optimizing various applications, particularly in studying the performance of catalysts and sensors. Its applications span across several critical areas:

2.4.2.1. Hydrogen Evolution Reaction (HER): This technique assesses catalysts used for hydrogen production. By analyzing metrics such as onset potential, current density, and overpotential, electrochemical analysis provides insights into the catalytic efficiency and performance of HER catalysts, which are essential for hydrogen fuel production.[19]

2.4.2.2. Oxygen Evolution Reaction (OER): For catalysts involved in oxygen generation, electrochemical analysis measures their effectiveness in water splitting processes. It provides data on the catalysts' activity, stability, and the energy required for oxygen production, helping in the development of efficient OER catalysts for renewable energy applications.[20,21,22]

2.4.2.3. Oxygen Reduction Reaction (ORR): In fuel cells and other electrochemical devices, ORR catalysts are evaluated to understand their efficiency in reducing oxygen to water. Electrochemical analysis reveals important details about catalytic activity, reaction kinetics, and long-term stability, which are crucial for enhancing fuel cell performance and lifespan.[23]

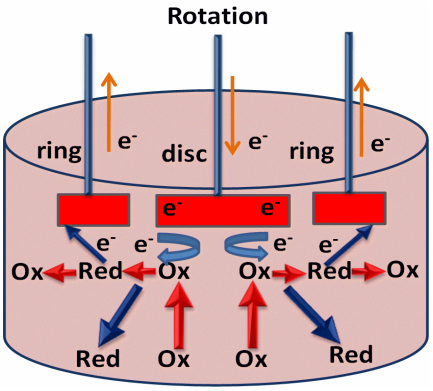

Figure 2.13. Schematic diagram of RRDE configuration during ORR.

2.4.2.4. Overall Water Splitting (OWS): Electrochemical methods are used to study catalysts involved in the overall water electrolysis reaction, where both HER and OER occur. This analysis provides a comprehensive understanding of the catalysts' performance in generating hydrogen and oxygen from water, supporting advancements in sustainable energy technologies.[24]

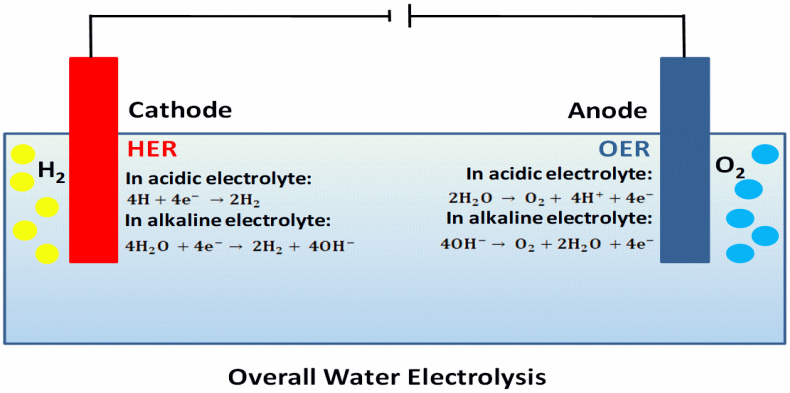

Figure 2.14. Schematic diagram of overall water electrolysis.

2.4.2.5. Sensing Applications: Electrochemical analysis is also vital for developing and optimizing sensors used in detecting various substances, including gases, ions, and biomolecules. It offers insights into the sensitivity, selectivity, and stability of electrochemical sensors, enabling precise and reliable measurements in environmental monitoring, healthcare, and industrial processes.[25,26]

Overall, electrochemical analysis provides essential data on the activity, stability, and efficiency of catalysts and sensors, driving progress in energy conversion, environmental monitoring, and advanced material development.

2.5. Photoelectrochemical Analysis (PEC): Photoelectrochemical analysis is a powerful technique that combines the principles of photochemistry and electrochemistry to investigate the interaction between light and electrochemical processes, such as energy conversion and environmental remediation.[27] To thoroughly analyze and optimize photoelectrochemical systems, a combination of electrochemical techniques and semiconductor characterization methods is employed. These techniques include CV, LSV, CA, EIS, as well as Mott-Schottky analysis, band gap determination, and HOMO-LUMO energy levels. Here, we integrate these methods to provide a comprehensive understanding of photoelectrochemical systems.

2.5.1. Cyclic Voltametry. In photoelectrochemistry, CV is employed to investigate the redox properties of photoactive materials under illumination. CV helps in understanding how light affects the electrochemical behavior of these materials by cycling the electrode potential and observing the resulting current. This technique provides critical information about the electrochemical reversibility of photo-induced reactions, the stability of the photoelectrodes, and the efficiency of light-induced charge separation and transfer. The shape of the cyclic voltammogram, including peak currents and potentials, reflects the performance and mechanisms of photoelectrochemical processes.

2.5.2. Linear Sweep Voltametry. LSV is used to evaluate the performance of photoelectrodes by applying a linearly increasing potential and recording the resulting current. This technique is particularly useful for determining the onset potentials of photoinduced reactions and assessing the catalytic activity of photoelectrodes. The data obtained from LSV can reveal the efficiency of light absorption, charge separation, and the overall photoelectrochemical performance of the material. LSV is instrumental in optimizing the conditions for photoelectrochemical reactions and improving the design of photoelectrochemical systems.

2.5.3. Chronoamperometry. CA provides insights into the time-dependent behavior of photoelectrochemical reactions. By applying a step change in potential and monitoring the resulting current over time, CA reveals the dynamics of photo-induced charge transfer processes and the stability of photoelectrochemical systems. This technique is valuable for studying the transient response of photoelectrodes to illumination and understanding the kinetics of light-induced reactions. The time-course analysis of current can help in evaluating the durability and efficiency of photoelectrodes under continuous illumination.

2.5.4. Electrochemical Impedance Spectroscopy. EIS is a powerful technique for characterizing the impedance of photoelectrochemical systems across a range of frequencies. EIS provides detailed information about the resistive and capacitive properties of photoelectrodes, including charge transfer

resistance, double-layer capacitance, and diffusion processes. The Nyquist plot, commonly used in EIS, offers insights into the resistance and capacitance associated with the photoelectrode interface, while equivalent circuit modeling helps in interpreting the impedance data. EIS is crucial for understanding the charge transport dynamics, evaluating the efficiency of photoelectrochemical reactions, and optimizing the performance of photoelectrochemical devices.

2.5.5. Mott-Schottky Analysis. Mott-Schottky analysis provides essential information about the electronic properties of semiconductor materials used in photoelectrochemistry. This technique involves measuring the capacitance of a semiconductor electrode as a function of the applied potential. The key parameters derived from Mott-Schottky analysis include the carrier concentration and the flat band potential.

The Mott-Schottky equation relates the capacitance C to the applied potential E:

$$\frac{1}{C^2} = \frac{2}{e\epsilon\epsilon_0 N_D}\left(E - E_{FB} - \frac{K_B T}{e}\right) \qquad \text{Eq.2.16}$$

Where e is the elementary charge (1.602×10^{-19} C), ϵ is the relative permittivity (dielectric constant) of the semiconductor, ϵ_0 is the permittivity of free space (8.854×10^{-12} F m^{-1}), N_D is the donor density (for n-type semiconductors) or acceptor density (for p-type semiconductors), E_F is the Fermi level.

Carrier concentration: The slope of the Mott-Schottky plot ($1/C^2$ vs potential) reveals the density of charge carriers in the semiconductor.

- **Flat band potential**: The flatband potential, obtained from the intercept of the Mott-Schottky plot, indicates the potential at which the charge distribution in the semiconductor is flat.

Mott-Schottky analysis helps in understanding the electronic structure of the photoelectrode, which is essential for optimizing its performance in photoelectrochemical reactions.

2.5.6. Band Gap Determination. The band gap of a semiconductor material determines its ability to absorb light and drive photoelectrochemical reactions. Band gap determination can be achieved using methods such as:

- **Tauc's Plot**: The optical band gap can be estimated by plotting $(\alpha h\nu)^2$ vs $h\nu$, where α denotes the absorption coefficient and $h\nu$ represents the photon energy. The band gap E_g is obtained by extrapolating the linear portion of the plot to the energy axis.

$$(\alpha h\nu)^2 = A(h\nu - E_g) \qquad \text{Eq.2.17}$$

Where α is the absorption coefficient, $h\nu$ is the photon energy, A is a constant related to the transition probability.

- **Photoluminescence (PL)**: The emission spectrum of the material under excitation can also be used to estimate the band gap by analyzing the emission peaks

Knowledge of the band gap is critical for designing photoelectrodes that can efficiently absorb light and participate in desired photoelectrochemical reactions.

2.5.7. HOMO-LUMO Energy Levels. The HOMO-LUMO energy levels are fundamental for understanding the electronic transitions and charge transfer processes in photoelectrochemical systems. It is related to the band gap in semiconductors and is indicative of the energy required for electronic transitions.

$$E_g = E_{LUMO} - E_{HOMO} \qquad \text{Eq. 2.18}$$

Where E_{LUMO} represents the energy of the Lowest Unoccupied Molecular Orbital and E_{HOMO} represents the energy of the Highest Occupied Molecular Orbital.

These energy levels are related to:

- **Charge Transfer Efficiency**: The alignment of HOMO and LUMO levels with the redox potentials of the photoelectrochemical reactions influences the efficiency of charge transfer between the photoelectrode and the electrolyte.
- **Design of Photoelectrodes**: By selecting materials with appropriate HOMO-LUMO energy levels, researchers can enhance the photoelectrochemical performance and optimize the reaction pathways.

Techniques such as UV-Vis spectroscopy and cyclic voltammetry can be used to estimate the HOMO-LUMO energy levels, providing insights into the electronic structure of the photoelectrode materials.

The integration of CV, LSV, CA, EIS, Mott-Schottky analysis, band gap determination, and HOMO-LUMO energy levels provides a comprehensive toolkit for analyzing and optimizing photoelectrochemical systems. Each technique offers unique insights into the electronic properties, charge transfer dynamics, and efficiency of photoelectrodes, facilitating the development of advanced photoelectrochemical technologies for sustainable energy and environmental applications.

In the following chapters, we delved into detailed case studies and applications of the analysis techniques discussed in this chapter. These examples will illustrate how these methods contribute to a deeper understanding of the materials being studied and highlight their importance in advancing both the characterization and application of the synthesized materials.

REFERENCES

(1) He, B.B., *Two-dimensional X-ray Diffraction*. John Wiley & Sons. Edition 2, New Jersey & Canada, **2018**, 1-426, ISBN: 9780470502648, DOI: 10.1002/9780470502648.

(2) Van der Heide, P. 2011. *X-ray photoelectron spectroscopy: an introduction to principles and practices*. John Wiley & Sons, Inc. **2011**, 1-237. ISBN: 9781118162897, DOI: 10.1002/9781118162897.

(3) https://en.wikipedia.org/wiki/Scanning_electron_microscope.

(4) Mignot, C. *Color (and 3D) for scanning electron microscopy*, Microscopy Today, Volume 26, Issue 3, **1 May 2018**, 12-17, DOI: 10.1017/S1551929518000482.

(5) https://en.wikipedia.org/wiki/Transmission_electron_microscopy.

(6) Franken, L.E.; Grünewald, K.; Boekema, E.J. and Stuart, M.C. A technical introduction to transmission electron microscopy for soft-matter: Imaging, possibilities, choices, and technical developments. *Small*, **2020**, *16*, 1906198 (1-15).

(7) Thomas, J.M. and Midgley, P.A. High-resolution transmission electron microscopy: the ultimate nanoanalytical technique. *Chemcomm.* **2004**, 11, 1253-1267.

(8) Hamuyuni, J.; Daramola, M.O. and Oluwasina, O.O.; Energy-Dispersive X-Ray Spectroscopy: Theory and Application in Engineering and Science. *Encyclopedia of Phys. Org. Chem.* **2016,** 1-23.

(9) Ambroz, F.; Macdonald, T.J.; Martis, V.; Parkin, I.P. Evaluation of the BET theory for the characterization of meso and microporous MOFs. *Small Methods* **2018**, 2, 1800173 (1-17).

(10) Torrent, J.O.S.E. and Barron, V. *Diffuse Reflectance Spectroscopy*, Methods of Soil Analysis Part 5-Mineralogical Methods, **2008**, 367-385. ISBN: 9780891188575, DOI: 10.2136/sssabookser5.5.c13.

(11) Tissue, B. M. *Ultraviolet and Visible Absorption Spectroscopy*. Characterization of Materials, Edition 2, **2012**, 1-13, DOI: 10.1002/0471266965.com059.pub2.

(12) https://en.wikipedia.org/wiki/Fourier-transform_infrared_spectroscopy.

(13) Griffiths P. R. , De Haseth J. A. *Fourier Transform Infrared Spectrometry*, Chemical Analysis: A Series of Monographs on Analytical Chemistry and Its Applications, John Wiley & Sons, 2006, ISBN: 9780470106310, DOI: 10.1002/9780470106310.ch4.

(14) https://en.wikipedia.org/wiki/Raman_spectroscopy.

(15) Toney J. E. *Photoluminescence Spectroscopy*, Characterization of Materials, Spire Corporation, Bedford, Massachusetts, **2012**, 681-688, DOI: 10.1002/0471266965.com058.pub2

(16) Bard, A. J.; Faulkner, L. R. and White, H.S. *Electrochemical methods: fundamentals and applications*. John Wiley & Sons, **2022**, Edition 3, ISBN: 978-1-119-33405-7.

(17) Bockris, J.O.M. and Reddy, A.K. *Modern electrochemistry 2B: electrodics in chemistry, engineering, biology and environmental science*. Springer Science & Business Media, **1998**, 1539-2040, ISBN 0-306-48036-0.

(18) Wang, S.; Zhang, J.; Gharbi, O.; Vivier, V.; Gao, M. and Orazem, M.E. Electrochemical impedance spectroscopy. *Nat. Rev. Methods Primers* **2021**, *1*, 41 (1-58).

(20) Zou, X. and Zhang, Y. Noble metal-free hydrogen evolution catalysts for water splitting. *Chem. Soc. Rev*. **2015**, 44, 5148-5180.

(21) Li, X.; Cheng, Z. and Wang, X. Understanding the mechanism of the oxygen evolution reaction with consideration of spin. *Electrochem. Energy Rev*. **2021**, *4*, 136-145.

(22) Yoo, J. S.; Rong, X.; Liu, Y. and Kolpak, A. M. Role of lattice oxygen participation in understanding trends in the oxygen evolution reaction on perovskites. *ACS Catal*. **2018**, *8*, 4628-4636.

(23) Suntivich, J.; May, K. J.; A.Gasteiger, H.; Goodenough, J. B. and Shao-Horn, Y. A perovskite oxide optimized for oxygen evolution catalysis from molecular orbital principles. *Science* **2011**, *334*, 1383-1385.

(24) Ghorui, U.K.; Show, B.; Roy, D.; Basak, A.; Adhikary, B. and Mondal, AStrategically designed Pd-induced changes in alkaline hydrogen evolution reaction and oxygen evolution reaction performances of electrochemical water oxidation by the galvanically synthesized MoO_2/MoO_3 composite thin film. *ACS Appl. Mater. Interfaces* **2024**, *16*, 3460-3475.

(25) Baranwal, J.; Barse, B.; Gatto, G.; Broncova, G. and Kumar, A. Electrochemical sensors and their applications: A review. *Chemosensors* **2022**, *10*, 363 (1-22).

(26) Singh, R.; Gupta, R.; Bansal, D.; Bhateria, R. and Sharma, M. A review on recent trends and future developments in electrochemical sensing. *ACS Omega* **2024**, *9*, 7336-7356.

(27) https://en.wikipedia.org/wiki/Photoelectrochemistry.

CHAPTER 3

Tetraphenylporphyrin decorated Bi_2MoO_6 nanocomposites: its twin affinity of oxygen reduction reaction and electrochemical detection of 4-nitrophenol

Objectives

Creating efficient electrocatalysts through surface modification to enhance the catalytic activities

GRAPHICAL ABSTRACT

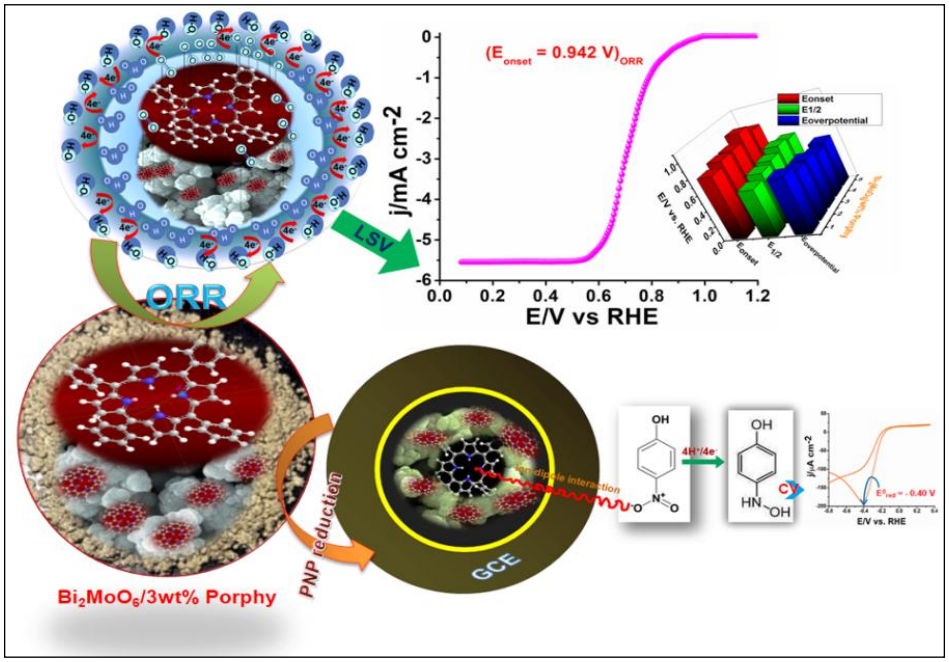

HIGHLIGHTS

- Bi_2MoO_6/H_2TPP, a cost-effective, ingenious organic-inorganic heterostructured nanocatalyst with high active site density, high electrochemical surface area (ECSA), and good stability, enhances good catalytic activity.
- Pyrrolic- and pyridinic-N atoms in C, N-based mesoporous materials enforce O_2 adsorption, boosting ORR activities with a high onset potential (0.942 V).
- Electrochemical sensor for detection of 4-Nitrophenol with good reproducibility, stability, low RSD (3.75%) and also applied for real matrix samples.

ABSTRACT

A selective electrode for Oxygen Reduction Reaction (ORR) and electrocatalytic reduction of 4-nitrophenol (p-NP) was fabricated on glassy carbon electrode using organic-inorganic Bi_2MoO_6/H_2TPP nanocomposites with different wt % tetraphenylporphyrin, synthesized by the solvothermal process. Materials thus synthesized were characterized through UV-Vis diffuse reflectance spectroscopy, X-ray photoelectron spectroscopy (XPS), Field emission scanning electron microscopy (FE-SEM), Energy dispersive X-ray spectroscopy (EDX), High-resolution transmission electron microscopy (HR-TEM), Fourier transform Infrared spectroscopy (FTIR) and X-ray diffraction (XRD) analysis. The electrocatalytic performance of the modified electrode toward ORR in 0.1 M KOH solution, the onset potential E_{onset} (0.942 V), $E_{½}$ (0.704 V) vs. RHE, J_d (-5.545 mA cm^{-2}) and n = 4 physicochemical parameters were well appreciable. It exhibits good catalytic activity toward ORR through a four-electron pathway with excellent stability and high active site density, and thus the in-situ Porphy decorated metal oxide system facilitates the electron transport process. High selectivity and efficacy for the oxygen reduction reaction (ORR) is a significant measure for several energy-converting applications. The decorated electrode, GCE/Bi_2MoO_6/3 wt % Porphy serves as an electrochemical sensor that exhibited good sensitivity (0.4683 μA μM^{-1} cm^{-2}), good reproducibility, a low detection limit (0.0940 μM), and long-term stability in the aqueous phase without any appreciable effect in the presence of some common organic and inorganic interferences for the detection of p-NP in a linear concentration range of 0.5-350 μM. Therefore, the material performs as an effective electrode for both the ORR and the electrocatalytic reduction of p-NP with real matrix samples at room conditions.

KEYWORDS: Mixed-Metal oxide, Tetraphenylporphyrin, Oxygen Reduction Reaction, Electrochemical Sensor, Interference Effects.

3.1. INTRODUCTION

Advanced technologies for sustainable energy storage and conversion have received a great deal of scientific and industrial consideration in recent years owing to the quickened consumption of fossil fuels and consequent environmental pollution.[1] There have been many attempts to develop renewable proton exchange membrane fuel cells (PEMFC) and rechargeable metal-air batteries (MAB), microbial fuel cells, and water splitting for profitable clean power generation.[2] Conversely, microbial fuel cells that convert waste into electrical energy are notable due to their environmental acceptability, rich in resources and their mild operating procedures. Oxygen is generally used as the oxidant in fuel cells, where an enormous amount of energy is extracted from the fuel, yielding water that is a toxicless safe reduced product. However, facing difficulties in cleaving the O=O bond with a binding energy of 498 kJ mol^{-1} by an electrochemical process, Pt and Pt-based alloy nanoparticles are believed to be effective ORR catalysts.[3] But Pt-based catalysts are less tolerant to methanol[4] and generate CO, which blocks the active sites of Pt and reduces catalytic activity. It is an ideal situation to develop a new low-cost, active, and ORR-prone catalyst to replace Pt-based catalysts in wide range of applications.[5] Furthermore, the growing global concern over ecological effluence has prompted important research on heterogeneous photocatalysis, trying to construct a nanocomposite material serving against remediation of water and atmospheric organic pollutants.[6] The US Environmental Protection Agency (EPA)[7] has designated P-nitrophenol, a class of substituted phenols, as a priority pollutant due to its negative effects on human, animal, and plant growth and metabolism.[8,9] The concentration of environmentally friendly p-NPs must be accurately determined. Earlier reports on p-NP sensing have mostly focused on gas chromatography, liquid chromatography, capillary electrophoresis, fluorescence detection, UV-Vis spectrophotometry, and high-performance liquid chromatography. These techniques have some limitations for the broad application of p-NP sensing due to their pre-treatment complications, low selectivity, and high cost of equipment. Electrochemical detection has become a beneficial technique due to its accuracy, sensitivity, stability, short detection time, and low cost.[10] Electrode modification and microstructure tuning is a crucial step in developing new materials to improve electrochemical performance.

In recent times, metal molybdate ($MMoO_4$ and $M_2O_3.nMoO_3$, where M = metal) based electrodes have been used in lithium-ion batteries and supercapacitors due to their stable crystal structure and redox behaviour of the metals (Ni, Co, Mn) in aqueous alkaline electrolytes.[11] Bismuth molybdates are an important class of semiconductor materials with the general chemical formula $Bi_2O_3.nMoO_3$ (n = 3, 2, 1). Bismuth molybdate (Bi_2MoO_6) is a typical layered ternary oxide,[12]

comprising of $[Bi_2O_2]^{2+}$ layers sandwiched between $[MoO_4]^{2-}$ slabs,[13] and is an excellent electrode material for different applications. Metalloporphyrins have become very popular catalysts for oxygen reduction as well as for oxygen activation. Several cobalt porphyrins were effectively used for direct ORR at low overpotentials to substitute platinum catalysts.[14] Metalloporphyrins, the basis of artificial photosynthetic systems, are designed to generate electricity and facilitate the splitting of water into H_2 and O_2.[15,16] Cobalt porphyrins with MWCNTs demonstrate oxygen reduction activities in different media (acidic, basic, neutral media, etc.).[17] Among various metalloporphyrins, complexes of meso-tetraphenylporphyrin (MTPP) complexes have been notably studied due to their reasonably high synthetic yields and ease of purification.[18]

In light of these thoughts, a new type of organic-inorganic nanocatalyst, Bi_2MoO_6/Tetraphenylporphyrin (Bi_2MoO_6/Porphy), was efficiently prepared and investigated the loading effect of tetraphenylporphyrin (H_2TPP) over Bi_2MoO_6 nanospheres on their catalytic performance. To the best of the author's information, the synthesis and studies of Bi_2MoO_6/Porphy composites were performed for the first time to determine the impact of functionalization on ORR, supported by kinetic studies, and the electrochemical performances for p-NP sensing were evaluated using modified glassy carbon electrode (GCE). The activity of Bi_2MoO_6 is remarkably enhanced upon the loading of Porphy, providing pyrrolic- and pyridinic-N atoms.[19] Bi_2MoO_6/Porphy shows excellent catalytic activity and persistent stability with high current density, low η, and also with a low Tafel slope.

3.2. EXPERIMENTAL SECTION

3.2.1. Materials. All the chemicals were used as received. Analytical grade Pyrrole (C_4H_5N), Benzaldehyde (C_7H_6O), Bismuth nitrate ($Bi(NO_3)_3.5H_2O$), Sodium molybdate ($Na_2MoO_4.2H_2O$), Ethanol (EtOH), Methanol (CH_3OH), Commercial Pt/C catalyst (20 wt % Pt), Ethylene glycol ($C_2H_6O_2$), Propionic acid ($CH_3CH_2CO_2H$), Sulfuric acid (H_2SO_4), Phosphoric acid (H_3PO_4), Potassium hydroxide (KOH), Sodium hydroxide (NaOH), Nafion ($C_7HF_{13}O_5S{\cdot}C_2F_4$), p-Nitrophenol ($C_6H_5NO_3$), Potassium chloride (KCl), Potassium ferricyanide ($K_3Fe(CN)_6$), Potassium ferrocyanide ($K_4Fe(CN)_6$), Disodium hydrogen phosphate (Na_2HPO_4) were purchased from Sigma-Aldrich. All water used throughout the experiments was demineralized and ultra-filtered by a Millipore Milli-Q system (resistivity >18.2 MΩ, TOC < 5 ppb).

3.2.2. Synthesis of Materials

3.2.2.1. Synthesis of Bi_2MoO_6 nanoparticles. Under controlled conditions, Bi_2MoO_6 nanoparticles were synthesized by a facile solvothermal process. First, 2 mmol of bismuth nitrate ($Bi(NO_3)_3.5H_2O$) and 2 mmol of sodium molybdate ($Na_2MoO_4.2H_2O$) were separately added to 20 mL of ethylene glycol solution and sonicated for 20 min to get a homogeneous suspension. The mixture was then transferred to a 50 ml Teflon-lined stainless steel autoclave and heated at 160 °C for 15 hours. After cooling it to room temperature, the precipitate was centrifuged and washed several times with deionized water and ethanol. After that, the product was dried under a vacuum at room temperature.

3.2.2.2. Synthesis of Bi_2MoO_6/Porphy nanocomposites. For the above mentioned synthesis route of Bi_2MoO_6 nanoparticles, a certain weight percent of Porphy was added to the homogenous suspended phase and sonication was done for another 30 minutes for complete dispersion. Again, the mixture solution was transferred to a Teflon-lined 50 ml stainless steel autoclave, heated at 160 °C for 15 hours, cooled, washed as above, and finally procured the nanocomposite system, i.e., Bi_2MoO_6/Porphy. For a better understanding of different electrocatalytic as well as electroactive performances, a series of Bi_2MoO_6/Porphy composites with different Porphy mass ratios ranging from 0% to 4% were fabricated (**Scheme 3.1**).

3.2.2.3. Synthesis of tetraphenylporphyrin (H_2TPP). Tetraphenylporphyrin was synthesized by taking 40 mL of propionic acid in a 100 mL round-bottom flask fitted with a reflux condenser and boiled vigorously. A mixture of an equimolar amount of (0.03 mol) benzaldehyde and pyrrole was added to it under boiling conditions and allowed to reflux for 1 hr. Finally, the deep purple compound was collected through filtration and washed with MeOH.

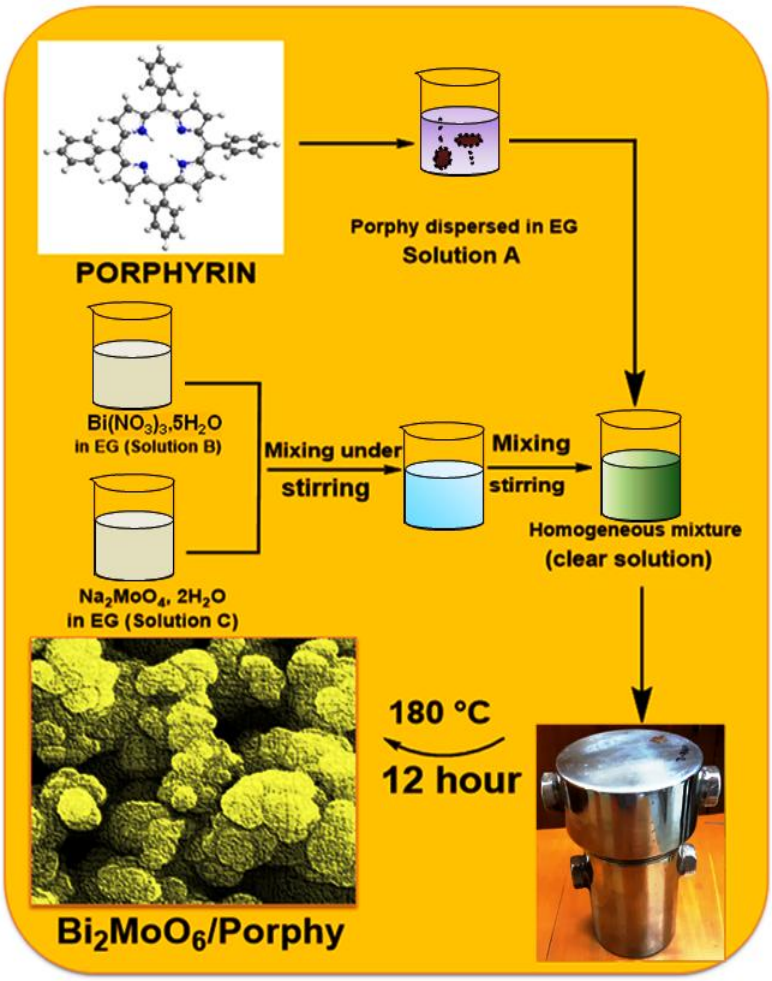

Scheme 3.1. Sequential steps for preparing and decoration of Bi_2MoO_6 with Porphy by solvothermal technique.

3.2.3. Characterization and Instrumentation. The crystallinity and phase formation of the as-prepared samples were investigated by the Philips PW 1140 parallel beam X-ray diffractometer using monochromatic Cu-Kα radiation (λ = 1.5405 Å). The surface morphologies and internal structure of the catalysts were characterized using field emission scanning electron microscopy (FE-SEM JEOL JSM 7100F) with energy dispersive X-ray spectroscopy (EDX) and transmission electron microscopy (TEM-JEOL JEM-2100) operated at 200 kV. The samplings were done by a simple drop cast of Bi_2MoO_6 and Bi_2MoO_6/Porphy solution, dispersed in ultra-pure water onto a strong carbon-coated Cu grid (300 mesh size, purchased from Ted Pella), and the sample grid was stored in a vacuum desiccator before TEM analysis. In order to determine the composition of the samples, selected area

electron diffraction (SAED) pattern was used. X-ray photoelectron spectra (XPS, Perkin-Elmer Physical Electronics 5600 spectrometer) were recorded to identify the chemical states of surface atoms and to confirm the existence of Porphy along with Bi_2MoO_6. Infrared spectra were recorded using a Perkin-Elmer Spectrum Two with ATR Mode analyses to establish the purity of the material. The optical properties of the samples were studied by UV DRS (Agilent UV 5000) with an integrating sphere arrangement in the wavelength range of 1000 to 200 nm and the band gap energies of different composites were calculated by using Kubelka-Munk plot. The specific surface area (S_{BET}), pore size distribution, and pore volume of the catalysts were measured by the N_2 sorption isotherms performed in an Autosorb iQ2 gas sorption instrument (Quantachrome Instruments, USA). Prior to N_2-sorption experiments, all the samples were degassed at 100 °C under vacuum in the attached FLOVAC Degasser sample preparation unit. The pore volume and pore size distribution were estimated by the 2D- Non-Local Density Functional Theory (2D-NLDFT) method.

3.2.4. Electrode preparation for electrochemical measurements. The electrochemical properties of different catalysts were investigated using a rotating ring-disk electrode (RRDE-3A) and a CH17014E electrochemical analyzer (CH Instruments, USA) using a traditional three electrode system at room temperature. The RRDE (disk and ring diameter of 4 and 3 mm, respectively), a Pt electrode, and Ag/AgCl electrode (with saturated KCl solution) were employed as working, counter, and reference electrode, respectively. RRDE was first polished with slurry of alumina powder followed by ultrasonic vibration for 10 min in water. In order to prepare the working electrode for ORR, 5 mg of catalyst was well dispersed into the mixture containing 40 µL of nafion (0.5%) and 1 mL of H_2O by ultrasonication for 2 h. After that, 5 µL of the above suspension was deposited onto the pre-polished glassy carbon disc surface of RRDE and dried in air for 4 h. For comparison, Pt/C (for ORR) electrodes with the same mass loading were prepared by the same method using commercial Pt/C.

Before starting all the experiments, the cell and all the glassware were rigorously cleaned by storing them overnight in concentrated H_2SO_4 to remove metals and organic contaminants. Before use, all were rinsed and boiled three times in H_2O to ensure the cleanliness of the system. The electrochemical experiments were carried out with O_2 - saturated KOH solution, which was bubbled with high purity O_2 for 30 min before the experiment due to O_2/HO^- equilibrium at 1.23 Vs RHE. The ORR was conducted in 0.1 M KOH solution. Also, the electrochemical impedance spectra (EIS) were recorded from 5 mHz to 100 kHz in 1.0 M KOH solution.

3.3. RESULTS AND DISCUSSION

3.3.1. Material Characterizations

3.3.1.1. PXRD analysis of Bi_2MoO_6/Porphy nanocomposites. X-ray diffraction technique was used to characterize the crystallinity and phase structure of Bi_2MoO_6 and a series of Bi_2MoO_6/Porphy nanocomposites. All diffraction peaks are perfectly indexed to orthorhombic Bi_2MoO_6 (JCPDS No. 84-0787, simulated pattern in Figure 3.1b) with a scan rate of 0.5 sec per step over the range of 2θ from 20° to 80° under ambient conditions. The diffraction pattern of Bi_2MoO_6 shows a well-defined and intense reflection at 2θ = 28.2°, which resembles with Bi_2MoO_6. Four peaks of Bi_2MoO_6 at 28.2°, 46.32°, 49.78°, and 54.33° are in good agreement with (131), (251), (232), and (271) crystal faces of Bi_2MoO_6 (Figure 3.1a). Debye-Scherrer equation (crystallite size, $D = 0.9 \times \lambda/\beta \cos\theta$), and the dislocation density ($\delta = 1/D^2$) were applied to calculate the crystallite size, symbols bearing their physical significance and, it was found that the dislocations or defects per unit area of the crystallites have a grain size of ~ 11 nm and ~ 82.64×10^{-4} nm^2 for the diffracted planes with notable intensities, respectively.

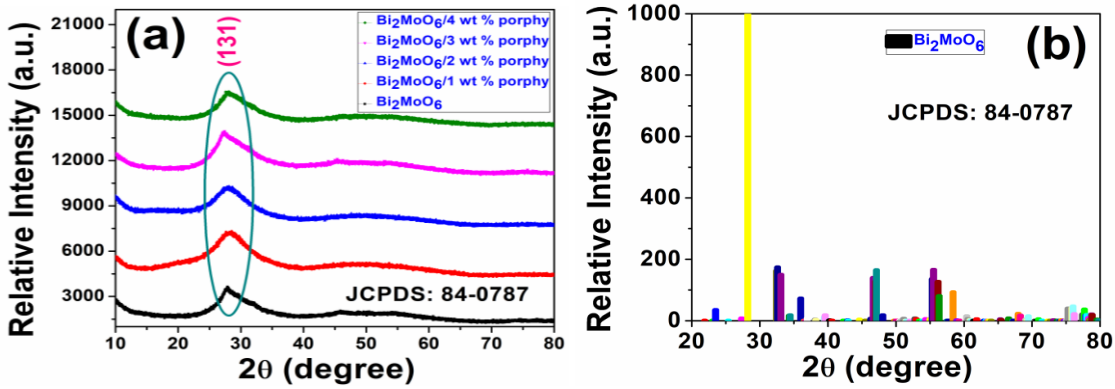

Figure 3.1. XRD pattern of (a) Bi_2MoO_6 and Bi_2MoO_6/Porphy nanocomposites with different wt % Porphy (b) Simulated pattern of Bi_2MoO_6.

For the Bi_2MoO_6/Porphy nanocomposites, only Bi_2MoO_6 crystal peaks were detected, though the introduction of Porphy into Bi_2MoO_6 caused some peak shifts (Table 3.1), indicating that the hybrid materials were formed due to the presence of Porphy content having a clear effect on the crystalline phase of Bi_2MoO_6.

Table 3.1. XRD data of Bi_2MoO_6/Porphy nanocomposites.

Nanocomposites	2θ (degree)				FWHM (131) plane	Grain size (nm)
Bi_2MoO_6	28.20° (131)	46.32° (251)	49.78° (232)	54.33° (271)	0.738	11.23
Bi_2MoO_6/1 wt % Porphy	28.18° (131)	48.84° (222)			0.774	10.71
Bi_2MoO_6/2 wt % Porphy	28.05° (131)	48.50° (222)			0.592	14.00
Bi_2MoO_6/3 wt % Porphy	27.63° (131)	45.55° (171)	53.89° (123)		0.628	13.18
Bi_2MoO_6/4 wt % Porphy	27.87° (131)	46.44° (251)	54.14° (321)		0.689	12.02

3.3.1.2. Morphological Studies. Structure, size, and morphology were investigated by FE-SEM and HR-TEM analyses. The morphology of the Bi_2MoO_6 composite shown by the relatively low magnification FE-SEM image (Figure 3.2a) reveals an uneven distribution of quasi-spherical structure and the magnified image (Figure 3.2b) shows a stacking geometry of spherical grains throughout the region (Figure 3.2c and 3.2d, inset), indicating the decoration of Bi_2MoO_6 with 3 wt % Porphy on its surface. In the modified system, surface topology changes with spinose structures on the quasi-spherical grains, which directly affect the electrocatalytic sensing abilities. The linkage with adjacent particles is much clearer in the high magnification image. The size of Bi_2MoO_6 nanoparticles is ~ 70-90 nm whereas, in its modified form, the size decreases to ~ 50-60 nm due to the change in seeding kinetics of nanoparticles. At this juncture, Porphy controls the growth of quasi-spherical crystals, slowly changing to spinose structures.

The elemental distribution of Bi_2MoO_6 and Bi_2MoO_6/3 wt % Porphy was further confirmed by Energy dispersive X-ray spectroscopy (EDX) and E-mapping. The EDX pattern (Figure 3.2e and inset table) indicates the presence of Bi, Mo, and O in the appropriate stoichiometry (Bi/Mo molar ratio of 2.005), which resembles the precursors, confirming the composition of elements of Bi_2MoO_6. The presence of Bi, Mo, and O, along with C and N, was also confirmed by the EDX spectra (Figure 3.2f and inset table), suggesting that Bi_2MoO_6 is the main component of the Bi_2MoO_6/3 wt % Porphy nanocomposite. Furthermore, Figures 3.2(g→h) present the corresponding e-mappings of respective elements Bi (La), Mo (La), O (Ka) in Bi_2MoO_6 and Bi (La), Mo (La), O (Ka), C (Ka), N (Ka) in Bi_2MoO_6/3 wt % Porphy, indicating that materials were well dispersed throughout the surface and

were successfully prepared. This analysis is very important for any electrocatalytic reaction and its practical application viewpoint.

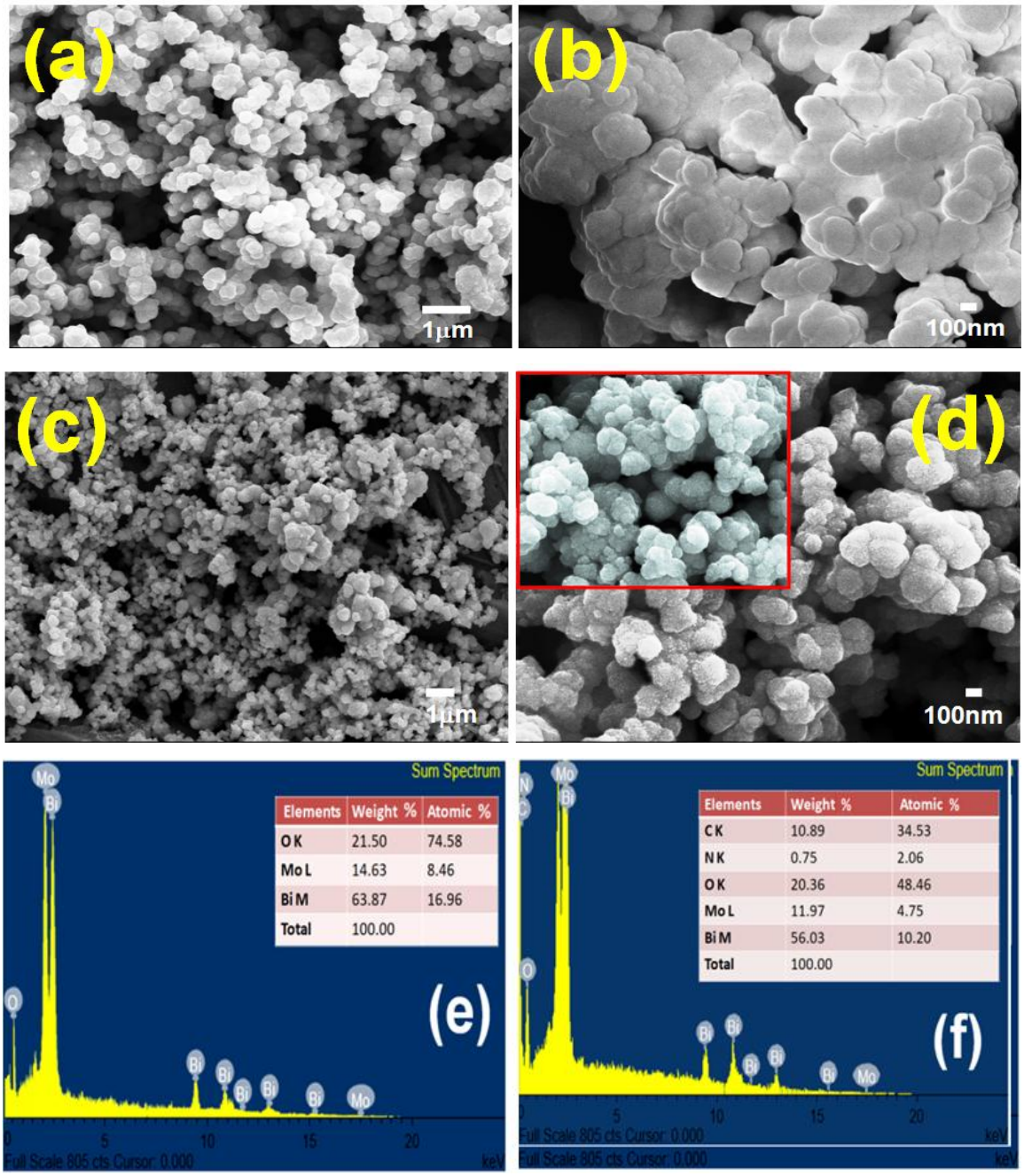

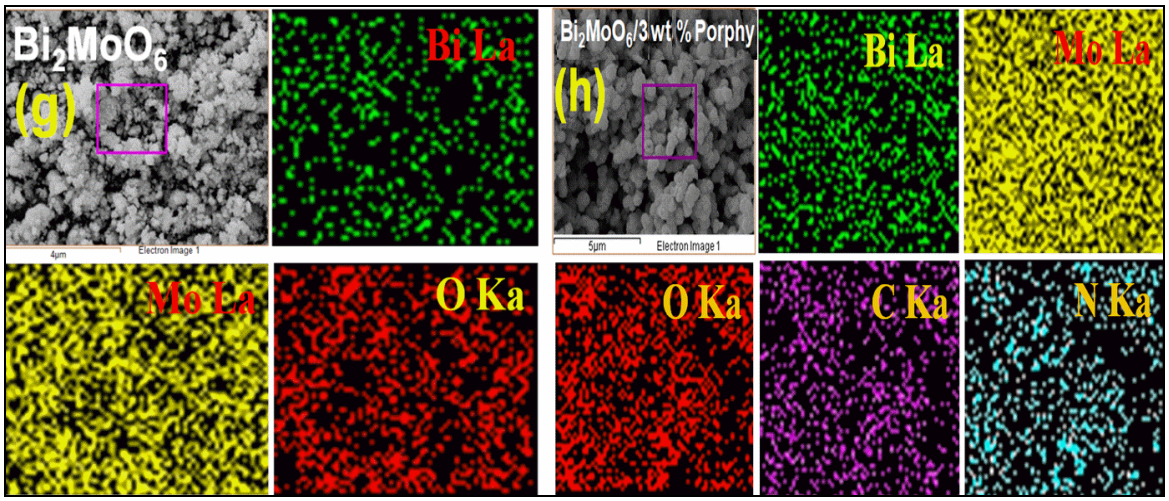

Figure 3.2. FE-SEM image of (a, b) Bi_2MoO_6 (c, d) Bi_2MoO_6/3 wt % Porphy in low as well as high magnification and (e, f) EDX and (g, h) E-mapping of Bi_2MoO_6 and Bi_2MoO_6/3 wt % Porphy nanocomposite.

Apart from that, TEM could again be used to gain insight into the morphology and stocking details of the Porphy on Bi_2MoO_6. During sample preparation, the particles were well dispersed onto the C-coated Cu grid. Figures 3.3a and b show TEM images of nano spherical Bi_2MoO_6 particles with soft edges and smooth surfaces. This is in accordance with the images revealed by FE-SEM (Figure 3.2). There are no such structural or morphological changes in Bi_2MoO_6 as shown by the TEM image (Figure 3.3a), but they are observed upon further magnification (Figure 3.3b). In the inset of Figure 3.3b, the histogram indicates the particle size distribution (PSD) of mixed-metal oxide nanoparticles having an average size of 7 nm, particles are indicated with dotted yellow lines. The HR-TEM image (Figure 3.3c, inset image) exhibits lattice fringes of different planes of Bi_2MoO_6 to justify the purity and phase of the material. The FFT and inverse FFT analyses of different areas of electron micrograph for finding the other lattice fringes with d-spacing of different planes, the fringe pattern of Bi_2MoO_6 nanoparticles (Figures 3.3(d→h)) with the noticeable appearance of the (131), (251), (232), and (120) planes having respective d-spacing's of 0.330 nm, 0.266 nm, 0.262 nm, and 0.471 nm, well confirmed with slight changes to our literature value, further confirms polycrystalline Bi_2MoO_6.

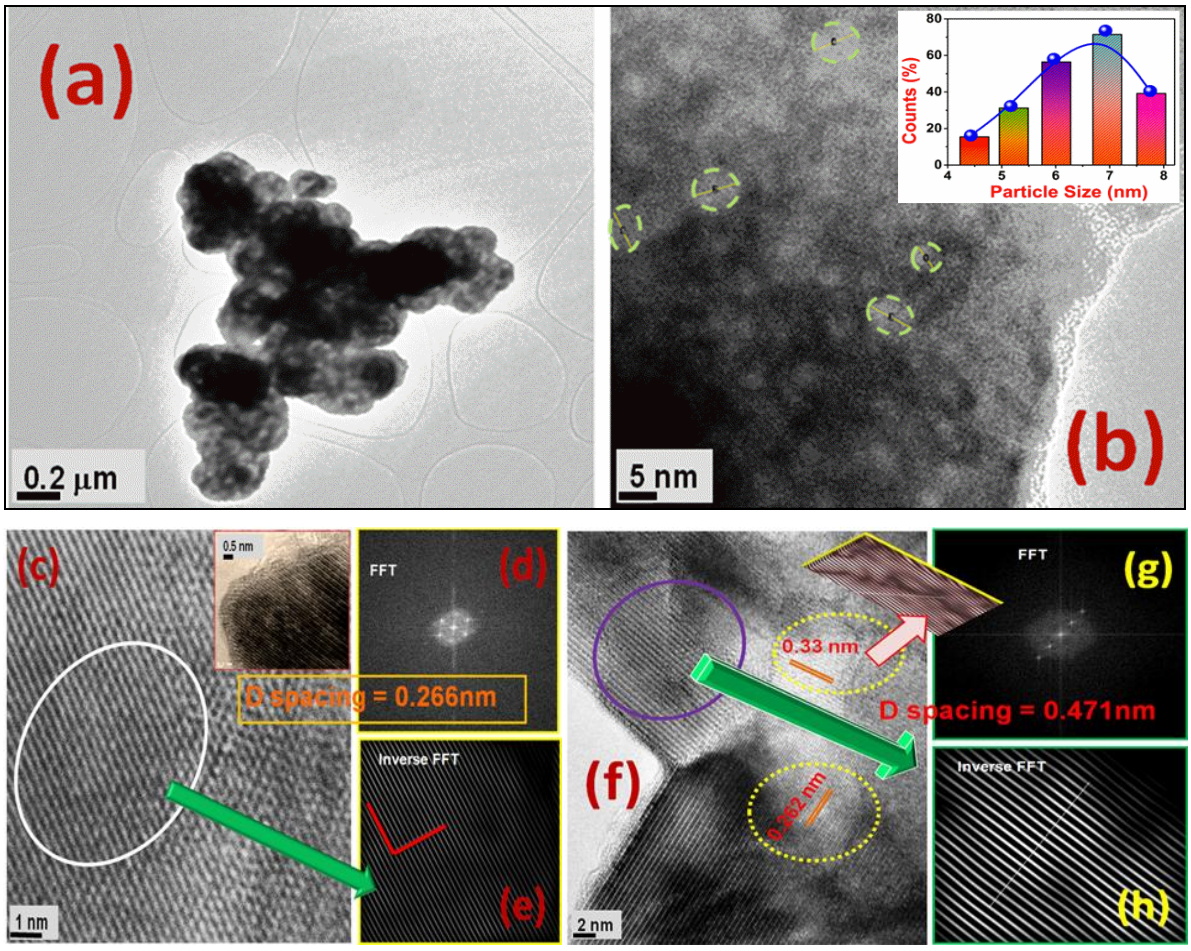

Figure 3.3. TEM image (a) Bi_2MoO_6 nanoparticles (b) magnified image indicated with dotted yellow circles of nanoparticles, inset figure: histogram plot for PSD and HR-TEM image (c) lattice fringes obtained from the magnification of inset figure (d→e) FFT and Inverse FFT image of (251) plane (f) composed of 3-different lattice fringes of (131), (232), and (120) planes with their d-spacings (g→h) FFT and Inverse FFT image of (120) plane.

The uniform coating of Porphy units on the surface of Bi_2MoO_6 nanocrystals was further confirmed by the TEM image of Porphy-decorated Bi_2MoO_6 nanocomposite (Figures 3.4a and b, inset), representing PSD of 9 nm, and the downward arrow image depicts the amorphous as well as crystalline part within the composite. When we move to the modification with 3 wt % Porphy into the crystal matrix, the d-spacing (~ 0.3075 nm closer to 131 planes) between the atomic planes will be somewhat distorted. It is visible in inverse FFT analysis of electron micrograph studies (Figures 3.4c→e) that the polycrystalline nature of Bi_2MoO_6 differs w.r.t Bi_2MoO_6/3 wt % Porphy

nanocomposites, and certain surface modifications have been induced onto the sample, which may directly influence the electrocatalytic performance.

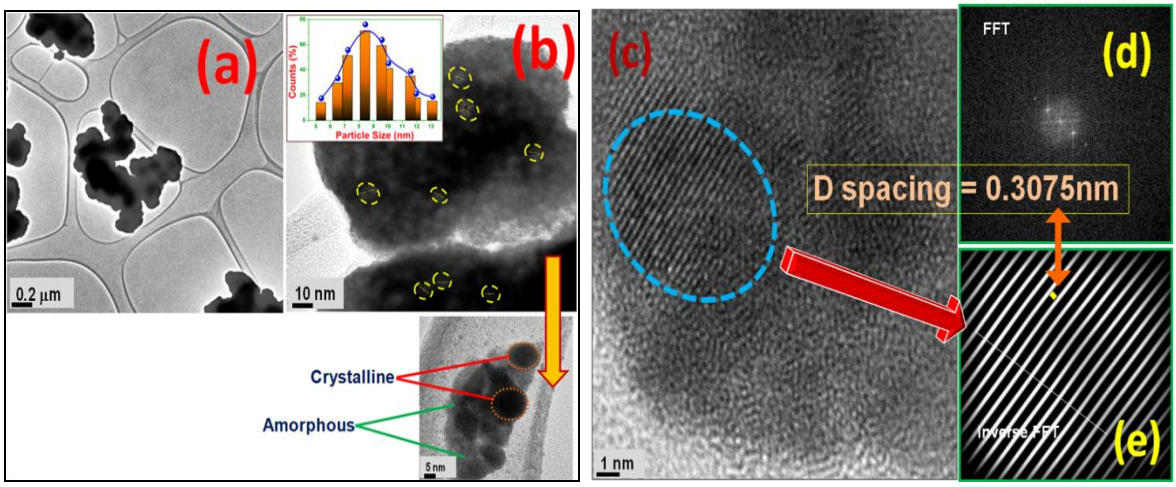

Figure 3.4. TEM image (a) Bi_2MoO_6/3 wt % Porphy nanocomposite (b) magnified image indicated with dotted yellow circles of nanoparticles, inset figure: histogram plot for PSD, amorphous (green line) and crystalline (red line) part of nanocomposite; HR-TEM image (c) lattice fringe obtained from the magnification (d→e) FFT and Inverse FFT image of (131) plane.

The Selected area electron diffraction pattern (SAED) of Bi_2MoO_6 and Bi_2MoO_6/3 wt % Porphy nanocomposite (Figures 3.5(a→b)) exhibits strong concentric ring patterns of (131), (123), (251), and (131), (123) planes respectively, which resembles the XRD data of Bi_2MoO_6. As shown in the images, the well-crystalline behaviour of Bi_2MoO_6 gradually deteriorates as the Porphy concentration in the matrix increases. Crystal points are randomly oriented as well as concentric rings are diffused in nature, which reveals that the Porphy decorated Bi_2MoO_6 matrix gains amorphicity within the crystal matrix.

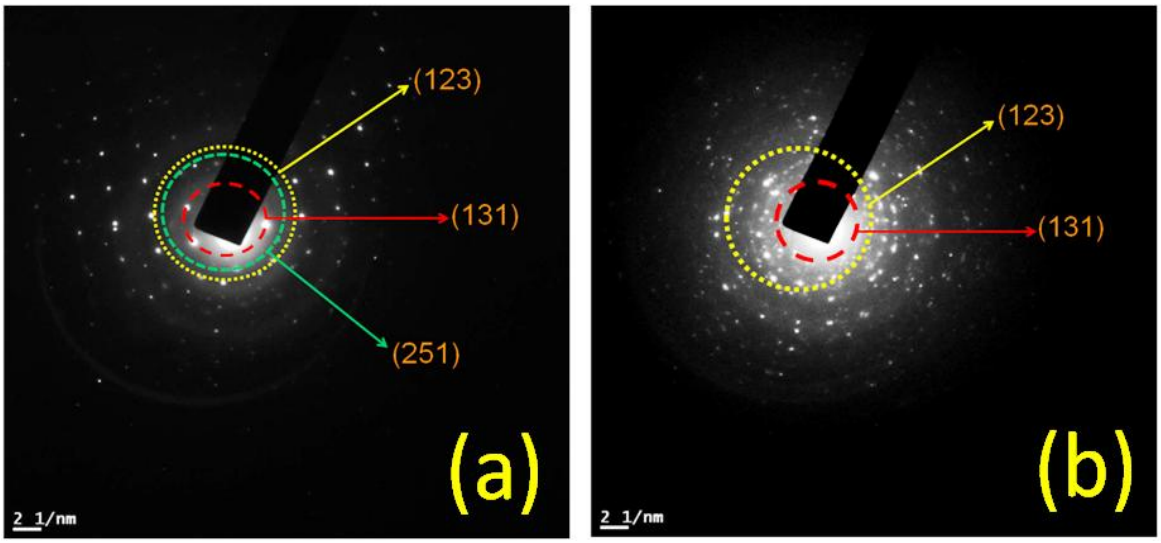

Figure 3.5. SAED pattern of (a) Bi_2MoO_6 and (b) Bi_2MoO_6/3 wt % Porphy nanocomposite.

3.3.1.3. XPS analysis of Bi_2MoO_6/3 wt % Porphy composite. The chemical composition and surface states of Porphy, Bi_2MoO_6, and Bi_2MoO_6/3 wt % Porphy nanocomposite were characterized by X-ray photoelectron spectroscopy (XPS). The XPS spectra clearly show that the Porphy is composed of the elements O, C, and N. The total survey spectrum confirms the presence of Bi, Mo, and O in Bi_2MoO_6 and Bi, Mo, O, C, and N in Bi_2MoO_6/3 wt % Porphy (Figure 3.6a). The high-resolution XPS spectrum of Bi 4f region was seen, and the peaks were identified in two distinct regions (Figure 3.6b). Now, the two asymmetric peaks for Bi $4f_{7/2}$ are resolved at 158.6 eV as well as for Bi $4f_{5/2}$ at 163.9 eV respectively.[20] The binding energies of Bi at 158.6 eV and 163.9 eV correspond to the oxidation state of Bi^{+3}. The binding energies of Mo $3d_{5/2}$ and Mo $3d_{3/2}$ in the Bi_2MoO_6/Porphy composite are centered at 231.6 eV and 234.6 eV, respectively[20] (Figure 3.6c), suggesting that the hexavalent oxidation state of Mo^{+6} is present in the composite. The N 1s core level spectrum of Bi_2MoO_6/Porphy corresponds to three peaks at 397.43 eV, 399.08 eV, and 401.51 eV (three peaks gave the best fit). Deconvolution of the N 1s peak yields two Gaussian peaks at 397.43 eV and 399.08 eV (Figure 3.6e), corresponding to pyrrolic-N (-NH) and pyridinic-N (-N=), respectively.[21,22] The presence of the third peak of N 1s, at 401.51 eV, could be attributed to a small amount of physisorbed nitrogen or slight oxidation of the attached Porphy molecule. Moreover, the C 1s peaks at 284.1 eV, 285.7 eV, and 287.6 eV (Figure 3.6f) correspond to C = C, C = N, and C-N bonds. The O 1s peaks at 529.54 eV and 530.67 eV (Figure 3.6d) indicate the crystal lattice oxygen and adsorbed oxygen, respectively. This result indicates that the macrocyclic Porphy remains in free

base state without being metalized in the nanocomposite. Here, the pyrrolic- and pyridinic-N atoms of the Porphy may behave like a carbon system incorporated with N, with excellent conductivity, high stability, and high surface content, which are well accepted in the energy sector. The pyridine-N peak was slightly shifted compared to the pure Porphy. This may be attributed to the surface interactions between the lone electron pairs of the pyridinic-N atoms of Porphy and the metal ions that exist on the outer surface of the material.

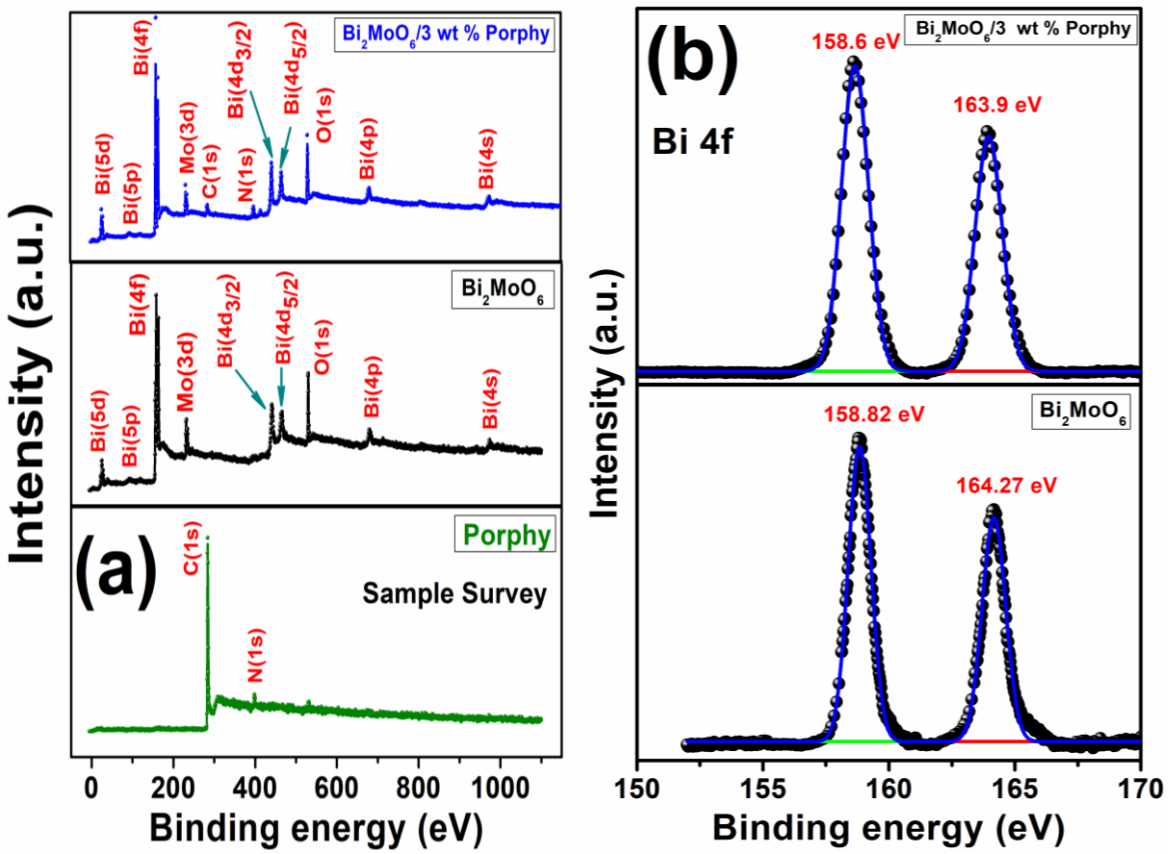

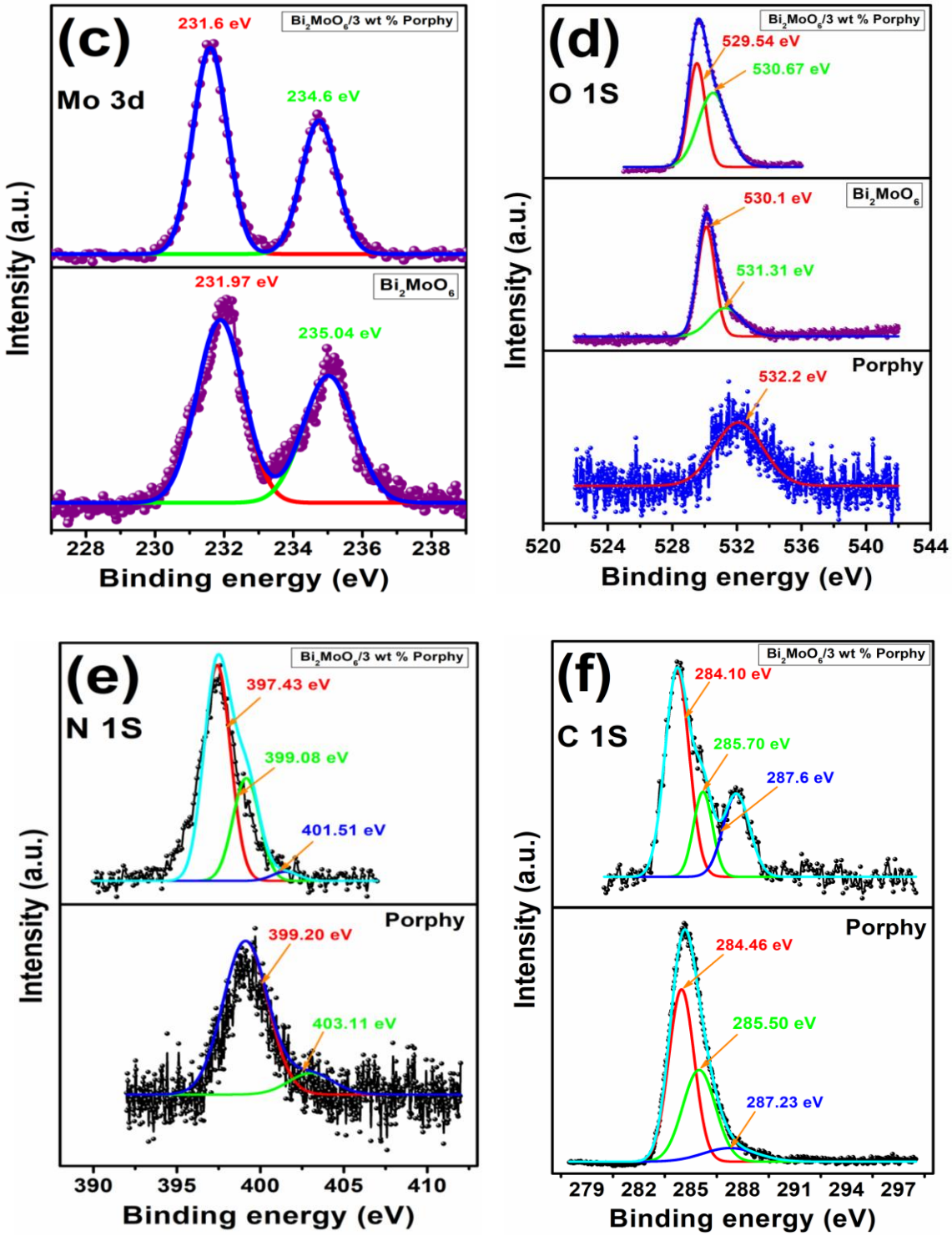

Figure 3.6. XPS spectra of Porphy, Bi_2MoO_6 and Bi_2MoO_6/3 wt % Porphy nanocomposite (a) Sample survey (b) Bi 4f (c) Mo 3d (d) O 1s (e) N 1s (f) C1s.

It was confirmed that there was no significant change between the bare Bi_2MoO_6 sample and the Bi_2MoO_6/3 wt % Porphy sample for the Bi, Mo, and O XPS peaks (Figures 3.6(b→d)). From the analysis of peak shifts and peak intensities, the formation of Bi_2MoO_6/Porphy hybrid materials was confirmed. This result indicates that the surfaces of Bi_2MoO_6 were effectively changed by Porphy and that Bi_2MoO_6 is bound to the Porphy surface via charge transfer phenomena.

3.3.1.4. FTIR Analysis. The Fourier transform infrared spectra (FTIR) of Bi_2MoO_6/3 wt % Porphy nanocomposite are presented in Figures 3.7a and b. The absorption bands at 3289 and 1610 cm^{-1} for Bi_2MoO_6 are ascribed to O-H vibrations for the absorbed water molecules.[20] The corner-sharing $(MoO_6)^{-6}$ octahedron has two absorption bands at 785 cm^{-1} and 821 cm^{-1} for symmetric and asymmetric vibrational modes (Mo-O stretching).[23] The peak at 715 cm^{-1} was assigned to the asymmetric stretching vibrations of the equatorial oxygen atoms of MoO_6, while the absorption band for the bending vibration of the MoO_6 octahedron[24] appeared at 556 cm^{-1}. For the free base H_2TPP (Tetraphenylporphyrin), the bands at ~ 1610 cm^{-1} and ~ 1350 cm^{-1} represent the symmetric angular deformations in the N-H plane and δ vibrations of the pyrrole ring. The bands at 3316, 3111, and 3027 cm^{-1} represent γN-H, C-H (phenyl), and C-H (pyrrole) stretching. Among other bands related to skeletal ring vibrations, bands related to in-plane δN-H and out-of-plane δN-H appeared at 970 cm^{-1} and 750 cm^{-1} respectively.

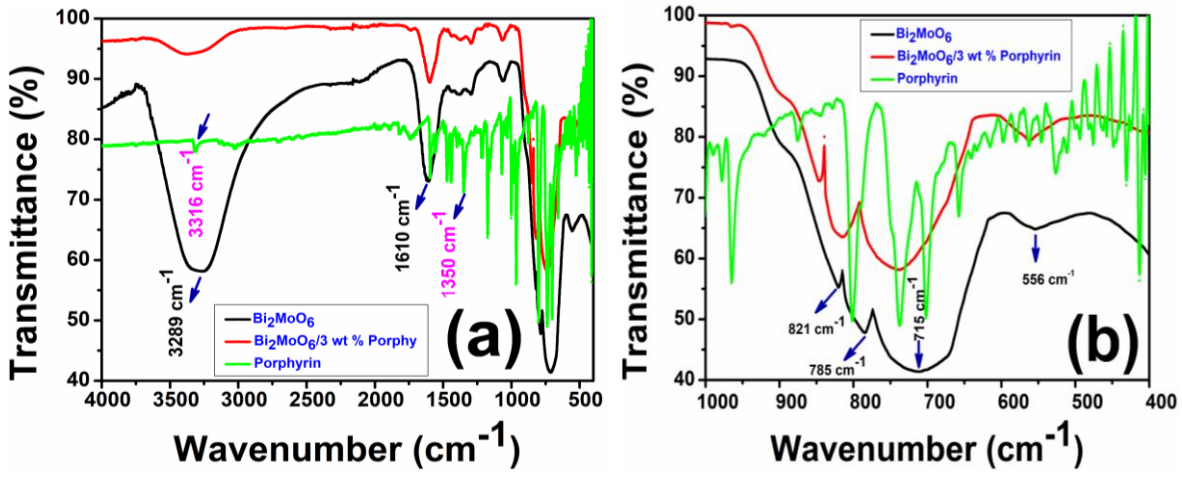

Figure 3.7. FTIR analysis of (a) Bi_2MoO_6 and (b) Bi_2MoO_6/3 wt % Porphy nanocomposite.

In the case of the Bi_2MoO_6/3 wt % Porphy composite, the characteristic bands for Bi_2MoO_6 still remain, indicating the presence of Bi_2MoO_6, while the band vibration of Porphy was observed less

significantly. This may be attributed to the low concentration of well-dispersed Porphy on the surface sites of Bi_2MoO_6 in the composite. Bi_2MoO_6 nanocrystals can interact with prophy through physisorption, electrostatic bonding, interfacial electronic, or charge transfer interactions. The prompt peaks of pure Bi_2MoO_6 have been slightly shifted to higher wave numbers due to the incorporation of 3 wt % Porphy. A little blue shift takes place for the composite, Bi_2MoO_6/3 wt % Porphy, which confirms that the two components come into the same chemical environment to form a heterogeneous composite system and appreciable interfacial interaction occurs between them. Hence, the presence of Porphy in the nanocomposites was further confirmed by the FTIR spectrum. The successful formation of Porphy-decorated Bi_2MoO_6 was established by XRD, XPS, FTIR, and elemental analysis altogether.

3.3.1.5. UV-Vis Diffuse Reflectance Spectroscopic Study (DRS). The UV-Vis diffuse reflectance spectra were also used to investigate the interactions between Bi_2MoO_6 and Porphy. Porphy decorated nanocomposites displayed a strong spectral response in the UV-Vis regions (Figure 3.8a) from 200-800 nm. The optical absorption edge of Bi_2MoO_6 was found at 449.26 nm, whereas for Bi_2MoO_6/3 wt % Porphy nanocomposite, it was reflected at 479.87 nm. The DRS spectrum of Porphy (Figure 3.8b) showed a strong absorption peak at 425.84 nm. This corresponds to the Soret band originating from the π-π* transition of the macrocycle ring.[25] After modification of Bi_2MoO_6 with Porphy, the Soret band was red-shifted to 479.87 nm, indicating a broadening of the absorption in the solar region. More importantly, the four relatively weak absorption peaks in the range of 500-700 nm, corresponding to the characteristic Q-band of Porphy,[26] were also observed in the DRS spectrum of the Bi_2MoO_6/3 wt % Porphy nanocomposite, suggesting the successful introduction of Porphy into Bi_2MoO_6.

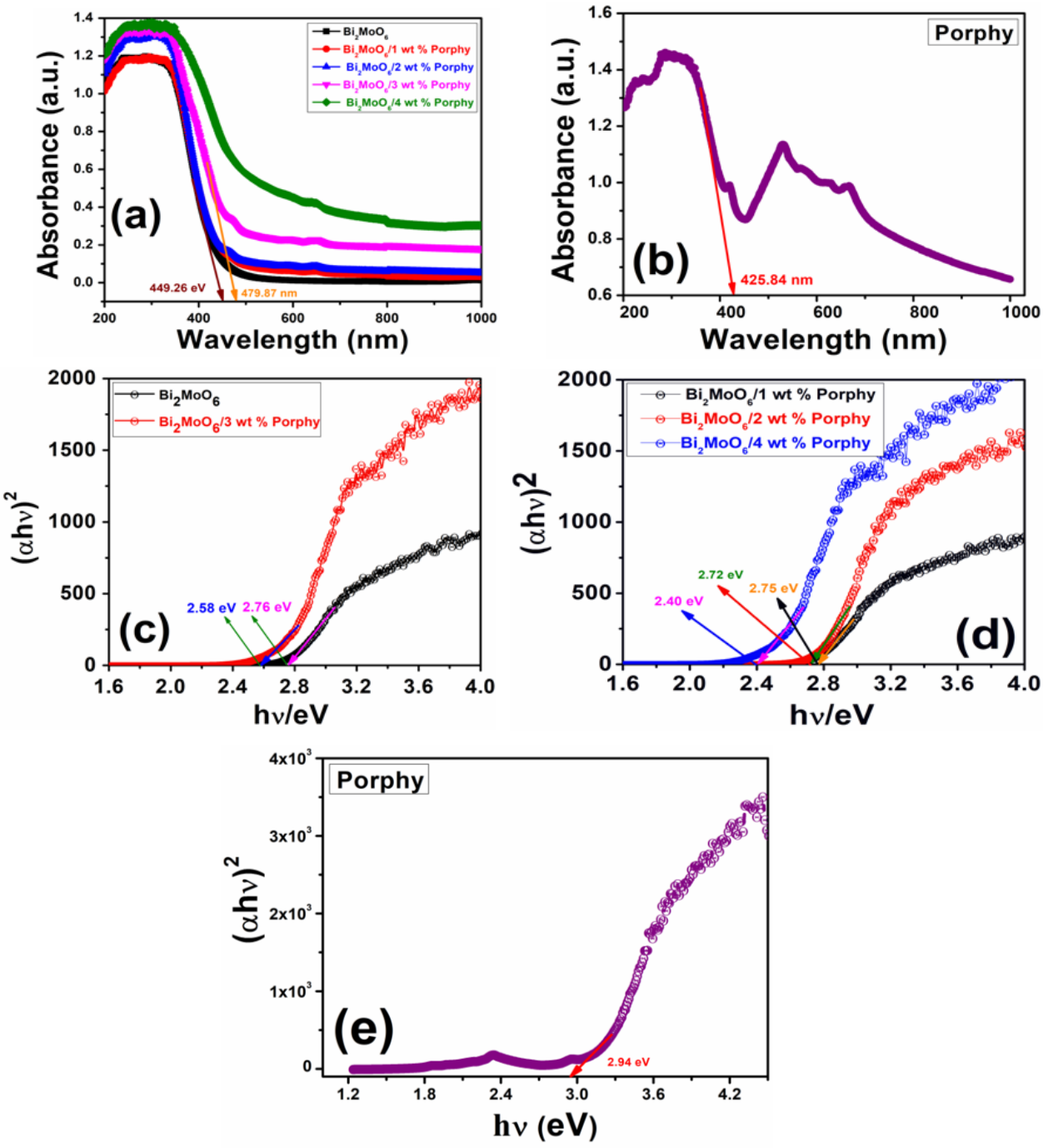

Figure 3.8. (a) UV-Vis diffuse reflectance spectroscopy of Bi_2MoO_6 and Bi_2MoO_6/Porphy nanocomposite (b) Porphy; Kubelka-Munk plot of (c) Bi_2MoO_6 and Bi_2MoO_6/3 wt % Porphy nanocomposite (d) Bi_2MoO_6/1 wt % Porphy, Bi_2MoO_6/2 wt % Porphy, Bi_2MoO_6/4 wt % Porphy (e) Porphy.

To determine the optical behavior of Bi_2MoO_6 and Bi_2MoO_6/3 wt % Porphy, the band gap energies were evaluated using the Kubelka-Munk function.[27] Figures 3.8(c→e) show the $(\alpha h\nu)^2$ versus photon energy ($h\nu$) curves of Bi_2MoO_6 and Bi_2MoO_6/3 wt % Porphy and other materials, which imply that the band gap energy (BGE) of 2.76 eV for Bi_2MoO_6 was significantly reduced to 2.40 eV for Bi_2MoO_6/4 wt % Porphy (Table 3.2). As a result of the strong molecular interactions between Bi_2MoO_6 and Porphy, the absorption edge of the Bi_2MoO_6/3 wt % Porphy nanocomposite exhibited a significant red shift compared to Bi_2MoO_6. Structural and morphological studies also showed changes from the bare Bi_2MoO_6 to the decorated form of the Bi_2MoO_6/Porphy nano-dimensional system. Therefore, it can be said that there is a high possibility of such an absorption band being generated due to the existence of sub-band gap defects.

Table 3.2. Band gap energy (BGE) from the absorption plot of different nanocomposites using Kubelka-Munk function.

Nanocomposites	λ_{max} (nm)	Band gap energy (eV)
Porphy	425.84	2.94
Bi_2MoO_6	449.26	2.76
Bi_2MoO_6/1 wt % Porphy	460.53	2.75
Bi_2MoO_6/2 wt % Porphy	492.10	2.72
Bi_2MoO_6/3 wt % Porphy	479.87	2.58
Bi_2MoO_6/4 wt % Porphy	579	2.40

3.3.1.6. Brunauer-Emmett-Teller (BET) Surface Area Analysis. To evaluate their characteristics, BET analysis was used to calculate the surface areas of Bi_2MoO_6 and Bi_2MoO_6/3 wt % Porphy (Figure 3.9). The Bi_2MoO_6/3 wt % Porphy nanocomposite has a mesoporous structure with a surface area of 52.50 $m^2 g^{-1}$ which is greater than Bi_2MoO_6 (31.30 $m^2 g^{-1}$), indicating a better electrocatalytic behaviour toward ORR (Table 3.3). A larger BET surface area allows more contact between the catalyst and the electrolyte. This result plays an important role in enhancing ESCA.

Table 3.3. Surface properties of Bi_2MoO_6 and Bi_2MoO_6/3 wt % Porphy nanocomposites.

Samples	BET surface area ($m^2 g^{-1}$)	Pore volume ($cm^3 g^{-1}$)	Pore diameter (nm)
Bi_2MoO_6	31.30	0.0403	1.564
Bi_2MoO_6/3 wt % Porphy	52.50	0.081	1.549

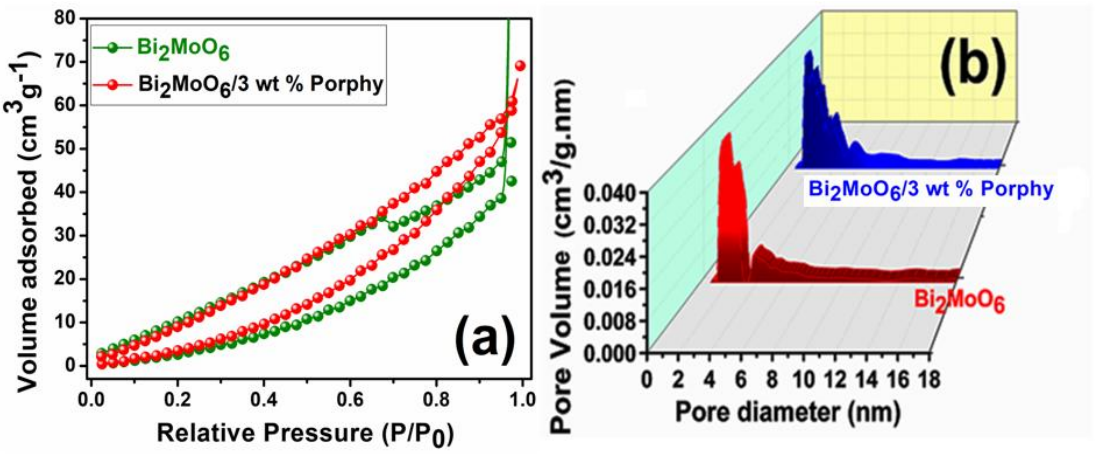

Figure 3.9. BET isotherm of Bi_2MoO_6 and Bi_2MoO_6/3 wt % Porphy nanocomposite (a) and (b).

However, after the introduction of Porphy to Bi_2MoO_6, the surface area increased and the isotherms for all samples resembled type IV (IUPAC) isotherms, indicating the mesoporous nature of materials. The cumulative pore volumes of Bi_2MoO_6 and Bi_2MoO_6/3 wt % Porphy were 0.0403 and 0.081 $cm^3\ g^{-1}$, respectively. The texture parameters of Bi_2MoO_6 and Bi_2MoO_6/3 wt % Porphy nanocomposite are listed in Table 3.3. Significantly, this mesoporous nanocomposite can provide a large number of active sites, which enhances its mass and charge transport capabilities, improving its catalytic performance.

3.3.2. Measurement of Oxygen Reduction Reaction (ORR) performance. The ORR activities of the synthesized catalysts were measured by using linear sweep voltammograms (LSVs) with different rotational speeds (400 to 2000 rpm) at a scan rate of 5 mV s^{-1}. The disk and ring current densities were normalized using the geometric immersed surface area of the electrode 0.126 and 0.071 cm^2 respectively. The chronoamperometric measurements were carried out to investigate the durability and MeOH tolerance of the catalysts. For the MeOH crossover study, 3.0 M MeOH (20 vol %) was added into O_2 saturated 0.1 M KOH solution after ~ 150 s. All obtained data was corrected by iR compensation. The number (n) of electron transfer at the electrode potentials of 0.15-0.40 V was obtained from the Koutecky-Levich (K-L) plots by the following equation:

$$\frac{1}{j} = \frac{1}{j_K} + \frac{1}{j_L} = \frac{1}{j_K} + \frac{1}{B\omega^{1/2}} \qquad \text{Eq. 3.1}$$

Where j, j_K, and j_L are the measured current density, kinetic current density, and diffusion-limited current density (mA cm^{-2}) respectively and ω is the electrode rotating speed in rpm.

Here, B stands for the Levich slope that is

$$B = 0.62nFC_0(D_0)^{2/3}(\nu)^{-1/6} \quad \text{Eq. 3.2}$$

Where n is the electron transfer number per oxygen molecule, F (Faraday constant) = 96,485 C mol^{-1}, C_0 (the bulk concentration of O_2 in 0.1 M KOH solution) = 1.2×10^{-6} mol cm^{-3}, D_0 (the diffusion coefficient of O_2 in 0.1 M KOH) = 1.90×10^{-5} cm^2 s^{-1} and ν (the kinematic viscosity in 0.1 M KOH) = 0.01 cm^2 s^{-1}. The number of electron transfer (n) is obtained from the slope of the linear plot of j^{-1} vs. $\omega^{-½}$. Tafel plots [E vs. log (j_k)] were collected from the LSV curves at 1600 rpm. For the RRDE measurement, catalyst inks and electrodes were prepared following the same procedure as for that RDE. The n value and percentage of HO_2^- yield can be determined quantitatively at a rotation speed of 1600 rpm based on the ring and disk currents by applying a constant ring potential of 1.5 V vs. RHE according to the followed equations.

$$n = \frac{4I_d}{I_d + \frac{I_r}{N}} \quad \text{Eq. 3.3}$$

$$HO_2^- \% = \frac{2 \times \frac{I_r}{N}}{I_d + \frac{I_r}{N}} \times 100\ \% \quad \text{Eq. 3.4}$$

Where I_r and I_d are the ring and disk currents (mA cm^{-2}) respectively and N is the current collection efficiency (0.43) of the ring.

3.3.2.1. Mechanism of ORR. In alkaline media, the ORR takes place via overall $4e^-$ pathway[28]

$$O_2 + 2H_2O + 4e^- \rightarrow 4\,OH^- \quad E^0 = +0.401\ V\ vs.\ SHE \quad \text{Eq. 3.5}$$

Alternatively, O_2 is reduced to peroxide ion, via the following $2e^-$ pathway,

$$O_2 + H_2O + 2e^- \rightarrow HO_2^- + OH^- \quad E^0 = -0.076\ V\ vs.\ SHE \quad \text{Eq. 3.6}$$

The generated peroxide may follow two possible pathways to decompose itself.

$$\text{Reduction: } HO_2^- + H_2O + 2e^- \rightarrow 3OH^- \quad E^0 = +0.878\ V\ vs.\ SHE \quad \text{Eq. 3.7}$$

$$\text{Disproportionation: } 2OH_2^- \rightarrow 2OH^- + O_2 \quad \text{Eq. 3.8}$$

Where, SHE stands for standard hydrogen electrode.

The RRDE technique is an effective tool for the evolution of ORR activity. Also, the deposited thin films served as the working electrodes, a GCE was the counter electrode, and an Ag/AgCl (saturated

KCl) was the reference electrode. All measured potentials vs. the Ag/AgCl (saturated KCl) were converted to the reversible hydrogen electrode (RHE) using the Nernst equation.

$$E_{RHE} = E_{Ag/AgCl} + 0.197 + 0.059\ pH \qquad \text{Eq. 3.9}$$

Here, the converted potential vs RHE is the experimentally measured potential against the Ag/AgCl reference electrode, and the standard potential of Ag/AgCl at 25 °C was 0.197 V. The electrochemical active surface area (ECSA) of all electrocatalysts were calculated from the double-layer capacitance (C_{dl}) (Table 3.7) according to the following equation:

$$ECSA = \frac{C_{dl}}{C_s} \qquad \text{Eq. 3.10}$$

Where, C_s is the ideal specific capacitance of a smooth planar surface made of the same material per unit area under identical electrolyte conditions. In our estimation of surface area, we have used the general specific capacitances of C_s = 40 μF cm^{-2} in 1.0 M KOH. The roughness factor (R_f) of the materials were determined by the equation:

$$R_f = \frac{ECSA}{GSA} \qquad \text{Eq. 3.11}$$

Where, the geometric surface area (GSA) of the electrode is 0.125 cm^2.

3.3.2.2. ORR analysis with the decorated GCE by Bi_2MoO_6/3 wt % Porphy nanocomposite. To understand the oxidation and reduction states using a modified GC electrode with Bi_2MoO_6, Bi_2MoO_6/Porphy nanocomposites, and Porphy, cyclic voltammograms (CV) were performed in N_2-saturated 20 mL of 0.1 M KCl/TBAP solution as the supporting electrolyte at 50 mV s^{-1} scan rate (Figure 3.10c). The catalytic activity of the Bi_2MoO_6/Porphy series towards the ORR was first investigated by cyclic voltammetry (CV) in a 0.1 M KOH solution that was separately saturated with N_2 and O_2 (Figures 3.10a and b). A sharp cathodic oxygen reduction peak was observed in the potential window from 0.5 V to 1.5 V under O_2 saturated conditions (Figure 3.10b). This peak showed a positive shift when Bi_2MoO_6 was loaded with Porphy. Remarkably, the dramatic positive shift of the cathodic oxygen reduction peak for Bi_2MoO_6/3 wt % Porphy shows its improved ORR activity.

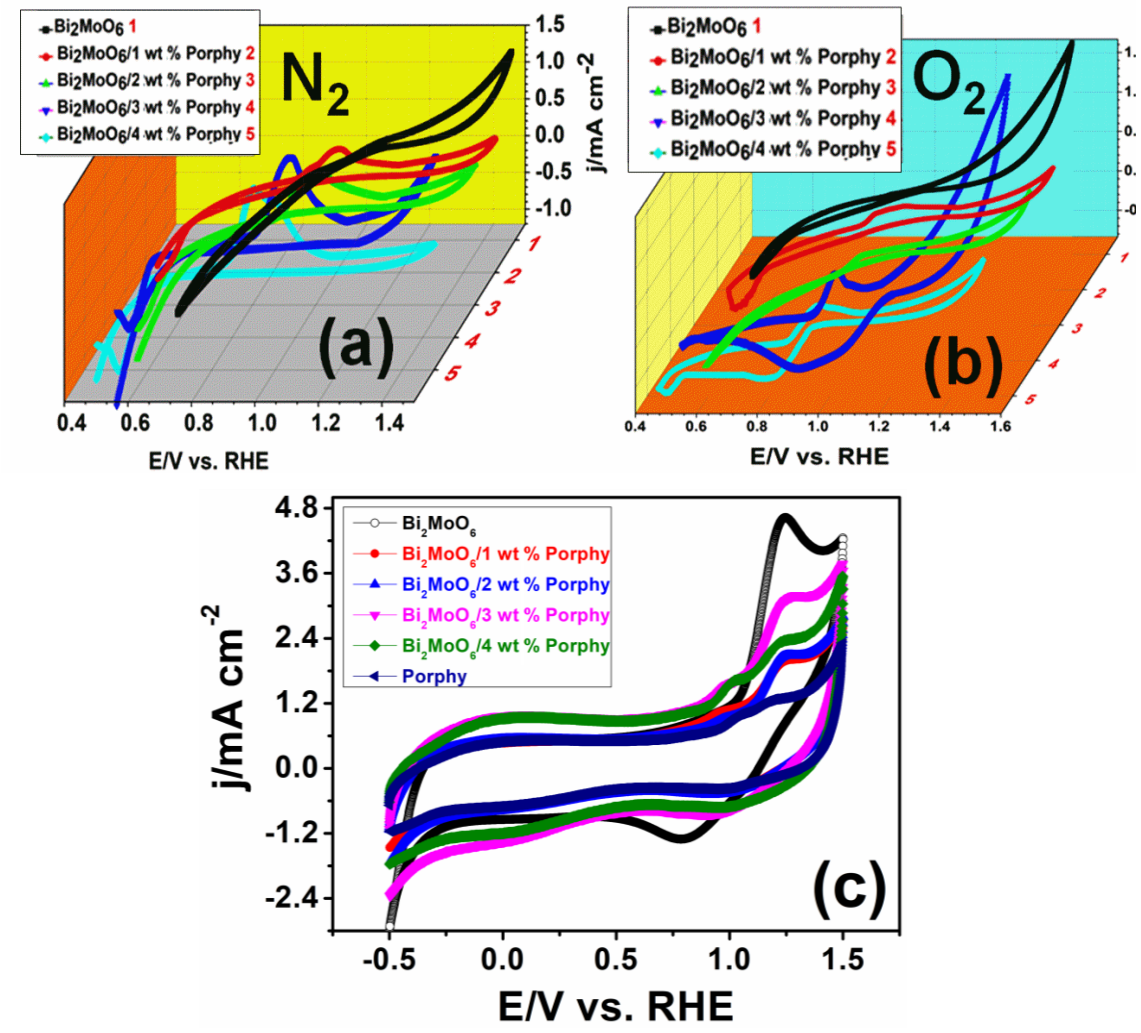

Figure 3.10. Overlay plot of cyclic voltammograms of bare Bi_2MoO_6 as well as different wt % of Porphy decorated Bi_2MoO_6 in (a) N_2 and (b) O_2 saturated condition (c) in 0.1 M KCl/TBAP with a scan rate of 50 m V s^{-1}.

Linear sweep voltammograms (LSV) were recorded at rotating speeds ranging from 400 to 2000 rpm using a rotating ring-disk electrode (**Scheme 3.2**) to investigate the kinetic characteristics of all catalysts and found that increasing rotating speed increased the limiting current densities (Figures 3.11(a→f)**)**. Bi_2MoO_6/3 wt % Porphy (Figure 3.11g) exhibited enhanced onset potential (0.942 V), half-wave potential (0.704 V), and limiting current density (-5.545 mA cm^{-2}) at a rotating speed of 1600 RPM when compared to Bi_2MoO_6, Bi_2MoO_6/1 wt % Porphy, Bi_2MoO_6/2 wt % Porphy, Bi_2MoO_6/4 wt % Porphy, and commercial Pt/C, showing its excellent electrochemical activity (Table

3.4). The enhanced ORR catalytic activity is plausibly due to Porphy which promotes the binding to the ORR intermediates, enhancing the redox capacity to readily adsorb O_2 onto the electrode surface. Not only that, beyond the optimum amount of Porphy (above 3 wt %), a surfeit amount of Porphy increases the thickness of the surface and interferes with the ORR activity of the materials.

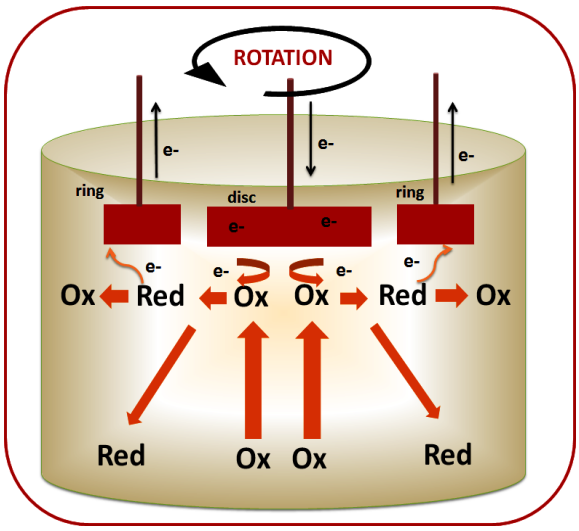

Scheme 3.2. Representation of different catalytic reactions occurring at the solid-liquid junction of rotating ring-disk electrode (RRDE).

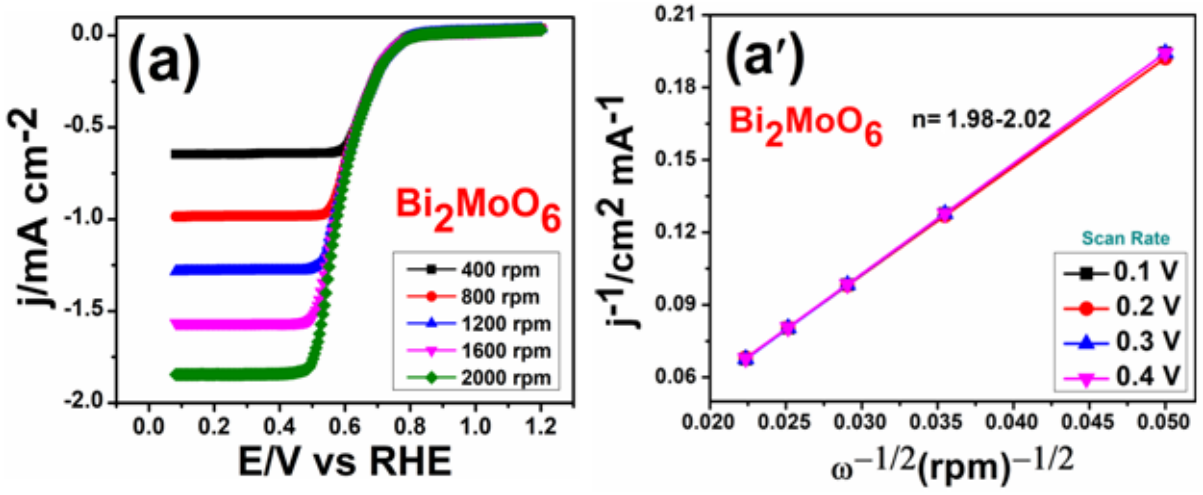

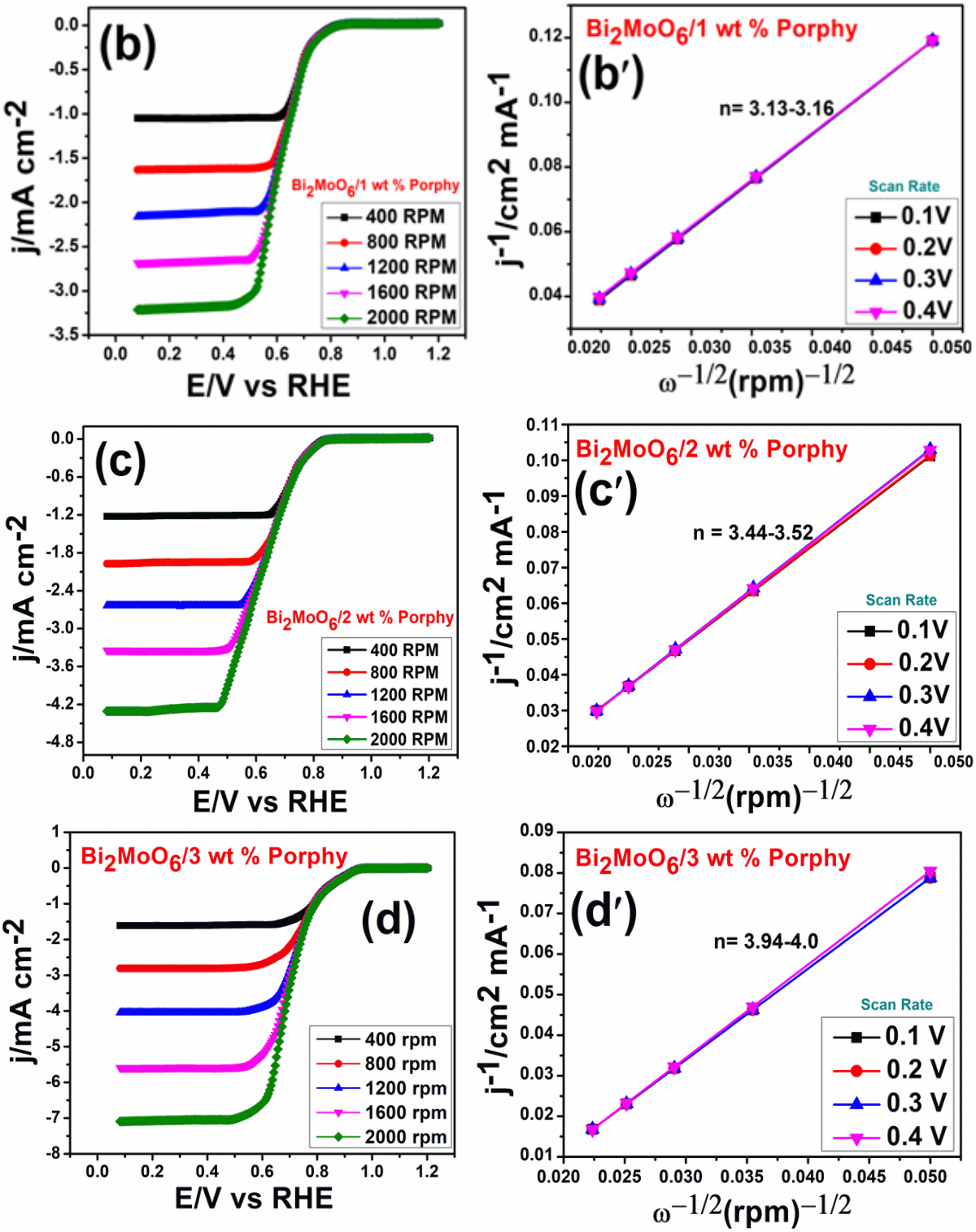
(b)
j/mA cm-2
E/V vs RHE
Bi2MoO6/1 wt % Porphy
400 RPM
800 RPM
1200 RPM
1600 RPM
2000 RPM
Bi2MoO6/1 wt % Porphy
(b′)
n= 3.13-3.16
Scan Rate
0.1V
0.2V
0.3V
0.4V
j-1/cm2 mA-1
ω−1/2(rpm)−1/2
(c)
Bi2MoO6/2 wt % Porphy
(c′)
n = 3.44-3.52
(d)
Bi2MoO6/3 wt % Porphy
(d′)
n= 3.94-4.0
0.1 V
0.2 V
0.3 V
0.4 V

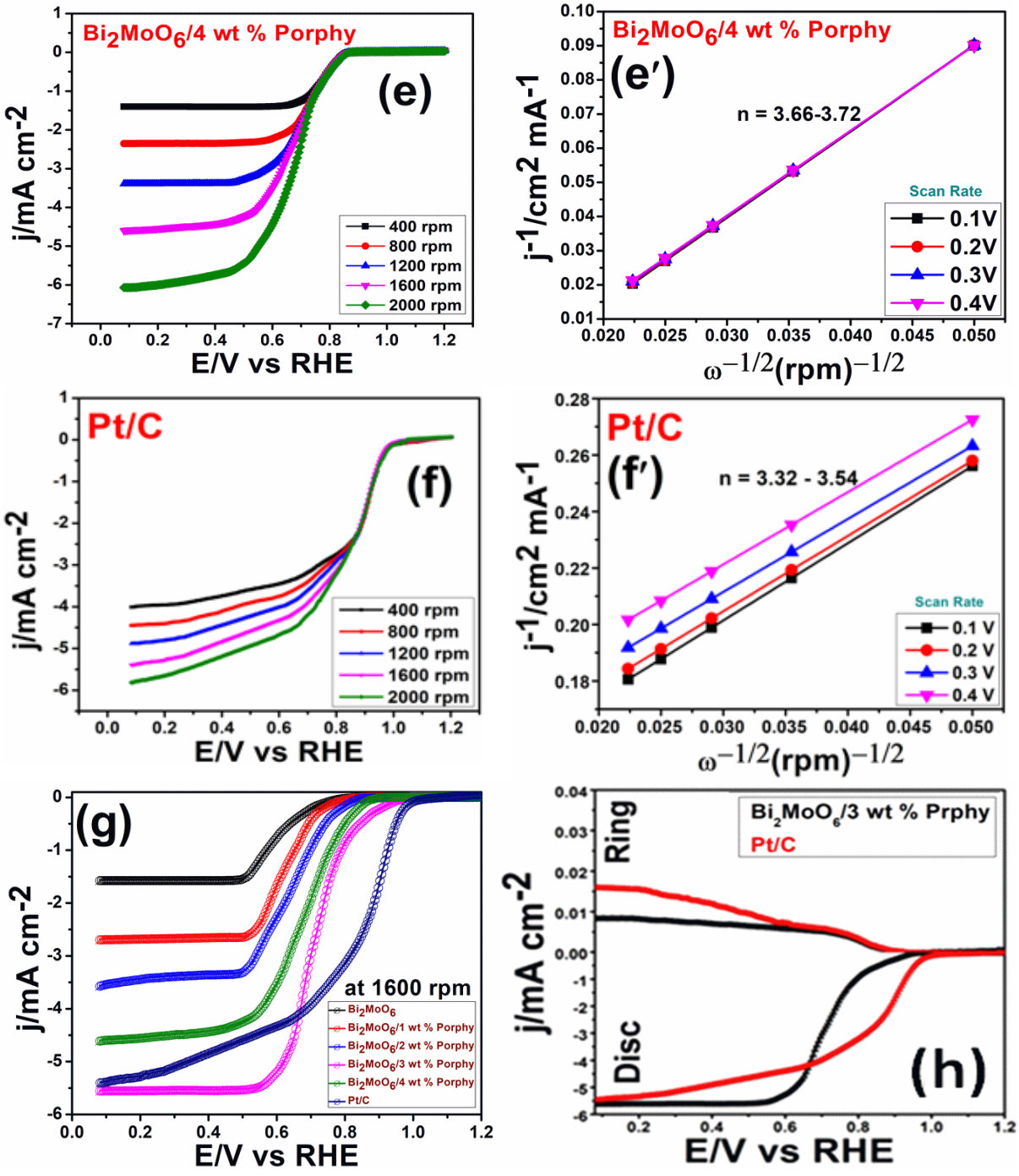

Figure 3.11. LSV plots (a→f) and K-L plots (a'→f') of bare Bi_2MoO_6 and different wt % Porphy-decorated Bi_2MoO_6 nanocomposite at rotating speeds from 400 to 2000 rpm (g) LSV plots at 1600 rpm for all electrodes (h) LSV-RRDE plots of Bi_2MoO_6/3 wt % Porphy and Pt/C.

Table 3.4. ORR performance of various materials during the electrocatalytic process.

Material	E_{onset} (V vs RHE)	$E_{½}$ (V vs RHE)	J_d (mA cm^{-2}) at 0.1 V	n	Tafel slope (mV dec^{-1})	η (V) (ΔE_{ORR} = 1.23 - $E_{½}$)	Δ $E_{½}$ (mV)
Bi_2MoO_6	0.782	0.571	-1.561	2	102.26	0.66	12.28
Bi_2MoO_6/1 wt % Porphy	0.839	0.626	-2.672	3.146	98	0.59	15.8
Bi_2MoO_6/2 wt % Porphy	0.842	0.648	-3.528	3.48	88	0.59	10.53
Bi_2MoO_6/3 wt % Porphy	0.942	0.704	-5.545	4	49.26	0.53	4.07
Bi_2MoO_6/4 wt % Porphy	0.864	0.671	-4.603	3.624	94.5	0.56	9.19
Pt/C	0.998	0.862	-5.4	3.54	75.62	0.368	5.89

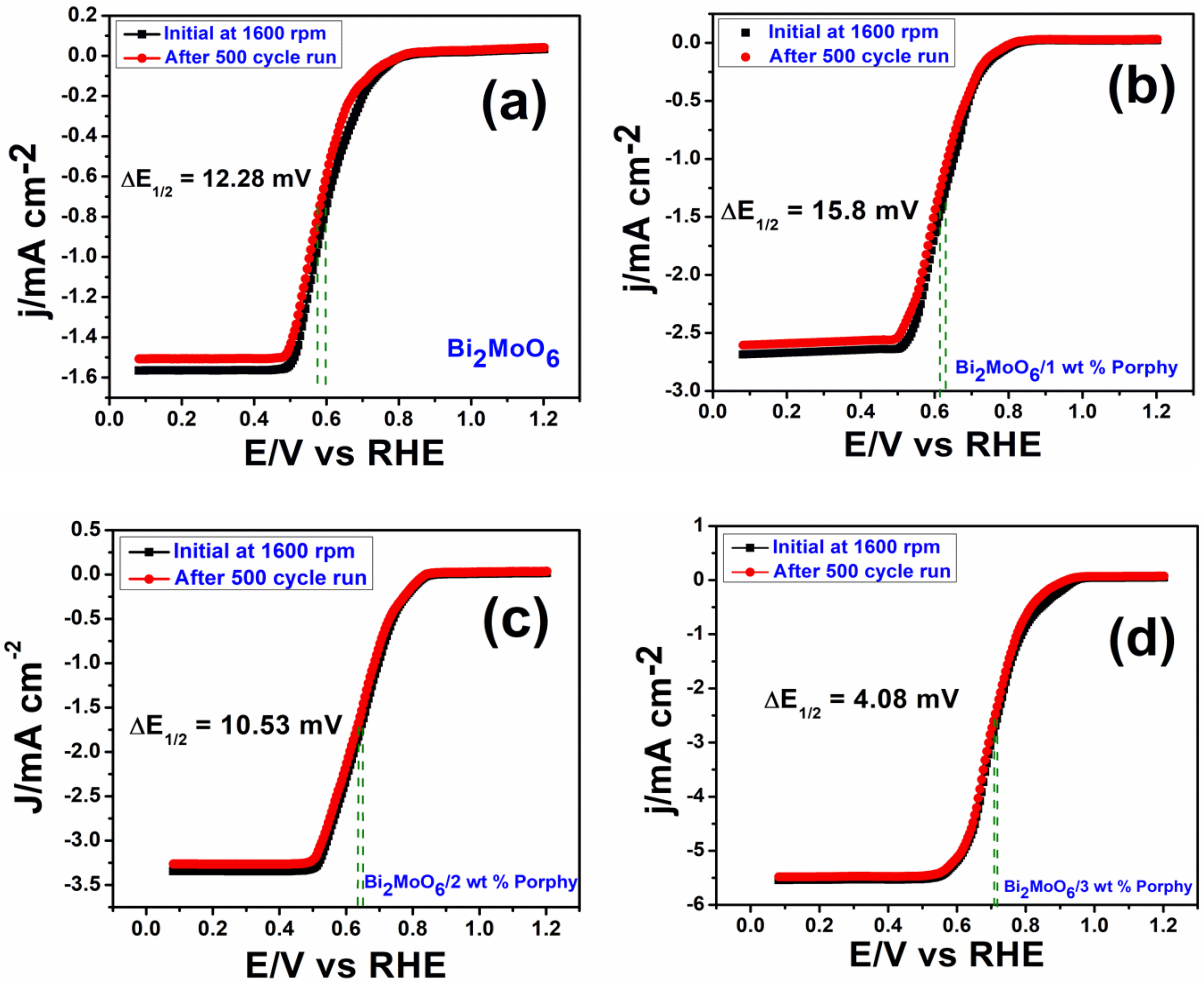

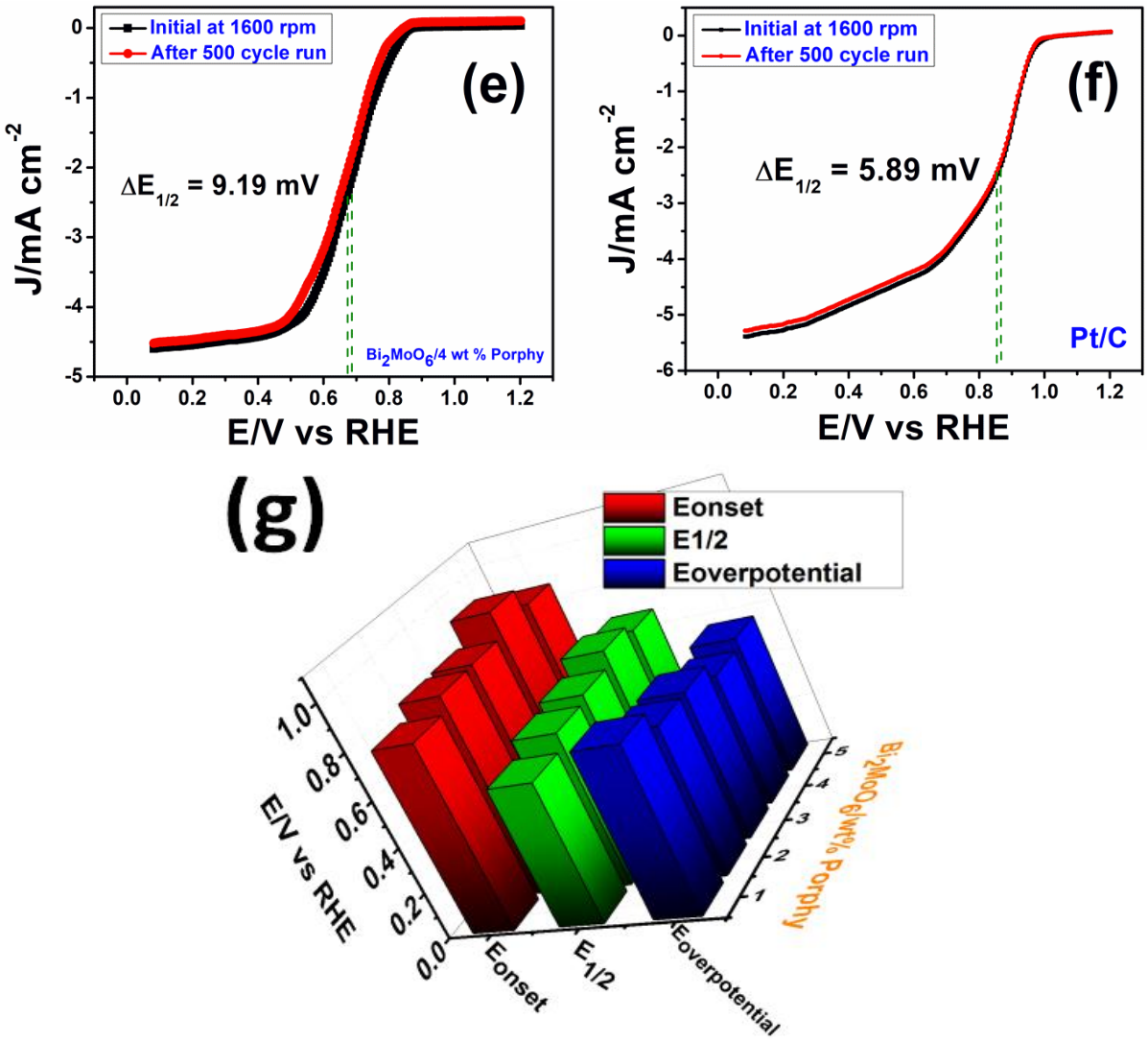

Figure 3.12. $\Delta E_{½}$ of (a) bare Bi_2MoO_6 (b→e) 1, 2, 3 and 4 wt % of Porphy-decorated nanocomposite (f) commercial Pt/C electrode at 1600 rpm, initial and final cycle (g) bar diagram of obtained onset potential, $E_{½}$ and overpotential values of bare Bi_2MoO_6 and different wt % of Porphy decorated Bi_2MoO_6 nanocomposites.

LSV plots of all electrocatalysts before and after 500 cycles are shown in Figure 3.12(a→f). The η (efficiency) of all electrocatalysts follows the given trend (Figure 3.12g): Bi_2MoO_6/3 wt % Porphy > Bi_2MoO_6/4 wt % Porphy > Bi_2MoO_6/2 wt % Porphy > Bi_2MoO_6/1 wt % Porphy > Bi_2MoO_6, further exhibiting the enhanced ORR activity of the Bi_2MoO_6/3 wt % Porphy nanocomposite. These superior kinetics are also reflected in the low Tafel slope (49.26 mV dec^{-1}) (Figure 3.13a), which is the lowest

among the other five, and this increased activity indicates its fast and favourable catalytic reaction kinetics, possibly due to faster charge transport and improved surface contact through ORR. This indicates superiority to previously reported catalysts (Table 3.5). The ORR reaction pathway was investigated using the K-L (Koutechy-Levich) equation (Figures 3.11(a′ and f′)), and the transferred number of electrons (n) was calculated. Typical plots showed good linearity of the K-L plots at various potentials, indicating first-order kinetics having the same electron transferred number per O_2 molecule. The n value for Bi_2MoO_6/3 wt % Porphy was found to be 4.0 in the potential range of 0.15-0.40 V, which is the highest among the other four catalysts and also for Pt/C (Table 3.4), indicating the complete reduction of O_2 to H_2O. This result, therefore, showed that the ORR activity remained unaffected in presence of Pt electrode during the electrochemical measurement. Thus, our noble element free nanocomposite was liable for the improved ORR activity, not for Pt counter electrode.[21,29,30]

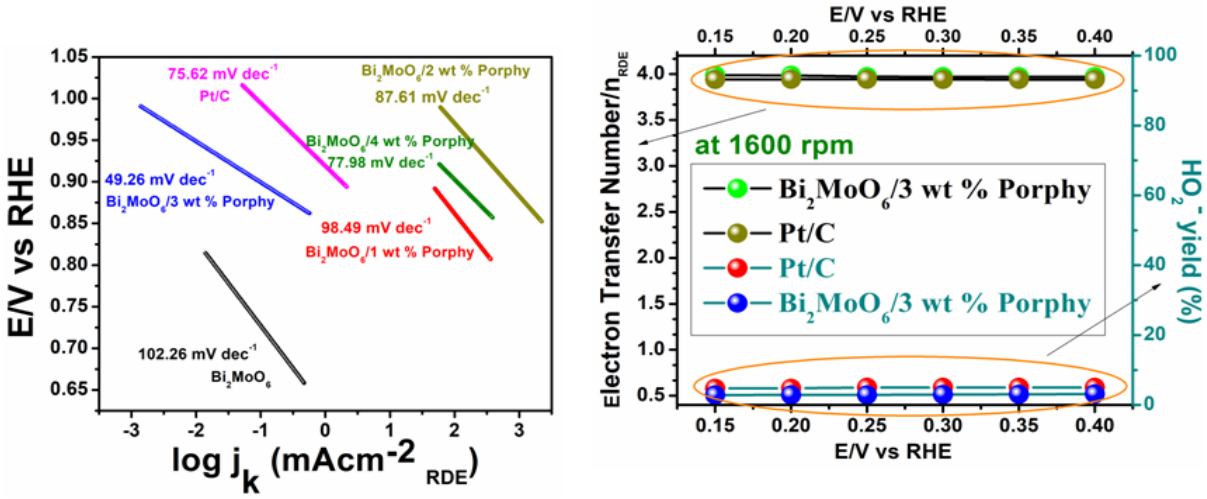

Figure 3.13. (a) Tafel slope of bare Bi_2MoO_6 as well as different wt % of Porphy decorated Bi_2MoO_6 nanocomposites compared with commercial Pt/C electrode (b) Representation of electron transfer number (n) and percentage of peroxide (HO_2^-) yield w.r.t. potential throughout ORR at a rotating speed of 1600 rpm for Bi_2MoO_6/3 wt % Porphy and Pt/C electrodes.

Again, the calculated values of n for Bi_2MoO_6 (2), Bi_2MoO_6/1 wt % Porphy (3.146), Bi_2MoO_6/2 wt % Porphy (3.48), Bi_2MoO_6/4 wt % Porphy (3.624), and commercial Pt/C (3.54) in the same potential range show that instead of only H_2O both H_2O_2 and H_2O are formed. H_2O_2 production decreases with increasing wt % of loaded Porphy over Bi_2MoO_6, but eventually disappears for Bi_2MoO_6/3 wt %

Porphy (Figure 3.13b) and increases again for Bi_2MoO_6/4 wt % Porphy. Furthermore, the value of n for Bi_2MoO_6/3 wt % Porphy obtained from RRDE measurements (Figure 3.11h) is approximately 4.0, indicating negligible (~ 0.8%) formation of HO_2^- for Bi_2MoO_6/3 wt % Porphy nanocomposite in 0.15 to 0.40 V potential range (Table 3.6).

Table 3.5. Comparison of electrocatalytic performance of Bi_2MoO_6/3 wt % Porphy with various reported catalysts toward ORR in 0.1 M KOH Solution.

Materials	E_{onset} (V vs. RHE)	$E_{½}$ (V vs. RHE)	J_d (mA cm^{-2})	n	Ref.
Bi_2MoO_6/3 wt % Porphy	0.942	0.704	-5.545	4	**This work**
FeTPyP + Co	-0.1	-0.22	-1.4	-	31
Cu_2ZnSnS_4-AuAg	0.87	0.73	-5.32	~ 3.9	32
g-C_3N_4/GO	0.984	0.859	-5.98	4.0	33
Co_3O_4/Au	0.99	0.83	-5.3	4.0	34
GPHox + Co(II)OEP	-0.08 vs. Ag/AgCl	-	-	4.0	35
Hollow Mo_2C-C microspheres	0.832	0.713	-5.52	~ 3.2- 3.6	36
C-FeZIF-900-0.84	0.95	0.85	-5.3	3.8	37
Fe-N-CNT/OMC	1.01	~ 0.85	-6.5	~ 3.97	38
G-Mo_2C	0.75	0.85	-3.6	2.13-3.21	39
CuAg@Ag/N-GNS	0.94	0.85	-6.5	3.8-4.0	40
Fe-N-C/rGO	0.94	0.81	-6.5	3.8-4.0	41
Mo_2C/NPCNFs	0.9	-	~ -4.8	~ 3.8	42
Co0.6Mo1.4N_2	0.713	-	-6.2	4.1	43
α-Fe_2O_3@MoS_2/NGNS	0.9476	0.8546	~ 7.0	~ 3.91-3.96	44
Mo_2C/CXG	0.89	-	~ -4.1	3.0	45
ppy/$AgVO_3$/porphy	1.05	0.89	-17.32	4.0	46
MWNT-Fe Porphyrin	0.1	-	-	3.97	47

This result shows that introduction of N-containing π-conjugated organic moiety to Bi_2MoO_6 considerably enhanced its ORR efficacy. The result further reveals that the decoration of Porphy over Bi_2MoO_6 offers both pyrrolic- and pyridinic-N, which provides a rough surface that delivers numerous active sites for electrocatalytic reactions, leading to a considerable enhancement in ORR activity. The presence of both pyrrolic- and pyridinic-N and the enhanced surface area considerably increases the ORR activity of Bi_2MoO_6/3 wt % Porphy.

Table 3.6. Electron transfer number (n) and peroxide yield during ORR activity.

Electrocatalysts	Number of Electron Transfer (n) from RDE	Number of Electron Transfer (n) from RRDE	% H_2O_2
Bi_2MoO_6/3 wt % Porphy	4.0	4.0	0.8
Pt/C	3.54	3.6	1.5

3.3.2.3. Mechanism of ORR of Bi_2MoO_6/3 wt % Porphy nanocomposite. Due to the screening effect, the negatively charged N causes the surrounding carbon atoms to get partial positive positively charged. Pyrrolic-N atoms in Porphy can donate electrons to the conjugated system, which sequentially increases the nucleophilicity of neighbouring carbon atoms.

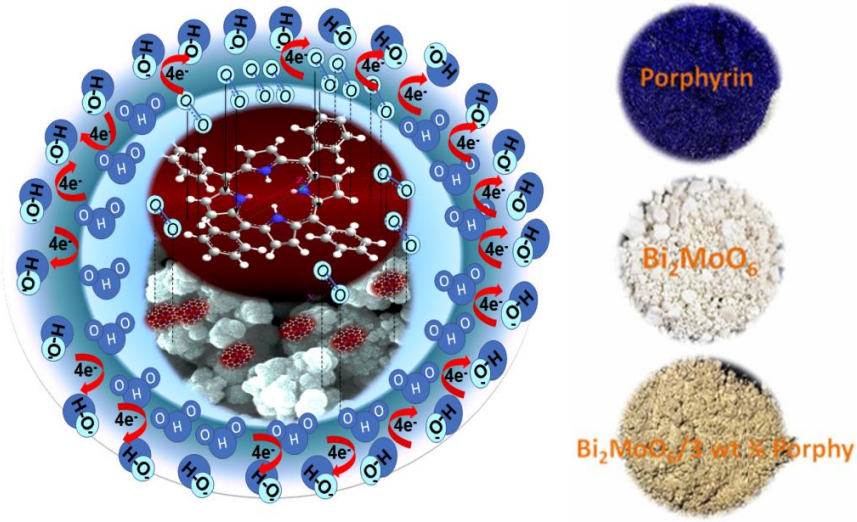

Scheme 3.3. Mechanism of ORR of Bi_2MoO_6/3 wt % Porphy nanocomposite via $4e^-$ transfer pathway.

As a result, O_2 adsorption was enhanced and ORR activity was accelerated. This N-induced charge delocalization also changes the O_2 chemisorption mode from end-on adsorption on the N-free Bi_2MoO_6 surface to side-on adsorption on the surface of N-containing composites, thereby weakening the O-O bonding parameters through parallel diatomic adsorption, assisting ORR activity (**Scheme 3.3**). Therefore, the presence of both pyrrolic- and pyridinic-N atoms plays an important role in increasing the active site density of Bi_2MoO_6/Porphy, significantly improving its kinetics compared to others. The abnormal trend of ORR activities of different wt % of Porphy decorated Bi_2MoO_6

nanocomposites are also supported by the findings of electrochemical surface area and roughness of the modified electrodes (Table 3.7).

Table 3.7. C_{dl}, ESCA and R_f for the different catalyst from cyclic voltammograms in non-faradic region.

Nanocomposites	C_{dl} (mF cm^{-2})	ECSA (cm^2)	R_f
Bi_2MoO_6	6.58	164.5	1316
Bi_2MoO_6/1 wt % Porphy	7.79	194.75	1558
Bi_2MoO_6/2 wt % Porphy	7.94	198.5	1558
Bi_2MoO_6/3 wt % Porphy	8.62	215.5	1724
Bi_2MoO_6/4 wt % Porphy	7.32	183	1464

3.3.2.4. Electrochemical Active Surface Area (ECSA) Analysis. For ORR, the ECSA and roughness factor (R_f) of the catalysts were evaluated to better understand the surface accessibility of the catalysts. In general, electrocatalysts with more exposed active sites have higher catalytic activity. We estimated ECSA by cyclic voltammetry (CV) measurements of the electrochemical double layer capacitance (C_{dl}) determined by the linear slope of the capacitive current density versus scan rate (Figure 3.14f). Cyclic voltammograms were recorded at various scan rates of 20, 40, 60, 80, and 100 mV s^{-1}, with potentials ranging between 0.90 V and 1.10 V (Figures 3.14(a→e)). The C_{dl} value of Bi_2MoO_6/3 wt % Porphy (8.62 mF cm^{-2}) is larger than that of other catalysts, suggesting the higher ECSA of Bi_2MoO_6/3 wt % Porphy (Table 3.7) as well as better charge transfer ability, which might be the responsible factor for the fast charge transfer rate for the efficient ORR process. EIS was recorded in the frequency range from 0.1 to 10^5 Hz with AC amplitude of 5 mV. Figure 3.15 shows the Nyquist plot, where Z' and Z" represent the real and imaginary parts of the impedance, respectively. The extended Nyquist plot (at 0.8 V vs. RHE) for Porphy decorated Bi_2MoO_6 shown in Figures 3.15(b→c) represents a semicircle with an equivalent circuit composed according to the Randless cell structure (inset figures 3.15b and c). The electrolyte resistance (R_s) corresponds to the lower frequency point, while the electron-transfer resistance (R_{ct}) corresponds to the higher frequency point where the curves intersect the real impedance axis (Z′). For Bi_2MoO_6/3 wt % Porphy nanocomposite, double arc curvature implies the different modes of interfacial charge transfer resistance, in which the first arc is smaller than that of the second arc due to the increased conductivity at the electrode-electrolyte junction at both 0 rpm and 1600 rpm rotating speeds for ORR kinetics. The low-frequency semicircles are associated with the adsorption of reactive intermediates

such as HO_2^- (common intermediates in ORR) to the electrode surface. The smaller R_{ct} value of Bi_2MoO_6/3 wt % Porphy (Table 3.8), which is considerably better than the others, indicates a more rapid charge transfer for ORR. For ORR kinetics, electrochemical impedance spectroscopic (EIS) analysis was further used to measure the double layer capacitance (C_{dl}) at rotating speeds of 0 rpm and 1600 rpm. The above measured C_{dl} values (Table 3.8) for different electrodes follow a similar trend of results to the C_{dl} values calculated from CV techniques (Table 3.7). The highest ECSA and R_f values for Bi_2MoO_6/3 wt % Porphy also support the above result, revealing that its surface was remarkably rich in active sites, resulting in its excellent intrinsic activity. The overall results also reinforce the electrocatalytic activity of Bi_2MoO_6/3 wt % Porphy compared with other Porphy-decorated nanocomposites through CV, LSV, EIS, K-L, and Tafel plots.

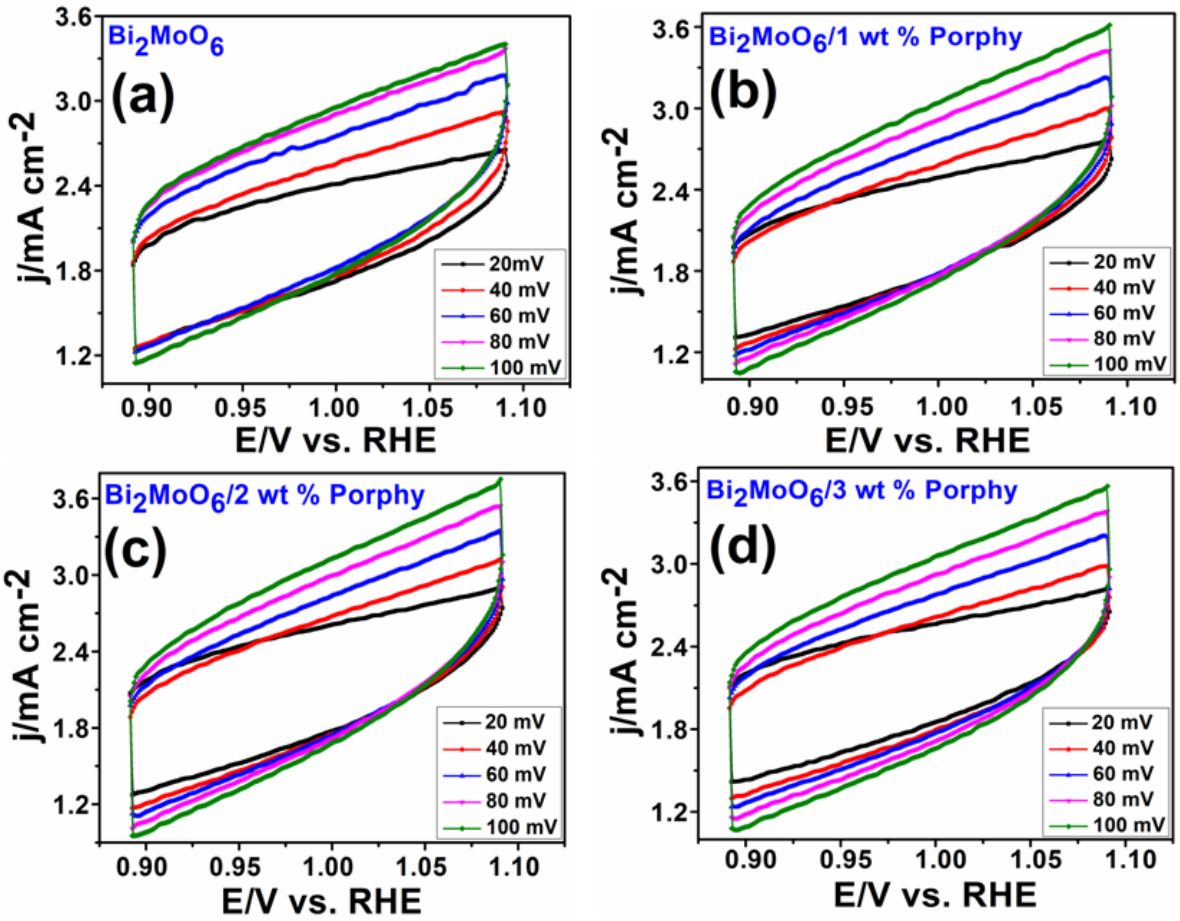

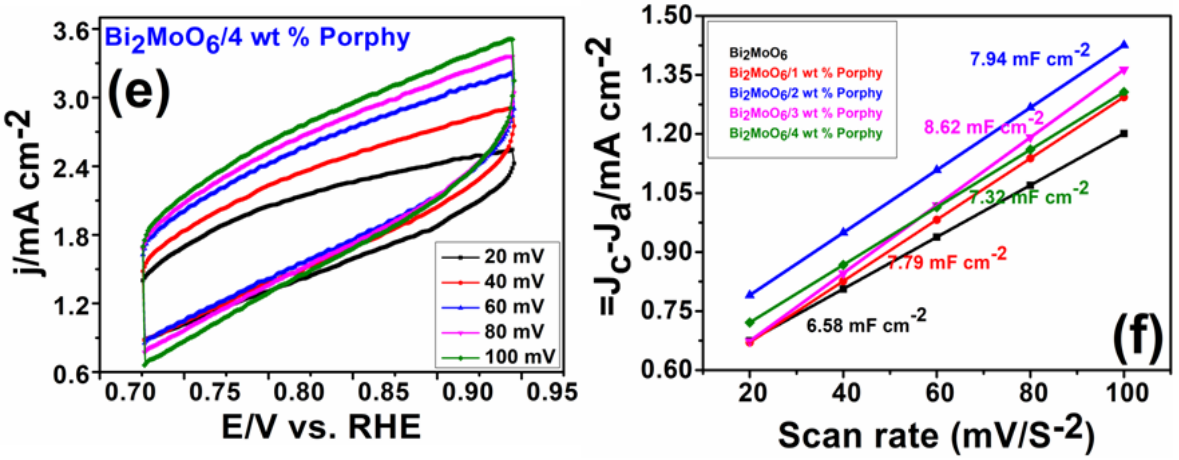

Figure 3.14. CV curves recorded in the double layer capacitance charging region at increasing scan rates (a→e) of bare Bi_2MoO_6 as well as decorated with different wt % Porphy nanocomposites (f) Linear fitting of respective capacitive current density vs. scan rate for measuring the ECSA.

Table 3.8. R_s, R_{ct} and Z′ for the different composites from 1 wt % to 3 wt % Porphy for both 0 rpm and 1600 rpm.

RDE at 1600 rpm	R_s (Ω cm^2)	$R_s + R_{ct}$ (Ω cm^2)	R_{ct} (Ω cm^2)	Z′ (Ω cm^2)	C_{dl} (mF cm^{-2})
Bi_2MoO_6	13.72	163.25	149.53	89.74	0.8794
Bi_2MoO_6/1 wt % Porphy	14.51	150.37	135.86	85.38	1.7145
Bi_2MoO_6/2 wt % Porphy	12.30	124.52	112.22	73.72	1.7195
Bi_2MoO_6/3 wt % Porphy	14.02	107.78	93.76	61.15	2.058
Bi_2MoO_6/4 wt % Porphy	13.52	135.68	122.16	79.19	1.0761
RDE at 0 rpm	**R_s (Ω cm^2)**	**$R_s + R_{ct}$ (Ω cm^2)**	**R_{ct} (Ω cm^2)**	**Z′ (Ω cm^2)**	**C_{dl} (mF cm^{-2})**
Bi_2MoO_6	13.87	151.20	137.33	86.63	0.5384
Bi_2MoO_6/1 wt % Porphy	18.2	169.48	151.28	95.50	0.5922
Bi_2MoO_6/2 wt % Porphy	14.44	199.58	185.14	110.35	0.8590
Bi_2MoO_6/3 wt % Porphy	11.30	122.36	111.06	67.50	0.9753
Bi_2MoO_6/4 wt % Porphy	17.69	189.13	171.44	103.87	0.7669

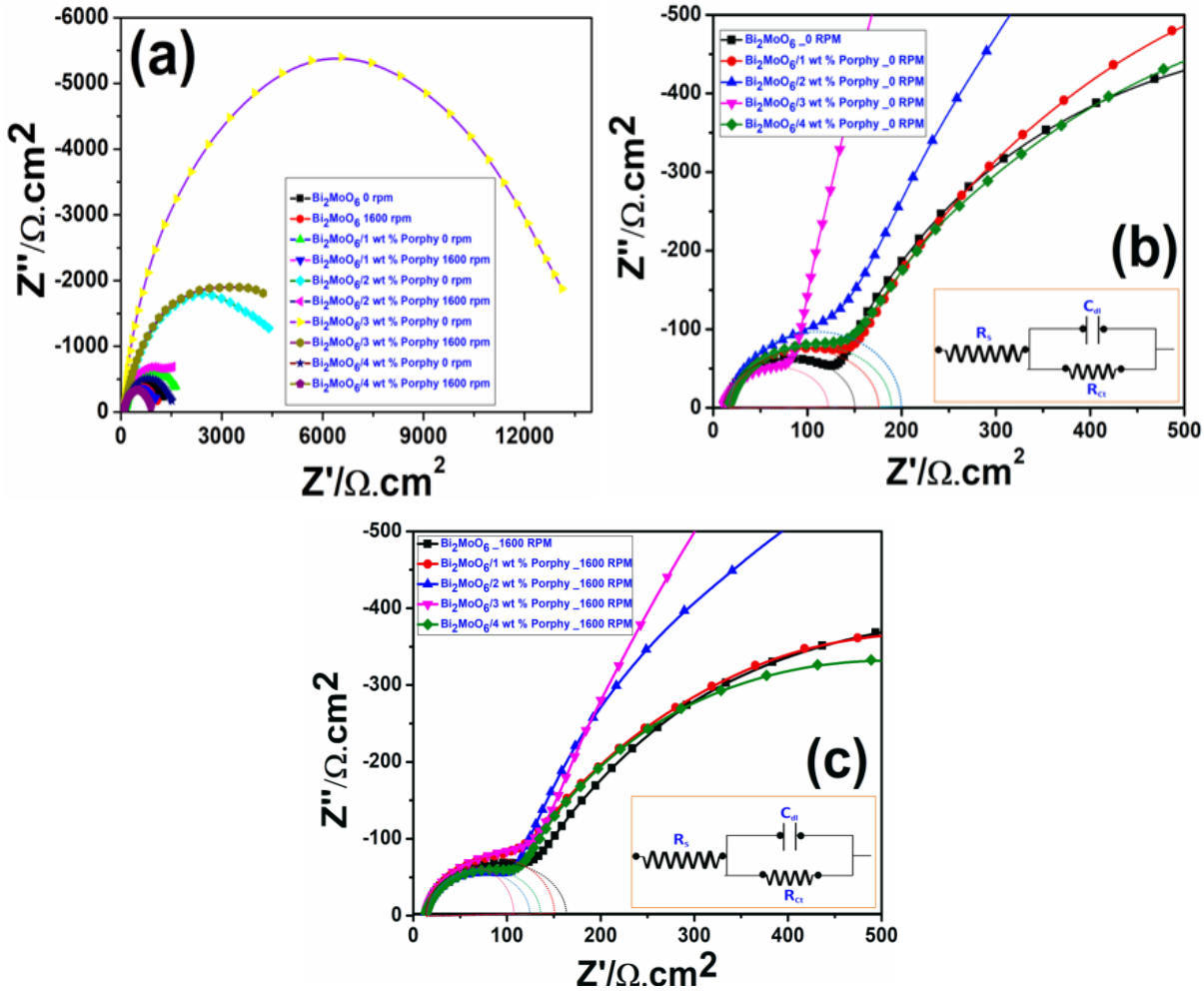

Figure 3.15. (a) Nyquist plots of bare Bi_2MoO_6 and modified Bi_2MoO_6 with different wt % Porphy nanocomposites on GCE in 1.0 M KOH medium; Extended Nyquist's plot for bare Bi_2MoO_6 and modified Bi_2MoO_6 with different wt % Porphy nanocomposites on GCE in 1.0 M KOH for the determination of charge transfer resistance (inset: Equivalent circuit analogue of electrode-electrolyte resistance) at 0 rpm (b) and at 1600 rpm (c).

3.3.2.5. Durability test by chronoamperometric analysis. The chronoamperometric analysis and the LSV measurements were employed to investigate the accelerated durability and potential cycling stability. After 20,000 s, the retention (%) of the currents for Bi_2MoO_6/3 wt % Porphy and for commercial Pt/C was 99.6 and 84 (Figure 3.16a), showing outstanding stability and durability of Bi_2MoO_6/3 wt % Porphy nanocomposite. Figures 3.12(a→f) illustrated the effect of potential cycling stability after 500 cycles of Bi_2MoO_6, Bi_2MoO_6/1 wt % Porphy, Bi_2MoO_6/2 wt % Porphy, Bi_2MoO_6/4

wt % Porphy, and Pt/C catalysts. There was a negative shift in the half-wave potential ($E_{½}$) of approximately 12.28, 15.80, 10.53, 9.19, and 5.89 mV, respectively (Table 3.4). Remarkably, the polarization curve of Bi_2MoO_6/3 wt % Porphy showed a negligible decrease in limiting current density with a negative shift of $E_{½}$ of 4.08 mV, further confirming its excellent stability.

Furthermore, during chronoamperometric measurements, when 3.0 M CH_3OH (20 vol %) was injected into an O_2-saturated 0.1 M KOH solution, it showed impressive tolerance toward CH_3OH poisoning effects compared to Pt/C. The CH_3OH crossover is a major problem in direct methanol fuel cells. This is because CH_3OH and its oxidative intermediates can toxin the active sites of the catalyst through electrode material imbalances in their equlibria, which consecutively reduces the energy density and increases the overpotential of the cathodic reaction. Figure 3.16b showed that there was no obvious change in the current density of Bi_2MoO_6/3 wt % Porphy after CH_3OH addition, while for Pt/C there was a sudden and sharp decrease in the current density. This result confirms that the Bi_2MoO_6/3 wt % Porphy nanocomposite possesses exceptional ORR performance such as catalytic activity, durability, stability, and CH_3OH tolerance.

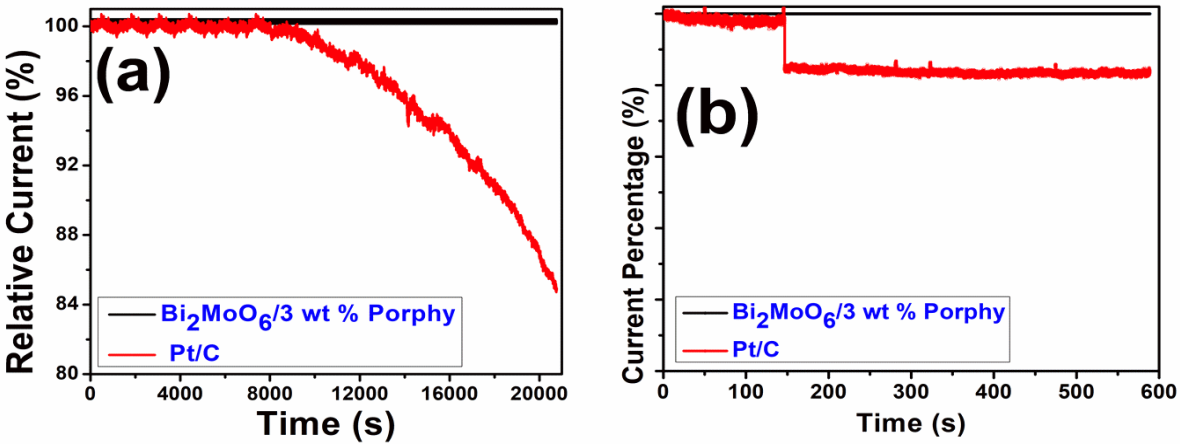

Figure 3.16. (a) Chronoamperometric durability test at 0.66 V, rotating speed of 1600 rpm, up to 20000 seconds (b) CH_3OH tolerance test of Pt/C and Bi_2MoO_6/3 wt % Porphy, 18ml of CH_3OH was added to 72 ml of 0.1 M KOH solution after about 150 s.

3.3.2.6. Structural analysis of Bi_2MoO_6/3 wt % Porphy nanocomposite after ORR has been done by PXRD. The structural, as well as phase analysis of Bi_2MoO_6/Porphy nanocatalysts, were confirmed after the ORR electrocatalysis process by XRD analysis. Figure 3.17 showed its excellent structural stability, suggesting that the material can be reused for these catalytic reactions. The

improved stability of the Bi_2MoO_6/3 wt % Porphy nanocatalyst might be owing to the protection of the Porphy coat around the Bi_2MoO_6 nanoparticles.

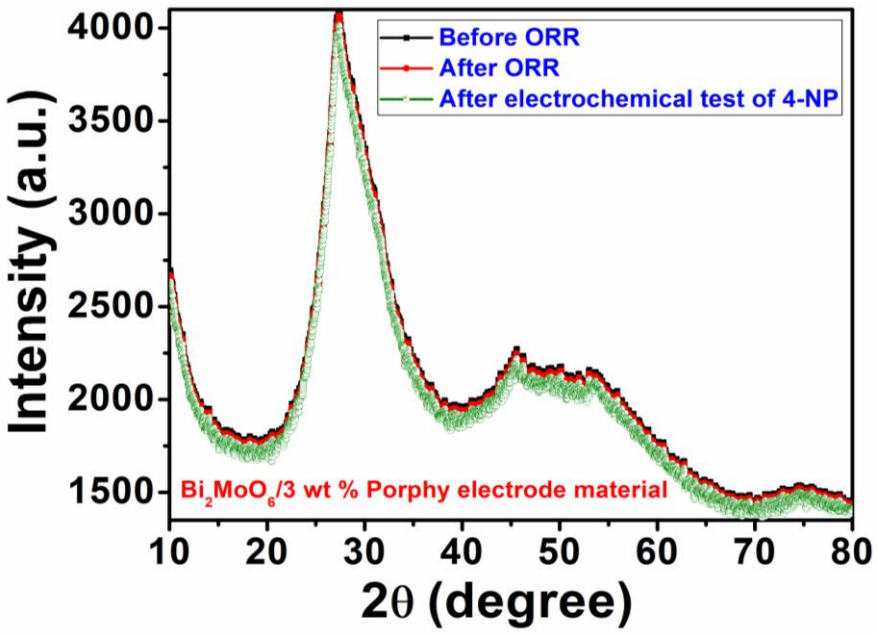

Figure 3.17. X-ray diffraction analyses of Bi_2MoO_6/3 wt % Porphy nanocomposites before, after ORR as well as p-NP electrochemical reduction.

3.3.3. Electrocatalytic reduction of p-nitrophenol using modified GCE/Bi_2MoO_6/3 wt % Porphy.

To investigate any other catalytic activity besides its ORR activity, the electrocatalytic reduction of p-NP was performed with the help of electrochemical techniques. Figure 3.18a showed the CV responses of bare GCE, GCE/Bi_2MoO_6, GCE/Bi_2MoO_6/1 wt % Porphy, GCE/Bi_2MoO_6/2 wt % Porphy, GCE/Bi_2MoO_6/3 wt % Porphy, GCE/Bi_2MoO_6/4 wt % Porphy in 0.1 M KCl solution with a redox couple of 2.5 mM $K_3[Fe(CN)_6]$ and 2.5 mM $K_4[Fe(CN)_6]$ in an electrolytic bath under N_2 purging for 2 minutes to study the electrochemical behaviour of different fabricated electrode. Here, we observed that the GCE/Bi_2MoO_6/3 wt % Porphy showed better electrochemical signals and utilized this specific electrode for further studies of p-NP at a particular pH through cyclic voltammogram. The presence of abundant active sites for electrocatalytic reaction may be attributed to the better electrochemical response of p-NP for GCE/Bi_2MoO_6/3 wt % Porphy. The GCE/Bi_2MoO_6/3 wt % Porphy exhibited a reduction peak due to the formation of p-(hydroxyamino)-phenol. The irreversible reduction corresponded to a direct reduction mechanism involving a 4-

electron and 4-proton transfer process from p-nitrophenol to p-(hydroxyamino)-phenol, which is consistent with previous reports.[48,49] Higher cathodic current for reduction is owing to ion-dipole interactions through electrostatic interactions[50] (**Scheme 3.4**).

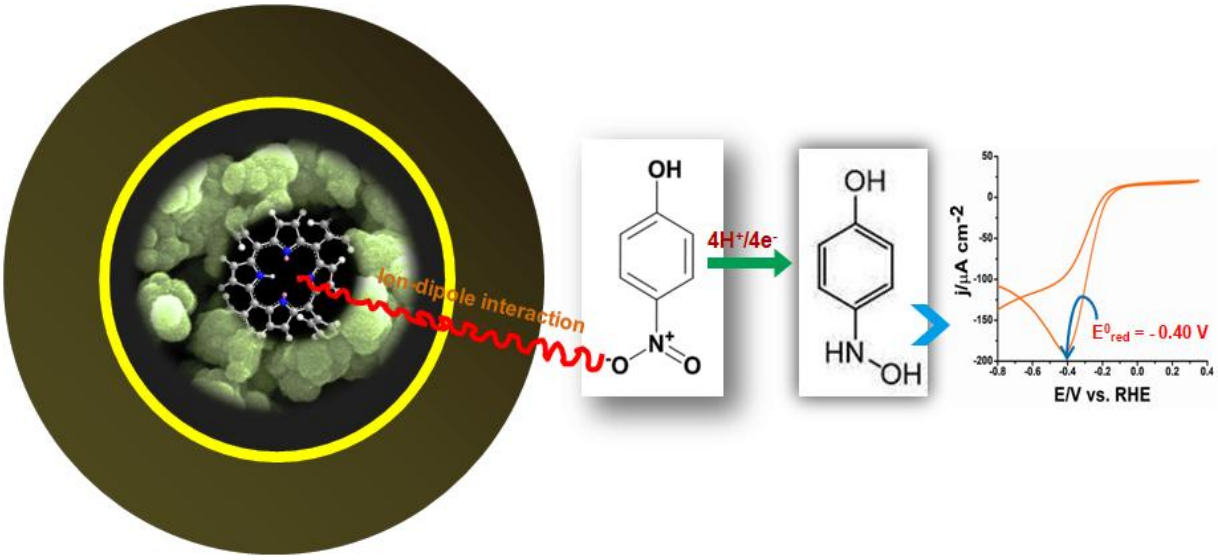

Scheme 3.4. Electron transfer mechanism for the direct reduction of p-nitrophenol to p-hydroxylaminophenol.

3.3.3.1. Effect of pH

The effect of the pH on the electrochemical behaviour of p-nitrophenol was investigated by cyclic voltammogram for GCE/Bi_2MoO_6/3 wt % Porphy. Figure 3.18b illustrated the CV response of p-NP at 20 mVs^{-1} scan rate with different pH of 5.0, 6.0, 7.0, and 8.0. The reduction peak shifts positively and linearly with increasing pH,[51] and a slope of 0.06 V/pH was calculated based on the corresponding linear fit (Figure 3.18c). This is close to the theoretical value of 0.059 V/pH, and, the electrons and protons involved in p-NP reduction were identical. This corresponds to the electro-reduction mechanism described above for p-NP, and the linear regression equation is as follows:

$$E_{pc}(V) = 0.06\ pH - 0.705 \quad R^2 = 0.808 \qquad \text{Eq. 3.12}$$

The relationship between peak potential and pH is given by equation[52] below:

$$E_{pc} = E' - \left[\frac{2.303mRT}{nF}\right]pH \qquad \text{Eq. 3.13}$$

Where m and n indicate the number of electrons and protons transferred during the reduction process. T is the temperature (298 K), R is the gas constant (8.314 J K^{-1} mol^{-1}), and F is the Faraday constant.

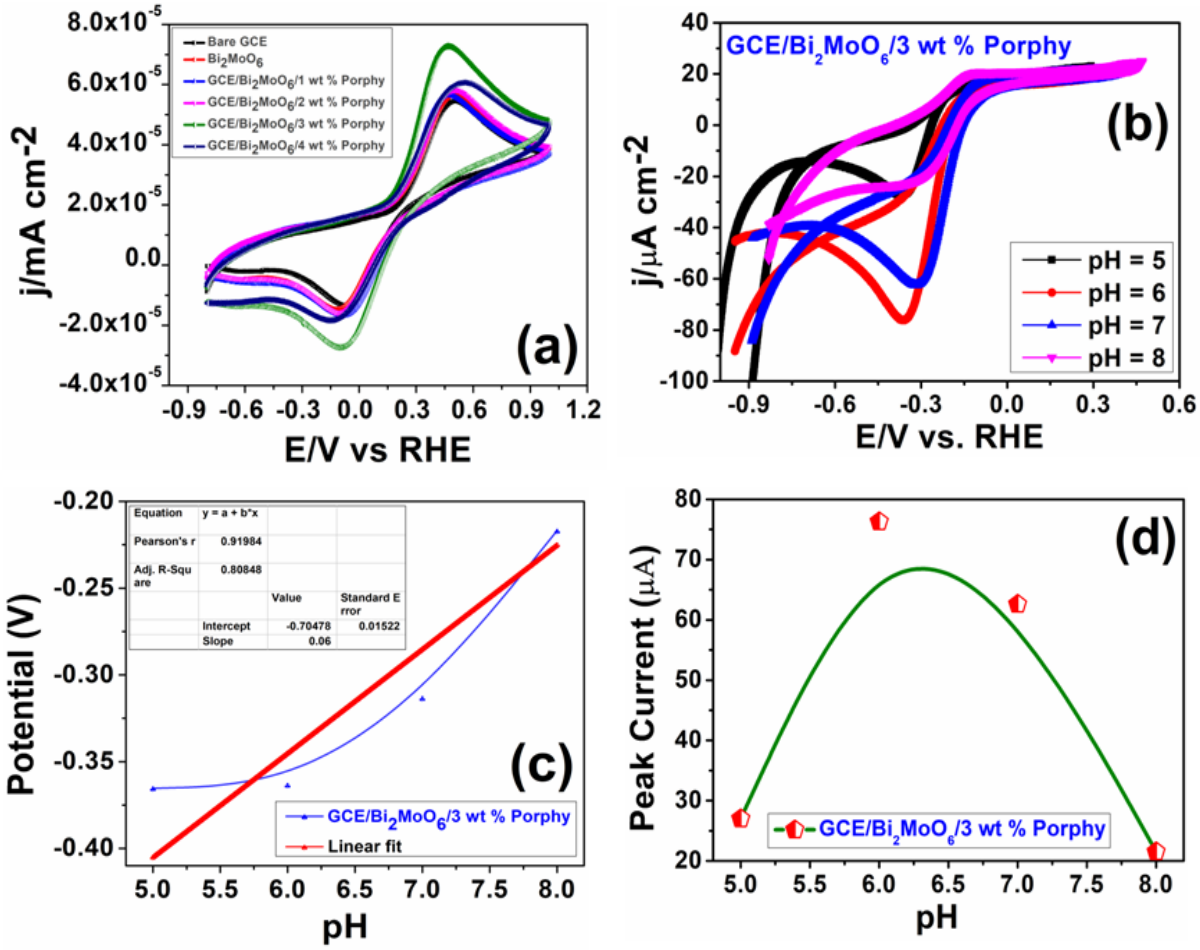

Figure 3.18. (a) CVs of bare GCE, GCE/Bi_2MoO_6 and GCE/ Bi_2MoO_6 with different wt % of Porphy in $[Fe(CN)_6]^{3-}$/$[Fe(CN)_6]^{4-}$/KCl redox couple (b) CVs of GCE/Bi_2MoO_6/3 wt % Porphy in 0.1 M PBS medium containing 200 μM p-NP at 20 mV s^{-1} scan rate (pH ~ 5.0, 6.0, 7.0, 8.0) (c) Potential against pH (d) Peak current against pH of Bi_2MoO_6/3 wt % Porphy nanocomposite for electrochemical sensing of p-NP.

It was established that the reduction peak current (j_{pc}) gradually increased from pH 5.0 to 8.0 and attained a maximum value at pH 6.0. Therefore, an optimal pH 6.0 was used for further electrochemical investigations. Figure 3.18d showed a plot of peak reduction current versus solution pH. The electrochemical reduction of p-NP depends on the pH of the solution, and the electrode

exhibited excellent catalytic performance in the weakly acidic condition. Again, we studied the electrochemical behaviour of different electrodes under similar conditions and concluded that GCE/Bi_2MoO_6/3 wt % Porphy is the best for electrochemical reduction tendency, with sensing abilities among all of them (Figures 3.19a and b)), which may be due to the presence of both pyrrolic- and pyridinic-N of Porphy enhancing the active sites on the surface bed of the nanocomposite.

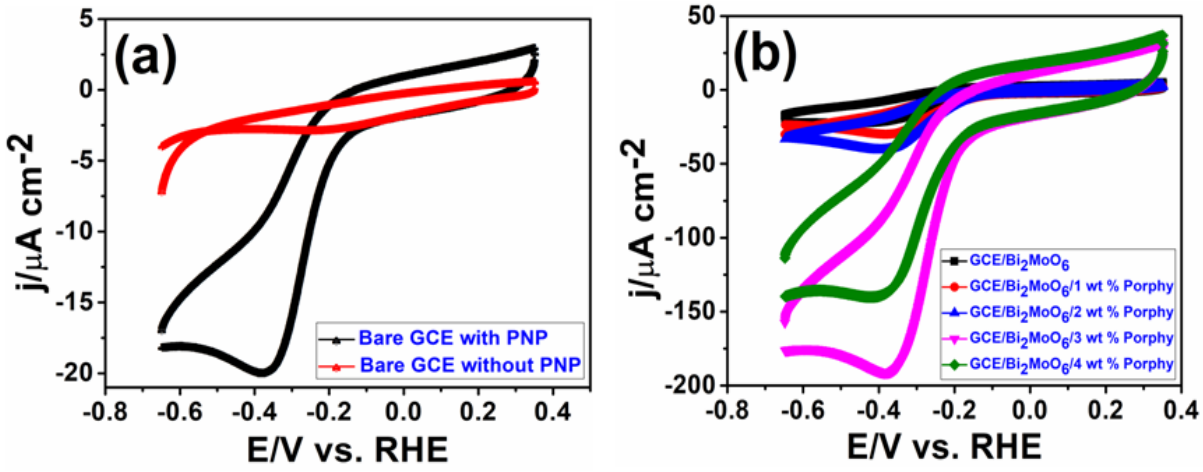

Figure 3.19. (a) CVs of 200 μM p-NP with Bare GCE (b) GCE/Bi_2MoO_6, GCE/Bi_2MoO_6/1 wt % Porphy, GCE/Bi_2MoO_6/2 wt % Porphy, GCE/Bi_2MoO_6/3 wt % Porphy, GCE/Bi_2MoO_6/4 wt % Porphy in 0.1 M 20 mL PBS at a scan rate of 250 mV s^{-1} (pH 6.0).

3.3.3.2. Effect of scan rate. The effect of scan rates during electrochemical analysis of p-NP on GCE/Bi_2MoO_6/3 wt % Porphy was examined by CV at constant concentration (200 μM p-NP) and pH 6.0. The reduction current increases with the rise of the scan rate from 20 mV s^{-1} to 250 mV s^{-1} (Figures 3.20 (a→g)).

A linear relationship was observed between the peak cathodic current (j_{pc}) and the square root of the scan rate ($\nu^{1/2}$), (Figures 3.20b, e and h) and the observed linear regression equation is as follows:

$$j_{pc} = -7.49\nu^{\frac{1}{2}}\left(mV^{\frac{1}{2}}S^{-\frac{1}{2}}\right) - 76.347 \quad R^2 = 0.993 \qquad \text{Eq. 3.14}$$

This suggests that the reduction of p-NP on GCE/Bi_2MoO_6/3 wt % Porphy is a diffusion-controlled process. Moreover, the peak potential shifted in the negative direction as the scan rate increased. The peak cathodic potential (E_{pc}) has a linear relationship with the logarithm of the scan rate (ln ν) (Figures 3.20c, f and i) and the observed linear regression equation is:

$$E_{pc} = -0.024 \ln \nu - 0.250 \quad R^2 = 0.973 \qquad \text{Eq. 3.15}$$

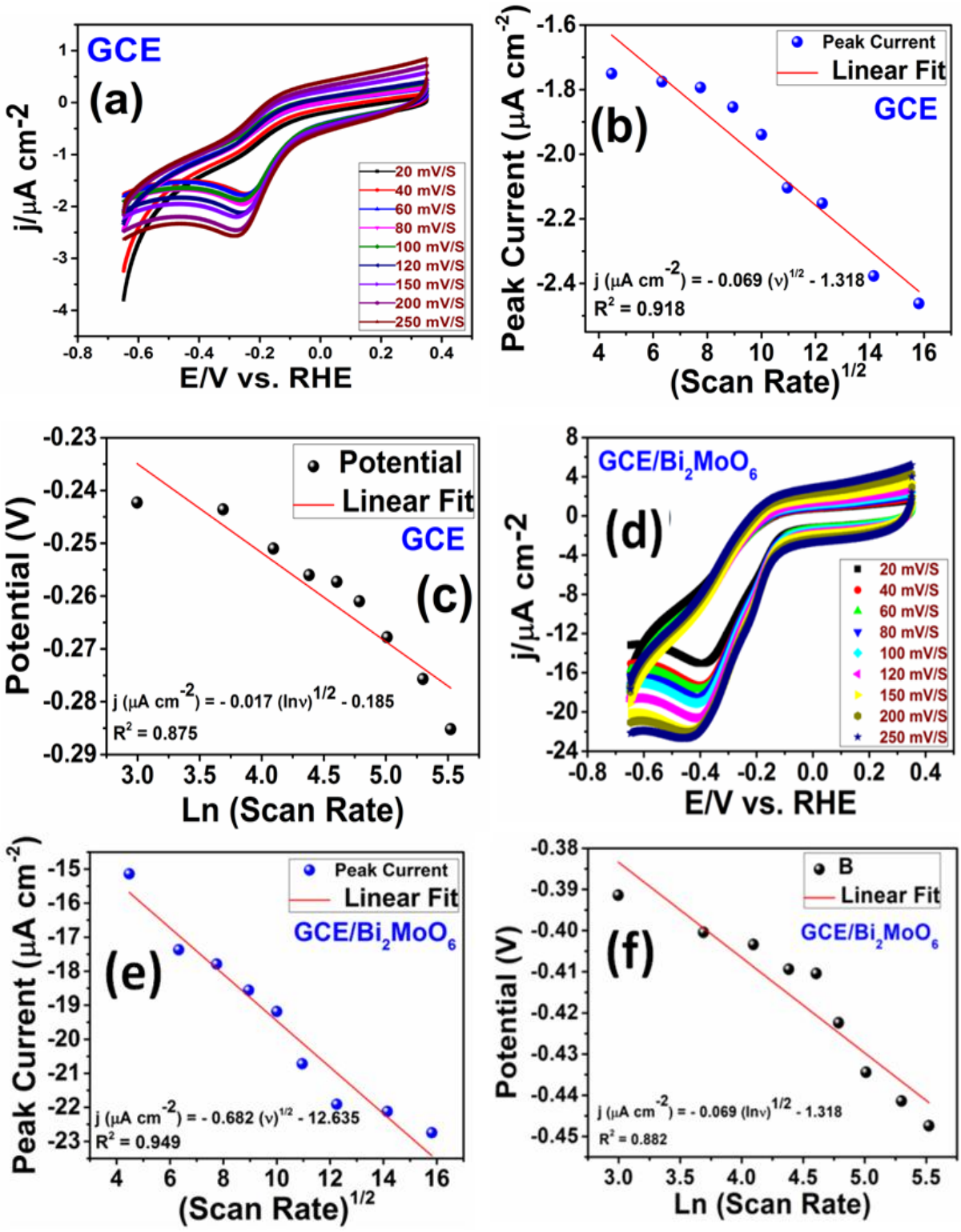

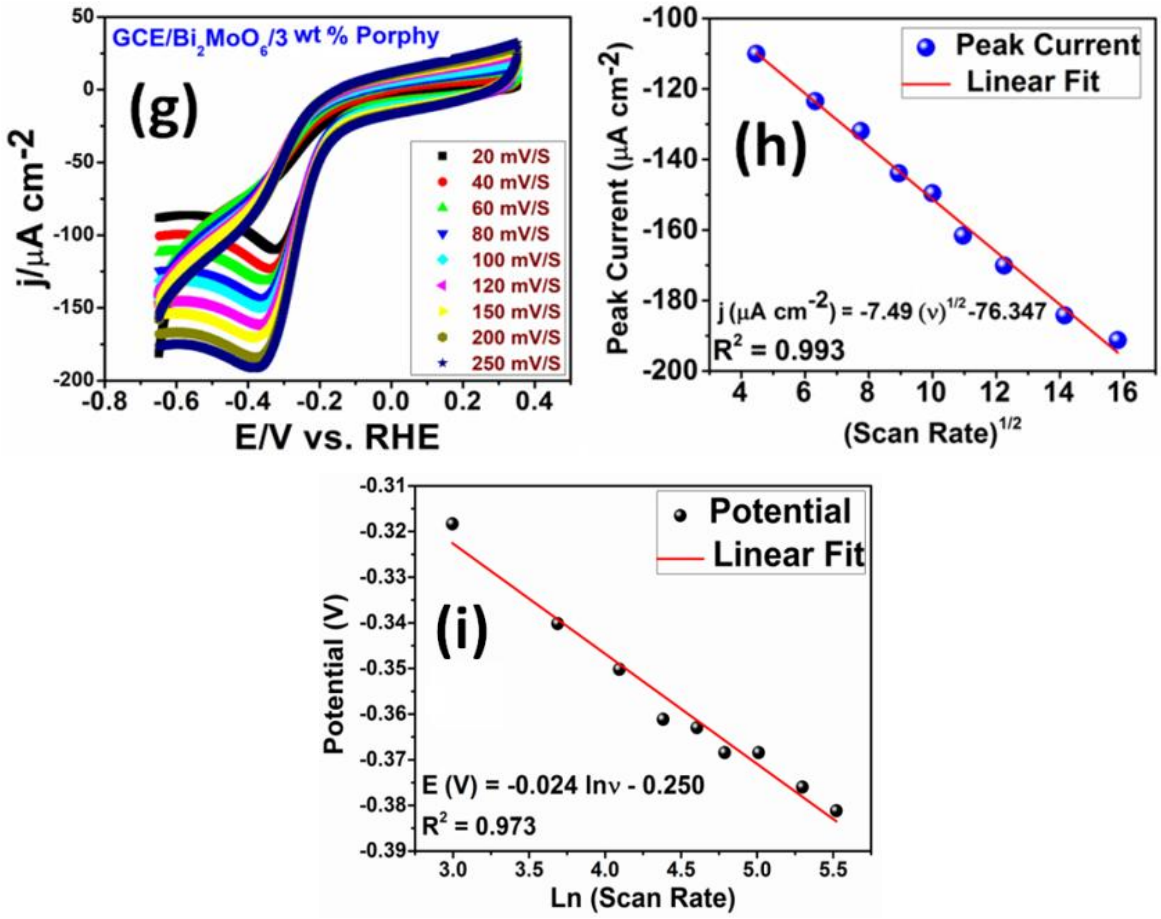

Figure 3.20. (a, d and g) CVs of GCE/Bi_2MoO_6/3 wt % Porphy, GCE and GCE/Bi_2MoO_6 in 0.1 M PBS medium (pH 6) containing 200 μM p-NP at different scan rates (20-250 mV s^{-1}) (b,e and h) Plot of peak current versus square root of scan rate (c, f and i) Plot of potential versus logarithm of scan rate.

Substituting the values in Laviron equation,[53] it obtained a value of 0.2654 for the electron transfer coefficient (α) and 3.163 s^{-1} for the rate constant (K_s) of the GCE/Bi_2MoO_6/3 wt % Porphy.

$$E_{pc} = E^0 + \frac{2.303RT}{\alpha nF}\log \nu \qquad \text{Eq. 3.16}$$

$$\log K_s = \alpha\log(1-\alpha) + (1-\alpha)\log\alpha - \log\left(\frac{RT}{nF\nu}\right) - \frac{\alpha(1-\alpha)nF\Delta E_p}{2.303RT} \qquad \text{Eq. 3.17}$$

$$K_s = \frac{n\alpha F\nu_c}{RT} \qquad \text{Eq. 3.18}$$

Here, ν_c is the x-axis intercept of the lines for the cathodic branch (j_{pc} vs. $\nu^{1/2}$ plot).

The electron transfer rate constant (k_s) can also be determined using the value of α by applying the constraint $E\text{-}E^0 = 0$ to Equation 3.17, reducing it to Equation 3.18.[54,55] The electrochemical response of p-NP on GCE/Bi_2MoO_6/3 wt % Porphy in comparison to GCE/Bi_2MoO_6 (k_s = 0.548 s^{-1}) and bare GCE (k_s = 0.082 s^{-1}) was significantly improved. This surprising current enhancement enables the development of a highly sensitive electrochemical sensor for detecting p-NP.

3.3.3.3. Electrochemical sensing of p-nitrophenol with GCE/Bi_2MoO_6/3 wt % Porphy. Cyclic voltammetry (CV) was applied to determine the electrochemical measurement of p-NP on GCE/Bi_2MoO_6/3 wt % Porphy. The CV response of the reduction curve for GCE/Bi_2MoO_6/3 wt % Porphy increases linearly with the continuous addition of p-NP (Figure 3.21a). The sharp reduction peak is apparently due to the addition of 0.5-350 µM p-NP to the electrochemical bath.

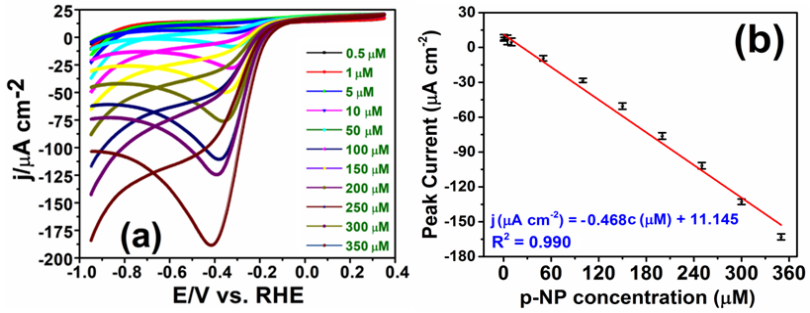

Figure 3.21. (a) CVs of GCE/Bi_2MoO_6/3 wt % Porphy in 0.1 M PBS medium (pH 6) at different concentrations (0.5-350 µM); scan rate: 20 mV s^{-1} (b) Plot of peak current versus concentration of p-NP.

The corresponding calibration equation of the linear plot (Figure 3.21b) can be expressed as

$$j_{pc} = -0.468c + 11.145 \quad R^2 = 0.990 \qquad \text{Eq. 3.19}$$

The sensitivity and limit of detection (LOD) were evaluated to be 0.4683 µA μM^{-1} cm^{-2} and 0.0940 µM, respectively. The electrochemical sensor GCE/Bi_2MoO_6/3 wt % Porphy has improved performance for p-NP detection owing to its wide linear range, low detection limit, and high sensitivity. This was mainly due to the superior electrocatalytic activity and fast electron transfer process. The performance of Bi_2MoO_6/3 wt % Porphy and its comparison with various previously reported electrochemical sensors for detecting p-NP are summarized in Table 3.9. The GCE/Bi_2MoO_6/3 wt % Porphy exhibited better performance, especially in the linear region.

Table 3.9. Comparison of the performance of Bi_2MoO_6/3 wt % Porphy with various previously reported electrochemical sensors for the detection of p-NP.

Electrode materials	Methods	Linear range (µM)	Current sensitivity (µA μM^{-1} cm^{-2})	LOD (µM)	Ref.
Bi_2O_3@MWCNTs	CV	1,000-10,000	-	0.10	56
MoS_2	DPV	4-0.02	0.491	0.01	57
$ZnBi_{38}O_{60}$/GCE	DPV	0.59-8.33	-	0.035	58
O-g-C_3N_4/SPE	DPV	0.0033-0.313	-	0.000075	59
S-GCN/SPCE	i-t	0.05-90	12.655	0.0016	60
β -CD/SiC/GCE	i-t	0.01-150	-	0.023	61
Ag NPs -decorated TA@Fe_3O_4/GCE	DPV	0.1-680.1	0.573	0.033	62
FeOx/TiO_2@mC/GCE	CV	5-310	-	0.183	63
α- MnO_2/MWCNTs	CV	30-475	0.186	0.64	64
2D $ZnCo_2O_4$ Nanosheets	DPV	1-4,000	0.318	0.30	65
GCE/Bi_2MoO_6/3 wt % Porphy	CV	0.5-350	0.4683	0.0940	**This work**
	CA	20-180	0.395	0.0254	

3.3.3.4. Determination of p-NP by chronoamperometry (CA). The electrochemical performance of GCE/Bi_2MoO_6/3 wt % Porphy was evaluated toward p-NP with successive addition of 20 µM p-NP at every 100 s intervals at an applied potential ~ -0.30 V (Figure 3.22a). The electrodes, GCE/Bi_2MoO_6 and GCE/Bi_2MoO_6/3 wt % Porphy showed rapid current responses with the successive increase in p-NP concentration. Linearity was observed over the concentration range of 20-180 µM (Figure 3.22b). According to the linear regression equations 3.20 and 3.21 sensitivity toward p-NP of GCE/Bi_2MoO_6 and GCE/Bi_2MoO_6/3 wt % Porphy was calculated to be 0.094 µA μM^{-1} cm^{-2} and 0.395 µA μM^{-1} cm^{-2}, respectively, and their respective LOD values are 0.248 µM and 0.0254 µM.

$$j(\mu A\ cm^{-2}) = -0.094c - 0.693 \quad R^2 = 0.999 \qquad \text{Eq. 3.20}$$

$$j(\mu A\ cm^{-2}) = -0.395c - 4.833 \quad R^2 = 0.999 \qquad \text{Eq. 3.21}$$

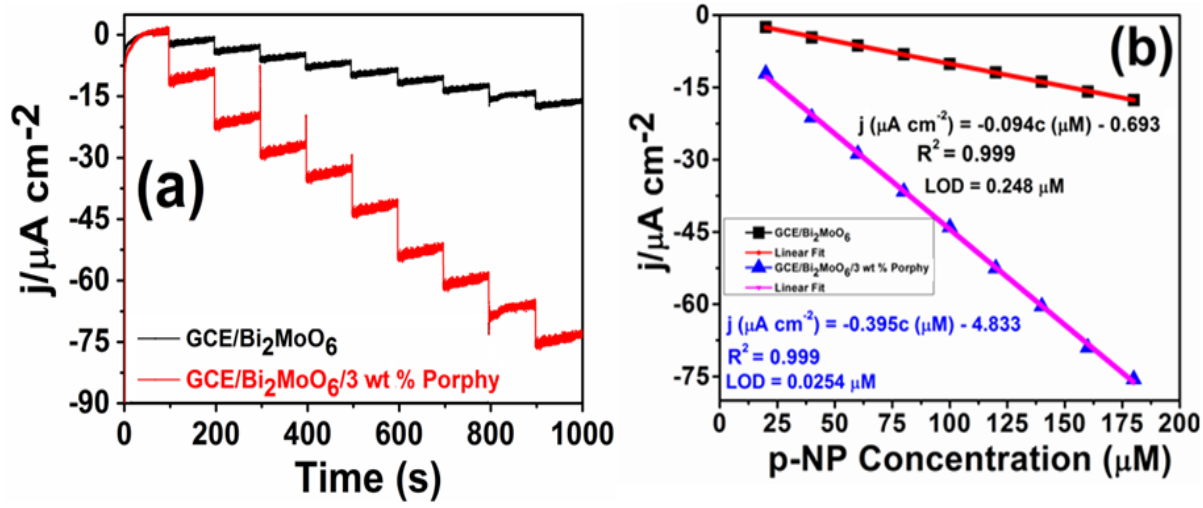

Figure 3.22. (a) Chronoamperograms with increasing concentration of p-NP (20-180 μM) in 0.1 M PBS medium (pH 6.0) (b) Response current versus p-NP concentration on GCE/Bi_2MoO_6 and GCE/Bi_2MoO_6/3 wt % Porphy at ~ - 0.30V.

3.3.3.5. Reproducibility and Stability analysis. The reproducibility of the GCE/Bi_2MoO_6/3 wt % Porphy was investigated independently by fabricating five modified electrodes for the detection of p-NP under the same physicochemical conditions (Figures 3.23a and b), and the relative standard deviation (RSD) was determined to be 3.75%. The stability of the GCE/Bi_2MoO_6/3 wt % Porphy was also studied by CV over 1 week (Figure 3.23c). When not in use, electrodes were stored in a regular refrigerator at 4 °C. The current response remained nearly same, reflecting better long-term stability of the electrode. Its good structural stability was also confirmed by XRD measurement (Figure 3.17).

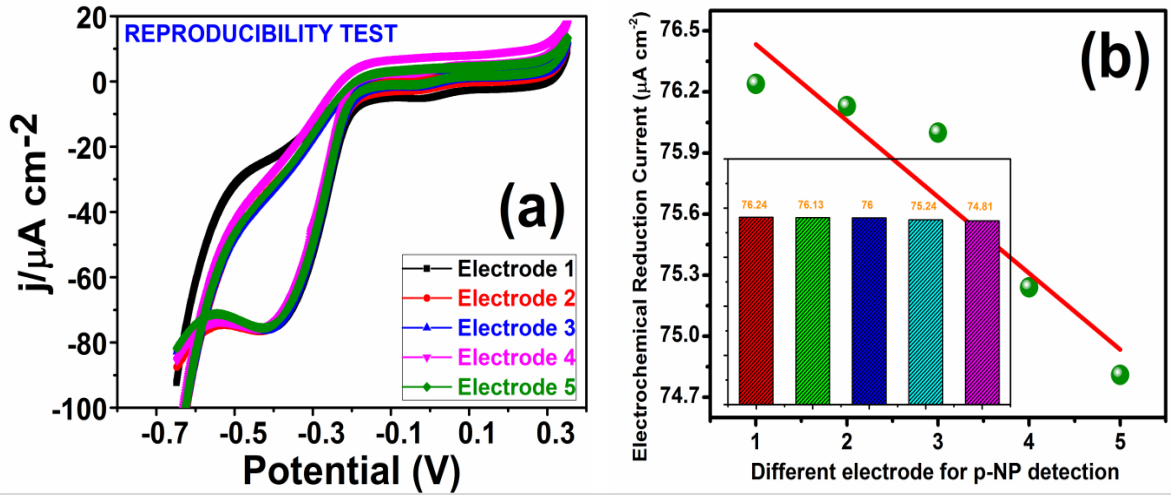

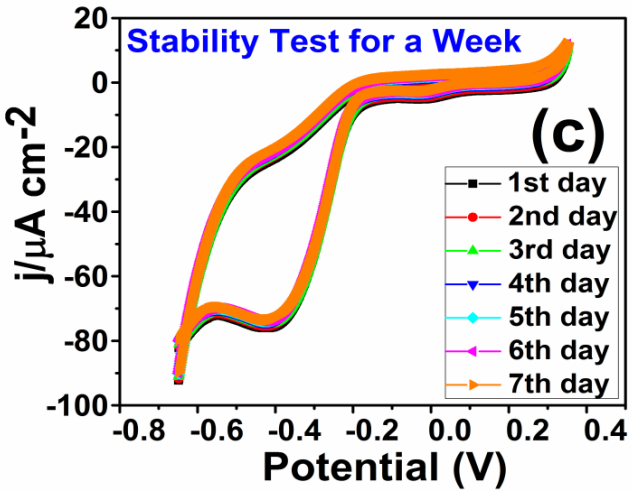

Figure 3.23. (a) Reproducibility test (b) Electrochemical reduction cycle (c) Stability test for a week.

3.3.3.6. Interference and selectivity Study. The selectivity of Bi_2MoO_6/3 wt % Porphy for the detection of p-NP was determined by investigating the effect of some common organic and inorganic interferents in 0.1 M PBS (pH 6.0) in the presence of 200 μM p-NP. The % variation in the CV cathodic peak current (j_{pc}) is given by the formula: Percentage variation of j_{pc} (p-NP) = [j_{pc} (p-NP) - j_{pc} (interference)]/j_{pc} (p-NP).

In this equation, j_{pc} (p-NP) was the peak cathodic current of the p-NP and j_{pc} (interferent) was the peak cathodic current of the interference. The results are shown in Table 3.10. The % variation of j_{pc} (p-NP) for p-NP detection (200 μM) was less than 5% in the presence of phenol (C_6H_6O), benzaldehyde (C_7H_6O), or benzoic acid ($C_7H_6O_2$) (2 mM each) studied separately. Similarly, for o-NP ($C_6H_5O_3N$, 2-Nitrophenol) (400 μM) and m-NP ($C_6H_5O_3N$, 3-Nitrophenol) (400 μM), the % variation of j_{pc} (p-NP) was 13.91% and 12.59%, respectively.

This might be due to the presence of similar reductive groups which are reduced near the p-NP detection potential (Figure 3.24a). When the concentrations of Na^+ (Sodium ion), Mg^{2+} (Magnesium ion), K^+ (Potassium ion), SO_4^{2-} (Sulphate ion), PO_4^{3-} (Phosphate ion), NO_3^- (Nitrate ion), OAc^- (Acetate ion), and CO_3^{2-} (Carbonate ion) (~ 0.02 M) were much higher than that of p-NP, there was no appreciable effect on p-NP detection (Figure 3.24b).

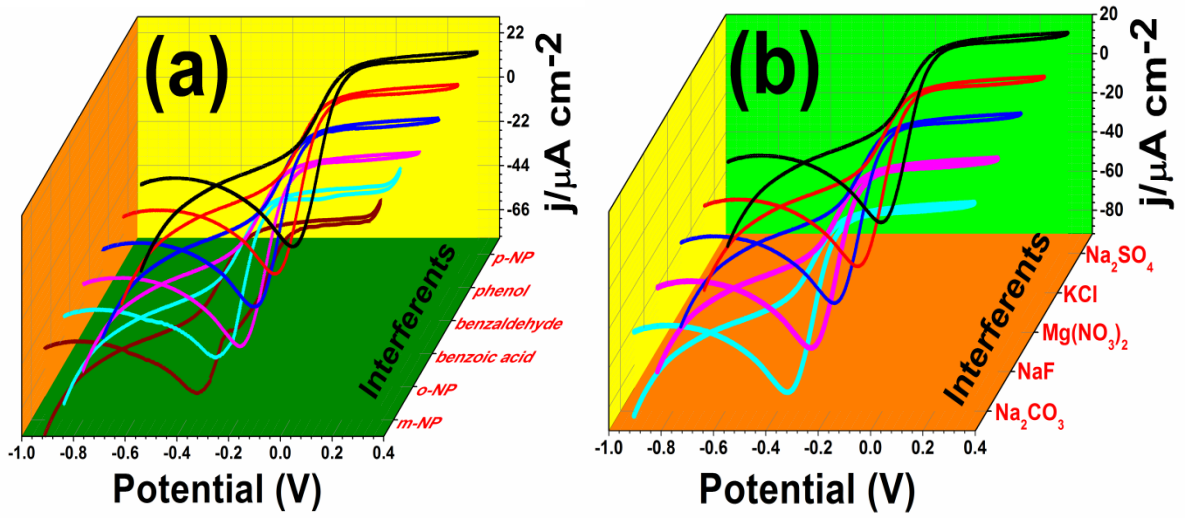

Figure 3.24. (a) CV curves at 20 mV s^{-1} of GCE/Bi_2MoO_6/3 wt % Porphy for 200 µM p-NP in 0.1 M PBS (pH 6.0) in comparison to organic interferents: phenol, benzaldehyde, benzoic acid, o-NP and m-NP (b) possible inorganic interferents: Na_2SO_4, KCl, $Mg(NO_3)_2$, NaF and Na_2CO_3 salts.

Table 3.10. Percentage variation (%) in j_{pc} of GCE/Bi_2MoO_6/3 wt % Porphy for p-NP detection in presence of common organic interferents.

Interferents	Concentration (mM)	Percentage Variation, j_{pc} (%)
Phenol	2.0	4.19
Benzaldehyde	2.0	4.77
Benzoic acid	2.0	0.60
ortho-nitrophenol (o-NP)	0.40	13.91
meta-nitrophenol (m-NP)	0.40	12.59

3.3.3.7. Analysis of p-nitrophenol in real matrix samples. To confirm the practicality of the proposed method, we measured p-NP in model samples of RO, distilled, and tap water in the micromolar range. To prepare the sample, 5.0 mL of various real water samples were mixed with 15.0 mL of 0.1 M PBS at pH 6.0. The CV of real water samples before and after adding the p-NP was shown in Figure 3.25(a→d). In real water samples, p-NP was not detected. Furthermore, 50 µM and 100 µM p-NP samples were added to phosphate buffer containing real water samples. The average recoveries[66] ranged from 90.89% to 102.40%, indicating that the p-NP detection method proposed in this study is promising for the direct analysis of real samples (Table 3.11).

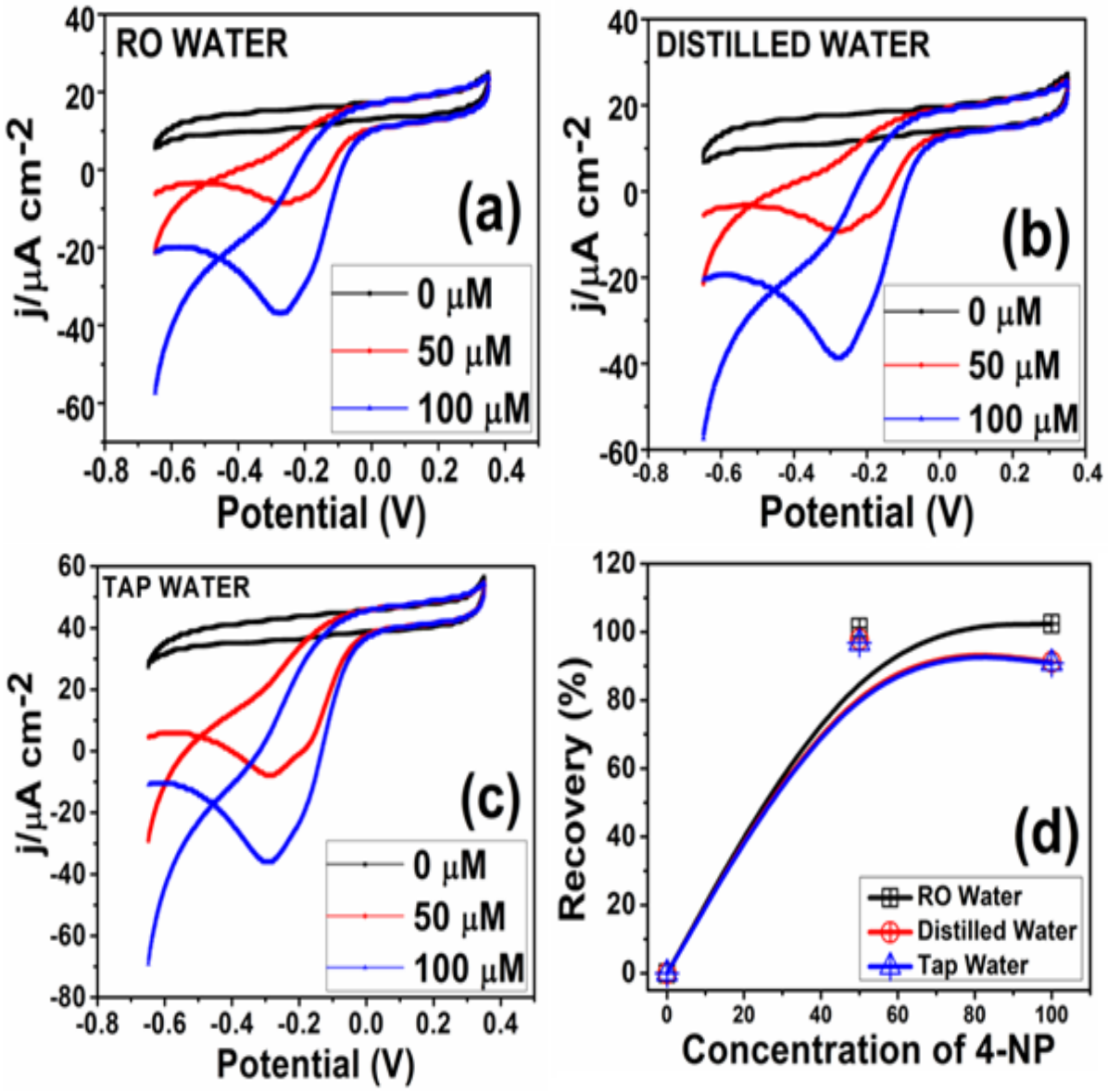

Figure 3.25. Analysis of p-NP in real matrix samples (a) RO water (b) Distilled water (c) Tap water (d) Recovery (%) in presence of Bi_2MoO_6/3 wt % Porphy nanocomposite; scan rate: 20 mV s^{-1}.

Table 3.11. Determination of p-NP in real matrix samples by standard addition method at the electrolytic cell in presence of GCE/Bi_2MoO_6/3 wt % Porphy.

Samples	Added (µM)	Average found (µM)	Recovery (%)	LOD (µM))
RO Water 1	0	0	0	0.295
RO Water 2	50	50.65	101.3	
RO Water 3	100	102.39	102.4	
Distilled Water 1	0	0	0	0.323
Distilled Water 2	50	48.94	97.88	
Distilled Water 3	100	91.23	91.23	
Tap Water 1	0	0	0	0.364
Tap Water 2	50	48.94	96.78	
Tap Water 3	100	91.23	90.89	

3.4. CONCLUSIONS

In summary, a new composite has been developed with the solvothermal process to design organic-inorganic nanocomposites, Bi_2MoO_6/Porphy, exhibiting remarkable electrochemical behaviour. The structure, electronic and chemical performance of Bi_2MoO_6 quasi-nanospheres have been tuned by different wt % of tetraphenylporphyrin. The adequate surface area, the mesoporous structure of the 3 wt % Porphy decorated Bi_2MoO_6 nanocomposite, and its better electroreduction for pure O_2 through RRDE and electrochemical quantitative detection from standard and real samples of p-NP showed an appreciable interest. The ECSA and improved charge transport phenomenon, along with other electrochemical ensuing parameters confirm the efficient performances of Bi_2MoO_6/3 wt % Porphy nanocomposites. The presence of pyrrolic- and pyridinic-N atoms synergistically improved its functionality more than that of other formerly reported catalysts in view of its low η, and low Tafel slope for ORR activity. The reproducibility of the electrode material and interference assay during the elctroreduction of p-NP has been done. We believe that our effort may provide positive insight for a fundamental understanding of the intrinsic activity of organic-inorganic catalyst Bi_2MoO_6/3 wt % Porphy, which serves as a promising catalyst in water electrolysis, sensing towards p-NP, and ongoing work. It also opens different thoughts on fabricating an effective catalyst for multidirectional utility.

REFERENCES

(1) Winter, M. and Brodd, R. J. What are batteries, fuel cells, and supercapacitors? *Chem. Rev.* **2004**, *105*, 1021-1021.

(2) Guo, Y.; Yang, D.; Li, B.; Yang, D.; Ming, P. and Zhang, C. Effect of dispersion solvents and ionomers on the rheology of catalyst inks and catalyst layer structure for proton exchange membrane fuel cells. *ACS Appl. Mater. Interfaces* **2021**, *13*, 27119-27128.

(3) Li, Y. and Dai, H. Recent advances in zinc-air batteries. *Chem. Soc. Rev*. **2014**, *43*, 5257-5275.

(4) Zhang, Z.; Li, H.; Yang, Y.; Key, J.; Ji, S.; Ma, Y.; Wang, H. and Wang, R. Cow dung-derived nitrogen-doped carbon as a cost effective, high activity, oxygen reduction electrocatalyst. *RSC Adv.* **2015**, *5*, 27112-27119.

(5) Wang, H.; Wang, K.; Song, H.; Li, H.; Ji, S.; Wang, Z.; Li, S. and Wang, R. N-doped porous carbon material made from fish-bones and its highly electrocatalytic performance in the oxygen reduction reaction. *RSC Adv.* **2015**, *5*, 48965-48970.

(6) Balasubramanian, P.; Balamurugan, T. S. T.; Chen, S. M. and Chen, T. W. Simplistic synthesis of ultrafine $CoMnO_3$ nanosheets: an excellent electrocatalyst for highly sensitive detection of toxic 4-nitrophenol in environmental water samples. *J. Hazard. Mater.* **2019**, *361*, 123-133.

(7) Rather, J. A.; Debnath, P. and De Wael, K. Fullerene-β-cyclodextrin conjugate based electrochemical sensing device for ultrasensitive detection of p-nitrophenol. *Electroanalysis* **2013**, *25*, 2145-2150.

(8) Li, C.; Wu, Z.; Yang, H.; Deng, L. and Chen, X. Reduced graphene oxide-cyclodextrin-chitosan electrochemical sensor: effective and simultaneous determination of o-and p-nitrophenols. *Sen. Actuators B: Chem.* **2017**, *251*, 446-454.

(9) Jain, S.; Chakraborty, A.; Sharma, B. and Sarma, T. K. Cu^{2+} Ion doping-induced self-assembled ZnO-Cu_xO nanostructures for electrochemical sensing of hydrogen peroxide and p-nitrophenol. *ACS Appl. Nano Mater.* **2022**, *5*, 11973-11983.

(10) Yang, L.; Fan, S.; Deng, G.; Li, Y.; Ran, X.; Zhao, H. and Li, C. P. Bridged β-cyclodextrin-functionalized MWCNT with higher supramolecular recognition capability: the simultaneous electrochemical determination of three phenols. *Biosens. Bioelectron.* **2015**, *68*, 617-625.

(11) Zhang, L.; Xu, T.; Zhao, X. and Zhu, Y. Controllable synthesis of Bi_2MoO_6 and effect of morphology and variation in local structure on photocatalytic activities. *Appl. Catal. B: Environ.* **2010**, *98*, 138-146.

(12) Chen, F.; Niu, C.; Yang, Q.; Li, X. and Zeng, G. Facile synthesis of visible-light-active BiOI modified Bi_2MoO_6 photocatalysts with highly enhanced photocatalytic activity. *Ceram. Int.* **2016**, *42*, 2515-2525.

(13) Yue, D.; Chen, D.; Wang, Z.; Ding, H.; Zong, R. and Zhu, Y. Enhancement of visible photocatalytic performances of a Bi_2MoO_6-BiOCl nanocomposite with plate-on-plate heterojunction structure. *Phys. Chem. Chem. Phys.* **2014**, *16*, 26314-26321.

(14) Zhang, W.; Shaikh, A. U.; Tsui, E. Y. and Swager, T. M. Cobalt porphyrin functionalized carbon nanotubes for oxygen reduction. *Chem. Mater.* **2009**, *21*, 3234-3241.

(15) Song, E.; Shi, C. and Anson, F. C. Comparison of the behavior of several cobalt porphyrins as electrocatalysts for the reduction of O_2 at graphite electrodes. *Langmuir* **1998**, *14*, 4315-4321.

(16) Du, J.; Cheng, F.; Wang, S.; Zhang, T. and Chen, J. M (Salen)-derived nitrogen-doped M/C (M = Fe, Co, Ni) porous nanocomposites for electrocatalytic oxygen reduction. *Sci. Rep.* **2014**, *4*, 1-7.

(17) Sonkar, P. K.; Prakash, K.; Yadav, M.; Ganesan, V.; Sankar, M.; Gupta, R. and Yadav, D. K. Co(II)-porphyrin-decorated carbon nanotubes as catalysts for oxygen reduction reactions: an approach for fuel cell improvement. *J. Mater. Chem. A* **2017**, *5*, 6263-6276.

(18) Buttry, D. A. and Anson, F. C. New strategies for electrocatalysis at polymer-coated electrodes. Reduction of dioxygen by cobalt porphyrins immobilized in Nafion coatings on graphite electrodes. *J. Am. Chem. Soc.* **1984**, *106*, 59-64.

(19) Hu, X.; Chen, S.; Chen, L.; Tian, Y.; Yao, S.; Lu, Z.; Zhang, X. and Zhou, Z. What is the real origin of the activity of Fe-N-C electrocatalysts in the O_2 reduction reaction? critical roles of coordinating pyrrolic N and axially adsorbing species. *J. Am. Chem. Soc.* **2022**, *144*, 18144-18152.

(20) Wang, D.; Shen, H.; Guo, L.; Wang, C. and Fu, F. Porous BiOBr/$B_{i2}Mo_{O6}$ heterostructures for highly selective adsorption of methylene blue. *ACS Omega* **2016**, *1*, 566-577.

(21) Bu, Y.; Chen, Z. Role of polyaniline on the photocatalytic degradation and stability performance of the polyaniline/silver/silver phosphate composite under visible light. *ACS Appl. Mater. Interfaces* **2014**, *6*, 17589-17598.

(22) Bera, R.; Jana, B.; Mondal, B. and Patra, A. Design of CdTeSe-porphyrin-graphene composite for photoinduced electron transfer and photocurrent generation. *ACS Sustain. Chem. Eng.* **2017**, *5*, 3002-3010.

(23) Wang, R.; Li, D.; Wang, H.; Liu, C. and Xu, L. Preparation, characterization, and performance analysis of S-doped Bi_2MoO_6 nanosheets. *Nanomaterials* **2019**, *9*, 1341.

(24) Zhao, W.; Li, C.; Wang, A.; Lv, C.; Zhu, W.; Dou, S.; Wang, Q. and Zhong, Q. Polyaniline decorated Bi_2MoO_6 nanosheets with effective interfacial charge transfer as photocatalysts and optical limiters. *Phys. Chem. Chem. Phys.* **2017**, *19*, 28696-28709.

(25) Koposova, E.A.; Offenhausser, A.; Ermolenko, Y.E. and Mourzina, Y.G. Photoresponsive porphyrin nanotubes of meso-tetra (4-Sulfonatophenyl) porphyrin and Sn (IV) meso-tetra (4-pyridyl) porphyrin. *Front. Chem.* **2019**. *7*, 351 (1-16).

(26) Zhao, P.; Huang, Y.; Chen, J.; Shao, S.; Miao, H.; Xia, J.; Jia, C. and Hua, M. Preparation of meso-tetraphenyl porphyrin modified defect-rich BiOCl with enhanced visible-light photocatalytic activity for antibiotic degradation and mechanism insight. *J. Photochem. Photobiol.* **2020**, *3*, 100014 (1-11).

(27) Ri, C. N.; Kim, S. G.; Ju, K. S.; Ryo, H. S.; Mun, C. H. and Kim, U. H. The synthesis of a $Bi_2MoO_6/Bi_4V_2O_{11}$ heterojunction photocatalyst with enhanced visible-light-driven photocatalytic activity. *RSC Adv.* **2018**, *8*, 5433-5440.

(28) Ge, X.; Sumboja, A.; Wuu, D.; An, T.; Li, B.; Goh, F.T.; Hor, T.A.; Zong, Y. and Liu, Z. Oxygen reduction in alkaline media: from mechanisms to recent advances of catalysts. *ACS Catal.* **2015**, *5*, 4643-4667.

(29) Liu, L.; Wei, Q.; Yu, X. and Zhang, Y. Metal-organic framework-derived Co_3O_4/Au heterostructure as a catalyst for efficient oxygen reduction. *ACS Appl. Mater. Interfaces* **2018**, *10*, 34068-34076.

(30) Maiti, K.; Balamurugan, J.; Gautam, J.; Kim, N. H. and Lee, J. H. Hierarchical flowerlike highly synergistic three-dimensional iron tungsten oxide nanostructure-anchored nitrogen-doped graphene as an efficient and durable electrocatalyst for oxygen reduction reaction. *ACS Appl. Mater. Interfaces* **2018**, *10*, 32220-32232.

(31) Hotger, D.; Etzkorn, M.; Morchutt, C.; Wurster, B.; Dreiser, J.; Stepanow, S.; Grumelli, D.; Gutzler, R. and Kern, K. Stability of metallo-porphyrin networks under oxygen reduction and evolution conditions in alkaline media. *Phys. Chem. Chem. Phys.* **2019**, *21*, 2587-2594.

(32) Yu, X.; Liu, J.; Genc, A.; Ibanez, M.; Luo, Z.; Shavel, A.; Arbiol, J.; Zhang, G.; Zhang, Y. and Cabot, A. Cu_2ZnSnS_4-Ag_2S nanoscale p-n heterostructures as sensitizers for photoelectrochemical water splitting. *Langmuir* **2015**, *31* 10555-10561.

(33) Xiang, Q.; Liu, Y.; Zou, X.; Hu, B.; Qiang, Y.; Yu, D.; Yin, W.; Chen, C. Hydrothermal synthesis of a new kind of N-doped graphene gellike hybrid as an enhanced ORR electrocatalyst. *ACS Appl. Mater. Interfaces* **2018**, *10*, 10842-10850.

(34) Liu, L.; Wei, Q.; Yu, X.; Zhang, Y. Metal organic frameworks-derived Co_3O_4/Au heterostructure as a catalyst for efficient oxygen reduction. *ACS Appl. Mater. Interfaces* **2018**, *10*, 34068-34076.

(35) Canales, C.; Gidi, L.; Arce, R.; Armijo, F.; Aguirre, M. J. and Ramirez, G. Electro-reduction of molecular oxygen mediated by a cobalt (II) octaethylporphyrin system onto oxidized glassy carbon/oxidized graphene substrate. *Catalyst* **2018**, *8*, 629.

(36) Luo, Y.; Wang, Z.; Fu, Y.; Jin, C.; Wei, Q. and Yang, R. In situ preparation of hollow Mo 2C-C hybrid microspheres as bifunctional electrocatalysts for oxygen reduction and evolution reactions. *J. Mater. Chem. A* **2016**, *4*, 12583-12590.

(37) Deng, Y.; Dong, Y.; Wang, G.; Sun, K.; Shi, X.; Zheng, L.; Li X.; Liao, S. Well-defined ZIF-derived Fe-N codoped carbon nanoframes as efficient oxygen reduction catalysts. *ACS Appl. Mater. Interfaces* **2017**, *9*, 9699-9709.

(38) Zhao, L.; Wang, Q.; Zhang, X.; Deng, C.; Li, Z.; Lei, Y.; Zhu, M. Combined electron and structure manipulation on Fe-containing N-doped carbon nanotubes to boost bifunctional oxygen electrocatalysis. *ACS Appl. Mater. Interfaces* **2018**, *10*, 35888-35895.

(39) Huang, K.; Bi, K.; Liang, C.; Lin, S.; Wang, W.J.; Yang, T.Z.; Liu, J.; Zhang, R.; Fan, D.Y.; Wang, Y.G. and Lei, M. Graphite carbon-supported Mo_2C nanocomposites by a single-step solid state reaction for electrochemical oxygen reduction. *Plos one* **2015**, *10*, e0138330 (1-11).

(40) Thanh, T. D.; Chuong, N. D.; Hien, H. V.; Kim, N. H.; Lee, J. H. CuAg@Ag core-shell nanostructure encapsulated by N-doped graphene as a high-performance catalyst for oxygen reduction reaction. *ACS Appl. Mater. Interfaces* **2018**, *10*, 4672-4681.

(41) Zhang,C.; Liu, J.; Ye, Y.; Aslam, Z.; Brydson, R.; Liang, C. Fe-N-doped mesoporous carbon with dual active sites loaded on reduced graphene oxides for efficient oxygen reduction catalysts. *ACS Appl. Mater. Interfaces* **2018**, *10*, 2423-2429.

(42) Wang, H.; Sun, C.; Cao, Y.; Zhu, J.; Chen, Y.; Guo, J.; Zhao, J.; Sun, Y. and Zou, G. Molybdenum carbide nanoparticles embedded in nitrogen-doped porous carbon nanofibers as a dual catalyst for hydrogen evolution and oxygen reduction reactions. *Carbon* **2017**, *114*, 628-634.

(43) Cao, B.; Neuefeind, J. C.; Adzic, R. R. and Khalifah, P. G. Molybdenum nitrides as oxygen reduction reaction catalysts: structural and electrochemical studies. *Inorg. chem.* **2015**, *54*, 2128-2136.

(44) Chuong, N. D.; Thanh, T. D.; Kim, N. H. and Lee, J. H. Hierarchical heterostructures of ultrasmall Fe_2O_3-encapsulated MoS_2/N-graphene as an effective catalyst for oxygen reduction reaction. *ACS Appl. Mater. Interfaces* **2018**, 10, 24523-24532.

(45) Mladenovic, D.; Vujkovic, M.; Mentus, S.; Santos, D.M.; Rocha, R.P.; C Sequeira, C.A.; Figueiredo, J. L. and Sljukic, B. Carbon-supported Mo_2C for oxygen reduction reaction electrocatalysis. *Nanomaterials* **2020**, *10*, 1805.

(46) Mondal, P.; Ghorui, U. K.; Satra, J.; Mardanya, S.; Srivastava, D. N.; Bhadu, G. R. and Adhikary, B. $AgVO_3$ Nanorods decorated with polypyrrole and tetraphenylporphyrin as ternary catalysts for oxygen electrode reactions. *ACS Appl. Nano Mater.* **2020**, *3*, 3876-3891.

(47) Hanana, M.; Arcostanzo, H.; Das, P.K.; Bouget, M.; Le Gac, S.; Okuno, H.; Cornut, R.; Jousselme, B.; Dorcet, V.; Boitrel, B. and Campidelli, S. Synergic effect on oxygen reduction reaction of strapped iron porphyrins polymerized around carbon nanotubes. *New J. Chem.* **2018**, *42*, 19749-19754.

(48) He, Q.; Tian, Y.; Wu, Y.; Liu, J.; Li, G.; Deng, P. and Chen, D. Facile and ultrasensitive determination of 4-nitrophenol based on acetylene black paste and graphene hybrid electrode. *Nanomaterials* **2019**, *9*, 429.

(49) Pontie, M.; Thouand, G.; De Nardi, F.; Tapsoba, I. and Lherbette, S. Antipassivating electrochemical process of glassy carbon electrode (GCE) dedicated to the oxidation of nitrophenol compounds. *Electroanalysis* **2011**, *23*, 1579-1584.

(50) Giribabu, K.; Suresh, R.; Manigandan, R.; Kumar, S. P.; Muthamizh, S.; Munusamy, S. and Narayanan, V. Preparation of nitrogen-doped reduced graphene oxide and its use in a glassy carbon electrode for sensing 4-nitrophenol at nanomolar levels. *Microchim. Acta* **2014**, *181*, 1863-1870.

(51) Ramalingam, M.; Ponnusamy, V. K. and Sangilimuthu, S. N. Electrochemical determination of 4-nitrophenol in environmental water samples using porous graphitic carbon nitride-coated screen-printed electrode. *Environ. Sci. Pollut. Res.* **2020**, *27*, 17481-17491.

(52) Izumi, I.; Dunn, W. W.; Wilbourn, K. O.; Fan, F. R. F. and Bard, A. J. Heterogeneous photocatalytic oxidation of hydrocarbons on platinized titanium dioxide powders. *J. Phys. Chem.* **1980**, *84*, 3207-3210.

(53) Laviron, E. General expression of the linear potential sweep voltammogram in the case of diffusionless electrochemical systems. *J. Electroanal. Chem. Interfacial Electrochem.* **1979**, *101*, 19-28.

(54) Eckermann, A. L.; Feld, D. J.; Shaw, J. A. and Meade, T. J. Electrochemistry of redox-active self-assembled monolayers. *Coord. Chem. Rev.* **2010**, *254*, 1769-1802.

(55) Luz, R. A.; Pereira, A. R.; de Souza, J. C.; Sales, F. C. P. F. and Crespilho, F. N. Enzyme biofuel cells: thermodynamics, kinetics and challenges in applicability. *ChemElectroChem* **2014**, *1*, 1751-1777.

(56) Raviraj, P. D.; Ajay, V. M.; Balaji, B. M. and Bhaskar, R. S. Bi_2O_3 nanoparticles decorated carbon nanotube: an effective nanoelectrode for enhanced electrocatalytic 4-nitrophenol reduction. *Front. Chem.* **2020**, *8*, 10-3389.

(57) Jeyapragasam, T. and Ganesh, V. Molybdenum disulfide-based modifier for electrochemical detection of 4-nitrophenol. *Ionics* **2018** *24*, 4033-4041.

(58) Padmanaban, A.; Dhanasekaran, T.; Manigandan, R.; Kumar, S. P.; Gnanamoorthy, G.; Stephen, A. and Narayanan, V. Facile solvothermal decomposition synthesis of single phase $ZnBi_{38}O_{60}$ nanobundles for sensitive detection of 4-nitrophenol. *New J. Chem.* **2017**, *41*, 7020-7027.

(59) Ramalingam, M.; Ponnusamy, V. K. and Sangilimuthu, S. N. Electrochemical determination of 4-nitrophenol in environmental water samples using porous graphitic carbon nitride-coated screen-printed electrode. *Environ. Sci. Pollut. Res.* **2020**, *27*, 17481-17491.

(60) Rajkumar, C.; Veerakumar, P.; Chen, S. M.; Thirumalraj, B. and Lin, K. C. Ultrathin sulfur-doped graphitic carbon nitride nanosheets as metal-free catalyst for electrochemical sensing and catalytic removal of 4-nitrophenol. *ACS Sustainable Chem. Eng.* **2018**, *6*, 16021-16031.

(61) Wu, S.; Fan, S.; Tan, S.; Wang, J. and Li, C. P. A new strategy for the sensitive electrochemical determination of nitrophenol isomers using β-cyclodextrin derivative-functionalized silicon carbide. *RSC Adv.* **2018**, *8*, 775-784.

(62) Sangili, A.; Annalakshmi, M.; Chen, S. M.; Balasubramanian, P. and Sundrarajan, M. Synthesis of silver nanoparticles decorated on core-shell structured tannic acid-coated iron oxide nanospheres for excellent electrochemical detection and efficient catalytic reduction of hazardous 4-nitrophenol. *Compos. B. Eng.* **2019**, *162*, 33-42.

(63) Wang, M.; Liu, Y.; Yang, L.; Tian, K.; He, L.; Zhang, Z.; Jia, Q.; Song, Y. and Fang, S. Bimetallic metal-organic framework derived FeO_x/TiO_2 embedded in mesoporous carbon

nanocomposite for the sensitive electrochemical detection of 4-nitrophenol. *Sens. Actuators B: Chem.* **2019**, *281*, 1063-1072.

(64) Anbumannan, V.; Dinesh, M.; Kumar, R. R. and Suresh, K. Hierarchical α-MnO_2 wrapped MWCNTs sensor for low level detection of p-nitrophenol in water. *Ceram. Int.* **2019**, *45*, 23097-23103.

(65) Zhu, G.; Sun, H.; Zou, B.; Liu, Z.; Sun, N.; Yi, Y. and Wong, K. Y. Electrochemical sensing of 4-nitrochlorobenzene based on carbon nanohorns/graphene oxide nanohybrids. *Biosens. Bioelectron.* **2018**, *106*, 136-141.

(66) Zhou, Y.; Zhao, J.; Li, S.; Guo, M., and Fan, Z. An electrochemical sensor for the detection of p-nitrophenol based on a cyclodextrin-decorated gold nanoparticle-mesoporous carbon hybrid. *Analyst* **2019**, *144*, 4400-4406.

CHAPTER 4

β-Bi_2O_3-Bi_2WO_6 Nanocomposite Ornated with *meso*-Tetraphenylporphyrin: Interfacial Electrochemistry and Photoresponsive Detection of Nanomolar Hexavalent Cr

Objectives

Surface modification enhancing the photocatalytic and electrocatalytic performances

GRAPHICAL ABSTRACT

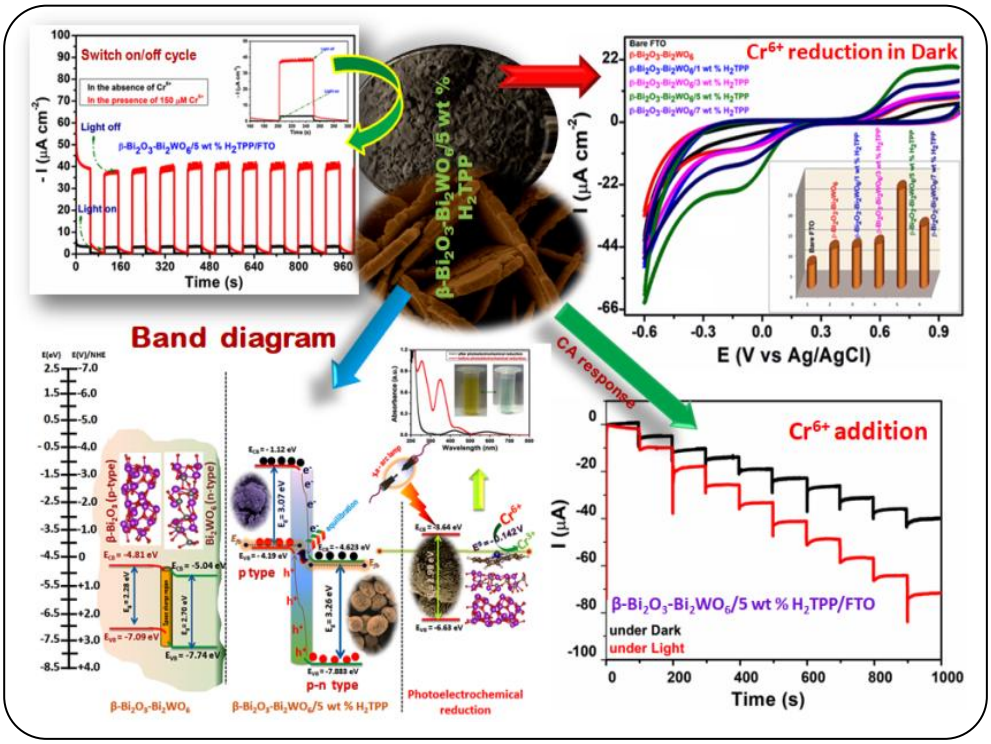

HIGHLIGHTS

- The cost-effective, inovative organic-inorganic heterostructured nanocatalyst β-Bi_2O_3-Bi_2WO_6/H_2TPP, featuring long-term stability, enhanced electrochemical surface area (ECSA), plays a significant role in reducing Cr^{6+} ions through an adsorption-reduction mechanism, illustrated with projected density of states (PDOS).
- Pyrrolic- and pyrridinic-N in mesoporous C, N-based nanocomposites appreciably improved sensing, achieving an impressive LOD of 0.008 µM.
- Cr^{6+} detection in real samples exhibits low RSD (%), high sensitivity (8.005 µA mM cm^{-2}), and excellent reproducibility.

ABSTRACT

Hexavalent chromium exposure via inhalation, ingestion, or both has been proven to adversely affect internal organs, induce toxic effects, cause allergies, and contribute to the development of cancer. It requires a substantial and challenging effort to detect several heavy metal ions conveniently, sensitively, and reliably using materials that are easy to synthesize and have a high yield. The impact of light on electrocatalytic oxidation/reduction process proves an environmentally friendly methodology with numerous applications in pollution control. The extensive use of photoactive materials in photoelectrochemical (PEC) sensors necessitates the development of stable and highly effective photoactive materials. Hence, the solvothermal synthesis of the organic-inorganic hybrid nanocomposite β-Bi_2O_3-Bi_2WO_6/H_2TPP with varying weight percentages of *meso*-tetraphenylporphyrin (H_2TPP) resulted in a selective electrode for electrocatalytic and photoelectrocatalytic reduction of Cr^{6+} on fluorine-doped tin oxide (FTO) by an adsorption-reduction mechanism. H_2TPP increases the active site density and provides an effective surface area for efficient adsorption by providing both pyridinic- and pyrrolic-N atoms to β-Bi_2O_3-Bi_2WO_6/H_2TPP. H_2TPP could effectively adsorb Cr^{6+} in the β-Bi_2O_3-Bi_2WO_6/H_2TPP composite system through electrostatic interaction, and the adsorbed Cr^{6+} ions were reduced to trivalent chromium Cr^{3+}, resulting in the promising Cr^{6+} sensing. The projected density of states and Bader charge calculations result in the electrostatic attraction among the N-2p orbital of H_2TPP and the 3d and 4s orbitals of the Cr atom, resulting in the adsorption of the hexavalent Cr atom onto the active centre of H_2TPP. Moreover, the addition of H_2TPP results in the development of a mesoporous surface that offers strong electrical conductivity, a substantial surface area, improved charge-mass transport, intimate contact between electrolyte and catalyst, an extended fluorescence lifetime, and increased stability. The role of pH values was thoroughly investigated. All electrochemical and photoelectrochemical studies were carried out on 5 wt % H_2TPP ornated β-Bi_2O_3-Bi_2WO_6. Nanocomposite β-Bi_2O_3-Bi_2WO_6/5 wt % H_2TPP demonstrated reliable cyclic stability, reproducibility, good sensitivity (8.005 µA mM cm^{-2}), and a low detection limit (LOD) (8.0 nM) towards photoelectrocatalytic reduction of Cr^{6+}. The interference study in the presence of a few inorganic entities exhibited excellent selectivity. This tale amplification approach for developing a β-Bi_2O_3-Bi_2WO_6/5 wt % H_2TPP nanocomposite system suggests a deeper understanding of the application of photoelectrocatalytic reduction of Cr^{6+} in environmental remediation with real samples under light irradiation.

KEYWORDS: β-Bi_2O_3-Bi_2WO_6, nanocomposite, *meso*-tetraphenylporphyrin, heterojunction, photolectrochemical sensor, hexavalent chromium.

4.1. INTRODUCTION

The development of sensitive and prompt methods for heavy metal ion determination has been necessitated by the need for environmental protection and public safety due to the significant biological toxicity of heavy metal ions and their cumulative effects on the human body.[1,2] Cr^{6+} is the most conspicuous toxic ion and has received considerable research attention due to its ability to cause mutations in the human body,[3-6] even though it is also extremely hazardous to underground safety and drinking water due to its widespread use in industries such as leather tanning and stainless steel production[7]. Numerous sensitive techniques, such as atomic adsorption spectrophotometry,[8,9] spectrofluorimetry,[10] luminescence,[11-13] etc., have been used to determine the heavy metal ions, though they are all time-consuming, challenging to use, or involve expensive equipment. However, the better sensitivity, shorter time requirements, reproducibility, selectivity, and low cost of electrochemical techniques have led to their pervasive application[14-16] whereas the photocatalytic approach is considered a successful and promising method to detect Cr^{6+} due to its pronounced efficacy.[17] As a result, the photoelectrochemical method,[18] which combines photocatalytic and electrochemical technologies, emerges as an attractive option for detecting Cr^{6+}. Since the photoelectrochemical process largely depends on the characteristics of the materials, significant effort must be put into developing electrochemical sensing materials for the detection of heavy metal ions. TiO_2, graphitic carbon nitride (g-C_3N_4), and bismuth-based semiconductors are frequently employed for Cr^{6+} detection.[19,20] Bismuth-based semiconductors such as BiOI, Bi_2S_3, Bi_2XO_6 (X = Mo, W), and others[21] are a few examples that have drawn considerable attention in the study of photoelectrochemical analysis due to their exceptional optical and electrical qualities and also for their abundance, low toxicity, and low cost. Because of its high chemical and thermal stability, acceptable band-gap energies (between 2.5 and 2.7 eV), and nontoxic properties, an aurivillius-type oxide, Bi_2WO_6, is regarded as a promising photocatalyst[22-24] and is now commonly used in photoelectrocatalytic solar cells,[25] photoelectrocatalytic sensing, photoelectrocatalytic hydrogen synthesis, and water splitting.[26] CuS/Bi_2WO_6 sensors have more practical application possibilities[27] for detecting Cr^{6+}. But the restricted surface area, poor photo-reduction capacity, rapid photo-carrier reunion,[28] and low sunlight-capturing capability of the original Bi_2WO_6 substantially decrease its photocatalytic activity.[29,30]

Besides, among bismuth oxide polymorphs, β-Bi_2O_3 is highly promising for various electrochemical and photochemical applications due to its narrow band gap.[31,32] Creating a p-n junction between n-type Bi_2WO_6 and p-type β-Bi_2O_3 is expected to significantly enhance photocatalytic efficiency. The

goal is to develop a composite photocatalyst that combines Bi_2WO_6 with β-Bi_2O_3 to broaden the visible-light photoresponse and improve the separation of photogenerated carriers by aligning their band potentials.[33,34]

For the reduction of Cr^{6+}, lots of adsorbent materials have been widely employed. However, traditional adsorbents frequently exhibit poor adsorption ability and may even produce secondary pollution due to a lack of surface area, functional groups, and hydrophilic surface.[12] As a consequence, it is crucial to synthesize nanocomposites with superior adsorption properties[35] for the sensing of Cr^{6+}. Among the numerous materials, *meso*-tetraphenylporphyrin, with its hydrophilic head and pyrrolic N, which is thought to facilitate the adsorption of Cr^{6+}, has been employed as a highly efficient adsorbent for the reduction of heavy metal ions. The electrostatic interaction between H_2TPP and Cr^{6+} leads to the adsorption of Cr^{6+} on the active site of H_2TPP, near the four N atoms. The +R effect of the phenyl group of H_2TPP enhances the electronic cloud around the N-centres. The N-centres, rich in electrons, exhibit a prompt tendency to adsorb Cr^{6+} through electrostatic interaction. This leads to the transfer of charge from the N-atoms to Cr^{6+}, also showing a slight reducing ability of H_2TPP. In addition, β-Bi_2O_3 and Bi_2WO_6 effectively initiate the reduction of Cr^{6+}, both electrochemically and photoelectrochemically, in acidic medium with a specific pH. The incorporation of H_2TPP on the surface of β-Bi_2O_3-Bi_2WO_6 enhances the reduction process due to its ornamental role in facilitating the adsorption of Cr^{6+} at its active site. Besides, due to photoelectronic characteristics such as a broad photoresponsive range in the visible and near-infrared spectrum and rapid charge recombination between the HOMO orbital and the hole of their oxidized forms, porphyrins were used as photosensitizers to increase photocurrent intensity. Furthermore, the numerous possibilities for accumulating these macrocycles on various substrates encourage the development of highly stable composite materials that mimic the performance of the sensor.[36,37]

In the meantime, it is worth noting that a single semiconductor photocatalyst cannot effectively address the inherent challenge of balancing strong light absorption with efficient carrier separation. To tackle this issue, the creation of a heterojunction using two semiconductor photocatalysts has proven to be an effective solution, as indicated by previous studies.[38] Furthermore, when the nanocomposite system is modified by introducing an organic component on the surface, it enhances the photoelectrochemical activity by promoting better adsorption of Cr^{6+}. Moreover, organic-inorganic nanocomposites are of great interest in sensing applications because of their room-temperature operation, synergistic effects, and structural tunablity.[39,40,41] In response to these ideas, a new class of organic-inorganic nanophotoelectrocatalyst, β-Bi_2O_3-Bi_2WO_6/*meso*-tetraphenylporphyrin

(β-Bi_2O_3-Bi_2WO_6/H_2TPP), was successfully synthesized, capitalizing on the enhancement in charge separation, light absorption improvements, heterojunction formation, and additional reactive sites provided by β-Bi_2O_3, while H_2TPP enhances the Cr^{6+} adsorption, making it highly efficient in sensing applications.

The electro-/photoelectrochemical performance of H_2TPP ornated β-Bi_2O_3-Bi_2WO_6 nanomaterials for Cr^{6+} sensing using electrochemical impedance spectroscopy (EIS), current-time curves (i-t) analysis, and cyclic voltammetry (CV) was systematically examined for the first time. The adsorption of chromium ions on the active site of H_2TPP in β-Bi_2O_3-Bi_2WO_6/H_2TPP facilitates the electro- or photoelectrochemical reduction of Cr^{6+} with a low detection limit, high and quick sensitivity, and persisting stability by increasing the fluorescence life-time of the photocarrier and decreasing the charge recombination rate of the photogenerated electron-hole pair,[42,43] making our sample a promising sensor for hexavalent chromium. Thus, H_2TPP is a reliable electronic match between the material surface and hexavalent chromium. This work provides a quick, efficient, and ecologically friendly method for finding Cr^{6+} in polluted wastewater.

4.2. EXPERIMENTAL SECTION

4.2.1. Materials. All the chemicals were used as received. Analytical grade Pyrrole (C_4H_5N), Benzaldehyde (C_7H_6O), Bismuth nitrate ($Bi(NO_3)_3.5H_2O$), Sodium tungstate ($Na_2WO_4.2H_2O$), Ethanol (EtOH), Methanol (CH_3OH), Commercial Pt/C catalyst (20 wt % Pt), Ethylene glycol ($C_2H_6O_2$), Propionic acid ($CH_3CH_2CO_2H$), Sulfuric acid (H_2SO_4), Phosphoric acid (H_3PO_4), Nafion ($C_7HF_{13}O_5S{\cdot}C_2F_4$), Potassium chloride (KCl), cetyltrimethylammonium bromide (CTAB, $C_{19}H_{42}BrN$) were purchased from Sigma-Aldrich. All water used throughout the experiments was demineralized and ultrafiltered by a Millipore Milli-Q system (resistivity >18.2 MΩ, TOC < 5 ppb).

4.2.2. Synthesis of Materials

4.2.2.1. Synthesis of β-Bi_2O_3-Bi_2WO_6 nanocomposite. A controlled solvothermal process was used to synthesize β-Bi_2O_3-Bi_2WO_6 nanocomposite. CTAB, a commonly used surfactant, can play a role in regulating the shape and size of nanoparticles by selectively or strongly binding to various emerging crystalline facets. CTAB exhibits micelle formation at concentrations exceeding the critical micelle concentration (CMC).[44] Selective adsorption of CTAB on the surface induces the orientation growth of the nanocomposite. In the process of preparing the β-Bi_2O_3-Bi_2WO_6 nanocomposites, we thus introduced a specific concentration of CTAB to regulate the preferential adsorption on the surface of the nanocrystals, which facilitates anisotropic growth in the nanocomposite[45]. Thus, first,

15 mL of ethylene glycol solution was mixed with 4 mmol of CTAB and 4 mmol of $Bi(NO_3)_3.5H_2O$ separately, and the mixture was homogenized using a sonicator for 20 min. Consequently, a solution of 1 mmol of $Na_2WO_4.2H_2O$ in 15 mL of ethylene glycol was gently added to the above mixture, and then it was again sonicated for 30 min. After that, the mixture was poured into an airtight 100 mL Teflon-lined autoclave and heated at 180 °C for 12 h. After cooling to room temperature, filtering, and three rounds of washing with distilled water and ethanol, the solid residue was left to dry at that temperature.

4.2.2.2. Synthesis of β-Bi_2O_3-Bi_2WO_6/H_2TPP nanocomposites. For the aforesaid synthesis pathway of β-Bi_2O_3-Bi_2WO_6 nanocomposites, a certain weight percentage of H_2TPP was added to the homogeneous mixture, followed by an additional 30 min of sonication. The nanocomposite system, namely β-Bi_2O_3-Bi_2WO_6/H_2TPP, was then obtained by pouring the mixture solution into an airtight 100 mL Teflon-lined stainless steel autoclave. The autoclave was then heated at 180 °C for 12 h, cooled, and washed as before. To better understand various electrocatalytic and photoelectroactive performances, a series of β-Bi_2O_3-Bi_2WO_6/H_2TPP nanocomposites with H_2TPP weight percentages ranging from 1 to 7% were synthesized (**Scheme 4.1**).

4.2.2.3. Synthesis of *meso*-Tetraphenylporphyrin (H_2TPP). H_2TPP was synthesized by boiling vigorously 40 mL of propionic acid in a 100 ml round-bottom flask fitted to a reflux condenser. A mixture of equimolar (0.03 mol) benzaldehyde and pyrrole was added to it under boiling conditions and allowed to reflux for 1 h. Finally, the deep purple compound was collected through filtration and washed with MeOH.

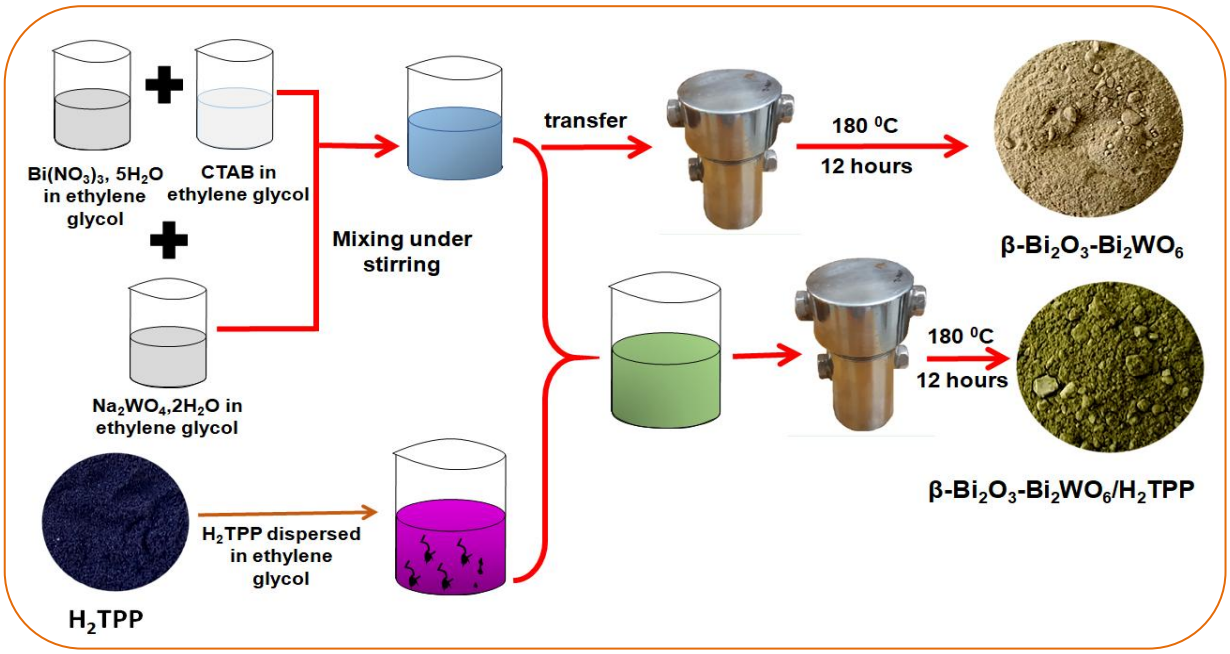

Scheme 4.1. Stepwise Process for the Synthesis and Ornamentation of β-Bi_2O_3-Bi_2WO_6 with H_2TPP via a Solvothermal Process.

4.2.3. Characterization and Instrumentation. The crystallinity and phase formation of the as-prepared samples were investigated by the Philips PW 1140 parallel beam X-ray diffractometer using monochromatic Cu-Kα radiation (λ = 1.540598 Å). The surface morphologies and internal structure of the catalysts were characterized using field emission scanning electron microscopy (FE-SEM JEOL JSM 7100F) with energy dispersive X-ray spectroscopy (EDX) and transmission electron microscopy (HR-TEM-JEOL JEM-2100) operated at 200 kV. The sampling was done by a simple drop cast of β-Bi_2O_3-Bi_2WO_6 and β-Bi_2O_3-Bi_2WO_6/H_2TPP solution dispersed in ultra-pure water onto a carbon-coated 300 mesh sized Cu grid (purchased from Ted Pella), and the sample grid was stored in vacuum desiccator before HR-TEM analysis. In order to determine the composition of the samples, selected area electron diffraction (SAED) pattern was used. X-ray photoelectron spectra (XPS, Perkin-Elmer Physical Electronics 5600 spectrometer) were recorded to identify the chemical states of surface atoms and to confirm the existence of H_2TPP along with β-Bi_2O_3-Bi_2WO_6. The optical properties of the samples were studied by a UV-Vis diffuse reflectance spectrophotometer (DRS) (Agillent carry 5000), and the band gap energies of different composites were calculated using Kubelka-Munk plots. The UV-Vis spectra were performed on a JASCO V-730 UV-Vis spectrophotometer. The photoluminescence (PL) spectra were recorded using a Duetta™ with

EzSpec™ self-contained fully automated spectroflurometer system. Raman analysis was done on HORIBA XploRA Plus, Japan under laser excitation at 532 nm. High-resolution Raman measurements were performed using a micro Raman spectrometer (LabRam HR, Jobin Yvon) equipped with a 488 nm Argon ion laser and a Peltier cooled CCD detector. The specific surface area (S_{BET}), pore size distribution and pore volume of the catalysts were measured by the N_2 sorption isotherms performed in an Autosorb iQ_2 gas sorption instrument (Quantachrome Instruments, USA). Prior to N_2-sorption experiments, all the samples were degassed at 100 °C under vacuum in the attached FLOVAC Degasser sample preparation unit. The pore volume and pore size distribution were estimated by the 2D-Non-Local Density Functional Theory (2D-NLDFT) method. In the dark adsorption equilibrium experiments, the experimental conditions included a 6 mg quantity of adsorbent, a Cr^{6+} ion concentration of 10 mg L^{-1}, a solution volume of 100 mL, an adsorption temperature of 30 °C, and a pH of 4. After stability test, the sample was collected from the FTO surface through soft scratching with doctors blade and washed several times with distilled water (8 films were used). It was then dried and taken for further characterisation of XRD, XPS, HR-TEM, FE-SEM to study the stability of the catalyst. The electrochemical impedance spectroscopy (EIS) was recorded at an amplitude of 5 mV from 5 mHz to 100 kHz in 1.0 M KCl solution. Also the Mott-Schottky analyses of the FTO coated glass slide fabricated with β-Bi_2O_3-Bi_2WO_6, β-Bi_2O_3-Bi_2WO_6/5 wt % H_2TPP nanocomposite and H_2TPP were carried out separately in 0.1 M KCl solution (pH 4.0) using an AC frequency of 10 kHz with a scan rate of 0.05 V s^{-1} and an AC voltage magnitude of 5 mV.

4.2.4. Sample Preparation for Optical Analysis. UV-Vis, photoluminescence (PL) spectral analyses, and nanosecond time-resolved transient fluorescence decay measurement of β-Bi_2O_3-Bi_2WO_6 and different weight percent H_2TPP ornated β-Bi_2O_3-Bi_2WO_6 were carried out by dispersing these solid materials in H_2O separately.

4.3. RESULTS AND DISCUSSION

4.3.1. Material Characterizations

4.3.1.1. PXRD analysis of β-Bi_2O_3-Bi_2WO_6/H_2TPP nanocomposites. The XRD analysis was employed for the characterization of the crystallinity and structure of β-Bi_2O_3-Bi_2WO_6 and H_2TPP ornated different β-Bi_2O_3-Bi_2WO_6/H_2TPP nanocomposites. The presence of both pure orthorhombic Bi_2WO_6 (JCPDS No. 73-1126) and the tetragonal phases of β-Bi_2O_3 (JCPDS No. 74-1374) can be

discerned simultaneously within the sample prepared, spanning the 2θ range of 20° to 80°, as depicted in Figures 4.1(a→e). The characteristic peaks observed for β-Bi_2O_3 are assigned to the diffraction from the (310), (221), (400), (421), (402), (442), and (802) planes. The characteristic peaks of Bi_2WO_6 correspond to the diffraction from the (113), (200), (125), (313), (400), (402), and (145) planes. This implies the coexistence of β-Bi_2O_3 and Bi_2WO_6 in the system.[46] The presence of sharp diffraction peaks in the sample suggests its high crystallinity.

However, in the case of β-Bi_2O_3-Bi_2WO_6/H_2TPP nanocomposites, only the characteristic peak of β-Bi_2O_3-Bi_2WO_6 was observed in the pattern, with no peak of H_2TPP. It could be because H_2TPP has a lower concentration and diffraction intensity than β-Bi_2O_3-Bi_2WO_6. Nonetheless, it was shown that the intensity of the diffraction peaks in the nanocomposites decreased, and some peak shifting occurred as a result of H_2TPP loading (Figure 4.1e). This indicates that the incorporation of H_2TPP led to a reduction in the crystallinity of β-Bi_2O_3-Bi_2WO_6/H_2TPP.

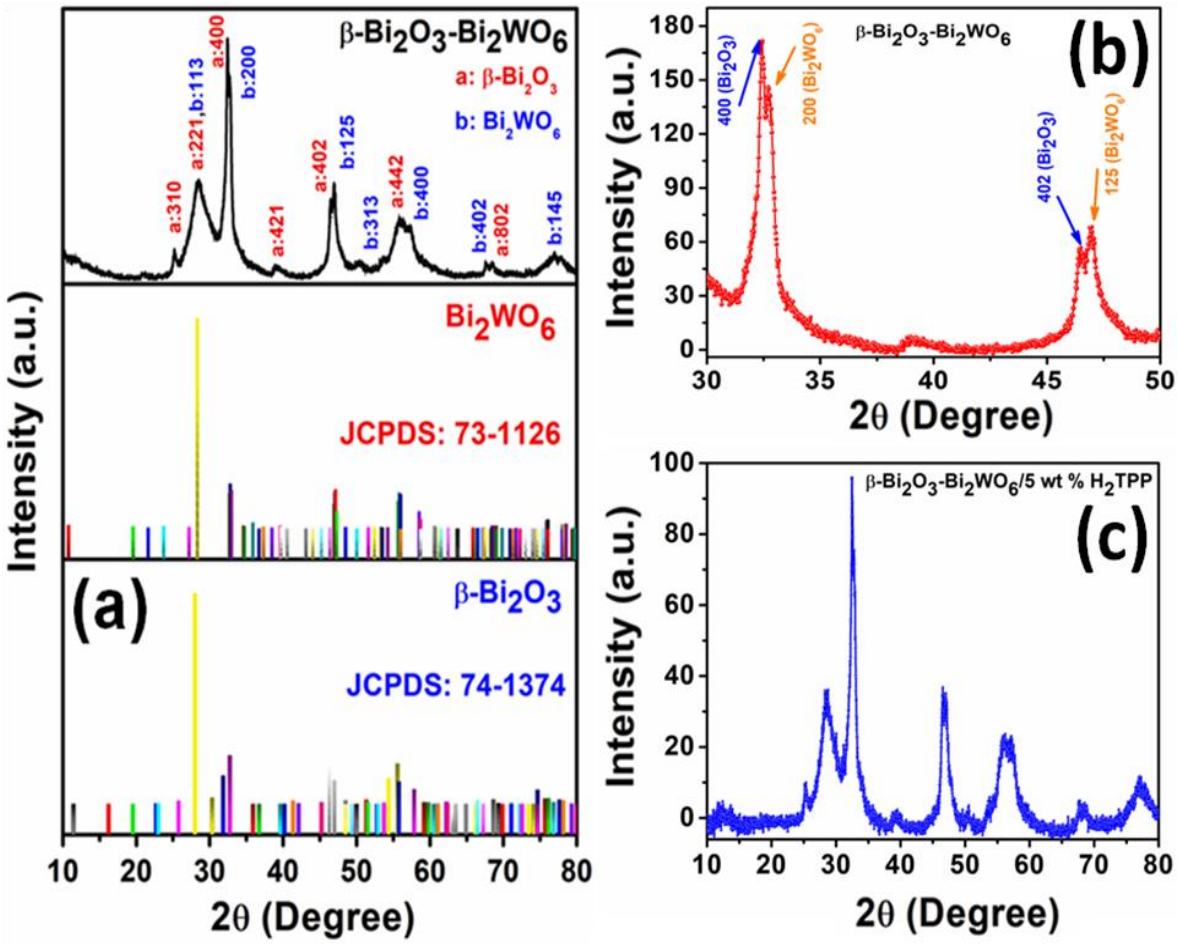

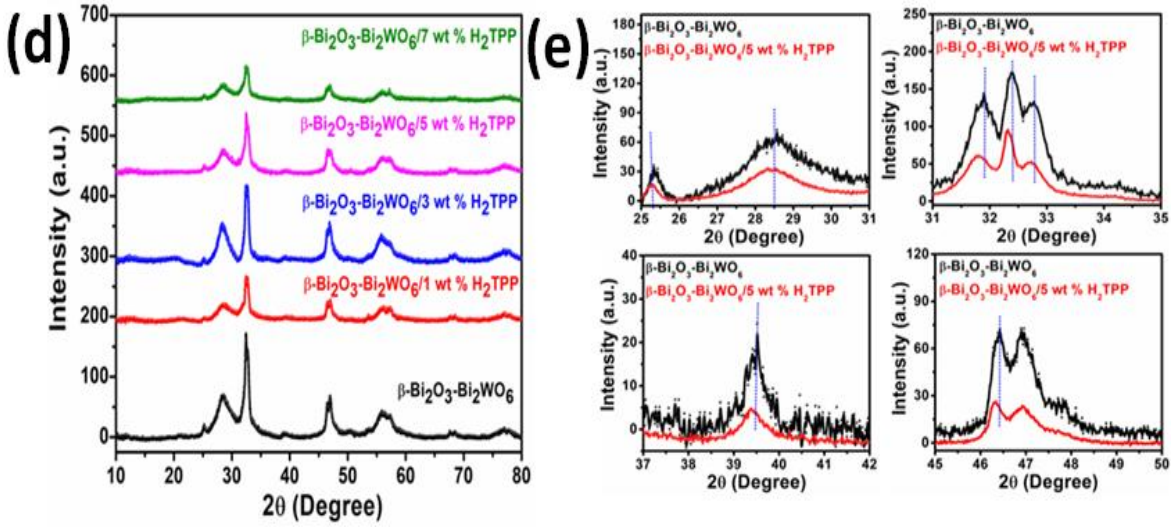

Figure 4.1. XRD of (a) β-Bi_2O_3-Bi_2WO_6 with a simulated pattern of β-Bi_2O_3 and Bi_2WO_6 (b) small range plot to identify the peaks in support of coexistence of β-Bi_2O_3 and Bi_2WO_6 (c) decrease in peak intensity along with peak broadening due to incorporation of H_2TTP, leading to a gradual reduction in crystallinity. (d) XRD pattern of β-Bi_2O_3-Bi_2WO_6 and different wt % of H_2TPP ornated β-Bi_2O_3-Bi_2WO_6 nanocomposites (e) slow scan PXRD of β-Bi_2O_3-Bi_2WO_6 and β-Bi_2O_3-Bi_2WO_6/5 wt % H_2TPP.

4.3.1.2. XPS analysis. X-ray photoelectron spectroscopy (XPS) also established the co-occurrence of β-Bi_2O_3 and Bi_2WO_6 in the nanocomposite. A full range of investigations supported the existence of Bi, W, O, C, and N, representing the chemical constituents of the nanocomposite (Figure 4.2a). The binding energies of 158.21 eV for Bi $4f_{7/2}$ and 163.59 eV for Bi $4f_{5/2}$ in the Bi 4f region represent the 3+ oxidation state of Bi (Figure 4.2b), whereas the binding energies in the W 4f region of the XPS spectrum, which are 34.54 eV for W $4f_{7/2}$ and 36.62 eV for W $4f_{5/2}$, respectively, indicate that W is in the 6+ oxidation state (Figure 4.2c).[47] The existence of non-equivalent lattice oxygen atoms resulted in the deconvolution of the XPS spectrum of O 1s, yielding two peaks at 530.10 and 532.05, corresponding to Bi-O and W-O in Bi_2WO_6, respectively[46,48] (Figure 4.2d). In the spectrum of N 1s of β-Bi_2O_3-Bi_2WO_6/5 wt % H_2TPP, two distinct peaks at 398.68 and 402.93 eV (Figure 4.2e) correspond to pyridinic and pyrrolic N, respectively. Besides, in the C 1s spectrum, three different peaks represent C=C (283.79 eV), C=N (285.59 eV), and C-N (287.94 eV) bonds (Figure 4.2f). This suggests that the macrocyclic H_2TPP in the nanocomposite stays in it's free-base state without undergoing metallization.

Here, the pyridinic and pyrrolic N-atoms in H_2TPP possibly behave as an N-containing carbon system, and such species are becoming increasingly popular in the field of sensing due to their excellent adsorption capacity, good stability, and high surface area. The shifting of the pyridinic N peak to a low energy level as compared to pristine H_2TPP could be due to the interaction between metal ions present on the external surface of the nanocomposite and the lone pair of N atoms present in the pyridine group of H_2TPP. The overall findings demonstrate that H_2TPP successfully ornated the surface of β-Bi_2O_3-Bi_2WO_6, with H_2TPP bound to the β-Bi_2O_3-Bi_2WO_6 surface through electrostatic interaction.[49,50]

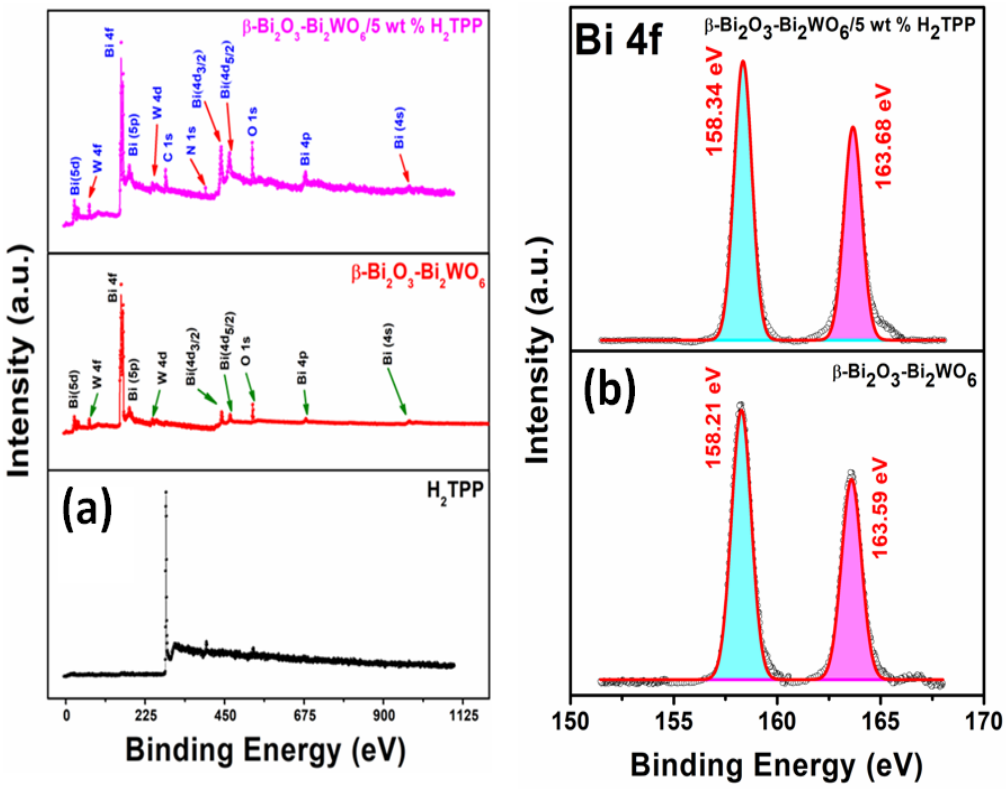

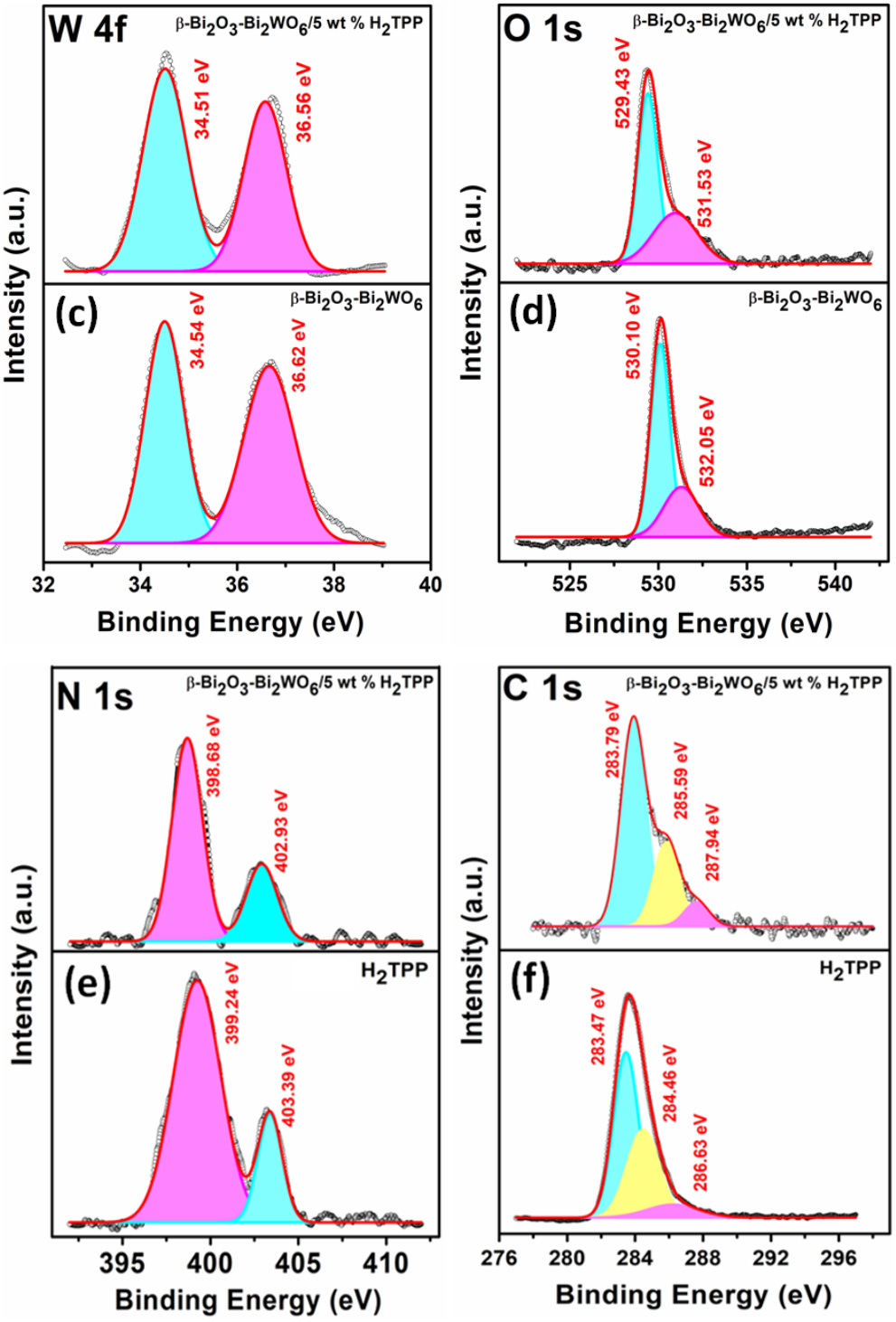

Figure 4.2. XPS spectra of H_2TPP, β-Bi_2O_3-Bi_2WO_6 and β-Bi_2O_3-Bi_2WO_6 /5 wt % H_2TPP nanocomposites (a) Sample survey (b) Bi 4f (c) W 4f (d) O 1s (e) N 1s (f) C1s.

4.3.1.3. Morphological Analysis. The morphological investigation of the β-Bi_2O_3-Bi_2WO_6 nanocomposite, as observed in the low magnification FE-SEM images (Figures 4.3a and b), reveals that the prepared sample consists of numerous uniform, sphere-like (flaky-flower) hierarchical microspheres with diameters ranging from 1 to 4 μm. Further, the high-magnification images (Figures 4.3c and d) reveal that β-Bi_2O_3-Bi_2WO_6 microspheres are built from small 2D crystalline interconnected nanosheets, each having an average thickness of approximately 19-20 nm. This phenomenon is primarily attributed to the presence of CTAB in the reaction system. Mesopores are created as a result of the aggregation of these nanosheets within each flaky-flower structure. Moreover, the internal nanosheets were well separated, with an average distance of ~ 49 nm, as represented in the inset of Figure 2d. This separation is consistent throughout the morphological analysis and suggests that the crystallites aggregate to form each quasi-spherical flower-like structure, maintaining a uniform surface roughness. In the β-Bi_2O_3-Bi_2WO_6/5 wt % H_2TPP nanocomposites, it displays similar quasi-spherical flower-like morphologies (Figures 4.4(a→c)) with diameters ranging from 1 to 3 μm (Figure 4.4d).

The FE-SEM images of bare H_2TPP, as shown in Figure 4.5, reveal discrete polymorphism grains. Conversely, the incorporation 5 wt % of H_2TPP to ornament the solid matrix resulted in well-dispersed, tiny spherical entities throughout the mixed metal oxide, with an average diameter of ~ 13.75 nm, as shown in Figure 4.4b, which enhance the active sites of the material, ultimately promoting favorable catalytic behavior. This observed morphology is likely influenced by the reaction conditions on the outer surface of the β-Bi_2O_3-Bi_2WO_6.

Energy-dispersive X-ray spectroscopy (EDX) confirmed the presence of Bi, W, and O in the β-Bi_2O_3-Bi_2WO_6 nanocomposites, as illustrated in Figure 4.6a and the inset table. In the case of β-Bi_2O_3-Bi_2WO_6/5 wt % H_2TPP, the existence of C, N, O, Bi, and W, as shown in Figure 4.6b and the inset table, indicated the successful surface ornamentation of β-Bi_2O_3-Bi_2WO_6 nanocomposite with H_2TPP. Furthermore, element mapping of the corresponding elements Bi (Lα), W (Lα), and O (Kα) in β-Bi_2O_3-Bi_2WO_6 and Bi (Lα), W (Lα), O (Kα), C (Kα), and N (Kα) in β-Bi_2O_3-Bi_2WO_6/5 wt % H_2TPP, as depicted in Figures 4.6a and b, used to analyze in depth the distribution of specific elements, confirms that the materials were successfully prepared and that H_2TPP is uniformly distributed across the surface of the β-Bi_2O_3-Bi_2WO_6 nanocomposite.

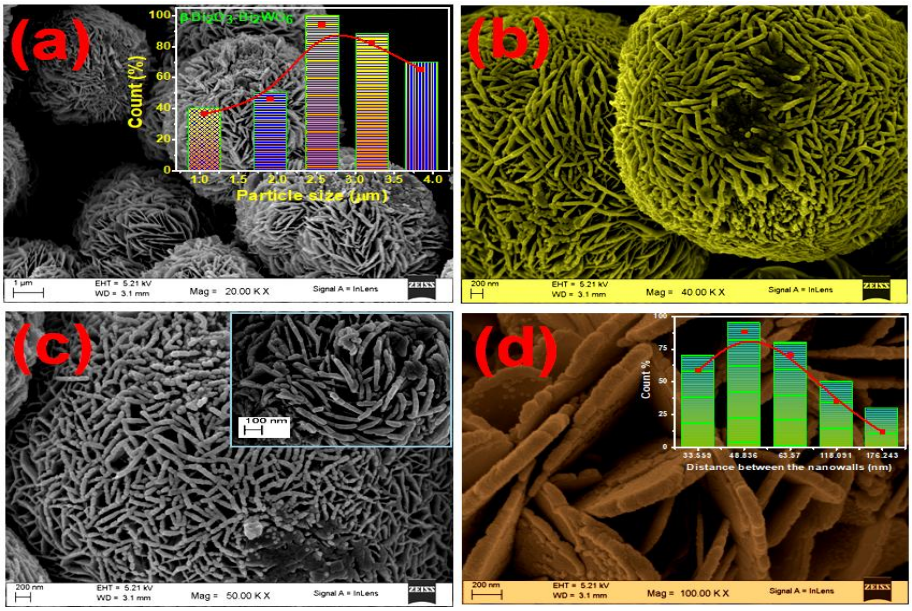

Figure 4.3. FE-SEM image of β-Bi_2O_3-Bi_2WO_6 (a) in low magnification and inset of (a) particle size distribution (b, c, d) in high magnification and inset of (d) internal distance between the nanosheets.

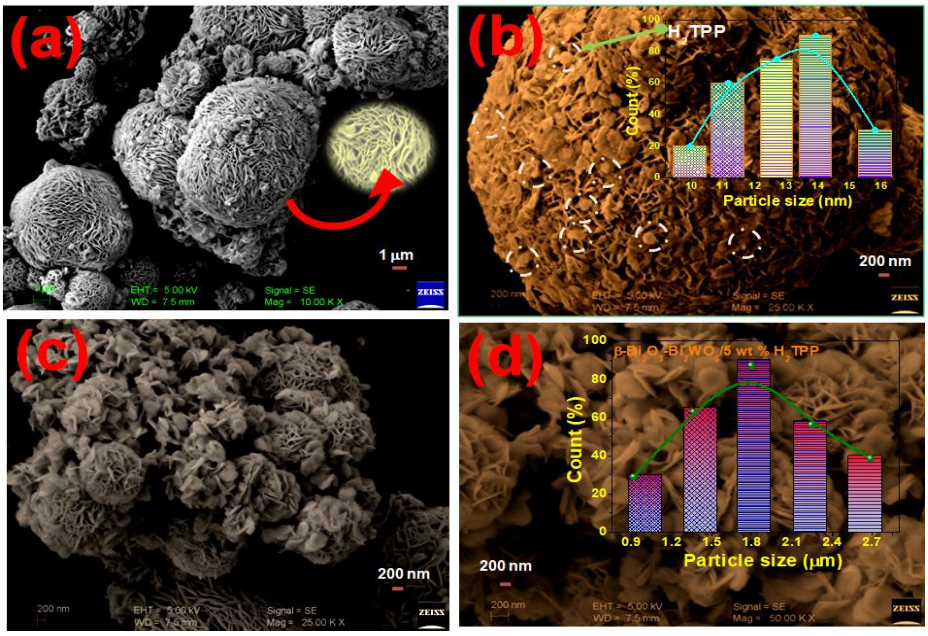

Figure 4.4. FE-SEM image of β-Bi_2O_3-Bi_2WO_6/5 wt % H_2TPP (a) in low magnification (b, c, and d) in high magnification and inset of (b) particle size distribution curve of H_2TPP and inset of (d) particle size distribution curve of β-Bi_2O_3-Bi_2WO_6/5 wt % H_2TPP nanocomposite.

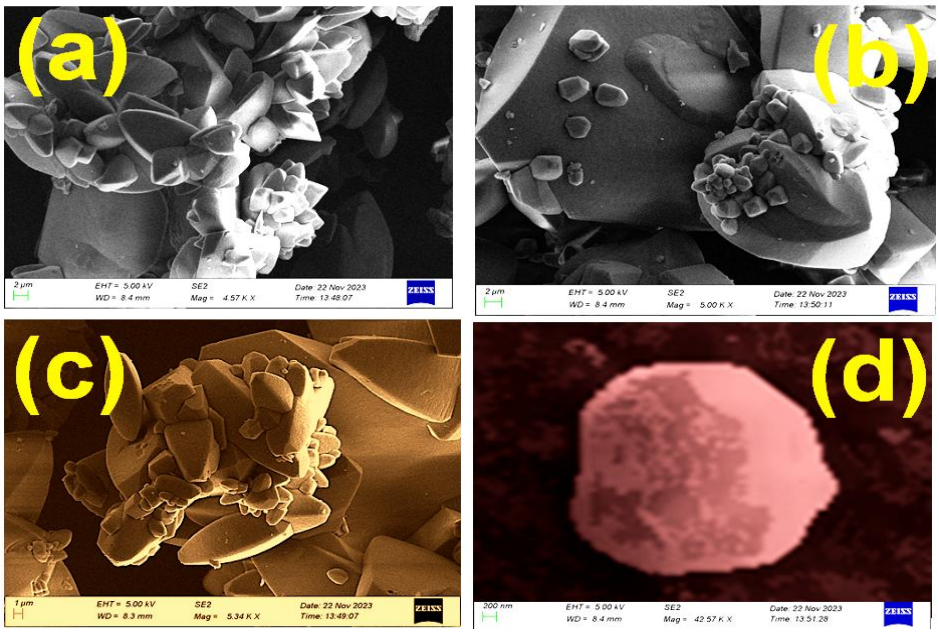

Figure 4.5. FE-SEM image of H_2TPP (a → d) with different magnifications from 2 μm to 200 nm scaling image.

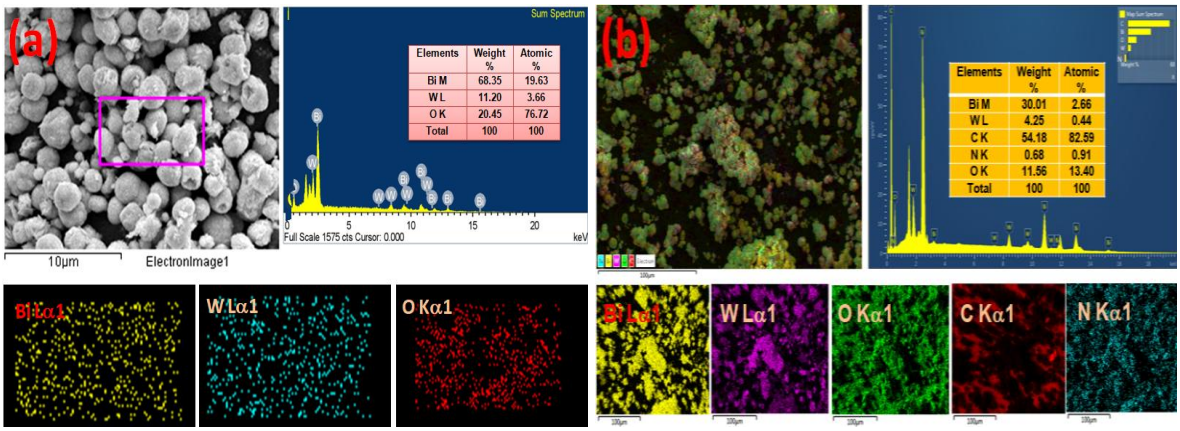

Figure 4.6. (a) EDX and E-mapping of β-Bi_2O_3-Bi_2WO_6 and (b) β-Bi_2O_3-Bi_2WO_6/5 wt % H_2TPP nanocomposites.

However, for a more comprehensive insight into the morphology and the presence of H_2TPP on β-Bi_2O_3-Bi_2WO_6, high-resolution transmission electron microscopy (HR-TEM) was employed. The HR-TEM images, as shown in Figures 4.7(a→e), revealed an isolated β-Bi_2O_3-Bi_2WO_6 microsphere composed of 2D nanosheets, closely resembling the structure observed in the FE-SEM images

(Figures 4.3(a→d)). A histogram illustrating the size distribution of the β-Bi_2O_3-Bi_2WO_6 nanocomposite, displaying an average crystallite size of 11.28 nm, is presented, with the crystallites highlighted by a yellow dotted line (Figure 4.7b). In the HR-TEM images of the β-Bi_2O_3-Bi_2WO_6 (Figures 4.7(f→h)), the lattice fringes with d-spacing were measured to be about 0.34, 0.317, 0.273, 0.193, and 0.123 nm for Bi_2O_3 and 0.136, 0.165, and 0.272 nm for Bi_2WO_6, respectively. These values correspond to the (310), (221), (400), (402), and (802) planes of β-Bi_2O_3 and the (400), (313), and (200) planes of Bi_2WO_6, respectively. The above-mentioned result confirmed the successful formation of the β-Bi_2O_3-Bi_2WO_6 composite.

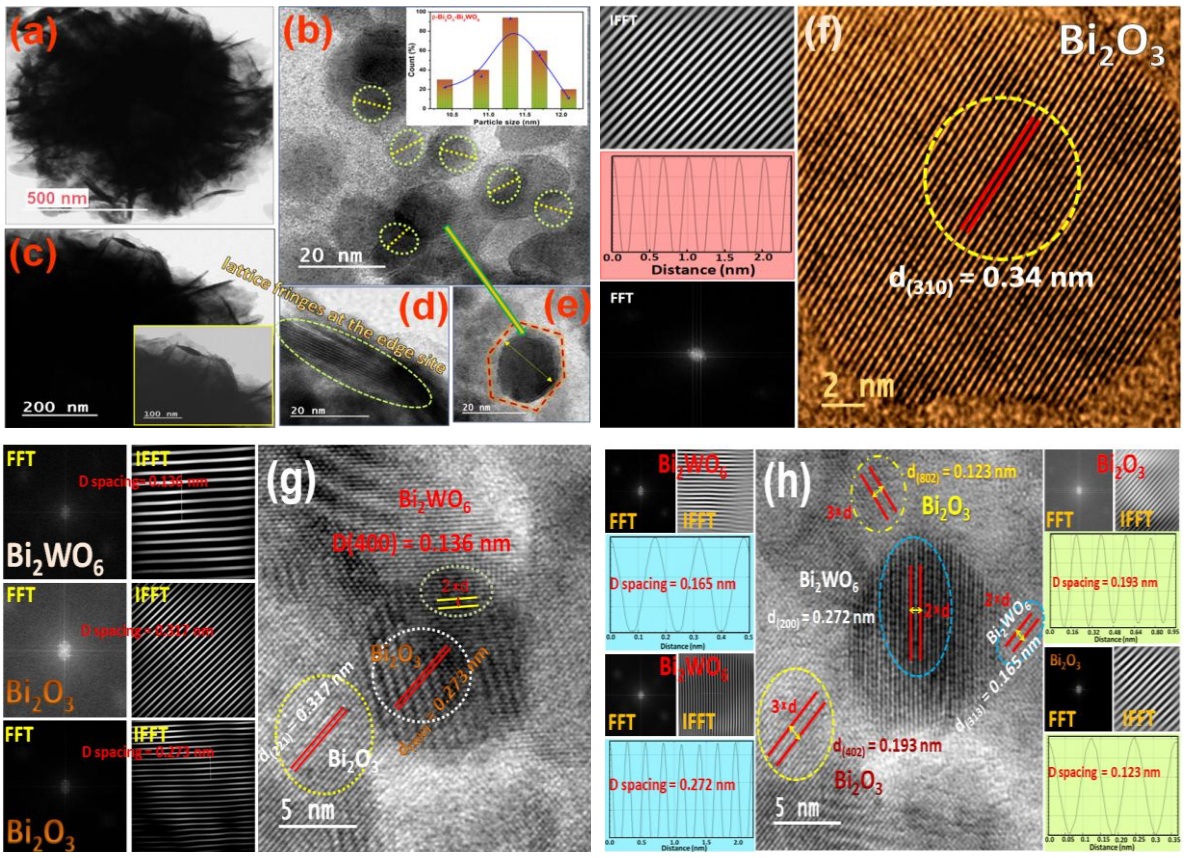

Figure 4.7. HR-TEM image β-Bi_2O_3-Bi_2WO_6 nanocomposite (a and c) in low magnification (b) magnified image shown with dotted yellow circles of nanocomposite, inset figure: Particle size distribution (d) lattice fringes at the edge site (e) a single crystallite (f→h) different lattice fringes of (310), (221), (400), (402) and (802) planes of β-Bi_2O_3, and (400), (313), and (200) planes of Bi_2WO_6 with their FFT and Inverse FFT images.

The HR-TEM images of the H_2TPP ornated β-Bi_2O_3-Bi_2WO_6 nanocomposite (Figures 4.8(a→e)) confirm the homogeneous enfolding of H_2TPP over the β-Bi_2O_3-Bi_2WO_6 surface via electrostatic interaction with an average crystallite size of ~ 11 nm as shown in Figure 4.8b, and the images shown in Figures 4.8(c→e) demonstrate the amorphous and crystalline natures of the nanocomposite. Figures 4.8(f→h)) also revealed the lattice fringes of 0.33, and 0.273 nm for the (310) and (400) planes of β-Bi_2O_3 and 0.167 and 0.272 nm for the (313) and (200) planes of Bi_2WO_6. The lattice fringes of 0.33 nm for the (310) plane of Bi_2O_3 and 0.167 nm for the (313) plane of Bi_2WO_6 are slightly distorted. H_2TPP, acting as a topping ligand, causes the aggregation of the β-Bi_2O_3-Bi_2WO_6/H_2TPP nanocomposite, and this type of surface morphology suggests that the nanocomposite possesses a substantial specific surface area.

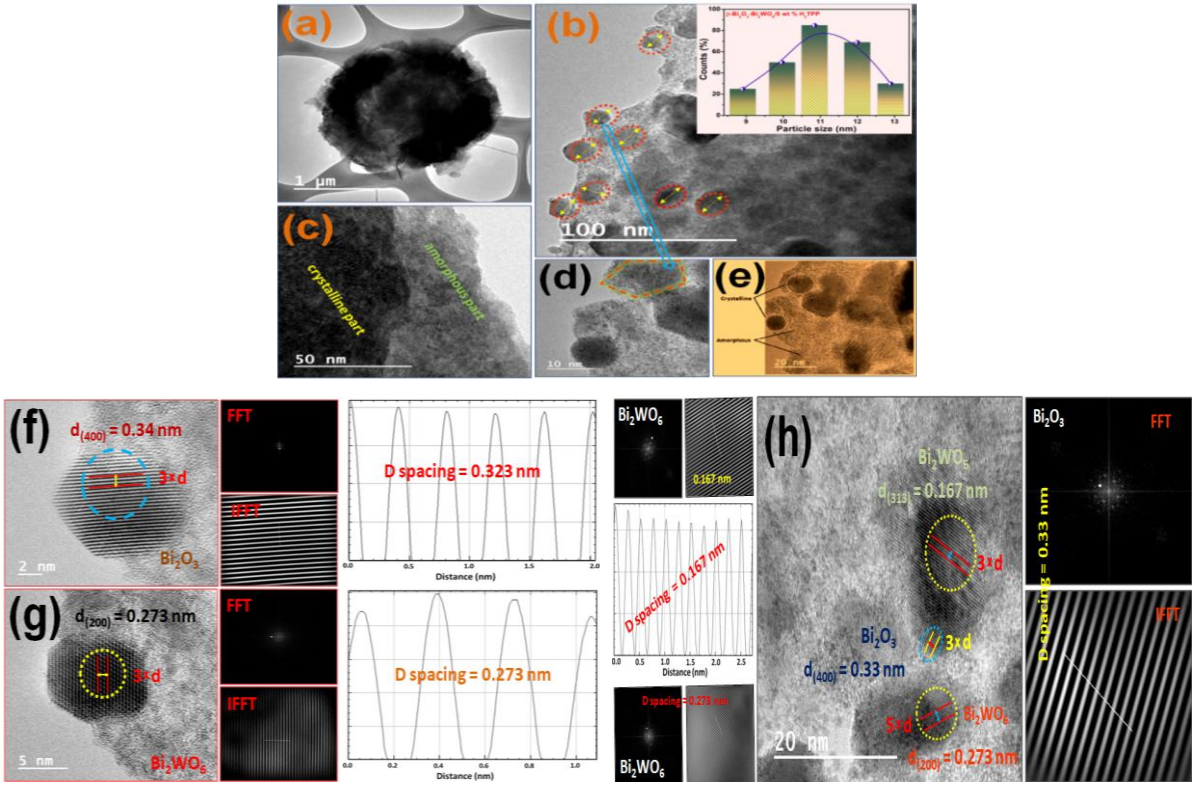

Figure 4.8. HR-TEM image of β-Bi_2O_3-Bi_2WO_6/5 wt % H_2TPP nanocomposite (a) in low magnification (b) magnified image indicated with dotted red circles of nanoparticles, inset figure: histogram plot for PSD (c→e) amorphous and crystalline part of nanocomposite (f→h) different lattice fringes of (310), and (400) planes of β-Bi_2O_3, and (313) plane Bi_2WO_6 with their FFT and Inverse FFT images.

The distinct selected area electron diffraction (SAED) patterns for both β-Bi_2O_3-Bi_2WO_6 and β-Bi_2O_3-Bi_2WO_6/5 wt % H_2TPP (Figures 4.9a and b) exhibit strong concentric rings corresponding to the planes (221), (400), (421), (402) for Bi_2O_3 and the planes (400), (402) for Bi_2WO_6, respectively. These patterns align well with the XRD result of β-Bi_2O_3-Bi_2WO_6, further confirming the existence of β-Bi_2O_3-Bi_2WO_6 as a key component.

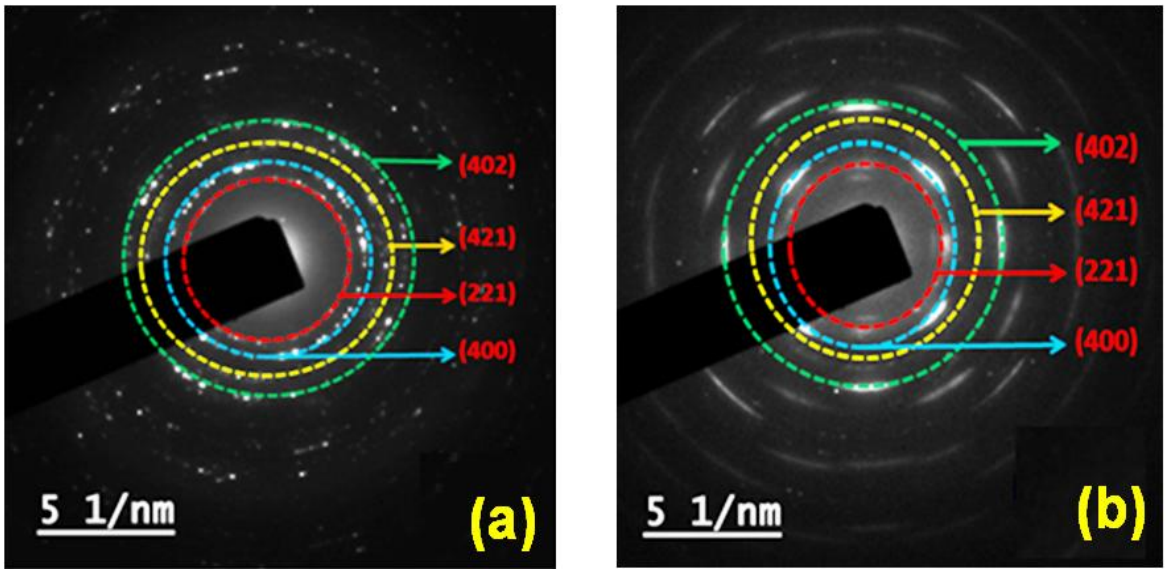

Figure 4.9. SAED pattern of (a) β-Bi_2O_3-Bi_2WO_6 and (b) β-Bi_2O_3-Bi_2WO_6/5 wt % H_2TPP nanocomposites.

4.3.1.4. Ramam Analysis. To validate our findings, the Raman spectra and mapping of β-Bi_2O_3-Bi_2WO_6 and β-Bi_2O_3-Bi_2WO_6/5 wt % H_2TPP were performed, which are displayed in Figures 4.10(a→d). In pure β-Bi_2O_3-Bi_2WO_6, the peaks at 600-1000 cm^{-1} are due to the stretching vibration of W-O, while the band at 305 cm^{-1} is responsible for the simultaneous translational modes of Bi^{3+} and WO_6^{6-}. The peaks at 692 and 822 cm^{-1} are also attributed to the anti-symmetric bridging mode accompanying the tungstate chain and the anti-symmetric A_g mode of the terminal O-W-O groups.[51] The band at 116 cm^{-1} originates from A_g symmetry, which is mostly due to the involvement of the Bi atoms. The displacements of Bi and O atoms in the β-Bi_2O_3 lattice may be the source of the band at 161 cm^{-1} (B_g).[52] The Raman peaks at higher frequencies, specifically at 306, 383, 467, and 562 cm^{-1} are ascribed to the displacements of oxygen atoms in β-Bi_2O_3. However, none of the Raman peaks of

β-Bi_2O_3-Bi_2WO_6 shifted significantly in β-Bi_2O_3-Bi_2WO_6/5 wt % H_2TPP but showed a little tendency to move towards the lower wave number region (Figure 4.10a).

Moreover, the 1549 cm^{-1} mode in the β-Bi_2O_3-Bi_2WO_6/H_2TPP spectrum (Figure 4.10b) corresponds to asymmetric stretching and bending in C_α-C_m-$C_{\alpha'}$ and C_α-NH-$C_{\alpha'}$/C_α-N-$C_{\alpha'}$ bonds, C_β-$C_{\beta'}$ bond stretching, symmetric stretching of the C_α-C_m-$C_{\alpha'}$ bond, and bending deformation of the C_α-NH-$C_{\alpha'}$/C_α-N-$C_{\alpha'}$ bonds, involving rocking of Hs on C_β atoms of H_2TPP.[53,54,55] The 1223 cm^{-1} band is attributed to the rocking of Hs and bending deformation within the phenyl groups, along with C_m-C_φ bond stretching and relatively weak skeletal deformation of the macro-cycle. The 1002 cm^{-1} Raman band indicates in-plane bending of phenyl rings, while the 990 cm^{-1} peak arises from pyrrolenine/pyrroline group expansion along N· · ·N and NH· · ·NH directions, involving C_α-C_m-C_α bond bending and weak skeletal deformation of phenyl rings. The 990 cm^{-1} band is attributed to pyrroline (primarily) and pyrrolenine rings along HN· · ·NH/N· · ·N direction, resulting from bending of H(N)-C_α-C_β/(H)N-$C_{\alpha'}$-$C_{\beta'}$ and N-C_α-C_β/N-$C_{\alpha'}$-$C_{\beta'}$ bonds in the same phase. Another band at 954 cm^{-1} is observed from the expansion of pyrrolenine (predominantly) and pyrroline rings along the N· · ·N/NH· · ·NH direction, involving the bending of N-C_α-C_β/N-$C_{\alpha'}$-$C_{\beta'}$ and H(N)-C_α-C_β/(H)N-$C_{\alpha'}$-$C_{\beta'}$ bonds in the same phase. The Raman features at 828 cm^{-1} are attributed to wagging of Hs on phenyl groups; 636 cm^{-1} is due to diagonal expansion of phenyl groups, including relatively weak wagging of Hs on the macrocycle; and 441 cm^{-1} result from twisting of phenyl rings caused by their out-of-plane bending deformations. The Raman bands at 383 and 194 cm^{-1} may be indicative of dimerization or aggregation of the H_2TPP.[54] These overall results suggest that the H_2TPP molecule may be attached to β-Bi_2O_3-Bi_2WO_6 through electrostatic interaction, confirming the successful fabrication of β-Bi_2O_3-Bi_2WO_6 with H_2TPP.

Additionally, Figure 4.10c reveals that the β-Bi_2O_3-Bi_2WO_6 nanocomposites are well-dispersed, exhibiting relatively consistent roughness across the scanning zone. However, as shown in Figure 4.10d, a few distinct red spots at the top sites become noticeable when an organic system is added to activate its catalytic activity. Additionally, a significant number of these spots are evenly distributed throughout the image. The Raman spectra thus provide additional evidence of the existence of H_2TPP in the nanocomposite. Overall, the XRD and XPS studies, elemental analyses, and Raman analyses collectively demonstrate the successful formation of H_2TPP ornated β-Bi_2O_3-Bi_2WO_6.

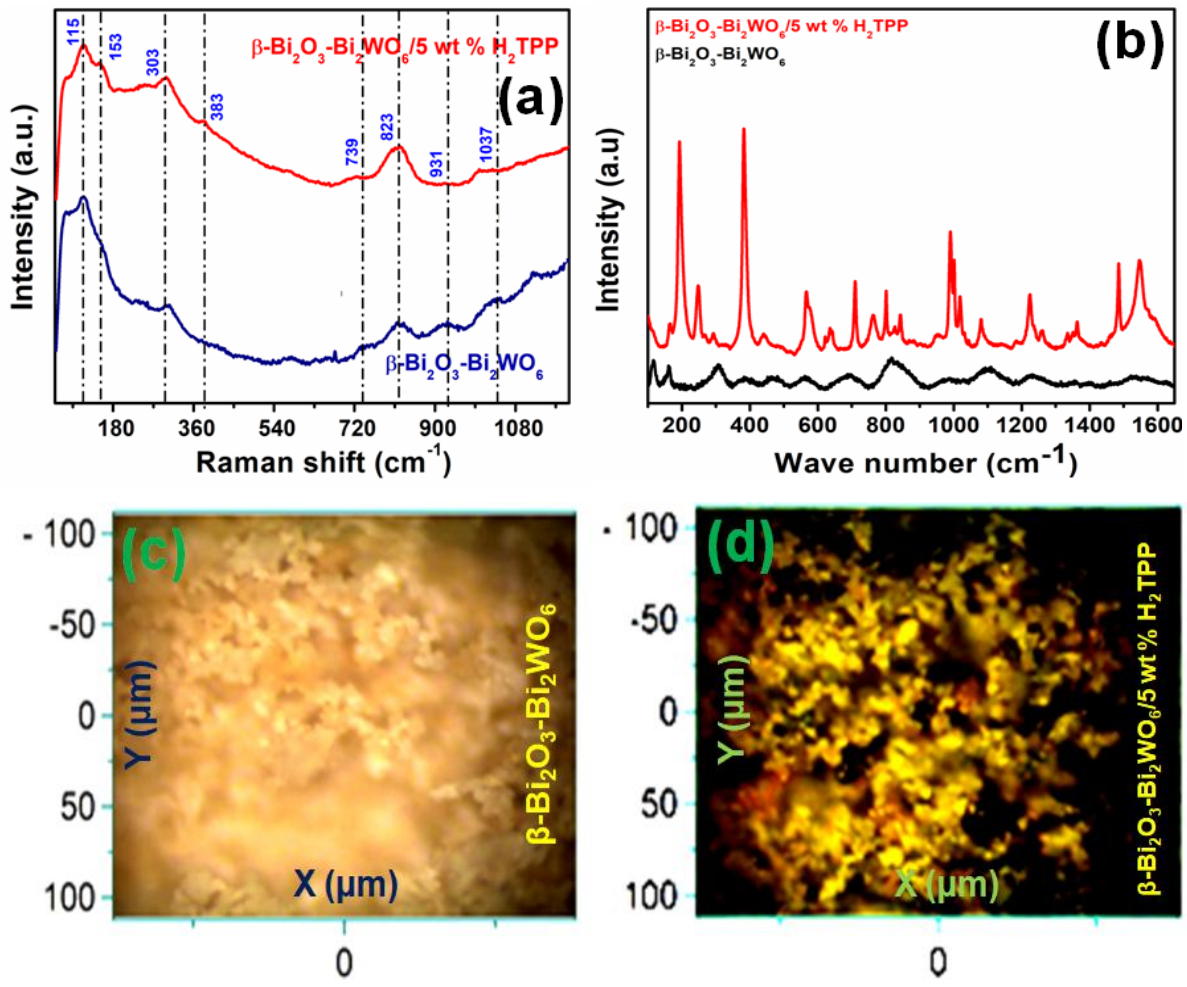

Figure 4.10. (a) Raman spectra; Excitation wavelength: 532 nm; Excitation power: 0.4 mW; (b) Excitation wavelength: 488 nm; Excitation power: 0.4 mW. Residual, small background has been subtracted and (c and d) Raman mapping of β-Bi_2O_3-Bi_2WO_6 and β-Bi_2O_3-Bi_2WO_6/5 wt % H_2TPP nanocomposites.

4.3.1.5. Brunauer-Emmett-Teller (BET) Surface Area Analysis. To evaluate the specific surface area and their pore size distribution (PSD), the nitrogen adsorption-desorption isotherms of β-Bi_2O_3-Bi_2WO_6 and β-Bi_2O_3-Bi_2WO_6/5 wt % H_2TPP composites were performed as shown in Figures 4.11a and b, which can be assigned to type IV isotherm. The pore size distribution analysis of β-Bi_2O_3-Bi_2WO_6 demonstrated a large number of pores with diameters of 1.515 (Figure 4.11a), possibly present on the crystalline nanosheets within the β-Bi_2O_3-Bi_2WO_6 microspheres.[35] Conversely, smaller pores with sharp peaks around 3.38 are likely a result of the crystal growth process.[56] The calculated

BET surface area for β-Bi_2O_3-Bi_2WO_6 is 19.756, accompanied by cumulative pore volumes of 0.068 cm^3 g^{-1}. The incorporation of 5 wt % H_2TPP into β-Bi_2O_3-Bi_2WO_6 results in a higher BET surfac e area of 34.085 m^2 g^{-1}, along with a larger pore size of 2.48 nm (Figure 4.11b) and an increased pore volume of 0.705 cm^3 g^{-1} (Table 4.1). This enhancement in surface area and pore volume for the β-Bi_2O_3-Bi_2WO_6/5 wt % H_2TPP nanocomposite suggests improved adsorption and reaction sites, as well as enhanced mechanical strength and electrocatalytic behavior for Cr^{6+} reduction. These results also play a dominant role in the enhancement of ECSA.

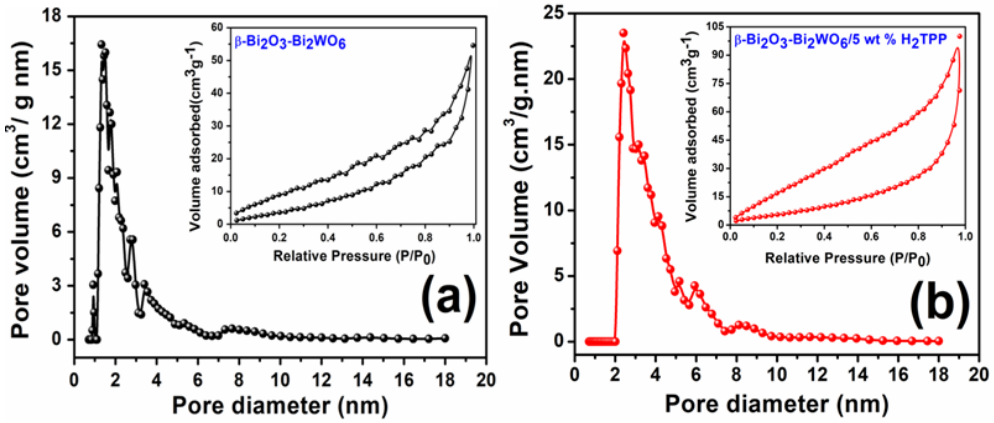

Figure 4.11. BET isotherms of (a) β-Bi_2O_3-Bi_2WO_6 and (b) β-Bi_2O_3-Bi_2WO_6/5 wt % H_2TPP nanocomposites.

Table 4.1. Surface properties of β-Bi_2O_3-Bi_2WO_6 and β-Bi_2O_3-Bi_2WO_6/5 wt % H_2TPP nanocomposites.

Samples	BET surface area (m^2 g^{-1})	Pore volume (cm^3 g^{-1})	Pore diameter (nm)
β-Bi_2O_3-Bi_2WO_6	19.756	0.068	1.515
β-Bi_2O_3-Bi_2WO_6/5 wt % H_2TPP	34.085	0.705	2.480

4.3.1.6. UV-Vis Diffuse Reflectance Spectroscopic Study (DRS). To investigate the optical characterization, UV-Vis diffuse reflectance spectroscopy of the nanocomposites was performed to determine their photoelectrocatalytic activity. Figure 4.12a indicates that all nanocomposites have strong absorption in the visible region. A significant Soret band at 438.57 nm due to the π-π* transition of the macrocyclic ring was observed[42,57] in the DRS spectrum of H_2TPP, as shown in Figure 4.12b. The red-shifting of the Soret band of H_2TPP in β-Bi_2O_3-Bi_2WO_6/5 wt % H_2TPP at

526.28 nm indicates increased absorption in the solar region and the quick generation of photogenerated electron and hole pairs. The characteristic absorption peaks corresponding to the Q bands of H_2TPP,[58] ranging from 500 to 700 nm, were also observed in the DRS spectrum of β-Bi_2O_3-Bi_2WO_6/H_2TPP nanocomposite, which further confirmed the successful introduction of H_2TPP into β-Bi_2O_3-Bi_2WO_6. The optical absorption edges of β-Bi_2O_3-Bi_2WO_6 and β-Bi_2O_3-Bi_2WO_6/5 wt % H_2TPP were found at 453.77 and 526.28 nm, respectively. Within the visible region (400-800 nm), β-Bi_2O_3-Bi_2WO_6/H_2TPP shows a higher absorbance than that of β-Bi_2O_3-Bi_2WO_6, signifying that the loading of H_2TPP can enhance the activities of the synthesized nanocomposite, as depicted in Figure 4.12a.

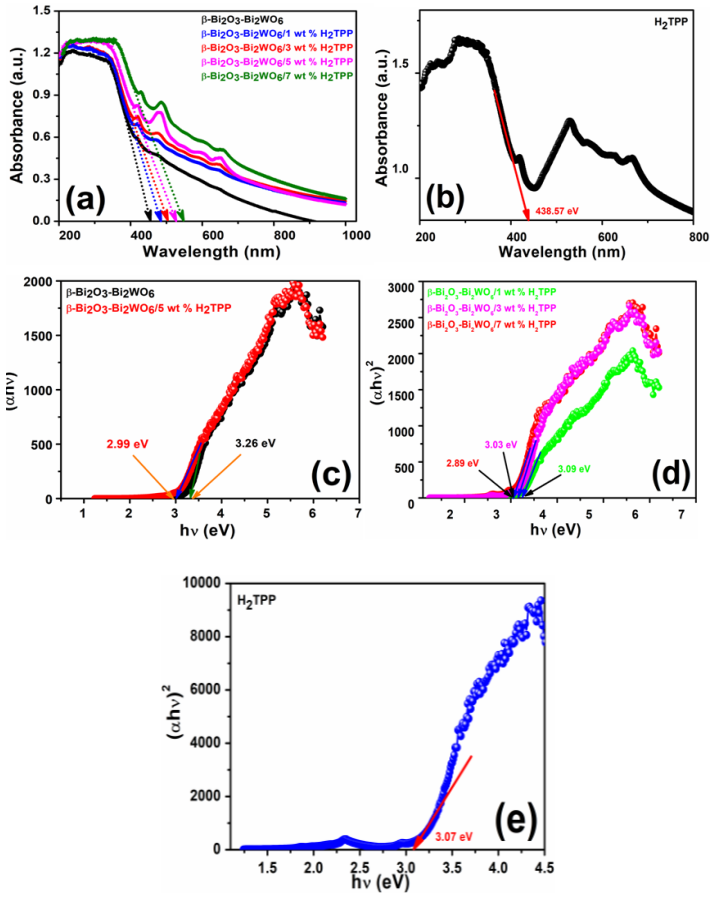

Figure 4.12. UV-Vis diffuse reflectance spectroscopy of (a) β-Bi_2O_3-Bi_2WO_6 and different weight percentages of H_2TPP ornated β-Bi_2O_3-Bi_2WO_6 nanocomposites (b) H_2TPP; Kubelka-Munk plot of (c) β-Bi_2O_3-Bi_2WO_6 and β-Bi_2O_3-Bi_2WO_6/5 wt % H_2TPP nanocomposites (d) β-Bi_2O_3-Bi_2WO_6/1 wt % H_2TPP, β-Bi_2O_3-Bi_2WO_6/3 wt % H_2TPP and β-Bi_2O_3-Bi_2WO_6/7 wt % H_2TPP nanocomposites (e) H_2TPP.

The Kubelka-Munk equation was used to calculate the band gap energies of the nanocomposites.[59] The band gap energies calculated from the plots of $(\alpha h\nu)^2$ against photon energy ($h\nu$), as shown in Figures 4.12(c→e), display that an increase in the concentration of H_2TPP decreases the band gap energy significantly (Table 4.2), suggesting that the loading of H_2TPP can effectively reduce the band gap of the synthesized nanocomposites, resulting in the nanocomposite being advantageous to separate the photogenerated electron and hole pairs.

Table 4.2. Band gap energy (BGE) from the absorption plot of different nanocomposites using Kubelka-Munk function.

Nanocomposites	λ_{max} (nm)	Band gap energy (eV)
H_2TPP	438.57	3.07
β-Bi_2O_3-Bi_2WO_6	453.77	3.26
β-Bi_2O_3-Bi_2WO_6/1 wt % H_2TPP	485.34	3.09
β-Bi_2O_3-Bi_2WO_6/3 wt % H_2TPP	503.38	3.03
β-Bi_2O_3-Bi_2WO_6/5 wt % H_2TPP	526.28	2.99
β-Bi_2O_3-Bi_2WO_6/7 wt % H_2TPP	544.84	2.89

4.3.1.7. Thermogravimetric analysis (TGA). The TGA profile of *meso*-tetraphenylporphyrin was performed (Figure 4.13). The H_2TPP showed a weight loss of approximately 32.07% at approximately 545 °C corresponding to the decomposition of macrocyclic ligands that clearly indicates its thermal stability till 600 °C.

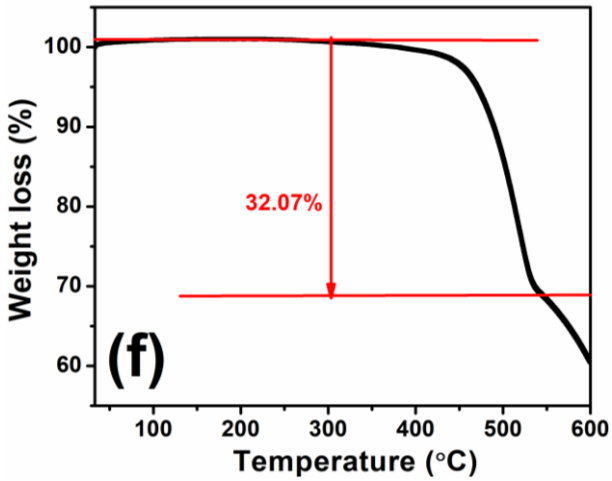

Figure 4.13. TGA profile of H_2TPP.

4.3.1.8. FTIR Analysis. Figures 4.14(a, a′, and b, b′) showed the FTIR spectra of the groups containing oxygen atoms and the chemical interactions of β-Bi_2O_3-Bi_2WO_6/H_2TPP. The absorption bands at 400-1100 cm^{-1} are ascribed to the bridging stretching modes of the O atom attached to the metal atom; the peak at 515 cm^{-1} is responsible for the stretching vibration mode of Bi-O, while the bands at 693 and 883 cm^{-1} are due to the stretching vibration modes of WO_6 in Bi_2WO_6.[60] The absorption peak positions between β-Bi_2O_3-Bi_2WO_6 and H_2TPP ornated β-Bi_2O_3-Bi_2WO_6 nanocomposites were not substantially different, but there were some differences at 1744, 1612, and 1039 cm^{-1}. The IR absorption bands at 1612, 1039, and 1083 cm^{-1} dropped with the increase in the concentration of H_2TPP on the surface of the nanocomposites.[60] However, the absorption peak at 1744 cm^{-1} increased with the increasing amount of H_2TPP, indicating an increase in the N-containing π-conjugated organic species on the nanocomposites thus prepared.[61] The peaks at 2854 and 2918 cm^{-1} are responsible for the symmetric and asymmetric stretching vibrations of the -CH_2 group.[46,62] The absorption bands at 963 and 798 cm^{-1} appeared due to the in-plane and out-of-plane δ N-H of H_2TPP[42]. This further confirmed the effective surface modification of β-Bi_2O_3-Bi_2WO_6 by H_2TPP, wherein H_2TPP is firmly attached to the surface through electrostatic interactions.

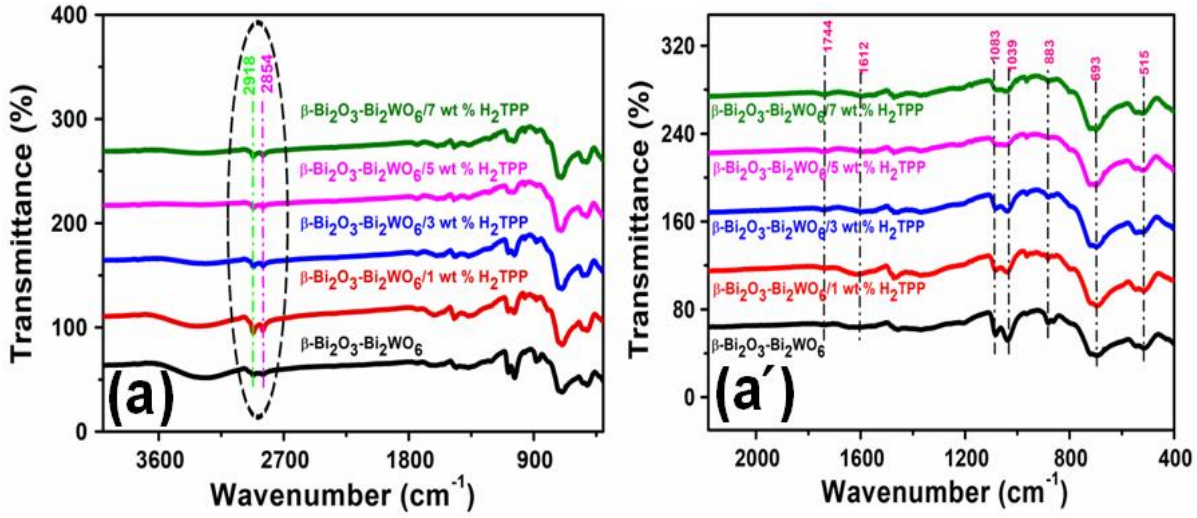

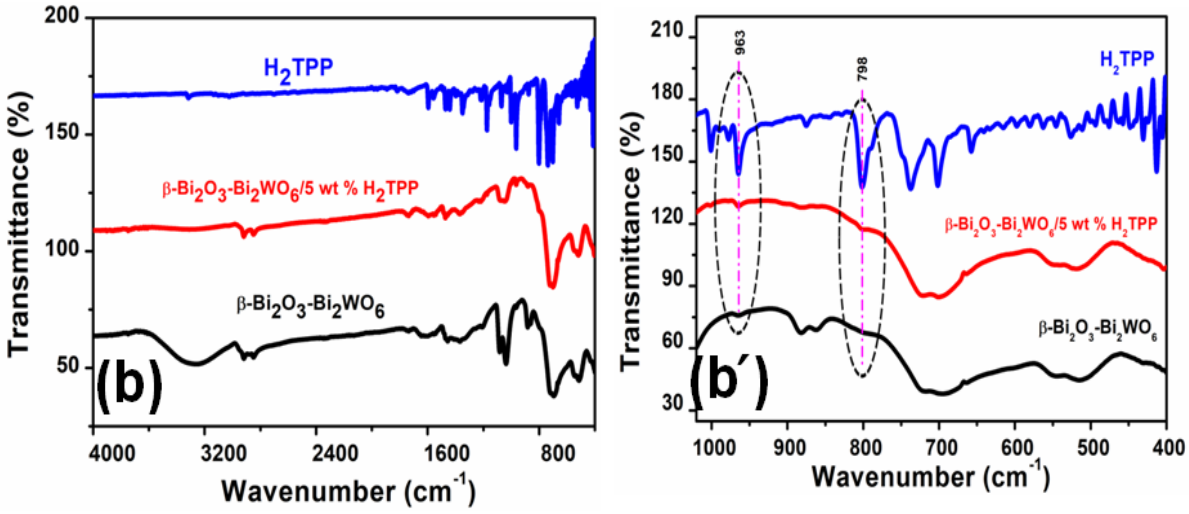

Figure 4.14. FTIR analysis of (a and a′) β-Bi_2O_3-Bi_2WO_6 and H_2TPP ornated different β-Bi_2O_3-Bi_2WO_6 nanocomposites (b and b′) β-Bi_2O_3-Bi_2WO_6, β-Bi_2O_3-Bi_2WO_6/5 wt % H_2TPP nanocomposites and H_2TPP.

4.3.2. Electrochemical Activity for Cr^{6+} Detection. The concentration of Cr^{6+} after a 30 min dark adsorption period was used as the initial concentration for the analysis. An adsorption-desorption equilibrium, as shown in Figure 4.15h, for Cr^{6+} was established after 30 min when the adsorption amount of Cr^{6+} was below 10%. In order to understand the reduction potential of Cr^{6+}, cyclic voltammetric (CV) measurements in 0.1 M KCl without and with 150 μM Cr^{6+} mixed solution at pH 4.0 were performed under dark conditions in an N_2 atmosphere (Figures 4.15(a→g)). In the presence of Cr^{6+}, bare FTO showed no reduction peak, indicating that bare FTO is not responsible for the reduction of Cr^{6+} (Figure 4.15a). However, in the presence of Cr^{6+}, a reduction peak was observed with β-Bi_2O_3-Bi_2WO_6/FTO and H_2TPP/FTO. The presence of electron-rich N in H_2TPP may be responsible for the weak reduction peak. After the incorporation of different wt % H_2TPP with β-Bi_2O_3-Bi_2WO_6, the electrostatic interaction of the 2p orbital of N of H_2TPP to the 3d and 4s orbitals of Cr^{6+} facilitates the adsorption of Cr^{6+} to the pore of H_2TPP, resulting in a significant enhancement of the reduction peak, which may be due to the three-electron reduction of Cr^{6+} (Equation 4.1). Compared with H_2TPP/FTO, β-Bi_2O_3-Bi_2WO_6/FTO, β-Bi_2O_3-Bi_2WO_6/1 wt % H_2TPP/FTO, β-Bi_2O_3-Bi_2WO_6/3 wt % H_2TPP/FTO, and β-Bi_2O_3-Bi_2WO_6/7 wt % H_2TPP/FTO electrodes, the reduction current for the β-Bi_2O_3-Bi_2WO_6/5 wt % H_2TPP-modified electrode was strong, as shown in Figures 4.16a and b. Surface modification by H_2TPP greater than 5% by weight may thicken the surface,

resulting in inhibition of the adsorption of Cr^{6+}, which decreases the electrochemical reduction performance of the nanocomposite.

$$HCrO_4^- + 7H^+ + 3e^- \rightarrow Cr^{3+} + 4H_2O \qquad \text{Eq. 4.1}$$

The reduction current increases with increasing Cr^{6+} concentration[63] (Figures 4.16(c→h) and exhibits good linearity, as shown in Figures 4.16(c′→h′). Among all the nanocomposites, β-Bi_2O_3-Bi_2WO_6/5 wt % H_2TPP has the greatest electrocatalytic activity for Cr^{6+} reduction in the concentration range of 0-200 µM (Figure 4.16g), and the calibration plot has a correlation coefficient (R^2 = 0.992) as displayed in Figure 4.16g′. The computed values of sensitivity and LOD are determined to be 0.131 µA $µM^{-1}$ cm^{-2} and 0.101 µM, respectively, as given in Table 4.3. Moreover, β-Bi_2O_3-Bi_2WO_6/5 wt % H_2TPP could enhance the effective surface area for high electron transport and electrocatalytic activity for the detection of Cr^{6+}, as is evidenced by BET and ECSA, suggesting its high electrocatalytic activity for the detection of Cr^{6+} in comparison to that of other nanocomposites.

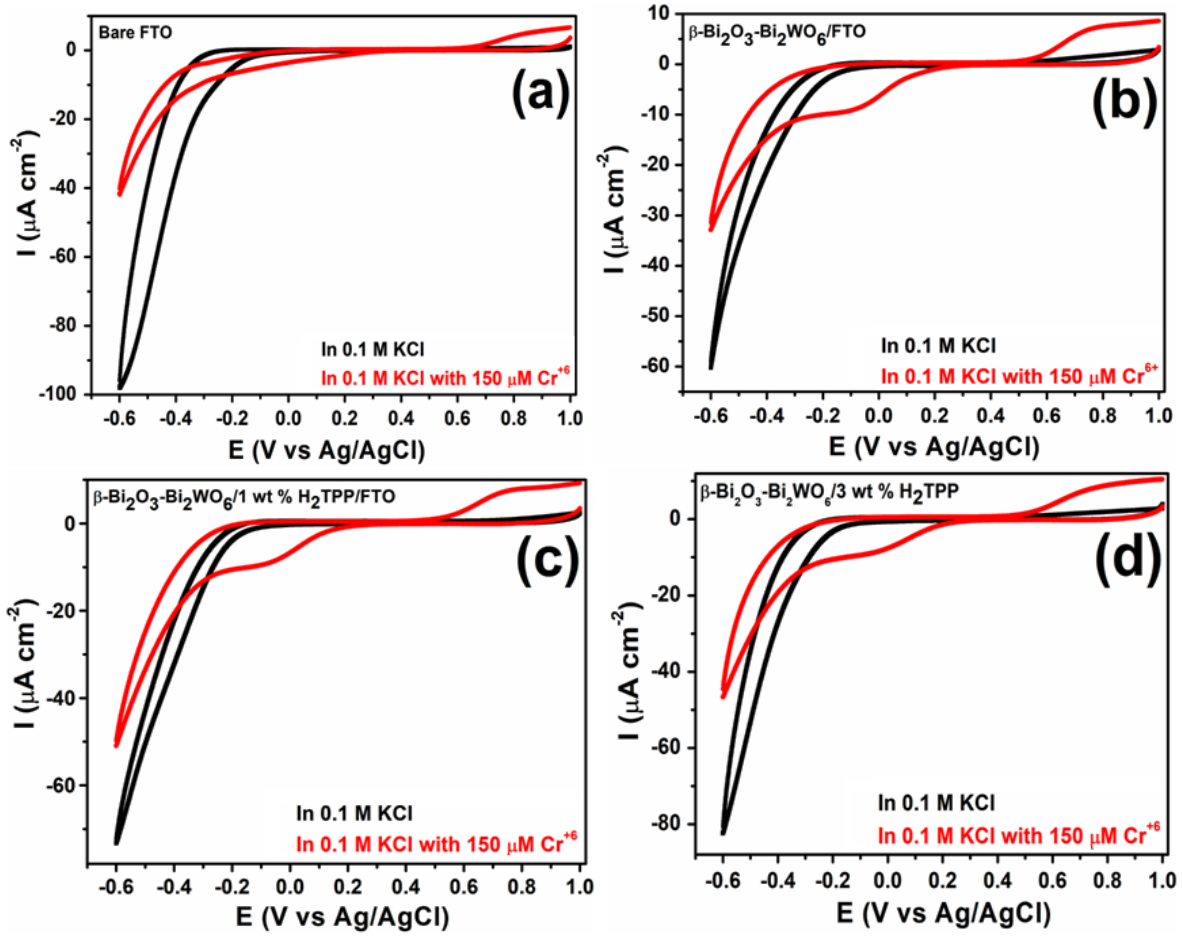

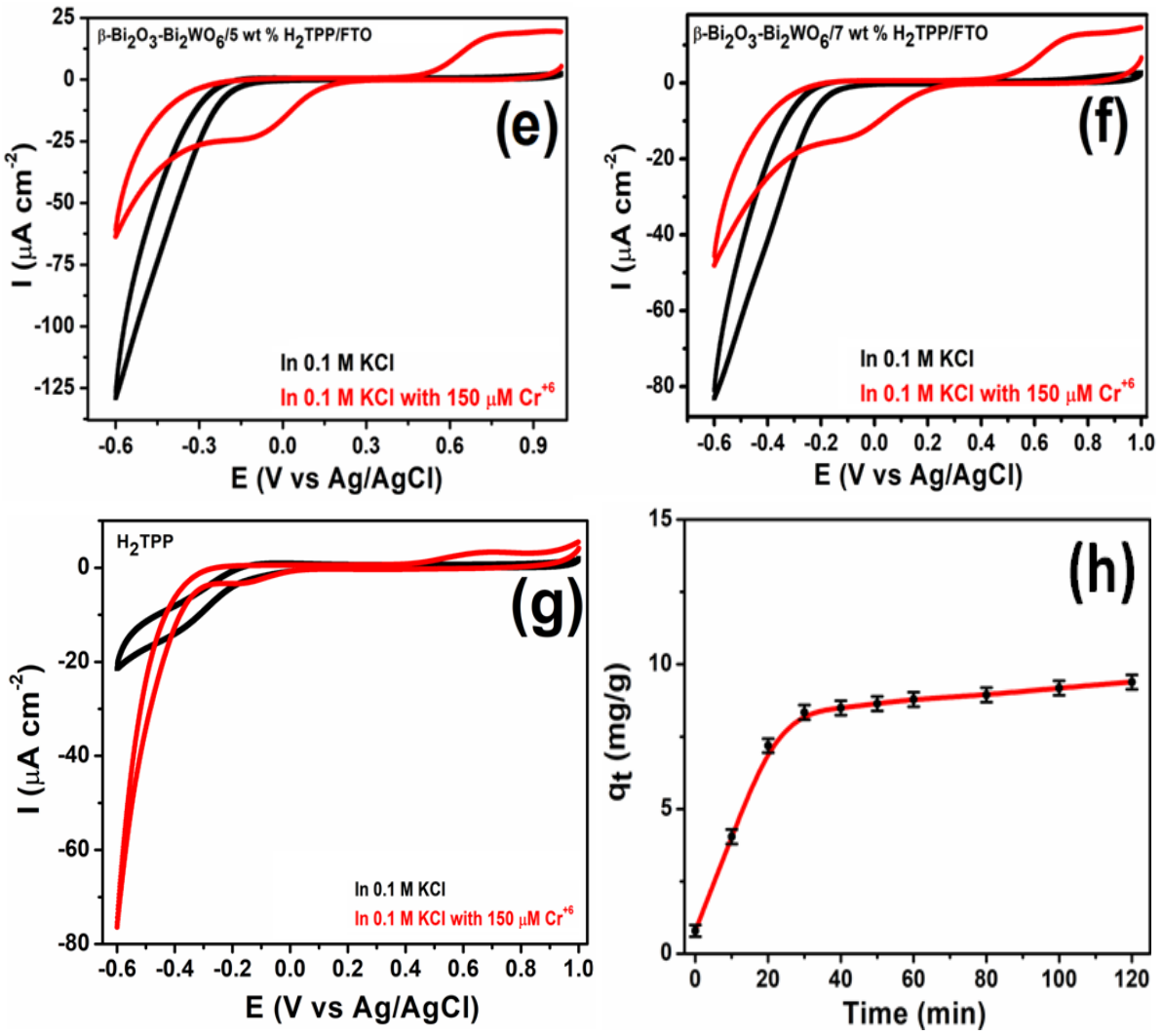

Figure 4.15. Cyclic voltammetric response of (a) bare FTO (b) β-Bi_2O_3-Bi_2WO_6/FTO (c) β-Bi_2O_3-Bi_2WO_6/1 wt % H_2TPP/FTO (d) β-Bi_2O_3-Bi_2WO_6/3 wt % H_2TPP/FTO (e) β-Bi_2O_3-Bi_2WO_6/5 wt % H_2TPP/FTO (f) β-Bi_2O_3-Bi_2WO_6/7 wt % H_2TPP/FTO (g) H_2TPP/FTO in 0.1 M KCl and 0.1 M KCl with 150 μM of Cr^{6+} (pH 4.0) at a scan rate of 20 mV s^{-1} under dark conditions (h) effect of adsorption on Cr^{6+} reduction.

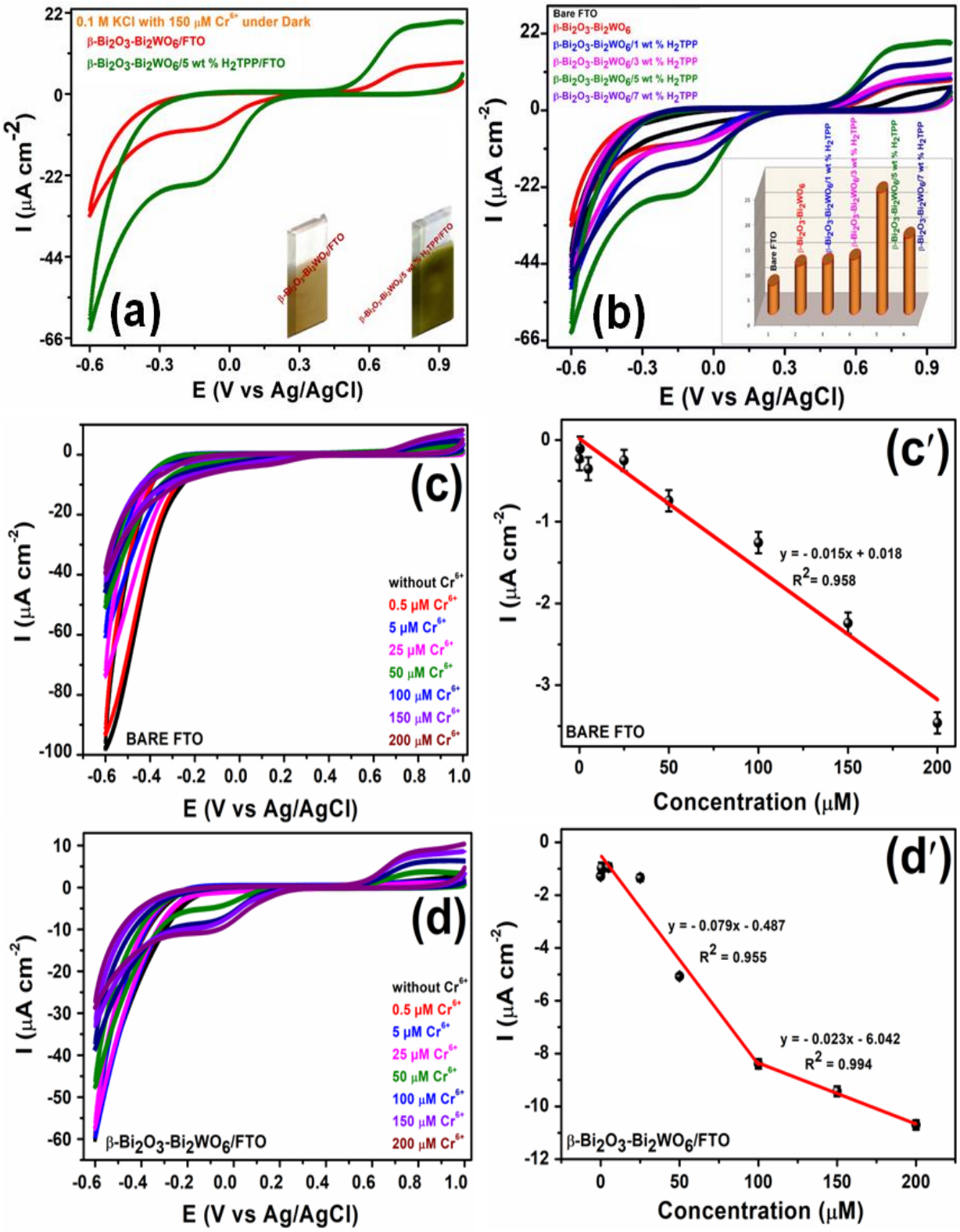
0.1 M KCl with 150 μM Cr6+ under Dark
β-Bi2O3-Bi2WO6/FTO
β-Bi2O3-Bi2WO6/5 wt % H2TPP/FTO
(a)
I (μA cm-2)
E (V vs Ag/AgCl)
Bare FTO
β-Bi2O3-Bi2WO6
β-Bi2O3-Bi2WO6/1 wt % H2TPP
β-Bi2O3-Bi2WO6/3 wt % H2TPP
β-Bi2O3-Bi2WO6/5 wt % H2TPP
β-Bi2O3-Bi2WO6/7 wt % H2TPP
(b)
(c)
without Cr6+
0.5 μM Cr6+
5 μM Cr6+
25 μM Cr6+
50 μM Cr6+
100 μM Cr6+
150 μM Cr6+
200 μM Cr6+
BARE FTO
(c′)
y = - 0.015x + 0.018
R2= 0.958
Concentration (μM)
(d)
β-Bi2O3-Bi2WO6/FTO
(d′)
y = - 0.079x - 0.487
R2 = 0.955
y = - 0.023x - 6.042
R2 = 0.994

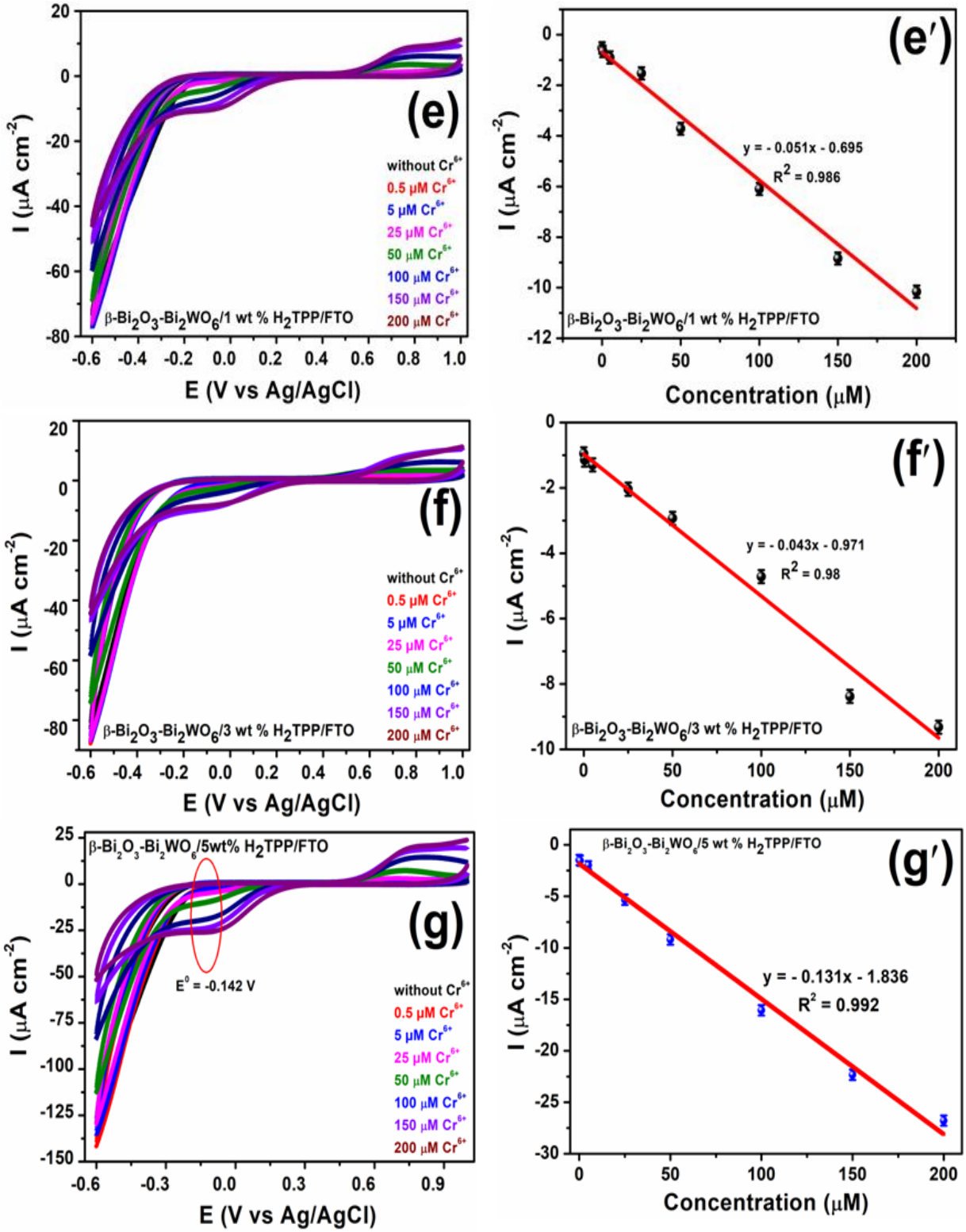
(e)
β-Bi2O3-Bi2WO6/1 wt % H2TPP/FTO
without Cr6+
0.5 μM Cr6+
5 μM Cr6+
25 μM Cr6+
50 μM Cr6+
100 μM Cr6+
150 μM Cr6+
200 μM Cr6+
I (μA cm-2)
E (V vs Ag/AgCl)
(e′)
y = - 0.051x - 0.695
R2 = 0.986
Concentration (μM)
(f)
β-Bi2O3-Bi2WO6/3 wt % H2TPP/FTO
(f′)
y = - 0.043x - 0.971
R2 = 0.98
(g)
β-Bi2O3-Bi2WO6/5wt% H2TPP/FTO
E0 = -0.142 V
(g′)
β-Bi2O3-Bi2WO6/5 wt % H2TPP/FTO
y = - 0.131x - 1.836
R2 = 0.992

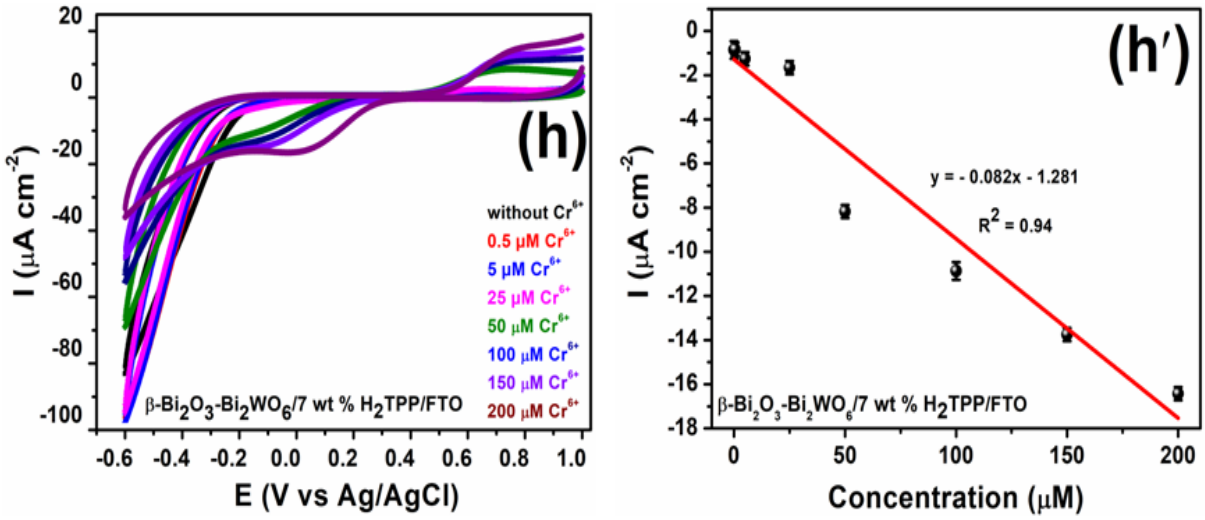

Figure 4.16. Cyclic voltammetric response under dark conditions at a scan rate of 20 mV s^{-1} (pH 4.0) of (a) β-Bi_2O_3-Bi_2WO_6/FTO and β-Bi_2O_3-Bi_2WO_6/5 wt % H_2TPP/FTO (b) bare FTO, β-Bi_2O_3-Bi_2WO_6/FTO, β-Bi_2O_3-Bi_2WO_6/1 wt % H_2TPP/FTO, β-Bi_2O_3-Bi_2WO_6/3 wt % H_2TPP/FTO, β-Bi_2O_3-Bi_2WO_6/5 wt % H_2TPP/FTO, β-Bi_2O_3-Bi_2WO_6/7 wt % H_2TPP/FTO in 0.1 M KCl with 150 µM of Cr^{6+} (c→h) at different Cr^{6+} concentrations (c′→h′) Calibration plot of reduction peak current against concentration of Cr^{6+} of bare FTO, β-Bi_2O_3-Bi_2WO_6/FTO, β-Bi_2O_3-Bi_2WO_6/1 wt % H_2TPP/FTO, β-Bi_2O_3-Bi_2WO_6/3 wt % H_2TPP/FTO, β-Bi_2O_3-Bi_2WO_6/5 wt % H_2TPP/FTO, β-Bi_2O_3-Bi_2WO_6/7 wt % H_2TPP/FTO under dark conditions.

With the increase in scan rate, the reduction peak current increases; however, the peak potential was slightly moved to the negative side (Figures 4.17(a→f)). The reduction peak current and the square root of the scan rate show a linear relationship (Figures 4.17(a′→f′)), having a correlation coefficient R^2 = ~ 0.992 for all nanocomposites, suggesting that it is a diffusion-controlled process. Furthermore, the electrochemical performance of various wt % H_2TPP-adorned β-Bi_2O_3-Bi_2WO_6/FTO electrodes with reference to Cr^{6+} sensing was estimated from the amperometric current response. Different modified electrodes displayed rapid current responses with the gradual addition of 10 µM Cr^{6+} at 100 s intervals under a potential of ~ -0.142 V, as shown in Figure 4.18a, and exhibited an incredible linear relationship between the response current and concentrations in the range of (0-90) µM of Cr^{6+}, having correlation coefficients (R^2) greater than 0.99 (Figures 4.18(b→f)). The current response in the case of β-Bi_2O_3-Bi_2WO_6/5 wt % H_2TPP nanocomposite is the fastest among all other nanocomposites, signifying that the nanocomposite had quick electrochemical sensing for Cr^{6+} and

would inhibit the build-up of reduction intermediates on the electrode surface.[64] From the amperometric current response, the sensitivity and LOD values of the β-Bi_2O_3-Bi_2WO_6/5 wt % H_2TPP nanocomposite were found to be 4.915 µA mM cm^{-2} and 0.017 µM, whereas the sensitivity and LOD values of the β-Bi_2O_3-Bi_2WO_6 nanocomposite were 0.797 µA mM cm^{-2} and 0.072 µM in the linear concentration range of (0-90) µM, as detailed in Table 4.3.

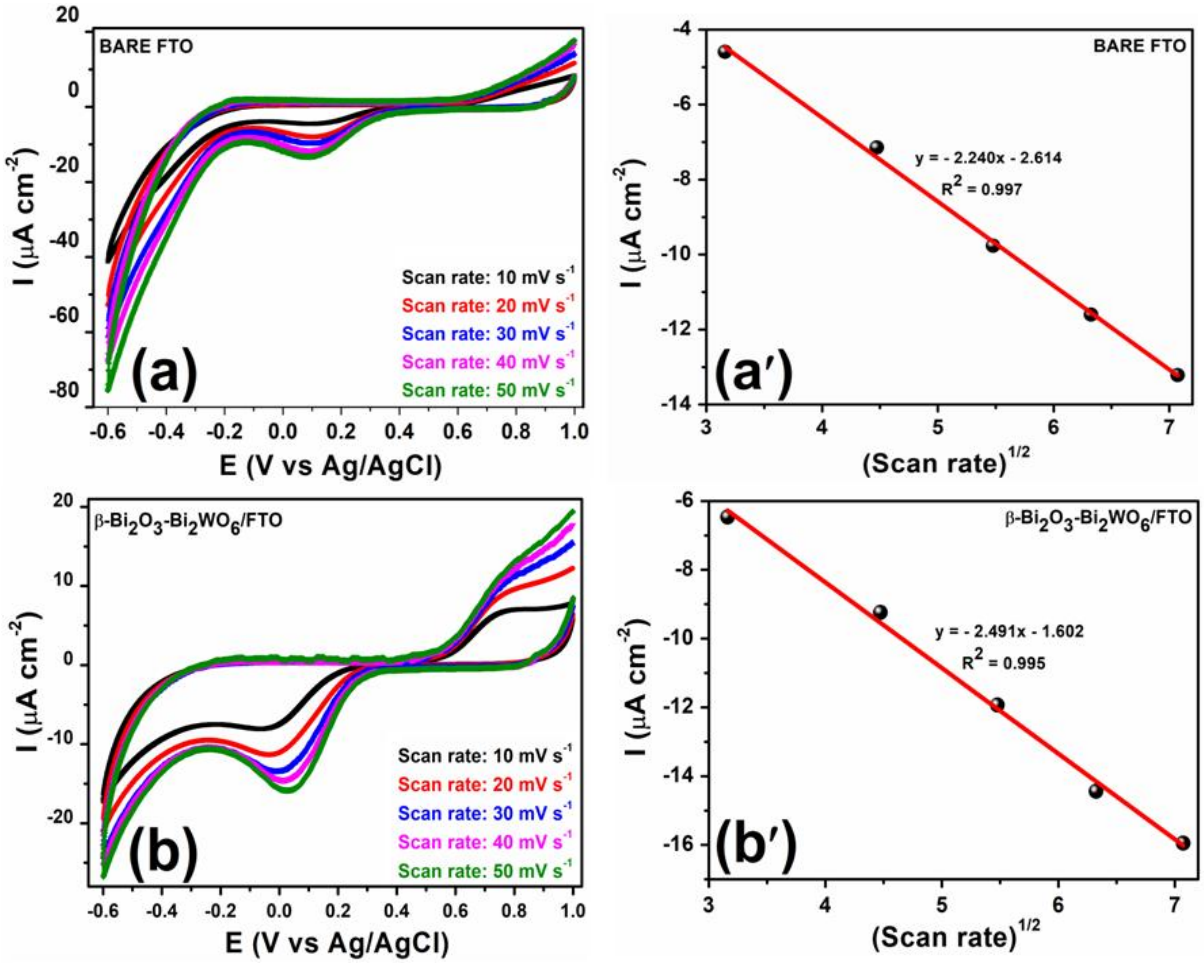

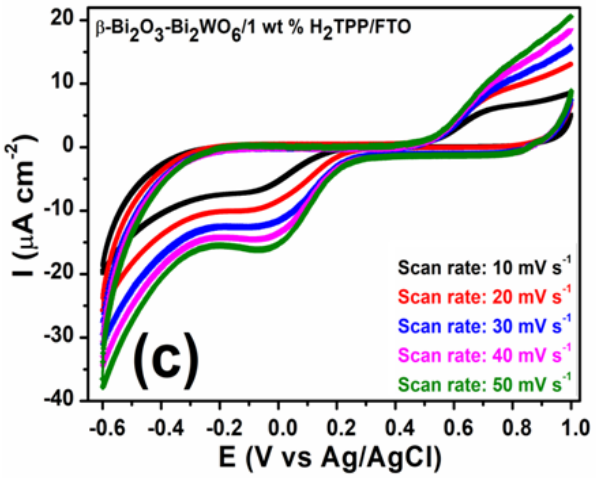
β-Bi2O3-Bi2WO6/1 wt % H2TPP/FTO
I (μA cm-2)
E (V vs Ag/AgCl)
Scan rate: 10 mV s-1
Scan rate: 20 mV s-1
Scan rate: 30 mV s-1
Scan rate: 40 mV s-1
Scan rate: 50 mV s-1
(c)

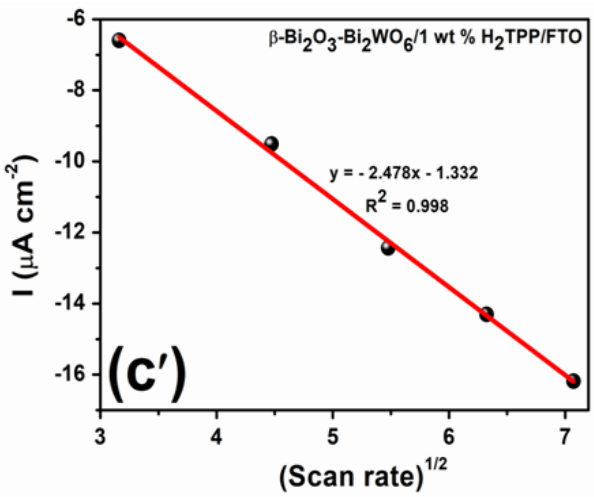
β-Bi2O3-Bi2WO6/1 wt % H2TPP/FTO
y = - 2.478x - 1.332
R2 = 0.998
I (μA cm-2)
(Scan rate)1/2
(c′)

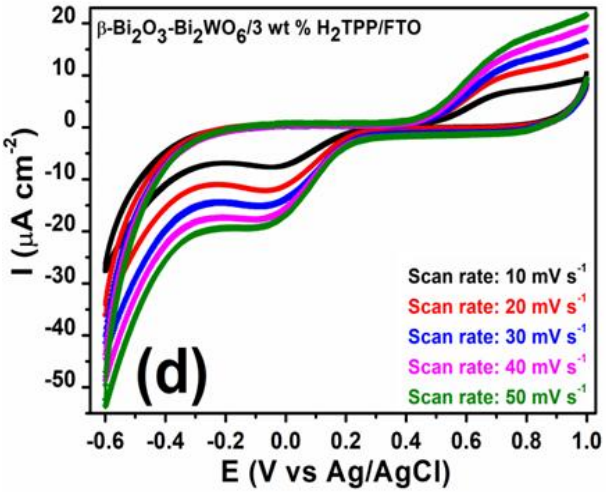
β-Bi2O3-Bi2WO6/3 wt % H2TPP/FTO
I (μA cm-2)
E (V vs Ag/AgCl)
Scan rate: 10 mV s-1
Scan rate: 20 mV s-1
Scan rate: 30 mV s-1
Scan rate: 40 mV s-1
Scan rate: 50 mV s-1
(d)

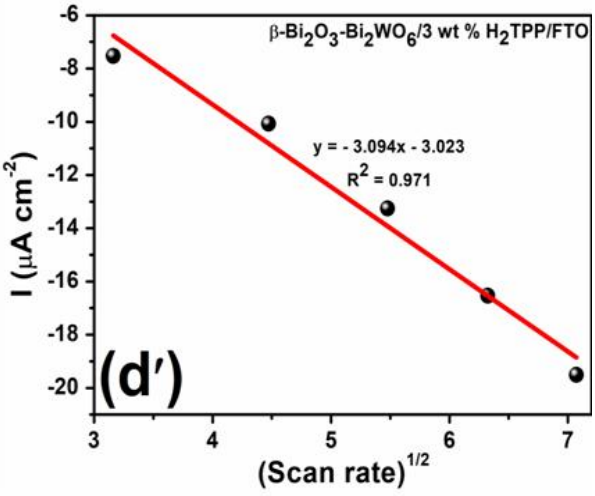
β-Bi2O3-Bi2WO6/3 wt % H2TPP/FTO
y = - 3.094x - 3.023
R2 = 0.971
I (μA cm-2)
(Scan rate)1/2
(d′)

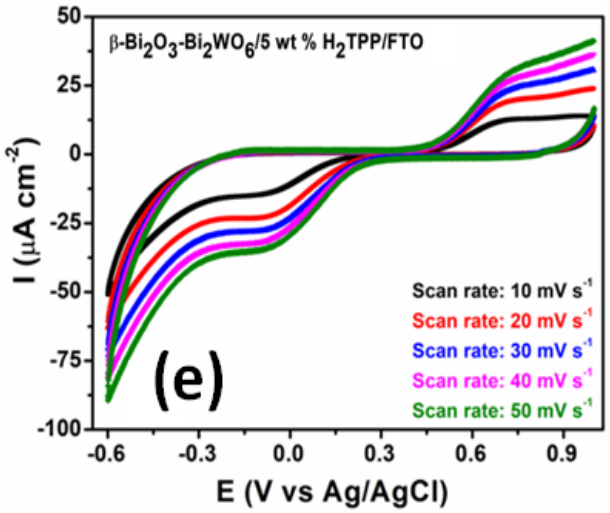
β-Bi2O3-Bi2WO6/5 wt % H2TPP/FTO
I (μA cm-2)
E (V vs Ag/AgCl)
Scan rate: 10 mV s-1
Scan rate: 20 mV s-1
Scan rate: 30 mV s-1
Scan rate: 40 mV s-1
Scan rate: 50 mV s-1
(e)

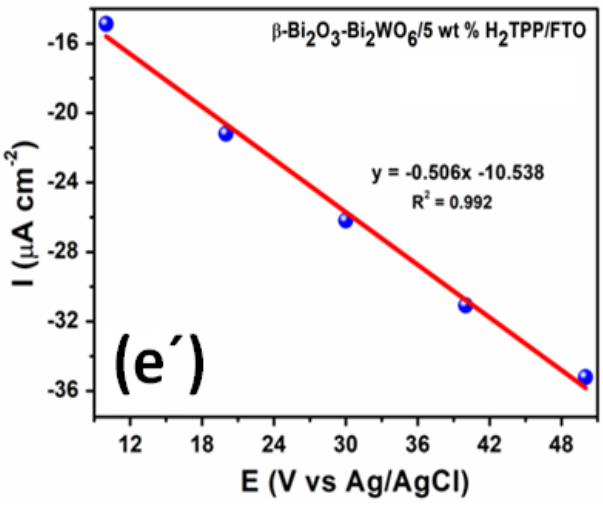
β-Bi2O3-Bi2WO6/5 wt % H2TPP/FTO
y = -0.506x -10.538
R2 = 0.992
I (μA cm-2)
E (V vs Ag/AgCl)
(e´)

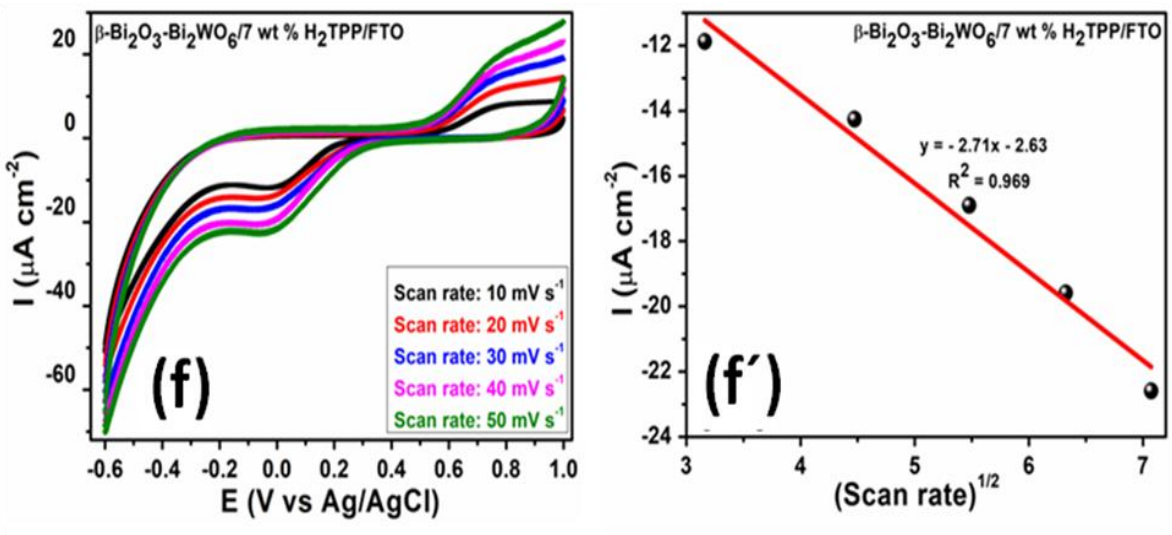

Figure 4.17. (a→e) Cyclic voltammetric response at different scan rates and (a′→e′) Linear relationships between the reduction peak currents and the square root of scan rate ($\nu^{1/2}$) for bare FTO, β-Bi_2O_3-Bi_2WO_6/FTO, β-Bi_2O_3-Bi_2WO_6/1 wt % H_2TPP/FTO, β-Bi_2O_3-Bi_2WO_6/3 wt % H_2TPP/FTO, β-Bi_2O_3-Bi_2WO_6/5 wt % H_2TPP/FTO, β-Bi_2O_3-Bi_2WO_6/7 wt % H_2TPP/FTO in 0.1 M KCl with 150 μM of Cr^{6+} (pH 4.0) under dark conditions.

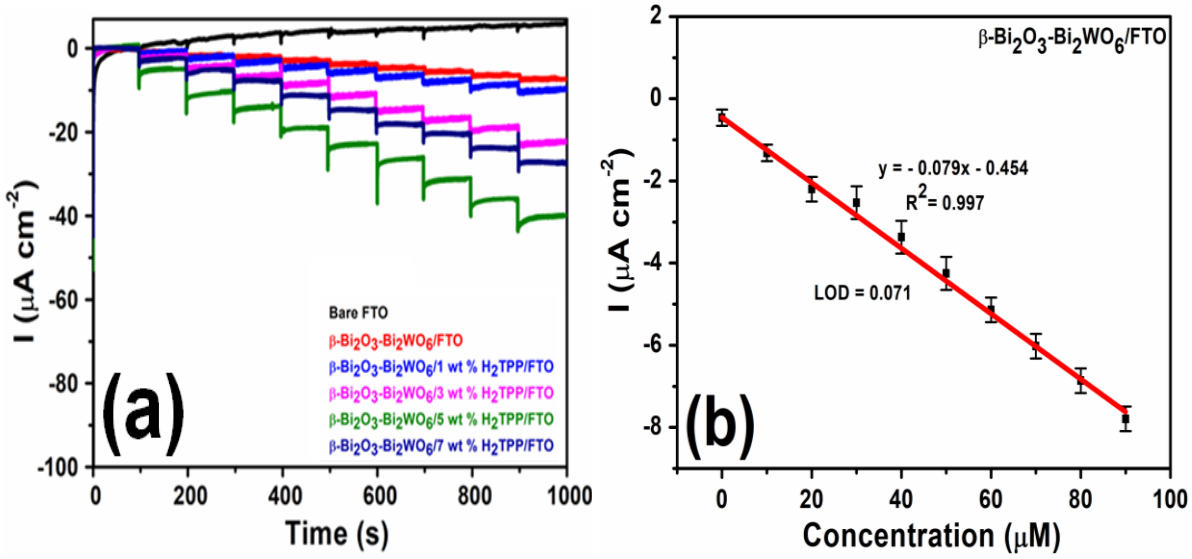

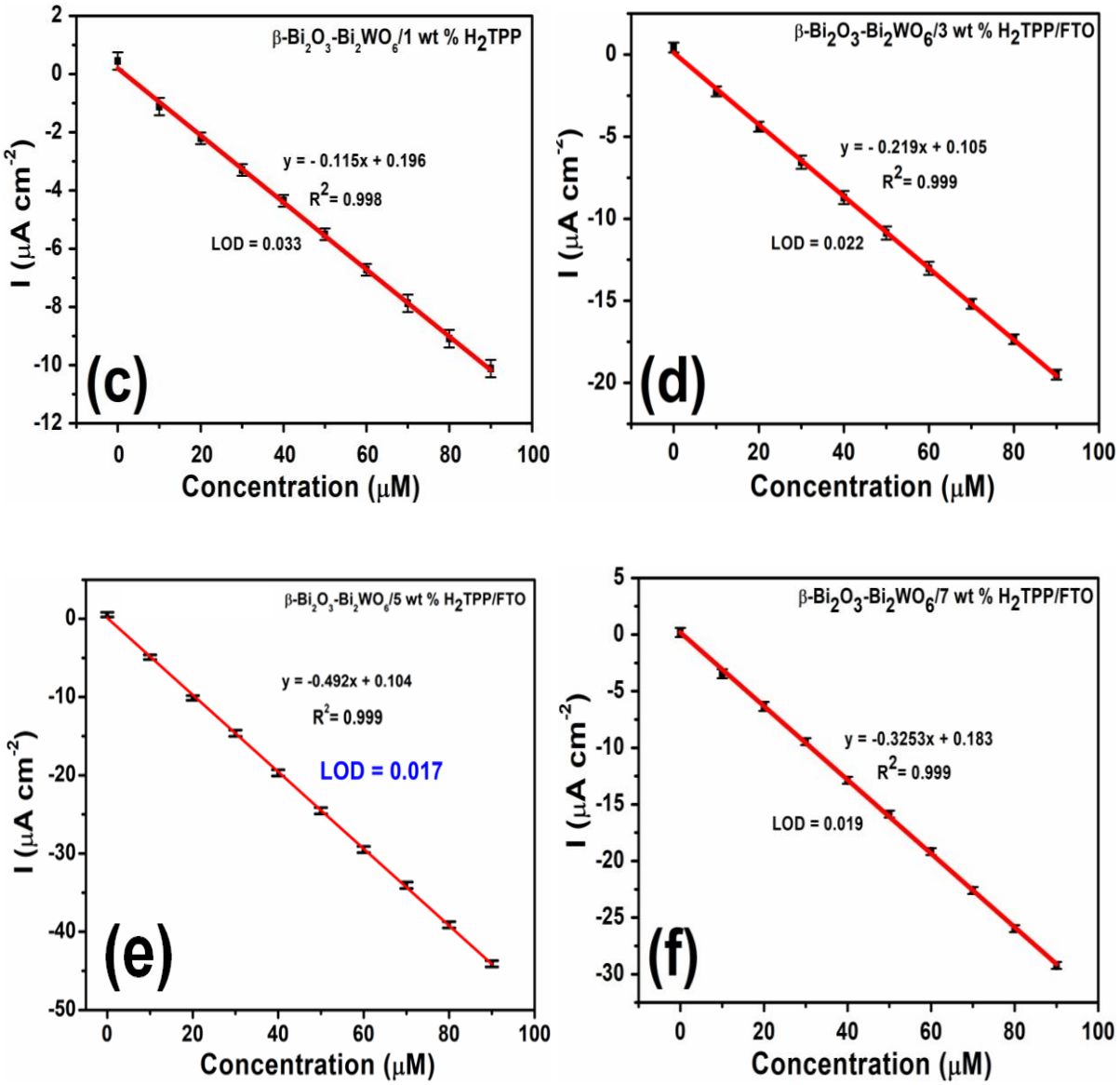

Figure 4.18. (a) Chronoamperometric current responses of bare FTO, β-Bi_2O_3-Bi_2WO_6/FTO, and various weight percentages of H_2TPP ornated β-Bi_2O_3-Bi_2WO_6/FTO electrodes upon addition of 10 μM Cr^{6+} ion in 0.1 M KCl medium (pH 4.0) at ~ -0.142 V (b→f) Calibration plot of amperometric current response for β-Bi_2O_3-Bi_2WO_6 and different wt % H_2TPP decorated β-Bi_2O_3-Bi_2WO_6 nanocomposite under dark conditions.

Table 4.3. Performances of β-Bi_2O_3-Bi_2WO_6/FTO and 1 to 5 wt % H_2TPP ornated β-Bi_2O_3-Bi_2WO_6/FTO electrodes.

Nanocomposites	Methods	Sensitivity (μA mM cm^{-2})	LOD (μM)
β-Bi_2O_3-Bi_2WO_6/FTO under dark	CV	0.079	0.376
	i-t	0.797	0.072
β-Bi_2O_3-Bi_2WO_6/1 wt % H_2TPP/FTO under dark	CV	0.051	0.138
	i-t	1.159	0.033
β-Bi_2O_3-Bi_2WO_6/3 wt % H_2TPP/FTO under dark	CV	0.043	0.164
	i-t	2.185	0.022
β-Bi_2O_3-Bi_2WO_6/5 wt % H_2TPP/FTO under dark	CV	0.131	0.101
	i-t	4.915	0.017
β-Bi_2O_3-Bi_2WO_6/5 wt % H_2TPP/FTO under light	CV	0.487	0.052
	i-t	8.005	0.008
β-Bi_2O_3-Bi_2WO_6/7 wt % H_2TPP/FTO under dark	CV	0.082	0.285
	i-t	3.253	0.019

4.3.3. Photoelectrochemical Activity for Cr^{6+} Detection. As β-Bi_2O_3-Bi_2WO_6/5 wt % H_2TPP has good electrochemical sensing properties, its photoelectrochemical sensing properties towards Cr^{6+} sensing under light irradiation were also investigated (Figures 4.19a and b). Figure 4.19c demonstrated a swift and uniform photocurrent response on the addition of 150 μM Cr^{6+} in 0.1 KCl, showing on/off cycle mode under chopping irradiation every 50 s at ~ -0.142 V vs. Ag/AgCl, indicating that the lower electron-hole recombination process allows more electrons to participate in the reduction process to improve the photoelectrochemical signal. Thus, a "signal-on" strategy for Cr^{6+} detection has been designed using a β-Bi_2O_3-Bi_2WO_6/5 wt % H_2TPP nanostructure-based photoelectrode. The enhanced adsorption of Cr^{6+} on the active centre of H_2TPP in β-Bi_2O_3-Bi_2WO_6/5 wt % H_2TPP nanocomposite in 0.1 M KCl containing 150 μM Cr^{6+} at pH 4.0 results in the rapid increase of photocurrent, nearly ten times under light, representing the enhanced sensitivity and consistent current levels towards Cr^{6+} reduction facilitated by the modified material.

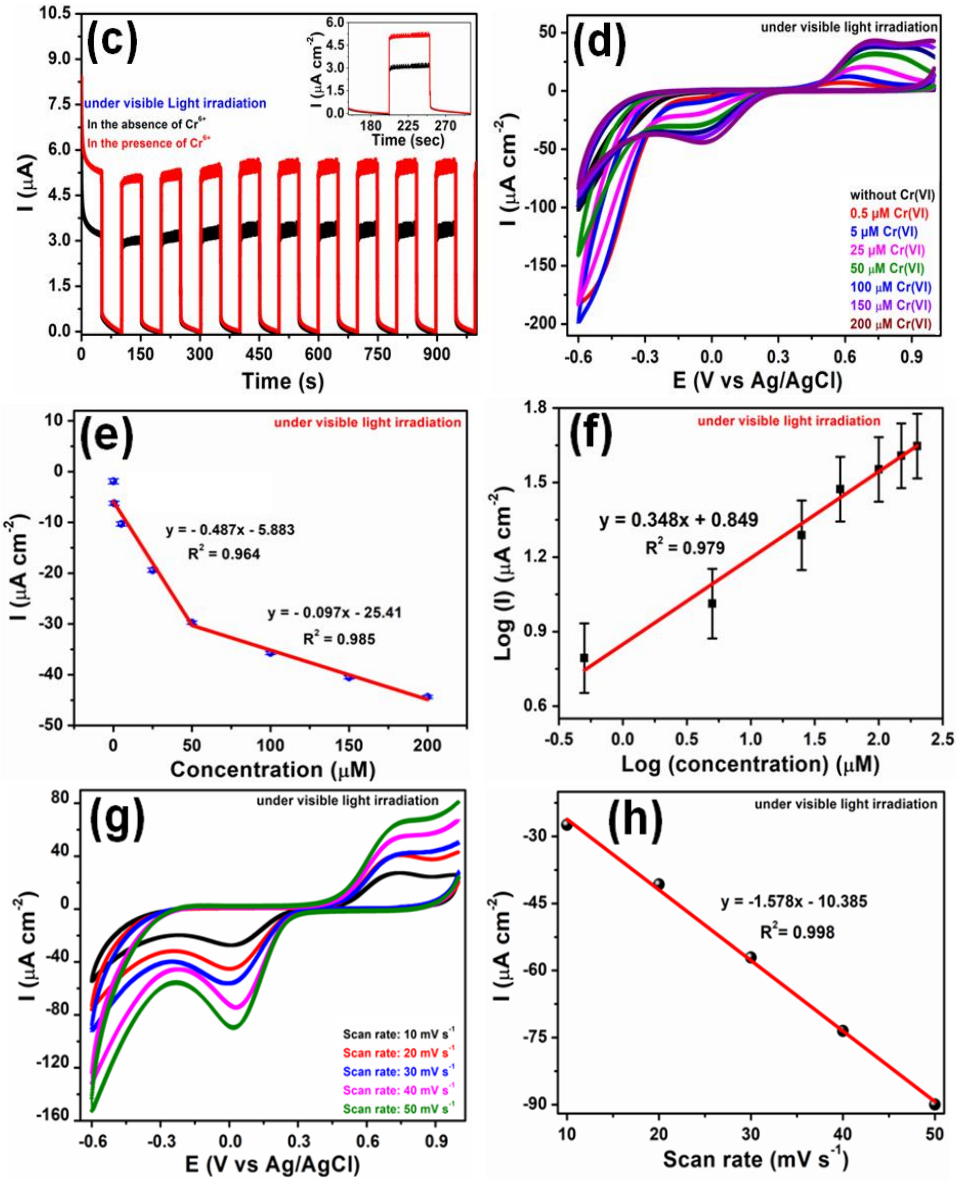

Figure 4.19. Cyclic voltammetric response at a scan rate of 20 mV s^{-1} at pH 4.0 (a) under light irradiation in 0.1 M KCl and 0.1 M KCl with 150 μM of Cr^{6+} (b) under dark and light irradiation in 0.1 M KCl with 150 μM of Cr^{6+} (c) Photocurrent response in the presence and absence of 150 μM Cr^{6+} at ~ -0.142 V in each switch on/off cycle (d) Photocurrent response towards increasing concentrations of Cr^{6+} (e) Linear relationships between the reduction peak currents and the concentration of Cr^{6+} (f) Linear relationships between the log of reduction peak currents and the log of Cr^{6+} concentration (g) Photocurrent response at different scan rates (h) Calibration plot of reduction peak current against square root of scan rate ($\nu^{1/2}$) of β-Bi_2O_3-Bi_2WO_6/5 wt % H_2TPP/FTO.

The photoelectrochemical sensor based on β-Bi_2O_3-Bi_2WO_6/5 wt % H_2TPP/FTO electrode for different concentrations of Cr^{6+} (Figure 4.19d) showed that the photocurrent response gradually increases with increasing the concentration of Cr^{6+}. From the calibration plots (Figures 4.19e and f), the linear concentration ranges were calculated as 0-200 μM. Moreover, the sensitivity and LOD were calculated as 0.487 μA mM cm^{-2} and 0.052 μM (Table 4.3). Due to its broad linear range, better sensitivity, and low detection limit, the electrochemical sensor displayed better performance for the detection of Cr^{6+}. Moreover, Table 4.4 shows the comparison of the photoelectrochemical reduction of Cr^{6+} for β-Bi_2O_3-Bi_2WO_6/5 wt % H_2TPP nanocomposite with other reported Cr^{6+} sensors. The superior photoelectrocatalytic performance of β-Bi_2O_3-Bi_2WO_6/5 wt % H_2TPP nanocomposite is due to its outstanding charge transfer rate, reduced charge recombination, and moderate concentration of H_2TPP. Figures 4.19g and h demonstrated that the reduction peak current exhibited a linear increase as the scan rate increased, signifying the diffusion-controlled process.

Table 4.4. Analytical comparison of β-Bi_2O_3-Bi_2WO_6/5 wt % H_2TPP with previously reported modified catalysts for determination of Cr^{6+}.

Materials	Method	Linear range (μM)	LOD (μM)	Ref.
CuS-BSA	Colorimetric	0-1 × 10^{-3} 1-20	5 × 10^{-2} 6.8	65
Au NP/rGO	SWV	0.1-30	4.6 × 10^{-2}	66
	CV	5-100	2	
g-C_3N_4/AgM/Nf	Amperometry	0.1-0.7	16 × 10^{-4}	67
CP_5	i-t	-	1.61	68
{$Ni(P_4Mo_6)_2$}	i-t	-	0.321	69
$Pb_5S_2I_6$	PEC	0.01-80	3 × 10^{-3}	70
Bi/BiOI	PEC	1-230	0.3	71
MoS_2/BiOI	PEC	0.05-160	0.01	72
PbS	PEC	2 × 10^{-5}- 2	10 × 10^{-6}	73
0.05-Bi-BPI-6%	PEC	0.5-180	0.15	74
5%-CuS/BW-180	PEC	1-80	0.95	75
5%-CuS/BM-160	PEC	0.5-230	0.12	76
NiCo-LDHs/TiO_2NTAs	PEC	0.5-20, 20-400, 400-1800	0.12	77
β-Bi_2O_3-Bi_2WO_6/5 wt % H_2TPP/FTO	i-t (Dark)	0-90	1.7 × 10^{-2}	**This work**
	i-t (Light)	0-90	8 × 10^{-3}	
	CV (Dark)	0.131	0.101	
	CV (Light)	0.487	5.2 × 10^{-2}	

UV-Vis measurements were performed at different time intervals using the desired material and 10 mg/L Cr^{6+} to examine the reduction of Cr^{6+} to Cr^{3+} (Figure 4.20a), which also showed that the catalytic activity of the modified system enhances under light irradiation and follows pseudo-first-order kinetics[78] (Figure 4.20b). The experiment was repeated five times using the same catalyst, consistently demonstrating the robustness of the material despite a minor reduction in the catalytic activity (Figure 4.20c), which may be due to the deactivation of the surface induced by the adsorption of reduction products of Cr^{6+} on the catalyst.[79] Both photocatalysis and photoelectrocatalysis favor the reduction of Cr^{6+}, with the latter proving to be not only faster but also more easily detectable, especially at very low concentrations.

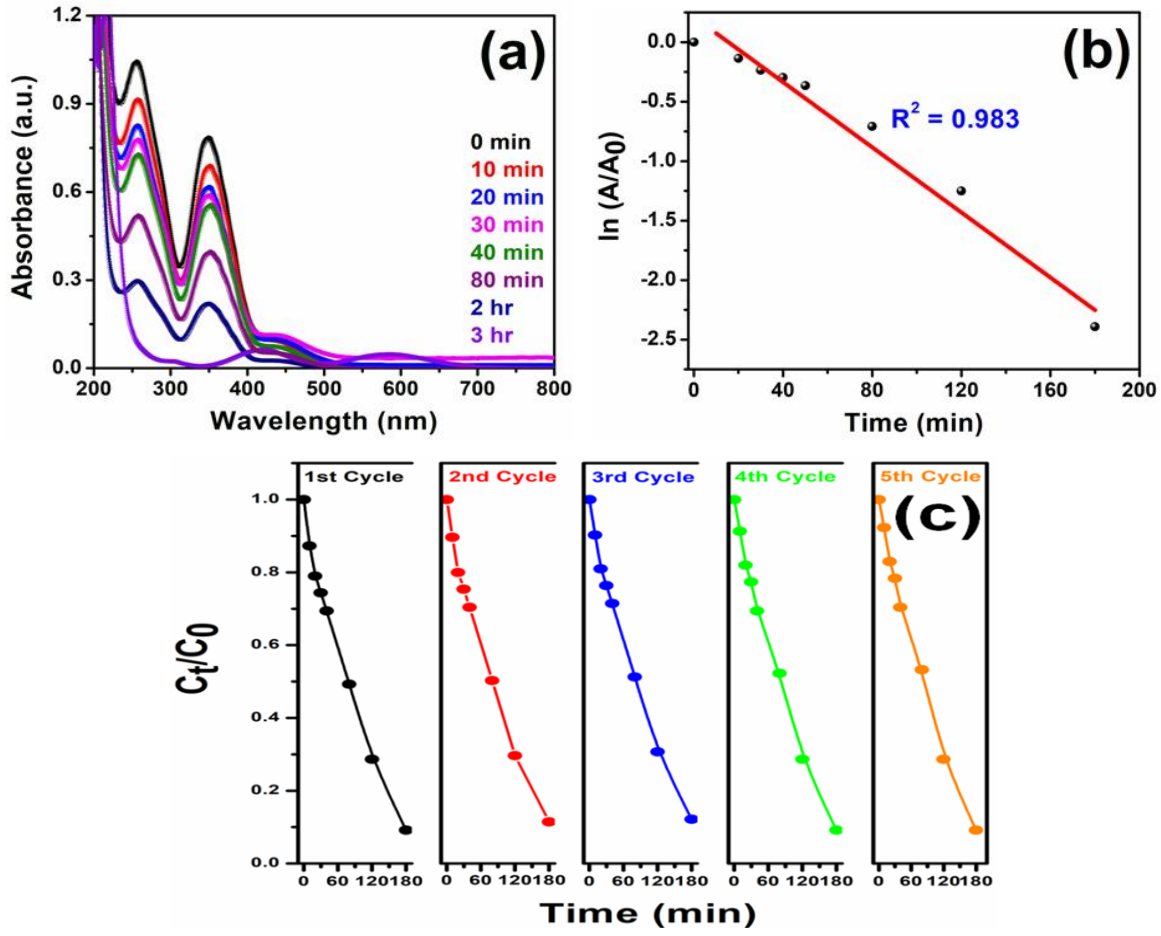

Figure 4.20. (a) UV-Vis spectral plots of Cr^{6+} reduction at different time intervals (b) corresponding reaction rate kinetic plot (c) recycle test for the photocatalytic reduction of Cr^{6+} by β-Bi_2O_3-Bi_2WO_6/5 wt % H_2TPP.

Besides, the chronoamperometric study of β-Bi_2O_3-Bi_2WO_6/5 wt % H_2TPP nanocomposite showed a more quick current response under the irradiation of light with the gradual addition of 10 μM Cr^{6+} at 100 s intervals under a potential of ~ -0.142 V (Figure 4.21a) and showed linearity between the reduction current and the concentration of Cr^{6+}, with correlation coefficients (R^2) of 0.999 (Figure 4.21b). The sensitivity and LOD values of the β-Bi_2O_3-Bi_2WO_6/5 wt % H_2TPP nanocomposite in the presence of light were found to be 8.005 μA mM cm^{-2} and 0.008 μM, respectively, in the concentration range of (0-90) μM, which are much better than those in the absence of light (Tables 4.3 and 4.4), indicating its excellent photoelectrochemical performance towards Cr^{6+} reduction owing to the presence of a large number of active sites that assist the effective separation of photogenic electron-hole pair and boost the photocurrent.

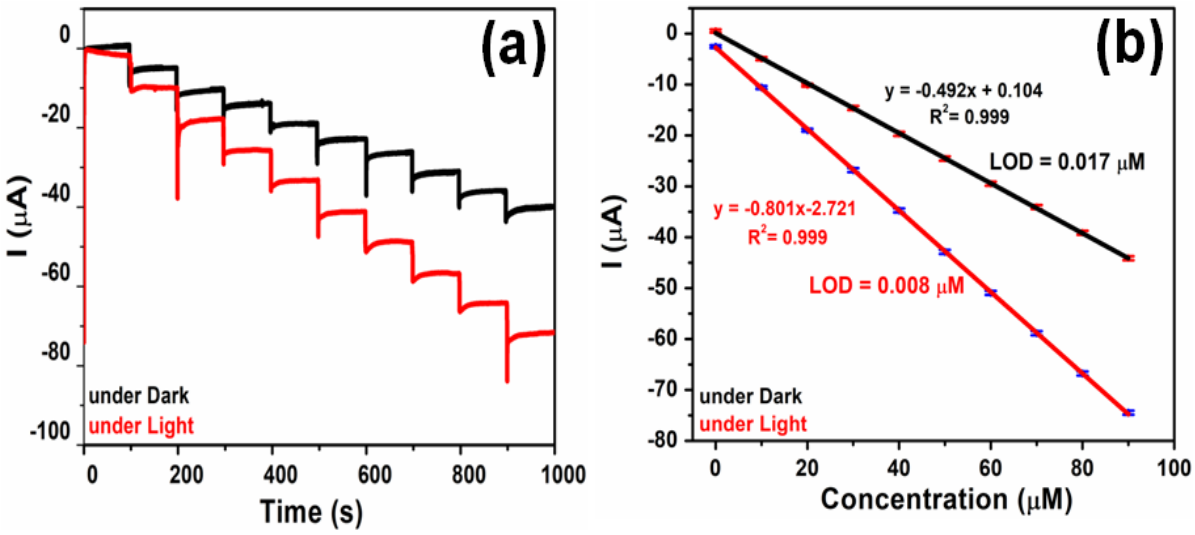

Figure 4.21. (a) Chronoamperometric current responses upon addition of 10 μM of Cr^{6+} ion in 0.1 M KCl medium (pH 4.0) under dark and light irradiation (b) Response current versus Cr^{6+} concentration on β-Bi_2O_3-Bi_2WO_6/5 wt % H_2TPP nanocomposite at ~ -0.142 V.

In the absence of light, the reduction peak totally diminished after the 200th cycle, whereas under light irradiation conditions, the reduction peak completely disappeared after the 100th cycle for 150 μM Cr^{6+} in 0.1 M KCl (Figure 4.22a), indicating that Cr^{6+} was completely reduced to Cr^{3+}, as is evidenced from the UV-Vis spectral study of the initial solution of Cr^{6+} and the solution after photoelectrochemical reduction (Figure 4.34). The PXRD analysis as shown in Figure 4.22b of the catalyst after the photoelectrochemical process confirmed the presence of accumulated Cr^{3+} (JCPDS

No. 38-1479) on the surface of the catalyst, indicating the reduction of Cr^{6+} to Cr^{3+}. The photoelectrochemical reduction of Cr^{6+} into Cr^{3+} was further confirmed by UV-Vis spectroscopic study. The optical absorption bands at 255.39, 349.18, and 441.35 nm are responsible for chromium ions in the 6+ oxidation state. The band at 441.35 nm is ascribed to the $^4A_{2g} \rightarrow {}^2A_{1g}$ transition, whereas the additional band at 349.18 nm is assigned to the $^4A_{2g} \rightarrow {}^4T_{1g}$ (p) transition.[80] Two bands at 422.29 and 585.92 nm are owing to the d-d transition of Cr^{3+} ions and are assigned to $^4A_{2g} \rightarrow {}^4T_{1g}$ and $^4A_{2g} \rightarrow {}^4T_{2g}$ transitions, respectively, and another band at 308.68 nm in the UV region is observed due to the charge transfer transistion.[81] The pH of the solution was also monitored during the photoelectrochemical reduction of Cr^{6+} in the presence of β-Bi_2O_3-Bi_2WO_6/5 wt % H_2TPP nanocomposite and was found to remain at a pH of ~ 4.0 throughout the process.

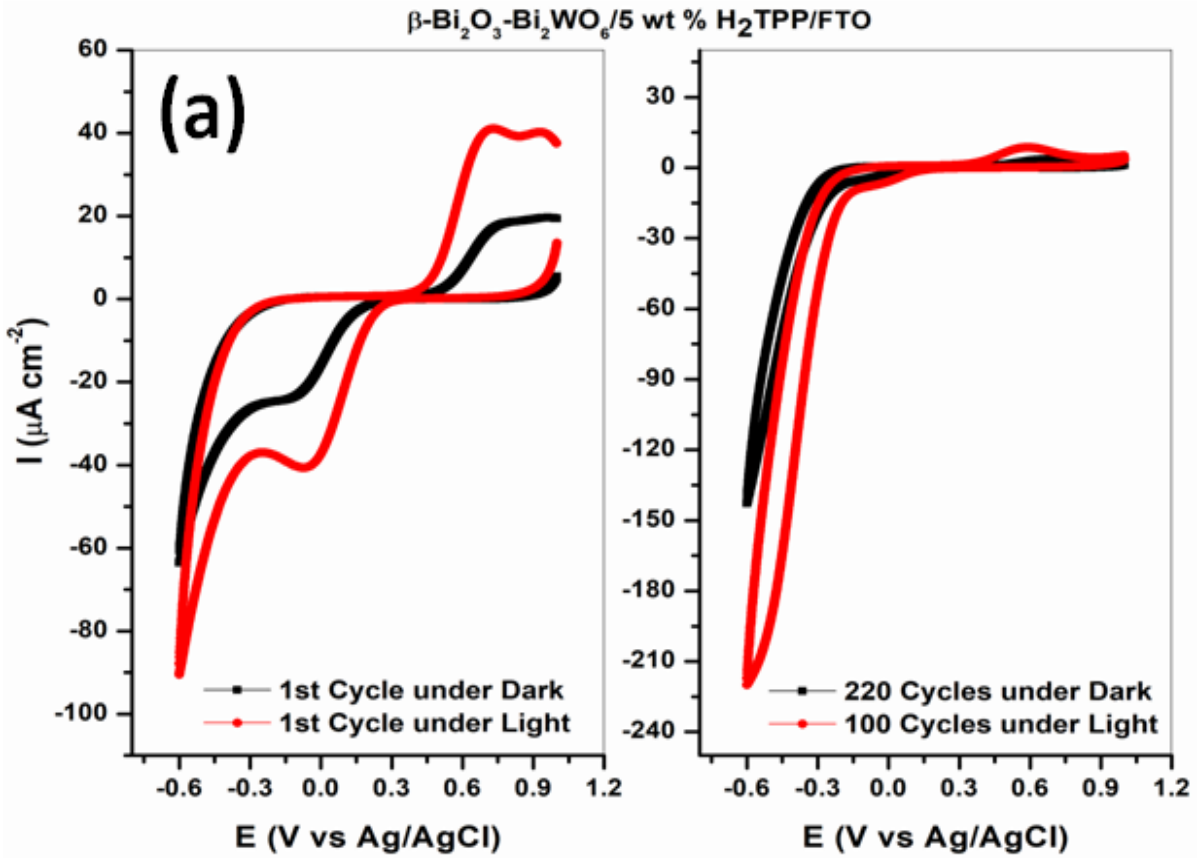

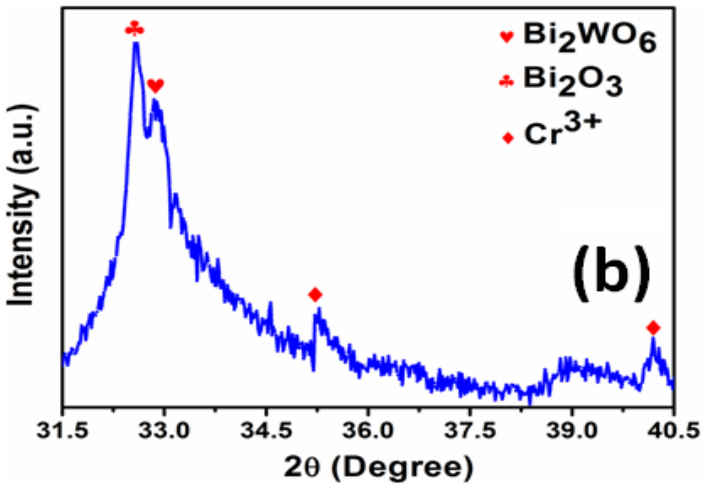

Figure 4.22. (a) Comparison of Cyclic voltammetric response for the first; and 220th cycles and the 100th cycles for β-Bi_2O_3-Bi_2WO_6/5 wt % H_2TPP/FTO in 0.1 M KCl with 150 μM Cr^{6+} under dark and light irradiation conditions, respectively, (b) XRD of β-Bi_2O_3-Bi_2WO_6/5 wt % H_2TPP after photoelectrochemical reduction of Cr^{6+} (small scale plot).

4.3.3.1. PL Study. To better understand the charge transfer efficiency and recombination rate of photoexcitations of the as-synthesized nanocomposites, photoluminescence (PL) spectra were measured, as shown in Figures 4.23(a→c). The high photoluminescence (PL) intensity observed in β-Bi_2O_3-Bi_2WO_6 is a result of rapid recombination of photogenerated electrons and holes, which leads to a shortening of the lifetime of these excitations, as depicted in Figures 4.23a and b. However, in the case of β-Bi_2O_3-Bi_2WO_6/5 wt % H_2TPP nanocomposite, the lower photoluminescence (PL) intensity and an extended lifetime of excitations are due to reduced electron-hole recombination. Significantly, incorporation of H_2TPP into β-Bi_2O_3-Bi_2WO_6 leads to a decrease in the emission intensity, indicating that H_2TPP favors photogenerated electron-hole separation and that the rate of recombination can be controlled through the optimization of the concentration of H_2TPP. The longest fluorescence lifetime of β-Bi_2O_3-Bi_2WO_6/5 wt % H_2TPP among all other nanocomposites (Table 4.5) confirms its greater charge separation efficacy, which in turn enhances its photocatalytic performances.[29] The average fluorescence lifetime can be calculated according to equation 4.2.

$$\tau_{ave} = \frac{\sum_{i=1}^{n} \alpha_i \tau_i^2}{\sum_{i=1}^{n} \alpha_i \tau_i} \qquad \text{Eq.4.2}$$

Where, α_i is the pre-exponential coefficient, τ_i is fluorescence lifetimes and chi squared (χ^2) values obtained from fitting of the emission decays.

Table 4.5. Lifetime of materials.

Materials	τ_1 (ns)	τ_2 (ns)	τ (av) (ns)	$(\chi)^2$
β-Bi_2O_3-Bi_2WO_6	0.165	2.176	0.204	1.278
β-Bi_2O_3-Bi_2WO_6/1 wt % H_2TPP	0.734	7.421	2.389	1.120
β-Bi_2O_3-Bi_2WO_6/3 wt % H_2TPP	0.954	7.6308	3.00	1.137
β-Bi_2O_3-Bi_2WO_6/5 wt % H_2TPP	0.883	8.544	4.009	1.075
β-Bi_2O_3-Bi_2WO_6/7 wt % H_2TPP	1.237	8.027	3.255	1.091

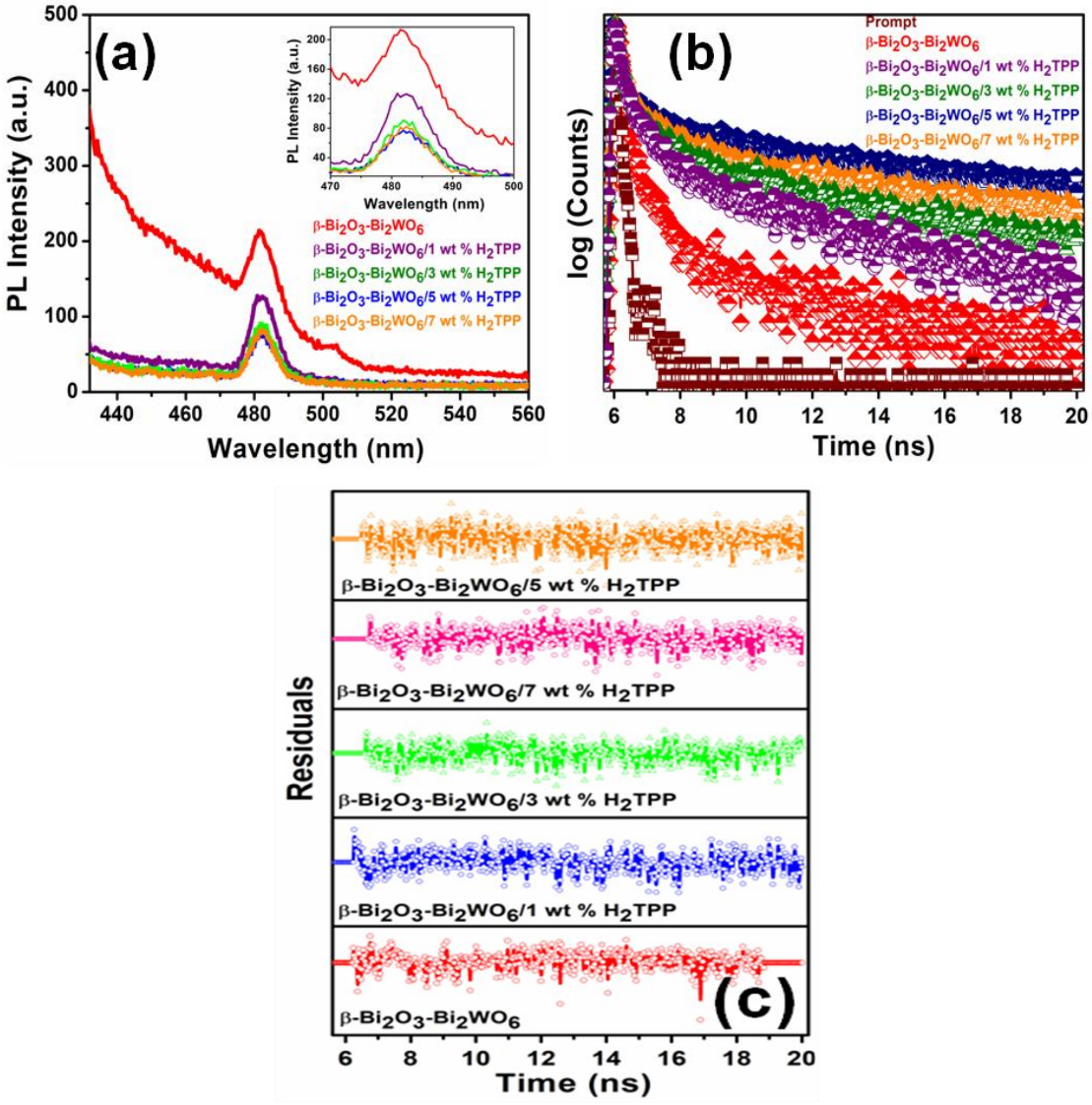

Figure 4.23. (a) Photoluminescence (PL) spectra and (b) PL decay (c) Residual plot of β-Bi_2O_3-Bi_2WO_6 and different weight percentages of H_2TPP ornated β-Bi_2O_3-Bi_2WO_6 nanocomposites.

4.3.3.2. Photoelectrochemical sensor. To further investigate the charge transfer efficiency, the amperometric current-time (i-t) curve was used to study the current densities of the nanocomposites under chopping illumination every 50 s at ~ -0.142 V vs. Ag/AgCl, as depicted in Figure 4.24. All of the photoelectrocatalysts responded to light irradiation with a quick and consistent photocurrent response during each switch-on/off cycle. The photocurrent response of the nanocatalysts is further correlated with the production and separation of photogenerated carriers in the photocatalytic process, with strong obliteration of photoexcited charge carriers that are significantly delayed for the β-Bi_2O_3-Bi_2WO_6/5 wt % H_2TPP/FTO electrode. A lower electron-hole recombination rate indicates a higher photoresponsive character of the heterojunction. The higher photocurrent response of β-Bi_2O_3-Bi_2WO_6/5 wt % H_2TPP heterojunction indicates the most efficient separation of photogenarated carriers, as illustrated in Figure 4.24. Therefore, the β-Bi_2O_3-Bi_2WO_6/5 wt % H_2TPP nanocomposite is obviously effective in promoting the separation of photogenerated charge carriers,[82,83] which agrees well with the EIS spectral results shown in Figure 4.25b. Similar photocurrent results were found in each switch on/off cycle during different cycle measurements, demonstrating the good reproducibility of the photoelectrocatalyst. The reproducibility of photoresponsive behavior suggests that the photogenerated carriers might be easily transported to the back contact (on the FTO surface) across the material to generate photocurrent responses under light irradiation.

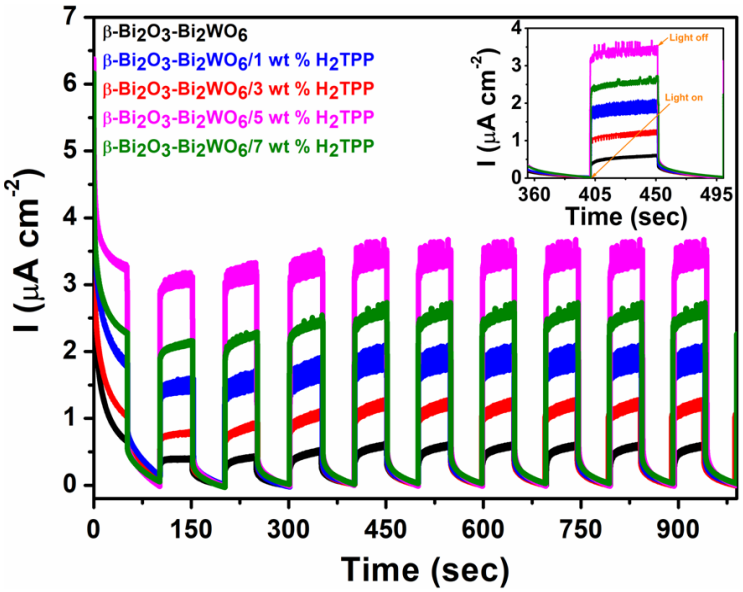

Figure 4.24. Photocurrent responses for β-Bi_2O_3-Bi_2WO_6/FTO and different weight percentages of H_2TPP ornated β-Bi_2O_3-Bi_2WO_6/FTO electrode at ~ -0.142 V in each switch on/off cycle.

4.3.3.3. Electrochemical Impedance Spectra. In addition, as an influential tool, the electrochemical impedance spectra (EIS) were performed to gain a deeper insight into the photoresponsive characteristics and charge separation efficiency of the β-Bi_2O_3-Bi_2WO_6/5 wt % H_2TPP nanocomposite heterojunction, as shown in Figures 4.24 and 4.25 (a→d). Studying the capacitance and resistance of the electrode materials using the EIS Nyquist plots, where Z' and Z'' stand for the corresponding real and imaginary parts of the impedance, confirmed the efficiency of separating the photogenerated electron-hole pairs and the charge carrier properties.[83,84] It was investigated by the Randles cell model[29] equivalent circuit (inset of Figures 25(c→d)), which includes charge transfer resistance (R_{ct}), solution resistance (R_s), and double-layer capacitance (C_{dl}). The R_{ct} of the as-synthesized β-Bi_2O_3-Bi_2WO_6/5 wt % H_2TPP nanocomposite is smaller in comparison to other nanocomposites (Tables 4.6 and 4.7) in spite of being under dark and light conditions, confirming the significant enhancement of the interfacial charge-transfer efficiency in the β-Bi_2O_3-Bi_2WO_6/5 wt % H_2TPP heterojunction.[82] The ECSA of the β-Bi_2O_3-Bi_2WO_6/5 wt % H_2TPP nanocomposite under the irradiation of light is higher than that of the other nanocomposites, suggesting its superior photoelectrochemical activity towards Cr^{6+} sensing. H_2TPP (greater than 5% by weight) thickens the surfaces of the material, preventing light absorption and the effective transport of photogenerated electrons. This result suggests that the β-Bi_2O_3-Bi_2WO_6/5 wt% H_2TPP heterojunction achieved more efficient charge separation as well as improved the photoinduced electron transport properties. The electrochemical active surface area (ECSA) of all electrocatalysts were calculated from the double-layer capacitance (C_{dl}) according to following equation 4.3.

$$ECSA = \frac{C_{dl}}{C_s} \qquad \text{Eq. 4.3}$$

Where C_s is the ideal specific capacitance of a smooth planar surface made of the same material per unit area under identical electrolyte conditions. In our estimation of surface area, we have used the general specific capacitance of C_s = 40 μF cm^{-2}.[85] The roughness factor (R_f) of the materials were determined by equation 4.4.

$$R_f = \frac{ECSA}{GSA} \qquad \text{Eq. 4.4}$$

Where the geometric surface area (GSA) of the electrode is 1 cm^2.

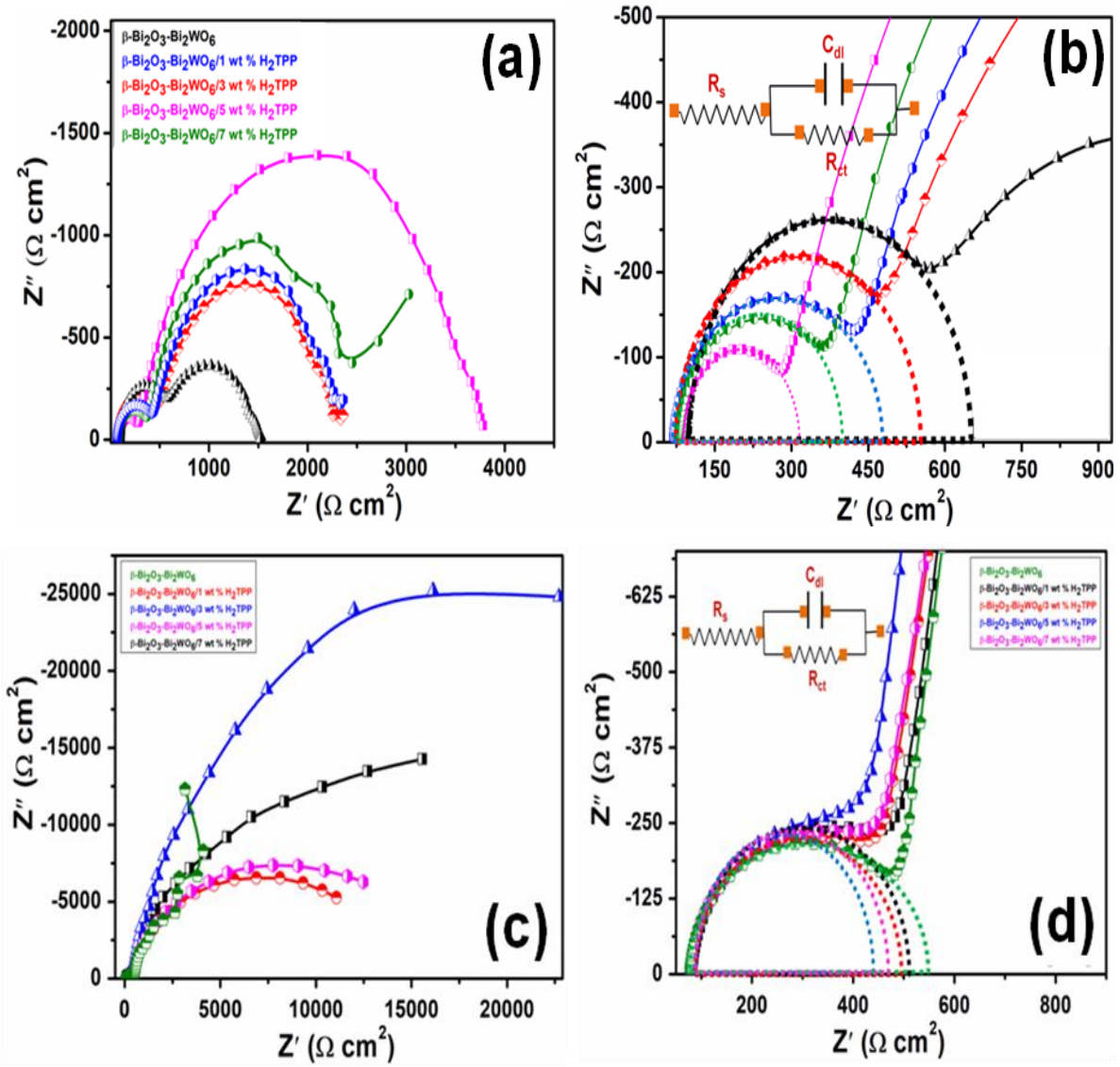

Figure 4.25. (a) Nyquist's plot (b) Extended Nyquist's plot of β-Bi_2O_3-Bi_2WO_6 and different weight percentages of H_2TPP ornated β-Bi_2O_3-Bi_2WO_6 nanocomposites under light; (c) Nyquist's plot (b) Extended Nyquist's plot of β-Bi_2O_3-Bi_2WO_6 and different weight percentages of H_2TPP ornated β-Bi_2O_3-Bi_2WO_6 nanocomposites under dark.

Table 4.6. R_s, R_{ct}, Z′, C_{dl}, ECSA and R_f for β-Bi_2O_3-Bi_2WO_6 and 1 to 5 wt % H_2TPP ornated β-Bi_2O_3-Bi_2WO_6 nanocomposites under light irradiation.

Materials	R_s (Ω cm^2)	$R_s + R_{ct}$ (Ω cm^2)	R_{ct} (Ω cm^2)	Z′ (Ω cm^2)	C_{dl} (μF cm^{-2})	ECSA (cm^2)	R_f
β-Bi_2O_3-Bi_2WO_6	93.18	649.61	556.43	391.40	0.509	0.013	0.013
β-Bi_2O_3-Bi_2WO_6/1 wt % H_2TPP	77.65	552.14	474.49	320.82	0.723	0.018	0.018
β-Bi_2O_3-Bi_2WO_6/3 wt % H_2TPP	69.22	476.01	406.79	288.09	1.03	0.026	0.026
β-Bi_2O_3-Bi_2WO_6/5 wt % H_2TPP	81.33	314.42	233.09	202.69	2.64	0.066	0.066
β-Bi_2O_3-Bi_2WO_6/7 wt % H_2TPP	77.71	397.62	319.91	252.06	1.81	0.045	0.045

Table 4.7. R_s, R_{ct}, Z′, C_{dl}, ECSA and R_f for β-Bi_2O_3-Bi_2WO_6 and 1 to 5 wt % H_2TPP ornated β-Bi_2O_3-Bi_2WO_6 nanocomposites under dark conditions.

Materials	R_s (Ω cm^2)	$R_s + R_{ct}$ (Ω cm^2)	R_{ct} (Ω cm^2)	Z′ (Ω cm^2)	C_{dl} (μF cm^{-2})	ECSA (cm^2)	R_f
β-Bi_2O_3-Bi_2WO_6	77.72	546.85	469.13	322.99	0.411	0.011	0.011
β-Bi_2O_3-Bi_2WO_6/1 wt % H_2TPP	82.68	509.02	426.34	358.72	0.649	0.016	0.016
β-Bi_2O_3-Bi_2WO_6/3 wt % H_2TPP	78.09	495.16	417.07	303.45	0.768	0.019	0.019
β-Bi_2O_3-Bi_2WO_6/5 wt % H_2TPP	78.24	439.74	361.50	244.65	0.952	0.024	0.024
β-Bi_2O_3-Bi_2WO_6/7 wt % H_2TPP	78.56	469.76	391.20	296.56	0.785	0.020	0.020

4.3.4. Computational analysis in support of Cr^{6+} reduction on heterolayered nanocomposites. To investigate the orbital interactions when the Cr atom was adsorbed to the *meso*-tetraphenylporphyrin attached bilayer nanocomposite β-Bi_2O_3-Bi_2WO_6, density functional theory (DFT) based calculations were performed. The DFT calculations are carried out by using the Vienna ab-initio simulation package[86-89] with Perdew-Burke-Ernzehof (PBE)[90] exchange-correlation functional along with the generalized gradient approximation scheme. We have considered a kinetic energy cut-off of 500 eV for the plane wave basis expansion and employed a Monkhorst-pack[91] k-grid of 7×7×1 k points for the sampling of Brillouin zone. We also set a limit of 0.01 eV/Å and 10^{-5} eV for the convergence of Hellman-Feyman forces and total energies, respectively. The van der Waals interactions between

Bi_2O_3 and Bi_2WO_6 surfaces, porphyrin attached to the Bi_2O_3-Bi_2WO_6 nanocomposite, and Cr adsorbed on the porphyrin-attached nanocomposite Bi_2O_3-Bi_2WO_6 are accounted for by employing the Grimme's dispersion corrections of DFT-D3.[92]

A porphyrin (C18H10N4) molecule was attached to the nanocomposite heterostructure since it is the reactive part of *meso*-tetraphenylporphyrin and responsible for the adsorption process. First, optimization of the bulk structures of Bi_2O_3 and Bi_2WO_6 was done, and then the (400) and (200) planes of these structures were made, respectively, as these planes are responsible for the intense peaks in the XRD pattern of the nanocomposite Bi_2O_3-Bi_2WO_6. Thereafter, one porphyrin molecule was relaxed on top of the nanocomposite Bi_2O_3-Bi_2WO_6. Again, one Cr atom was placed above 2.5 Å on the porphyrin-attached nanocomposite, and geometry optimization calculations were performed. The optimized geometries of Bi_2O_3-Bi_2WO_6 and Cr adsorbed on Porphyrin-attached Bi_2O_3-Bi_2WO_6 nanocomposite and the relaxed structures of H_2TPP and porphyrin are presented in Figures 4.26(a→d) of the supplementary information.

To explore the orbital interactions between Cr atom and porphyrin-attached Bi_2O_3-Bi_2WO_6 nanocomposite, the projected density of states (PDOS) of the valence 4s and 3d orbitals of Cr atom before and after its adsorption to porphyrin-attached Bi_2O_3-Bi_2WO_6 surfaces was plotted, as shown in Figures 4.27a and b, respectively. Some additional electronic states below the Fermi energy level corresponding to the 4s and 3d orbitals of Cr when the Cr atom is adsorbed on the porphyrin-attached Bi_2O_3-Bi_2WO_6 nanocomposite (dotted circles in Figure 4.27b) were noticed. These electronic states represent the transfer of charge from porphyrin to the 3d and 4s orbitals of Cr, which is responsible for changing the oxidation state of Cr. To further confirm this charge transfer, the PDOS of the 2s and 2p orbitals of the N atom of the porphyrin molecule before and after the adsorption of Cr was plotted, as shown in Figures 4.27c and d, respectively. A significant depletion in the electronic states of the N-2p orbital can be observed in Figure 4.27d compared to Figure 4.27c, close to the Fermi energy level, indicating the participation of the N-2p orbital of porphyrin with the 3d and 4s orbitals of the Cr atom. The adsorption of Cr^{6+} to porphyrin-attached Bi_2O_3-Bi_2WO_6 takes place through electrostatic interaction[63] between the 3d orbital of Cr and the 2p orbital of N of H_2TPP of β-Bi_2O_3-Bi_2WO_6/H_2TPP nanocomposite. To get an estimation of the oxidation state of Cr atom adsorbed to porphyrin-attached nanocomposite, a grid based charge analysis calculation using the Bader charge portioning[93] method was performed. It was found that the valence orbitals of the Cr atom had a total charge of 4.32e when it was adsorbed to the porphyrin-attached Bi_2O_3-Bi_2WO_6, indicating that its

oxidation state is close to +3, and the reduction of Cr^{6+} took place due to the charge transfer from the N-2p orbitals of the porphyrin molecule.

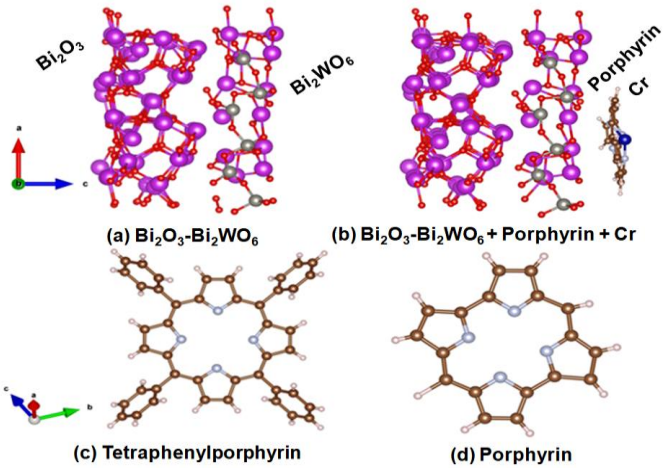

Figure 4.26. The relaxed structures of (a) Bi_2O_3-Bi_2WO_6 nanocomposite, (b) Cr adsorbed on Porphyrin-attached Bi_2O_3-Bi_2WO_6 (c) Tetraphenylporphyrin (H_2TPP) (d) Porphyrin.

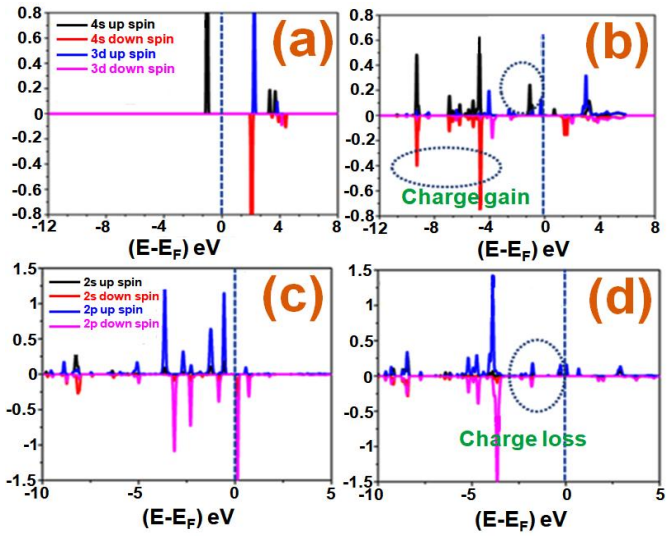

Figure 4.27. The PDOS of (a) 3d and 4s orbitals of the Isolated Cr atom, (b) 3d and 4s orbitals of Cr adsorbed to the porphyrin-attached Bi_2O_3-Bi_2WO_6 (c) 2s and 2p orbitals of the N atom in Porphyrin attached Bi_2O_3-Bi_2WO_6 (d) 2s and 2p orbitals of the N atom in Porphyrin-attached Bi_2O_3-Bi_2WO_6 when Cr is adsorbed on it.

4.3.5. Stability Tests. Stability plays a vital role in the determination of the characteristics of the nanocomposite for Cr^{6+} reduction. To examine the stability of the photoelectrochemical sensor based on β-Bi_2O_3-Bi_2WO_6/5 wt % H_2TPP nanocomposite, the photoexcitation process was repeated within 1000 s (Figure 4.28a). During the act of averting light, the dark current is seen to be extremely stable. The photocurrent rapidly rises in the presence of light and maintains its stability for 20 s. The photocurrent and dark currents stayed stable throughout the entire test. The extended stability of the nanocomposite was investigated by the amperometric current responses to Cr^{6+} (Figure 4.28b). After nonstop operation for 12 h, β-Bi_2O_3-Bi_2WO_6/5 wt % H_2TPP nanocomposite was still able to retain its initial current response, suggesting its good stability and potentiality towards Cr^{6+} sensing. Figure 4.28c also shows its extended stability over 10 days. After every use, the electrode was kept in a refrigerator at 4 °C. After 10 days, the photocurrent response was 98.77% of its initial state, indicating its high extended stability. The stability of the sample was further explored by HR-TEM, FE-SEM, PXRD, and XPS measurements (Figures 4.29 and 4.30). The FE-SEM and HR-TEM images shown in Figures 4.29(a→d) and 4.29e express its excellent structural stability, showing the lack of such morphological change; only a slight distortion in plane took place in the HR-TEM image after several times of use of the electrode material. The structural stability was again established by PXRD studies, which show no significant changes in the peak intensity (Figure 4.30a) as well as the spectra for Bi 4f, W 4f, O 1s, C 1s, and N 1s (Figures 4.30(b→f)) of the nanocomposite after undergoing a stability test, indicating excellent compositional stability. The improved stability of the β-Bi_2O_3-Bi_2WO_6/5 wt % H_2TPP nanocomposite may be attributed to the protective H_2TPP layer around the β-Bi_2O_3-Bi_2WO_6 nanocatalyst.

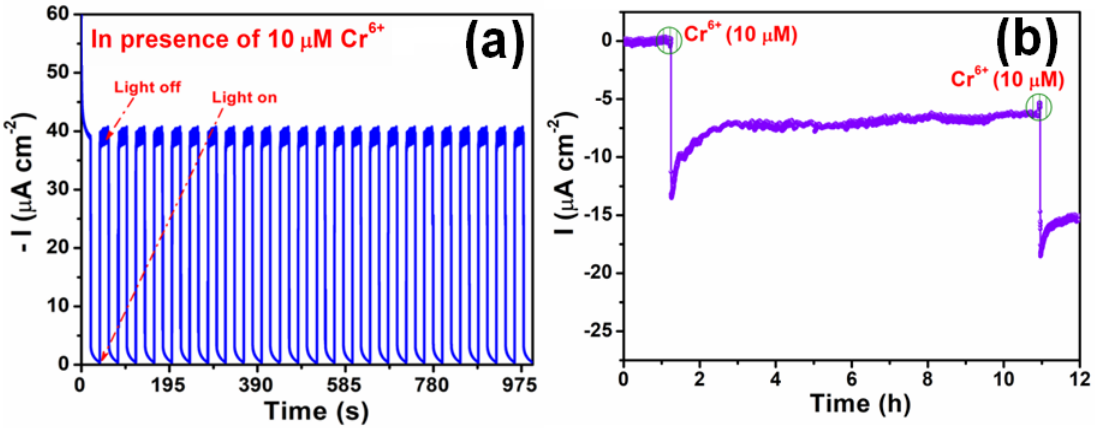

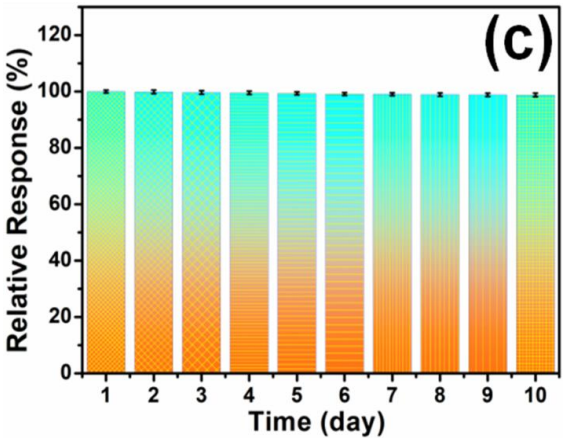

Figure 4.28. (a) Stable photocurrent response over 1000 s (b) Stability of amperometric responses for 12 h (c) Stability test for 10 days of the β-Bi_2O_3-Bi_2WO_6/5 wt % H_2TPP/FTO towards Cr^{6+} reduction under light irradiation.

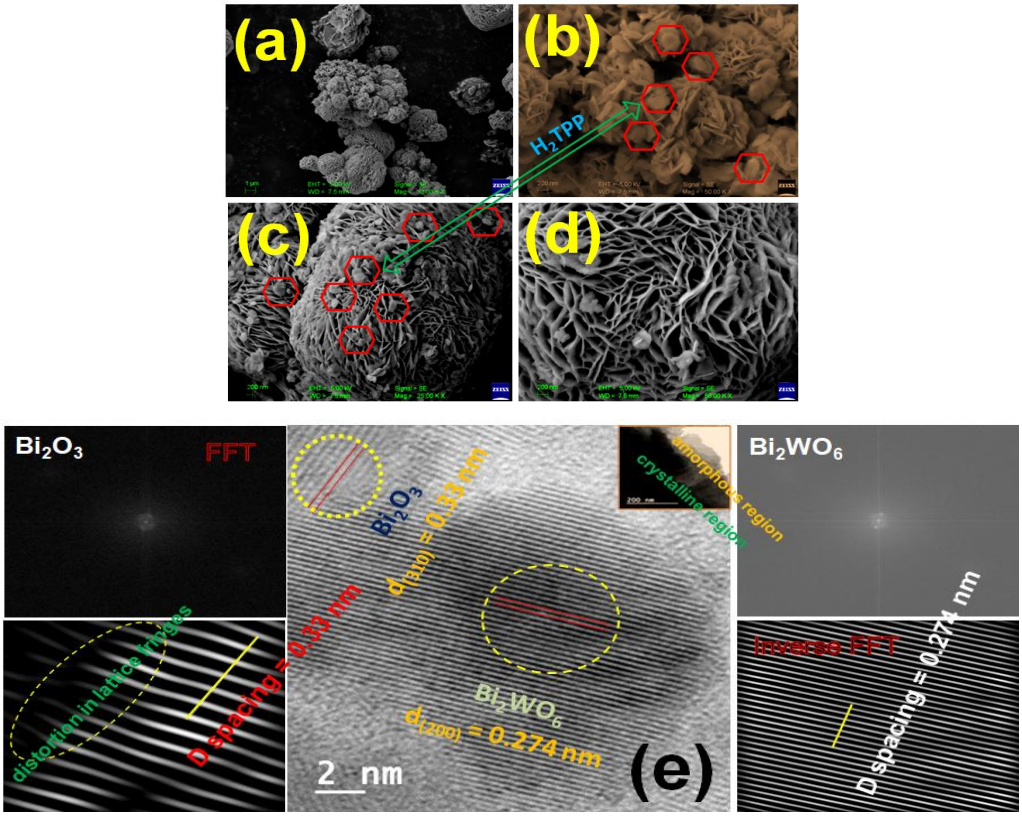

Figure 4.29. HR-TEM and FE-SEM images of β-Bi_2O_3-Bi_2WO_6/5 wt % H_2TPP after the photoelectrochemical reduction of Cr^{6+}.

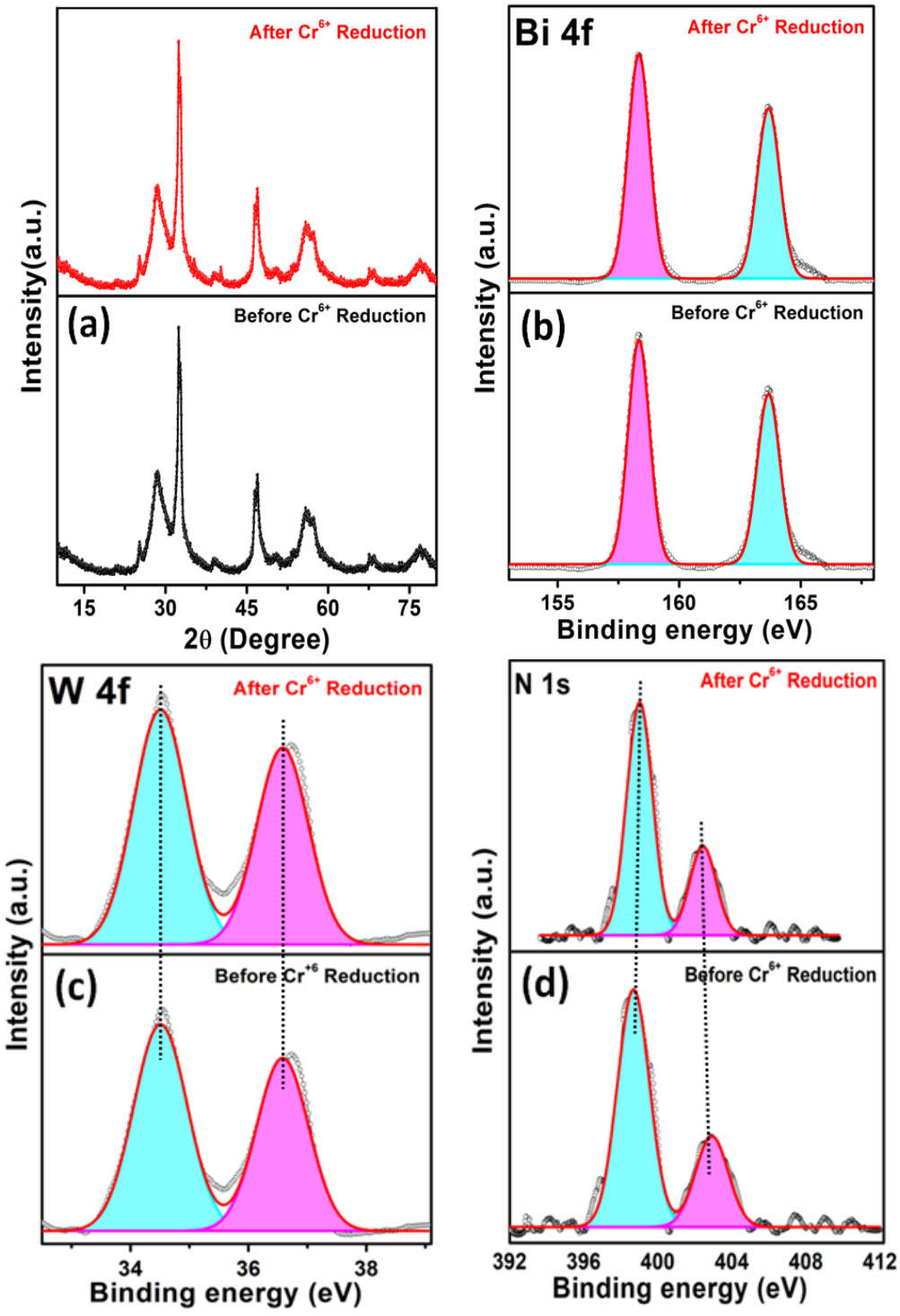
After Cr6+ Reduction
Before Cr6+ Reduction
(a)
Intensity(a.u.)
15
30
45
60
75
2θ (Degree)
Bi 4f
After Cr6+ Reduction
Before Cr6+ Reduction
(b)
Intensity (a.u.)
155
160
165
Binding energy (eV)
W 4f
After Cr6+ Reduction
Before Cr+6 Reduction
(c)
Intensity (a.u.)
34
36
38
Binding energy (eV)
N 1s
After Cr6+ Reduction
Before Cr6+ Reduction
(d)
Intensity (a.u.)
392
396
400
404
408
412
Binding energy (eV)

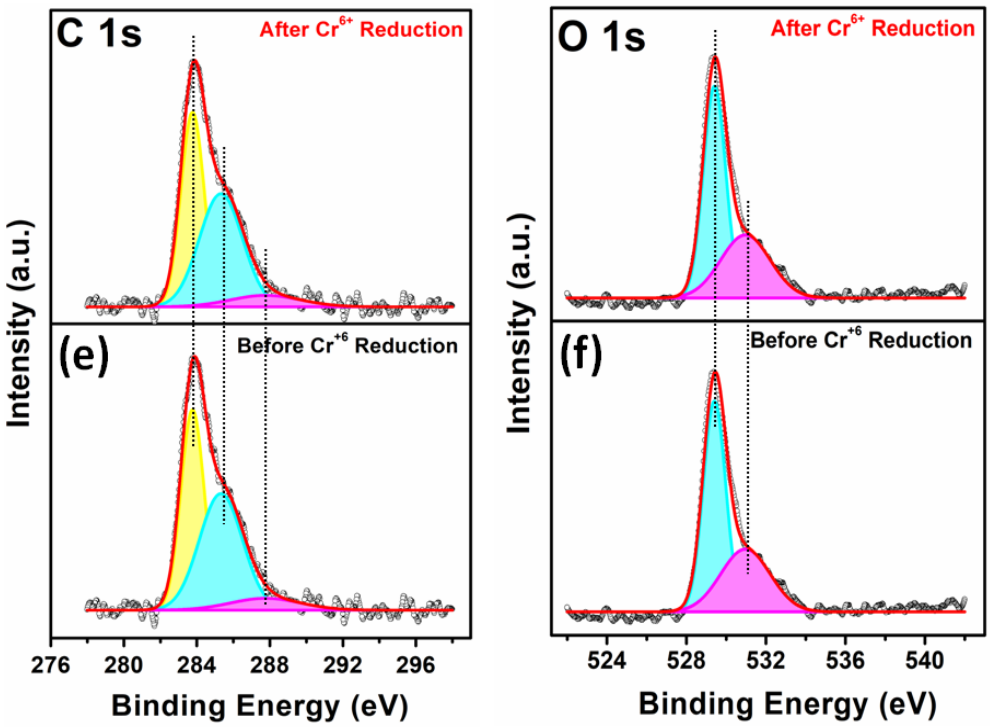

Figure 4.30. (a) XRD of β-Bi_2O_3-Bi_2WO_6/5 wt % H_2TPP before and after stability test; XPS spectrum of (b) Bi 4f, (c) W 4f, (d) N 1s, and (e) c 1s (f) O 1s of β-Bi_2O_3-Bi_2WO_6/5 wt % H_2TPP nanocomposite before and after stability test.

4.3.6. Effect of pH and temperature. The pH of the solution has a significant impact on the adsorption process caused by electrostatic interactions because it can affect the surface charge of β-Bi_2O_3-Bi_2WO_6/5 wt % H_2TPP and the Cr^{6+} species. At a high acidic pH, the material may be exhausted due to the presence of an organic-inorganic system in our modified electrodes, but it is crucial for the study of heavy metal remediation through the reduction process in a moderate pH condition. To determine the optimal conditions for Cr^{6+} reduction, a pH study[16] was performed briefly using cyclic voltammetric measurements in 0.1 M KCl medium with a variation of pH using 1:10 HCl solution. The peak current gradually increases with an increase in pH from 2.0 to 4.0 and suddenly starts decreasing at pH 5 under both dark and light irradiated conditions, demonstrating that pH 4.0 is the optimal condition for the reduction of Cr^{6+} as shown in Figures 4.31(a→d). Between pH 2.0 and 6.0, $HCrO_4^-$ is the main species[63] and the surface of the catalyst became protonated to make a positive bed for the accumulation of $HCrO_4^-$, whereas at higher pH, the catalyst surface became more negatively charged, tending to reject the $Cr_2O_7^{2-}$ ions and reduce the rate of electro- and

photoelectrocatalytic reduction of Cr^{6+}. The maximum adsorption of Cr^{6+} on the active sites of H_2TPP at pH 4.0 makes our material a promising catalyst at this definite pH. Figures 4.31(e→h) show the temperature study at pH 4.0, indicating that 30 °C is the optimal condition for both electro- and photoelectrochemical reduction of Cr^{6+}.

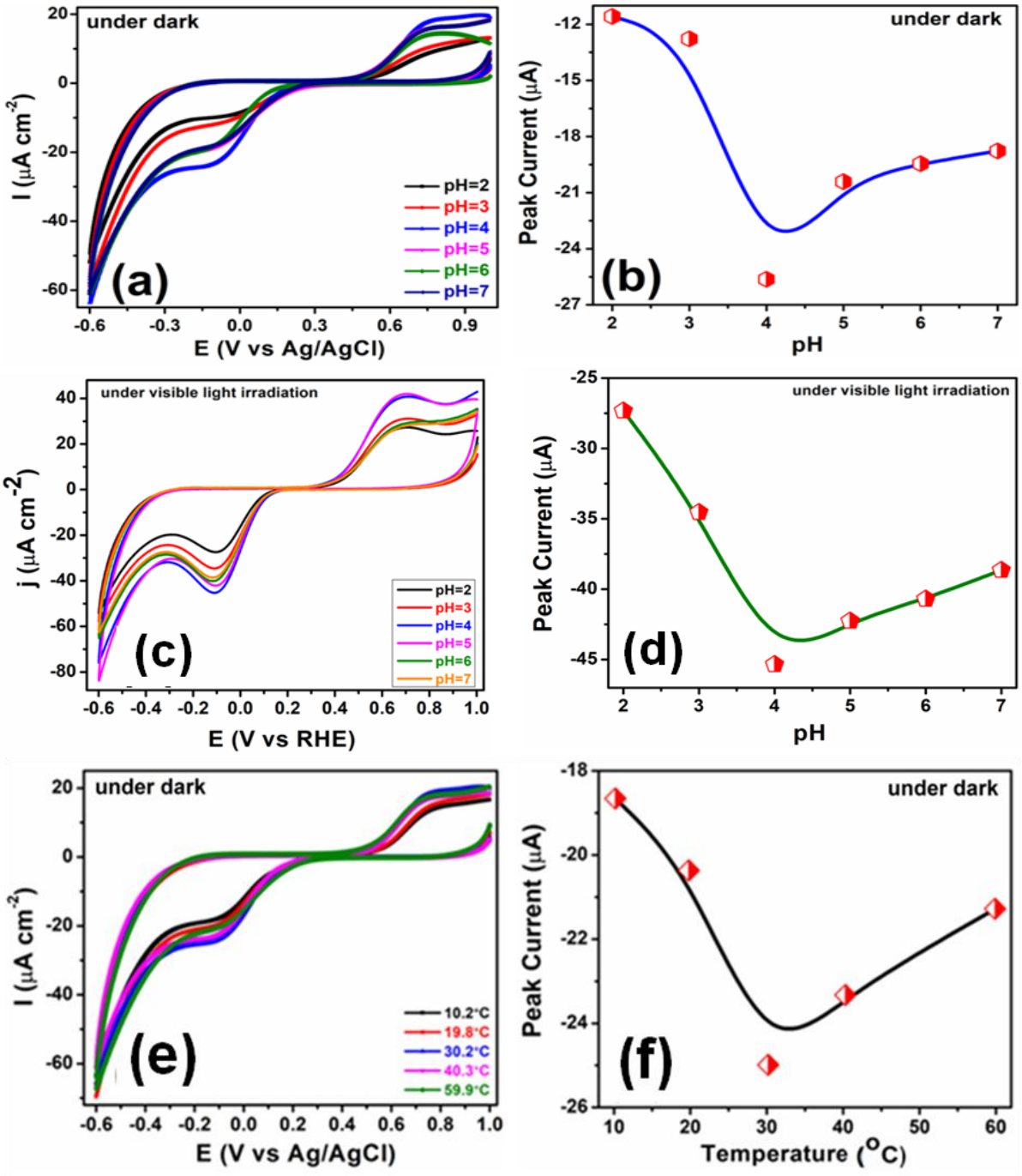

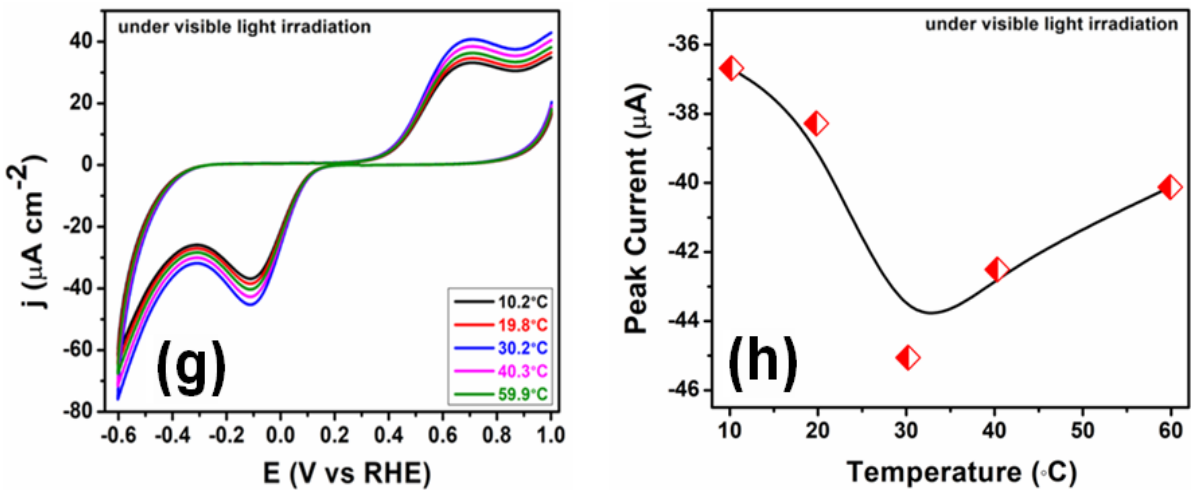

Figure 4.31. (a) CVs at different pH under dark (b) Peak potential vs. pH under dark (c) CVs at different pH under light (d) Peak potential vs. pH under light (e) CVs at different temperatures under dark (f) Peak current vs. temperature under dark (g) CVs at different temperatures under light (h) Peak current vs. temperatures under light in 0.1 M KCl at pH 4.0 with 150 μM Cr^{6+} of β-Bi_2O_3-Bi_2WO_6/5 wt % H_2TPP at a scan rate of 20 mV s^{-1}.

4.3.7. Selectivity, Reproducibility, and Repeatability study. The selectivity and interference studies of the proposed method were performed to evaluate the practical application of photoelectrochemical detection of Cr^{6+} in the presence of 10 fold other 14 interfering cations having Cd^{2+}, Al^{3+}, Mg^{2+}, Zn^{2+}, Co^{2+}, Ni^{2+}, Na^{+}, Pb^{2+}, Ca^{2+}, NH_4^{+}, Mn^{2+}, Cu^{2+}, Fe^{3+}, and K^{+} ions, as shown in Figures 4.32a and a′, and also 10 fold 14 types of anions such as F^{-}, Cl^{-}, Br^{-}, I^{-}, $H_2PO_4^{-}$, HPO_4^{2-}, PO_4^{3-}, NO_3^{-}, NO_2^{-}, HSO_4^{-}, SO_4^{2-}, SO_3^{2-}, HCO_3^{-}, and CO_3^{2-}, as depicted in Figures 4.32b and b′. An appreciable current response of β-Bi_2O_3-Bi_2WO_6/5 wt % H_2TPP nanocomposite was observed when Cr^{6+} was added to 0.1 M KCl medium, whereas the subsequent addition of other 14 interfering cations and 14 interfering anions produced no obvious change in the amperometric response, exhibiting outstanding selectivity and sensitivity in the photoelectrochemical sensing of Cr^{6+}.

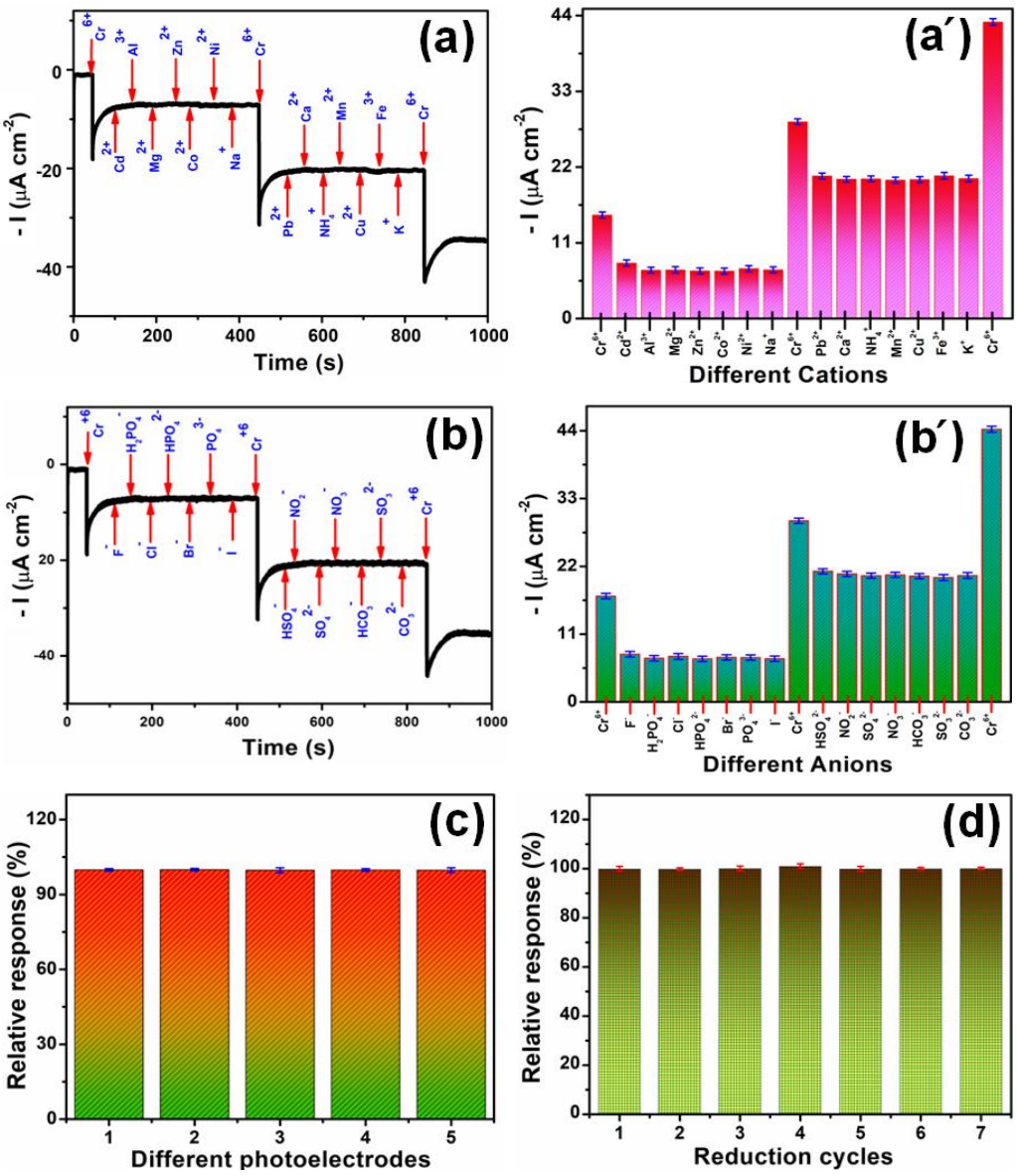

Figure 4.32. Selectivity of β-Bi_2O_3-Bi_2WO_6/5 wt % H_2TPP photoelectrode with Cr^{6+} ions towards some common interferences with a 10 fold concentration of Cr^{6+} in the testing solution: (a) metal ions such as Cd^{2+}, Al^{3+}, Mg^{2+}, Zn^{2+}, Co^{2+}, Ni^{2+}, Na^{+}, Pb^{2+}, Ca^{2+}, NH_4^{+}, Mn^{2+}, Cu^{2+}, Fe^{3+}, and K^{+} and (b) anions such as F^{-}, Cl^{-}, Br^{-}, I^{-}, $H_2PO_4^{-}$, HPO_4^{2-}, PO_4^{3-}, NO_3^{-}, NO_2^{-}, HSO_4^{-}, SO_4^{2-}, SO_3^{2-}, HCO_3^{-}, CO_3^{2-} (c) Relative photocurrent responses of five independently prepared β-Bi_2O_3-Bi_2WO_6/5 wt % H_2TPP photoelectrodes to 150 μM Cr^{6+} (d) Relative photocurrent responses of the same β-Bi_2O_3-Bi_2WO_6/5 wt % H_2TPP photoelectrode to Cr^{6+} from seven consecutive measurements under light irradiation conditions.

The reproducibility of the sensor was examined for detecting Cr^{6+} with five similar electrodes, as depicted in Figure 4.32c. The photoelectrochemical current response of the five similar electrodes remained almost the same, with an RSD value of 2.53 %, representing good reproducibility of the sensing electrode. The repeatability of the sensing electrode was also examined for seven consecutive measurements, as illustrated in Figure 4.32d, with an RSD value of 2.41%, showing good repeatability of the sensor.

4.3.8. Photoelectrochemical analysis of Cr^{6+} in real samples. To examine the practical sensing performance of the synthesized sensor photoelectrochemically, three water samples from various sources of laboratory tap water (pH 7.0), commercial potable mineral water (pH 7.0), and Kestopur canal water (pH 8.0), South Dum Dum, Kolkata, West Bengal (Latitude 22.6177°; Longitude 88.4045°) were used to detect Cr^{6+} using the standard addition technique. The sample was prepared by adding 6.0 mL of different water samples to 14.0 mL of 0.1 M KCl solution (pH 4.0). Different amounts of Cr^{6+} ions in the micromolar concentration range were added to 0.1 M KCl solution in the presence of real water samples, as shown in Figures 4.33(a→c). The findings from these experiments are compiled and presented in Table 4.8. The average recoveries, as shown in Figure 4.33d, were found to be (101.30-102.40%), (91.23-97.93%), and (97.90-103.20%), respectively. Furthermore, the LOD values showcased in Figure 4.33e provide strong evidence that the proposed method for photoelectrochemical detection of Cr^{6+} is promising for the analysis of real samples. Notably, laboratory tap water and potable mineral water were found to be free of Cr^{6+}, while the average Cr^{6+} concentration in Kestopur canal water was measured at 309.4 ppb.

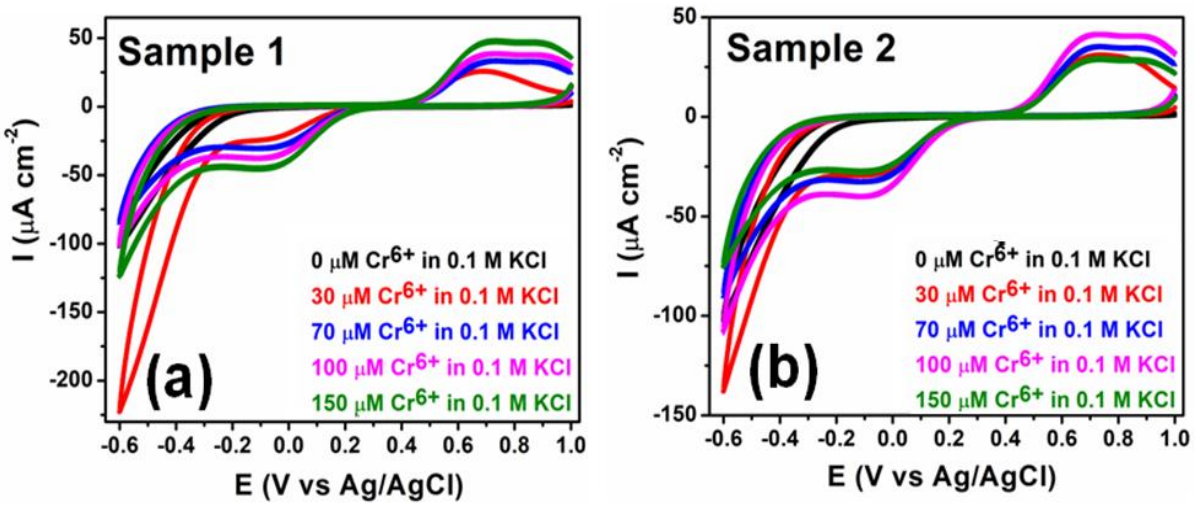

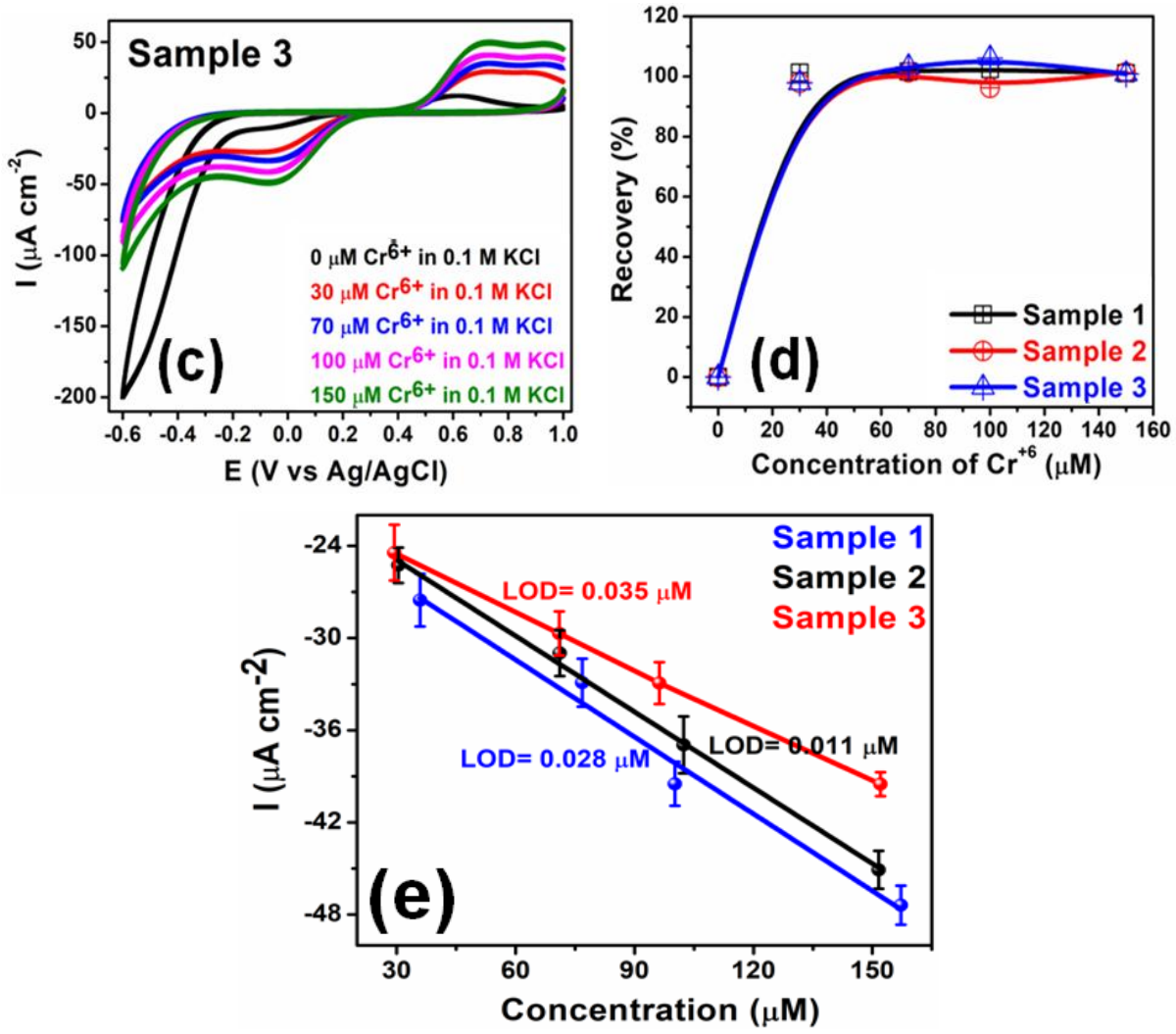

Figure 4.33. Analysis of Cr^{6+} in (a) Laboratory Tap water (Sample 1) (b) Commercial Potable Mineral water (Sample 2) (c) Kestopur Canal Water (Sample 3) (d) Recovery percentage (e) LOD plots in the presence of β-Bi_2O_3-Bi_2WO_6/5 wt % H_2TPP/FTO electrode under light at 20 mV s^{-1} scan rate.

Table 4.8. Detection of Cr^{6+} in real samples by the proposed method.

Samples	Added (µM)	Average found (µM)	Recovery (%)	RSD (%) (n = 5)	LOD (µM)
Sample 1 (Laboratory Tap Water)	0	0	-	1.17	0.028
	30	30.39	101.3	1.15	
	70	71. 14	101.63	1.49	
	100	102.39	102.39	1.85	
	150	151.56	101.04	1.23	
Sample 2 (Commercial portable Mineral Water)	0	0	-	1.27	0.011
	30	29.98	99.93	1.81	
	70	70.97	101.39	1.43	
	100	99.23	99.23	1.36	
	150	152.04	101.36	0.78	
Sample 3 (Kestopur Canal Water)	0	5.95	-	1.21	0.035
	30	35.92	99.90	1.71	
	70	76.79	101.20	1.56	
	100	100.18	100.18	1.43	
	150	157.19	100.83	1.27	

4.3.9. Scavenger Study. To determine the role of the active species, active species trapping agents, specifically p-benzoquinone (BQ), isopropyl alcohol (IPA), citric acid, and $K_2S_2O_8$ of 1 mM concentrations[94] were used as scavengers of superoxide radicals ($\bullet O_2^-$), hydroxyl radicals (•OH), holes (h^+), and electrons (e^-), respectively. Figure 4.34d reveals that the addition of BQ, IPA, and citric acid did not alter the reduction rate of Cr^{6+}. However, the introduction of $K_2S_2O_8$ significantly decreased the Cr^{6+} reduction rates, suggesting that photogenerated electrons are the primary active species responsible for Cr^{6+} reduction.[78,95]

4.3.10. Proposed mechanism for photoelectrochemical detection of Cr^{6+}. Furthermore, the enhanced photoelectrocatalytic performance of the nanocomposite could be attributed to the formation of a p-n-p[96] heterojunction between a p-type H_2TPP organic moiety and a p-n type β-Bi_2O_3-Bi_2WO_6 nanocomposite, and the schematic representation of the probable energy band structure is shown in Figure 4.34. To determine the flat band potential (E_{fb}), capacitance measurements were performed. The E_{fb} of the materials can be measured by extrapolating the linear part of the Mott-Schottky plot to $C^{-2} = 0$ (Equation 4.5). The flat band potentials of β-Bi_2O_3-Bi_2WO_6 and H_2TPP were determined through Mott-Schottky measurements and found to be approximately -4.623 and -4.19 eV vs. RHE (Equations 4.6 and 4.7) (Figures 4.34a and b), resembling the conduction band minimum of

β-Bi_2O_3-Bi_2WO_6 and the valence band maximum of H_2TPP, respectively. In association with band gap energy (E_g), the valence band (E_{VB}) and the conduction band potential (E_{CB}) of β-Bi_2O_3-Bi_2WO_6 and H_2TPP could be evaluated to be -7.883 and -1.12 eV, respectively (Table 4.9). The E_{VB} and E_{CB} values of pure β-Bi_2O_3 are -7.09 and -4.81 eV,[97] while those of Bi_2WO_6 are -7.74 eV and -5.04 eV,[98] respectively (Table 4.9).

The E_{fb} values were determined using the Mott-Schottky equation.

$$\frac{1}{C^2} = \frac{2}{e\mathcal{E}\mathcal{E}_0 N_D}\left(E - E_{fb} - \frac{K_B T}{e}\right) \qquad \text{Eq. 4.5}$$

Where C is the space-charge capacitance (in F cm^{-2}), N_D is the carrier density (cm^{-3}), e is the electronic charge (C), Ɛ is the dielectric constant of the semiconductor, $Ɛ_0$ is the permittivity of free space, E_{fb} is the flat band potential (V), E is the applied potential (V), K_B is the Boltzmann constant and T is the temperature.

The band diagram of β-Bi_2O_3 and Bi_2WO_6 resembles our results obtained for the β-Bi_2O_3-Bi_2WO_6 composite. In light of the above results, the band positions of H_2TPP and β-Bi_2O_3-Bi_2WO_6 before and after internal junction formation have been represented in Figure 4.35. After inducing H_2TPP on the surface of β-Bi_2O_3-Bi_2WO_6, at the interface, a p-n-p heterojunction was built, and the transportation of electrons continued till their Fermi levels got aligned to attain equilibrium. Following the orientation, the E_{fb} was found to be -3.64 eV, as depicted in Figure 4.34c, and the corresponding band bending was noticed. The photoelectrochemical reduction of Cr^{6+} can be described according to the following equations (4.8→4.9). When the β-Bi_2O_3-Bi_2WO_6/5 wt % H_2TPP nanocomposite was exposed to light, both H_2TPP and β-Bi_2O_3-Bi_2WO_6 experienced excitation, and the photoexcited e^- could readily be transported from the LUMO of H_2TPP to the CB of β-Bi_2O_3-Bi_2WO_6. Simultaneously, the photogenerated h^+ in the VB of β-Bi_2O_3-Bi_2WO_6 quickly migrated to the HOMO of H_2TPP. Due to light, semiconducting materials have a tendency for photogenerated carriers, i.e., holes, to move in the upward direction, while electrons can move in the downward direction through the siphon process by increasing the band bending, and consequently, this is likely to result in greater efficiency in separating photogenerated charge carriers.[99] With the electronic cloud being concentrated on the adjacent moiety, the appropriate band bending between them enhances the reduction process in the respective potential region. Thus, the efficient internal charge transmission in the β-Bi_2O_3-Bi_2WO_6/5 wt % H_2TPP nanocomposite could lead to charge separation,[100] which can also be approved by the photoluminescence quenching effect (Figure 4.23b) and elongated fluorescence lifetime (4.009 ns), leading to excellent structural stability and a significant improvement in the

photoelectrochemical catalytic activity of the β-Bi_2O_3-Bi_2WO_6/5 wt % H_2TPP nanocomposite. Besides, the accumulated electrons on the CB of β-Bi_2O_3-Bi_2WO_6 of the nanocomposite could possibly reduce the hexavalent Cr ions adsorbed on its surface to trivalent Cr following equation 4.9. Due to the higher photocatalytic behaviour of β-Bi_2O_3 and H_2TPP and also to the high adsorption efficiency of cr^{6+} on the active site of H_2TPP in β-Bi_2O_3-Bi_2WO_6/5 wt % H_2TPP, our sample serves as a promising photoelectrochemical sensor for the reduction of Cr^{6+}.

$$E_{fb}(eV) = -4.5 - E_{fb}(V) \quad \text{Eq.4.6}$$

$$E_{CB} - E_{VB} = E_g \quad \text{Eq.4.7}$$

$$\beta - Bi_2O_3 - Bi_2WO_6/5\ \text{wt}\%\ H_2TPP + h\nu \rightarrow e^-_{CB} + h^+_{VB} \quad \text{Eq.4.8}$$

$$HCrO_4^- + 7H^+ + 3e^-_{CB} \rightarrow Cr^{3+} + 4H_2O \quad \text{Eq.4.9}$$

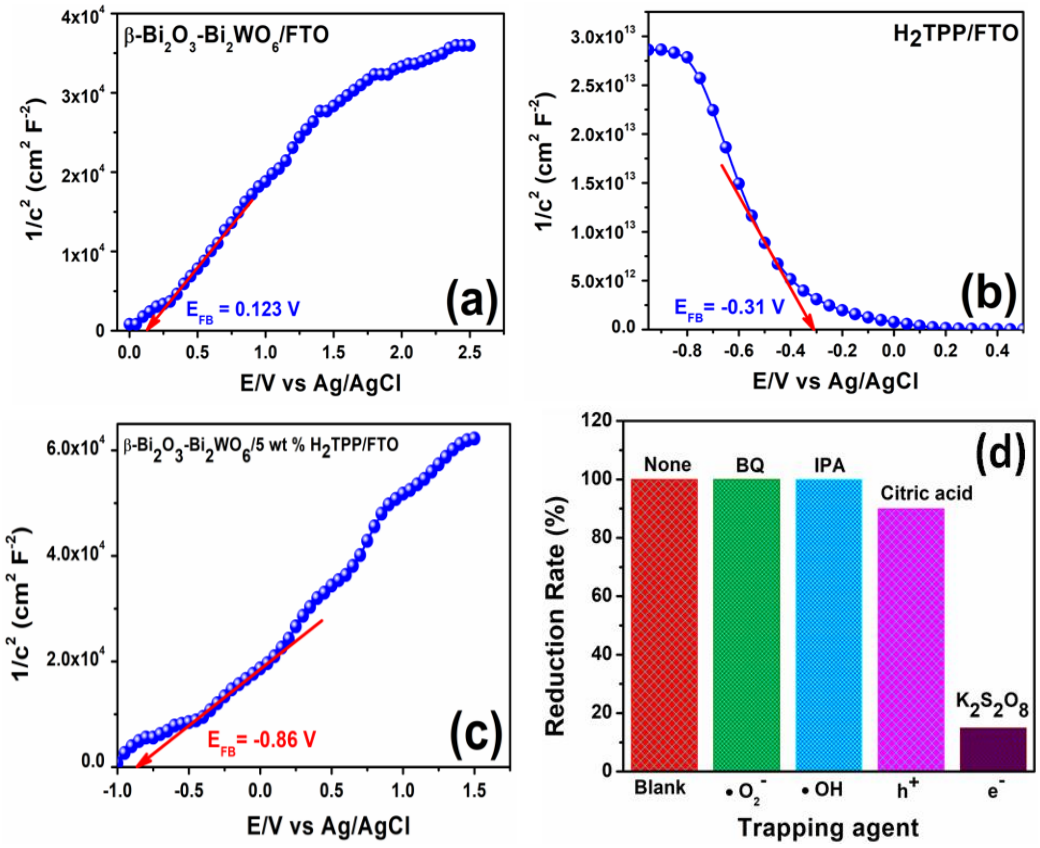

Figure 4.34. Mott-Schottky analyses of (a) β-Bi_2O_3-Bi_2WO_6 (b) H_2TPP (c) β-Bi_2O_3-Bi_2WO_6/5 wt % H_2TPP nanocomposite; (d) Effect of different scavengers on the photoelectrochemical reduction of Cr^{6+}.

Table 4.9. Flat band potentials of H_2TPP, β-Bi_2O_3, Bi_2WO_6, β-Bi_2O_3-Bi_2WO_6, and β-Bi_2O_3-Bi_2WO_6/5 wt % H_2TPP.

Materials	E_{fb}(V) vs. RHE	E_{fb} (eV) vs. RHE	Band gap (eV)	E_{vb}/HOMO (eV)	E_{cb}/LUMO (eV)
H_2TPP	-0.31	-4.19	3.07	-4.19	-1.12
β-Bi_2O_3	-	-	2.28	-7.09	-4.81
Bi_2WO_6	-	-	2.70	-7.74	-5.04
β-Bi_2O_3-Bi_2WO_6	0.123	-4.623	3.26	-7.883	-4.623
β-Bi_2O_3-Bi_2WO_6/5 wt % H_2TPP	-0.86	-3.64	2.99	-6.63	-3.64

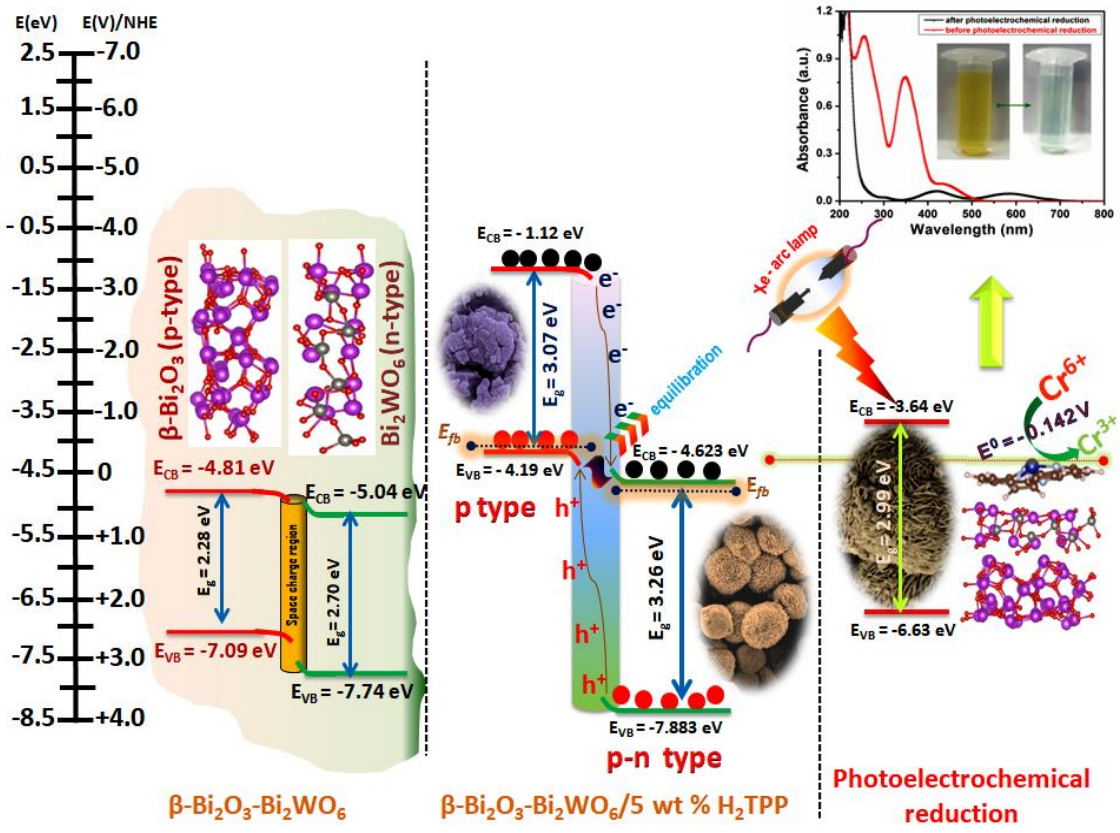

Figure 4.35. Schematic representation of the energy band structure of H_2TPP and β-Bi_2O_3-Bi_2WO_6 before and after internal junction formation for the reduction of Cr^{6+}.

4.4. CONCLUSIONS

In summary, a new organic-inorganic nanocomposite system, synthesized using the solvothermal process, exhibits a notable photocatalytic, electrochemical, and photoelectrochemical reduction of Cr^{6+}. By adjusting the weight percentages of *meso*-tetraphenylporphyrin, the morphology, optical, and electrochemical performances of the β-Bi_2O_3-Bi_2WO_6 composite were fine-tuned. Computational analysis confirmed the adsorption of hexavalent Cr due to the electrostatic attraction between the 2p-orbital of the N atom of H_2TPP and the 3d and 4s orbitals of hexavalent Cr. The mesoporous structure, adequate exposed surface area, and computable photoelectrochemical sensing of Cr^{6+} from standard and real samples of the β-Bi_2O_3-Bi_2WO_6/5 wt % H_2TPP nanocomposite drew a lot of attention. ECSA, enhanced charge transport phenomena, and electrochemical preceding factors validated its effective photoelectrochemical activities. The availability of pyrrolic- and pyridinic-N atoms synergistically enhanced its performance more than that of other known photoelectrochemical sensors due to its wide linear range, low LOD, and higher sensitivity values for photoelectrochemical reduction of Cr^{6+}. The scavenger study confirmed the significant role of photogenerated electrons in the reduction of Cr^{6+} ions. The interference study and the reproducibility of the electrode material throughout the photoelectrochemical reduction of Cr^{6+} underline its potential as a reliable choice for advanced, large-scale sensing of Cr^{6+}.

REFERENCES

(1) Bolisetty, S.; Peydayesh, M.; Mezzenga, R. Sustainable technologies for water purification from heavy metals: review and analysis. *Chem. Soc. Rev.* **2019**, *48*, 463-487.

(2) Pournara, A. D.; Margariti, A.; Tarlas, G. D.; Kourtelaris, A.; Petkov, V.; Kokkinos, C.; Economou, A.; Papaefstathiou, G. S.; Manos, M. J. A Ca^{2+} MOF combining highly efficient sorption and capability for voltammetric determination of heavy metal ions in aqueous media. *J. Mater. Chem. A* **2019**, *7*, 15432-15443.

(3) Li, X.; Li, C.; Xiang, D.; Zhang, C.; Xia, L.; Liu, X.; Zheng, F.; Xie, X.; Zhang, Y.; Chen, W. Self-limiting synthesis of Au-Pd core-shell nanocrystals with a near surface alloy and monolayer Pd shell structure and their superior catalytic activity on the conversion of hexavalent chromium. *Appl. Catal. B* **2019**, *253*, 263-270.

(4) Pang, Y.; Kong, L.; Chen, D.; Yuvaraja, G. Rapid Cr (VI) reduction in aqueous solution using a novel microwave-based treatment with MoS_2-$MnFe_2O_4$ composite. *Appl. Surf. Sci*. **2019**, *471*, 408-416.

(5) Veerakumar, P.; Thanasekaran, P.; Lin, K. C.; Liu, S. B. Biomass derived sheet-like carbon/palladium nanocomposite: an excellent opportunity for reduction of toxic hexavalent chromium. *ACS Sustain. Chem. Eng.* **2017**, *5*, 5302-5312.

(6) Xin, X.; Tian, X.; Yu, H.; Han, Z. Synthesis of hybrid phosphomolybdates and application as highly stable and effective catalyst for the reduction of Cr (VI). *Inorg. Chem.* **2018**, *57*, 11474-11481.

(7) Costa, M.; Klein, C. B. Toxicity and carcinogenicity of chromium compounds in humans. *Crit. Rev. Toxicol.* **2006**, *36*, 155-163.

(8) Cespon-Romero, R.M.; Yebra-Biurrun, M.C. and Bermejo-Barrera, M.P. Preconcentration and speciation of chromium by the determination of total chromium and chromium (III) in natural waters by flame atomic absorption spectrometry with a chelating ionexchange flow injection system. *Anal. Chim. Acta* **1996**, *327*, 37-45.

(9) de Paula Eiras, S.; Custodio, U. M. and Pavanin, L. A. Determination of chromium (III) using a homogenous mixture of water/ethanol methylisobutylketone solvents. *Talanta* **2003**, *59*, 621-625.

(10) Tang, B.; Yue, T.; Wu, J.; Dong, Y.; Ding, Y.; Wang, H. Rapid and sensitive spectrofluorimetric determination of trace amount of Cr (III) with O-vanillin-8-aminoquinoline. *Talanta* **2004**, *64*, 955-960.

(11) Ma, J.; Xu, N.; Liu, Y.; Wang, Y.; Li, H.; Liu, G.; Wang, X. and Li, J. A Stable 3D Zn-coordination polymer sensor based on dual luminescent ligands for efficient detection of multiple analytes under acid or alkaline environment. *Inorg. Chem.* **2020**, *59*, 15495-15503.

(12) Liu, G. C.; Li, Y.; Chi, J.; Xu, N.; Wang, X. L.; Lin, H. Y. and Chen, Y. Q. Multi-functional fluorescent responses of cobalt complexes derived from functionalized amide-bridged ligand. *Dyes Pigm.* **2020**, *174*, 108064 (1-9).

(13) Meng, X.; Song, S. Y.; Song, X. Z.; Zhu, M.; Zhao, S. N.; Wu, L. L. and Zhang, H. J. A Eu/Tb-codoped coordination polymer luminescent thermometer. *Inorg. Chem. Front.* **2014**, *1*, 757-760.

(14) Fang, X.; Chen, X.; Liu, Y.; Li, Q.; Zeng, Z.; Maiyalagan, T. and Mao, S. Nanocomposites of Zr (IV)-based metal-organic frameworks and reduced graphene oxide for electrochemically sensing ciprofloxacin in water. *ACS Appl. Nano Mater.* **2019**, *2*, 2367-2376.

(15) Wei, Y.; Gao, C.; Meng, F. L.; Li, H. H.; Wang, L.; Liu, J. H. and Huang, X. J. SnO_2/reduced graphene oxide nanocomposite for the simultaneous electrochemical detection of cadmium (II), lead (II), copper (II), and mercury (II): an interesting favorable mutual interference. *J. Phys. Chem. C* **2012**, *116*, 1034-1041.

(16) Wang, Y.; Ma, J. X.; Zhang, Y.; Xu, N. and Wang, X. L. A series of cobalt-based coordination polymer crystalline materials as highly sensitive electrochemical sensors for detecting Trace Cr (VI), Fe (III) Ions, and ascorbic acid. *Cryst. Growth Des.* **2021**, *21*, 4390-4397.

(17) Jaihindh, D. P.; Thirumalraj, B.; Chen, S. M.; Balasubramanian, P. and Fu, Y. P. Facile synthesis of hierarchically nanostructured bismuth vanadate: an efficient photocatalyst for degradation and detection of hexavalent chromium. *J. Hazard. Mater*. **2019**, *367*, 647-657.

(18) Zhao, W. W.; Xu, J. J. and Chen, H. Y. Photoelectrochemical DNA biosensors. *Chem. Rev.* **2014**, *114*, 7421-7441.

(19) Qiao, J.; Wang, Y.; Liang, Q.; Dong, S.; Zeng, Z. and Shao, S. A Photoelectrochemical sensor based on TiO_2 nanotube arrays decorated with nickel-cobalt layered double hydroxides for the effective and sensitive detection of chromium (VI). *ACS Appl. Nano Mater.* **2022**, *5*, 5535-5543.

(20) Wang, Y.; Ma, Y.; Zhao, Q.; Hou, L. and Han, Z. Polyoxometalate-based crystalline catalytic materials for efficient electrochemical detection of Cr (VI). *Sens. Actuators B Chem.* **2020**, *305*, 127469 (1-8).

(21) Stelo, F.; Kublik, N.; Ullah, S. and Wender, H. Recent advances in Bi_2MoO_6 based Z-scheme heterojunctions for photocatalytic degradation of pollutants. *J. Alloys Compd*. **2020**, *829*, 154591 (1-15).

(22) Liu, Y.; Wei, B.; Xu, L.; Gao, H. and Zhang, M. Generation of oxygen vacancy and OH radicals: a comparative study of Bi_2WO_6 and Bi_2WO_{6-x} nanoplates. *ChemCatChem*. **2015**, *7*, 4076-4084.

(23) Cai, M.; Liu, Y.; Wang, C.; Lin, W. and Li, S. Novel $Cd_{0.5}Zn_{0.5}S/Bi_2MoO_6$ S-scheme heterojunction for boosting the photodegradation of antibiotic enrofloxacin: Degradation pathway, mechanism and toxicity assessment. *Sep. Purif. Technol*. **2023**, *304*, 122401 (1-11).

(24) Li, S.; Cai, M.; Liu, Y.; Wang, C.; Lv, K. and Chen, X. S-scheme photocatalyst $TaON/Bi_2WO_6$ nanofibers with oxygen vacancies for efficient abatement of antibiotics and Cr (VI): intermediate eco-toxicity analysis and mechanistic insights. *Chinese J. Catal.* **2022**, *43*, 2652-2664.

(25) Huang, H.; Zhou, C.; Jiao, X.; Yuan, H.; Zhao, J.; He, C.; Hofkens, J.; Roeffaers, M.B.; Long, J. and Steele, J.A. Subsurface defect engineering in single-unit-cell Bi_2WO_6 monolayers boosts solar-driven photocatalytic performance. *ACS Catal.* **2019**, *10*, 1439-1443.

(26) Vairale, P.; Sharma, V.; Bade, B.; Waghmare, A.; Shinde, P.; Punde, A.; Doiphode, V.; Aher, R.; Subhash, P.; Nair, S. and Jadkar, V. Melanin sensitized nanostructured ZnO photoanodes for efficient photoelectrochemical splitting of water: synthesis and characterization. *J. Eng. Sci.* **2020**, *11*, 76-84.

(27) Zhang, G.; Cheng, D.; Li, M.; Feng, C.; Wu, H. and Mei, H. Enhanced the photoelectrochemical performance of Bi_2XO_6 (X = W, Mo) for detecting hexavalent chromium by modification of CuS. *J. Environ. Sci.* **2021**, *103*, 185-195.

(28) Liu, X.; Gu, S.; Zhao, Y.; Zhou, G. and Li, W. $BiVO_4$, Bi_2WO_6 and Bi_2MoO_6 photocatalysis: a brief review. *J. Mater. Sci. Technol.* **2020**, *56*, 45-68.

(29) Li, S.; Cai, M.; Liu, Y.; Wang, C.; Yan, R. and Chen, X. Constructing $Cd_{0.5}Zn_{0.5}S/Bi_2WO_6$ S-scheme heterojunction for boosted photocatalytic antibiotic oxidation and Cr (VI) reduction. *Adv. Powder Mater.* **2023**, *2*, 100073 (1-12).

(30) Li, S.; Wang, C.; Liu, Y.; Liu, Y.; Cai, M.; Zhao, W. and Duan, X. S-scheme MIL-101 (Fe) octahedrons modified Bi_2WO_6 microspheres for photocatalytic decontamination of Cr (VI) and tetracycline hydrochloride: synergistic insights, reaction pathways, and toxicity analysis. *J. Chem. Eng.* **2023**, *455*, 140943 (1-12).

(31) Zerjav, G.; Terzan, J.; Djinovic, P.; Barbierikova, Z.; Hajdu, T.; Brezova, V.; Zavasnik, J.; Kovac, J. and Pintar, A. TiO_2-β-Bi_2O_3 junction as a leverage for the visible-light activity of TiO_2 based catalyst used for environmental applications. *Catal. Today* **2021**, *361*, 165-175.

(32) Yang, J.; Xie, T.; Wang, J.; Peng, Y.; Liu, S.; Zhang, X.; Xu, L. and Liu, C. rGO/β-Bi_2O_3/$SrFe_{12}O_{19}$ magnetic photocatalyst: facile synthesis and its photocatalytic activity. *Mater. Res. Express* **2019**, *6*, 115912 (1-11).

(33) Li, C.X.; Song, S.Y.; Shi, D.S.; Ying, Y.; Zhang, X.X.; Wei, J.Q.; Hong, B.; Xu, J.C.; Jin, H.X.; Wang, P.F. and Wang, X.Q. Improved photocatalytic activity of Z-scheme β-Bi_2O_3/Bi_2WO_6 nanocomposites from band bending of p-n heterojunction. *J. Nanopart. Res*. **2020**, *22*, 1-11.

(34) Peng, Y.; Yan, M.; Chen, Q.G.; Fan, C.M.; Zhou, H.Y. and Xu, A.W. Novel one-dimensional Bi_2O_3-Bi_2WO_6 p-n hierarchical heterojunction with enhanced photocatalytic activity. *J. Mater. Chem. A* **2014**, *2*, 8517-8524.

(35) Yang, C.; Yu, J.M.; Zhai, L.; Jia, S.; Yang, T.; Xiong, W.W. and Zhang, Q. Two-dimensional layered organic hybrid selenidostannate coupled with polyaniline for high efficient photocatalytic Cr (VI) reduction. *Chem. Eng. J.* **2023**, *467*, 143511 (1-13).

(36) Arora, S.; Nagpal, R.; Gusain, M.; Singh, B.; Pan, Y.; Yadav, D.; Ahmed, I.; Kumar, V. and Parshad, B. Organic-inorganic porphyrinoid frameworks for biomolecule sensing. *ACS Sens.* **2023**, *8*, 443-464.

(37) Negut, C. C.; Stefan-van Staden, R. I. and van Staden, J. F. Porphyrins-as active materials in the design of sensors. An overview. *ECS J. Solid State Sci. Technol.* **2020**, *9*, 051005 (1-10).

(38) Lu, J.; Gu, S.; Li, H.; Wang, Y.; Guo, M. and Zhou, G. Review on multi-dimensional assembled S-scheme heterojunction photocatalysts. *J. Mater. Sci. Technol.* **2023**, *160*, 214-239.

(39) Chaudhary, V.; Talreja, R.K.; Rustagi, S.; Walvekar, R. and Gautam, A. High-performance H_2 sensor based on polyaniline-WO_3 nanocomposite for portable batteries and breathomics-diagnosis of irritable bowel syndrome. *Int. J. Hydrog. Energy*. **2023**, *8*, 151(1-8).

(40) Dong, C.; Yang, J.J.; Xie, L.H.; Cui, G.; Fang, W.H. and Li, J.R. Catalytic ozone decomposition and adsorptive VOCs removal in bimetallic metal-organic frameworks. *Nat. Commun.* **2022**, *13*, 4991(1-10).

(41) Liu, Y.H.; Lv, J.A.; Xu, M.M.; Dong, C.; Liu, X.M.; Li, J.R. and Xie, L.H. Birnessite-type manganese dioxide nanosheets on metal-organic frameworks with high catalytic activity in ozone decomposition. *ACS Appl. Nano Mater*. **2023**, *6*, 7794-7801.

(42) Pal, S.; Sarkar, A.; Satra, J.; Mondal, P.; Ray, P.; Srivastava, D.N.; Adhikary, B. and Show, B. Tetraphenylporphyrin decorated Bi_2MoO_6 nanocomposite: its twin affinity of oxygen reduction reaction and electrochemical detection of 4-nitrophenol. *Inorg. Chem.* **2022**, *61*, 17402-17418.

(43) Mondal, P.; Ghorui, U. K.; Satra, J.; Mardanya, S.; Srivastava, D. N.; Bhadu, G. R. and Adhikary, B. $AgVO_3$ nanorods decorated with polypyrrole and tetraphenylporphyrin as ternary catalysts for oxygen electrode reactions. *ACS Appl. Nano Mater*. **2020**, *3*, 3876-3891.

(44) Jin, W.; Liang, G.; Zhong, Y.; Yuan, Y.; Jian, Z.; Wu, Z. and Zhang, W. The influence of CTAB-capped seeds and their aging time on the morphologies of silver nanoparticles. *Nanoscale Res. Lett.* **2019**, *14*, 1-11.

(45) Wei, W.; Xie, J.; Lu, X.; Osei, P.B.; Yan, Z.; Meng, S. and Cui, H. CTAB-assisted synthesis and characterization of Bi_2WO_6 photocatalysts grown from $WO_3{\cdot}0.33H_2O$ nanoplate precursors. *Monatsh. Chem.* **2014**, *145*, 47-59.

(46) Wang, T.; Zhang, F.; Xiao, G.; Zhong, S. and Lu, C. Synthesis of Bi_2WO_6/Bi_2O_3 composite with enhanced photocatalytic activity by a facile one-step hydrothermal synthesis route. J. *Photochem. Photobiol.* **2015**, *91*, 291-297.

(47) Ge, M.; Li, Y.; Liu, L.; Zhou, Z. and Chen, W. Bi_2O_3-Bi_2WO_6 composite microspheres: hydrothermal synthesis and photocatalytic performances. *J. Phys. Chem. C.* **2011**, *115*, 5220-5225.

(48) Wu, K.; Qin, Z.; Zhang, X.; Guo, R.; Ren, X. and Pu, X. Z-scheme BiOCl/Bi-Bi_2O_3 heterojunction with oxygen vacancy for excellent degradation performance of antibiotics and dyes. *J. Mater. Sci.* **2020**, *55*, 4017-4029.

(49) D Urso, A.; Di Mauro, A.; Cunsolo, A.; Purrello, R. and Fragala, M.E. Solvophobic versus electrostatic interactions drive spontaneous adsorption of porphyrins onto inorganic surfaces: a full noncovalent approach. *J. Phys. Chem. C* **2013**, *117*, 17659-17665.

(50) Yang, J.; Wang, X.; Zhao, X.; Dai, J. and Mo, S. Synthesis of uniform Bi_2WO_6-reduced graphene oxide nanocomposites with significantly enhanced photocatalytic reduction activity. *J. Phys. Chem. C* **2015**, *119*, 3068-3078.

(51) Hao, J.; Qu, T.; Wang, Q. and Zhao, Z. Preparation and visible light responsive photocatalytic activity of Fe_3O_4/Ni-Al-Ce LDH/Bi_2WO_6 composites. *Quim Nova* **2017**, *40*, 849-853.

(52) Ho, C.H.; Chan, C.H.; Huang, Y.S.; Tien, L.C. and Chao, L.C. The study of optical band edge property of bismuth oxide nanowires α-Bi_2O_3. *Opt. Express* **2013**, *21*, 11965-11972.

(53) Nurhayati, Suendo, V.; Alni, A.; Nugroho, A.A.; Majima, Y.; Lee, S.; Nugraha, Y.P. and Uekusa, H. Revealing the real size of a porphyrin molecule with quantum confinement probing via temperature-dependent photoluminescence spectroscopy. *J. Phys. Chem. A* **2020**, *124*, 2672-2682.

(54) Aydin, M. DFT and Raman spectroscopy of porphyrin derivatives: tetraphenylporphine (TPP). *Vib. Spectrosc.* **2013,** *68*, 141-152.

(55) Aydin, M. Comparative study of the structural and vibroelectronic properties of porphyrin and its derivatives. *Molecules* **2014**, *19*, 20988-21021.

(56) Bai, J.; Ren, X.; Chen, X.; Lu, P. and Fu, M. Oxygen vacancy-enhanced ultrathin Bi_2O_3-Bi_2WO_6 nanosheets' photocatalytic performances under visible light irradiation. *Langmuir* **2021**, *37*, 5049-5058.

(57) Koposova, E.A.; Offenhausser, A.; Ermolenko, Y.E. and Mourzina, Y.G. Photoresponsive porphyrin nanotubes of *meso*-tetra (4-sulfonatophenyl) porphyrin and Sn (IV) *meso*-tetra (4-pyridyl) porphyrin. *Front. Chem*. **2019**, *7*, 351 (1-16).

(58) Zhao, P.; Huang, Y.; Chen, J.; Shao, S.; Miao, H.; Xia, J.; Jia, C. and Hua, M. Preparation of *meso*-tetraphenyl porphyrin modified defect-rich BiOCl with enhanced visible-light photocatalytic activity for antibiotic degradation and mechanism insight. *J. Photochem. Photobiol*. **2020**, 3, 100014 (1-11).

(59) Ri, C. N.; Kim, S. G.; Ju, K. S.; Ryo, H. S.; Mun, C. H. and Kim, U. H. The synthesis of a Bi_2MoO_6/$Bi_4V_2O_{11}$ heterojunction photocatalyst with enhanced visible-light-driven photocatalytic activity. *RSC Adv*. **2018**, *8*, 5433-5440.

(60) Zhong, S.; Zhang, F.; Lu, W.; Wang, T. and Qu, L. One-step synthesis of Bi_2WO_6/Bi_2O_3 loaded reduced graphene oxide multicomponent composite with enhanced visible-light photocatalytic activity. *RSC Adv*. **2015**, *5*, 68646-68654.

(61) Guo, H.; Guo, Y.; Liu, L.; Li, T.; Wang, W.; Chen, W. and Chen, J. Designed hierarchical synthesis of ring-shaped Bi_2WO_6@CeO_2 hybrid nanoparticle aggregates for photocatalytic detoxification of cyanide. *Green Chem.* **2014**, *16*, 2539-2545.

(62) Zhang, J.; Huang, Z. H.; Xu, Y. and Kang, F. Hydrothermal synthesis of graphene/Bi_2WO_6 composite with high adsorptivity and photoactivity for azo dyes. *J. Am. Ceram. Soc.* **2013**, *96*, 1562-1569.

(63) Wang, P.; Dong, F.; Liu, M.; He, H.; Huo, T.; Zhou, L. and Zhang, W. Improving photoelectrochemical reduction of Cr (VI) ions by building α-Fe_2O_3/TiO_2 electrode. *Environ. Sci. Pollut. Res.* **2018**, *25*, 22455-22463.

(64) Karthika, A.; Nikhil, S.; Suganthi, A. and Rajarajan, M. A facile sonochemical approach based on graphene carbon nitride doped silver molybdate immobilized nafion for selective and sensitive electrochemical detection of chromium (VI) in real sample. *Adv. Powder Technol.* **2020**, *31*, 1879-1890.

(65) Swaidan, A.; Borthakur, P.; Boruah, P.K.; Das, M.R.; Barras, A.; Hamieh, S.; Toufaily, J.; Hamieh, T.; Szunerits, S. and Boukherroub, R. A facile preparation of CuS-BSA nanocomposite as

enzyme mimics: application for selective and sensitive sensing of Cr (VI) ions. *Sens. Actuators B Chem.* **2019**, *294*, 253-262.

(66) Hussein, M. A.; Ganash, A. A. and Alqarni, S. A. Electrochemical sensor-based gold nanoparticle/poly(aniline-co-o-toluidine)/grapheme oxide nanocomposite modified electrode for hexavalent chromium detection: a real test sample. *Polym.-Plast. Technol. Mater.* **2019**, *58*, 1423-1436.

(67) Janik, P.; Zawisza, B.; Talik, E. and Sitko, R. Selective adsorption and determination of hexavalent chromium ions using graphene oxide modified with amino silanes. *Microchim. Acta* **2018**, *185*, 1-8.

(68) Karthika, A.; Nikhil, S.; Suganthi, A. and Rajarajan, M. A facile sonochemical approach based on graphene carbon nitride doped silver molybdate immobilized nafion for selective and sensitive electrochemical detection of chromium (VI) in real sample. *Adv. Powder Technol.* **2020**, *31*, 1879-1890.

(69) Wang, Y.; Ma, J. X.; Zhang, Y.; Xu, N. and Wang, X. L. A series of cobalt-based coordination polymer crystalline materials as highly sensitive electrochemical sensors for detecting trace Cr (VI), Fe (III) ions, and ascorbic acid. *Cryst. Growth Des.* **2021**, *21*, 4390-4397.

(70) Xin, X.; Hu, N.; Ma, Y.; Wang, Y.; Hou, L.; Zhang, H. and Han, Z. Polyoxometalate-based crystalline materials as a highly sensitive electrochemical sensor for detecting trace Cr (VI). *Dalton Trans.* **2020**, *49*, 4570-4577.

(71) Dashtian, K.; Ghaedi, M. and Hajati, S. Photo-sensitive $Pb_5S_2I_6$ crystal incorporated polydopamine biointerface coated on nanoporous TiO_2 as an efficient signal-on photoelectrochemical bioassay for ultrasensitive detection of Cr (VI) ions. *Biosens. Bioelectron.* **2019**, *132*, 105-114.

(72) Li, M.; He, R.; Wang, S.; Feng, C.; Wu, H. and Mei, H. Visible light driven photoelectrochemical sensor for chromium (VI) by using BiOI microspheres decorated with metallic bismuth. *Microchim. Acta* **2019**, *186*, 1-8.

(73) Chen, R.; Tang, R. and Chen, C. Photoelectrochemical detection of chromium (VI) using layered MoS_2 modified BiOI. *J. Chem. Sci*. **2020**, *132*, 1-9.

(74) Wang, P.; Cao, L.; Wu, Y.; and Di, J. A cathodic photoelectrochemical sensor for chromium (VI) based on the use of PbS quantum dot semiconductors on an ITO electrode. *Microchim. Acta* **2018**, *185*, 1-7.

(75) Li, M.; Zhang, G.; Feng, C.; Wu, H. and Mei, H. Highly sensitive detection of chromium (VI) by photoelectrochemical sensor under visible light based on Bi SPR-promoted $BiPO_4$/BiOI heterojunction. *Sens. Actuators B Chem.* **2020**, *305*, 127449 (1-33).

(76) Zhang, G.; Cheng, D.; Li, M.; Feng, C.; Wu, H. and Mei, H. Enhanced the photoelectrochemical performance of Bi_2XO_6 (X = W, Mo) for detecting hexavalent chromium by modification of CuS. *J. Environ. Sci.* **2021**, *103*, 185-195.

(77) Qiao, J.; Wang, Y.; Liang, Q.; Dong, S.; Zeng, Z. and Shao, S. A Photoelectrochemical sensor based on TiO_2 nanotube arrays decorated with nickel-cobalt layered double hydroxides for the effective and sensitive detection of chromium (VI). *ACS Appl. Nano Mater.* **2022**, *5*, 5535-5543.

(78) Zhang, G.; Chen, D.; Li, N.; Xu, Q.; Li, H.; He, J. and Lu, J. Fabrication of Bi_2MoO_6/ZnO hierarchical heterostructures with enhanced visible-light photocatalytic activity. *Appl. Catal. B: Environ.* **2019**, *250*, 313-324.

(79) Nan, J.; Guo, S.; Alhashmialameer, D.; He, Q.; Meng, Y.; Ge, R.; El-Bahy, S.M.; Naik, N.; Murugadoss, V.; Huang, M. and Xu, B.B. Hydrothermal microwave synthesis of Co_3O_4/In_2O_3 nanostructures for photoelectrocatalytic reduction of Cr (VI). *ACS Appl. Nano Mater.* **2022**, *5*, 8755-8766.

(80) Morshidy, H.Y.; Abd El-Fattah, Z.M.; Abul-Magd, A. A.; Hassan, M.A. and Mohamed, A.R. Reevaluation of Cr^{6+} optical transitions through Gd_2O_3 doping of chromium-borate glasses. *Opt. Mater.* **2021**, *113*, 110881 (1-10).

(81) Caiut, J.; Floch, N.; Messaddeq, Y.; Lima, O.J.D.; Rocha, L.A.; Ciuffi, K.J.; Nassar, E.J.; Friedermann, G.R. and Ribeiro, S.J. Cr^{3+} doped Al_2O_3 obtained by non-hydrolytic sol-gel methodology. *J. Braz. Chem. Soc.* **2019**, *30*, 744-751.

(82) Li, S.; Yan, R.; Cai, M.; Jiang, W.; Zhang, M. and Li, X. Enhanced antibiotic degradation performance of $Cd_{0.5}Zn_{0.5}S$/Bi_2MoO_6 S-scheme photocatalyst by carbon dot modification. *J. Mater. Sci. Technol.* **2023**, *164*, 59-67.

(83) Li, S.; Cai, M.; Wang, C. and Liu, Y. Ta_3N_5/CdS core-shell S-scheme heterojunction nanofibers for efficient photocatalytic removal of antibiotic tetracycline and Cr (VI): performance and mechanism insights. *Adv. Fiber Mater.* **2023**, *5*, 994-1007.

(84) Huang, J.; Tan, G.; Ren, H.; Yang, W.; Xu, C.; Zhao, C. and Xia, A. Photoelectric activity of a Bi_2O_3/$Bi_2WO_{6-x}F_{2x}$ heterojunction prepared by a simple one-step microwave hydrothermal method. *ACS Appl. Mater. Interfaces* **2014**, *6*, 21041-21050.

(85) Thakur, N., Chaturvedi, A., Mandal, D. and Nagaiah, T.C. Ultrasensitive and highly selective detection of dopamine by a NiFeP based flexible electrochemical sensor. *Chem. Commun.* **2020**, *56*, 8448-8451.

(86) Kresse, G. and Furthmuller, J. Efficient interative schemes for ab initio total-energy calculations using a plane-wave basis set. *Phys. Rev. B* **1996**, *54*, 11169 (1-18).

(87) Kresse, G. and Furthmuller, J. Efficiency of ab-initio total energy calculations for metals and semiconductors using a plane-wave basis set. *Comput. Mater. Sci.* **1996**, *6*, 15-50.

(88) Kresse, G. and Hafner, J. Ab initio molecular dynamics for liquid metals. *Phys. Rev. B* **1993**, *47*, 558 (1-8).

(89) Kresse, G. and Hafner, J. Ab initio molecular-dynamics simulation of the liquid-metal-amorphous-semiconductor transition in germanium. *Phys. Rev. B* **1994**, *49*, 14251 (1-20).

(90) Perdew, J.P., Burke, K. and Ernzerhof, M. Generalized gradient approximation made simple. *Phys. Rev. Lett*. **1996**, *77*, 3865-3868.

(91) Monkhorst, H.J. and Pack, J.D. Special points for brillouin-zone integrations. *Phys. Rev. B* **1976**, *13*, 5188 (1-5).

(92) Grimme, S., Antony, J., Ehrlich, S. and Krieg, H. A consistent and accurate ab initio parametrization of density functional dispersion correction (DFT-D) for the 94 elements H-Pu. *J. Chem. Phys.* **2010**, *132*, 154104 (1-20).

(93) Tang, W., Sanville, E. and Henkelman, G. A grid-based Bader analysis algorithm without lattice bias**.** *J. Phys. Condens. Matter*. **2009**, *21*, 084204 (1-7).

(94) Ahamed, S.T.; Ghosh, A.; Show, B. and Mondal, A. Fabrication of n-TiO_2/p-CuO thin-film heterojunction for efficient photocatalytic degradation of toxic organic dyes and reduction of metal ions in solution. *J. Mater. Sci. Mater. Electron.* **2020**, *31*, 16616-16633.

(95) Ren, Z.; Liu, X.; Zhuge, Z.; Gong, Y. and Sun, C.Q. $MoSe_2$/ZnO/ZnSe hybrids for efficient Cr (VI) reduction under visible light irradiation. *Chinese J. Catal.* **2020**, *41*, 180-187.

(96) Li, M.; Fu, H.; Wang, B.; Cheng, J.; Hu, W.; Yin, B.; Peng, P.; Zhou, S.; Gao, X.; Jia, C. and Guo, X. Dipole-modulated charge transport through PNP-type single-molecule junctions. *J. Am. Chem. Soc.* **2022**, *144*, 20797-20803.

(97) Hao, Y.; Deng, Z.; Zhao, Z. and Song, X. A facile synthesis of a highly efficient β-Bi_2O_3/$Bi_2O_2CO_3$ heterojunction with enhanced photocatalytic NO oxidation under visible light. *New J. Chem*. **2020**, *44*, 10989-10993.

(98) Qi, S.; Zhang, Y.; Zhang, R.; Liu, X. and Xu, H. First-principles and experiment investigation of Bi_2O_3/Bi_2WO_6 heterojunctions. *Colloids Interface Sci. Commun.* **2021**, *44*, 100502 (1-9).

(99) Murali, A.; Sarswat, P.K. and Free, M.L. Minimizing electron-hole pair recombination through band-gap engineering in novel ZnO-CeO_2-rGO ternary nanocomposite for photoelectrochemical and photocatalytic applications. *Environ. Sci. Pollut. Res.* **2020**, *27*, 25042-25056.

(100) Sharma, R., Khanuja, M., Sharma, S.N. and Sinha, O.P. Reduced band gap and charge recombination rate in Se doped α-Bi_2O_3 leads to enhanced photoelectrochemical and photocatalytic performance: theoretical and experimental insight. *Int. J. Hydrog. Energy* **2017**, *42*, 20638-20648.

CHAPTER 5

Asymmetric Harmonization of $CuWO_4$/CuO and Its rGO Blended Nanocomposite: Tuning the Electronic Relay to Optimize Advanced Water Electrolysis in Alkaline Medium

Objectives

Optimization of electronic properties to enhance catalytic performance for improved water electrolysis in alkaline conditions

GRAPHICAL ABSTRACT

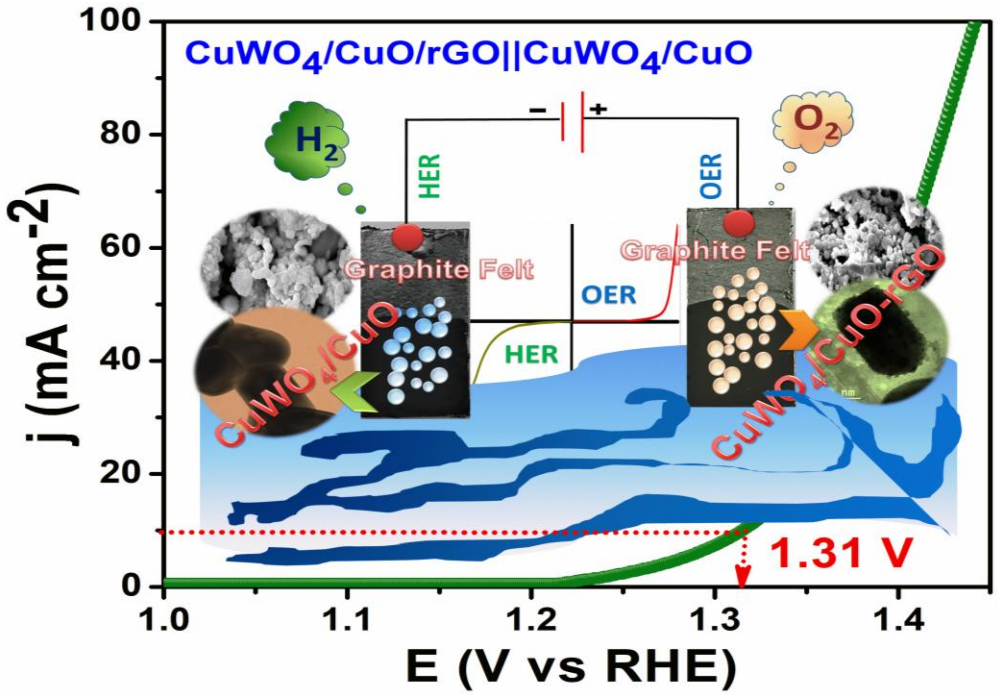

HIGHLIGHTS

- An emerging approach involving asymmetrically decorating electrodes, $CuWO_4$/CuO/GF (cathode) and $CuWO_4$/CuO-rGO/GF (anode), demonstrates the potential of cost effective catalysts in advancing water splitting.
- The morphology of the two distinct electrodes is crucial to their performance.
- $CuWO_4$/CuO/GF excels in HER, while $CuWO_4$/CuO-rGO/GF significantly enhances OER efficiency.
- It achieves an impressive current density of 10 mA cm^{-2} at a low cell voltage of 1.31 V, showing great potential for water electrolysis.

ABSTRACT

Affordable, high-performance electrocatalysts are crucial for advancing water electrolysis technology, which is essential for producing O_2 and H_2. A ground breaking approach is presented for developing a mixed morphological Cu-based $CuWO_4$/CuO heterostructure nanocomposite as a hydrogen evolution reaction (HER) catalyst and a reduced graphene oxide (rGO) blended $CuWO_4$/CuO nanocomposite as an oxygen evolution reaction (OER) catalyst. The distinct morphologies of CuO and $CuWO_4$, resulting from the different Cu-salt and synthesis processes, play a crucial role in optimizing the reaction kinetics. The exceptional OER activity of rGO blended $CuWO_4$/CuO nanocomposite is attributed to the exposed active sites and the faster electron transfer, facilitated by the cumulative effect of rGO. Remarkably, $CuWO_4$/CuO demonstrates remarkably low overpotential (η_{10}) of only 16 mV, accompanied by small Tafel slope of 16.33 mV dec^{-1} for HER. Meanwhile, $CuWO_4$/CuO-rGO exhibits low overpotential of 161 mV with small Tafel slope of 60.82 mV dec^{-1} for OER at 10 mA cm^{-2}. Inspired by these findings, we assemble an asymmetric alkaline electrolyzer, $CuWO_4$/CuO-rGO||$CuWO_4$/CuO, which achieves a water-splitting current of 10 mA cm^{-2} with just 1.31 V and displays impressive long-term stability at room temperature (28 °C). Furthermore, the cumulative effect of $CuWO_4$, CuO, and rGO highlights the potential of $CuWO_4$/CuO-rGO (anode)||$CuWO_4$/CuO (cathode) as a cost-effective catalyst candidate for water electrolysis. This study aims to demonstrate the contribution of unique morphologies to the efficiency of water splitting, highlighting the potential of asymmetrically decorated electrodes in advancing sustainable energy technologies.

KEYWORDS: rGO blended $CuWO_4$/CuO nanocomposite, cumulative effect, HER, OER, Overall Water Splitting.

5.1. INTRODUCTION

The escalating depletion of fossil fuels has propelled the search for viable alternative energy sources[1-3]. Hydrogen (H_2), known for its high gravimetric energy density (142 MJ kg^{-1}), is regarded as a promising clean energy carrier[4] for the future. One environmentally friendly method for H_2 production is water electrolysis, a process consisting of two fundamental half-reactions: OER and HER. This approach offers a greener means of generating H_2 without carbon emissions. In recent times, electrochemical water electrolysis has emerged as a focal point in the quest for efficient H_2 and O_2 production.[5-9] attracting considerable attention. However, a significant challenge lies in the sluggish kinetics of both the OER[10-15] and HER,[16-22] resulting in substantial overpotentials (η). These challenges have posed major impediments to the widespread adoption of water electrolysis for H_2O splitting, prompting the urgent need to develop highly efficient and durable electrocatalysts. Consequently, considerable efforts have been directed toward developing stable and cost-effective catalysts to address these limitations in water electrolysis. Most of these alternative electrocatalysts demonstrate exceptional OER performance in alkaline mediums and HER performance in acidic conditions, restricting their practical applicability. Currently, noble metals like Pt/C for HER[17] and IrO_2/RuO_2 for OER[23] remain preferred choices due to their activity across a wide pH range. However, challenges such as scarcity, high costs, susceptibility to poisoning, and limited durability impede their wide-range, long-term use. Recent research has been dedicated to the development of efficient electrocatalysts, encompassing various materials such as metal oxides[13] (hydroxides),[24] chalcogenides,[25-27] phosphides,[28] nitrides,[29] carbides,[30] noble-metal-based materials,[31-33] and diverse composites,[34,35] all of which have garnered significant interest for their promising catalytic performance. Over the past few decades, a substantial number of noble-metal-free catalysts have been developed for HER and OER. Among these, transition metal oxides have garnered considerable research interest owing to their abundance, tunable valence states, and excellent surface reaction kinetics.[36,37]

Copper tungsten oxide nanostructures have versatile applications as catalysts, sensors, and electrochemical performers. They catalyze photodegradation and water oxidation and find use in various sensing tasks. Integration with materials like reduced graphene oxide (rGO), polypyrrole (PPy), and carbon nanosheets enhances their functionality, enabling applications in sensors, photocatalysis, and solar cells. Studies have highlighted the impressive bifunctional electrocatalytic properties of pure $CuWO_4$ materials, showing their potential in applications such as supercapacitors and alkaline water electrolysis.[38] Additionally, investigations into copper tungsten oxide@reduced

graphene oxide nanocomposites have explored their enhanced electrocatalytic performance for both OER and HER in both alkaline and acidic media.[39] Recently, interest in copper-based oxides as OER catalysts has been increasing owing to their advantageous properties, including different oxidation states, non-toxicity, and abundance.[40] These oxides are recognized as effective oxygen carriers, capable of undergoing reversible transformations between Cu^{+} and Cu^{2+}. This unique feature allows precise control over the electronic environment of adjacent atoms, facilitating the mobility of oxygen atoms to surface-active sites during the OER.[41] Moreover, Cu-based oxides exhibit significant HER activity due to their low energy barriers for hydrogen adsorption.[42] Cu-based oxides have garnered interest as versatile catalysts for OER, HER, and bifunctional water splitting.[43,44] However, it is important to note that Cu-based materials have not yet achieved the same level of electrochemical performances as their Ni, Co, or Fe-based counterparts.[45] Hence, there is a growing need to identify effective Cu-based electrocatalysts with optimized electronic structures that can match or even surpass the performance of well-established catalysts.

To this end, Cu-based composites have been developed to enhance electrochemical OER and HER performance through their cumulative effects.[46,47] Additionally, structural modifications of Cu-oxide materials have been explored to fine-tune their electrochemical activity, exemplified by Zhou et al.'s work with hierarchical CuO_x/Co_3O_4 nanorods on Cu foam, which demonstrated remarkable efficiency as a bifunctional electrocatalyst.[48] Bifunctional OER and HER activities of CeO_2/CuO composites, influenced by cooperative redox properties and the presence of oxygen vacancies, were reported.[49] CuO supported $CuWO_4$ nanocomposites with unique structural properties enhancing active sites have been less studied till date for the overall water electrolysis, which may give the right path of methodology in a lower potential region.

Reduced graphene oxide is a two dimensional material with exceptional properties such as high conductivity, large capacitance, and long-term stability, as it exists as a 2D layer of sp^2-hybridized carbon atoms arranged in a hexagonal lattice.[50] rGO serves as excellent catalyst support, aiding hybridization, preventing nanoparticle aggregation, enhancing electronic conductivity, accelerating charge transfer, improving catalyst dispersion, and modulating electronic structures that convey signals through the active sites of semiconductor/graphene composites. The interfacial band structure of rGO blended heterostructure nanocomposite plays an important role for OER activities.[51]

This study explores the use of asymmetrically assembled electrodes, emphasizing Cu-based materials with distinct morphologies for enhanced efficiency. Monoclinic CuO, obtained from $CuCO_3.Cu(OH)_2$, develops into a spherical urchin-like structure, while triclinic $CuWO_4$, synthesized

from $CuSO_4.5H_2O$, exhibits dendritic growth resembling coral reefs. Incorporating rGO into $CuWO_4$/CuO enhances electrocatalytic performance by introducing oxygen vacancies. The unique morphologies of these materials optimize reaction kinetics for HER and OER, significantly improving water-splitting efficiency. The development of a mixed morphological heterostructure nanocomposite, $CuWO_4$/CuO, was designed for cathode application, while an rGO-blended $CuWO_4$/CuO nanocomposite was developed for anode application in the overall water electrolysis system.

Moreover, during the solvothermal synthesis of the rGO-blended $CuWO_4$/CuO nanocomposite calcinated at 400 °C, there is a risk of breaking the C-C linkage of rGO, which may demean the efficiency of the HER. To address this, we designed an effective electrode using the reflux method, in which rGO was incorporated into the reaction mixture of the $CuWO_4$/CuO heterostructure nanocomposite, with the expectation that the mixed metal oxide would be wrapped in the rGO layer-like structure. However, the resulting electrochemical behavior was suboptimal, suggesting that the anisotropy may not be suitable for HER and OER activities in alkaline medium. The expected lattice deformation to create a truly heterogeneous catalyst did not occur, affecting the interfacial charge separation essential for enhancing electrocatalytic behavior. To enhance electrocatalytic efficiency for overall water electrolysis, further modifications are planned to design an effective electrode and cell structure, such as $CuWO_4$/CuO-rGO/GF (anode)||$CuWO_4$/CuO/GF (cathode). Moreover, graphite felt (GF) was used as a catalyst substrate instead of nickel foam (NF) for overall water splitting. The electrolyzer exhibited promising performance in overall water splitting, showcasing minimal overpotential, selective OER, and enduring stability over extended operational periods. This innovative approach is expected to introduce a new concept for synthesizing highly efficient catalysts for overall water electrolysis.

5.2. EXPERIMENTAL SECTION

5.2.1. Materials. All the chemicals were used as received. Analytical grade copper carbonate hydroxide ($CuCO_3.Cu(OH)_2$), copper sulphate ($CuSO_4 \cdot 5H_2O$), Sodium tungstate ($Na_2WO_4.2H_2O$), Ethylene glycol ($C_2H_6O_2$), Ethanol (EtOH), Commercial Pt/C catalyst (20 wt % Pt), Nafion ($C_7HF_{13}O_5S \cdot C_2F_4$), KOH were purchased from Sigma-Aldrich. All water used throughout the experiments was demineralized and ultrafiltered by a Millipore Milli-Q system (resistivity >18.2 MΩ, TOC < 5 ppb).

5.2.2. Synthesis of Materials

5.2.2.1. Synthesis of CuO nanoparticles. A solution was prepared by initially mixing 2 mmol of copper carbonate hydroxide with 100 mL of ethylene glycol, followed by stirring to ensure thorough mixing and dispersion. Subsequently, 5 g of finely crushed NaOH was added to the solution, and the mixture was kept under continuous magnetic stirring for 4 h until a homogeneous suspension was achieved. This well-homogenized mixture was then subjected to reflux at 80 °C for 5 hours, resulting in the formation of a red precipitate of Cu_2O. After that the mixture was allowed to naturally cool to room temperature, and the black precipitate was separated from the solution through centrifugation, thoroughly washed with deionized water and absolute ethanol, and subsequently air-dried. Further the red residue of Cu_2O was calcined at 400 °C for half an hour to get CuO nanoparticles.

5.2.2.2. Synthesis of $CuWO_4$ nanocomposite. $CuWO_4$ nanocomposite was synthesized using a controlled solvothermal process. Initially, 2 mmol of $CuSO_4 \cdot 5H_2O$ was mixed with 15 mL of ethylene glycol, followed by 20 minutes of stirring. Subsequently, a solution containing 2 mmol of $Na_2WO_4 \cdot 2H_2O$ in 15 mL of ethylene glycol was gently added to the previous mixture and stirred for an another 20 minutes followed by additional ultrasonication of 1 h for thorough mixing. The resulting solution was then transferred into a sealed 100 mL Teflon-lined autoclave and heated at 180 °C for 12 hours. After cooling to room temperature, the mixture was filtered, followed by three cycles of washing with distilled water and ethanol. Finally, the solid residue was allowed to air dry at room temperature and calcined at 400 °C for half an hour.

5.2.2.3. Synthesis of $CuWO_4$/CuO Heterostructure Nanocomposite. $CuWO_4$/CuO nanocomposites were synthesized by a controlled solvothermal process. Initially, 2 mmol of $CuSO_4.5H_2O$, mixed with 15 mL of ethylene glycol, was stirred for 20 minutes. A solution containing 2 mmol of $Na_2WO_4.2H_2O$ mixed with 15 mL of ethylene glycol was stirred for another 30 minutes. To this mixture, 2 mmol of CuO was added, followed by 1 h of stirring and 3 h of ultrasonication. The solution was then heated in a sealed autoclave at 180 °C for 12 h. After cooling, the mixture was filtered and washed to obtain the desired nanocomposite, which was then calcinated at 400 °C for 30 min. The aim was to create a nanocomposite with materials of varied morphologies to introduce significant defects into the solid-state structure (**Scheme 5.1a**).

5.2.2.4. Synthesis of rGO Blended $CuWO_4$/CuO Nanocomposite. In the similar pathway for $CuWO_4$/CuO nanocomposite, the process was extended by adding 10 wt % of rGO to the well-mixed solution, followed by 1 h of stirring and 3 h of ultrasonication. The resulting organic-inorganic heterostructure nanocomposite system, referred to as rGO blended $CuWO_4$/CuO nanocomposite

($CuWO_4$/CuO-rGO), was produced by heating the mixture solution into a sealed 100 mL Teflon-lined stainless steel autoclave at 180 °C for 12 h, followed by cooling and the same washing procedure as previously outlined, followed by calcination at 400 °C for 30 min (**Scheme 5.1b**).

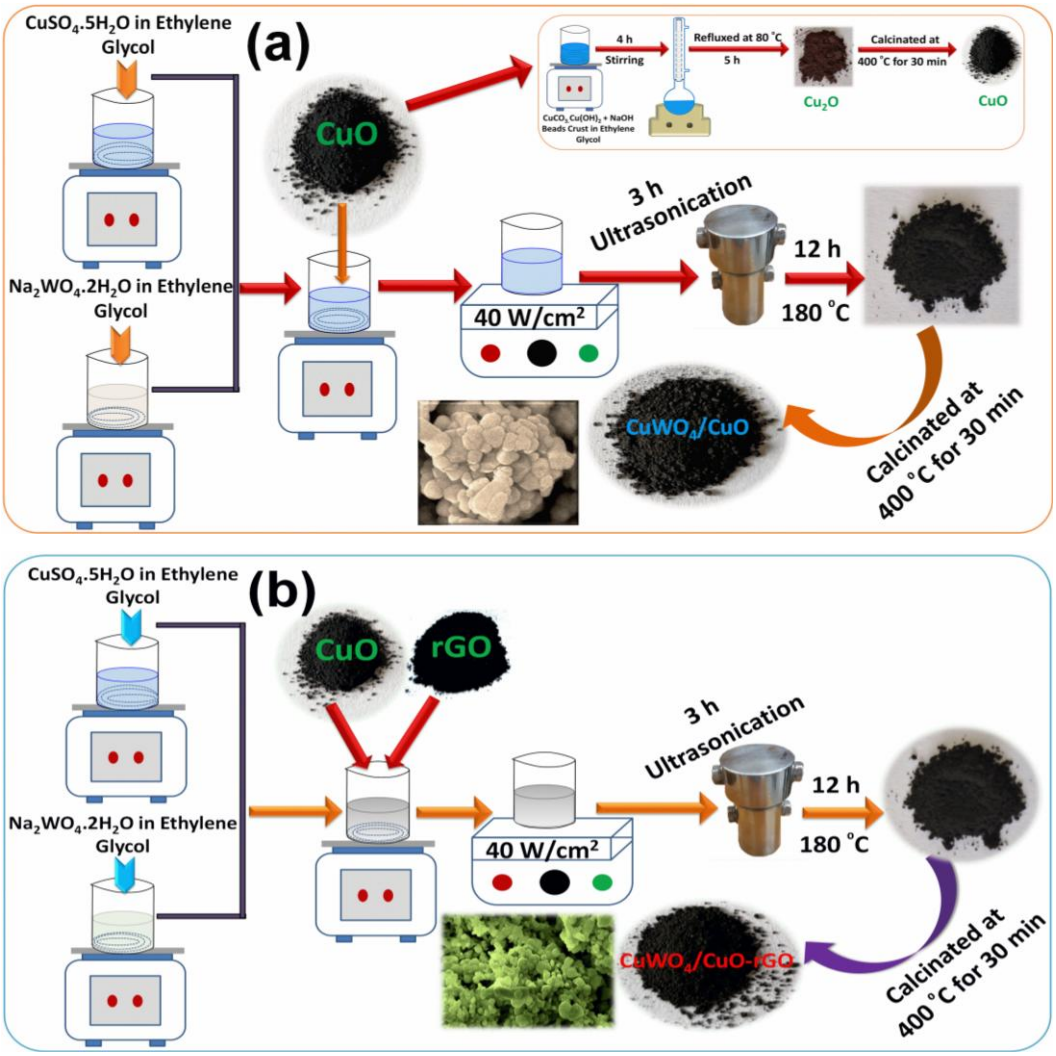

Scheme 5.1. Pictorial representation of the synthesis of (a) $CuWO_4$/CuO and (b) $CuWO_4$/CuO-rGO through a solvothermal technique.

5.2.3. Characterization and Instrumentation. The crystallinity and phase formation of the as-prepared samples were investigated by the Philips PW 1140 parallel beam X-ray diffractometer using monochromatic Cu-Kα radiation (λ = 1.540598 Å). The surface morphologies and internal structure of the catalysts were characterized using field emission scanning electron microscopy (FE-SEM

JEOL JSM 7100F) with energy dispersive X-ray spectroscopy (EDX) and transmission electron microscopy (HR-TEM-JEOL JEM-2100) operated at 200 kV. The sampling was done by a simple drop cast of $CuWO_4$/CuO and $CuWO_4$/CuO-rGO solution dispersed in ultra-pure water onto a carbon-coated 300 mesh sized Cu grid (purchased from Ted Pella), and the sample grid was stored in vacuum desiccator before HR-TEM analysis. In order to determine the composition of the samples, selected area electron diffraction (SAED) pattern was used. X-ray photoelectron spectra (XPS, Perkin-Elmer Physical Electronics 5600 spectrometer) were recorded to identify the chemical states of surface atoms and to confirm the existence of rGO along with $CuWO_4$/CuO. The optical properties of the samples were studied by a JASCO V-730 UV-Vis spectrophotometer, and the band gap energies of different composites were calculated using Tauc's plots. Raman analysis was done on HORIBA XploRA Plus, Japan under laser excitation at 532 nm. The specific surface area (S_{BET}), pore size distribution and pore volume of the catalysts were measured by the N_2 sorption isotherms performed in an Autosorb iQ_2 gas sorption instrument (Quantachrome Instruments, USA). Prior to N_2-sorption experiments, all the samples were degassed at 100 °C under vacuum in the attached FLOVAC Degasser sample preparation unit. The pore volume and pore size distribution were estimated by the Non-Local Density Functional Theory (2D-NLDFT) method. After stability test, the sample was collected from the GCE surface through soft scratching and washed several times with distilled water (30 times). It was then dried and taken for further characterisation of XRD, XPS, HR-TEM, FE-SEM to study the stability of the catalyst. The electrochemical impedance spectroscopy (EIS) was recorded at an amplitude of 5 mV from 5 mHz to 100 kHz in 1.0 M KOH solution.

5.2.4. Sample Preparation for Optical Analysis. UV-Vis measurement and photoluminescence (PL) spectral analyses of $CuWO_4$, CuO, $CuWO_4$/CuO, and $CuWO_4$/CuO-rGO were carried out by dispersing these solid materials in H_2O separately.

5.2.5. Calculation of ECSA, R_f, Mass activity, and TOF: Determination of Electrochemical active surface area and Roughness factor. The electrochemical active surface area (ECSA) of all electrocatalysts were calculated from the double-layer capacitance (C_{dl}) according to the following equation:

$$\mathrm{ECSA} = \frac{C_{dl}}{C_s} \qquad \text{Eq. 5.1}$$

Where C_s is the ideal specific capacitance of a smooth planar surface made of the same material per unit area under identical electrolyte conditions. In our estimation of surface area, we have used the

general specific capacitance of C_s = 40 μF cm^{-2}.[52] The roughness factor (R_f) of the materials were determined by the equation:

$$R_f = \frac{ECSA}{GSA} \quad \text{Eq. 5.2}$$

Where the geometric surface area (GSA) of the electrode is 0.125 cm^2.

The mass activity (A g^{-1}) of all catalysts was obtained from the measured current density j (mA cm^{-2}) by the catalyst loading m (mg cm^{-2}).[53] For OER, it was calculated at η = 260 mV whereas η = 50 mV used for HER.

$$\text{Mass Activity} = \frac{j}{m} \quad \text{Eq. 5.3}$$

For OER, the turnover frequency was determined through the following equation: [54]

$$TOF = \frac{js}{4Fn} \quad \text{Eq. 5.4}$$

Where, j is the obtained current density (A cm^{-2}) at η of 260 mV, S is the surface area (cm^2) of the electrode with active catalyst, the number 4 suggests 4 electrons transfer in OER, F is Faraday constant (96485 C mol^{-1}), and n is the number of moles of the catalytic material on the working electrode. It represents the number of moles of oxygen molecules evolved per second per mole of catalyst, providing valuable perception about the per-site activity of the catalysts.

Subsequently, TOF for HER can be calculated with the equation below: [55]

$$TOF = \frac{I}{2Fn} \quad \text{Eq. 5.5}$$

Where, I is the current of polarization curve in A at η of 50 mV during LSV measurements in 1 M KOH medium. Here, the factor 2 represents the required two electrons for the formation of one hydrogen molecule in HER.

$$n = \frac{Q}{2F} \quad \text{Eq. 5.6}$$

Q is the voltammetric charge (C); ν refers to the scan rate (V s^{-1}).

$$Q = \frac{\text{Integrated CV Area}}{\nu} \quad \text{Eq. 5.7}$$

From the above equations, we come to conclusion the following equation

$$TOF = \frac{I}{Q} \quad \text{Eq. 5.8}$$

5.2.6. Electrochemical cell set up. All electrochemical measurements were carried out by an electrochemical workstation (CHI660E, USA) in a standard three-electrode cell with a glassy carbon electrode (GCE, 3 mm in diameter) as the working electrode, an Ag/AgCl (Sat. KCl) electrode as the reference electrode, and Pt wire as the counter electrodes using N_2 saturated 1.0 M KOH electrolyte.

5.2.7. Electrode Preparation: First, the GCE was sequentially polished with 0.5 and 0.05 μm alumina powder which was subsequently cleaned with H_2O under sonication for 20 min. For both OER and HER, the working electrode was prepared as follows: ~ 3 mg of catalyst was ultrasonically dispersed into the mixture of 1 mL of H_2O and 40 μL of nafion (0.5%) for 1 h to generate a homogeneous ink. Then, 7 μL of the above catalyst ink was drop-casted on the prepolished glassy carbon disk surface of GCE which resulted in a catalyst loading 0.168 mg cm^{-2}. Finally the prepared electrode was air-dried for 3 h at room temperature for all electrochemical measurements.

We have used a non-glass based cell which was made of fluorinated ethylene propylene (FEP) to avoid the interference of impurities from the glass cell in alkaline electrolyte. As during electrochemical reaction, the leaching of glass from glass cell may affect on the catalytic activity of electrocatalyst. Additionally, prior to starting all measurements, the cell and all glassware were thoroughly cleaned through storing overnight in concentrated H_2SO_4 in order to eliminate all metals and organic contaminants. Then, all were boiled and washed several times with H_2O to make sure the cleanness of the system.

5.3. RESULTS AND DISCUSSION

5.3.1. MATERIAL CHARACTERIZATION

5.3.1.1. PXRD analysis. The structural information of the synthesized catalysts was evaluated through Powder X-Ray diffraction (PXRD) analysis, as shown in Figures 5.1. The PXRD pattern of $CuWO_4$ nanoparticles shows peaks at 19.02°, 22.94°, 23.56°, 24.13°, 25.96°, 28.70°, 30.15°, 32.12°, 34.34°, 35.66°, 36.87°, 38.59°, 41.08°, 42.92°, 48.72°, 53.26°, 54.39°, 59.61°, 63.94°, 66.54°, and 67.67° corresponding to the (100), (110), (0-11), (011), (-1-11), (111), (1-11), (120), (0-21), (002), (-120), (-102), (-121), (130), (-202), (-122), (310), (132), (1-32), and (3-11) planes of the triclinic phase of $CuWO_4$ (JCPDS No. 73-1823)[56] and are shown in Figure 5.1d.

Figure 5.1e shows the PXRD plot of CuO nanoparticles. The diffraction peaks at 32.51°, 35.54°, 38.90°, 46.26°, 48.72°, 51.34°, 53.49°, 58.27°, 61.53°, 66.22°, 66.45°, 68.13°, 72.37°, and 75.25° for (110), (11-1), (200), (11-2), (20-2), (112), (020), (202), (11-3), (31-1), (310), (220), (311) and (22-2) planes were related to the monoclinic phase of CuO (JCPDS No. 48-1548).[57] The crystallite sizes of

$CuWO_4$ and CuO nanoparticles calculated by the Debye-Scherrer equation[58] are found to be 89.31and 60.23 nm, respectively. Figure 5.1a presents the PXRD pattern of rGO, showing a main peak at 2θ = 25.60° for the (002) plane and a less intense peak at 2θ = 44.83° for the (001) plane.[59] Figures 5.1b and c illustrate the PXRD patterns of $CuWO_4$/CuO and $CuWO_4$/CuO-rGO nanocomposites, confirming the presence of both $CuWO_4$ and CuO through their characteristic planes. However, the PXRD patterns of rGO blended $CuWO_4$/CuO nanocomposite do not show the characteristic diffraction peaks of rGO, likely due to its limited quantity and the disrupted regular stacks of rGO within the heterostructure.[60]

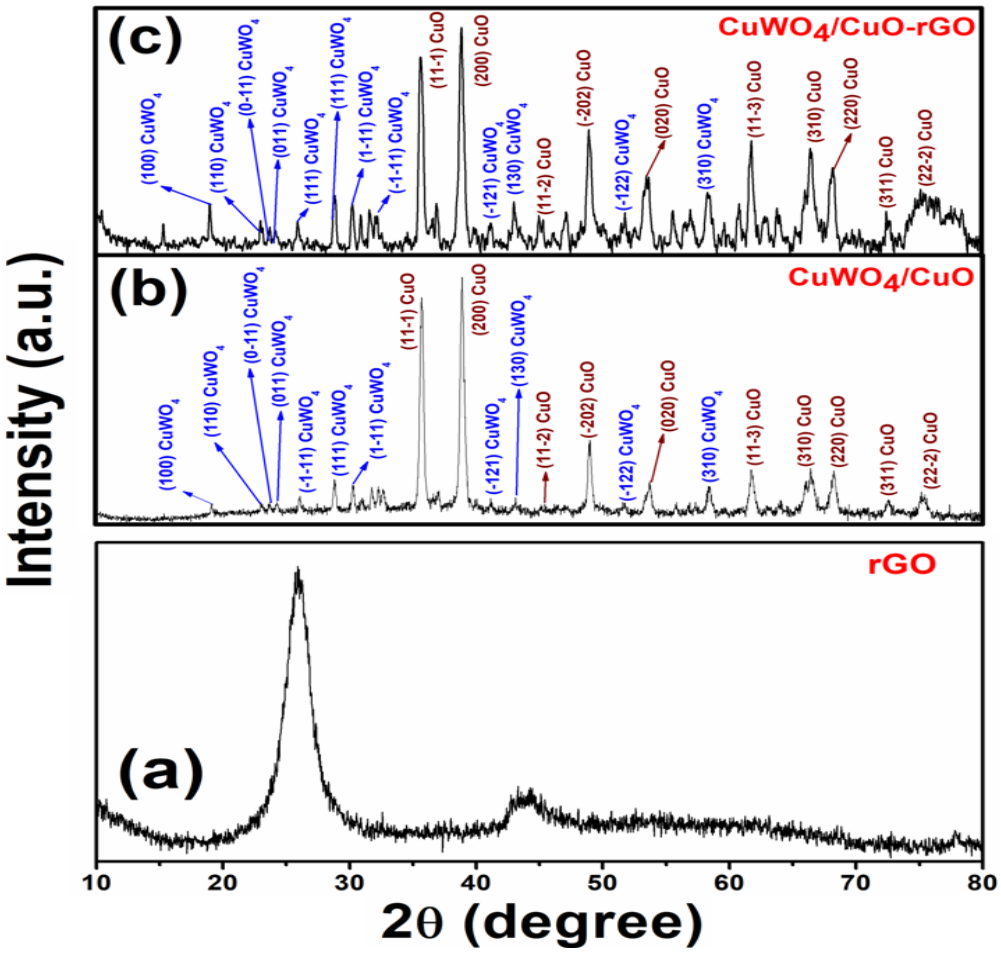

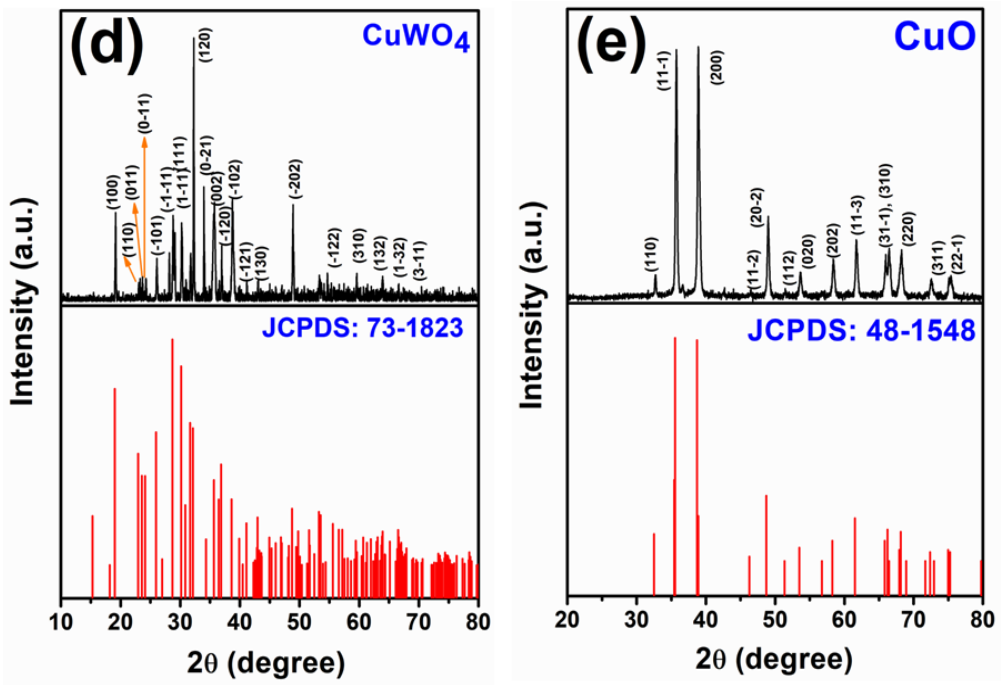

Figure 5.1. PXRD pattern of (a) rGO (b) $CuWO_4$/CuO and (c) rGO blended $CuWO_4$/CuO nanocomposite (d) $CuWO_4$ with their simulated pattern, and (e) CuO nanoparticles with simulated pattern.

5.3.1.2. XPS Analysis. X-ray photoelectron spectroscopy (XPS) was performed to investigate the surface chemical compositions and oxidation states of the $CuWO_4$/CuO and rGO blended $CuWO_4$/CuO nanocomposites. The high-resolution spectra of these samples, presented in Figures 5.2(b→e), were deconvoluted. Figure 5.2a demonstrates the full scan survey spectrum of the catalysts and the existence of Cu, W, and O in $CuWO_4$/CuO and Cu, W, O, and C in $CuWO_4$/CuO-rGO, respectively. In Figure 5.2b, the deconvolution of Cu 2p high-resolution XPS spectra reveals four distinct peaks at approximately 934.20, 942.63, 954.08, and 962.38 eV. These peaks are ascribed to Cu^{2+} species within the electronic structure of $CuWO_4$. Specifically, the peaks at 934.20 pertain to Cu $2p_{3/2}$, while those at 954.08 correspond to Cu $2p_{1/2}$, accompanied by distinct satellite peaks at 942.63 and 962.38 eV, collectively confirming the presence of Cu^{2+}.

In the high-resolution XPS spectra of W 4f as shown in Figure 5.2c, two discernible peaks emerge at approximately 35.34 and 37.43 eV, along with a very weak peak at around 41.08 eV. These peaks represent the spin-orbit splitting of W $4f_{7/2}$, W $4f_{5/2}$, and W $5p_{3/2}$ for the W^{6+} oxidation state, providing

further insight into the electronic configuration of the system.[61] The high-resolution O 1s spectra (Figure 5.2d) were analyzed to yield two peaks: a prominent peak at approximately 530.2 eV, characteristic of typical metal oxide, and a secondary shoulder peak at around 530.9 eV, associated with oxygen vacancies. Based on the core level C 1s XPS spectra of rGO blended $CuWO_4$/CuO nanocomposite (Figure 5.2e), the binding energies of 284.67, 285.42, 288.29, and 289.13 eV are attributed to sp^2 graphitic carbon, −C−O−, C=O, and −O−C=O functional groups, respectively, and the satellite peak at 293.04 eV may be due to electronic transition in core level.[62] Figure 5.2e depicts that the peak intensities related to oxygen-containing functional groups significantly diminished, while the sp^2 carbon bonds became more pronounced, suggesting that the majority of the oxygen-containing groups in GO have been removed.[59] The slight peak shift observed in the rGO-blended $CuWO_4$/CuO in comparison to $CuWO_4$/CuO may be attributed to the interaction of the $CuWO_4$/CuO heterostructure with the rGO surface, confirming that the $CuWO_4$/CuO nanocomposite was successfully stuck onto the rGO surface.

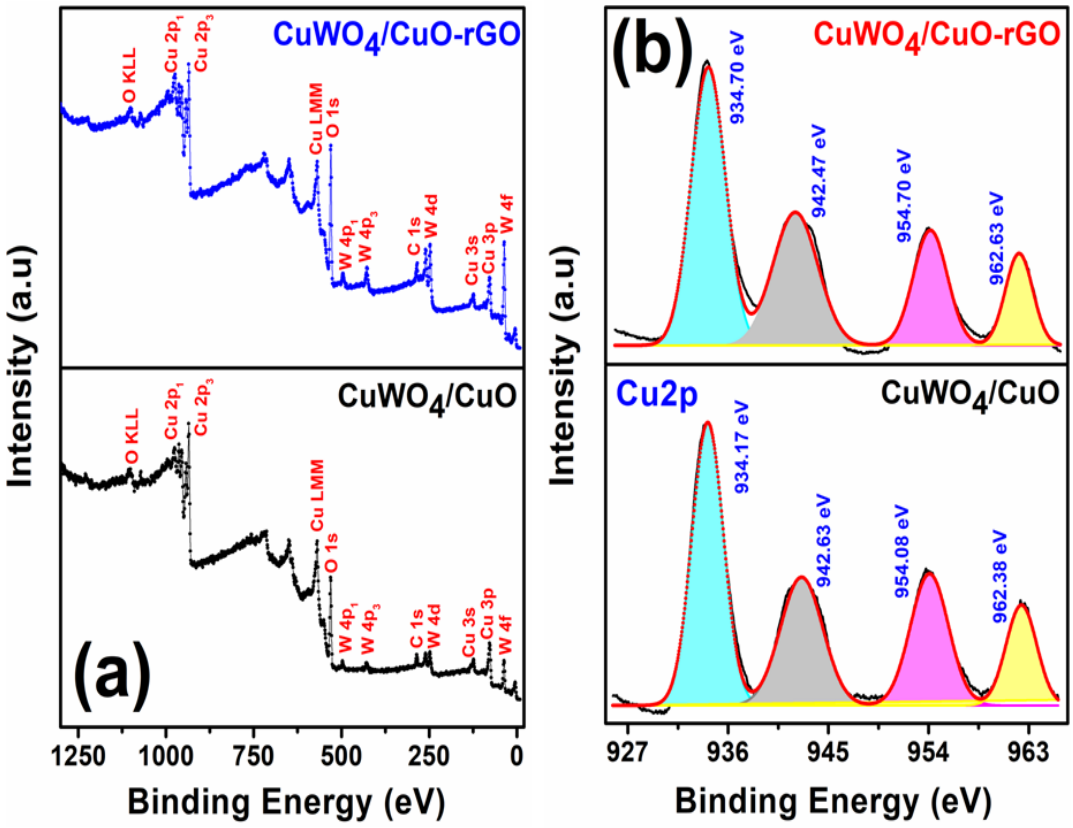

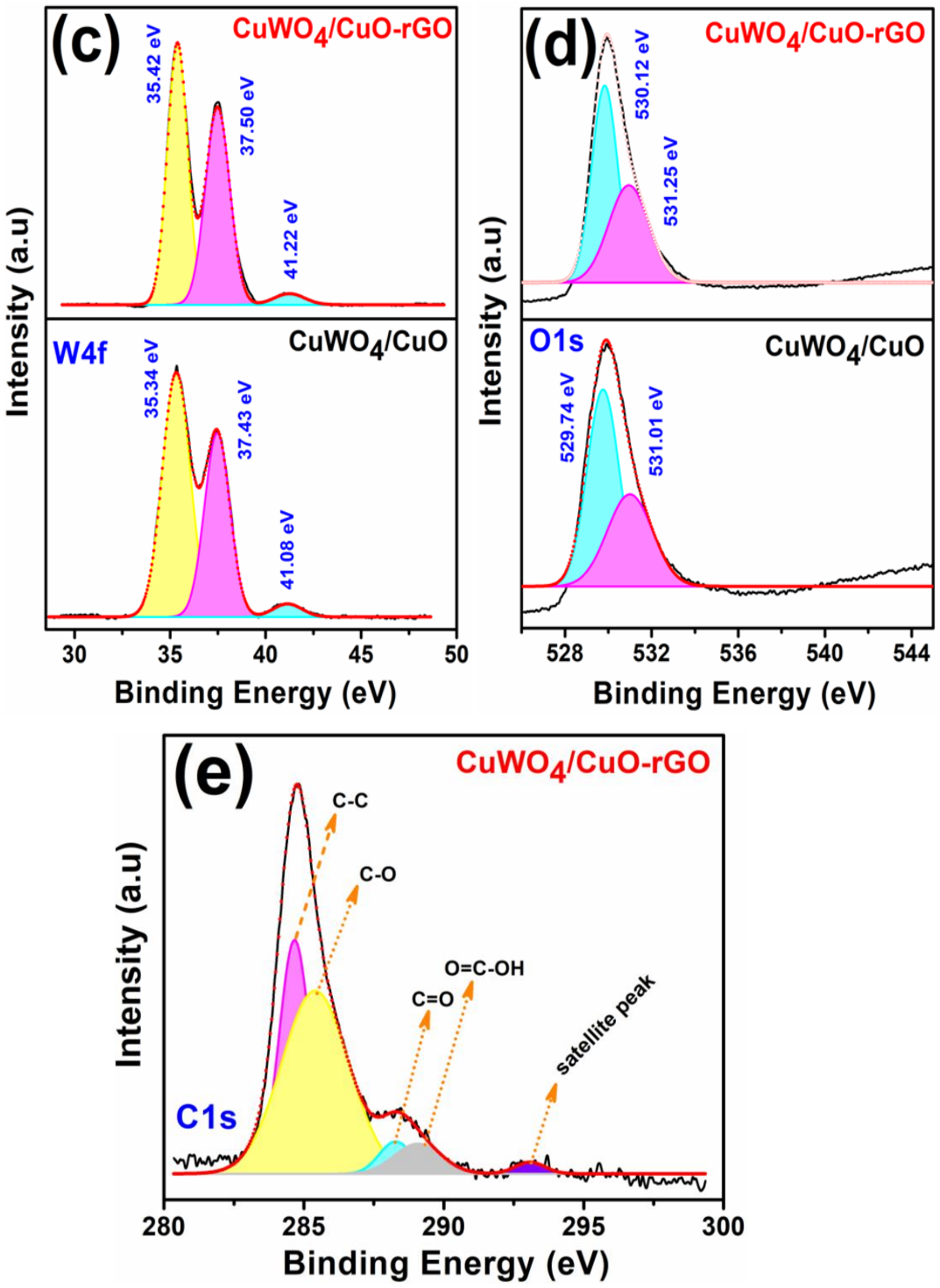

Figure 5.2. XPS spectra of $CuWO_4$/CuO, rGO blended $CuWO_4$/CuO nanocomposites (a) Sample survey (b) Cu 2p (c) W 4f (d) O 1s (e) C 1s.

5.3.1.3. Morphological Analysis. FE-SEM analysis was carried out to analyze the detailed structure, size, and morphology of the electrocatalysts. Figure 5.3a depicts FE-SEM images of triclinic $CuWO_4$, revealing dendritic growth resembling coral reefs, with an average particle size of ~ 92 nm. The FE-SEM image (Figure 5.3b) of monoclinic CuO illustrates uniformly distributed nanoparticles exhibiting nearly spherical urchin-like morphology, with a diameter of around 65 nm. The FE-SEM image of rGO is shown in Figure 5.3c. The FE-SEM image of $CuWO_4$/CuO, where $CuWO_4$ and CuO are well integrated, with the distinct morphologies of individual $CuWO_4$ and CuO metal oxides indicating a new, unique pattern of mixing, is displayed in Figure 3a. The respective triclinic and monoclinic phases of $CuWO_4$ and CuO are completely distorted. The high-magnification FE-SEM image reveals that two different crystallites are stacked together, with smaller crystallites attached to larger ones, creating surface roughness. This roughness suggests the presence of potential active sites for OER activity. The SEM images in Figures 3b illustrate the sheet-like morphologies of rGO blended $CuWO_4$/CuO heterostructure nanocomposites, indicating $CuWO_4$/CuO nanocomposites densely stacked on both sides of the lamellar rGO sheets, with some holes formed on the rGO sheet.[63,64] The $CuWO_4$/CuO mixed-phase system is well integrated onto the rGO sheet, creating visible active sites and enhanced surface roughness, which correlates with the observed electrolytic behavior. Additionally, the porous rGO sheet that arose from calcination at 400 °C provides a favorable environment for incorporating the mixed metal oxide. This porosity, clearly visible in the FE-SEM images, is responsible for the formation of defects in the rGO-blended mixed metal oxide.
These defects that enhance the OER activity may reduce the active sites for HER, and the electronic structure of rGO blended CuO/$CuWO_4$ nanocomposite prefers to adsorb oxygen intermediate adsorption over hydrogen intermediates. This selective site availability makes the CuO/$CuWO_4$-rGO nanocomposite more suitable for OER than HER, indicating that the fragmented, stacked rGO favors OER over the HER process. In the inset of Figures 5.3d and e, the particle sizes have also been calculated.

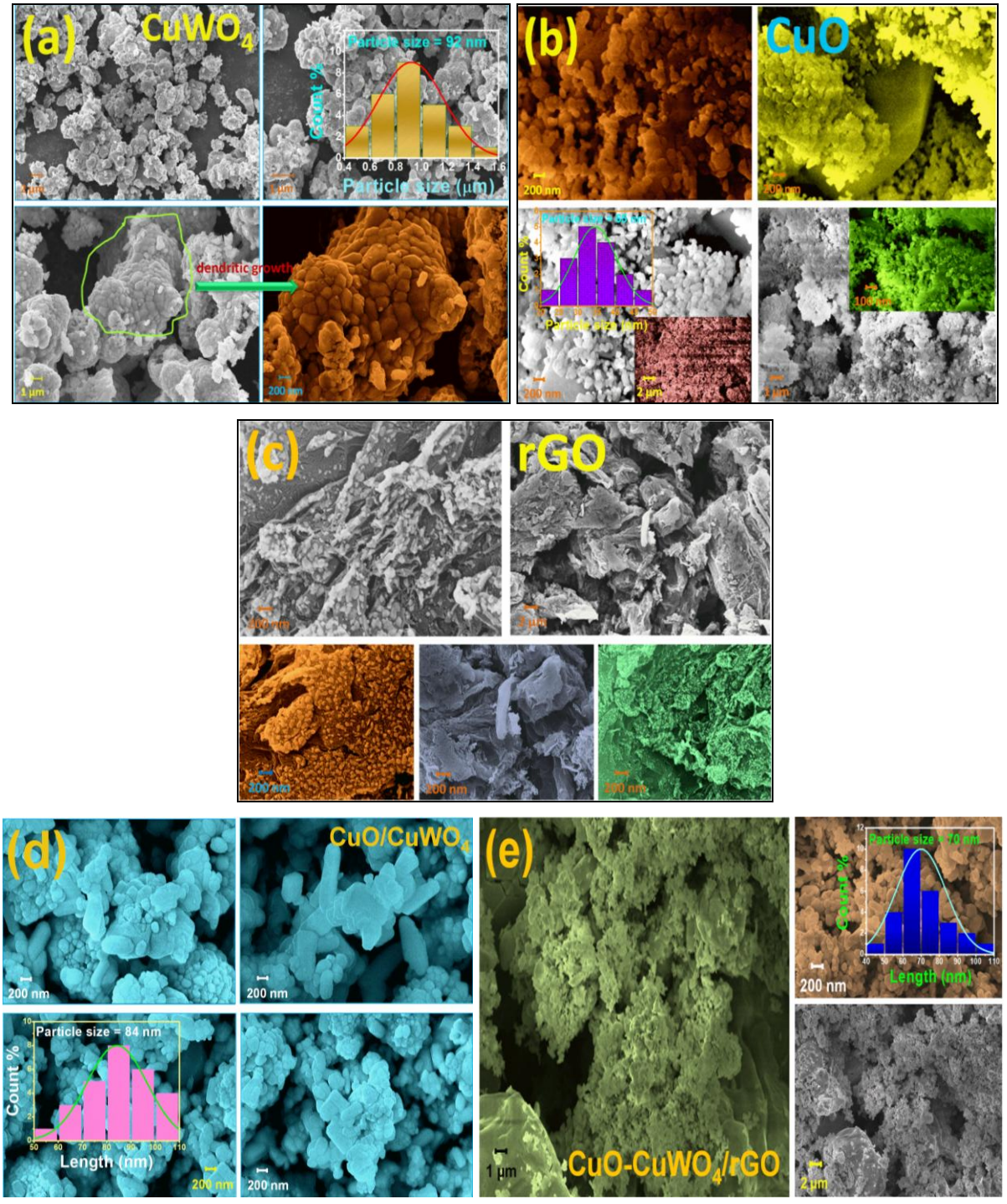

Figure 5.3. FE-SEM images of (a) $CuWO_4$ (b) CuO nanocomposite (c) rGO in low magnification and inset particle size distribution in high magnification; and FE-SEM images of (d) $CuWO_4$/CuO (e) rGO blended $CuWO_4$/CuO nanocomposites and particle size distribution.

To get a deeper understanding of the morphology of $CuWO_4$/CuO and the presence of rGO on $CuWO_4$/CuO, high-resolution transmission electron microscopy (HR-TEM) was performed. The HR-TEM images, depicted in Figures 5.4a, show the distribution of agglomerates adorned with small particles. Figure 5.4a shows a uniform agglomerate distribution with a regular morphology,[65] consistent with the parallelepiped agglomerates observed in the FE-SEM images (Figure 5.3d). Figures 5.4(a′-d′) indicate different electron-micrographs collected from distinct regions of the image in Figure 4a, which suggest that two different nanocrystallites, $CuWO_4$ and CuO, are well interlinked or stacked together throughout the material. Figure 5.5a clearly depicts that when rGO is blended with these nanocomposites, the two different sets of crystallites are connected through rGO sheets, indicating that rGO acts as a linker between the heterostructure. The heterostructure formation was confirmed due to the presence of lattice fringes (Figures 5.4b), with measured d-spacings of ~ 0.25 nm for $CuWO_4$ and 0.27 nm for CuO, respectively. These values align with the crystallographic planes, specifically the (0-21) and (110) planes of $CuWO_4$ and the (110) plane of CuO. The HR-TEM image of $CuWO_4$/CuO-rGO, as shown in Figure 5b, reveals numerous vermicular-like nanoparticles, which results from the recrystallization of $CuWO_4$/CuO nanoparticles on the rGO sheet[63], wherein the measured lattice fringes reveal d-spacings of about 0.29 and 0.23 nm for $CuWO_4$ and CuO, respectively, corresponding to the (111) plane of $CuWO_4$ and the (200) planes of CuO. This outcome provides the successful formation of both $CuWO_4$/CuO and $CuWO_4$/CuO-rGO.

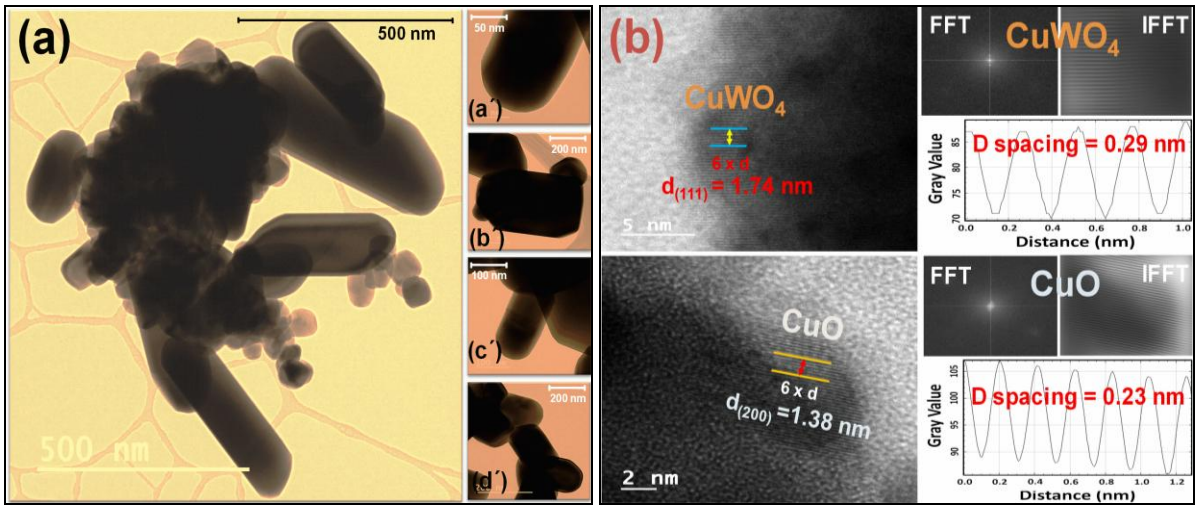

Figure 5.4. (a) HR-TEM images of $CuWO_4$/CuO and (b) Lattice fringes with FFT and Inverse FFT.

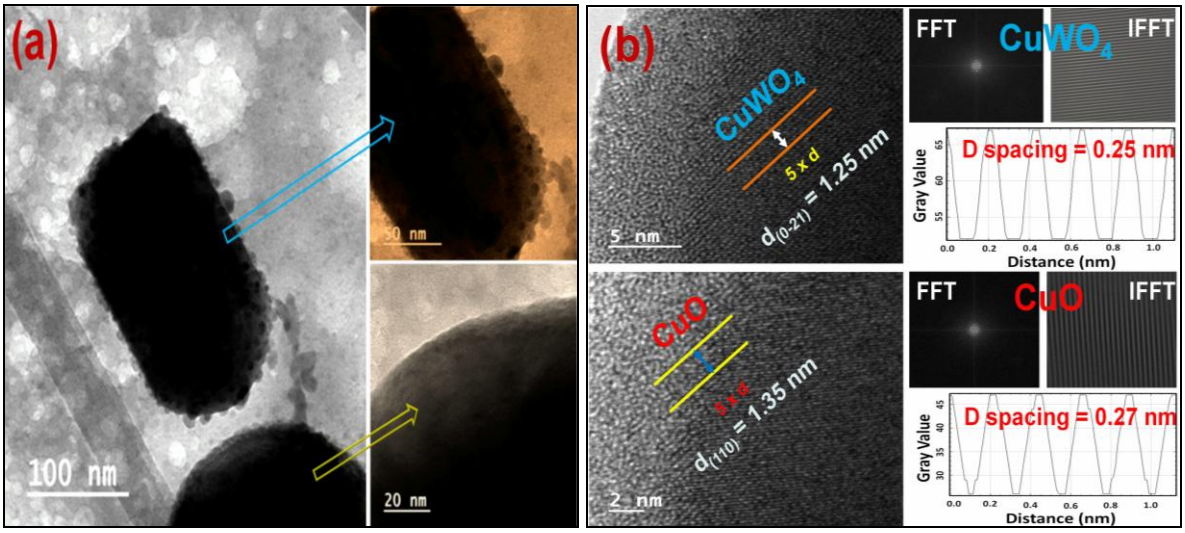

Figure 5.5. (a) HR-TEM images of rGO blended $CuWO_4$/CuO nanocomposite and (b) Lattice fringes with FFT and Inverse FFT.

Energy-dispersive X-ray spectroscopy (EDX) analysis verified the presence of Cu, W, and O in the $CuWO_4$/CuO nanocomposite, as demonstrated in Figure 5.6 and the inset table. For the $CuWO_4$/CuO blended with rGO nanocomposite, the inclusion of Cu, W, O, and N, depicted in Figure 5.7 and the inset table, indicated the effective surface modification of the $CuWO_4$/CuO-rGO nanocomposite with rGO. Additionally, element mapping of Cu (Kα), W (Lα), and O (Kα) in $CuWO_4$/CuO and Cu (Kα), W (Lα), O (Kα), and C (Kα) in rGO blended $CuWO_4$/CuO nanocomposite, as shown in Figures 5.6 and 5.7, was utilized for a detailed analysis of element distribution, confirming successful preparation of the catalysts and uniform distribution of rGO on the surface of the $CuWO_4$/CuO nanocomposite.

The distinctive selected area electron diffraction (SAED) patterns observed for $CuWO_4$/CuO and rGO blended $CuWO_4$/CuO nanocomposites depicted in Figures 5.8a and b display five robust concentric rings corresponding to the crystallographic planes (1-11), (100), (11-1), (-120), (130) for $CuWO_4$/CuO, and also five rings (11-1), (100), (11-1), (200), (-102) for $CuWO_4$/CuO-rGO, respectively, which closely resemble the XRD results. The diffused nature observed in the concentric rings of the rGO blended $CuWO_4$/CuO nanocomposite can be attributed to the introduction of rGO, leading to a reduction in the crystallinity of the $CuWO_4$/CuO heterostructure nanocomposite.

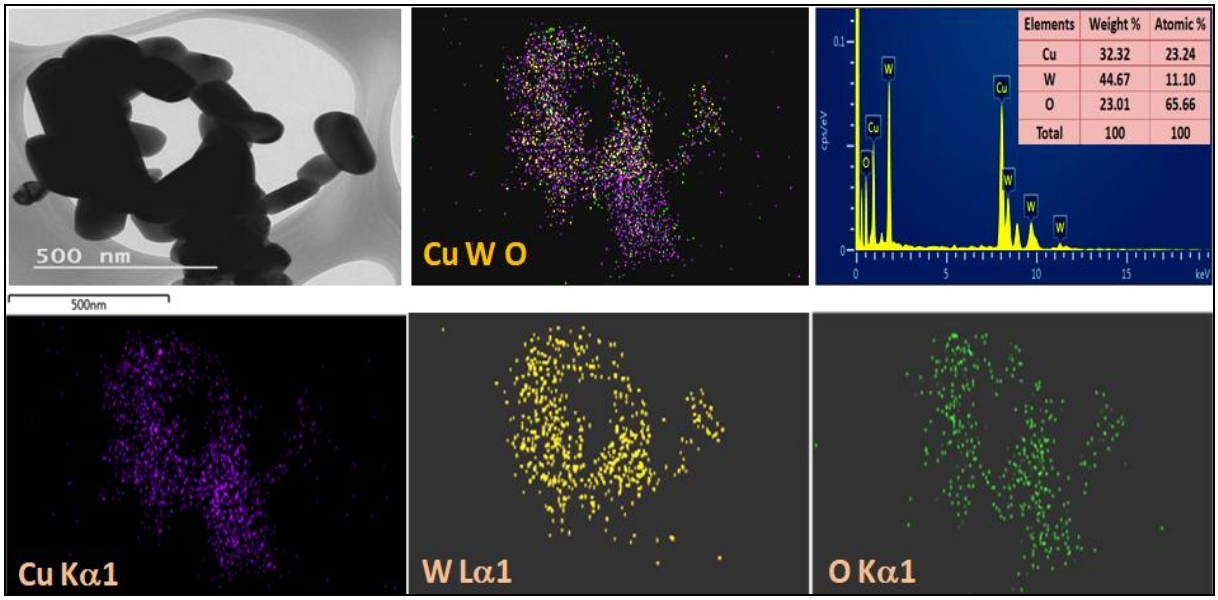

Figure 5.6. TEM images and EDX analysis with elemental percentages and E-mapping of $CuWO_4$/CuO nanocomposite.

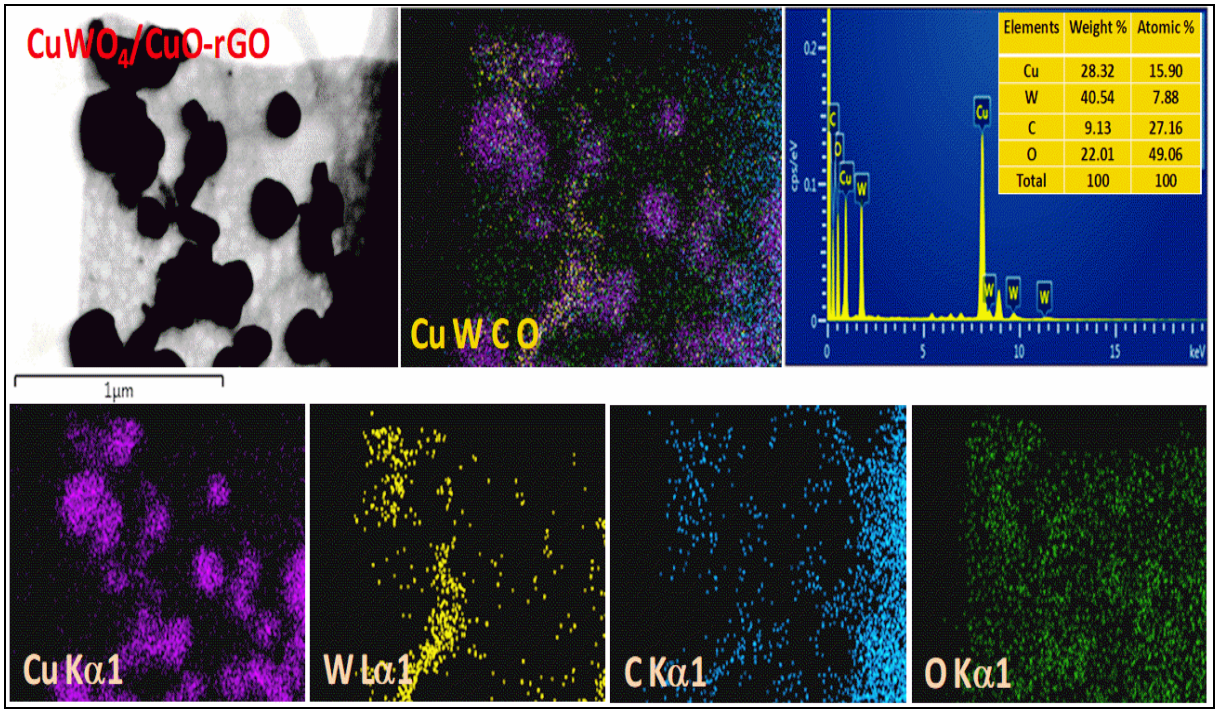

Figure 5.7. HR-TEM images and EDX analysis with elemental percentages and E-mapping of rGO blended $CuWO_4$/CuO nanocomposite.

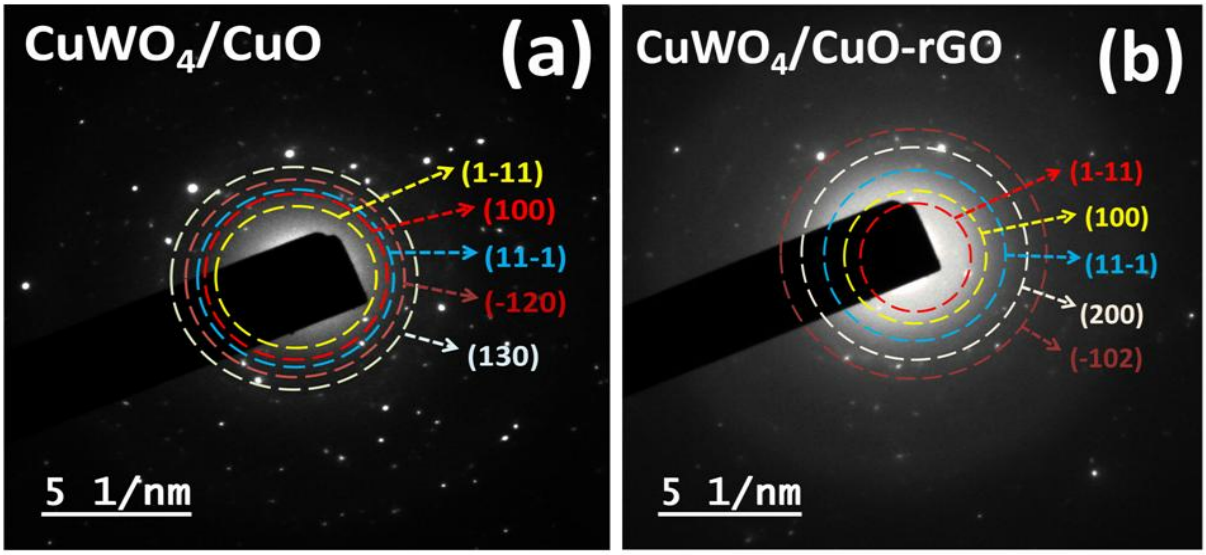

Figure 5.8. SAED Pattern of (a) $CuWO_4$/CuO and (b) rGO blended $CuWO_4$/CuO.

5.3.1.4. UV-Vis Spectroscopic Study. The UV-vis absorption spectra shown in Figures 5.9a and c demonstrated a significant increase in light absorption intensity, characterized by a discernible red shift towards longer wavelengths with the formation of the $CuWO_4$/CuO nanocomposite. This effect is further enhanced with the incorporation of rGO, attributed to its robust absorption capabilities across both the UV and visible regions. The band gap energy (E_g) for the catalysts was determined through linear extrapolation of the Tauc's plot depicted in Figures 5.9b and d, employing the Tauc's equation $(\alpha h\nu)^n = A(h\nu - E_g)$. In this equation, hν represents the photon energy, α denotes the absorption coefficient, A is a constant, and the value of n is set at ½ for an indirectly allowed transition and 2 for a directly allowed transition, respectively. The band gap for pristine $CuWO_4$ is established at 2.33 eV, while that of CuO is 2.49 eV. In contrast, both the $CuWO_4$/CuO and rGO blended $CuWO_4$/CuO nanocomposites exhibit reduced band gaps of 2.14 and 2.02 eV, respectively, compared to the individual band gaps of pure $CuWO_4$ and CuO (Table 5.1). A significant decrease in the band gap in rGO blended $CuWO_4$/CuO heterostructure nanocomposites may be due to an increase in oxygen vacancies, which raises the electron concentration in the energy gap region and brings some localized electronic states closer to the conduction band minimum.[66] This indicates band to band transition is much more prominent in the case of the rGO blended heterostructure in comparison to others, so the small agglomeration is influenced to create charge carriers, which may directly influence the electrocatalytic performance.

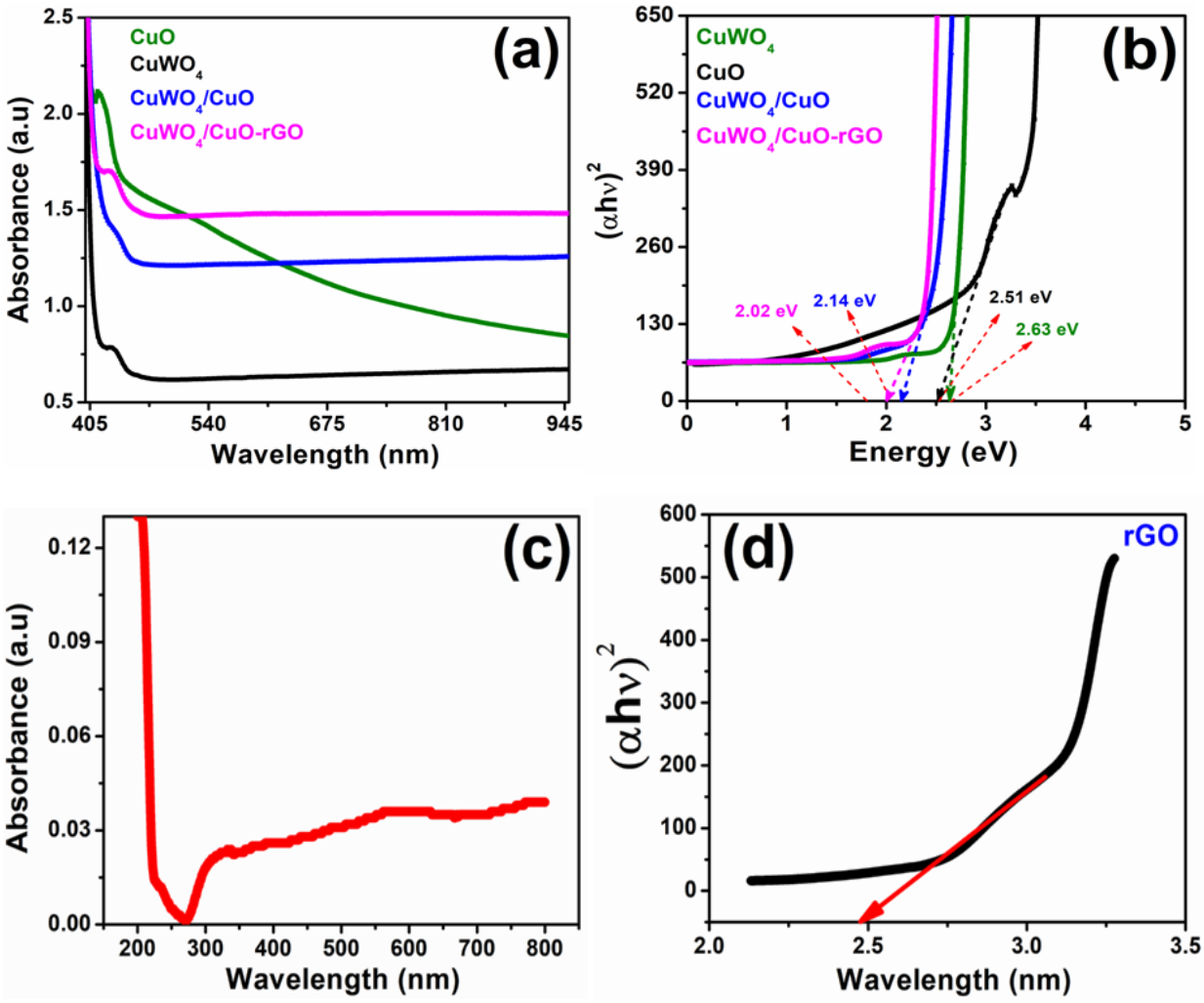

Figure 5.9. (a) UV-Vis spectroscopy of $CuWO_4$, CuO, $CuWO_4$/CuO, and rGO blended $CuWO_4$/CuO nanocomposite (b) Tauc's plot of all the nanocomposites; and (c) UV-Vis spectroscopy (d) Tauc's plot of rGO.

Table 5.1. Band gap energy (BGE) from the absorption plot of different materials using Tauc's plot function.

Nanocomposites	λ_{max} (nm)	Band gap energy (eV)
$CuWO_4$	532	2.63
CuO	499	2.51
$CuWO_4$/CuO	577	2.14
$CuWO_4$/CuO-rGO	610	2.02
rGO	563	2.47

5.3.1.5. FTIR Analysis. In the FTIR spectrum of the as-synthesized $CuWO_4$, depicted in Figure 5.10a, a broad vibrational band at 912 cm^{-1} is associated with the stretching vibration of W=O in WO_3 for $CuWO_4$. This band is slightly shifted in the $CuWO_4$/CuO and $CuWO_4$/CuO-rGO nanocomposites. Peaks at 541, 613, 723, 729, 912, and 1102 cm^{-1} are observed, which can be attributed to the tensile band and vibrations of $CuWO_4$. Within the WO_4 structure, the infrared absorption peaks at 613 and 912 cm^{-1} are likely due to the tensile mode of W-O. The small band at 803 cm^{-1} confirms the stretching mode of the W-O-W bond. The distinctive peaks observed at 528 cm^{-1} and 592 cm^{-1} correspond to the Cu-O vibrations of monoclinic CuO.[67] The peaks at 1102, 1061, 1087, and 1070 cm^{-1} for $CuWO_4$, CuO, $CuWO_4$/CuO, and rGO blended $CuWO_4$/CuO, respectively, are attributed to Cu-OH vibration. The band at 1223 cm^{-1} in $CuWO_4$/CuO-rGO nanocomposites is responsible for C-O stretching. The FTIR spectra further confirm the successful synthesis of $CuWO_4$/CuO and $CuWO_4$/CuO-rGO nanocomposites.

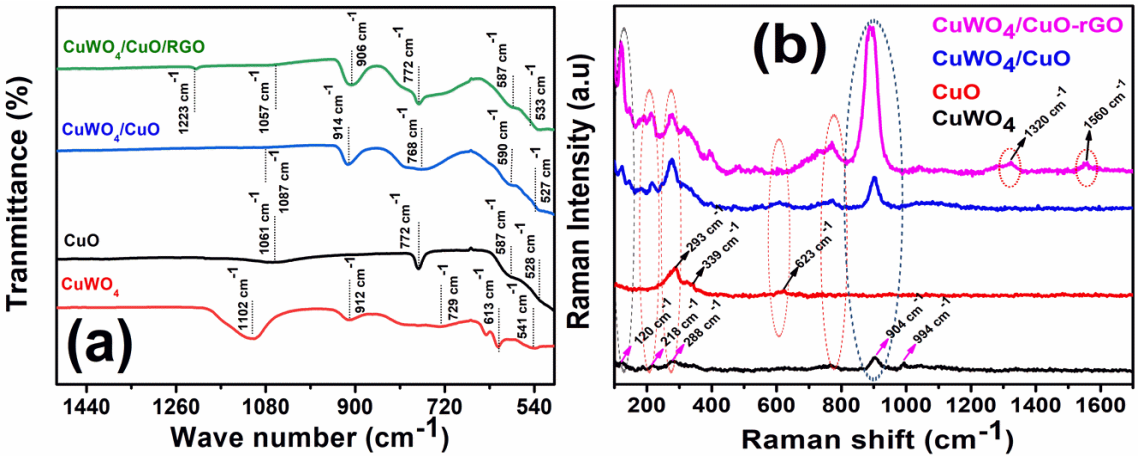

Figure 5.10. (a) FTIR analysis and (b) Raman spectra at 532 nm excitation wavelength with 0.4 mW excitation power of $CuWO_4$, CuO, $CuWO_4$/CuO, and $CuWO_4$/CuO-rGO.

5.3.1.6. Raman Analysis. The Raman scattering spectrum of CuO nanocomposite reveals distinctive phonon bands at 293 cm^{-1} (A_g mode), 339 cm^{-1}, and 623 cm^{-1} (B_g modes), confirming their congruence with expected values and consistent alignment with the characteristics observed in CuO nanoparticles. The observed Raman bands at 120, 218, 288, 772, and 904 cm^{-1} as shown in Figure 5.10b align closely with those found in $CuWO_4$ nanoparticles. It is noteworthy that the prominent Raman band at 904 cm^{-1}, associated with the symmetric stretching W-O vibration, serves as a distinctive marker for the presence of the $CuWO_4$ phase.[68] In the Raman spectrum of $CuWO_4$/CuO-

rGO nanocomposites, the peak around 1560 cm^{-1} (G band), which corresponds to an E_{2g} mode of graphite, is allied with sp^2 hybridized carbon atoms. Meanwhile, the peak around 1320 cm^{-1} (D band) relates to the breathing modes of rings or k-point phonons of A_{1g} symmetry, confirming the presence of rGO in the nanocomposite.[63]

5.3.1.7. EPR Analysis. To analyze the lattice defect and crystal imperfections present in the samples during the synthesis of rGO blended $CuWO_4$/CuO nanocomposite, the electron paramagnetic resonance (EPR) experiment was conducted for $CuWO_4$, CuO, and $CuWO_4$/CuO and rGO blended $CuWO_4$/CuO nanocomposites. In Figures 5.12a and b, the intense signal of $CuWO_4$/CuO-rGO has a g-tensor value of 2.005 (magnetic field of 325 mT), which could be ascribed to the surface unpaired electrons trapped on oxygen vacancies. Moreover, the intense signal observed in rGO blended $CuWO_4$/CuO nanocomposite indicated surface unpaired electrons trapped on oxygen vacancies (OV).[69] $CuWO_4$ nanocomposites showed stronger EPR intensity than pure CuO nanosheets, suggesting a higher presence of OV. Similarly, $CuWO_4$/CuO exhibited stronger EPR intensity than pure $CuWO_4$ nanosheets, and $CuWO_4$/CuO-rGO showed even stronger intensity, all confirming the increased existence of OV defects. This finding aligns with the reduced band gap observed in the nanocomposites, as shown in Table 5.1. Significantly, rGO has the potential to introduce additional OV defects, thereby decreasing the bandgap. Consequently, it is reasonable to expect that incorporating rGO into $CuWO_4$/CuO nanocomposites could introduce more OV defects, effectively reducing the band gap and enhancing catalytic activity.

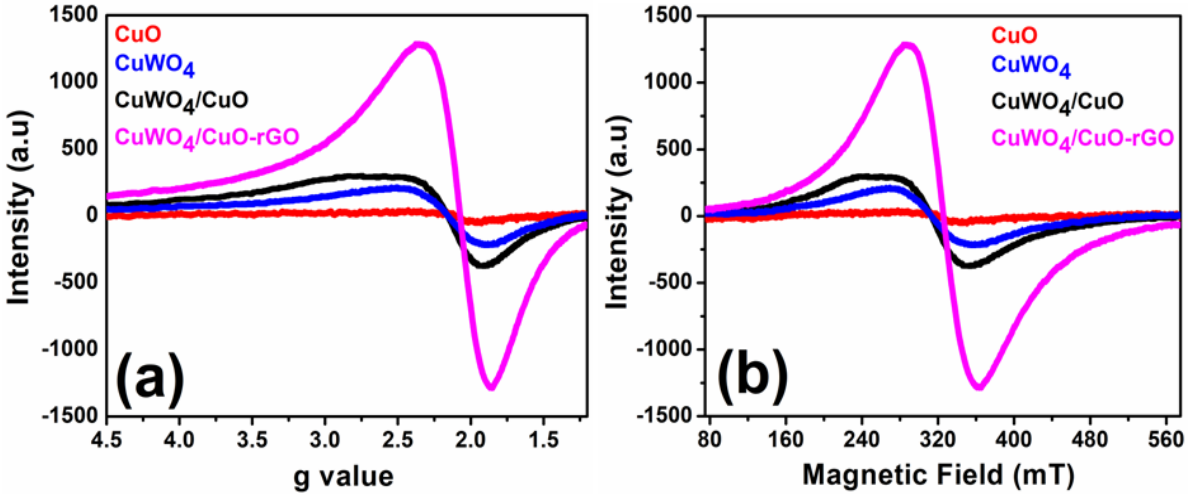

Figure 5.11. EPR spectra of CuO, $CuWO_4$, $CuWO_4$/CuO and $CuWO_4$/CuO-rGO.

5.3.1.8. PL Study. The photoluminescence (PL) spectra of $CuWO_4$ nanoparticles (Figue 5.11a) exhibit two emission peaks at 437 nm (blue region) and 536 nm (green region) due to WO_4^{2-} groups, resulting from the recombination of electrons in the $^3T_{1u}$ state and holes in the $^1A_{1g}$ ground state. The PL spectrum of CuO (Figure 5.11b) reveals a peak at 351 nm, which is attributed to near-band-edge UV emission resulting from the recombination of electron-hole pairs in free excitons. Additionally, a small hump at 416 nm is probably due to band-to-band radiative emission, while the emission peak at 455 nm can be attributed to defect-related emission or surface impurities within the CuO crystal. The PL spectra of $CuWO_4$/CuO and $CuWO_4$/CuO-rGO (Figure 5.11c and d) show all three emission peaks of CuO, along with a small peak of WO_4^{2-}, shifting in peak position.

Compared with pure $CuWO_4$ and CuO, the PL emission peak of the $CuWO_4$/CuO and $CuWO_4$/CuO-rGO systems was quenched after incorporating CuO into $CuWO_4$ to form close heterogeneous interfaces. This quenching indicates reduced charge pair recombination and enhanced charge migration in the $CuWO_4$/CuO and $CuWO_4$/CuO-rGO nanocomposites, which improves their catalytic activity.

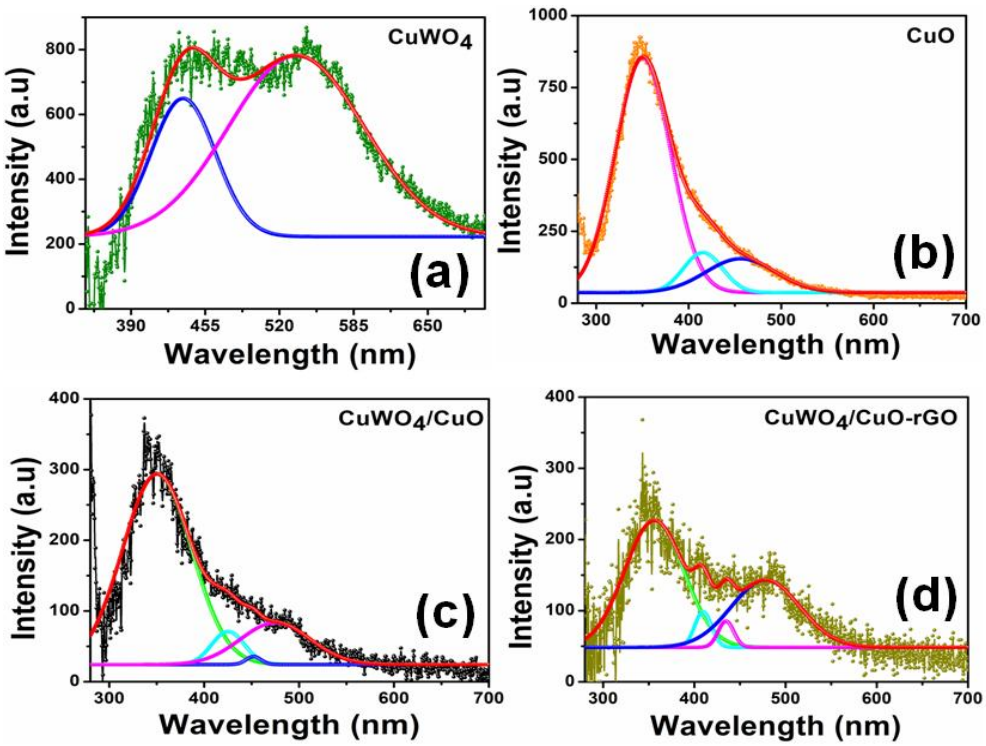

Figure 5.12. Photoluminescence (PL) spectra of (a) $CuWO_4$, (b) CuO, (c) $CuWO_4$/CuO, and (d) $CuWO_4$/CuO-rGO.

5.3.1.9. Brunauer-Emmett-Teller (BET) analysis. The N_2 adsorption-desorption isotherms for $CuWO_4$, CuO, $CuWO_4$/CuO, and $CuWO_4$/CuO-rGO are shown in Figures 5.13(a→d). These isotherms are analyzed to assess the specific surface area, while the inset shows their pore size distribution (PSD) using the Non-Local Density Functional Theory (2D-NLDFT) method. $CuWO_4$ exhibits a BET surface area of 8.77 m^2 g^{-1}, accompanied by a pore size and pore volume of 1.60 nm and 0.008 cm^3 g^{-1}, respectively. In comparison, CuO demonstrates a BET surface area of 30.54 m^2 g^{-1}, with a pore size and pore volume measuring 1.36 nm and 0.070 cm^3 g^{-1}, respectively. The $CuWO_4$/CuO composite displays a BET surface area of 37.69 m^2 g^{-1}, featuring a pore size and pore volume of 1.28 nm and 0.023 cm^3 g^{-1}, respectively (Table 5.2). Lastly, rGO blended $CuWO_4$/CuO nanocomposite shows a BET surface area of 45.09 m^2 g^{-1}, with a pore size and pore volume measuring 1.17 nm and 0.031 cm^3 g^{-1}, respectively. Table 5.2 presents the BET isotherm data for various nanocomposites. The characteristic nature of the isotherm graphs indicates a typical type IV class with H3 hysteresis loop for $CuWO_4$/CuO and type V class with H3 hysteresis loop for rGO blended $CuWO_4$/CuO. Notably, all the samples exhibit a microporous structure, as evidenced by an average pore size of < 2 nm based on the pore size distribution (PSD). More significantly, the organic-inorganic hybrid nanocomposites we have designed may offer abundant active sites, thereby facilitating mass and charge transport abilities and, consequently, significantly contributing to improved catalytic performances.

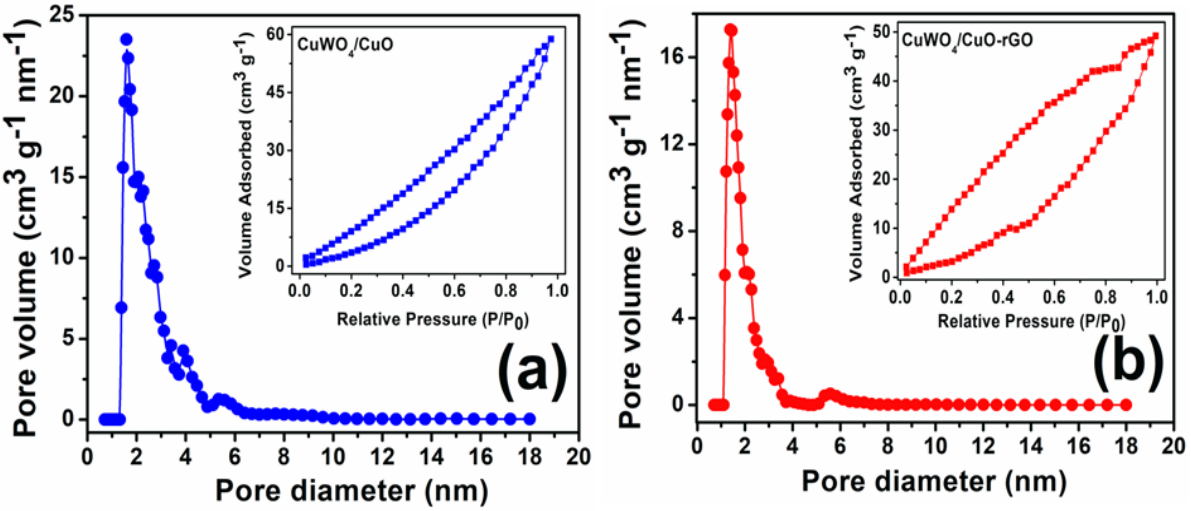

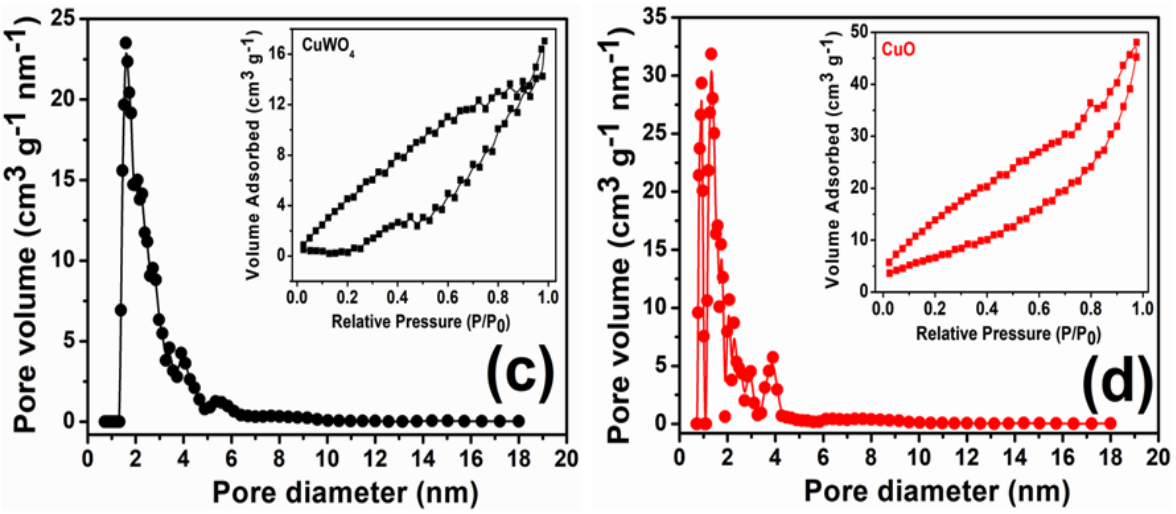

Figure 5.13. BET isotherms of (a) $CuWO_4$/CuO (b) $CuWO_4$/CuO-rGO (c) $CuWO_4$ and (d) CuO nanocomposites.

Table 5.2. BET surface area analysis of $CuWO_4$, CuO, $CuWO_4$/CuO and $CuWO_4$/CuO-rGO electrocatalysts.

Samples	BET surface area ($m^2\ g^{-1}$)	Pore volume ($cm^3\ g^{-1}$)	Pore diameter (nm)
$CuWO_4$	8.77	0.008	1.60
CuO	30.54	0.070	1.36
$CuWO_4$/CuO	37.69	0.023	1.28
$CuWO_4$/CuO-rGO	45.09	0.031	1.17

5.3.2. Electrochemical HER Performances

5.3.2.1. Measurements of HER Performances. The HER polarization curve (LSV) was measured under potential range from -0.5 to 0.0 V at a scanning rate of 5 mV s^{-1}. The EIS measurements were carried out at a constant overpotential of 50 mV. Tafel analyses and stability tests were the same as those for OER tests above. The chronoamperometric response of $CuWO_4$/CuO-rGO was performed at constant potential of 50 mV. All the polarization curves were corrected by iR compensation

5.3.2.2. HER Performances of catalysts. The HER activities of all electrocatalysts were performed in 1.0 M KOH, and intriguingly, $CuWO_4$/CuO exhibited a significant increase in cathodic current density (Figures 5.14a and b), with an onset potential of 2.48 mV (Table 5.5 and Figure 5.14a), surpassing the values for $CuWO_4$, CuO, $CuWO_4$/CuO-rGO, $CuWO_4$/CuO@rGO, Pt, and Pt/C

(102.32, 62.93, 49.41, 234.38, 9.5, and 0 mV), respectively. Moreover, $CuWO_4$/CuO demonstrated a significantly lower η_{10} of 16 mV compared to the other electrocatalysts, indicating its significant efficiency in HER performances. To enable a more accurate comparison, values of η_{20} for all electrocatalysts were also evaluated, revealing a consistent upward trend (Table 5.5). The introduction of rGO into $CuWO_4$/CuO demonstrates a negative influence on HER activity. The hydrophobic nature of the rGO surface in the CuO/$CuWO_4$-rGO nanocomposite may impede proton adsorption, which decreases the efficiency of HER activity. The CuO/$CuWO_4$@rGO nanocomposite displays exceptionally low HER activity compared to other electrocatalysts, suggesting that the anticipated lattice deformation to enhance electrocatalytic performance did not occur. To mitigate the mass loading effects, electrocatalytic activity was assessed based on mass-normalized current density (j_m). The CuO/$CuWO_4$ nanocomposite showed notable HER activity with a relatively low value of η (23 mV), achieving a current density of -100 A g^{-1}. This performance outperformed $CuWO_4$, CuO, $CuWO_4$/CuO-rGO, and Pt/C (153, 88, 74, and 35 mV, respectively) (Figure 5.14c). Furthermore, the mass activity of $CuWO_4$/CuO, reaching 595 A g^{-1} with an η value of ~ 53 mV, was considerably higher compared to $CuWO_4$, CuO, $CuWO_4$/CuO-rGO, and Pt/C, showing improvements of 176.6, 14.23, 11.9, and 2.12 times, respectively (Figure 5.14d). Remarkably, among all the electrocatalysts, $CuWO_4$/CuO again demonstrated its superior performance, attaining a higher current density of 100 mA cm^{-2} at 53 mV (Table 5.5).

To delve deeper into the consistently improved activity, the primary kinetics of the HER were analyzed using Tafel plots. Figure 5.14e depicts the lowest Tafel slope of 16.33 mV dec^{-1} for the $CuWO_4$/CuO heterojunction, surpassing those of $CuWO_4$, CuO, $CuWO_4$/CuO-rGO, Pt, and Pt/C (Table 5.5), which signifies a more efficient HER mechanism for the $CuWO_4$/CuO heterojunction. The data suggests that the $CuWO_4$/CuO heterojunction effectively enhances the Volmer step, and the HER mechanism for this heterojunction follows the Volmer-Tafel pathway. The rate-determining step in this process is the chemical desorption of hydrogen.[70] Pt wire shows a better Tafel slope (34.99 mV dec^{-1}) than Pt/C (51.32 mV dec^{-1}), attributed to its ease in releasing the H_2 bubble produced. In contrast, Pt/C, being coated onto GCE, faces difficulties in releasing H_2 bubbles owing to its larger diameter than that of Pt wire. It is noteworthy to highlight that $CuWO_4$/CuO exhibited exceptional catalytic performance, characterized by its low overpotential (η_{10}), low onset potential as shown in Figure 5.14f, and also its high mass activity, which establishes it as the top-performing electrocatalyst for HER.

5.3.2.3. HER Mechanism. In HER process, only 2 e^- are transferred for releasing one H_2 molecule and a theoretical thermodynamic voltage of 0 V is required to drive the HER. Typically, it is a two-step 2 e^- process which is expressed by the following equations (in alkaline media):[55]

Step I: $H_2O + e^- \rightarrow H_{ads} + OH^-$ Eq. 5.9

(Volmer Reaction, ~ 120 mV dec^{-1})

Step II: $H_{ads} + H_2O + e^- \rightarrow H_2 + OH^-$ Eq. 5.10

(Heyrovsky Reaction, ~ 40 mV dec^{-1})

Or $2H_{ads} \rightarrow H_2$ Eq. 5.11

(Tafel Reaction, ~ 30 mV dec^{-1})

Overall Reaction: $H_2O + 2e^- \rightarrow H_2 + 2OH^-$ Eq. 5.12

Here, M and H_{ads} represent the metal atom (active center) of the electrocatalyst and the H atom chemically adsorbed at the active center of the electrocatalyst, respectively. The Tafel slopes of the above steps are 120, 40, and 30 mV dec^{-1}, respectively. In accordance with the aforementioned steps, the adsorbed hydrogen intermediate (H_{ads}) is initially formed in the Volmer step (step I). Here, these hydrogen ions are originated from the cleaved water molecules.

In step II, H_2 molecules are produced that involves two different routes. One (in Heyrovsky step) is combination of one proton with the H_{ads} species generated from step I to give an H_2 molecule. And in the other route named as Tafel step, two as-formed H_{ads} species (in step I) are directly combined to generate an H_2 molecule. Thus, the Tafel slopes can easily establish the reaction mechanism of HER, mostly including the Volmer-Heyrovsky or Volmer-Tafel mechanism.

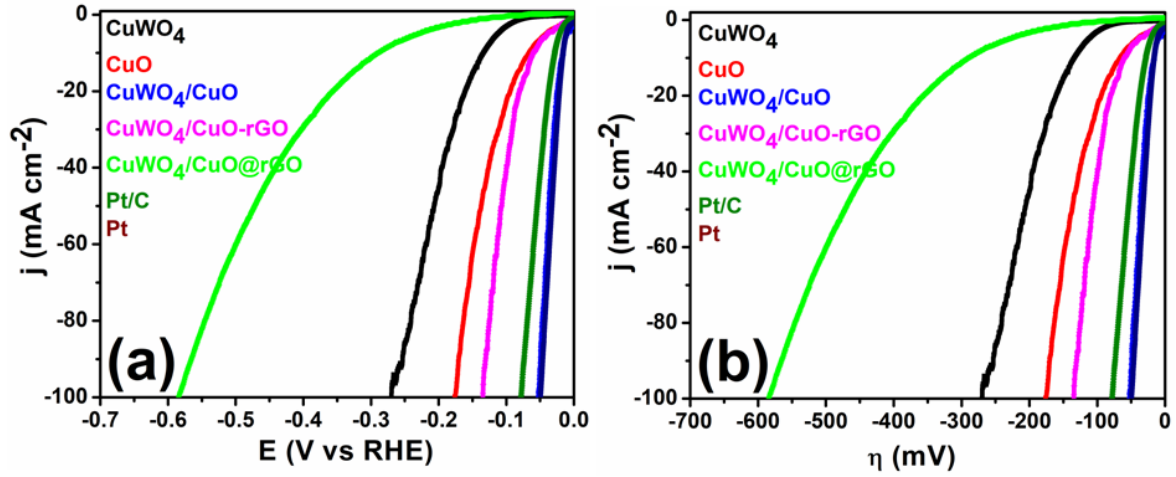

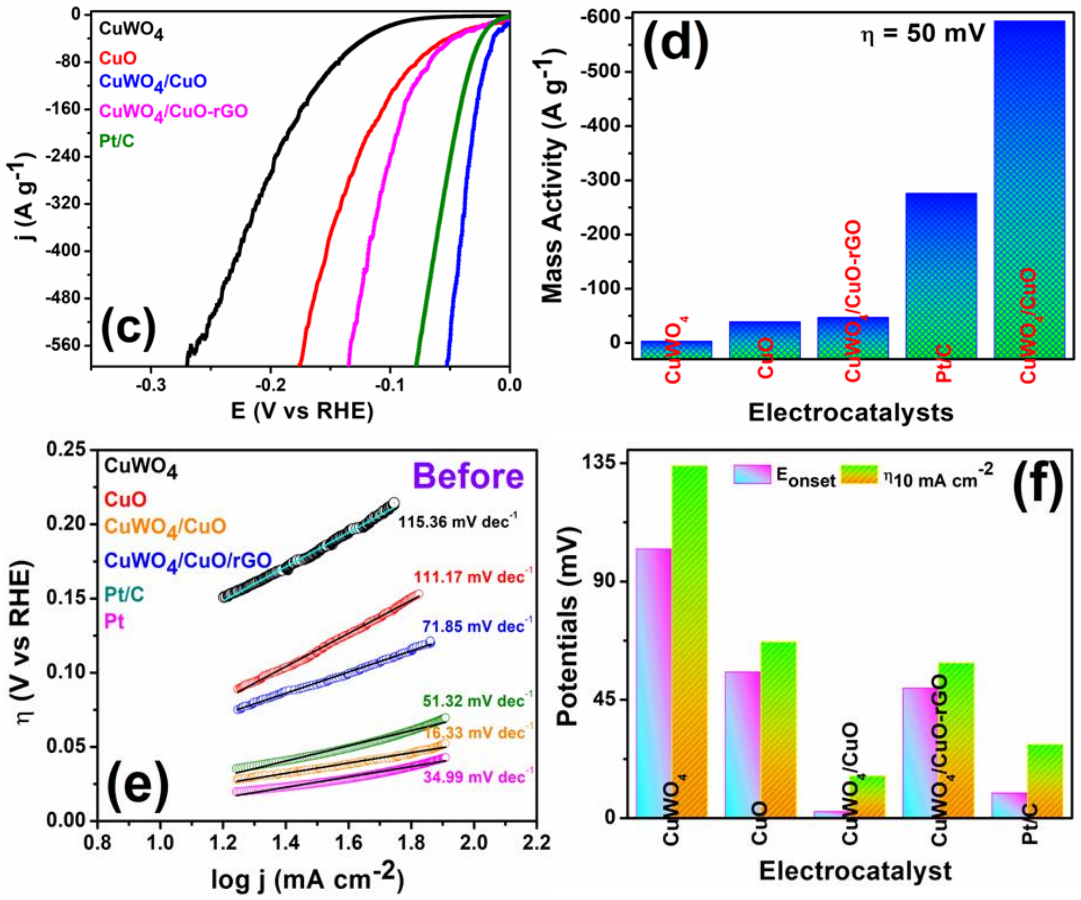

Figure 5.14. (a) HER LSV Plots and (b) current density vs corresponding η plots of $CuWO_4$, CuO, $CuWO_4$/CuO, $CuWO_4$/CuO-rGO, $CuWO_4$/CuO@rGO and Pt/C (c) Mass activity plots (d) bar diagram of mass activity at η = 50 mV and (e) corresponding Tafel plots (f) Bar diagram showing the onset potential and η_{10}.

5.3.2.4. ECSA Analysis. The electrochemical surface area (ECSA), closely linked to the double layer capacitance (C_{dl}), plays an important role in determining the HER activity. C_{dl} is determined from cyclic voltammetry (CV) measurements at various scan rates within the nonfaradaic region (0.2 V to 0.3 V vs. RHE) (Figure 5.15(a→d)). By plotting the current density differences, ΔJ ($J = J_{anodic} - J_{cathodic}$), at 250 mV vs. RHE across different scan rates, we can estimate C_{dl}, as depicted in Figure 5.15f. The C_{dl} values for the catalysts correspond with the ECSA in Table 5.9. Among these, $CuWO_4$/CuO exhibits the maximum ECSA (39 cm^2) value, accompanied by a robust roughness factor (R_f) of 312, indicating an enhancement in HER efficiency. In both the EIS and CV analyses, we observed a consistent trend in the results (Tables 5.3 and 5.9). The intrinsic HER activities were

further evaluated by determining the turnover frequency (TOF) at 50 mV overpotential (η). The TOF values (Table 5.4) follow a trend similar to the activity sequence presented in Table 5.5, where $CuWO_4$/CuO exhibits the highest TOF (2.197 s^{-1}). This maximum TOF of $CuWO_4$/CuO compared to others (Figure 5.16a and b) further confirms it's admirable HER activity. To gain deep insights into the fundamental properties of these electrocatalysts for HER activity, the EIS measurement was performed at η value of 50 mV (Figure 5.16c). To gain a more profound understanding of the resulting Nyquist plot, an equivalent circuit model (Randles cell structure) was used (inset of Figure 5.16c), which includes solution resistance (R_s), charge-transfer resistance (R_{ct}), and double-layer capacitance (C_{dl}). The smallest R_{ct} value of $CuWO_4$/CuO (Table 5.3) signifies a faster e^- transfer process[71] at the electrode-electrolyte interface during HER, indicating a contributing factor to enhanced electrical conductivity and heightened catalytic activity.

Table 5.3. R_s, R_{ct}, Z′, C_{dl}, ECSA and R_f of the electrocatalysts for HER.

Materials	R_s (Ω cm^2)	$R_s + R_{ct}$ (Ω cm^2)	R_{ct} (Ω cm^2)	Z′ (Ω cm^2)	C_{dl} (mF cm^{-2})	C_{dl} (μF)	ECSA (cm^2)	R_f
$CuWO_4$	28.97	65.30	36.33	13.29	2.13	266.25	6.66	53.28
CuO	29.04	56.13	27.09	10.96	5.78	722.50	18.06	144.48
$CuWO_4$/CuO	28.15	49.75	21.60	8.77	11.65	1456.25	36.41	291.28
$CuWO_4$/CuO-rGO	28.96	41.07	12.11	7.91	8.87	1108.75	27.72	221.76

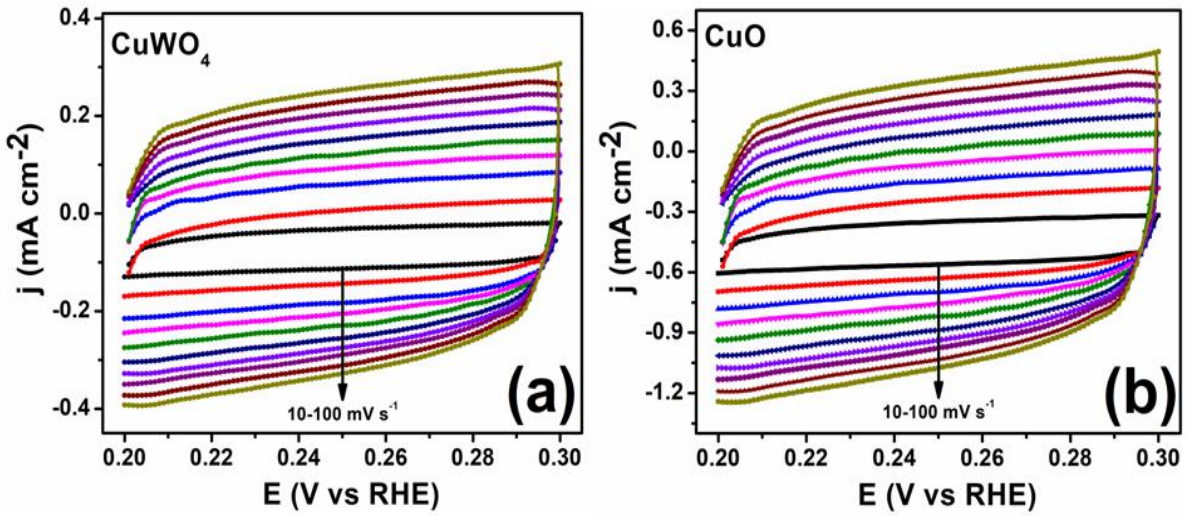

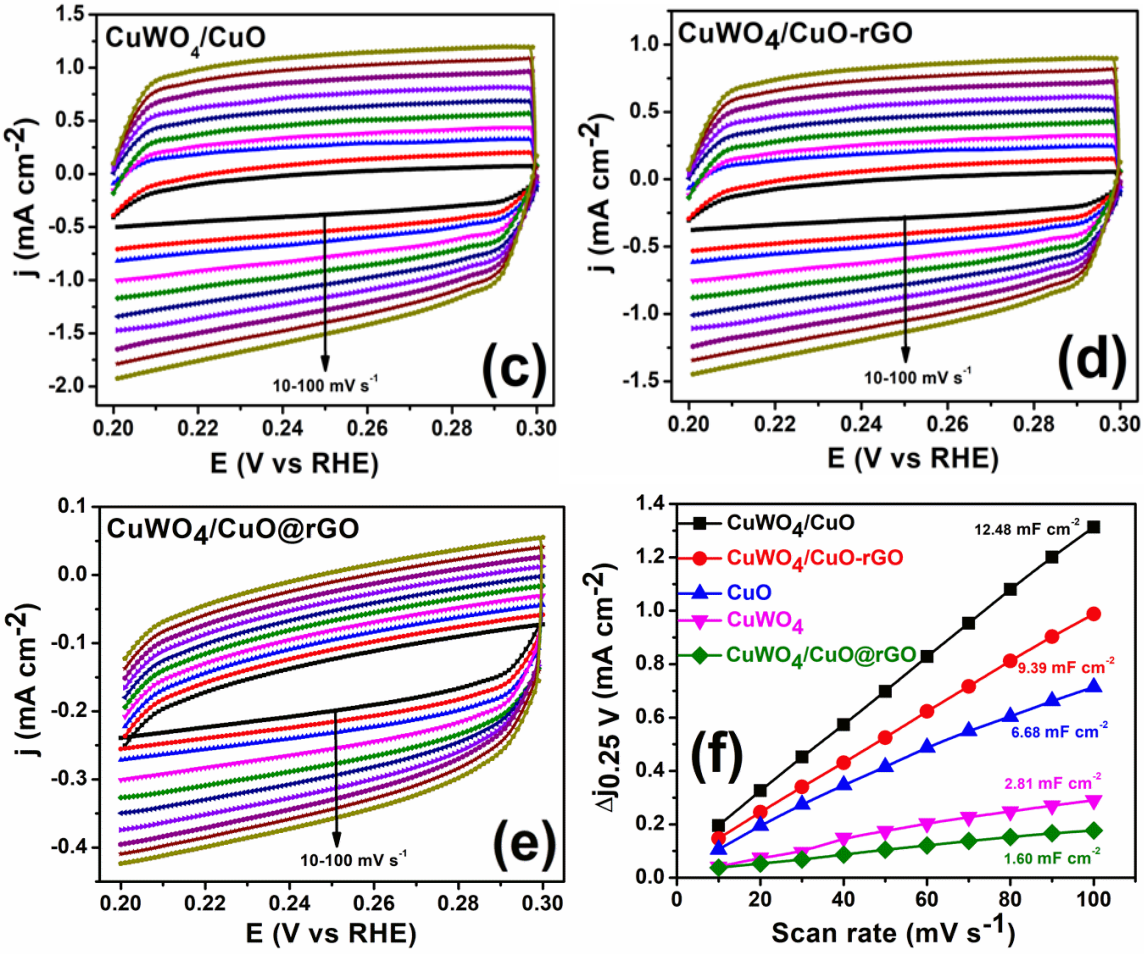

Figure 5.15. CV curves at increasing scan rates recorded in the double layer capacitance charging region for (a) $CuWO_4$, (b) CuO, (c) $CuWO_4$/CuO, (d) $CuWO_4$/CuO-rGO in 1.0 M KOH during HER.

Table 5.4. TOF of all the electrocatalysts at η = 0.050 V for HER and 0.260 V for OER.

Materials	Integrated CV Area (A.V)	TOF (s^{-1}) at 50 mV for HER	TOF (s^{-1}) at 260 mV for OER
$CuWO_4$	8.49×10^{-5}	0.039	0.081
CuO	2.77×10^{-4}	0.147	0.060
$CuWO_4$/CuO	2.63×10^{-4}	2.197	0.102
$CuWO_4$/CuO-rGO	1.52×10^{-4}	0.301	0.965

The exceptionally poor activity of $CuWO_4$ was significantly enhanced when combined with CuO. Specifically, the improved activity of $CuWO_4$/CuO can be attributed to various factors: (i) the introduction of CuO enhancing charge transportation, as evidenced by the EIS (Figure 5.16c); (ii) an

increased BET surface area (Table 5.2); (iii) the development of a porous surface facilitating mass transport; (iv) more exposed active sites, confirmed by the large available ECSA (Tables 5.3 and 5.9); and (v) a strong coupling between $CuWO_4$ and CuO. The equimolar mixture of $CuWO_4$ and CuO seems to create a cumulative effect, potentially reducing the H adsorption energy on the surface of the catalyst and thereby enhancing the HER.

Table 5.5. Electrocatalytic HER activity of the electrocatalysts in 1.0 M KOH solution.

Electrocatalyst	E_{onset} (mV vs RHE)	η_{10} (mV)	η_{20} (mV)	J_{HER} (mA cm^{-2}) at η = 53 mV	Mass activity (A g^{-1}) at 53 mV	$\Delta\eta_j$ at 10 mA cm^{-2} (mV) after HER	Tafel slope (mV dec^{-1}) (Before)	Tafel slope (mV dec^{-1}) (After)
$CuWO_4$	102.32	134	161	0.57	3.37	20	115.36	113.02
CuO	55.51	67	94	7.02	41.80	14	111.17	110.74
$CuWO_4$/CuO	2.48	16	25	100	595	4	16.33	15.32
$CuWO_4$/CuO-rGO	49.41	59	80	8.39	49.98	6	71.85	70.83
Pt/C	9.50	28	37	47.23	281.14	7	51.32	50.21

5.3.2.5. Life span of the modified electrode for HER: To evaluate the practical applicability of the electrocatalysts, long-term stability for the Hydrogen Evolution Reaction (HER) was performed by amperometric i-t response at 50 mV overpotential over a duration of 10 h (Figure 5.16d). During this assessment, it was observed that there is minimal degradation in HER performance because of the accumulation of H_2 bubbles around the electrode surface. This is because of the reduction of H^+ ions in the electrolyte, resulting in a delay in the subsequent H^+ ions reaching the electrode. This delay, in turn, disrupts the continuity of the reaction.[72]

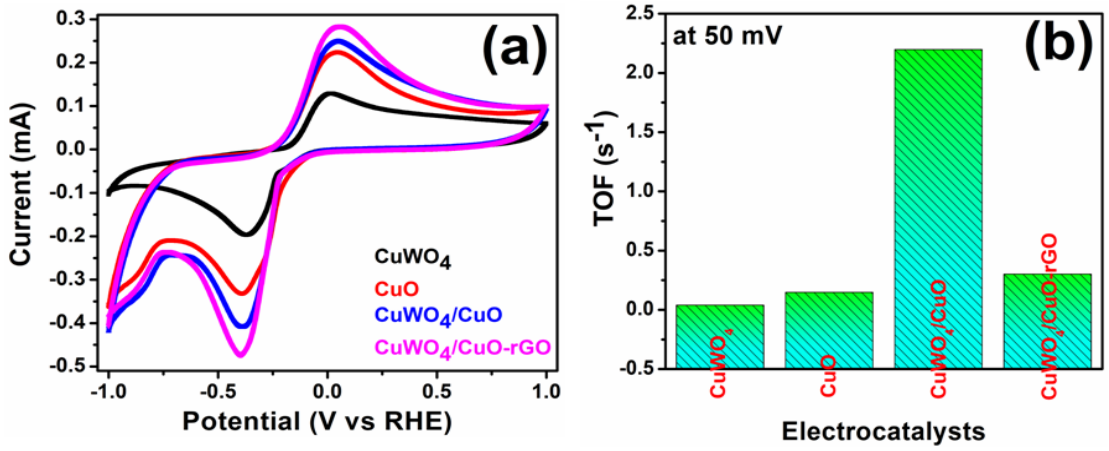

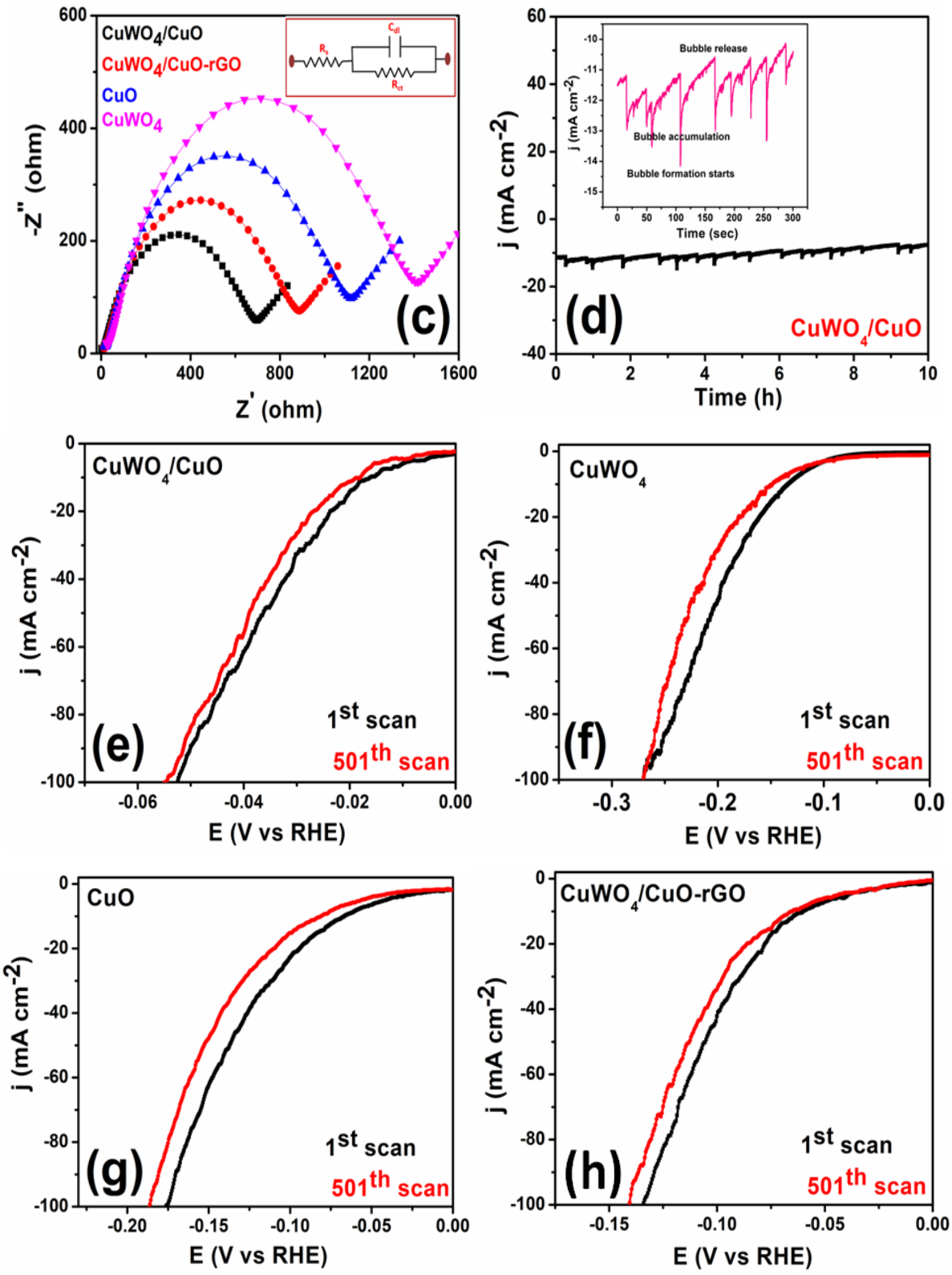
CuWO4/CuO
CuWO4/CuO-rGO
CuO
CuWO4
-Z'' (ohm)
Z' (ohm)
(c)
Bubble release
Bubble accumulation
Bubble formation starts
Time (sec)
j (mA cm-2)
Time (h)
(d)
CuWO4/CuO
(e)
1st scan
501th scan
E (V vs RHE)
(f)
CuWO4
(g)
CuO
(h)
CuWO4/CuO-rGO

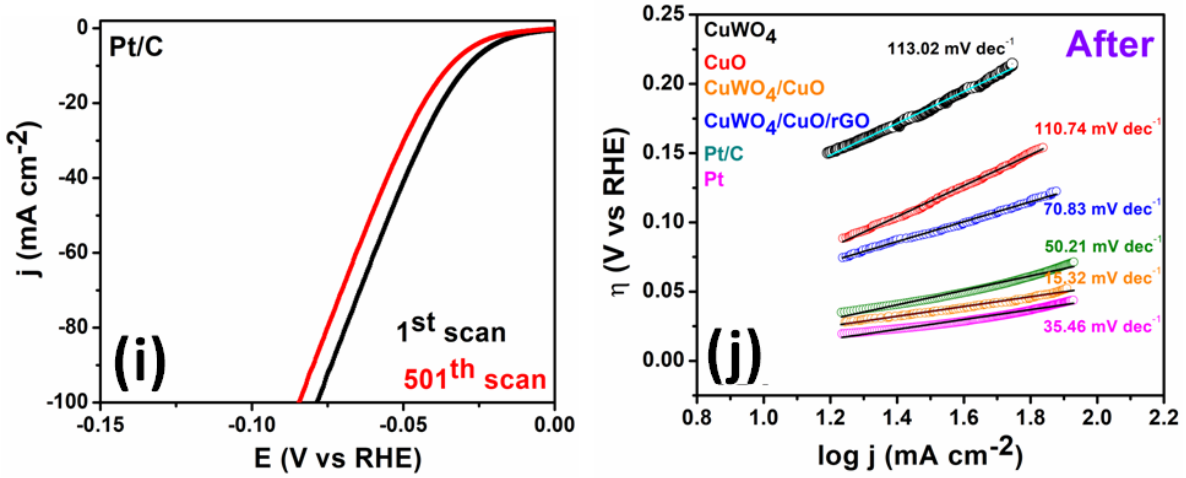

Figure 5.16. (a) Plots of current density vs the applied scan rate for C_{dl}. (b) CV curves in 0.1 M phosphate buffer (pH = 7) at 50 mV s^{-1} scan rate (c) TOF of all electrocatalysts at 50 mV (d) Nyquist plots at 50 mV overpotential in 1.0 M KOH (inset: corresponding equivalent circuit diagram and magnified image) (e) Amperometric i-t curve of $CuWO_4$/CuO at 50 mV in 1.0 M KOH for 10 h (inset: H_2 bubble accumulation) (f) LSV curves of $CuWO_4$/CuO electrodes before and after 500 cycles (g) Tafel plots of all samples after 500 cycles.

The stability and durability were also assessed using the LSV study, both before and after running 500 cycles. It was satisfactory to note a mere 4 mV overpotential increase after running to achieve a current density of 10 mA cm^{-2} for the $CuWO_4$/CuO electrocatalyst (Figure 5.16e), suggesting the remarkable stability of the electrocatalyst in such conditions. Figures 5.16(f→i) depicts changes in overpotentials for various electrocatalysts, as summarized in Table 5.5. Remarkably, the Tafel slope of the $CuWO_4$/CuO electrocatalyst after 500 cycles (15.32 mV dec^{-1}), shown in Figure 5.16j, signifies its long-lasting and consistent activity over other electrocatalysts. The poor stability and electrocatalytic performance of Pt/C may be attributed to the accumulation of Pt nanoparticles on the amorphous surface of the carbon moiety, making it more prone to corrosion.[73] Even after the 10 h stability test, the $CuWO_4$/CuO retained its morphology, as confirmed through XPS and FE-SEM analyses (Figures 5.17(b→e) and 5.18). The phase remained intact, with only a slight decrease in the diffraction peak intensity observed in the XRD pattern (Figure 5.17). These results collectively suggest the outstanding stability of $CuWO_4$/CuO for HER activity. Table 5.6 provides an in-depth analysis of OER performance for $CuWO_4$/CuO and electrocatalysts derived from copper transition metals, as reported in previous studies.

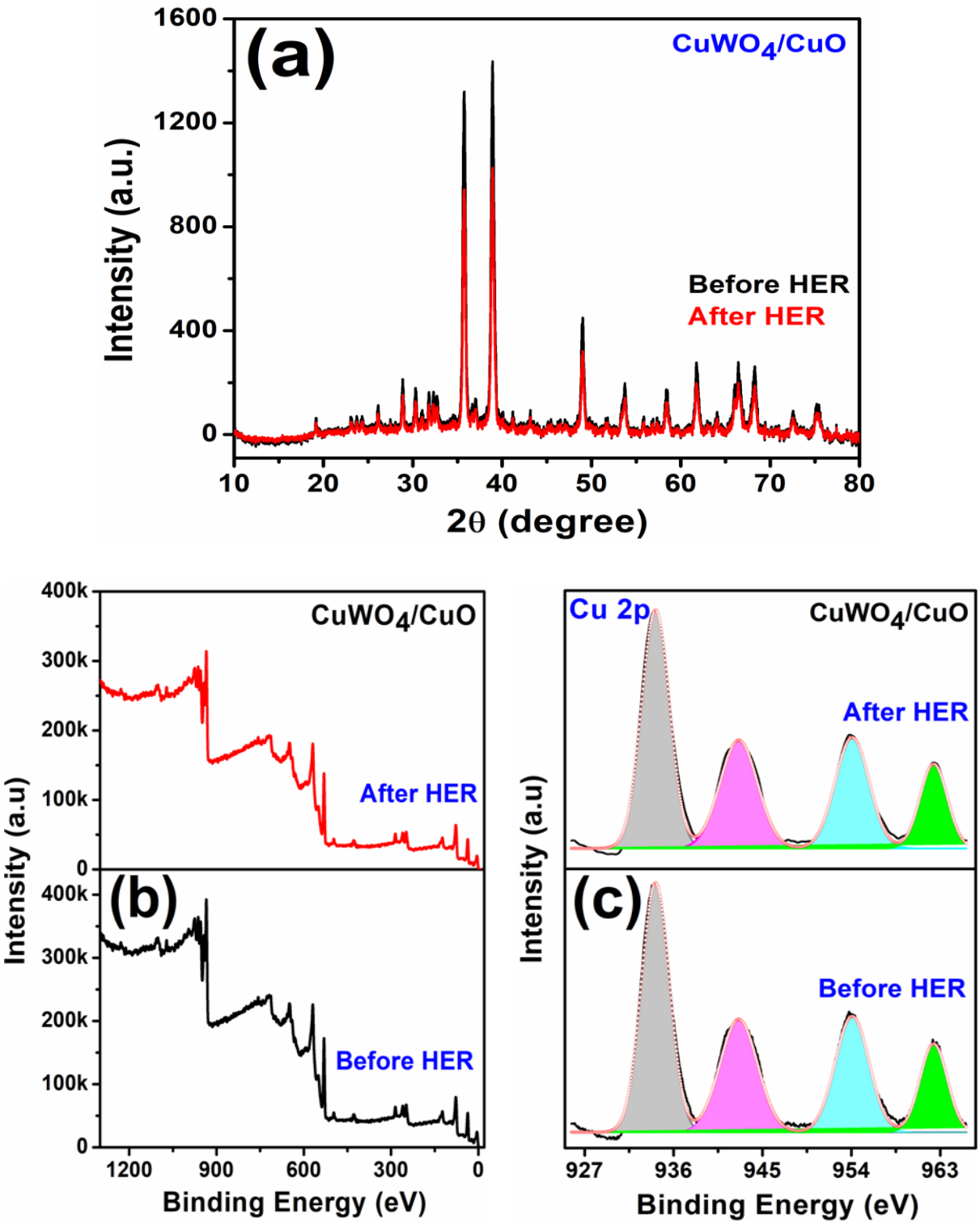
(a)
CuWO4/CuO
Before HER
After HER
Intensity (a.u.)
2θ (degree)
(b)
CuWO4/CuO
After HER
Before HER
Intensity (a.u)
Binding Energy (eV)
(c)
Cu 2p
CuWO4/CuO
After HER
Before HER
Intensity (a.u)
Binding Energy (eV)

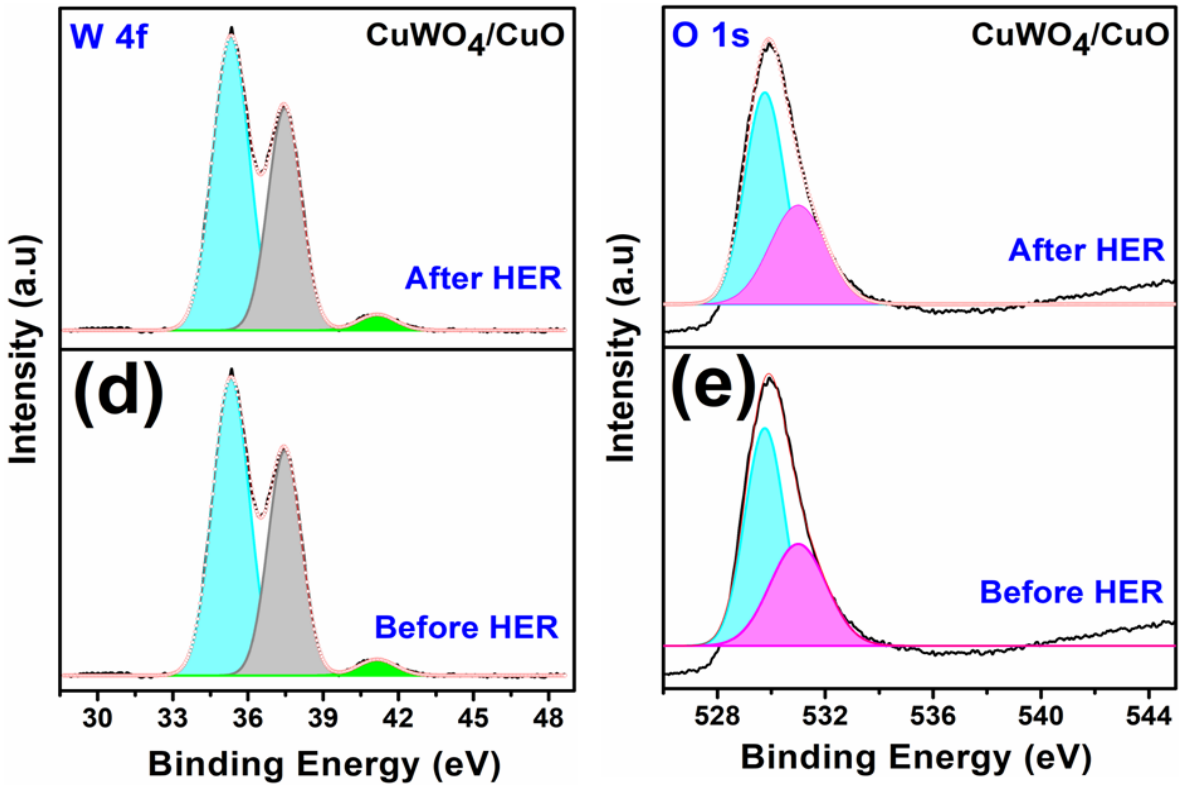

Figure 5.17. Post-catalytic characterizations of of $CuWO_4/CuO$ (a) XRD; and XPS spectra of (b) Sample survey (c) Cu 2p (d) W 4f (e) O 1s after HER stability test.

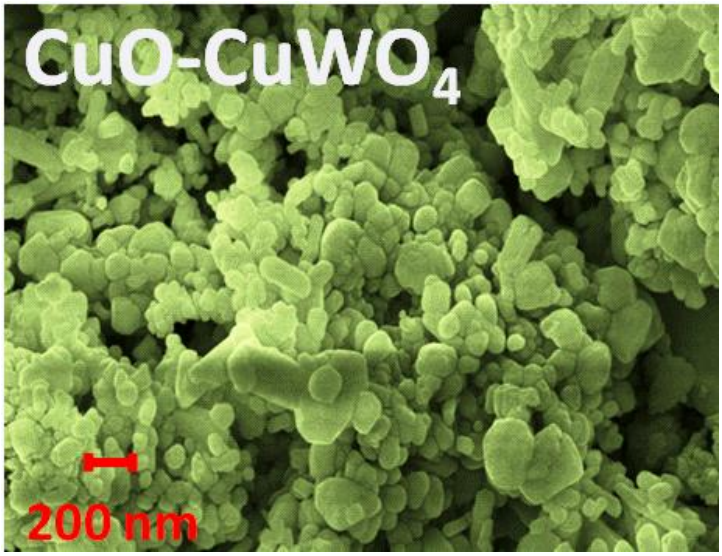

Figure 5.18. FE-SEM images of $CuWO_4/CuO$ after HER stability test.

Table 5.6. Comparison of $CuWO_4$/CuO with previously reported modified catalysts for HER in 1.0 M KOH.

Materials	Current Density (mA cm^{-2})	Overpotential (mV)	Tafel slope (mV dec^{-1})	Ref.
$CuWO_4$/CuO	10	16	16.33	**This work**
$CuNi_2N$-3DNi nano-patterns	10	48	51	74
Ru-doped CuO/MoS_2 (MSCR)	10	198	113	75
Cu_2O/RGO-2	10	142	65.62	76
$Ni_{1-x}Cu_x$	10			77
Ni-Gr-CNTs-Ni_2P-CuP_2	20	140	41	78
Ni_2P-Cu_3P@NiCuC	10	78	173	79
Cu_1Ni_2-N/Carbon Cloth	10	71.4	74.2	80
Cu NPs-TiO_x-Ti	10	108	122	81
NiCu in graphitic shells	10	74	44	82
NC/CuCo/$CuCoO_x$ nanowires	10	112	55	83
NiCoP@Cu_3P/CF	10	54	72	84
NiCu-P-Ni mesh	10	175	53	85
NC-NiCu-NiCuN	10	93	55	86
NiCuP	50	146	47	87
NC@$CuCo_2N_x$/CF	10	105	76	88

5.3.3. Electrochemical OER Performances

5.3.3.1. Measurements of OER Performances. Before measuring the polarization curves, first the catalyst electrodes were continually scanned through cyclic voltametric (CV) measurements until a static CV plot could be attained. Then, the OER activity of all catalysts was evaluated by linear sweep voltammetry (LSV) in the potential window ranging from 1.1 to 1.8 V (vs. RHE) with a scan rate of 2 mV s^{-1}. The current densities were normalized to the geometric immersed surface area of the electrode 0.125 cm^2. Electrochemical impedance spectroscopy (EIS) was conducted at a constant overpotential of 260 mV under the sweeping frequency from 5 mHz to 100 kHz with an AC voltage of 5 mV. The impedance data were fit to a simplified Randles cell model to analyze the charge transfer resistance (R_{ct}) and double layer capacitane (C_{dl}). The iR-compensation was adopted to minimize the conductivity impact on OER catalytic performance. The η at 10 mA cm^{-2} (η_{10}) was calculated as follows:

$$\eta_{10} = E_{10} - 1.23 \qquad \text{Eq. 5.13}$$

Here, E_{10} is OER polarization potential at current density of 10 mA cm^{-2} and the value 1.23 suggests the O_2/H_2O equilibrium potential. The Tafel slope was derived according to the Tafel equation as below:

$$\eta = a + b \log j \qquad \text{Eq. 5.14}$$

Where, η is the overpotential, b is the Tafel slope, and j is the current density.

5.3.3.2. OER Performances of catalysts. The OER performance of all electrocatalysts was assessed in 1M KOH, with RuO_2 serving as a benchmark for the anodic reaction of water splitting due to its balanced oxygen binding properties. However, the application of RuO_2 is limited by its low anodic stability, especially at high overpotentials.[89] $CuWO_4$/CuO-rGO/GCE showed higher current density and a significantly lower onset potential (1.246 V) than RuO_2 (1.415 V) and other electrocatalysts as synthesized, indicating its superior OER performance (Figure 5.19a). $CuWO_4$/CuO-rGO/GCE demonstrates exceptional OER performance with a remarkably low overpotential (η_{10}) of 161 mV at 10 mA cm^{-2}. The calcination of CuO/CuWO4-rGO nanocomposite at 400 °C introduces defects in the nanocomposite that act as active sites for OER, resulting in a lower overpotential required for the reaction, while $CuWO_4$/CuO@rGO/GCE shows suboptimal OER activity due to the absence of such lattice defects. Moreover, the $CuWO_4$/CuO-rGO/GCE exhibited a current density of 49.98 mA cm^{-2} at overpotential of 260 mV, outperforming the other electrocatalysts (Figure 5.19b). This surpasses the other synthesized electrocatalysts and even exceeds the performance of other previously reported electrocatalysts. Notably, it achieves a current density of approximately 100 A g^{-1} with a low overpotential of 197 mV, significantly exceeding other electrocatalysts, as illustrated in Figure 5.19c. These findings affirm the superior electrocatalytic performance of $CuWO_4$/CuO-rGO/GCE. This result confirms the vital role of rGO surface modification in improving the OER efficiency of the $CuWO_4$/CuO nanocomposite, indicating a high electron transfer rate between the surface of the catalyst and electrolyte. Improved OER efficiencies were confirmed through mass activity determination, notably $CuWO_4$/CuO-rGO/GCE achieves a current density of approximately 100 A g^{-1} at a low η of 200 mV, surpassing all other electrocatalysts as depicted in Figure 5.19d.

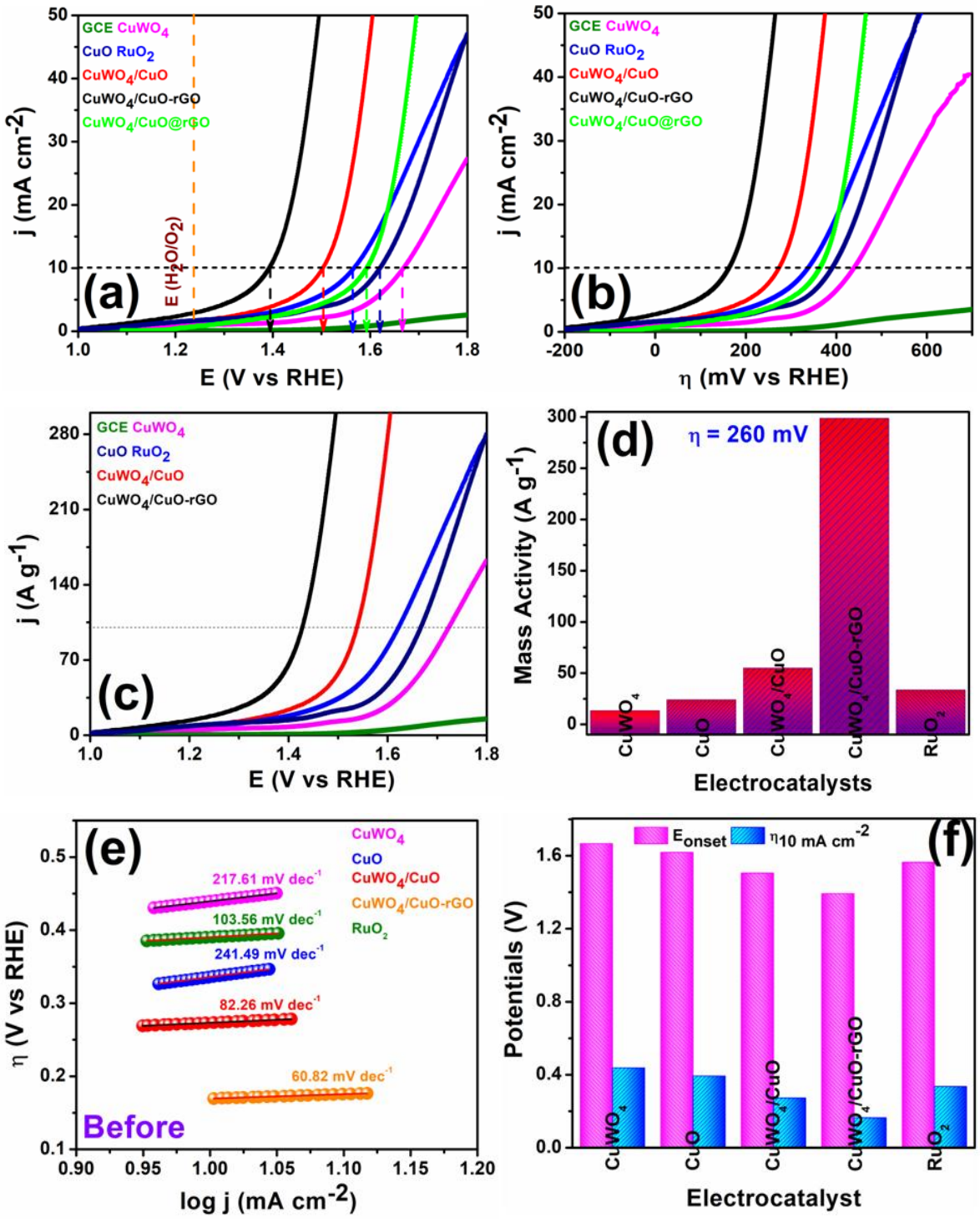

Figure 5.19. (a) OER LSV Plots (b) current density against η plots (c) Mass activity plots (d) bar diagram showing the onset potential and η_{10} of $CuWO_4$, CuO, $CuWO_4$/CuO, and $CuWO_4$/CuO-rGO,

$CuWO_4$/CuO@rGO, and RuO_2 (e) OER Tafel plots and (f) bar diagram of mass activity at 200 mV of $CuWO_4$, CuO, $CuWO_4$/CuO, and $CuWO_4$/CuO-rGO, and RuO_2.

Furthermore, surpassing all electrocatalysts, $CuWO_4$/CuO-rGO/GCE attains a notable mass activity of 298.61 A g^{-1} at η of 260 mV. Notably, it exhibits a 9-fold improvement over RuO_2 at the same overpotential. Tafel plots were used for deeper insight into the reaction kinetics. $CuWO_4$/CuO-rGO/GCE stands out with the smallest Tafel slope at 60.82 mV dec^{-1}, as shown in Figure 5.19e, indicating efficient OER kinetics (Table 5.7). The close match to the theoretical 59 mV dec^{-1} suggests the rate-determining step involves the first electron-transfer process in the four-electron/proton OER mechanism, implying first-order kinetics with respect to OH^- concentration[3]. Thus, it is once again evident that rGO on the $CuWO_4$/CuO surface is directly responsible for the increase in OER efficiency. It is important to emphasize that $CuWO_4$/CuO-rGO demonstrated outstanding catalytic performance, featuring a low overpotential (η_{10}), a low onset potential as depicted in Figure 5.19f, and remarkable mass activity, positioning it as the premier electrocatalyst for OER.

Table 5.7. Comparison of OER activities of electrocatalysts at various current densities with Tafel slopes in 1.0 M KOH solution.

Electrocatalyst	E_{onset} (V vs RHE)	η_{10} (mV)	η_{20} (mV)	j_{OER} (m A^{-2}) at η = 260 mV	Mass activity (A g^{-1}) at 1.49 V	$\Delta\eta_j$ at 10 mA m^{-2} (mV) after OER	Tafel slope (mV dec^{-1}) (Before)	Tafel slope (mV dec^{-1}) (After)
$CuWO_4$	1.487	425	514	2.31	13.19	20	217.61	221.42
CuO	1.458	396	454	4.08	23.84	16	241.49	222.64
$CuWO_4$/CuO	1.367	269	318	9.05	54.72	15	82.26	83.99
$CuWO_4$/CuO-rGO	1.246	161	209	49.98	298.61	11	60.82	62.13
RuO_2	1.415	335	413	5.68	33.42	14	103.56	111.70

5.3.3.3. OER Mechanism. During OER, 4 e^-s needs to be transferred for per O_2 molecule generation and this e^- transfer may be occurred through multiple steps. The theoretical thermodynamic voltage for multistep 4 e^- oxidation processes is 1.23 V. The widely accepted whole OER process which consists of four elementary steps can be ascribed below.[54]

In alkaline media:

Step I: $'*' + OH^- \rightarrow OH^* + e^-$ Eq.5.15

Step II: $OH^* + OH^- \rightarrow O^* + H_2O + e^-$ Eq.5.16

Step III: $O^* + OH^- \rightarrow HOO^* + e^-$ Eq.5.17

Step IV: $HOO^* + OH^- \rightarrow O_2 + H_2O + e^- + '*'$ Eq.5.18

Overall Reaction: $4OH^- \rightarrow O_2 + H_2O + 4e^-$ Eq.5.19

Here '*' implies the active sites of the electrocatalyst and during 4-step process, the generated three reaction intermediates OH*, O*, and HOO* represent the adsorbed oxygen-containing species on the catalysts surface. Typically, during the electrochemical oxidation condition, the oxidation of OH^- ions was initiated to form OH* in step I, followed by deprotonation in step II and then further oxidation for the generation of the oxygenated intermediate of HOO*, and finally O_2 will release in step IV.

5.3.3.4. ECSA Analysis. Again, C_{dl} values were determined (Figure 5.20f) from CV measurements in the non-faradaic region at various scan rates (Figures 5.20(a→e)). The obtained C_{dl} values were subsequently used to estimate the ECSA, and $CuWO_4$/CuO-rGO shows the highest ECSA (176.31 cm^2) and a robust roughness factor (R_f) of 1410.48, indicating enhanced OER efficiency (Table 5.9). Both EIS and CV analyses exhibit a consistent trend in results. However, BET analysis shows that the BET surface area determined by the DFT method consistently aligns with the ECSA value obtained from C_{dl} measurements. Nevertheless, the OER activity order among the electrocatalysts correlates with the ECSA results, emphasizing that both BET surface area and ECSA findings collectively determine OER performance.

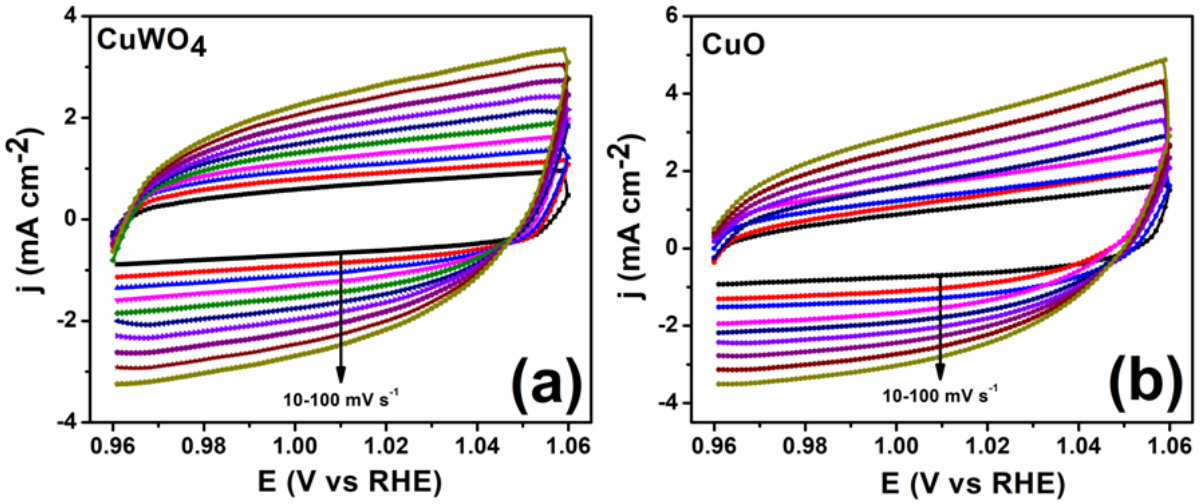

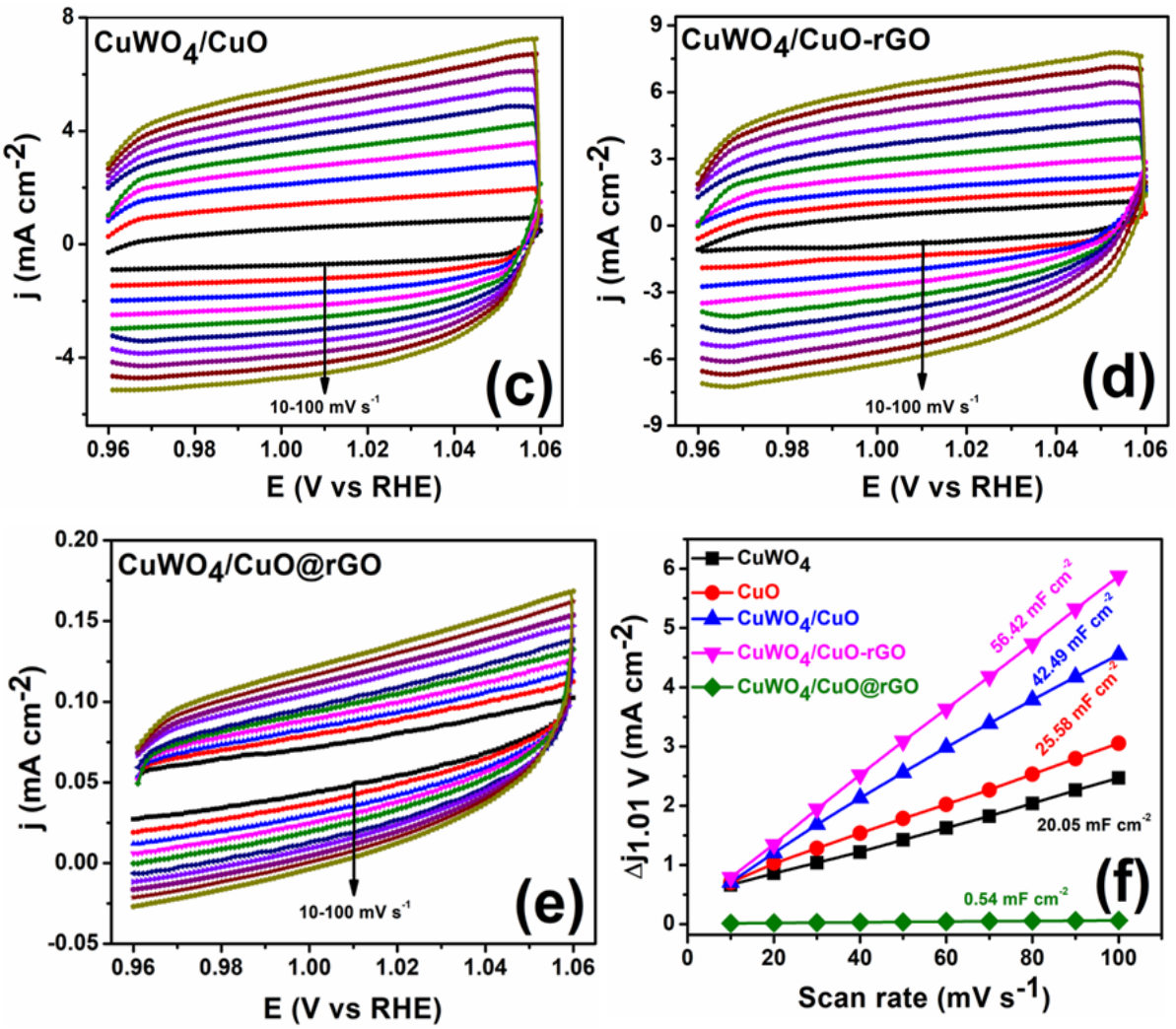

Figure 5.20. CV curves at increasing scan rates recorded in the double layer capacitance charging region for (a) $CuWO_4$, (b) CuO, (c) $CuWO_4$/CuO, (d) $CuWO_4$/CuO-rGO in 1.0 M KOH during OER.

To assess the fundamental characteristics of the electrocatalysts for OER, TOF was also calculated. The highest TOF of $CuWO_4$/CuO-rGO (9.65×10^{-1} s^{-1}) (Figure 5.21a and Table 5.4) suggests enriched and more exposed active sites, coupled with enhanced conductivity in $CuWO_4$/CuO-rGO, indicating its superior OER activity. The EIS measurement at 260 mV revealed the smallest R_{ct} value of $CuWO_4$/CuO-rGO (Table 5.8), offering a thorough understanding of the OER activity and confirming the crucial role of rGO in enhancing the OER activity as well as quick e^- transfer between the catalyst and substrate. The C_{dl} value calculated from EIS analyses (Figure 5.21b) suggests that $CuWO_4$/CuO-rGO (55.93 mF cm^{-2}) has the largest effective surface area, providing

numerous active sites and a rough surface, thereby contributing to its remarkable OER activity. This observation is further substantiated by the highest ECSA and R_f values of $CuWO_4$/CuO-rGO (Tables 5.8 and 5.9).

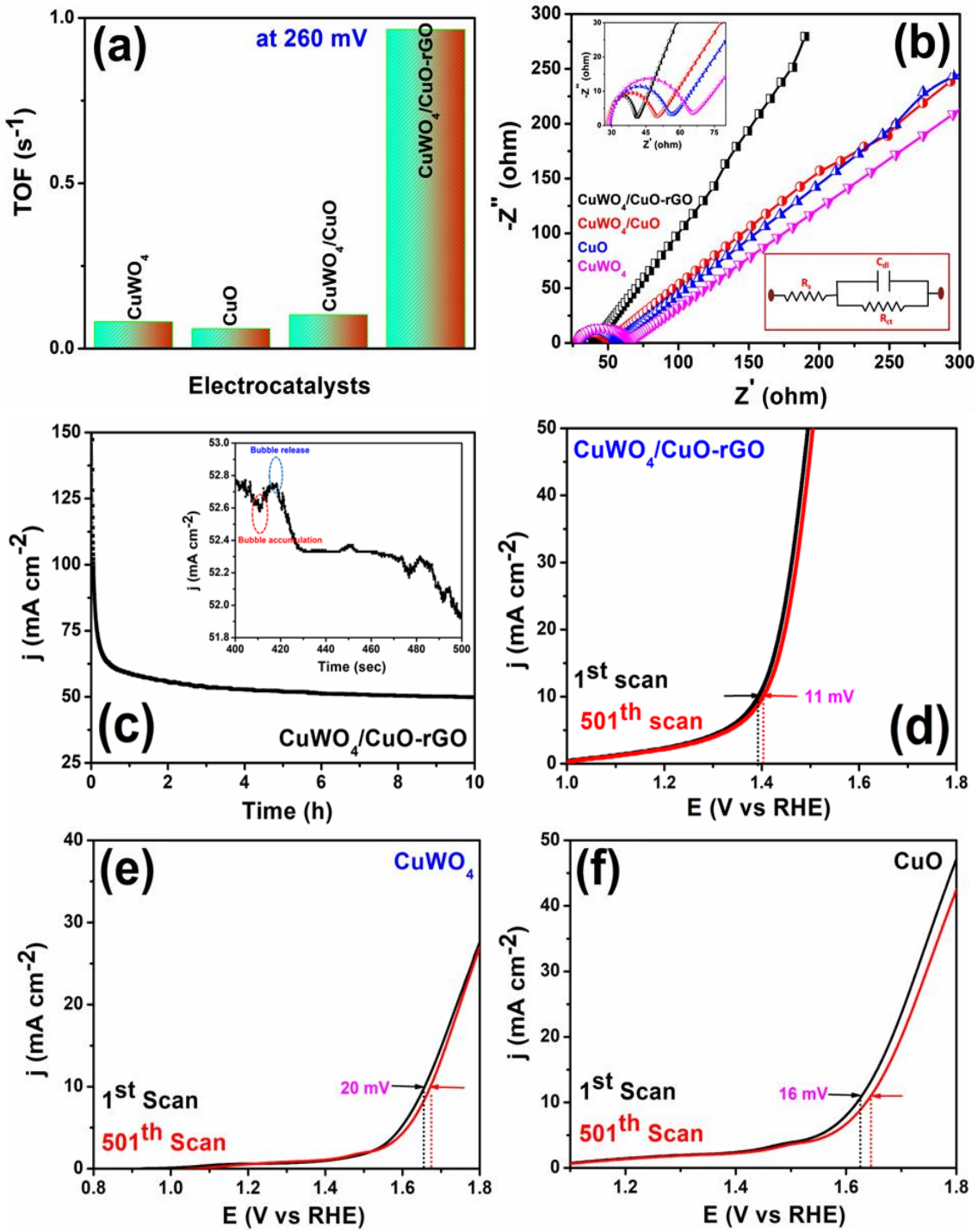

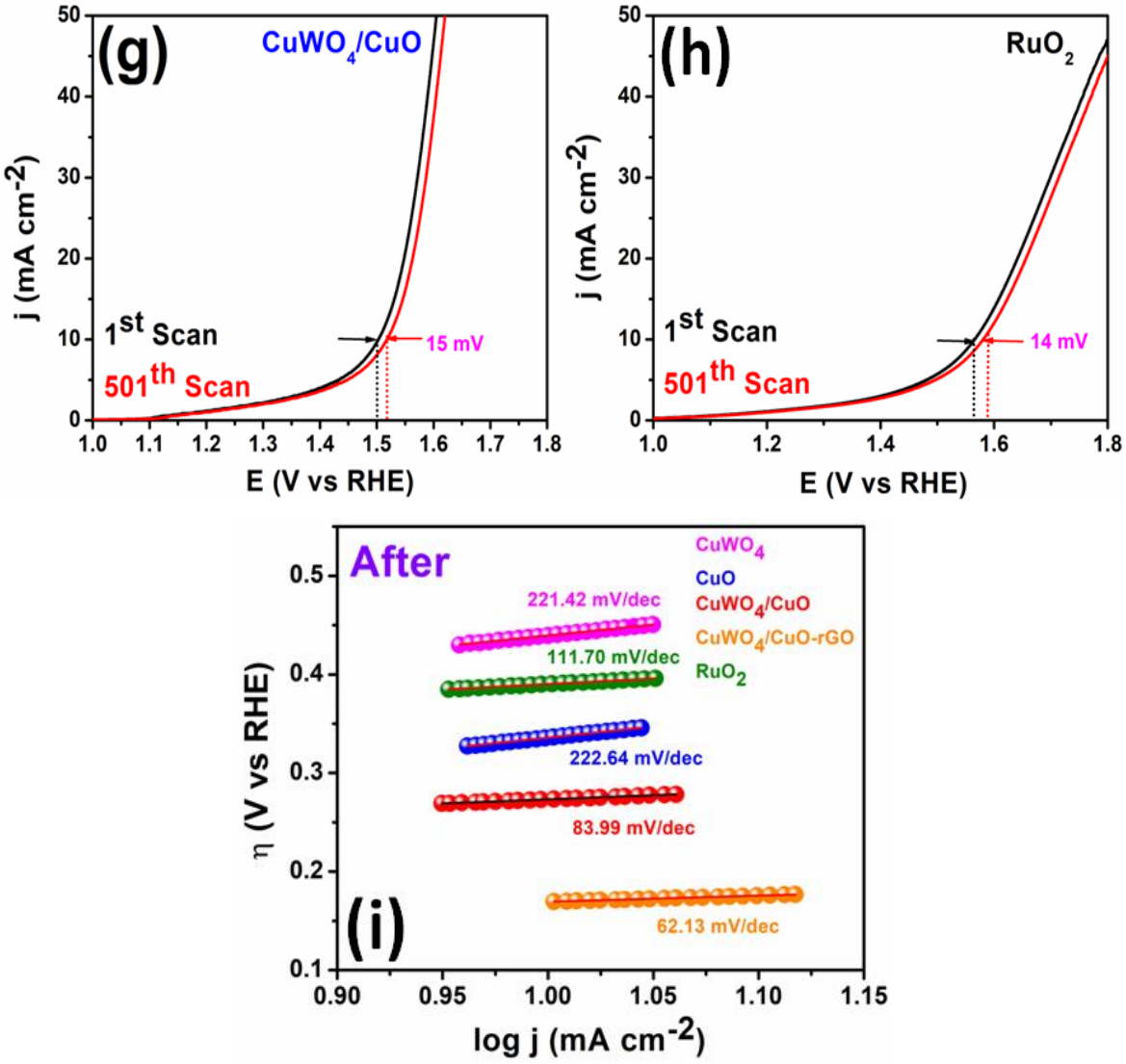

Figure 5.21. (a) Plots of current density vs the applied scan rate for C_{dl} (b) TOF of all electrocatalysts at 260 mV (c) Nyquist plots at 50 mV in 1.0 M KOH (inset: magnified image and equivalent circuit diagram) (d) Amperometric i-t curve of $CuWO_4$/CuO-rGO at 260 mV overpotential in 1.0 M KOH for 10 h (inset shows O_2 bubble accumulation) (e) LSV plots of $CuWO_4$/CuO before and after 500 cycles (f) Tafel plots of all electrocatalysts after 500 cycles.

Table 5.8. R_s, R_{ct}, Z′, C_{dl}, ECSA and R_f of the electrocatalysts for OER.

Materials	R_s (Ω cm^2)	$R_s + R_{ct}$ (Ω cm^2)	R_{ct} (Ω cm^2)	Z′ (Ω cm^2)	C_{dl} (mF cm^{-2})	C_{dl} (μF)	ECSA (cm^2)	R_f
$CuWO_4$	6.33	299.04	292.71	147.36	19.33	2416.25	60.41	483.28
CuO	4.09	236.93	232.84	119.75	25.88	3235	80.88	647.04
$CuWO_4$/CuO	1.21	188.31	187.10	73.76	41.95	5243.75	131.09	1048.72
$CuWO_4$/CuO-rGO	3.13	147.70	144.57	94.66	55.93	6991.25	174.78	1398.24

Table 5.9. Values of C_{dl} and ECSA from cyclic voltammograms of the electrocatalysts with different scan rates for HER and OER.

Materials	HER				OER			
	C_{dl} (mF cm^{-2})	C_{dl} (μF)	ECSA (cm^2)	R_f	C_{dl} (mF cm^{-2})	C_{dl} (μF)	ECSA (cm^2)	R_f
$CuWO_4$	2.81	351.25	8.78	70.24	20.05	2506.25	62.66	501.28
CuO	6.68	835	20.88	167.04	25.58	3197.50	79.94	639.52
$CuWO_4$/CuO	12.48	1560	39	312	42.49	5311.25	132.78	1062.24
$CuWO_4$/CuO-rGO	9.39	1173.75	29.34	234.72	56.42	7052.50	176.31	1410.48
$CuWO_4$/CuO@rGO	1.60	200	5	40	0.54	67.50	1.688	13.504

The enhanced OER performance can be attributed to various factors, including: (i) the enhanced surface area of $CuWO_4$/CuO-rGO and the even distribution of $CuWO_4$/CuO on rGO, confirmed through N_2 adsorption-desorption, exposing numerous active sites for enhanced performance; (ii) the positive impact of rGO in preventing $CuWO_4$/CuO restacking; (iii) introducing lattice defects due to calcinations at 400 °C in $CuWO_4$/CuO-rGO; (iv) integrating rGO maximizes the formation of OV defects in $CuWO_4$/CuO-rGO; (v) incorporating rGO enhances the electrical conductivity of $CuWO_4$/CuO, establishing strong chemical and electronic coupling between $CuWO_4$/CuO and rGO; (vi) the strong cumulative interaction between individual components of $CuWO_4$/CuO-rGO can lead to improved catalytic activity; and (vii) furthermore, the favorability of electrocatalysis may also be due to the tandem e^- transfer in $CuWO_4$/CuO-rGO.

5.3.3.5. Life span of the modified electrode for OER: In addition to catalytic efficiency, long-term durability is crucial. The amperometric i-t response (Figure 5.21c) conducted at 260 mV overpotential for 10 h revealed the superior stability of the $CuWO_4$/CuO-rGO electrocatalyst. The OER performance showed minimal degradation despite the accumulation of O_2 bubbles around the

electrode surface. In addition, the stability of the $CuWO_4$/CuO-rGO electrocatalyst was evaluated through LSV studies before and after running 500 cycles, revealing a mere 11 mV overpotential increase at 10 mA cm^{-2} current density (Figure 5.21d and Figure 5.21(e→h)). Overpotential changes and the Tafel slope of $CuWO_4$/CuO-rGO after 500 cycles (62.13 mV dec^{-1}) highlight its enduring stability compared to others, as illustrated in Table 5.7 and Figure 5.21i. Following the 10 h stability test, $CuWO_4$/CuO-rGO maintained its morphology, validated by XPS, and FESEM analyses (Figures 5.22(b→f) and 5.23). The phase integrity persisted, with a marginal reduction in diffraction peak intensity in the XRD pattern (Figure 5.22a). These findings collectively affirm the exceptional stability of $CuWO_4$/CuO-rGO in OER activity. A comprehensive comparison of the OER performance among $CuWO_4$/CuO-rGO and electrocatalysts derived from previously reported electrocatalysts derived from Cu transition metal is shown in Table 5.10.

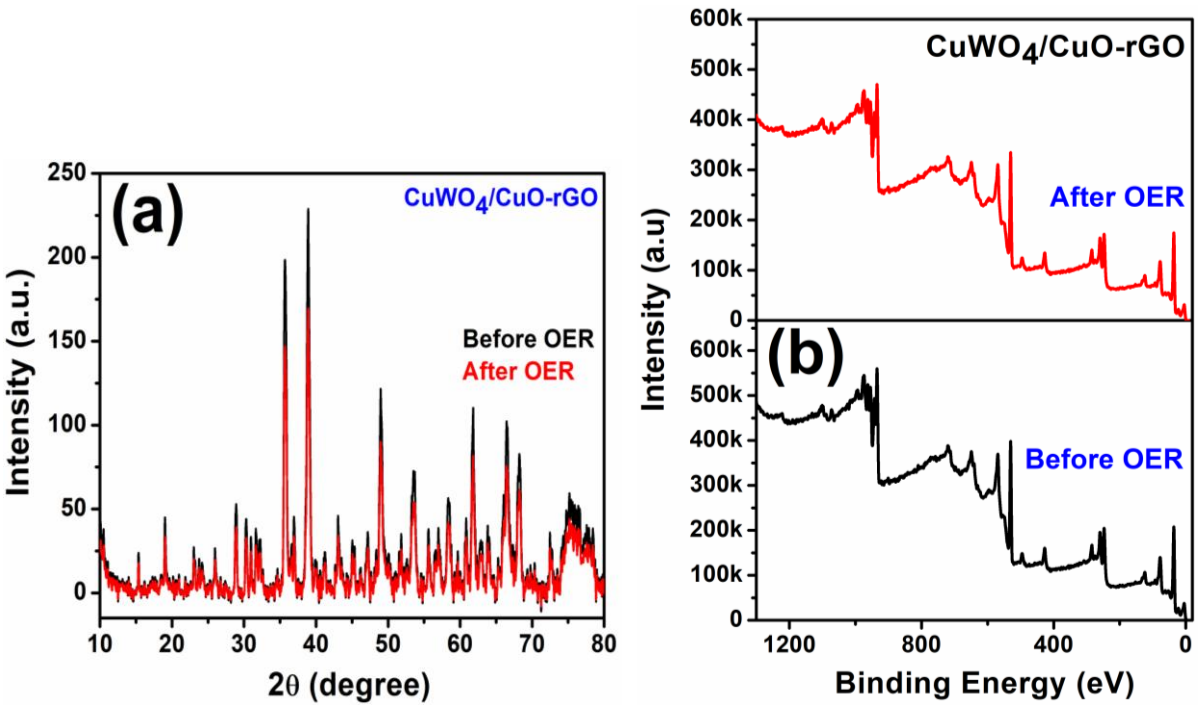

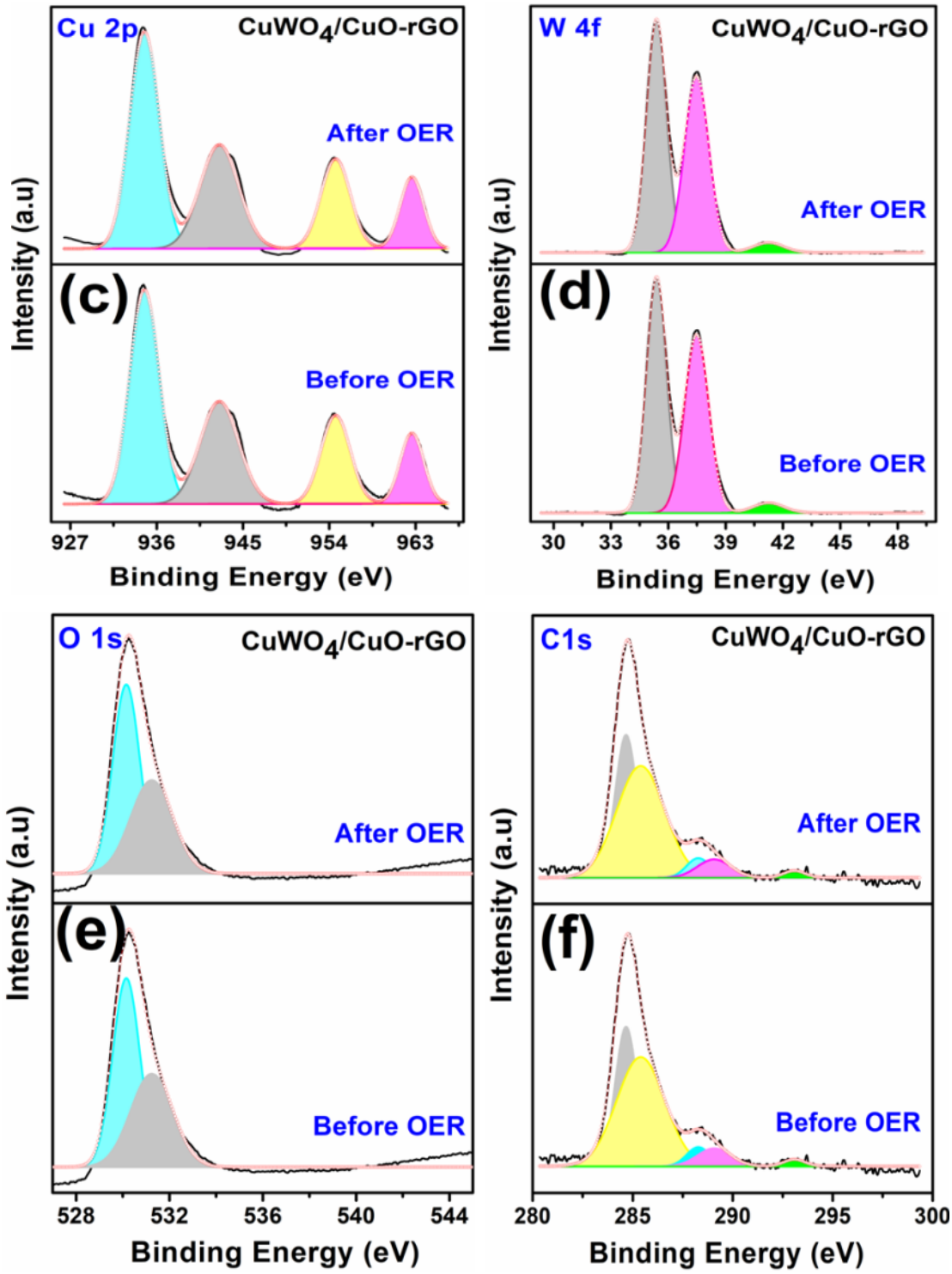

Figure 5.22. Post-catalytic characterizations of of $CuWO_4$/CuO-rGO (a) XRD; and XPS spectra of (b) Sample survey (c) Cu 2p (d) W 4f (e) O 1s (f) C 1s after OER stability test.

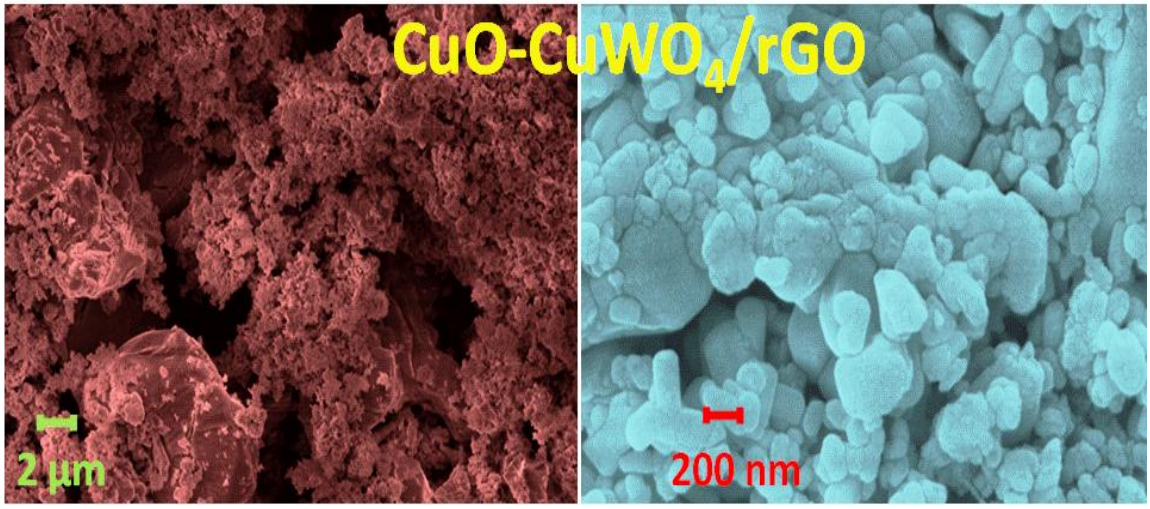

Figure 5.23. FE-SEM images of $CuWO_4$/CuO-rGO after OER stability test.

Table 5.10. Comparison of $CuWO_4$/CuO-rGO with previously reported modified catalysts for OER.

Materials	Current Density (mA cm^{-2})	Overpotential (mV)	Tafel slope (mV dec^{-1})	Ref.
$CuWO_4$/CuO-rGO	10	161	60.82	**This work**
Pd-Cu@HPCN (HPNC: Hexagonal porous carbon nanotube)	10	188	37	90
5% Co-doped CuO	10	120	118	91
Cu_2O/RGO-2	10	215	58.2	76
Ni-Gr-CNTs-Ni_2P-CuP_2 (NGCNC)	20	140	41	78
NiCuP	10	292	49	87
$CuCoO_2$ nanoplates	10	390	70	92
Co(OH)F/$CuCo_2S_4$	10	230	92	93
Cu_2S/CF (CF: Cu foam)	10	290	101	94
Co-Cu_7S_4	10	270	130	95
Ru-doped CuO/MoS_2 (MSCR)	10	201	229	75
Cu@CoS_x/CF (CF: Cu foam)	10	160	61	96
CuO/CF (CF: Cu foam)	10	290	64	97
Cu_2O/C	10	330	63	98
Cu_3P@NF (NF: Ni Foam)	10	320	54	99
CuO/FTO	10	430	61.4	100
Cu_3P NB/Cu	10	380	72	101

5.3.4. Overall Water Electrolysis. In the practical application of water electrolysis for H_2 production using a two-electrode configuration in a 1.0 M KOH solution, a water electrolyzer was implemented. The optimized amounts of electrocatalysts were loaded onto two GF of the same size. Before testing, the KOH solution was purged with N_2 for at least 30 min. Figure 5.24a represents the polarization plots for various assembled electrodes in overall water electrolysis, specifically comparing $CuWO_4$/CuO-rGO/GF (anode)||$CuWO_4$/CuO/GF (cathode), RuO_2/GF (anode)||Pt/C/GF (cathode), $CuWO_4$/CuO-rGO/GF (anode)||$CuWO_4$/CuO-rGO/GF (cathode), $CuWO_4$/CuO/GF (anode)||$CuWO_4$/CuO/GF (cathode), and GF (anode)||GF (cathode). Notably, the water-splitting performance of the bare GF (cathode)||GF (anode) configuration showed negligible contribution (Figure 5.24a). The data clearly indicates that the $CuWO_4$/CuO-rGO/GF (anode)||$CuWO_4$/CuO/GF (cathode) exhibited an excellent overall water splitting voltage of 1.31 V to achieve 10 mA cm^{-2} (Figures 5.24a and c), whereas RuO_2/GF (anode)||Pt/C/GF (cathode), $CuWO_4$/CuO-rGO/GF (anode)||$CuWO_4$/CuO-rGO/GF (cathode), $CuWO_4$/CuO/GF (anode)||$CuWO_4$/CuO/GF (cathode) require 1.47, 1.50 and 1.59 V, respectively. This performance is notably superior, with a lower voltage (180 mV) compared to RuO_2 (anode)||Pt/C (cathode) (240 mV), as depicted in Figure 5.24a and other advanced electrocatalysts mentioned in Table 5.11. Consequently, from the polarization plots, it is evident that the $CuWO_4$/CuO-rGO/GF (anode)||$CuWO_4$/CuO/GF (cathode) is the most efficient configuration for water electrolysis. However, when the configuration was reversed to $CuWO_4$/CuO/GF (anode)||$CuWO_4$/CuO-rGO/GF (cathode), it required a higher overall water-splitting voltage of 2.35 V to achieve 10 mA cm^{-2} (Figure 5.24d).

Table 5.11. Comparison of $CuWO_4$/CuO-rGO/GF (anode)||$CuWO_4$/CuO/GF (cathode) electrode with recently reported Cu-Based catalysts for two-electrode overall water splitting in 1.0 M KOH.

Materials	Catalyst Support	Current Density (mA cm^{-2})	Cell Voltage (V)	Ref.
$CuWO_4$/CuO-rGO (anode)||$CuWO_4$/CuO (cathode)	Graphite Felt	10	1.31	**This work**
Ru-doped CuO/MoS_2 (MSCR)	Ni Foam	10	1.68	75
Ni-Gr-CNTs-Ni_2P-CuP_2	Ni Foam	10	1.45	78
NiCuP	Ni Foam	10	1.60	87
$CuCo_2Se_4$	Ni Foam	10	1.782	102
$CuCo_2S_4$-WS_2	Ni Foam	10	1.54	103
Cu_3P NB/Cu	Cu Mesh	10	1.85	101

The Faradaic efficiency of all electrolyzers in operation was determined employing the water displacement method (Figure 5.25). The volume of accumulated H_2 was nearly twice that of the volume of accumulated O_2, affirming an approximate 100% Faradaic efficiency. The production of H_2 and O_2 in the two compartments was confirmed with gas chromatography analysis (Figure 5.26). In gas chromatography analysis, the signals at 1.12 min (Figure 5.26a) and 1.40 min (Figure 5.26b) confirm the identification of produced H_2 and O_2 gas. Significantly, this electrolyzer demonstrated remarkable long-term stability, showing no noticeable decay over 10 h of amperometric i-t response under an applied potential of 1.31 V (Figure 5.24b). Moreover, after the 10 h stability test, the polarization curve indicated a negative shift of about 10 mV for η_{10} compared to the initial measurement (Figure 5.24e), signifying the exceptional durability of our fabricated device. The overall findings emphasize the promise of $CuWO_4$/CuO-rGO/GF (anode)||$CuWO_4$/CuO/GF (cathode) as a prospective electrocatalyst, showing enhanced efficiency and durability for the process of overall water splitting.

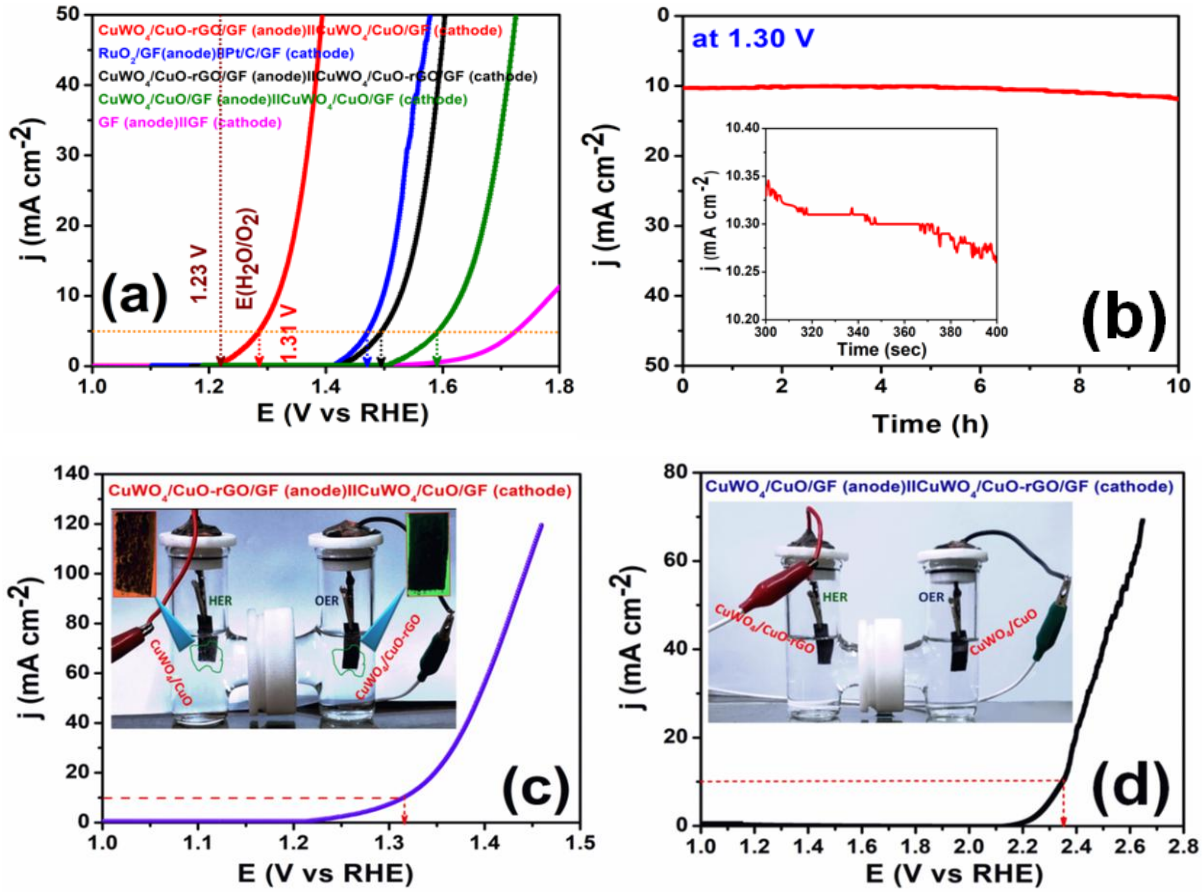

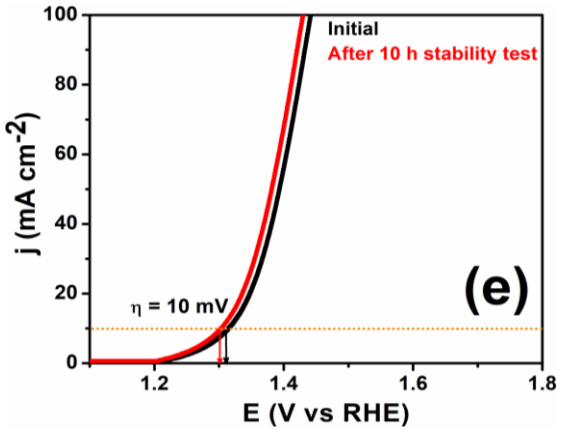

Figure 5.24. (a) LSV plots for alkaline electrolyzers employed in water electrolysis. (b) Chronoamperometric stability test of the CuO/$CuWO_4$-rGO electrolyzer at 1.30 V for 10 h (c) Polarization curve along with digital image of overall water electrolysis with CuO/$CuWO_4$ as the cathode and CuO/$CuWO_4$-rGO as the anode (d) Reverse set-up of digital image of overall water electrolysis with related polarization curve (e) LSV curves of CuO/$CuWO_4$-rGO before and after the stability test.

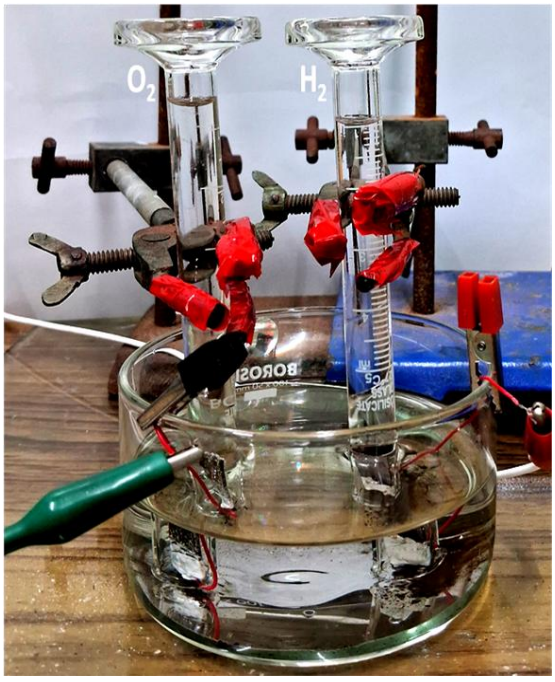

Figure 5.25. Measurement of H_2 and O_2 volumes by water displacement method in lab made electrolyzer.

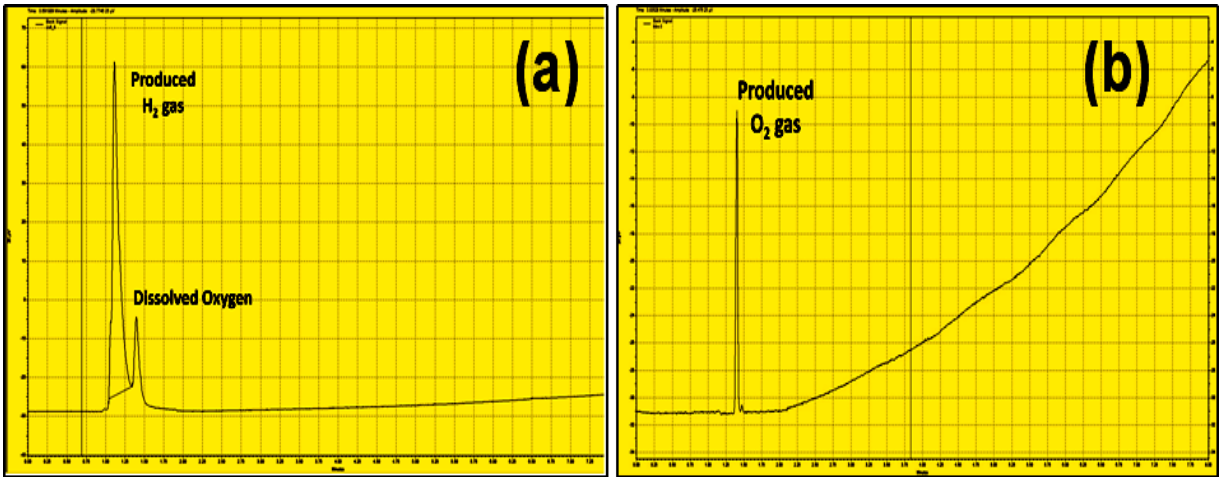

Figure 5.26. Gas chromatography data after overall water splitting.

5.3.4.1. Band Structure for Overall Water Splitting. Our method effectively creates p-n and p-n-n heterojunctions, significantly enhancing electrocatalytic performance. The Mott-Schottky plot (Figure 5.27) reveals that $CuWO_4$ and CuO act as n-type and p-type semiconductors, respectively, with flat-band potentials (E_{fb}) of -0.147 V and 1.61 V. These potentials align with the conduction band (E_{CB}) of $CuWO_4$ and the valence band (E_{VB}) of CuO. Based on UV-Vis spectroscopy data (Figure 5.9), the determined E_{VB} and E_{CB} values for $CuWO_4$ and CuO are 2.483 V and -0.9 V, respectively (Table 5.12). These results enable us to present schematic band diagrams for $CuWO_4$/CuO and $CuWO_4$/CuO-rGO nanocomposites (Figure 5.28), illustrating the formation of space-charge regions and changes in charge distribution.

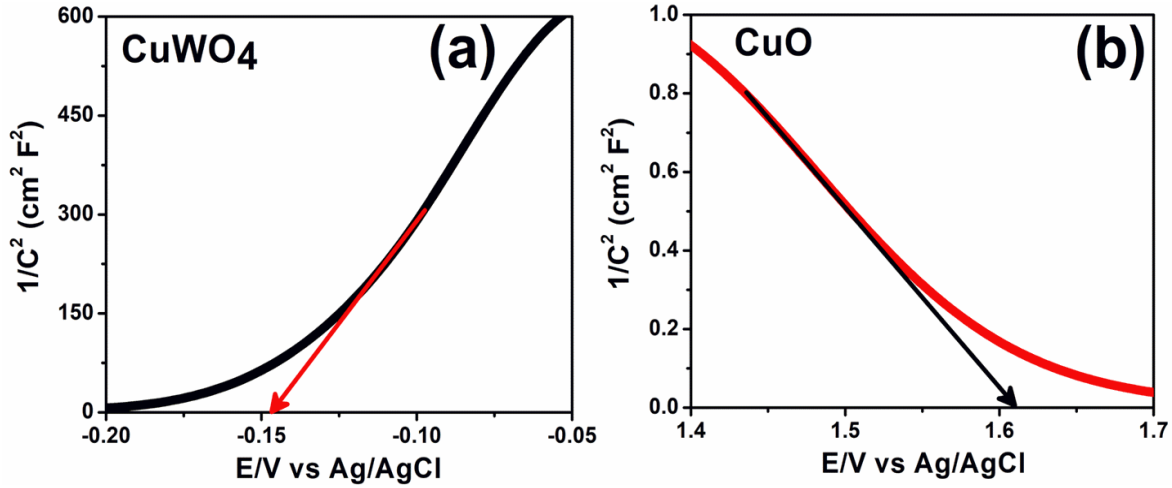

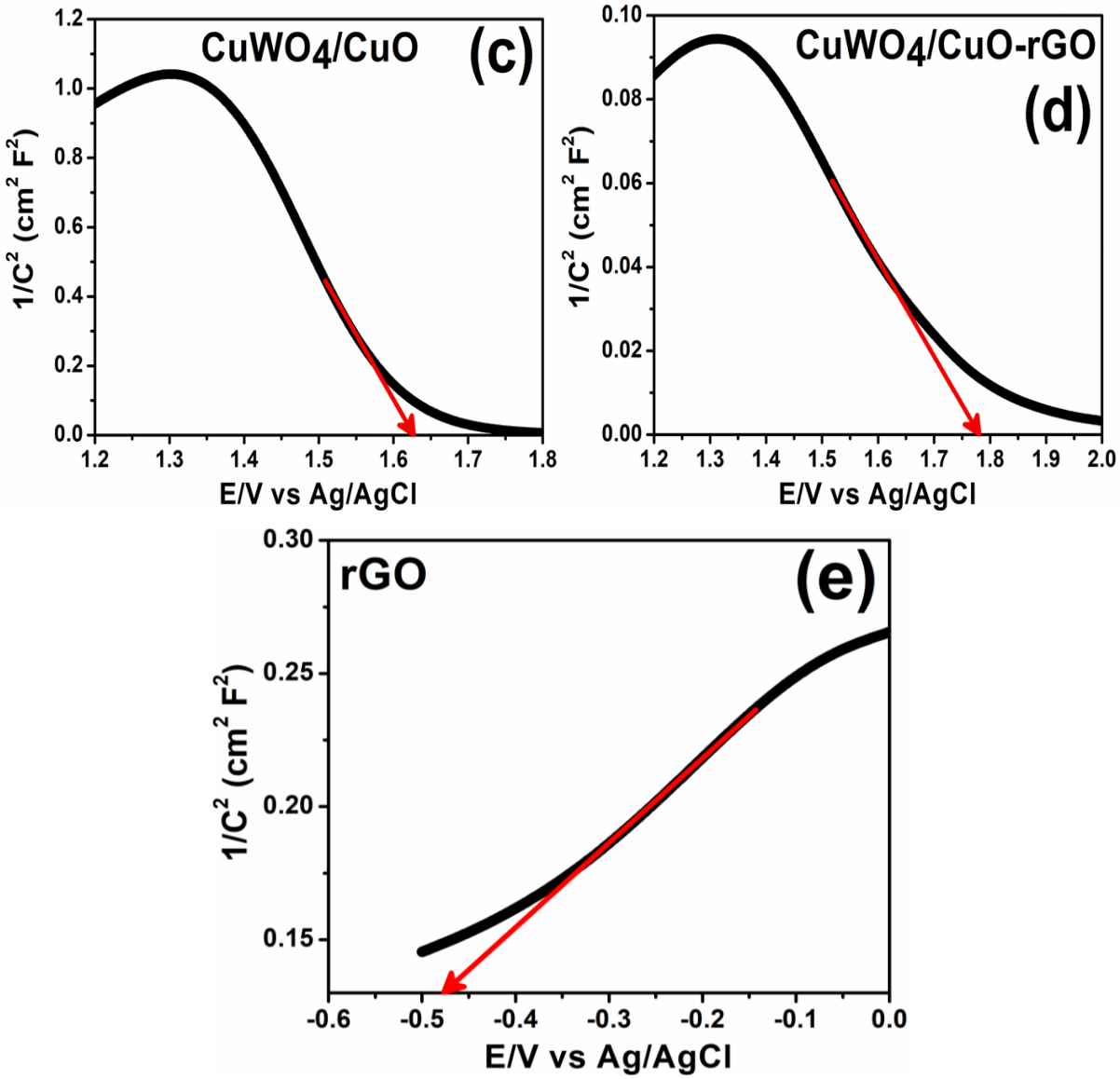

Figure 5.27. Mott-Schottky plots of (a) $CuWO_4$, (b) CuO, (c) $CuWO_4$/CuO, (d) $CuWO_4$/CuO -rGO and (e) rGO.

Initially, p-type CuO carries positive charge, and n-type $CuWO_4$ and n-type rGO carry negative charges. After alignment, E_{fb} values were estimated to be 1.63 V and 1.78 V for $CuWO_4$/CuO and $CuWO_4$/CuO-rGO nanocomposites, respectively (Figure 5.28). In this scenario, local regions of CuO and $CuWO_4$ within the $CuWO_4$/CuO heterojunction accumulate positive and negative charges,

forming a space-charge region and subsequently creating an electric field from CuO to $CuWO_4$. This interaction generates several active sites in the contact region, enhancing the HER activity by consuming a significant number of electrons from the biased zone. Furthermore, the incorporation of porous rGO in $CuWO_4$/CuO nanocomposite alters the band structure of the p-n heterojunction into a p-n-n heterojunction. This modification hinders electron transport, as evidenced by the increased charge transfer resistance (R_{ct}) value observed for HER (Figure 5.16c). The overall results (Figure 5.24c) indicate that the enhanced OER activity of $CuWO_4$/CuO-rGO and HER activity of $CuWO_4$/CuO align well with the design of the effective electrodes and cell structure. Specifically, a configuration using $CuWO_4$/CuO-rGO/GF as the anode and $CuWO_4$/CuO/GF as the cathode proves to be promising for overall water electrolysis. This setup optimizes the electrocatalytic properties of the materials, harnessing their respective strengths in OER and HER to achieve efficient water electrolysis.

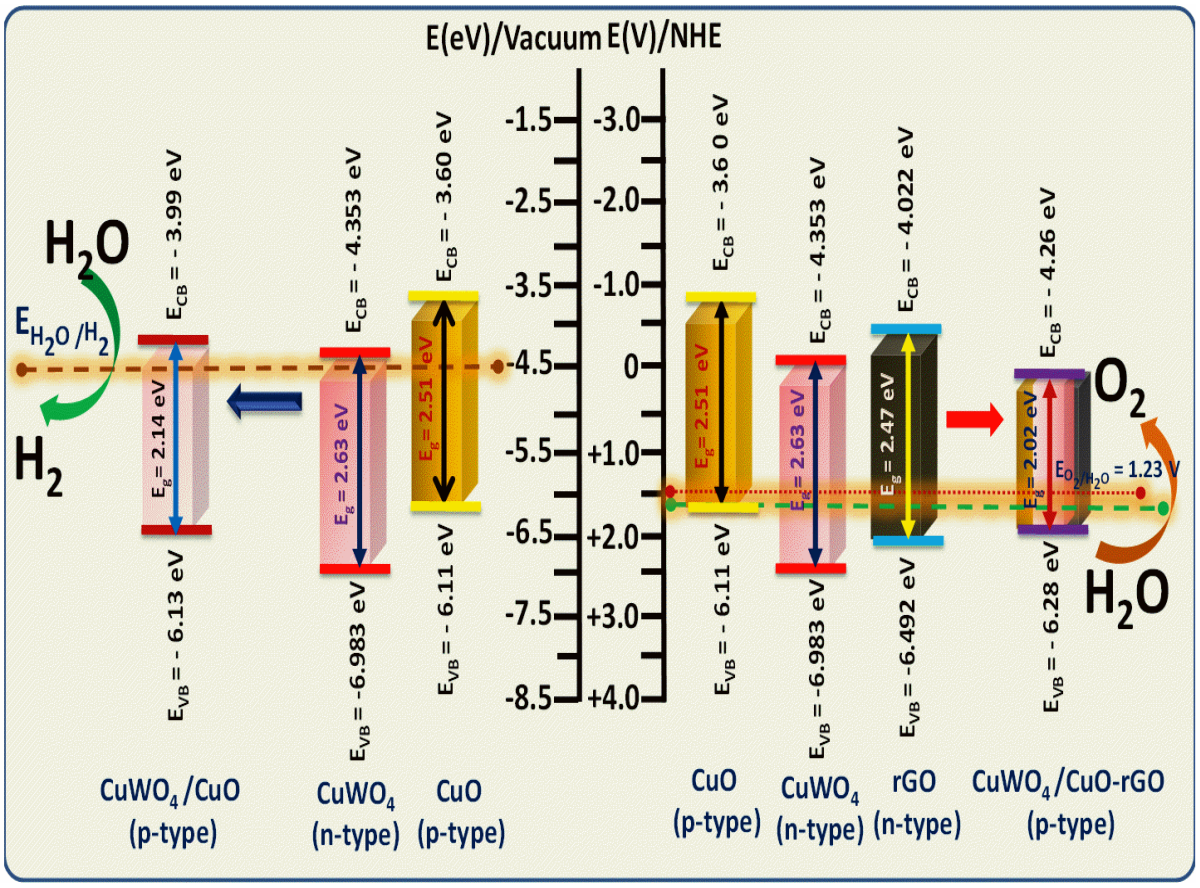

Figure 5.28. Band Structure for Overall Water Splitting.

Table 5.12. Flat band potentials of $CuWO_4$, CuO, $CuWO_4$/CuO, $CuWO_4$/CuO-rGO, and rGO.

Materials	E_{fb} (V) vs. RHE	E_{fb} (eV) vs. RHE	Band gap (eV)	E_{vb}/HOMO (eV)	E_{cb}/LUMO (eV)
$CuWO_4$	-0.147	-4.353	2.63	-6.983	-4.353
CuO	1.61	-6.11	2.51	-6.11	-3.60
$CuWO_4$/CuO	1.63	-6.13	2.14	-6.13	-3.99
$CuWO_4$/CuO-rGO	1.78	-6.28	2.02	-6.28	-4.26
rGO	-0.478	-4.022	2.47	-6.492	-4.022

CONCLUSIONS

In conclusion, this article emphasizes the significance of asymmetrically decorating electrodes, specifically $CuWO_4$/CuO for the cathode and rGO blended $CuWO_4$/CuO for the anode, in alkaline medium for achieving efficient water electrolysis via reduction and oxidation processes occurring simultaneously at low overpotentials. The use of GF as the catalyst support enhances the availability of active sites and improves electrolyte diffusion. The distinct morphologies of the electrodes play a pivotal role in optimizing the reaction kinetics of HER and OER, as revealed through various electrochemical analyses. The findings underscore the potential of tailored electrode structures for optimizing electronic properties and advancing the effectiveness of water-splitting technologies. Remarkably, the asymmetric assembly of $CuWO_4$/CuO and $CuWO_4$/CuO-rGO achieves a current density of 10 mA cm^{-2} at a low cell voltage of 1.31 V while also displaying excellent durability, making it the most promising among reported two-electrode water electrolyzers to date. Our study suggests the potential of employing transition metal-based catalysts for practical water electrolysis applications.

REFERENCES

(1) Wang, Y.; Leung, D. Y. C.; Xuan, J.; Wang, H. A Review on unitized regenerative fuel cell technologies, part B: unitized regenerative alkaline fuel cell, solid oxide fuel cell, and microfluidic fuel cell. *Renew. Sustain. Energy Rev*. **2017**, *75*, 775-795.

(2) Zhao, L.; Wang, Q.; Zhang, X.; Deng, C.; Li, Z.; Lei, Y.; Zhu, M. Combined electron and structure manipulation on Fe-containing N-doped carbon nanotubes to boost bifunctional oxygen electrocatalysis. *ACS Appl. Mater. Interfaces* **2018**, *10*, 35888-35895.

(3) Mondal, P.; Satra, J.; Srivastava, D.N.; Bhadu, G.R. and Adhikary, B. $Pd^{\delta+}$-mediated surface engineering of $AgMnO_4$ nanorods as advanced bifunctional electrocatalysts for highly efficient water electrolysis. *ACS Catal*. **2021**, *11*, 3687-3703.

(4) Yu, L.; Zhu, Q.; Song, S.; McElhenny, B.; Wang, D.; Wu, C.; Qin, Z.; Bao, J.; Yu, Y.; Chen, S.; Ren, Z. Non-noble metal-nitride based electrocatalysts for high-performance alkaline seawater electrolysis. *Nat. Commun*. **2019**, *10*, 5106 (1-10).

(5) Pu, Z.; Zhang, C.; Amiinu, I.S.; Li, W.; Wu, L. and Mu, S. General strategy for the synthesis of transition-metal phosphide/N-doped carbon frameworks for hydrogen and oxygen evolution. *ACS Appl. Mater. Interfaces* **2017**, *9*, 16187-16193.

(6) Pandey, A.; Mukherjee, A.; Chakrabarty, S.; Chanda, D.; Basu, S. Interface engineering of an RGO/MoS_2/Pd 2D heterostructure for electrocatalytic overall water splitting in alkaline medium. *ACS Appl. Mater. Interfaces* **2019**, *11*, 42094-42103.

(7) Anantharaj, S.; Ede, S. R.; Sakthikumar, K.; Karthick, K.; Mishra, S.; Kundu, S. Recent trends and perspectives in electrochemical water splitting with an emphasis on sulfide, selenide, and phosphide catalysts of Fe, Co, and Ni: a review. *ACS Catal.* **2016**, *6*, 8069-8097.

(8) Wang, A. L.; Xu, H.; Li, G. R. NiCoFe layered triple hydroxides with porous structures as high-performance electrocatalysts for overall water splitting. *ACS Energy Lett*. **2016**, *1*, 445-453.

(9) Yu, J.; He, Q.; Yang, G.; Zhou, W.; Shao, Z.; Ni, M. Recent advances and prospective in ruthenium-based materials for electrochemical water splitting. *ACS Catal*. **2019**, *9*, 9973-10011.

(10) Suen, N.T.; Hung, S.F.; Quan, Q.; Zhang, N.; Xu, Y.J.; Chen, H. M. Electrocatalysis for the oxygen evolution reaction: recent development and future perspectives. *Chem. Soc. Rev*. **2017**, *46*, 337-365.

(11) Suen, N. T.; Hung, S. F.; Quan, Q.; Zhang, N.; Xu, Y. J.; Chen, H. M. Electrocatalysis for the oxygen evolution reaction: recent development and future perspectives. *Chem. Soc. Rev*. **2017**, *46*, 337-365.

(12) Liu, K.; Zhang, C.; Sun, Y.; Zhang, G.; Shen, X.; Zou, F.; Zhang, H.; Wu, Z.; Wegener, E. C.; Taubert, C. J.; Miller, J. T.; Peng, Z.; Zhu, Y. High-performance transition metal phosphide alloy catalyst for oxygen evolution reaction. *ACS Nano* **2018**, *12*, 158-167.

(13) Fang, Z.; Peng, L.; Lv, H.; Zhu, Y.; Yan, C.; Wang, S.; Kalyani, P.; Wu, X.; Yu, G. Metallic transition metal selenide holey nanosheets for efficient oxygen evolution electrocatalysis. *ACS Nano* **2017**, *11*, 9550-9557.

(14) Maruthapandian, V.; Mathankumar, M.; Saraswathy, V.; Subramanian, B.; Muralidharan, S. A study of oxygen evolution reaction catalytic behavior of $Co_xNi_{1-x}Fe_2O_4$ in alkaline medium. *ACS Appl. Mater. Interfaces* **2017**, *9*, 13132-13141.

(15) Schofberger, W.; Faschinger, F.; Chattopadhyay, S.; Bhakta, S.; Mondal, B.; Elemans, J. A. A. W.; Millegger, S.; Tebi, S.; Koch, R.; Klappenberger, F.; Paszkiewicz, M.; Barth, J. V.; Rauls, E.; Aldahhak, H.; Schmidt, W. G.; Dey, A. A bifunctional electrocatalyst for oxygen evolution and oxygen reduction reactions in water. *Angew. Chem. Int. Ed.* **2016**, *55*, 2350-2355.

(16) Sumboja, A.; An, T.; Goh, H. Y.; Lübke, M.; Howard, D. P.; Xu, Y.; Handoko, A. D.; Zong, Y.; Liu, Z. One-step facile synthesis of cobalt phosphides for hydrogen evolution reaction catalysts in acidic and alkaline medium. *ACS Appl. Mater. Interfaces* **2018**, *10*, 15673-15680.

(17) Yu, J.; Guo, Y.; Miao, S.; Ni, M.; Zhou, W.; Shao, Z. Spherical ruthenium disulfide-sulfur-doped graphene composite as an efficient hydrogen evolution electrocatalyst. *ACS Appl. Mater. Interfaces* **2018**, *10*, 34098-34107.

(18) Shi, Y.; Zhang, B. Recent advances in transition metal phosphide nanomaterials: synthesis and applications in hydrogen evolution reaction. *Chem. Soc. Rev*. **2016**, *45*, 1529-1541.

(19) Ji, Z.; Liu, J.; Deng, Y.; Zhang, S.; Zhang, Z.; Du, P.; Zhao, Y.; Lu, X. Accurate synergy effect of Ni-Sn dual active sites enhances electrocatalytic oxidation of urea for hydrogen evolution in alkaline medium. *J. Mater. Chem. A* **2020**, *8*, 14680-14689.

(20) Liu, T.; Ma, X.; Liu, D.; Hao, S.; Du, G.; Ma, Y.; Asiri, A. M.; Sun, X.; Chen, L. Mn doping of CoP nanosheets array: an efficient electrocatalyst for hydrogen evolution reaction with enhanced activity at all pH values. *ACS Catal*. **2017**, *7*, 98-102.

(21) Chattopadhyay, S.; Sarkar, A.; Chatterjee, S.; Dey, A. Functional adlayers on Au electrodes: some recent applications in hydrogen evolution and oxygen reduction. *J. Mater. Chem. A* **2018**, *6*, 1323-1339.

(22) Ahmed, M. E.; Dey, S.; Mondal, B.; Dey, A. H_2 Evolution catalyzed by FeFe-hydrogenase synthetic model covalently attached to graphite surface. *Chem. Commun.* **2017**, *53*, 8188-8191.

(23) Hu, C.; Liu, J.; Wang, J.; She, W.; Xiao, J.; Xi, J.; Bai, Z.-W.; Wang, S. Coordination-assisted polymerization of mesoporous cobalt sulfide/heteroatom (N, S)-doped double-layered carbon tubes as an efficient bifunctional oxygen electrocatalyst. *ACS Appl. Mater. Interfaces* **2018**, *10*, 33124-33134.

(24) Friebel, D.; Louie, M. W.; Bajdich, M.; Sanwald, K. E.; Cai, Y.; Wise, A. M.; Cheng, M. J.; Sokaras, D.; Weng, T. C.; Alonso-Mori, R.; Davis, R.C. Identification of highly active Fe sites in (Ni, Fe) OOH for electrocatalytic water splitting. *J. Am. Chem. Soc.* **2015**, *137*, 1305-1313.

(25) Lu, Q.; Yu, Y.; Ma, Q.; Chen, B.; Zhang, H. 2D Transition-Metal-Di-chalcogenide-Nanosheet-Bassed Composites for Photocatalytic and Electrocatalytic Hydrogen Evolution Reactions. *Adv. Mater*. **2016**, *28*, 1917-1933.

(26) Zhang, J.; Wang, T.; Pohl, D.; Rellinghaus, B.; Dong, R.; Liu, S.; Zhuang, X.; Feng, X. Interface engineering of MoS_2/Ni_3S_2 heterostructures for highly enhanced electrochemical overall water-splitting activity. *Angew. Chem. Int. Ed*. **2016**, *55*, 6702-6707.

(27) Zhou, W.; Wu, X. J.; Cao, X.; Huang, X.; Tan, C.; Tian, J.; Liu, H.; Wang, J.; Zhang, H. Ni_3S_2 nanorods/Ni foam composite electrode with low overpotential for electrocatalytic oxygen evolution. *Energy Environ. Sci*. **2013**, *6*, 2921-2924.

(28) Tian, J.; Liu, Q.; Asiri, A. M.; Sun, X. Self-supported nanoporous cobalt phosphide nanowire arrays: an efficient 3D hydrogen-evolving cathode over the wide range of pH 0-14. *J. Am. Chem. Soc*. **2014**, *136*, 7587-7590.

(29) Anjum, M. A. R.; Lee, M. H.; Lee, J. S. Boron and nitrogen Co-doped molybdenum carbide nanoparticles imbedded in BCN network as a bifunctional electrocatalyst for hydrogen and oxygen evolution reactions. *ACS Catal*. **2018**, *8*, 8296-8305.

(30) Cui, W.; Cheng, N.; Liu, Q.; Ge, C.; Asiri, A. M.; Sun, X. Mo_2C nanoparticles decorated graphitic carbon sheets: biopolymer-derived solid-state synthesis and application as an efficient electrocatalyst for hydrogen generation. *ACS Catal*. **2014**, *4*, 2658-2661.

(31) Maiti, K.; Balamurugan, J.; Peera, S. G.; Kim, N. H.; Lee, J. H. Highly active and durable core-shell fct-PdFe@Pd nanoparticles encapsulated NG as an efficient catalyst for oxygen reduction reaction. *ACS Appl. Mater. Interfaces* **2018**, *10*, 18734-18745.

(32) Liu, L.; Wei, Q.; Yu, X.; Zhang, Y. Metal organic frameworks-derived Co_3O_4/Au heterostructure as a catalyst for efficient oxygen reduction. *ACS Appl. Mater. Interfaces* **2018**, *10*, 34068-34076.

(33) Luo, Y.; Luo, X.; Wu, G.; Li, Z.; Wang, G.; Jiang, B.; Hu, Y.; Chao, T.; Ju, H.; Zhu, J.; Zhuang, Z.; Wu, Y.; Hong, X.; Li, Y. Mesoporous Pd@Ru core-shell nanorods for hydrogen evolution reaction in alkaline solution. *ACS Appl. Mater. Interfaces* **2018**, *10*, 34147-34152.

(34) Mefford, J. T.; Rong, X.; Abakumov, A. M.; Hardin, W. G.; Dai, S.; Kolpak, A. M.; Johnston, K. P.; Stevenson, K. J. Water electrolysis on $La_{1-x}Sr_xCoO_{3-\delta}$ perovskite electrocatalysts. *Nat. Commun.* **2016**, *7*, 11053.

(35) Forslund, R. P.; Hardin, W. G.; Rong, X.; Abakumov, A. M.; Filimonov, D.; Alexander, C. T.; Mefford, J. T.; Iyer, H.; Kolpak, A. M.; Johnston, K. P.; Stevenson, K. J. Exceptional electrocatalytic oxygen evolution via tunable charge transfer interactions in $La_{0.5}Sr_{1.5}Ni_{1-x}$ $Fe_xO_{4\pm\delta}$ ruddlesden-popper oxides. *Nat. Commun.* **2018**, *9*, 3150 (1-11).

(36) McGee, S.; Fest, A.; Chandler, C.; Nova, N.N.; Lei, Y.; Goff, J.; Sinnott, S.B.; Dabo, I.; Terrones, M. and Zarzar, L.D. Direct laser writing of multimetal bifunctional catalysts for overall water splitting. *ACS Appl. Energy Mater.* **2023**, *6*, 3756-3768.

(37) Grimaud, A.; Diaz-Morales, O.; Han, B.; Hong, W. T.; Lee, Y. L.; Giordano, L.; Stoerzinger, K. A.; Koper, M. T. M.; Shao-Horn, Y. Activating lattice oxygen redox reactions in metal oxides to catalyse oxygen evolution. *Nat. Chem.* **2017**, *9*, 457-465.

(38) Ahmed, J.; Ahamad, T.; Alhokbany, N.; Almaswari, B.M.; Ahmad, T.; Hussain, A.; Al-Farraj, E.S.S. and Alshehri, S.M. Molten salts derived copper tungstate nanoparticles as bifunctional electro-catalysts for electrolysis of water and supercapacitor applications. *ChemElectroChem*, **2018**, *5*, 3938-3945.

(39) Ahmed, J.; Alhokbany, N.; Ahamad, T. and Alshehri, S.M. Investigation of enhanced electro-catalytic HER/OER performances of copper tungsten oxide@reduced graphene oxide nanocomposites in alkaline and acidic media. *New J. Chem.* **2022**, *46*, 1267-1272.

(40) Xiong, X.; You, C.; Liu, Z.; Asiri, A. M.; Sun, X. Co-doped CuO nanoarray: an efficient oxygen evolution reaction electrocatalyst with enhanced activity. *ACS Sustain. Chem. Eng*. **2018**, *6*, 2883-2887.

(41) Niu, W.; Shi, J.; Ju, L.; Li, Z.; Orlovskaya, N.; Liu, Y.; Yang, Y. Understanding synergism of cobalt metal and copper oxide toward highly efficient electrocatalytic oxygen evolution. *ACS Catal*. **2018**, *8*, 12030-12040.

(42) Macedo Andrade, A.; Liu, Z.; Grewal, S.; Nelson, A. J.; Nasef, Z.; Diaz, G.; Lee, M. H. MOF-derived Co/Cu-embedded N-doped carbon for trifunctional ORR/OER/HER catalysis in alkaline media. *Dalton Trans*. **2021**, *50*, 5473-5482.

(43) Chang, B.; Hao, S.; Ye, Z.; Yang, Y. A Self-supported amorphous Ni-P alloy on a CuO nanowire array: an efficient 3D electrode catalyst for water splitting in alkaline media. *Chem. Commun*. **2018**, *54*, 2393-2396.

(44) Wang, Y.; Du, R.; Qian, J.; Hu, Y. Self-supported CoP-decorated hierarchical CuO nanowire flowers toward enhanced oxygen evolution reaction. *ChemElectroChem* **2021**, *8*, 2101-2107.

(45) Xu, H.; Liu, W.; Zhao, Y.; Wang, D.; Zhao, J. Ammonia induced synergistic construction of Co_3O_4@CuO microsheets: an efficient electrocatalyst for oxygen evolution reaction. *J. Colloid Interface Sci*. **2019**, *540*, 585-592.

(46) Li, Y.; Li, G.; Xu, J.; Jia, L. Novel CuO-Cu_2O redox-induced self-assembly of hierarchical NiOOH@CuO-Cu_2O/$Co(OH)_2$ nanocomposite for efficient oxygen evolution reaction. *Sustain. Energ. Fuels* **2020**, *4*, 869-877.

(47) Wang, Z.; Du, H.; Liu, Z.; Wang, H.; Asiri, A. M.; Sun, X. Interface engineering of a CeO_2-Cu_3P nanoarray for efficient alkaline hydrogen evolution. *Nanoscale* **2018**, *10*, 2213-2217.

(48) Zhou, Q.; Li, T. T.; Qian, J.; Hu, Y.; Guo, F.; Zheng, Y. Q. Self supported hierarchical CuOx@Co_3O_4 heterostructures as efficient bifunctional electrocatalysts for water splitting. *J. Mater. Chem. A* **2018**, *6*, 14431-14439.

(49) Ghosh, D. and Pradhan, D. Effect of cooperative redox property and oxygen vacancies on bifunctional OER and HER activities of solvothermally synthesized CeO_2/CuO composites. *Langmuir* **2023**, *39*, 3358-3370.

(50) Mussa, Y.; Ahmed, F.; Arsalan, M. and Alsharaeh, E. Two dimensional (2D) reduced graphene oxide (RGO)/hexagonal boron nitride (h-BN) based nanocomposites as anodes for high temperature rechargeable lithium-ion batteries. *Sci. Rep.* **2020**, *10*, 1882 (1-13).

(51) Wakamatsu, S.; Islam, M.S.; Shudo, Y.; Fukuda, M.; Tagawa, R.; Goto, N.; Koinuma, M.; Sekine, Y. and Hayami, S. An efficient oxygen evolution reaction catalyst using Ni-Co layered double hydroxide anchored on reduced graphene oxide. *Energy adv.* **2023**, *2*, 1375-1380.

(52) Thakur, N.; Chaturvedi, A.; Mandal, D. and Nagaiah, T.C. Ultrasensitive and highly selective detection of dopamine by a NiFeP based flexible electrochemical sensor. *Chem. Commun.* **2020**, *56*, 8448-8451.

(53) Liu, Z. Q.; Cheng, H.; Li, N.; Ma, T. Y. and Su, Y. Z. $ZnCo_2O_4$ Quantum dots anchored on nitrogen-doped carbon nanotubes as reversible oxygen reduction/evolution electrocatalysts. *Adv. Mater*. **2016**, *28*, 3777-3784.

(54) Mondal, P.; Satra, J.; Srivastava, D.N.; Bhadu, G.R. and Adhikary, B. $Pd^{\delta+}$-mediated surface engineering of $AgMnO_4$ nanorods as advanced bifunctional electrocatalysts for highly efficient water electrolysis. *ACS Catal*. **2021**, *11*, 3687-3703.

(55) Das, D.; Santra, S. and Nanda, K. K. In situ fabrication of a nickel/molybdenum carbide-anchored N-doped graphene/CNT hybrid: an efficient (Pre) catalyst for OER and HER. *ACS Appl. Mater. Interfaces* **2018**, *10*, 35025-35038.

(56) Balasubramanian, V.; Kannan, S.; Nishanthi, S.T.; Sivakumar, G. and Mohanraj, K. Elucidate the pseudocapacitive behaviour of $CuWO_4$ electrode synthesized by solid-state reaction. *J. Mater. Sci.: Mater. Electron.* **2020**, *31*, 10142-10150.

(57) Ethiraj, A.S. and Kang, D.J. Synthesis and characterization of CuO nanowires by a simple wet chemical method. *Nanoscale Res. Lett.* **2012**, *7*, 1-5.

(58) Pal, S.; Sarkar, A.; Satra, J.; Mondal, P.; Ray, P.; Srivastava, D.N.; Adhikary, B. and Show, B. Tetraphenylporphyrin decorated Bi_2MoO_6 nanocomposite: its twin affinity of oxygen reduction reaction and electrochemical detection of 4-nitrophenol. *Inorg. Chem.* **2022**, *61*, 17402-17418.

(59) Sarkar, S.K.; Raul, K.K.; Pradhan, S.S.; Basu, S. and Nayak, A. Magnetic properties of graphite oxide and reduced graphene oxide. *Physica E Low Dimens. Syst. Nanostruct.* **2014**, *64*, 78-82.

(60) Deng, F.; Pei, X.; Luo, Y.; Luo, X.; Dionysiou, D.D.; Wu, S. and Luo, S. Fabrication of hierarchically porous reduced graphene oxide/$SnIn_4S_8$ composites by a low-temperature co-precipitation strategy and their excellent visible-light photocatalytic mineralization performance. *Catalysts*, **2016**, *6*, 113 (1-18).

(61) Loka, C.; Gelija, D.; Vattikuti, S.P. and Lee, K.S. Silver-boosted $WO_3/CuWO_4$ heterojunction thin films for enhanced photoelectrochemical water splitting efficiency. *ACS Sustain. Chem. Eng.* **2023**, *11*, 11978-11990.

(62) Nallal, M.; Park, K.H.; Park, S.; Kim, J.; Shenoy, S.; Chuaicham, C.; Sasaki, K. and Sekar, K. Cu_2O/reduced graphene oxide nanocomposites for electrocatalytic overall water splitting. *ACS Appl. Nano Mater.* **2022**, *5*, 17271-17280.

(63) Chen, G.; Guan, H.; Dong, C.; Xiao, X. and Wang, Y. Effect of calcination temperatures on the electrochemical performances of nickel oxide/reduction graphene oxide (NiO/RGO) composites synthesized by hydrothermal method. *J. Phys. Chem. Solids* **2016,** *98*, 209-219.

(64) Ortega-Amaya, R.; Matsumoto, Y.; Perez-Guzman, M.A. and Ortega-Lopez, M. In situ synthesis of Cu_2O and Cu nanoparticles during the thermal reduction of copper foil-supported graphene oxide. *J. Nanoparticle Res.* **2015**, *17*, 1-8.

(65) Raba-Paez, A.M.; Malafatti, J.O.D.; Parra-Vargas, C.A.; Paris, E.C. and Rincon-Joya, M.; Structural evolution, optical properties, and photocatalytic performance of copper and tungsten heterostructure materials. *Mater. Today Commun.* **2021**, *26*, 101886 (1-11).

(66) El-Nahass, M.M.; Soliman, H.S. and El-Denglawey, A. Absorption edge shift, optical conductivity, and energy loss function of nano thermal-evaporated N-type anatase TiO_2 films. *Appl. Phys. A* **2016**, *122*, 1-10.

(67) Shinde, S.K.; Dubal, D.P.; Ghodake, G.S.; Gomez-Romero, P.; Kim, S. and Fulari, V.J. Influence of Mn incorporation on the supercapacitive properties of hybrid $CuO/Cu(OH)_2$ electrodes. *RSC Adv.* **2015**, *5*, 30478-30484.

(68) Polyakov, B.; Kuzmin, A.; Vlassov, S.; Butanovs, E.; Zideluns, J.; Butikova, J.; Kalendarev, R. and Zubkins, M. A comparative study of heterostructured $CuO/CuWO_4$ nanowires and thin films. *J. Cryst. Growth* **2017**, *480*, 78-84.

(69) Dong, L.; Chu, H.; Wang, X.; Li, Y.; Zhao, S. and Li, D. Enhanced broadband nonlinear optical response of TiO_2/CuO nanosheets via oxygen vacancy engineering. J. *Nanophotonics* **2021**, *10*, 1541-1551.

(70) Chen, J.; Qian, G.; Zhang, H.; Feng, S.; Mo, Y.; Luo, L. and Yin, S. PtCo@PtSn heterojunction with high stability/activity for pH-universal H_2 evolution. *Adv. Function. Mater.* **2022**, 32, 2107597 (1-10).

(71) Pal, S.; Mahamiya, V.; Ray, P.; Sarkar, A.; Sultana, F.; Adhikary, B.; Chakraborty, B. and Show, B. β-Bi_2O_3-Bi_2WO_6 Nanocomposite ornated with meso-tetraphenylporphyrin: interfacial electrochemistry and photoresponsive detection of nanomolar hexavalent Cr. *Inorg. Chem.* **2023**, *62*, 21201-21223.

(72) Yang, J.; Zhu, J.; Xu, J.; Zhang, C.; Liu, T. $MoSe_2$ nanosheet array with layered MoS_2 heterostructures for superior hydrogen evolution and lithium storage performance. *ACS Appl. Mater. Interfaces* **2017**, *9*, 44550-44559.

(73) Jiang, P.; Yang, Y.; Shi, R.; Xia, G.; Chen, J.; Su, J.; Chen, Q. Pt-like electrocatalytic behavior of Ru-MoO_2 nanocomposites for the hydrogen evolution reaction. *J. Mater. Chem. A* **2017**, *5*, 5475-5485.

(74) Tiwari, A.P.; Bae, G.; Yoon, Y.; Kim, K.; Kim, J.; Lee, Y.L.; An, K.S. and Jeon, S. Chemical strain engineering of copper atoms on continuous three-dimensional-nanopatterned nickel nitride to accelerate alkaline hydrogen evolution. *ACS Sustain. Chem. Eng.* **2023**, *11*, 5229-5237.

(75) Maiti, A. and Srivastava, S.K. Ru-doped CuO/MoS_2 nanostructures as bifunctional water-splitting electrocatalysts in alkaline media. *ACS Appl. Nano Mater.* **2021**, *4*, 7675-7685.

(76) Nallal, M.; Park, K.H.; Park, S.; Kim, J.; Shenoy, S.; Chuaicham, C.; Sasaki, K. and Sekar, K. Cu_2O/reduced graphene oxide nanocomposites for electrocatalytic overall water splitting. *ACS Appl. Nano Mater*. **2022**, *5*, 17271-17280.

(77) Zhang, X.; Wang, J.; Wang, J.; Wang, J.; Wang, C. and Lu, C. Freestanding surface disordered NiCu solid solution as ultrastable high current density hydrogen evolution reaction electrode. *J. Phys. Chem. Lett.* **2021**, *12*, 11135-11142.

(78) Riyajuddin, S.; Azmi, K.; Pahuja, M.; Kumar, S.; Maruyama, T.; Bera, C. and Ghosh, K. Super-hydrophilic hierarchical Ni-foam-graphene-carbon nanotubes-Ni_2P-CuP_2 nano-architecture as efficient electrocatalyst for overall water splitting. *ACS Nano* **2021**, *15*, 5586-5599.

(79) Yu, L.; Zhang, J.; Dang, Y.; He, J.; Tobin, Z.; Kerns, P.; Dou, Y.; Jiang, Y.; He, Y. and Suib, S. L. In-situ growth of Ni_2P-Cu_3P bimetallic phosphide with bicontinuous structure on self-supported NiCuC substrate as an efficient hydrogen evolution reaction electrocatalyst. *ACS Catal*. **2019**, 9, 6919-6928.

(80) Wang, Z.; Xu, L.; Huang, F.; Qu, L.; Li, J.; Owusu, K. A.; Liu, Z.; in, Z.; Xiang, B.; Liu, X.; Yang, W.; Cheng, Y. and Mai, L. Copper-nickel nitride nanosheets as efficient bifunctional catalysts for hydrazine-assisted electrolytic hydrogen production. *Adv. Energy Mater*. **2019**, 9, 1900390 (1-11).

(81) Shinde, D.V.; Dang, Z.; Petralanda, U.; Palei, M.; Wang, M.; Prato, M.; Cavalli, A.; De Trizio, L. and Manna, L. In situ dynamic nanostructuring of the Cu-Ti catalyst-support system promotes hydrogen evolution under alkaline conditions. *ACS Appl. Mater. Interfaces* **2018**, *10*, 29583-29592.

(82) Yi, S.; Yongfang, Z.; Duo, W.; Xi, W.; Jia, L. and Jingyu, X. Nickel-copper alloy encapsulated in graphitic carbon shells as electrocatalysts for hydrogen evolution reaction. *Adv. Energy Mater*. **2018**, *8*, 1701759 (1-7).

(83) Jungang, H.; Yiqing, S.; Yunzhen, W.; Shuyan, C. and Licheng, S. Promoting active sites in core-shell nanowire array as Mott-Schottky electrocatalysts for efficient and stable overall water splitting. *Adv. Funct. Mater*. **2018**, *28*, 1704447 (1-12).

(84) Ma, X.; Chang, Y.; Zhang, Z. and Tang, J. Forest-like NiCoP@Cu_3P supported on copper foam as a bifunctional catalyst for efficient water splitting. *J. Mater. Chem. A* **2018**, *6*, 2100-2106.

(85) Asnavandi, M.; Suryanto, B. H. R.; Yang, W.; Bo, X. and Zhao, C. Dynamic hydrogen bubble templated NiCu phosphide electrodes for pH-insensitive hydrogen evolution reactions. *ACS Sustain. Chem. Eng.* **2018**, *6*, 2866-2871.

(86) Hou, J.; Sun, Y.; Li, Z.; Zhang, B.; Cao, S.; Wu, Y.; Gao, Z. and Sun, L. Electrical behavior and electron transfer modulation of nickel-copper nanoalloys confined in nickel-copper nitrides nanowires array encapsulated in nitrogen-doped carbon framework as robust bifunctional electrocatalyst for overall water splitting. *Adv. Funct. Mater.* **2018**, *28*, 1803278 (1-8).

(87) Wei, L.; Goh, K.; Birer, O.; Karahan, H. E.; Chang, J.; Zhai, S.; Chen, X. and Chen, Y. A Hierarchically porous nickel-copper phosphide nano-foam for efficient electrochemical splitting of water. *Nanoscale* **2017**, 9, 4401-4408.

(88) Zheng, J.; Chen, X.; Zhong, X.; Li, S.; Liu, T.; Zhuang, G.; Li, X.; Deng, S.; Mei, D. and Wang, J. G. Hierarchical porous NC@CuCo nitride nanosheet networks: highly efficient bifunctional electrocatalyst for overall water splitting and selective electrooxidation of benzyl alcohol. *Adv. Funct. Mater.* **2017**, *27*, 1704169 (1-11).

(89) Du, K.; Zhang, L.; Shan, J.; Guo, J.; Mao, J.; Yang, C.C.; Wang, C.H.; Hu, Z. and Ling, T. Interface engineering breaks both stability and activity limits of RuO_2 for sustainable water oxidation. *Nat. commun.* **2022**, *13*, 5448 (1-9).

(90) Fan, W.; Wang, A.; Wang, L.; Jiang, X.; Xue, Z.; Li, J. and Wang, G. Hollow carbon nanopillar arrays encapsulated with Pd-Cu alloy nanoparticles for the oxygen evolution reaction. *ACS Appl. Mater. Interfaces* **2023**, *15*, 13600-13608.

(91) Mishra, A. K. and Pradhan, D. Hierarchical urchin-like cobalt-doped CuO for enhanced electrocatalytic oxygen evolution reaction. *ACS Appl. Energy Mater.* **2021**, *4*, 9412-9419.

(92) Xiong, D.; Du, Z.; Xu, J.; Li, J.; Zhao, X. and Liu, L. Polyvinylpyrrolidone-assisted hydrothermal synthesis of $CuCoO_2$ nanoplates with enhanced oxygen evolution reaction performance. *ACS Sustain. Chem. Eng.* **2019**, *7*, 1493-1501.

(93) Sun, J.; Song, T.; Shao, Z.; Guo, N.; Huang, K.; He, F. and Wang, Q. Interfacial electronic structure modulation of hierarchical $Co(OH)F/CuCo_2S_4$ nanocatalyst for enhanced electrocatalysis and Zn-Air batteries performances. *ACS Appl. Mater. Interfaces* **2019**, *11*, 37531-37540.

(94) He, L.; Zhou, D.; Lin, Y.; Ge, R.; Hou, X.; Sun, X. and Zheng, C. Ultrarapid in situ synthesis of Cu_2S nanosheet arrays on copper foam with room-temperature-active iodine plasma for efficient and cost-effective oxygen evolution. *ACS Catal.* **2018**, *8*, 3859-3864.

(95) Li, Q.; Wang, X.; Tang, K.; Wang, M.; Wang, C. and Yan, C. Electronic modulation of electrocatalytically active center of Cu_7S_4 nanodisks by cobalt-doping for highly efficient oxygen evolution reaction. *ACS Nano* **2017**, *11*, 12230-12239.

(96) Liu, Y.; Li, Q.; Si, R.; Li, G.; Li, W.; Liu, D.; Wang, D.; Sun, L.; Zhang, Y. and Zou, X. Coupling sub-nanometric copper clusters with quasi-amorphous cobalt sulfide yields efficient and robust electrocatalysts for water splitting reaction. *Adv. Mater*. **2017**, *29*, 1606200 (1-8).

(97) Huan, T. N.; Rousse,G.; Zanna, S.; Lucas, I. T.; Xu, X.; Menguy, N.; Mougel, V. and Fontecave, M. A Dendritic nanostructured copper oxide electrocatalyst for the oxygen evolution reaction. *Angew. Chem. Int. Ed*. **2017**, *56*, 4792-4796.

(98) Zhang, H.; Zhang, Z.; Li, N.; Yan, W. and Zhu, Z. Cu_2O@C core/shell nanoparticle as an electrocatalyst for oxygen evolution reaction. *J. Catal*. **2017**, *352*, 239-245.

(99) Han, A.; Zhang, H.; Yuan, R.; Ji, H. and Du, P. Crystalline copper phosphide nanosheets as an efficient janus catalyst for overall water splitting. ACS *Appl. Mater. Interfaces* **2017**, *9*, 2240-2248.

(100) Liu, X.; Cui,S.; Sun, Z.; Ren, Y.; Zhang, X. and Du, P. Self-supported copper oxide electrocatalyst for water oxidation at low overpotential and confirmation of its robustness by Cu K-edge X-ray absorption spectroscopy. *J. Phys. Chem. C* **2016**, *120*, 831-840.

(101) Wei, S.; Qi, K.; Jin, Z.; Cao, J.; Zheng, W.; Chen, H. and Cui, X. One-step synthesis of a self-supported copper phosphide nanobush for overall water splitting. *ACS Omega* **2016**, *1*, 1367-1373.

(102) Cao, X.; Medvedeva, J. E. and Nath, M. Copper cobalt selenide as a high-efficiency bifunctional electrocatalyst for overall water splitting: combined experimental and theoretical study. *ACS Appl. Energy Mater*. **2020**, *3*, 3092-3103.

(103) Gautam, J.; Meshesha, M.M.; Chanda, D.; Gwon, J.S.; Lee, G.S.; Hong, D. and Yang, B.L. Rational design of a copper cobalt sulfide/tungsten disulfide heterostructure for excellent overall water splitting. *ACS Appl. Mater. Interfaces* **2023**, *15*, 40330-40342.

FUTURE GOAL

Our overarching future objective is to spearhead groundbreaking advancements in environmental remediation and energy conversion through the synthesis of highly efficient and effective nanomaterials. Our research will be centered on developing innovative surface engineering strategies to precisely tailor the properties of electrode materials. Leveraging advanced characterization techniques and computational modeling, we aim to design surfaces with enhanced catalytic activity, stability, and selectivity. This endeavor seeks to push the boundaries of electrocatalysis, revolutionizing the field and unlocking new opportunities for sustainable energy generation and storage.

Our goal is to pioneer a cost-effective and streamlined approach for producing advanced Cu- and Bi-based organic-inorganic nanocomposites and quaternary heterojunction structures. We aim to significantly enhance applications in electrocatalytic hydrogen evolution, metal-air batteries, fuel cells, and seawater splitting for green hydrogen production. In alignment with our commitment to sustainable development, we strive to develop surface-modified electrode materials that advance electrocatalytic applications. Furthermore, these innovative materials will be instrumental in the detoxification and demineralization of various organic and inorganic pollutants from natural sources, demonstrating the transformative impact of tailored surface modifications in advancing clean energy systems and promoting environmental sustainability.

Aligned with our vision for sustainable development, we are committed to addressing critical environmental challenges, such as the contamination of water bodies with pollutants like 4-nitrophenol. Our goal is to devise rapid and efficient processes for converting 4-nitrophenol into less harmful compounds, mitigating its impact on the environment. Furthermore, we are determined to combat the detrimental effects of heavy metal ions, including chromium (Cr), lead (Pb), mercury (Hg), and bismuth (Bi), on human health and the environment. By leveraging the catalytic capabilities of our nanomaterials, combined with organic components like reduced graphene oxide (rGO) and porphyrins, we endeavor to develop novel electrocatalysts capable of efficiently reducing these toxic metals through both electrochemical and photoelectrochemical approaches. Our synthesized material, $CuWO_4$/CuO-rGO, requires additional investigation to assess its efficiency in overall water splitting within an acidic environment. While we have generally explored its performance under alkaline conditions, further studies are necessary to comprehensively understand its behavior and efficiency in acidic media.

Our future endeavors will focus on overcoming key challenges in catalyst design and material synthesis, emphasizing the integration of organic matrices like polyaniline (PANI), polyindole, polypyrrole, etc. into our nanocomposites. Through interdisciplinary collaboration and a multidisciplinary approach, we aim to propel the field of nanotechnology towards the realization of sustainable solutions for environmental remediation and clean energy production.

With unwavering dedication and a steadfast commitment to innovation, we are poised to drive meaningful change and shape a more sustainable world for generations to come. Through interdisciplinary collaboration and surmounting pivotal obstacles in catalyst design and material synthesis, our ambition is to make substantial contributions to a cleaner, more sustainable future propelled by eco-friendly nanomaterials. Furthermore, our endeavors will focus on upscaling production methodologies and seamlessly integrating these nanocomposites into tangible devices and systems for practical deployment. Collaborations with industry partners and interdisciplinary research efforts may also be pursued to address emerging challenges and maximize the impact of these innovative materials. Ultimately, our goal is to advance towards the achievement of a cleaner and more sustainable future by harnessing the potential of advanced nanomaterial technology.

List of Publications

Publications related to the Thesis

(1) Pal, S.; Sarkar, A.; Satra, J.; Mondal, P.; Ray, P.; Srivastava, D.N.; Adhikary, B. and Show, B. Tetraphenylporphyrin decorated Bi_2MoO_6 nanocomposite: its twin affinity of oxygen reduction reaction and electrochemical detection of 4-nitrophenol. *Inorganic Chemistry*, **2022,** *61*, 17402-17418.

(2) Pal, S.; Mahamiya, V.; Ray, P.; Sarkar, A.; Sultana, F.; Adhikary, B.; Chakraborty, B. and Show, B. β-Bi_2O_3-Bi_2WO_6 nanocomposite ornated with meso-tetraphenylporphyrin: interfacial electrochemistry and photoresponsive detection of nanomolar hexavalent Cr. *Inorganic Chemistry*, **2023**, *62*, 21201-21223.

(3) Pal, S.; Sultana, F.; Ray, P.; Sarkar, A. and Show, B. Asymmetric harmonization of $CuWO_4$/CuO and Its rGO blended nanocomposite: tuning the electronic relay to optimize advanced water electrolysis in alkaline medium. Communicated on 12.08.2024 in *ACS Appl. Mater. Interfaces* (*under revision*).

Other Publications

(1) Ray, P.; Pal, S.; Sarkar, A.; Sultana, F.; Basu, A. and Show, B. Oyster pearl-shaped ternary iron chalcogenide, $FeSe_{0.5}Te_5$, films on FTO through electrochemical growth from the exchange of chalcogens boosted the enzyme-free urea-sensing ability toward real analytes. *ACS Appl. Bio Mater.* **2024**, 7, 3, 1621-1642.

(2) Show, B.; Ray, P.; Sarkar, A.; Pal, S.; Sultana, F.; Nandi A.; Bhaumik T.; Mukherjee N. and Mondal A. Influence of electrodeposited Cu_2ZnSnS_4 films for the reduction of 4-nitrophenol through electronic relay approach and serve as photoelectrode in PEC device. *Inorganica Chim. Acta* **2024**, 1222281 (1-13).

(3) Sarkar, L.; Das, S.; Sultana, F.; Pal, S.; Banerjee, A.; Show, B. and Nandi U. Fe^{3+}-doped nanocrystalline magnesium-cobaltite $MgCo_2O_4$ spinel synthesized by facile reflux method for high-performance supercapacitors. Communicated on 12.09.2024 in *ACS Appl. Energy Mater* (*under revision*).

National/International Symposium/Seminar/Conference

(1) Present in the "*National Seminar on Celebration of the International Year of the Periodic Table*" organised by Department of Chemistry, Jadavpur University, Kolkata, India on 13th and 14th August, 2019.

(2) Present in the "*National Seminar on Emerging Trends in Chemical Sciences*" organised by Department of Chemistry, Jadavpur University, Kolkata, India on 7th January, 2020.

(3) Present in the "*National Seminar on Recent Trends in Inorganic Chemistry*" organised by Department of Chemistry, Jadavpur University, Kolkata, India on 6th March, 2020.

(4) Present in the "*P. C Ray Memorial International Conference on Contemporary Ideas, Innovations & Initiatives in Chemical Sciences, CI3CS-2023*," held at Department of Chemistry, Presidency University, Kolkata, India on 23rd and 24th August, 2023.

(5) Present in the "*One-Day International Symposium on Recent Advanced in Chemistry and Chemistry-Biology Interface*" held at Department of Chemistry, Vivekananda Satavarshiki Mahavidyalaya, Manikpara, Jhargram, West Bengal, India on 5th January, 2024.